For information on all North-Holland publications
visit our website at https://www.elsevier.com/

Working together
to grow libraries in
developing countries

www.elsevier.com • www.bookaid.org

Contributors

Numbers in Parentheses indicate the pages on which the author's contributions begin.

G. Adachi (1), Faculty of Engineering, Osaka University, Suita, Osaka, Japan

C.D.S. Brites (339), CICECO—Aveiro Institute of Materials, University of Aveiro, Aveiro, Portugal

L.D. Carlos (339), CICECO—Aveiro Institute of Materials, University of Aveiro, Aveiro, Portugal

T. Hasegawa (1), Graduate School of Science and Technology, Niigata University, Niigata, Japan

M. Hoshino (129), Mineral Resource Research Group, National Institute of Advanced Industrial Science and Technology, Tsukuba, Japan

S.W. Kim (1), Graduate School of Science and Technology, Niigata University, Niigata, Japan

A. Millán (339), ICMA—Instituto de Ciencia de Materiales de Aragón, University of Zaragoza, Zaragoza, Spain

J.A. Mydosh (293), Kamerlingh Onnes Laboratory and Institute-Lorentz, Leiden University, Leiden, The Netherlands

L. Rademaker (293), Kavli Institute for Theoretical Physics, University of California Santa Barbara, CA, United States

K. Sanematsu (129), Mineral Resource Research Group, National Institute of Advanced Industrial Science and Technology, Tsukuba, Japan

M. Sato (1), Faculty of Engineering, Niigata University, Niigata, Japan

Y. Shimomura (1), Mitsubishi Chemical Corporation, Odawara, Kanagawa, Japan

K. Toda (1), Graduate School of Science and Technology, Niigata University, Niigata, Japan

Y. Watanabe (129), Akita University, Mining Museum of Akita University, Akita, Japan

Preface

These elements perplex us in our reaches [sic], baffle us in our speculations, and haunt us in our very dreams. They stretch like an unknown sea before us—mocking, mystifying, and murmuring strange revelations and possibilities.

Sir William Crookes (February 16, 1887)

Volume 49 of the *Handbook on the Physics and Chemistry of Rare Earths* adds four chapters to the series, covering subjects as diverse as phosphors for white light-emitting diodes, rare-earth mineralogy and resources, quantum critical matter and phase transitions in rare earths and actinides, and lanthanide luminescent thermometers.

The first chapter (Chapter 278) is devoted to luminescent materials for white light-emitting diodes. The subject is of importance with respect to energy-saving devices. Indeed, despite a sharp increase in the number of lighting devices worldwide, the share of electricity devoted to it is rather decreasing (about 12% presently). This is because of the prominent role played by rare earth phosphors in improving the efficiency of lighting devices, first in compact fluorescent lamps and presently in light-emitting diodes (LEDs). The electricity-to-light conversion efficiency has increased by a factor of 8–9 with respect to the traditional incandescent devices. In this chapter, the authors focus on LEDs based on blue indium gallium nitride chips coated with one or several lanthanide-containing phosphors. Both yellow-emitting trivalent cerium materials and polychromatic phosphors are discussed with respect to the choice of the matrix, of the active components, and of the synthetic methods yielding highly effective and both thermally and photo-stable materials.

Rare earth resources are the subject of Chapter 279. A growing number of critical technologies are vitally dependent on rare earth elements, making use of their unique chemical, magnetic, and spectroscopic properties. This has resulted in some of the rare earths, such as Nd, Eu, Tb, and Dy, deemed critical and prompted extensive efforts to find substitutes, which is hard and may not always be possible. Although not that rare in the earth crust, these elements are difficult to produce in the needed quantities because they always occur as intricate mixtures and because the compositions of these mixtures do not match the specific need for given elements. Geopolitical interferences add to the problem. The review provides insight into rare earth

resources according to their various sources and focuses particularly on the more critical heavy lanthanides (Gd–Lu).

With Chapter 280, the reader is transported into the select world of theoretical physics. While we are familiar with first-order phase transitions such as liquid to gas (e.g., water evaporation) or liquid to solid (e.g., water freezing) that are characterized by a discontinuous change in the material's properties and by the release or absorption of heat, second-order transitions such as ferromagnetic transitions are subtler because they are continuous, but they still feature discontinuity in the second derivative of the free energy. These transitions can be rationalized within the frame of well-established theories. When a second-order transition is thought to occur at zero temperature under the effect of pressure, magnetic field, or particle density, many unconventional properties develop around what is called a quantum critical point. The corresponding theories are challenging, and the authors discuss in detail the concept of quantum criticality in f-electron-based materials as well as successes and failures of existing theories such as the Hertz–Millis theory.

The final chapter (Chapter 281) deals with temperature measurements. Temperature is an important thermodynamic parameter which is central to many chemical and biochemical processes. In particular, the delicate equilibrium prevailing in living cell critically depends on temperature. Measuring temperature is also vital in totally different fields, such as microelectronics or materials testing, for instance. While macroscopic determination of this parameter seems to be rather simple, for instance with thermistors or thermocouples, moving to microscopic or nanoscopic scale is much more intricate. The size of the corresponding sensors must be reduced to molecular dimensions, and remote detection can no more rely on wire connections. Luminescence intensity is very often temperature dependent so that it offers a welcome possibility of designing noninvasive temperature micro- and nanosensors. The review concentrates on lanthanide sensors and describes how to optimize the thermal response of lanthanide-based luminescent thermometers, in particular the ratiometric single- and dual-center devices.

CHAPTER 278: RARE EARTH-DOPED PHOSPHORS FOR WHITE LIGHT-EMITTING DIODES
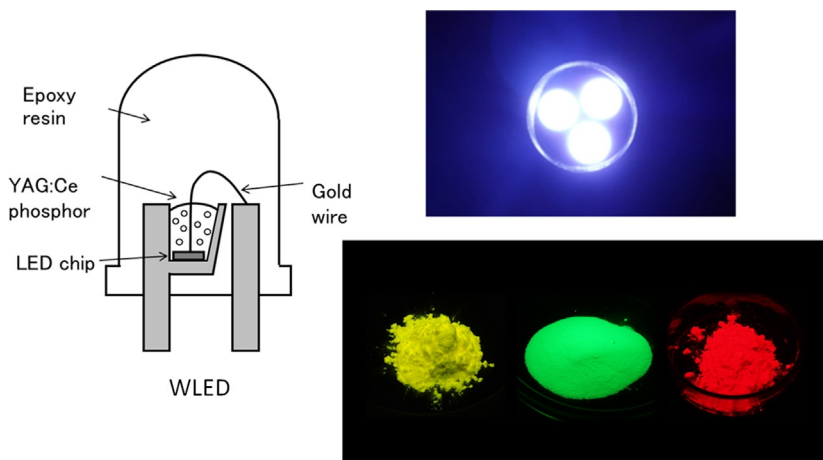
M. Sato*, S.W. Kim[†], Y. Shimomura[‡], T. Hasegawa[†], K. Toda[†], and G. Adachi[§]

*Faculty of Engineering, Niigata University, Niigata, Japan. E-mail: msato@eng.niigata-u.ac.jp

[†]Graduate School of Science and Technology, Niigata University, Niigata, Japan

[‡]Mitsubishi Chemical Corporation, Odawara, Kanagawa, Japan

[§]Faculty of Engineering, Osaka University, Suita, Osaka, Japan

In 1996, a new lighting device was proposed by Nichia Chemical Co., based on a blue InGaN LED chip coated with a yellow-emitting phosphor, cerium-doped yttrium aluminum garnet ($Y_{2.9}Ce_{0.1}Al_5O_{12}$, YAG:$Ce^{3+}$). The lighting device proved to have numerous advantages over traditional incandescent and fluorescent lamps, such as small size, long lifetime, robustness, fast switching, and high efficiency. Phosphor materials such YAG:Ce^{3+} play an unquestionable role for achieving high color-quality white emission in LED technology. However, conventional phosphors used in fluorescent lighting or displays are not good candidates for LED lighting because they are optimized for excitation at the wavelength of a mercury discharge tube at 254 nm, while InGaN chips emit in the blue. The aim of this review is to provide clues for the design of efficient lanthanide-based LED phosphors.

After a description of the principles of LED lighting and phosphor requirements, the structures and luminescence properties of LED phosphors are presented. The classification of phosphors is primarily based on the chemical composition such as oxide, nitride, and sulfide; on the emission color such as yellow, green, and red; and, finally, on the actual chemical formula. This is because it is convenient to understand the phosphor characteristics on the basis of the nature of chemical bonding, which controls the energy of electronic transitions, in the solid state. In practical applications for white light LED devices, powder technology is important so that the chapter describes synthesis methods of phosphor particles including morphology control. Implementation of phosphors in LED lighting devices is dealt with in the last section, as well as recent progresses in remote phosphors and wafer-level packaging.

CHAPTER 279: REE MINERALOGY AND RESOURCES

M. Hoshino*, K. Sanematsu*, and Y. Watanabe[†]

*Mineral Resource Research Group, National Institute of Advanced Industrial Science and Technology, Tsukuba, Japan. E-mail: hoshino-m@aist.go.jp

[†]Akita University, Mining Museum of Akita University, Akita, Japan

Deposit type

- ⬤ Carbonatite
- 🟩 Peralkaline-rock associated
- ⬛ Iron oxide apatite
- 🔺 Hydrothermal vein
- 🟪 Sediment-hosted hydrothermal
- ⭐ Ion adsorption
- ◆ Placer

Map labels:

Sarfartoq, Motzfeldt, Port Hope Simpson, Red Wine & Mann, Welsford, Niobec, Camaratuba, Pitinga, Serra Verde, Araxa, Chiriguelo, Rodeo de los Molles, Kvanefjeld & Tanbreez, Strange Lake, Elliot Lake, Montviel, Eldor, Kipawa, Pea Ridge, Elk Creek, Round Top Mountain, Hoidas Lake, Archie Lake, Athabasca, Bear Lodge, Bolero, Carbo, Diamond Creek, Nechalacho, Bokan, Mountain Pass

Tomtor, Bayan Obo, Longnan, Yen Phu, Hastings, Charley Creek, Nolans, Dubbo, Karasuginskoe, Khalzan Burged, Mushgia Khudag, Lugiin Gol, Khotgor, Maoniuping, Dong Pao, Mount Weld, John Galt, Cummins Range, Browns Range, Mynkuduk, Ulba, Kutessai II, Perak, Chavara, Manavalakurichi, Songwe, Mt Muambe, Tantalus, Machinga, Kangankunde, Belay-Analapatsy, Aksu Diamas, Kizilcaoren, Jabal Tawlah, Ghurayyah, Nile, Gakara, Mrima Hill, Wigu Hill, Ngualla, TRE, Steenkampskraal, Khibina, Korsnas, Lovozero, Olserun, Norra Karr, Bou Naga, Longonjo, Maliongue, Lofdal, Glenover, Xilluvo, Zandkopsdrift

Recent increase of the demand for rare earth elements (REEs), especially dysprosium and terbium used in the permanent magnet industry, is modifying the industrial approach to REE mineralogy and resources. This is amplified by the REE supply restrictions outside of China and by the fact that rare earths are never mined individually but always as mixtures with various compositions. These compositions however do not necessarily correspond to the demand for individual rare earths. Some elements are in surplus (La, Ce), while other ones are in tight supply (or more utilized) and are classified as "critical" (yttrium, neodymium, europium, terbium, dysprosium). Exploration has now been extended worldwide to secure the supply of REEs, especially the heavier ones (HREEs, Gd–Lu) that are globally three times less abundant than the lighter rare earths. In recent years, various attempts have been made to produce HREEs from unconventional sources, such as peralkaline igneous rocks, which have traditionally not been regarded as a REE source, or deep-sea muds (see Vol. 46, Chapter 268).

The chapter reviews the potential sources of REEs, with a focus on HREEs, which are regarded as the most critical group of elements for the future green technologies. It starts with a description of the geochemistry and mineralogy of rare earth elements before focusing on rare earth deposits. In this section, their classification into carbonatite, peralkaline rocks, iron oxide apatite, hydrothermal vein, ion-adsorption clays, and placer deposits is presented. More detailed properties of ion adsorption and apatite deposits are depicted in view of the importance of heavier rare earth elements. The authors conclude that in the future the most promising source of rare earths will be apatite ores.

CHAPTER 280: QUANTUM CRITICAL MATTER AND PHASE TRANSITIONS IN RARE EARTHS AND ACTINIDES

L. Rademaker* and J.A. Mydosh[†]

*Kavli Institute for Theoretical Physics, University of California Santa Barbara, CA, United States. E-mail: louk.rademaker@gmail.com

[†]Kamerlingh Onnes Laboratory and Institute-Lorentz, Leiden University, Leiden, The Netherlands. E-mail: mydosh@physics.leidenuniv.nl
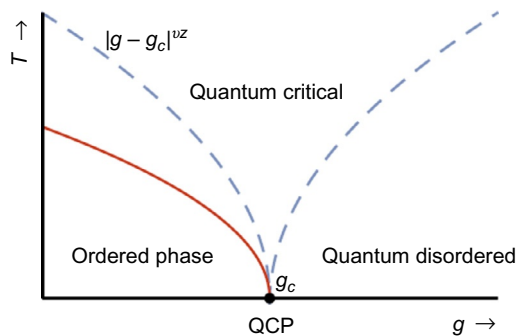
Many intermetallic compounds based on rare earth and actinide elements display unusual electronic and magnetic properties in that standard Fermi liquid theory is not applicable. However, theoretical developments have shown that these properties can be rationalized within the frame of the "quantum-phase transition" (QPT) concept. In this chapter the authors discuss quantum criticality, the notion that properties of a material are governed by the existence of a phase transition at zero temperature. The point where a second-order (continuous) phase transition takes place is known as a quantum critical point (QCP). Materials that exhibit quantum critical points can be tuned through their QPT by, for example, pressure, chemical doping or disorder, frustration, and magnetic field. The study of QPTs was initially theoretically driven, showing that high-temperature properties of a material with a QPT are directly influenced by the properties of the QCP itself.

The chapter starts by discussing the predictions of quantum critical and Hertz–Millis (H–M) theories. Experimentally, the authors mainly limit themselves to f-electron-based materials: the rare earths $Li(Ho,Y)F_4$, $Ce(Cu,Au)_6$, and $YbRh_2Si_2$, the cerium series $Ce(Co,Rh,Ir)In_5$, and one actinide-based material, URu_2Si_2. These heavy fermion 4f or 5f metals represent prototype materials of quantum critical matter, and their experimental signatures are critically reviewed as well as their evolving theoretical descriptions. The authors then elaborate on the shortcomings of H–M theory and list attempts toward better theories. Difficulties arising in hidden QCPs evidence the challenges and opportunities associated with the concept of QPT. The review concludes with the description of other manifestations of QPTs beyond the rare earths and actinides.

CHAPTER 281: LANTHANIDES IN LUMINESCENT THERMOMETRY

C.D.S. Brites*, A. Millán[†], and L.D. Carlos*

*CICECO—Aveiro Institute of Materials, University of Aveiro, Aveiro, Portugal. E-mail: lcarlos@ua.pt

[†]ICMA—Instituto de Ciencia de Materiales de Aragón, University of Zaragoza, Zaragoza, Spain
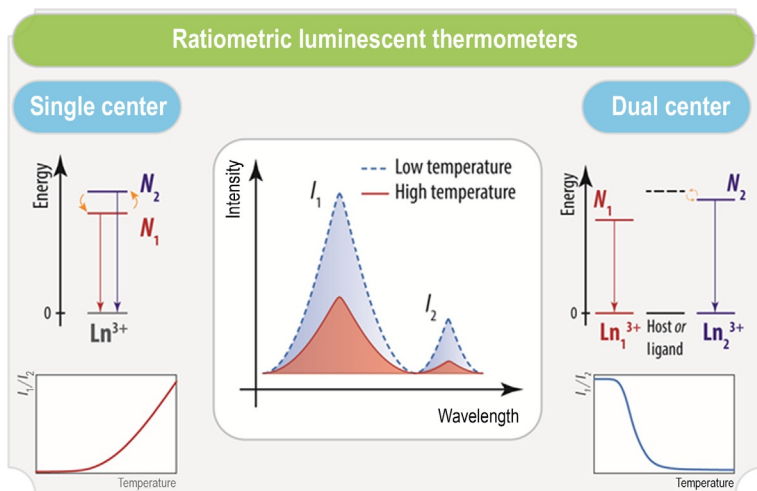
Luminescent ratiometric thermometers combining high spatial and temporal resolution at the micro- and nanoscale, where the conventional methods are ineffective, have emerged over the last decade as an effervescent field of research, essentially motivated by potential applications in nanotechnology, photonics, and biosciences. Applications of nanothermometry are developing in microelectronics, microoptics, photonics, micro- and nanofluidics, nanomedicine, and in many other conceivable fields, such as thermally induced drug release, phonon-, plasmonic-, magnetic-induced hyperthermia, and wherever exothermal chemical or enzymatic reactions occur at submicron scale. Among suitable luminescent thermal probes, trivalent lanthanide-based materials play a central role due to their unique thermometric response and intriguing emission features such as high quantum yield, narrow bandwidth, long-lived emission, large ligand-induced Stokes shifts, and ligand-dependent luminescence sensitization.

The chapter offers a general overview of recent examples of single- and dual-center lanthanide-based thermometers, emphasizing those working at nanometric scale. Important focus is given to how to quantify their performance according to the relevant parameters: relative sensitivity, experimental uncertainty on temperature, spatial and temporal resolution, repeatability (or test–retest reliability), and reproducibility. The emission mechanisms supporting single- and dual-center emissions are reviewed, together with the advantages and limitations of each approach. Illustrative examples of the rich variety of systems designed and developed to sense temperature are provided and explored: crystals of ionic complexes, molecular thermometers,

metal–organic frameworks, upconverting and NIR-emitting nanoparticles, among others. The review ends with a discussion of the challenges and opportunities in the development of highly sensitive luminescent ratiometric thermometers that scientists are currently facing in this exciting research field.

Jean-Claude G. Bünzli
Vitalij K. Pecharsky

Contents of Volumes 1–48

Index of Contents of Volumes 1–49

Chapter 278

Rare Earth-Doped Phosphors for White Light-Emitting Diodes

M. Sato[*,1]**, S.W. Kim**[†]**, Y. Shimomura**[‡]**, T. Hasegawa**[†]**, K. Toda**[†]
and G. Adachi[§]

[*]*Faculty of Engineering, Niigata University, Niigata, Japan*

[†]*Graduate School of Science and Technology, Niigata University, Niigata, Japan*

[‡]*Mitsubishi Chemical Corporation, Odawara, Kanagawa, Japan*

[§]*Faculty of Engineering, Osaka University, Suita, Osaka, Japan*

[1]*Corresponding author: e-mail: msato@eng.niigata-u.ac.jp*

Chapter Outline

1

1   INTRODUCTION

Two decisive advances in semiconductor electroluminescence have led to the production of visible light for illumination by light-emitting diodes (LEDs). First, red light emission was developed in 1962 (Holonyak and Bevacqua, 1962). In the decades that followed, LEDs were used only in numerical displays and signaling applications, but not in major lighting devices. The second advance was the demonstration of a bright blue LED by Nakamura in 1993 (Nakamura et al., 1994), along with earlier materials advances by Akasaki and Amano group (Amano et al., 1986, 1989), to whom the Nobel Prizes in Physics 2014 were awarded, for honoring their significant invention of the blue LEDs. Importantly, since blue is at the short wavelength side of the visible spectrum, this LED has significant potential to "down-convert" its blue light into green, yellow, and even red light using passive phosphorescent and fluorescent materials (Shimizu et al., 2003).

Traditional incandescent and fluorescent lamps rely on either heat or discharge of gases, associated with large energy consumption that occurs due to high temperatures and large Stokes shifts (Xie et al., 2007). On the other hand, LEDs have numerous advantages over these lamps, such as small size, long lifetime, robustness, fast switching, and high efficiency. Indeed, as illustrated in Fig. 1, the rapid increase in the luminous efficacy of LEDs is quite remarkable. There is now virtually no question that solid-state lighting (SSL) will eventually displace all conventional technologies in general illumination applications, leading to a considerable reduction of worldwide electricity consumption.

Phosphor materials in LED technology play a definite role for achieving high color quality white light. They are photon conversion materials which
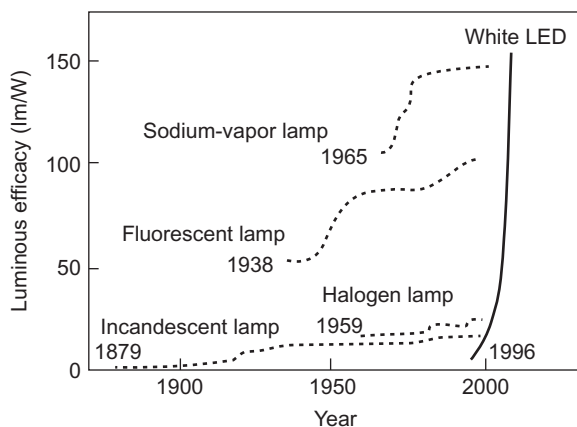
FIG. 1   Luminous efficacy improvements of various light sources. *Redrawn from Nakamura, S., Mukai. T., Senoh, M., 1994. Candela-class high-brightness InGaN/AlGaN double-heterostructure blue-light-emitting diodes. Appl. Phys. Lett. 64, 1687.*

themselves have a long history. Some of them have been used for fluorescent lighting or displays. However, these phosphors are not good candidates for searching phosphors suitable for SSL because they are optimized for excitation at the wavelength of a mercury discharge tube at 254 nm. Similarly, the phosphors used for television screens and other emissive displays are not helpful because they are optimized for electron beam excitation and, in addition, have sharp emission lines rather than the broad emission that, at least in the green and red, are desirable for high color rendering quality.

The main requirements that should be satisfied for phosphors for SSL are the following:

(1) High quantum efficiencies of emission.
(2) Excitation spectrum well matched to emission wavelengths and linewidths of LED.
(3) Short photoluminescence lifetimes in order to avoid saturation at high excitation intensities.
(4) Chemical compositions allowing easy tunability of excitation and emission wavelengths.
(5) Thermal and photochemical stability consistent with long-term SSL goals, including operation for up to 100,000 h under 100 W/cm^2 ultraviolet (UV) irradiation and at temperatures up to 200°C.
(6) Stable color (CIE chromaticity) at operating temperatures.
(7) Absence of thermal quenching at operating temperatures.
(8) Ease of manufacture and low cost.
(9) Nontoxicity of the components used to manufacture the phosphors.

Simultaneous fulfilling of these stringent requirements is likely to be difficult when using host materials that have been used in conventional phosphor matrices. As a consequence, the discovery of entirely new classes of photon conversion materials is required.

From these viewpoints, it is important and useful to provide a comprehensive review on LED-based SSL for scientists and material developers. We wish that this review can help many scientists and researchers providing answers for questions regarding the kinds of host materials that should be selected, the kinds of robust structures that should be targeted, which rare earth elements should be selected for the desired color emissions, and how the materials should be synthesized. In this review, our interest will be focused on phosphors, which are not only activated by rare earth ions but also excited by LED radiation. Therefore, the classification of phosphor materials in Section 4 is primarily based on chemical composition such as oxide, nitride, sulfide, and so on, and then on emission color such as yellow, green, red, and so on, and, finally, on the actual chemical formula. This is because it is convenient for materials scientists and chemists to understand the phosphor characteristics on the basis of the nature of chemical bonding, which controls the energy of the transitions, absorption, and emission, in solid state.

The literature reviewed here is meant to be as comprehensive as possible although it is restricted to entries which are academically and/or technologically important and valuable. Each phosphor quoted in the review is accompanied with excitation and emission spectra as well as its crystal structure and, if possible, some crystallographic data to understand how/where the emission centers are located in the crystal. Among numerous physical data that have already been reported in the literatures, reliable data are tabulated in Section 7 as a useful source of information on phosphors.

2   WHAT IS LED LIGHTING?

2.1   Principle of White Light Generation in LEDs

In 1996, a new lighting device was proposed by Nichia Chemical Co., using a blue InGaN LED chip coated with a yellow-emitting phosphor of yttrium aluminum garnet ($Y_{2.9}Ce_{0.1}Al_5O_{12}$, YAG:$Ce^{3+}$) (Nakamura and Fasol, 1997). A schematic structure of this device is shown in Fig. 2A. Blue light with wavelength around 450 nm (varying from 420 to 480 nm depending on the composition of $In_{1-x}Ga_xN$), is emitted by the driving chip through electron–hole
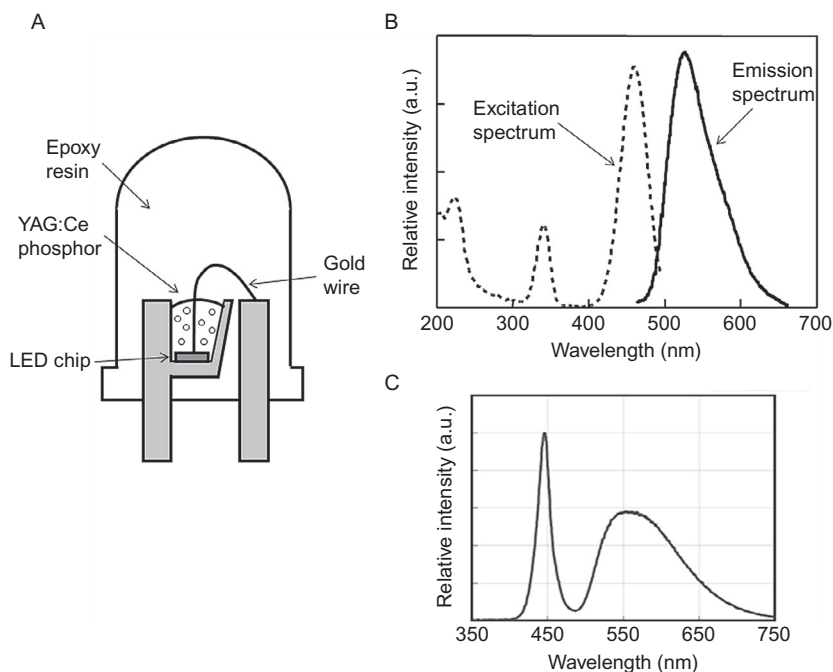
FIG. 2   LED-base lighting device. (A) A schematic structure of the device, (B) represents images for excitation and emission spectra of YAG:Ce^{3+} phosphor, and (C) represents an image of the emission spectra of the device.

recombination in the p–n junctions. Some of the blue light from the LED excite the YAG:Ce^{3+} phosphor to emit yellow light, and then the rest of the blue light is mixed with the yellow light to generate a white light. Typical excitation and emission spectra of YAG:Ce^{3+} phosphors are shown in Fig. 2B, and the overall emission spectrum for the device is also given in Fig. 2C. In the excitation spectrum of the phosphor, there are three excitation bands with relatively wide peak widths, where the bands at 220, 340, and 450 nm correspond to the transitions O → Ce (charge transfer, CT), 4f → 5d (higher level), and 4f → 5d (lower level), respectively, as discussed in detail later. Among the excitation bands, the band at around 450 nm is in excellent match with the emission wavelength of the InGaN LED.

Advantages of SSL are high luminous efficiency, energy savings, environment friendliness, small volume, and long persistence (Krames et al., 2007). For the conventional incandescent lamps and fluorescent lamps, a large amount of energy is radiated as heat from the high-temperature tungsten filament or from the mercury vapor discharge. The luminescence efficiency of white LEDs can be greatly improved by reducing the nonradiative recombination of electron–hole pairs in p–n junctions and by designing a new structure to enhance external quantum efficiency. The luminous efficacy of white LEDs will most probably reach 200 lm/W by 2020, which will be far greater than that of incandescent lamps and fluorescent lamps.

2.2 Types of LED Lighting Devices

Generally, four different approaches can be considered in order to generate white light from LEDs, as schematically illustrated in Fig. 3. In type (a), white light is obtained using a blue LED to excite a yellow phosphor. In other types,

A

Blue LEDs + yellow

B

UV–LEDs + RGB phosphors

C

Blue LEDs + RG phosphors

D

RGB LEDs
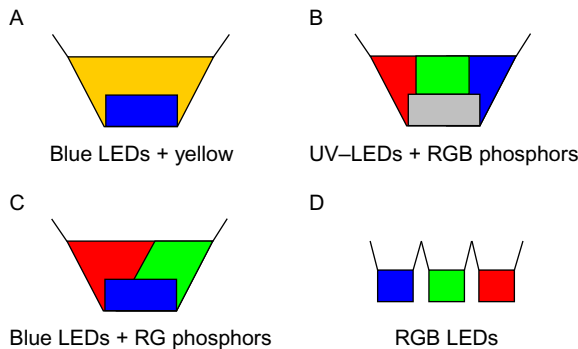
FIG. 3 Four methods of generating white light from LEDs: (A) *blue*-LEDs (*gray* in the print version) + *yellow* (*light gray* in the print version) phosphor, (B) UV-LEDs + *red–green–blue* (RGB) (*gray–light gray–dark gray* in the print version) phosphors, (C) *blue*-LEDs (*gray* in the print version) + *red–green* (RG) (*dark gray–light gray* in the print version) phosphors, and (D) *red–green–blue* (RGB) (*dark gray–light gray–gray* in the print version) LEDs.

white light is obtained using an UV LED to excite red–green–blue (RGB) phosphors (b), using a blue LED to excite red–green (RG) phosphors (c), and by mixing reds, greens, and blues, ie, RGB, LEDs (d). Type (a) is now most commonly used with InGaN LED chips and yellow YAG:Ce^{3+} phosphors because of easy fabrication and low cost. However, the white light obtained by this device has some problems such as poor color rendering index (CRI) and low stability of color temperature (Sheu et al., 2003; Steigerwald et al., 2002). Type (d) has the advantage to be able to create not only white colors but also various colors, although electronic tuning is complicated to require different driving currents for different color LEDs (Shur and Zukauskas, 2005). Type (b) has similar advantages of easy color rendering as type (d), using only one LED, while it has the drawbacks of complex blending of different phosphors and lack of efficient red phosphor.

2.3   Color Evaluation Indices

What are the colors suitable for human sight? First, we have to define various colors of light on the basis of physical quantities (Phillips, 2006).

The color of a light source can be described by the Commission Internationale de l'Éclairage (CIE) chromaticity coordinates, calculated as follows. Fig. 4A displays the three color-matching functions, $\bar{x}(\lambda)$, $\bar{y}(\lambda)$, and $\bar{z}(\lambda)$, which define the "1931 CIE Standard Observer." The function, $\bar{y}(\lambda)$ is defined to be identical to the photopic luminous efficiency function, V_λ, which describes the brightness perceived by the human eye of a light of a particular wavelength under day-brightness conditions. The other two color-matching functions, $\bar{x}(\lambda)$ and $\bar{z}(\lambda)$, do not have such simple physical interpretations
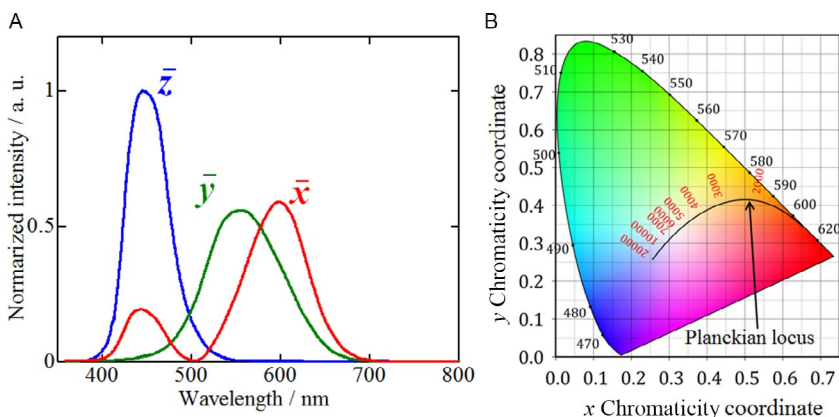
FIG. 4   CIE 1931 (1978) Color-matching functions (A) and CIE 1931 (x,y) chromaticity diagram and color temperature locus (B). The *triangular area* in the chromaticity diagram covers the gamut of colors defined by standard *green* (*light gray* in the print version), *red* (*dark gray* in the print version), and *blue* (*dark gray* in the print version) colors.

(Brill, 1998; Fairman et al., 1977) but, together with the first, are necessary to determine the color of light. The tristimulus values X, Y, and Z of a light source are defined as,

$$X = k \int P(\lambda)\,\bar{x}(\lambda)\mathrm{d}\lambda, \quad Y = k \int P(\lambda)\,\bar{y}(\lambda)\mathrm{d}\lambda, \quad Z = k \int P(\lambda)\,\bar{z}(\lambda)\mathrm{d}\lambda$$

where k is a proportionality constant and $P(\lambda)$, named as spectral power distribution (SPD), is the radiant power emitted by a source at each wavelength or band of wavelengths over the entire spectrum (eg, in units of W/nm). The SPD provides a complete description of the spectral properties of a light source. The Y value is equal to one of the photometric quantities (such as luminous flux) of the light source if $k = 683$ lm/W is used (see later, luminous efficacy of radiation, LER). Tristimulus values were derived such that $X = Y = Z$ is equal-energy white. The chromaticity coordinates (x,y) are calculated as $x = X/(X+Y+Z)$ and $y = Y/(X+Y+Z)$. Any color of light can be represented on the CIE 1931 (x,y) chromaticity diagram, which is shown in Fig. 4B. The chromaticity diagram is a guitar pick shaped 2D plot of all possible hue and saturation values of a light source, independent of luminance. The perimeter of the guitar pick is the locus of chromaticity coordinates for the spectral colors (ie, monochromatic light, wavelengths in nm).

2.3.1 Correlated Color Temperature

The black arc plotted in the interior of the chromaticity diagram gives the chromaticity coordinates of emission from a blackbody at temperatures between 1000 K and infinity. It is called the Planckian locus and is a convenient way of representing a white light source. Positions along the Planckian locus can be specified by the temperature of the blackbody, called the color temperature, thereby reducing the hundreds of numbers in an SPD, or the two numbers of chromaticity coordinate, to a single number. A nonblackbody source is often described by the correlated color temperature (CCT), which is the temperature of a blackbody radiator that most closely resembles the color from a source of equal brightness. Lines of a specified (constant) CCT would cross the Planckian locus at coordinates of that blackbody temperature, as indicated in Fig. 4B. A powerful feature of the chromaticity diagram is that light produced by mixing output from two sources having different chromaticity coordinates will fall on the line connecting the coordinates of the sources alone; the position along the line is determined by the weighted average of the brightness of each source. Similarly, the chromaticity coordinate of light produced by mixing three light sources will fall within the triangle formed by the chromaticity coordinates of the three sources as the vertices. It is important to note that any color falling outside this triangle cannot be produced by mixing the three sources.

How can we determine whether the spectrum of a light source is suitable for general lighting? The two major issues of the efficiency of the radiation and the color quality of the light are important.

2.3.2 Luminous Efficacy of Radiation

Luminous efficacy (lm/W), where the term "efficacy" is usually used instead of "efficiency" for radiation sources, is a parameter describing how bright the radiation is perceived by the average human eye. It scales with the eye sensitivity curve. The highest human eye sensitivity is located around at 555 nm, green, with the highest possible LER (=683 lm/W on photopic vision). Therefore, 683 lm/W is the highest possible efficiency that can ever be obtained from a light source: When 100% of the electrical power is converted to light at a wavelength of 555 nm, the efficacy of the light source is 683 lm/W. Any other spectrum will yield a lower LER, as the human eye is less sensitive for other wavelengths. In order to obtain white light, emission in the red and blue is necessary, so the LER of white light is significantly lower than 683 lm/W, being on the order of 350 lm/W. In general, one has to find a compromise between high LER and good color quality of the light source.

2.3.3 Color Rendering Index

CRI is a measure for color quality. The CRI gages how colors of certain standard reference objects appear when illuminated by a test light source, compared to the colors observed under illumination by a reference light source of the same CCT. If there is no difference between the colors rendered by the reference and test light sources, the test source would have a CRI of 100. Obviously, the choice of this reference is very important, since it defines what the "true" colors of objects are. In the definition of the CRI, a several reference sources are used depending on the type of test source. First, the spectrum of the test source is compared to that of a blackbody radiator. When the CCT of the test source is below 5000 K, the reference source used for the calculation of the CRI is a black body radiator of the same CCT. Above 5000 K, a standard daylight spectrum of the same CCT, derived from the D65 standard illuminant and defined by the CIE, is used. Light from a standard incandescent light bulb has a CRI near 100. CRI is calculated from the SPD of the test light source. To evaluate the CRI of real light sources, the SPD must be measured, although mathematical models exist to simulate the SPDs of various white LEDs (Ohno, 2004).

The value often quoted as "CRI" on commercially available lighting products is properly called the R_a (formally CIE R_a) value, ie, CRI is a term for general use, while R_a is an international standard term which is called "general color rendering index." Fourteen different color standard samples are used to evaluate R_a, of which the first eight are used for calculating R_a. Here, the special CRI, R_i, is calculated for each of the eight samples using the following equation:

$$R_i = 100 - 4.6\Delta E_i$$

where ΔE_i is the color coordinate difference between the test color and the eight standard samples, on the CIE 1964 W*U*V* uniform color space

(Schanda, 2007). Thus, R_i gives the CRI with respect to each sample. Then, R_a is obtained by calculating the arithmetic mean of R_i. However, it was realized that the definition of CRI or R_a is far from perfect, and several improvements were proposed, details of which are not described here (Davis and Ohno, 2005).

3   PHOSPHOR REQUIREMENTS FOR LED LIGHTING

The phenomena which involve absorption of energy and subsequent emission of light are classified generically under the term luminescence. Phosphors are luminescent materials that emit light when excited by radiation. In luminescent materials, absorption of energy takes place either by the host lattice or by intentionally doped impurities (localized emission center) such as rare earth and transition metal ions. The 4f electronic energy levels of rare earth ions are the mostly responsible for luminescence phenomena via both transitions of f–f and f–d/d–f. The energy levels are not affected much by the environment because the 4f electrons are shielded from external electric fields by the outer $5s^2$ and $5p^6$ electrons. This feature is in contrast with transition metal ions, whose 3d electrons, located in an outer orbit, are considerably affected by the environment or crystal electric field.

Among the requirements for the development of LED lighting, as pointed out before, issues regarding phosphor materials are the following:

(a) high quantum efficiencies of emission;
(b) excitation spectrum matched to LED emission wavelengths;
(c) short photoluminescence lifetimes; and
(d) absence of thermal quenching at operating temperatures.

Here, restricting our attention to rare earth ions, the items that are important for understanding the luminescence phenomena are introduced.

3.1   Features of Rare Earth Ions with Respect to Luminescence

3.1.1   Configurational Coordinate Diagram

First, let us explain the configurational coordinate diagram because it is very useful for describing the luminescence mechanism of rare earth ions. In solids, the emission of rare earth ions is observed at different spectral position from the absorption. The difference between the absorption and emission wavelength is described as the Stokes shift. The configurational coordinate diagram can well explain not only Stokes shift but also optical properties of a localized center on the basis of potential curves (Yamamoto, 2006), as shown in Fig. 5. The total energy U of the activator is plotted as a function of configurational coordinates. Here, the total energy U means the sum of the electron energy and ion energy for an isolated molecule, which is regarded as the environment around an emission center ion. The configurational coordinate can describe one aspect of the geometrical configuration of the active
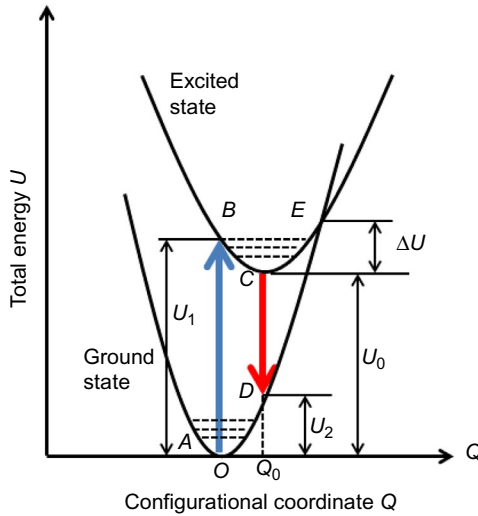
FIG. 5 Schematic illustration of configurational coordinate model.

ion with its nearest neighbors, usually regarded as the average distances between the active ion and the nearest neighbors. The horizontal dashed lines in ground state and excited state curves denote the vibrational states. For the total energy U, it is presumed that the bonding force between the active ion and the nearest neighbors can be expressed by Hooke's law, so that the energies of the ground state, U_g, and that of the excited state, U_e, are given by the following equations.

$$U_g = K_g \frac{Q^2}{2}$$

$$U_e = K_e \frac{(Q - Q_0)^2}{2} + U_0$$

where K_g and K_e are the force constants of the chemical bond, Q_0 represents the equilibrium distances of the ground state and the excited state, and U_0 is the total energy at $Q = Q_0$. When the activator absorbs some radiation light, an expansion of the lattice occurs in the vicinity of the activator ion and the activator is promoted to the excited state. The excitation and emission processes are illustrated by vertical arrows, showing that the nucleus of the activator stays at approximately the same position during these processes (so-called Franck–Condon principle). The energy difference between excitation and emission is the Stokes shift, equal to $U_1 - (U_0 - U_2)$. When the temperature of the phosphor exceeds some value, the vibrational energy makes the excited activator reach the E point of the excited state curve and then the activator relaxes to the ground state without radiation, which is called

temperature quenching. One can assume that this nonradiative relaxation process with activation energy, ΔU, and transition probability, N, is given by $N \propto \exp(-\Delta U/kT)$. The spatial distribution of an electronic orbital is different between the ground and excited states, giving rise to differences in the electron wave function overlaps with neighboring ions. This difference further includes a change in the equilibrium position and the force constant of the ground and excited states, and is the origin of the Stokes shift.

Since the phosphor may be heated up to about 100°C by a LED chip, this phenomenon is crucially important for selecting the host material. How can the thermal quenching at the operating temperature be reduced? One of the answers may be to increase ΔU. As U is a parabolic function of Q, the increase in ΔU can be achieved by increasing the curvature of the excited state U_e, this corresponding to an increase in K_e, ie, a decrease in lattice vibrations. In addition, the magnitude of the Stokes shift has a large influence on the efficiency of the emission because its value is related to the waste of the absorption energy. As shown in Fig. 5, the reduction of Stokes shift corresponds to the decrease in Q_0, requiring the suppression of electron cloud expansion in the excite state.

3.1.2 Electronic Transitions in Rare Earth Ions

The characteristic properties of the rare earth ions are attributable to the presence of a deep-lying 4f shell. The electrons of this shell are screened by those in the outer shells, and, as a result, they give rise to number of discrete energy levels. Since environment around a rare earth ion in a crystal lattice scarcely affects the position of these levels, there is a resemblance with the energy level diagrams of the free ions. In spite of this, there is an important difference in the emission properties. Rare earth ions are usually trivalent. For understanding the luminescent properties of rare earth ions, it is necessary to know their key energy levels. The energy level may be divided into three categories: those corresponding to $4f^n$ configuration, $4f^{n-1}5d$ configuration, and those corresponding to CT involving the neighboring ions.

3.1.2.1 4f–4f Transitions

This is concerned with the $4f^n$ configurations. Except for Ce^{3+} and Yb^{3+}, the number of discrete 4f energy levels is large. These levels further increase in number due to crystal-field splitting. Electric dipole transitions within the 4f shell are strictly forbidden because the parity does not change. However, the forbidden transitions are actually observed due to the fact that the interaction of rare earth ion with crystal field or with the lattice vibrations can mix states of different parities into 4f states. Coupling of 4f electrons with transient dipoles induced in the ligands by the radiation field leads to an amplification of the even-parity multipolar transition amplitudes for transitions within the 4f shell. These transitions are called "induced (or forced) electric dipole transitions." The transitions that are not allowed as electric dipole may take

place as magnetic dipole since in this case the parity exclusion rule does not apply. Spin-orbit coupling weakens selection rules on ΔL and ΔS. As a consequence of these facts, many trivalent rare earth ions exhibit luminescence with intensities high enough for practical uses. The decay times of the luminescence due to 4f–4f transitions are mostly in the range μs–ms, while, in the case of luminescence due to a spin-allowed transition between levels having equal spin multiplicity, they are much shorter, $\sim 10^{-5}$ s. The spectra of the 4f–4f transitions are line shaped and the energies of the levels involved in the transitions are well defined and mostly independent of the nature of the host. The energy level diagram for trivalent rare earth is commonly referred to as Dieke diagram (Peijzel et al., 2005). This diagram is useful because the energies of the J multiplets vary by only a small amount in different host crystals. The diagram allows rapid identification of the energy levels in new hosts and has been a crucial tool in the design of materials suitable for phosphors or lasers.

3.1.2.2 4f–5d Transitions

This is concerned with the $4f^{n-1}5d^1$ configurations. $4f^{n-1}5d^1$ levels may be understood as formed by the electron in the 5d orbital interacting with the $4f^{n-1}$ core. The 5d orbitals interact strongly with the surroundings (crystal field) so that $4f^{n-1}5d$ configurations of rare earth ions in solids are very different from those of the free ions. The $4f^n \rightarrow 4f^{n-1}5d^1$ absorption consists of parity-allowed intense and broad, bands corresponding to the components of 5d electronic levels split by the crystal field. For most of the trivalent rare earth ions, interconfigurational transitions $4f^n \rightarrow 4f^{n-1}5d^1$ correspond to wavenumbers exceeding $50{,}000$ cm^{-1}, and are thus not accessible to UV excitation. In the case of Ce^{3+} and Eu^{2+}, however, they have smaller energies and are usually accessible from near-UV to visible radiations. The spectra of the 4f–5d transitions are broad band shaped and can be tuned by modifying the coordination environment. The decay times of the luminescence arising from 4f to 5d transitions are short, usually in the range of 40–70 ns for Ce^{3+} and ~ 1 μs for Eu^{2+}.

3.1.3 Energy Transfer

The process by which the excitation energy of an ion migrates to another ion is called energy transfer. It is very important to understand this effect in order to develop efficient luminescent materials. There are several types of energy transfer processes (Goldberg, 1966). Here, it is convenient to introduce terms which are frequently used, such as donor/acceptor. A donor (D), sometimes called sensitizer, is a species giving out energy, while an acceptor (A), sometimes called activator, is a species accepting the energy of the donor.

(1) *Resonant energy transfer*

The energy of an excited ion migrates to another one of the same species that is in its ground state. This mechanism of this type of transfer is divided into three categories.

(i) *Multipolar interaction*. The energy transfer occurs in the case where both transitions in D and A are of electric multipole character. There are three types of interactions, that is, dipole–dipole (dd), dipole–quadrupole (dq), and quadrupole–quadrupole (qq). The probability of the energy transfer through multipolar interaction is expressed as:

$$P_s(R) = \frac{\alpha_{dd}}{R^6} + \frac{\alpha_{dq}}{R^8} + \frac{\alpha_{qq}}{R^{10}} + \ldots$$

where R is the distance between D and A and α_s s are the magnitudes of the interactions (Yamamoto, 2006). Among the three interactions, the dd interaction yields the highest transfer probability. However, if the dipole transition is not completely allowed for D and/or A, as in the case of 4f–4f transitions, it is probable that the higher order interactions, dq or qq, may have a larger probability for small distance (R) ion pairs (Nakazawa and Shionoya, 1967).

(ii) *Exchange interaction*. This energy transfer occurs when the donor and the acceptor are located closely enough for their electronic wave functions to overlap and the transfer is due to a quantum mechanical interaction.

(iii) *Phonon-assisted energy transfer*. This energy transfer occurs when there is a difference ΔE between the transition energies of D and A, that is compensated by either a phonon emission or an absorption. The transfer probability is given by the equation (Miyakawa and Dexter, 1970):

$$P_{as}(\Delta E) = P_{as}(0)e^{-\beta \Delta E}$$

where $P_{as}(0)$ is equal to the resonant transfer probability and β is a parameter that depends on the energy and occupation number of participating phonons. The energy difference ΔE is equal to the largest phonon energy. The energy transfer rates for various systems of rare earth ions in Y_2O_3 host showed excellent agreement with the above equation (Yamada et al., 1972).

(2) *Sensitization of luminescence*

This energy transfer process is often used in practical phosphors in order to enhance the emission efficiency. A donor (sensitizer) that absorbs strongly transfers its excitation energy very efficiently to an acceptor (activator). The resulting emission is greatly enhanced. For instance, the emission of Tb^{3+} is sensitized by Ce^{3+} ions in many green-emitting phosphors, as will be discussed later. Sensitization is the most important process for developing various color-emitting phosphors excited by LEDs and based on trivalent rare earth ions such as Sm^{3+}, Eu^{3+}, Tb^{3+}, etc.

(3) *Concentration quenching of luminescence*

An unwanted, and very common, feature of energy transfer is reduction in emission intensities when the emitting ions lie too close to each other.

The origin of concentration quenching is thought to be one of the following (Nakazawa, 2006):

  (i) Excitation energy is lost from the emitting state due to cross-relaxation between the acceptor ions.

 (ii) Excitation migration due to the resonance between the acceptor ions increases with their concentration, so that the energy reaches remote killers or the crystal surface acting as quenching centers.

(iii) The acceptor ions are paired or coagulated, forming a quenching center.

When concentration quenching due to cross-relaxation (relaxation due to the resonant energy transfer between the same element ions; Liu and Jacquier, 2005) occurs on a particular level among several emitting levels, the emission color of the phosphor changes with the acceptor concentration. A typical example of this was observed in Tb^{3+}-doped LaP_5O_{14} phosphors (Nakazawa and Shionoya, 1970).

3.2   Crystal-Field Effects on Luminescence

The 5d wave functions of ions such as Ce^{3+} and Eu^{2+} interact strongly with the orbitals of surrounding ligands and ions. The resulting splitting is usually much larger than the splitting induced by spin-orbit coupling. Therefore, the crystal field at an emission center ion in Ce^{3+}- and Eu^{2+}-doped phosphors has much more drastic influence on luminescence properties of the phosphors, compared with the cases of other trivalent rare earth-doped phosphors relying on 4f–4f transitions. Crystal-field splitting depends on several factors, some of which are as follows:

(1) Number of electrons in the d orbitals.
(2) Oxidation state of the ion (a high oxidation state will lead to a larger splitting).
(3) Arrangement of the ligands around the crystal (symmetry).
(4) Nature of the ligands.

A schematic diagram of 5d levels and emissions of rare earth ions such as Eu^{2+} or Ce^{3+} lying on a center with cubic O_h symmetry is illustrated in Fig. 6. First, the nephelauxetic effect caused by the expansion of the electron cloud of ligands toward the central metal ion lowers the energy of 5d orbitals, which is also called "*centroid shift*." Second, the O_h crystal field divides the five degenerated d orbitals into e_g orbitals with higher energy and t_{2g} with lower energy. Additional effects such as symmetry distortions or anion order may further modify the splitting. In luminescence phenomena in Eu^{2+}- or Ce^{3+}-doped phosphors, excitation/emission processes correspond 4f$\leftrightarrow$5d transitions.

The introduction of nitrogen in an oxide compound has expanded the possibilities of tuning the properties of phosphors, as will be shown in Section 4. Nitrogen is less electronegative and more polarizable than oxygen, which
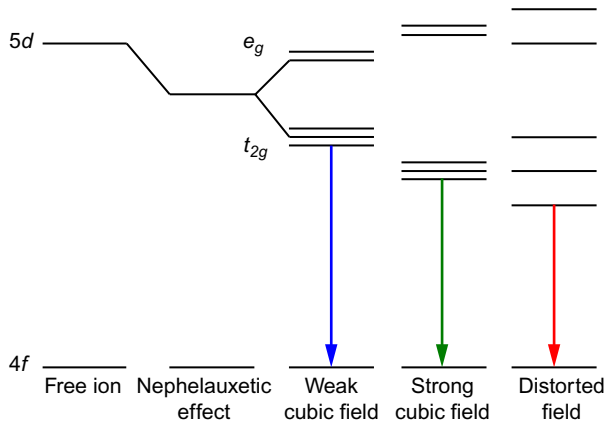
FIG. 6 Schematic diagram of energies of 5d levels and emissions of rare earth ions such as Eu^{2+} or Ce^{3+} affected by bonding (nephelauxetic effect) and crystal-field splitting in various environments.

increases the covalency of bonding. Interelectronic repulsion decreases and the nephelauxetic effect increases. The crystal-field splitting becomes larger as a consequence of the higher charge of nitride. The latter allows the formation of new compounds where cations show higher oxidation states than in oxides. These effects induce important changes in properties.

4 PHOSPHOR MATERIALS FOR WHITE LEDs

4.1 Oxides

Oxide phosphors are presently the most frequently available phosphors. Since they can be synthesized at a lower temperature compared with nitride phosphors, control of the morphology of the powders is easy when using conventional ceramic synthetic methods. Red shifting emission and excitation spectra are difficult for these phosphors due to reduced nephelauxetic effect. However, if an appropriate crystal matrix is carefully chosen, the red shift can be obtained with an oxide matrix. In general, the production costs of oxide phosphors are less than those of conventional nitride phosphors because of inexpensive starting materials and low synthesis temperatures.

4.1.1 Yellow-Emitting Phosphors
4.1.1.1 $Y_3Al_5O_{12}$:Ce^{3+} Phosphors
Ce^{3+}-activated yttrium aluminum garnet YAG:Ce^{3+} has been often used as a commercial yellow phosphor in phosphor-converted white LEDs (Chen et al., 2010a; Tamaki and Murazaki, 2007; Xie et al., 2011). The YAG:Ce^{3+} phosphor has a strong optical absorption band in the blue which well matches with the emission band of InGaN-based blue-LED chips, and it exhibits a strong and broad yellow emission. As shown in Fig. 7, the excitation spectrum
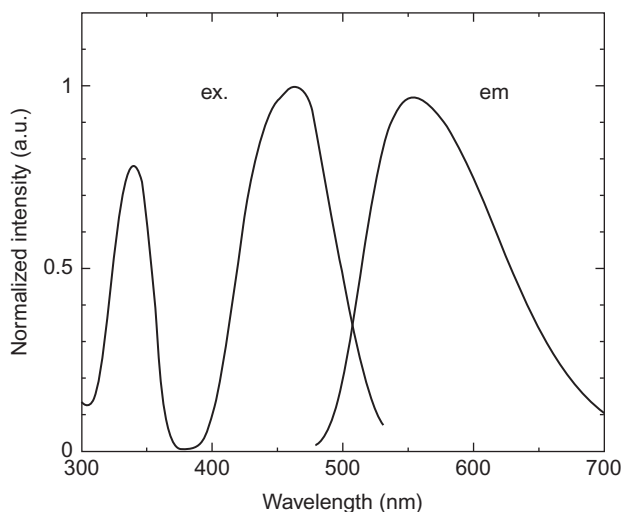
FIG. 7 Excitation and emission spectra of YAG:Ce^{3+} phosphor. Data were collected from a commercial phosphor by the authors.

consists of two broad bands with peaks at about 340 and 450 nm due to the $4f^1 \rightarrow 4f^0 5d^1$ transition of Ce^{3+}, and these excitation bands correspond to transitions to the two lowest energy levels of the 5d orbital (Xie et al., 2011): when an electron is excited from 4f to 5d, the 5d electron of the excited $4f^0 5d^1$ configuration forms a ^{2}D term, which is split by spin-orbit coupling into two lower energy levels, ^{2}D$_{3/2}$ and ^{2}D$_{5/2}$ (Dong et al., 2006; Jacobs et al., 1978). The emission spectrum of YAG:Ce^{3+} shows a broad yellow emission band with a full width at half maximum (FWHM) of 120 nm (Fig. 7) assigned to the $4f^0 5d^1 \rightarrow 4f^1$ transition of Ce^{3+}. The large FWHM of YAG:Ce^{3+} is caused by the vibronic broadening of the emitting ^{2}D$_{3/2}$ level and by the presence of two overlapping components due to transitions to the ^{2}F$_{5/2}$ and ^{2}F$_{7/2}$ spin-orbit levels, usually separated by about 2000 cm^{-1} (Dorenbos, 2006; Feldmann et al., 2003). The strong optical absorption in the blue and the broad yellow emission of YAG:Ce^{3+} are the main reasons for its use in blue-LED-based white LEDs. In addition, the phosphor has a high optical absorption of ~95% and an external quantum efficiency of ~83% under blue light excitation (440–470 nm) (Xie et al., 2011).

However, the resulting white LEDs have a low CRI and a high CCT (~5000 K), so that it is considerably difficult to generate a warm white light with YAG:Ce^{3+} phosphors. This is because YAG:Ce^{3+} has a weak emission intensity in the red. Therefore, effort has been devoted to improve the performances YAG:Ce^{3+}. The most frequently employed approach for tuning the emission color of YAG:Ce^{3+} is the substitution of yttrium with other rare earth elements in the host YAG lattice. When Y^{3+} sites are partially substituted by larger La^{3+}, Gd^{3+}, or Tb^{3+} (TAG), the emission band tends to shift
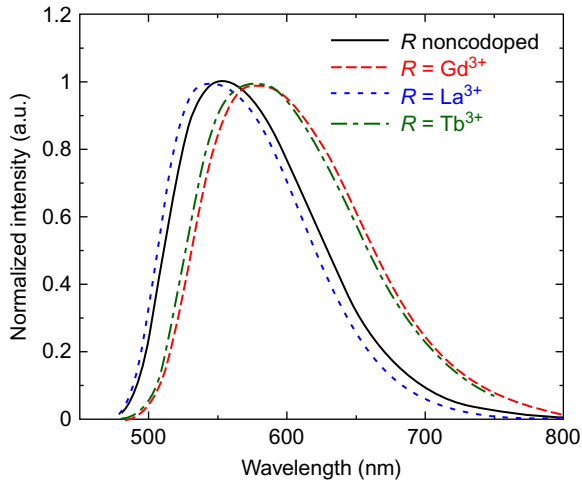
FIG. 8 Emission spectra of R codoped YAG:Ce^{3+} phosphors (R=La, Gd, and Tb). *Redrawn from Shao, Q., Li, H., Dong, Y., Jiang, J., Liang, C., He, J., 2010. Temperature-dependent photoluminescence studies on Y$_{2.93-x}$Ln$_x$Al$_5$O$_{12}$:Ce$_{0.07}$ (Ln=Gd, La) phosphors for white LEDs application. J. Alloy Compd. 498, 199–202; Jang, H.S., Im, W.B., Lee, D.C., Jeon, D.Y., Kim, S.S., 2007. Enhancement of red spectral emission intensity of Y$_3$Al$_5$O$_{12}$:Ce^{3+} phosphor via Pr co-doping and Tb substitution for the application to white LEDs. J. Lumin. 126, 371–377.*

to a longer wavelength (Fig. 8), and nowadays, Gd^{3+}-doped YAG:Ce^{3+} is commonly used in white LEDs. On the other hand, the partial substitution of Al^{3+} sites with larger Ga^{3+} ions results in a shift of the emission band to a shorter wavelength (blue shift; Kanke and Navrotsky, 1998; Pavese et al., 1995). In addition, the emission band also shifts to a shorter wavelength when smaller Lu^{3+} ions substitute the Y^{3+} site (Bachmann et al., 2009a; Chenavas et al., 1978; Meagher, 1975; Wu et al., 2007a).

As mentioned earlier, the emission wavelength of Ce^{3+}-activated YAG is strongly dependent on the crystal field. From the viewpoint of crystal-field theory, the emission band corresponding to 5d→4f transition generally shifts to a longer wavelength by doping smaller cations into the host lattice because the crystal-field strength around the activator is increased by lattice shrinkage. The enhancement of the crystal-field strength contributes to increase the crystal-field splitting of the 5d excited level, and the energy gap between the lowest 5d excited level and 4f ground level becomes smaller; consequently, the emission bands shift to a longer wavelength. However, the emission band of YAG:Ce^{3+} is blue shifted by doping smaller Lu^{3+} into the Y^{3+} site, and Lu$_3$Al$_5$O$_{12}$:Ce^{3+} (LuAG:Ce^{3+}) shows a broad green emission with a peak at 530 nm. LuAG is now a commercially available green emission phosphor for white LEDs.

Wu et al. (2007a,b) reported a surprising emission band shift in a series of Mg$_3$Y$_{2-y}$Gd$_y$Ge$_{3-z}$Si$_z$O$_{12}$:Ce (0≤y≤2, z=0, 1) garnets with respect to
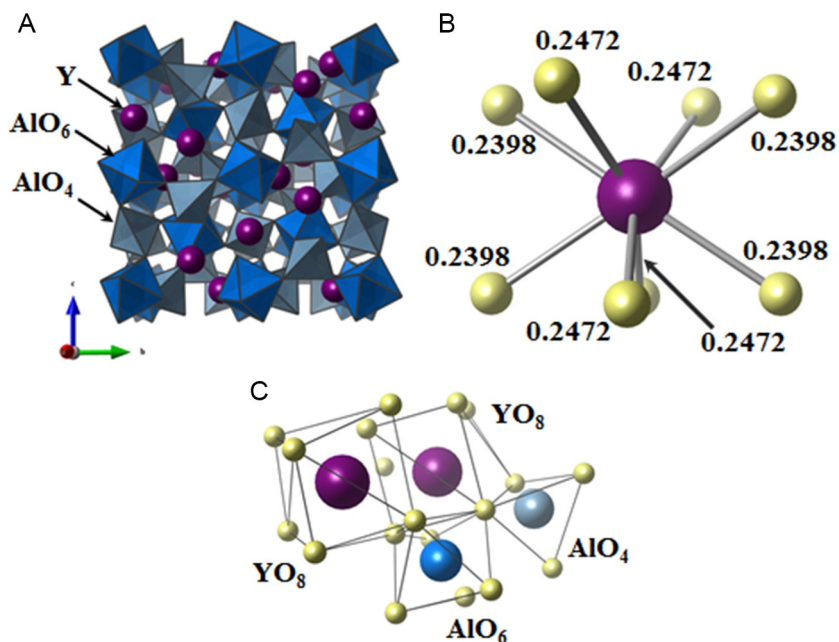
FIG. 9   The crystal structure of YAG (A), coordination environment of YO_8 polyhedron in YAG lattice (B), and schematic of oxygen coordination and interatomic distances for a portion of YAG structure (C). The unit of bond distance is nm. *Pictures were drawn based on the structure data obtained from the database (ICSD #16825).*

$YAG:Ce^{3+}$ and explained it based on the crystal structure of YAG. YAG has a cubic lattice with a space group of $Ia3d$, and the lattice constants, $a = 1.20136(9)$ nm (Chenavas et al., 1978; Meagher, 1975; Pavese et al., 1995; Xie et al., 2011) (Fig. 9A). Y^{3+} ions adopt eightfold oxygen coordination, and the YO_8 dodecahedron can be represented as a distorted cube in between a regular cube and an antiprism (Fig. 9B) (Kanke and Navrotsky, 1998). Al^{3+} occupies two independent sites within an AlO_4 tetrahedron and an AlO_6 octahedron, which share edges with the YO_8 dodecahedron, whereas they do not share any edge with themselves (Fig. 9C). When an ion substitutes the Y^{3+} site, the distance of Y–O in the lattice is strongly influenced by the ionic radius of the ion, while the Al–O distance does not change so much (Kanke and Navrotsky, 1998; Wu et al., 2007a,b). In other words, the change in the O–O distance in edges shared with another YO_8 dodecahedron is larger than when the edge is shared with the AlO_4 tetrahedron. Therefore, the distortion of the YO_8 dodecahedron is relaxed by substituting smaller ions in the Y^{3+} site, which reduces the crystal-field splitting of 5d excited level of Ce^{3+}.

In white LED applications, the effect of thermal stability of phosphors on temperature quenching is significantly important because it has great influence
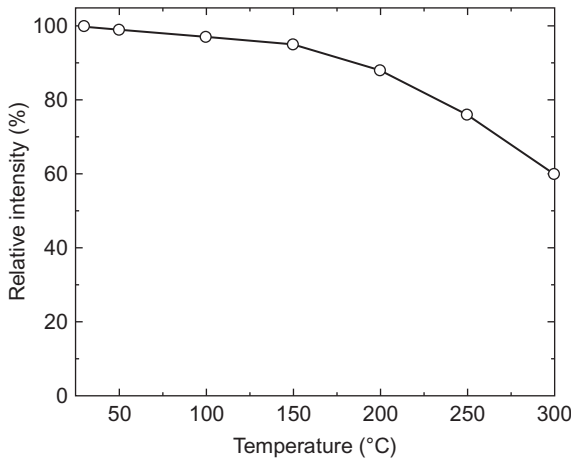
FIG. 10 Temperature dependence of the emission intensity of YAG:Ce^{3+}. *Redrawn from Chen, L., Lin, C.C., Yeh, C.W., Liu, R.S., 2010. Light converting inorganic phosphors for white light-emitting diodes. Materials 3, 2172–2195.*

on light output and CRI of white LEDs. According to a configuration-coordinate model, a nonradiative transition from an excited level to a ground level increases with increasing temperature; consequently, the emission intensity of phosphors generally decreases with increasing temperature. Fig. 10 shows the temperature dependence of the emission intensity, normalized with respect to the value at 25°C, of a YAG:Ce^{3+} phosphor. Between 25 and 150°C, the emission intensity decreases by about 13% and the emission band red shifts from 550 to 560 nm. On the other hand, the emission intensities at each temperature obtained upon cooling or heating are the same, indicating that there is little thermal degradation in YAG:Ce^{3+}. Furthermore, the emission intensity of a commercial YAG:Ce^{3+} phosphor measured at 150°C remains ≥95% of that measured at room temperature.

4.1.1.2 Sr-Rich (Ba,Sr)$_2$SiO$_4$ Phosphors

Sr-rich (Ba,Sr)$_2$SiO$_4$:Eu^{2+} (BOS or BOSE), in which the Ba:Sr ratio is about 2:8, is one of the promising yellow emission phosphors used in blue-LED-based white LEDs. The crystal structure of alkaline-earth orthosilicate, AE_2SiO$_4$ (AE = Ba, Sr, and Ca), was determined more than 30 years ago by Fields et al. (1972), Catti et al. (1983), and Barbier and Hyde (1985). AE_2SiO$_4$ (AE = Ba and Sr) have two morphologies: monoclinic (β-type) phase, which crystallizes at temperatures below 85°C; and orthorhombic (α′-type) phase, which crystallizes at temperatures above 85°C. Both β-type and α′-type phases have two kinds of cation sites which have fairly different crystallographic environments; M(I) and M(II) sites have 10-fold and ninefold oxygen coordination, respectively. AE_2SiO$_4$:Eu^{2+} (AE = Ba and Sr) phosphors have
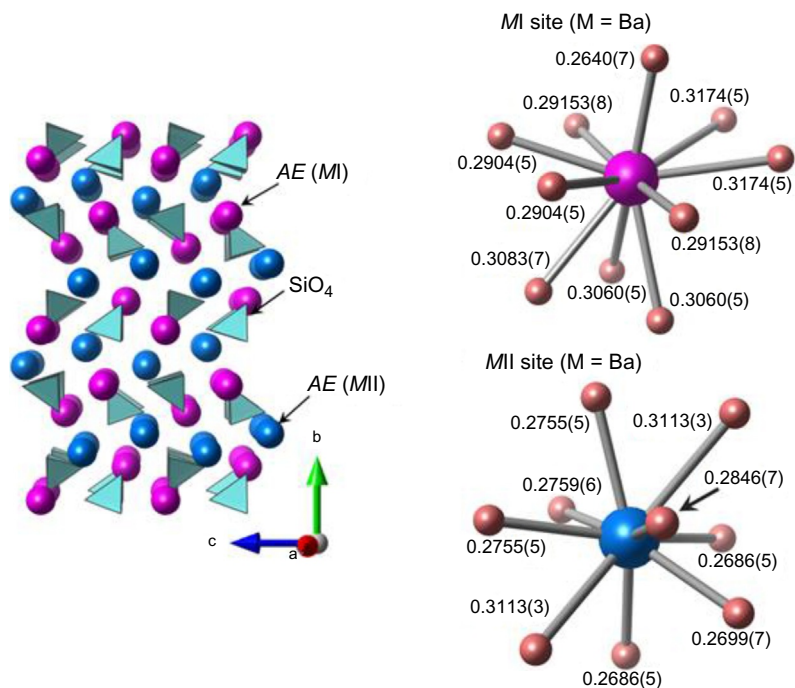
FIG. 11   Crystal structure of AE_2SiO_4 (AE = Ba, Sr, and Ca). The unit of bond distance is nm. *Pictures were drawn based on the structure data obtained from the database (ICSD #6246).*

an orthorhombic α'-type structure. The crystal structure of $(Ba,Sr)_2SiO_4$ is illustrated in Fig. 11. There are isolated SiO_4 tetrahedra. For Sr_2SiO_4, the average bond length of Sr–O is 0.2855 nm for Sr(I) and 0.2702 nm for Sr(II).

The photoluminescence properties of Eu^{2+}-activated $(Ba,Sr)_2SiO_4$ phosphors were first reported by Barry (1968) and have recently begun to receive attention again as conversion phosphors excitable by blue LEDs. The excitation and emission bands of $(Ba,Sr)_2SiO_4:Eu^{2+}$ can be tuned by controlling the Ba/Sr ratio (Barry, 1968). The Ba-rich $(Ba,Sr)_2SiO_4:Eu^{2+}$ phosphors with Ba:(Sr/Eu) ratio of about 1:1 exhibit a green emission, also available as a conversion phosphor for white LEDs, while the Sr-rich $(Ba,Sr)_2SiO_4:Eu^{2+}$ phosphors exhibit a yellow emission. Here, we mainly discuss the luminescence properties of the yellow-emitting Sr-rich $(Ba,Sr)_2SiO_4:Eu^{2+}$ phosphors. The excitation spectrum shows a broad absorption band ranging from 220 to 500 nm caused by both the CT from oxide ions to Eu^{2+} ions and the $4f^7 \rightarrow 4f^65d^1$ allowed transition of Eu^{2+} (Fig. 12). The absorption band well matches with a blue light emitted from an InGaN LED chip. The emission spectrum exhibits a broad yellow emission predominating at 575 nm.

In comparison with YAG:Ce^{3+}, Sr-rich $(Ba,Sr)_2SiO_4:Eu^{2+}$ show a higher emission intensity in the red spectral region and also have a higher CRI.
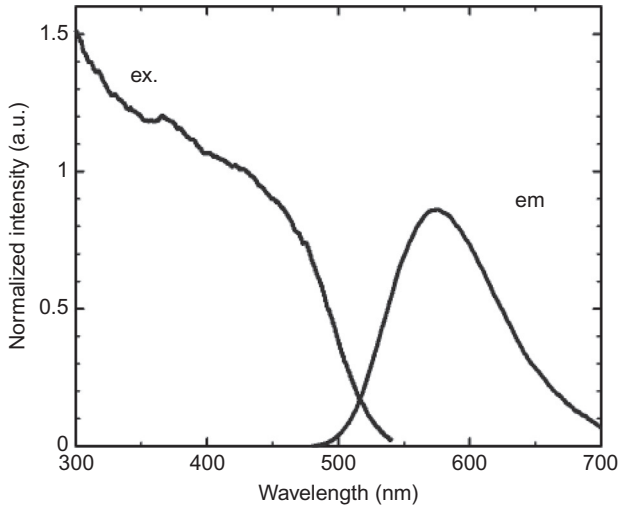
FIG. 12 Excitation and emission spectra of Sr-rich $(Ba,Sr)_2SiO_4:Eu^{2+}$. *Redrawn from Chen, L., Lin, C.C., Yeh, C.W., Liu, R.S., 2010. Light converting inorganic phosphors for white light-emitting diodes. Materials 3, 2172–2195.*
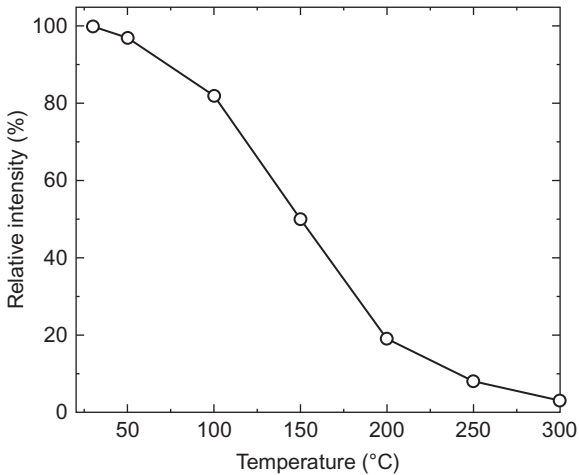
FIG. 13 Temperature dependence of emission intensity of Sr-rich $(Ba,Sr)_2SiO_4:Eu^{2+}$. *Redrawn from Chen, L., Lin, C.C., Yeh, C.W., Liu, R.S., 2010. Light converting inorganic phosphors for white light-emitting diodes. Materials 3, 2172–2195.*

However, Sr-rich $(Ba,Sr)_2SiO_4:Eu^{2+}$ have low thermal stability due to temperature quenching, this being a shortcoming of orthosilicate phosphors, ie, isolated SiO_4 tetrahedra, as a phosphor for white LEDs. The temperature dependence of the emission intensity of Sr-rich $(Ba,Sr)_2SiO_4:Eu^{2+}$ is given in Fig. 13. The emission intensity measured at 150°C is only 49% of that measured at room

temperature. In addition, it is necessary to improve the chemical stability of alkaline-earth orthosilicate phosphors since they are not so stable toward water. Further improvements are therefore necessary for these phosphors to be considered for practical applications.

4.1.1.3 $Sr_3SiO_5:Eu^{2+}$ Phosphors

In addition to alkaline-earth orthosilicate phosphors, $AE_2SiO_4:Eu^{2+}$ ($AE=$ Ca, Sr, and Ba), alkaline-earth silicate phosphors have been widely investigated and used in white LEDs owing to their excellent chemical and thermal stability, high luminescence efficiency, and low cost. Among them, $Sr_3SiO_5:Eu^{2+}$ is attracting attention as a promising candidate to replace the commercial yellow-emitting YAG:Ce^{3+} and Sr-rich $(Ba,Sr)_2SiO_4:Eu^{2+}$ phosphors (Chen et al., 2013; Jang et al., 2009a,b; Jee et al., 2006; Kang et al., 2011; Park et al., 2004, 2006; Shao et al., 2015; Sun et al., 2008; Wang et al., 2012a; Yang et al., 2014a). AE_3SiO_5 has a similar composition to that of alkaline-earth orthosilicates; however, the crystal structure of AE_3SiO_5, which was first reported by Glasser and Glasser (1965), has unique features different from those of AE_2SiO_4. Except for Ba_3SiO_5 (space group $I4/mcm$), CS_3SiO_5 ($CS=$ Ca and Sr) with space group $P4/ncc$ are built of CSO_6 octahedra and isolated SiO_4 tetrahedra, as shown in Fig. 14. One should pay attention to the existence of O^{2-} ions that do not bond to Si but are the ligands for CS. This fact may contribute to the high performance of the phosphors although
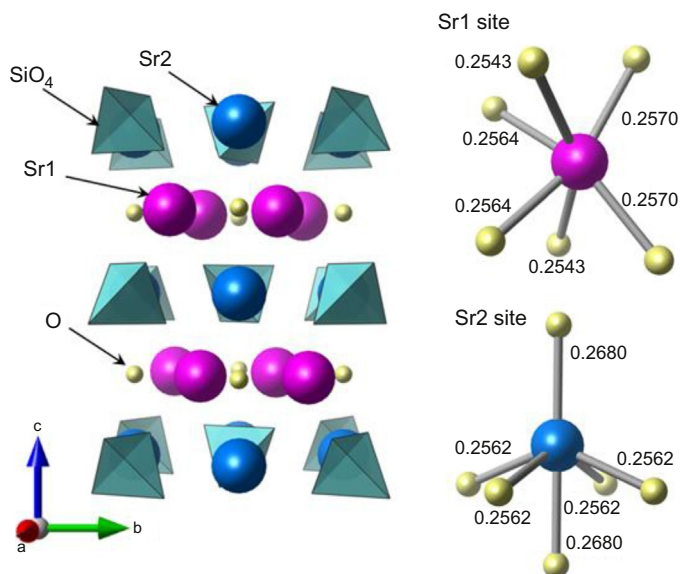
FIG. 14 Crystal structure of Sr_3SiO_5. The unit of bond distance is nm. *Pictures were drawn based on the structure data obtained from the database (ICSD #18151).*

they contain isolated SiO_4. On the other hand, Ba_3SiO_5 has extremely low chemical stability against water, lower than that of Ba_2SiO_4.

The luminescence properties of Eu^{2+}-activated AE_3SiO_5 was investigated almost 40 years ago by Blasse et al. (1968a,b). The emission band of the phosphors shifts to a longer wavelength by increasing the atomic number of the alkaline-earth element. Actually, the maximum emission wavelengths of of Eu^{2+}-activated AE_3SiO_5 are 510, 545, and 590 nm for Ca, Sr, and Ba, respectively. Furthermore, Park et al. (2004, 2006) reported that the partial substitution of Sr^{2+} in the larger Ba^{2+} sites in $Sr_3SiO_5:Eu^{2+}$ can red shift its emission. In addition, a white light LED based on a blue LED and the $(Sr,Ba)_3SiO_5:Eu^{2+}$ phosphor have a higher CRI and a lower color temperature than those of conventional white LEDs combining $YAG:Ce^{3+}$ with a blue LED. As shown in Fig. 15, the excitation spectra of $(Sr_{1-x}Ba_x)_3SiO_5:Eu^{2+}$ ($x=0$ and 0.25) consist of a broad band extending from 250 to 550 nm; the phosphors are consequently very suitable as color converters using any wavelength of excitation from a primary light source. As described earlier, the emission band of $Sr_3SiO_5:Eu^{2+}$ shifts to a longer wavelength by substituting Ba for Sr sites, and then $(Sr_{0.8}Ba_{0.2})_3SiO_5:Eu^{2+}$ exhibits a broad yellow emission with a peak at 580 nm, the tail of which covers the red region with high emission intensities. As to the red shift by Ba substitution, Park et al. (2004) pointed out the reason of it to be due to the lattice expansion along the c-axis and the lowered octahedral symmetry around Eu^{2+} sites. In addition, they also observed that the emission band was obviously red shifted by increasing the SiO_2 content in the composition, being ascribed to a larger centroid shift arising from an increase in covalency. However, on further increasing the Ba
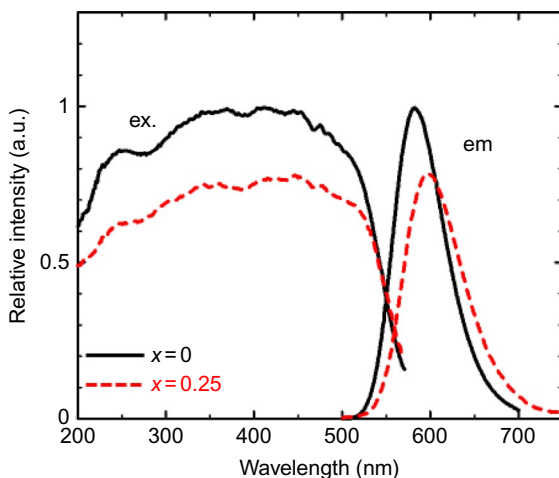
FIG. 15 Excitation and emission spectra of $(Sr_{1-x}Ba_x)_3SiO_5:Eu^{2+}$ ($x=0$ and 0.25). *Redrawn from Shao, Q., Lin, H., Dong, Y., Fu, Y., Liang, C., He, J., Jiang, J., 2015. Thermostability and photostability of $Sr_3SiO_5:Eu^{2+}$ phosphors for white LED applications. J. Solid State Chem. 225, 72–77.*
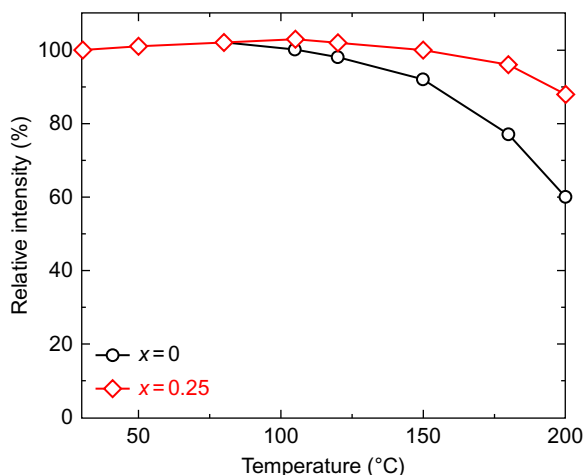
FIG. 16   Temperature-dependent emission intensity of the $(Sr_{1-x}Ba_x)_3SiO_5:Eu^{2+}$ ($x=0$ and 0.25). *Redrawn from Shao, Q., Lin, H., Dong, Y., Fu, Y., Liang, C., He, J., Jiang, J., 2015. Thermostability and photostability of $Sr_3SiO_5:Eu^{2+}$ phosphors for white LED applications. J. Solid State Chem. 225, 72–77.*

content, the emission intensity of $Sr_3SiO_5:Eu^{2+}$ decreases and its quantum yield is down to about 68% under excitation at 450 nm.

The effect of thermal stability on temperature quenching is significantly important for practical applications in white LEDs. The emission intensity of the $(Sr_{1-x}Ba_x)_3SiO_5:Eu^{2+}$ ($x=0$ and 0.2) phosphors decreases when they are heated from room temperature up to 200°C, but one can note that the thermal quenching is effectively minimized by Ba substitution (Fig. 16). The emission intensity of $Sr_3SiO_5:Eu^{2+}$ and $(Sr_{0.75}Ba_{0.25})_3SiO_5:Eu^{2+}$ at 150°C remains at 92% and 100%, respectively, relative to that at room temperature (Shao et al., 2015), showing that the phosphors are promising as a yellow-emitting materials for white LEDs.

In addition, Ce^{3+}-activated Sr_3SiO_5 phosphors have been widely investigated as phosphors for white LEDs, because of their efficient yellow emission under blue light irradiation (Jang and Jeon, 2007a,b; Jang et al., 2008, 2009a,b). Li^+-doped $Sr_3SiO_5:Ce^{3+}$ phosphors show a broad emission band covering the spectral region 465–700 nm (Jang and Jeon, 2007a). The LER of blue-LED-pumped white LEDs using this phosphor is 31.7 lm/W, which is higher than that of commercial white LEDs (15–30 lm/W); the CCT and the CRI (R_a) are 6857 K and 81, respectively (Jang and Jeon, 2007b).

4.1.1.4 $Li_2SrSiO_4:Eu^{2+}$ Phosphors

Besides alkaline-earth orthosilicate phosphors AE_2SiO_4 ($AE=$ alkaline earth), other orthosilicate materials have been widely investigated as host materials for phosphor for wihte LEDs because of their excellent chemical and thermal
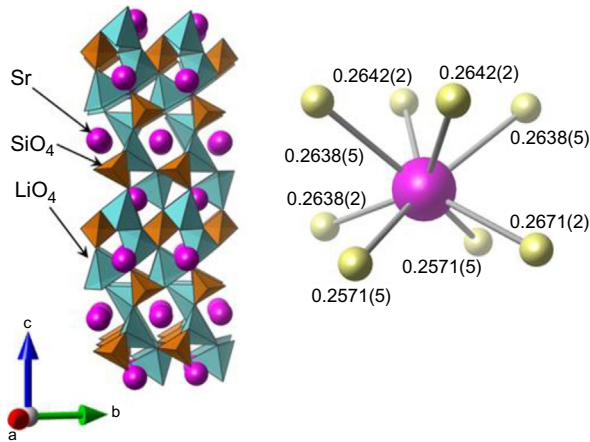
FIG. 17 Crystal structure and coordination environment of SrO_8 dodecahedron in Li_2SrSiO_4. The unit of bond distance is nm. *Pictures were drawn based on the structure data obtained from the database (ICSD #167334).*

stability. $Li_2SrSiO_4:Eu^{2+}$ is also one of the recently reported orthosilicate phosphors used in white LEDs (He et al., 2010; Kulshreshtha et al., 2009; Levshov et al., 2011; Pardha Saradhi and Varadaraju, 2006; Toda et al., 2006). Li_2SrSiO_4 has a trigonal (usually expressed by hexagonal setting) structure with space group $P3_121$, $a = 0.5030$ nm, $c = 1.2470$ nm, and $V = 0.3155$ nm^3 (Fig. 17), being isostructural with Li_2EuSiO_4 (Haferkorn and Meyer, 1998). The LiO_4 and SiO_4 tetrahedra are connected by sharing corners, forming a three-dimensional (3D) network able to accommodate Sr^{2+} with a distorted eightfold coordination (Fig. 17). The activator Eu^{2+} ions can substitute the Sr sites. The average Sr–O bond distance is 0.2633 nm. The SrO_8 dodecahedron can be represented as a distorted cube in between a regular cube and an antiprism, like in YAG:Ce^{3+} phosphors. Furthermore, the shape of the SrO_8 dodecahedron is a little closer to a regular antiprism than YO_8 in YAG:Ce^{3+}. It is expected then that inducing a lower symmetry of the Sr site in SrO_8 would result in $Li_2SrSiO_4:Eu^{2+}$ displaying longer wavelength emission compared to YAG:Ce^{3+}.

$Li_2SrSiO_4:Eu^{2+}$ is efficiently excited by near-UV and blue light and shows a reddish–yellow emission with a peak at around 570 nm (Fig. 18). The emission band is located at a longer wavelength than that of YAG:Ce^{3+} (550 nm), rather similar to that of Sr-rich $(Ba,Sr)_2SiO_4$ (575 nm). The emission intensity under excitation at 450 nm is almost the same as that of YAG:Ce^{3+}. Furthermore, the phosphor has better thermal stability with respect to temperature quenching compared with Sr-rich $(Ba,Sr)_2SiO_4$. As shown in Fig. 19, the decrease in the emission intensity of the phosphor is only a 10% and 20% at 100 and 150°C, respectively, indicating less thermal quenching.
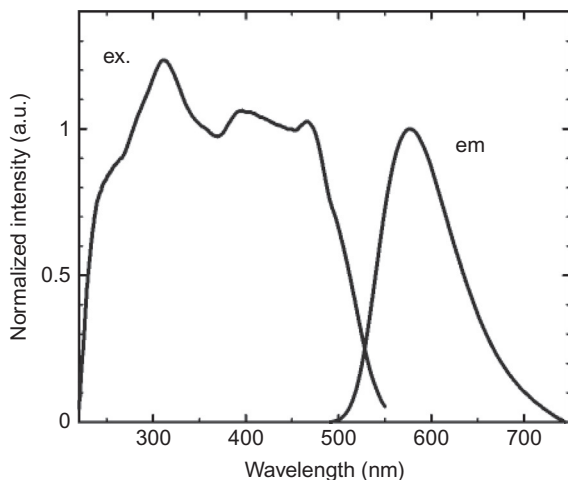
FIG. 18   Excitation and emission spectra of Li_2SrSiO_4:Eu^{2+}. *Redrawn from Toda, K., Kawakami, Y., Kousaka, S., Ito, Y., Komeno, A., Uematsu, K., Sato, M., 2006. New silicate phosphors for a white LED. IEICE Trans. Electron. E89-C, 1406–1412.*
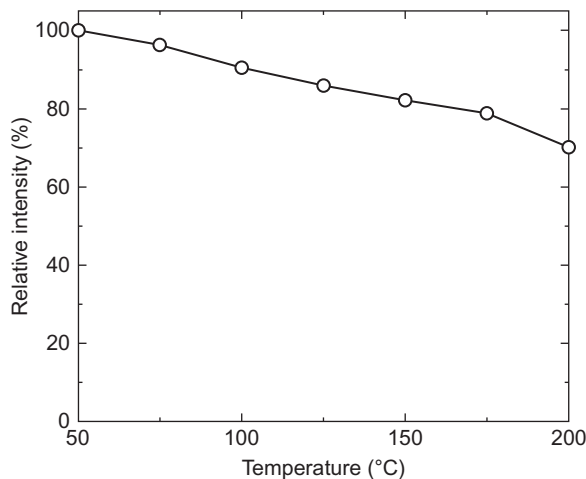
FIG. 19   Temperature dependence of the emission intensity of Li_2SrSiO_4:Eu^{2+} phosphor. *Redrawn from Toda, K., Kawakami, Y., Kousaka, S., Ito, Y., Komeno, A., Uematsu, K., Sato, M., 2006. New silicate phosphors for a white LED. IEICE Trans. Electron. E89-C, 1406–1412.*

4.1.1.5 $Ba_3Sc_4O_9$:Ce^{3+} Phosphors

Hasegawa et al. (2014) recently reported novel yellow-emitting Ce^{3+}-activated phosphors based on $Ba_3Sc_4O_9$ which crystallizes in a trigonal structure with space group $R3$ (Spitsyn et al., 1968) (Fig. 20). The structure is built up of BaO_n ($n=9$ and 12) polyhedra and ScO_6 octahedra forming
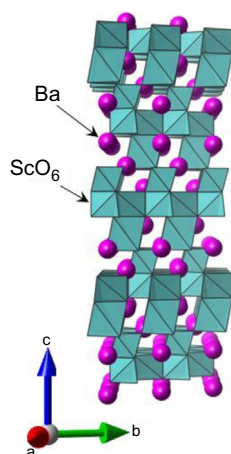
FIG. 20 Crystal structure of $Ba_3Sc_4O_9$. *Picture was drawn based on the structure data obtained from the database (ICSD #33239).*
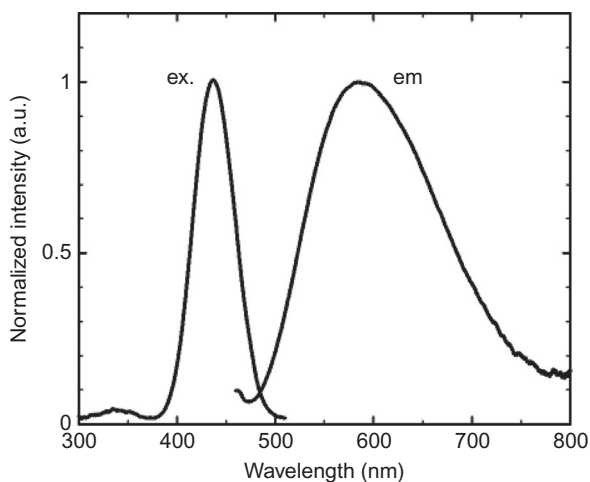
FIG. 21 Excitation and emission spectra of $Ba_3Sc_4O_9$:Ce^{3+}. *Redrawn from Hasegawa, T., Kim, S.W., Ishigaki, T., Uematsu, K., Takaba, H., Toda, K., Sato, M., 2014. Novel reddish yellow-emitting Ce^{3+}-doped $Ba_3Sc_4O_9$ phosphors for blue-light-based white LEDs. Chem. Lett. 43, 828–830.*

a 3D network, in which activator Ce^{3+} ions preferably occupy the Sc^{3+} sites. Rietveld refinement analysis, based on the structural data of $Ba_3Sc_4O_9$ (ICSD #20621) and $Ba_3Lu_4O_9$ (ICSD #38383) (ICSD, Inorganic Crystal Structure Database, 2015), confirms that the ScO_6 octahedron is slightly distorted from a regular octahedron with the distance Sc–O of 0.1739 nm.

$Ba_3(Sc_{1-x}Ce_x)_4O_9$ with $x = 0.001$ shows the highest emission intensity (Fig. 21). The excitation spectrum consists of a relatively narrow band

covering the region from near-UV to visible (400–500 nm). The emission spectrum exhibits a broad reddish–yellow band ranging from 480 to 750 nm with a peak at 583 nm under excitation at 437 nm. The emission peak wavelength of the phosphor is at longer wavelength compared to the commercial yellow-emitting YAG:Ce^{3+} phosphor (555 nm).

4.1.2   Green-Emitting Phosphors

4.1.2.1 $Ca_3Sc_2Si_3O_{12}$:Ce^{3+} Phosphors

$Ca_3Sc_2Si_3O_{12}$:Ce^{3+} (CSS:Ce^{3+}) phosphors, reported in 2007 by Shimomura, are of the garnet-type phosphors (Shimomura et al., 2007a). Ca^{2+}, Sc^{3+}, and Si^{4+} ions occupy dodecahedral, octahedral, and tetrahedral sites, respectively. The lattice parameter $a = 1.225$ nm is larger than that of YAG (1.2013 nm). In addition, Ce^{3+} ions preferably occupy the Ca^{2+} sites because the ionic radius of Ce^{3+} (0.128 nm for eightfold coordination and 0.115 nm for sixfold coordination; Shannon, 1976) is similar to that of Ca^{2+} (0.126 nm for eightfold coordination; Shannon, 1976), and much larger than that of Sc^{3+} (0.089 nm for sixfold coordination; Shannon, 1976). It is reasonable to consider that charge compensation is achieved by the formation of Ca vacancies because the formal valences of Ce and Ca ions are 3+ and 2+, respectively.

The excitation spectrum of CSS:Ce^{3+} consists of a strong broad absorption band covering the range of 380–500 nm with a peak at 455 nm (Fig. 22), which is very suitable for the color converter of a blue-LED chip as primary light
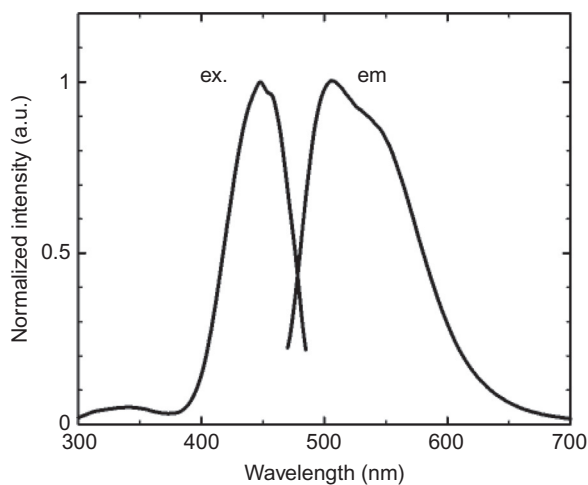
FIG. 22   Excitation and emission spectra of CSS:Ce^{3+}. *Redrawn from Shimomura, Y., Honma, T., Shigeiwa, M., Akai, T., Okamoto, K., Kijima, N., 2007. Photoluminescence and crystal structure of green-emitting $Ca_3Sc_2Si_3O_{12}$:Ce^{3+} phosphor for white light emitting diodes. J. Electrochem. Soc. 154, J35–J38.*
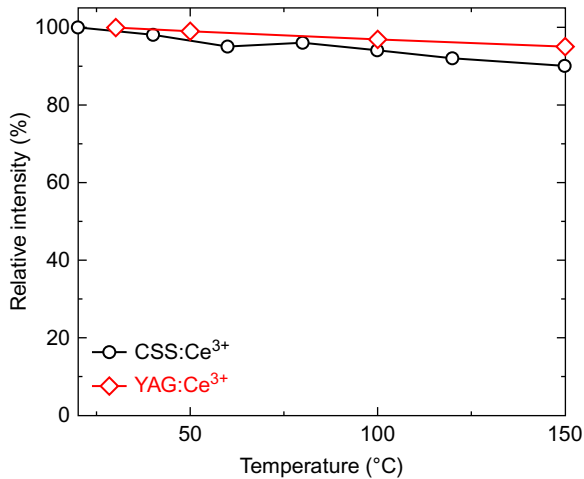
FIG. 23 Temperature dependence of emission intensity of CSS:Ce^{3+} and YAG:Ce^{3+}. *Redrawn from Shimomura, Y., Honma, T., Shigeiwa, M., Akai, T., Okamoto, K., Kijima, N., 2007a. Photoluminescence and crystal structure of green-emitting $Ca_3Sc_2Si_3O_{12}$:Ce^{3+} phosphor for white light emitting diodes. J. Electrochem. Soc. 154, J35–J38; Chen, L., Lin, C.C., Yeh, C.W., Liu, R.S., 2010a. Light converting inorganic phosphors for white light-emitting diodes. Materials 3, 2172–2195.*

source. The emission spectrum under excitation at 450 nm shows a broad green emission centered at 505 nm with a shoulder around 540 nm. The ground state of Ce^{3+} is well known, as stated before, to split into $^2F_{5/2}$ and $^2F_{7/2}$ due to spin-orbit coupling with the energy difference ~ 2000 cm^{-1} (Podhorodecki et al., 2011), surely responsible for the presence of the shoulder.

Fig. 23 shows the temperature dependence of the emission intensity of CSS:Ce^{3+}. For comparison, the data of YAG:Ce^{3+} are also plotted in Fig. 23. Phosphors used for white LEDs are required to exhibit enough luminescence up to 150°C. The emission intensity at 150°C of CSS:Ce^{3+} decreases to 92% of that at 25°C, which is higher compared to YAG:Ce^{3+} (87%). Thus, the phosphor has an excellent thermal stability with respect to temperature quenching and is a promising candidate as green-emitting phosphor for white LEDs.

4.1.2.2 CaSc$_2$O$_4$:Ce^{3+} Phosphors

Ce^{3+}-activated $CaSc_2O_4$ phosphors have been recently studied by Shimomura et al. (2007b). $CaSc_2O_4$ has a calcium ferrite ($CaFe_2O_4$) type orthorhombic structure with space group *Pnam* (no. 62), $a = 0.9453$ nm, $b = 1.1123$ nm, $c = 0.3141$ nm, and $V = 0.3303$ nm^3. The crystal structure of $CaSc_2O_4$ is composed of CaO_8 dodecahedra and ScO_6 octahedra, as shown in Fig. 24,
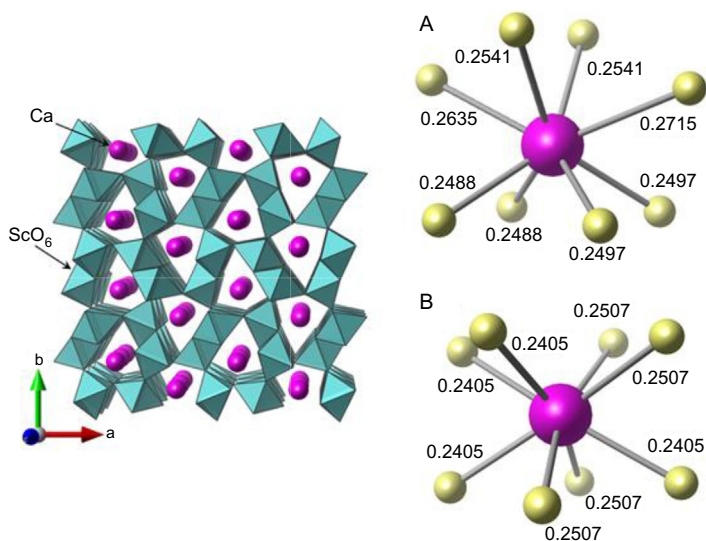
FIG. 24 Crystal structure of $CaSc_2O_4$, and coordination environment of CaO_8 in (A) $CaSc_2O_4$ and (B) $Ca_3Sc_2Si_3O_{12}$. The unit of bond distance is nm. *Pictures were drawn based on the structure data obtained from the database (ICSD #26074 ($CaSc_2O_4$), #27389 ($Ca_3Sc_2Si_3O_{12}$)).*

in which part of the Ca^{2+} sites are substituted by Ce^{3+} ions. In addition, the coordination environment of CaO_8 is similar to that in $Ca_3Sc_2Si_3O_{12}:Ce^{3+}$. The average Ca–O bond distance in CaO_8 is 0.2513 nm, which is longer than that in CaO_8 of $Ca_3Sc_2Si_3O_{12}$ (0.2461 nm).

$CaSc_2O_4:Ce^{3+}$ also shows a strong broad absorption band in the blue region and exhibits a broad green emission band with a peak at 515 nm (Fig. 25), which is a little red shifted compared to $Ca_3Sc_2Si_3O_{12}:Ce^{3+}$ (505 nm). Although the emission efficiency of $CaSc_2O_4:Ce^{3+}$ is lower than that of $Ca_3Sc_2Si_3O_{12}:Ce^{3+}$, it is greater than that of a commercial yellow-emitting YAG:Ce^{3+} phosphor (P46). Furthermore, the emission intensity at 100°C is 80% of that at 25°C. According to Shimomura et al. report, a white LED consisting of a blue InGaN LED, a red-emitting phosphor ($CaAlSiN_3:Eu^{2+}$) and a green-emitting $CaSc_2O_4:Ce^{3+}$ phosphor shows a high-color-rendering white light with CIE color coordinates of $x = 0.335$ and $y = 0.357$. Average R_a is 95, which is higher compared with a white LED consisting of a $Ca_3Sc_2Si_3O_{12}:Ce^{3+}$ phosphor instead of $CaSc_2O_4:Ce^{3+}$ ($R_a = 92$; Shimomura et al., 2007b). Thus, $CaSc_2O_4$: Ce^{3+} is a more suitable phosphor than $Ca_3Sc_2Si_3O_{12}:Ce^{3+}$ for application as a color-conversion material generating green light in white LEDs.

The emission band of the Ce^{3+}-activated phosphors is generally shifted to a longer wavelength by increasing the Ce(Y)–O bond distance because a longer bond distance usually generates a smaller crystal-field splitting of the 5d excited states, resulting in a shorter wavelength emission. The average Ca–O bond distance in $CaSc_2O_4$ is longer than that in $Ca_3Sc_2Si_3O_{12}$, as mentioned
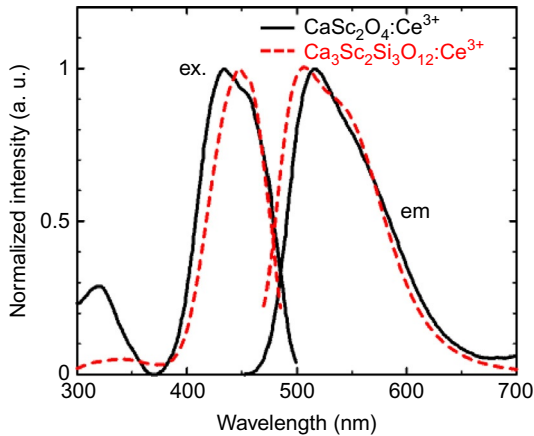
FIG. 25 Excitation and emission spectra of $CaSc_2O_4:Ce^{3+}$ and $Ca_3Sc_2Si_3O_{12}:Ce^{3+}$. *Redrawn from Shimomura, Y., Honma, T., Shigeiwa, M., Akai, T., Okamoto, K., Kijima, N., 2007. Photoluminescence and crystal structure of green-emitting $Ca_3Sc_2Si_3O_{12}:Ce^{3+}$ phosphor for white light emitting diodes. J. Electrochem. Soc. 154, J35–J38; Shimomura, Y., Kurushima, T., Kijima, N., 2007. Photoluminescence and crystal structure of green-emitting phosphor $CaSc_2O_4:Ce^{3+}$. J. Electrochem. Soc. 154, J234–J238.*

before, and however, the emission band of $CaSc_2O_4:Ce^{3+}$ is located at a slightly longer wavelength (Henderson and Imbush, 1989; Tamaki and Murazaki, 2007). Such a contradiction is probably explained by considering that CaO_8 in $CaSc_2O_4$ is somewhat more distorted than that of $Ca_3Sc_2Si_3O_{12}$. Namely, CaO_8 in $CaSc_2O_4$ is close to regular antiprism, which usually results in a strong interaction between the 5d and 2p electrons of O^{2-}. The strong interaction contributes to enhance the crystal-field strength around Ce^{3+}; consequently, causing the emission band shifting to longer wavelength.

4.1.2.3 $Ba_2MgSi_2O_7:Eu^{2+}$ Phosphors

Recently, Eu^{2+}-activated $AE_2MgSi_2O_7$ (AE = Ca, Sr, and Ba) phosphors have been widely investigated as a phosphor for white LEDs and as long-lasting phosphors (Aitasalo et al., 2007; Gong et al., 2009; Kim et al., 2012; Tam et al., 2014; Wu et al., 2011). Here, we mainly discuss the luminescence behavior of $Ba_2MgSi_2O_7:Eu^{2+}$ that is also expected to be a suitable candidate as a green-emitting phosphor for white LEDs.

The crystal structure of $Ba_2MgSi_2O_7$ was first reported by Shimizu et al. on the basis of a single crystal X-ray investigation (Lin et al., 2003; Shimizu et al., 1995). The structure is a tetragonal akermanite-type structure with space group $P\bar{4}2_1m$. However, the powder X-ray diffraction (XRD) pattern of the Eu^{2+}-activated $Ba_2MgSi_2O_7$ phosphor was not identical to the reported tetragonal structure (Toda et al., 2006). Fig. 26 shows a comparison of the powder pattern with the pattern simulated from single crystal data. The
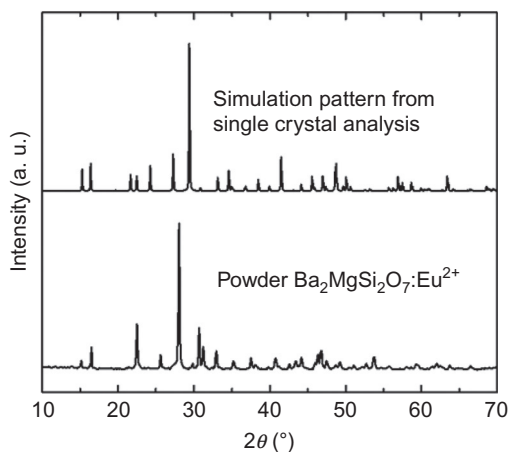
FIG. 26   XRD patterns of powder and single crystal $Ba_2MgSi_2O_7:Eu^{2+}$. *Redrawn from Toda, K., Kawakami, Y., Kousaka, S., Ito, Y., Komeno, A., Uematsu, K., Sato, M., 2006. New silicate phosphors for a white LED. IEICE Trans. Electron. E89-C, 1406–1412; Komeno, A., Uematsu, K., Toda, K., Sato, M., 2006. VUV properties of Eu-doped alkaline earth magnesium silicate. J. Alloy Compd. 408–412, 871–874.*
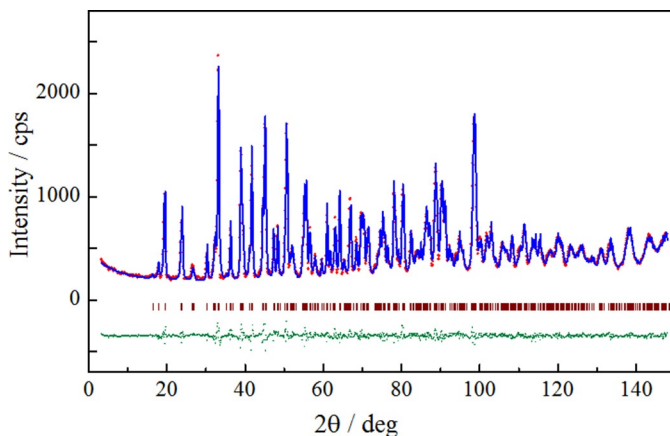
FIG. 27   Pattern fitting of the powder neutron diffraction of $Ba_2MgSi_2O_7:Eu^{2+}$. *Redrawn from Toda, K., Kawakami, Y., Kousaka, S., Ito, Y., Komeno, A., Uematsu, K., Sato, M., 2006. New silicate phosphors for a white LED. IEICE Trans. Electron. E89-C, 1406–1412; Komeno, A., Uematsu, K., Toda, K., Sato, M., 2006. VUV properties of Eu-doped alkaline earth magnesium silicate. J. Alloy Compd. 408–412, 871–874.*

pattern fitting figure calculated from the Rietveld refinement of powder neutron diffraction data of $Ba_2MgSi_2O_7$ is shown in Fig. 27, and the refined crystallographic data are summarized in Table 1. Indexing of the XRD patterns of $Ba_2MgSi_2O_7:Eu^{2+}$ certainly indicates a monoclinic symmetry with space group $C2/c$, $a = 0.8426$ nm, $b = 1.0726$ nm, $c = 0.8449$ nm, and

TABLE 1 Crystallographic Data of $Ba_2MgSi_2O_7$ (Komeno et al., 2006)

Space Group			$C2/c$			R_{wp}	5.65%
a (nm)			0.8425 (8)			R_p	4.34%
b (nm)			1.0732 (8)			R_R	9.84%
c (nm)			0.8454 (8)			R_e	4.57%
β (°)			110.723 (5)			S	1.23
Atoms	**Site**	**g**	**x**	**y**	**z**	**B (nm²)**	
Atomic parameters							
Ba1	8f	1	0.272(5)	0.044(1)	0.476(1)	0.0084(4)	
Mg1	4e	1	0.0	0.744(1)	0.25	0.009(2)	
Si1	8f	1	0.111(1)	0.282(5)	0.133(1)	0.007(1)	
O1	8f	1	0.100(1)	0.142(1)	0.120(2)	0.015(3)	
O2	8f	1	0.303(1)	0.342(1)	0.235(1)	0.003(1)	
O3	8f	1	0.479(1)	0.149(1)	0.042(1)	0.001(4)	
O4	4e	1	0.0	0.334(1)	0.25	0.009(4)	
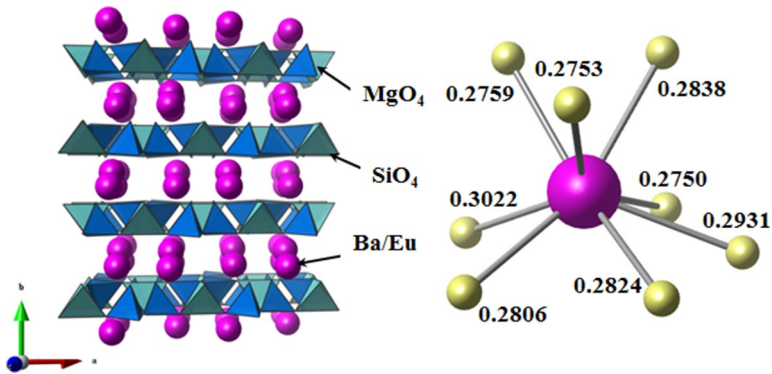
FIG. 28 Crystal structure and coordination environment of Ba/EuO_8 in $Ba_2MgSi_2O_7$. The unit of bond distance is nm. *Pictures were drawn based on the structure data obtained from the database (ICSD #154589).*

$\beta = 110.763°$ (Toda et al., 2006). The crystal structure of $Ba_2MgSi_2O_7{:}Eu^{2+}$ reported by Toda et al. is shown in Fig. 28. The structure has a layered structure, in which the Ba^{2+}/Eu^{2+} ions are separated by SiO_4 and MgO_4 tetrahedra layers perpendicular to b-axis. In the tetragonal $Ba_2MgSi_2O_7$ structure, Ba^{2+} ions have eightfold oxygen coordination in a centrosymmetric site.
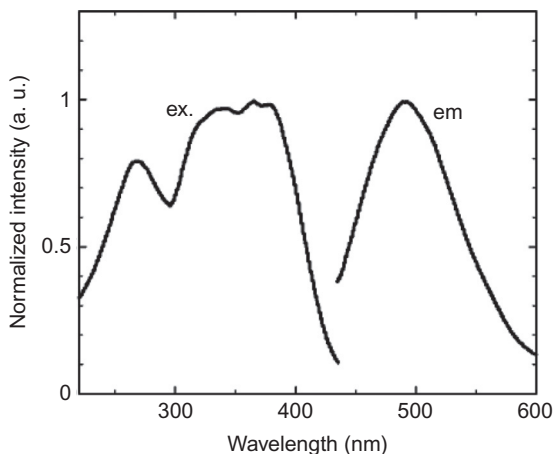
FIG. 29 Excitation and emission spectra of $Ba_2MgSi_2O_7$:Eu^{2+}. *Redrawn from Toda, K., Kawakami, Y., Kousaka, S., Ito, Y., Komeno, A., Uematsu, K., Sato, M., 2006. New silicate phosphors for a white LED. IEICE Trans. Electron. E89-C, 1406–1412; Komeno, A., Uematsu, K., Toda, K., Sato, M., 2006. VUV properties of Eu-doped alkaline earth magnesium silicate. J. Alloy Compd. 408–412, 871–874.*

On the other hand, the Ba^{2+}/Eu^{2+} ions in the monoclinic structure have also eightfold oxygen coordination, but a Ba/EuO$_8$ dodecahedron is much distorted with a noncentrosymmetric site as shown in Fig. 28. The average Ba/Eu–O bond distance in the monoclinic structure is 0.2854 nm, a relatively large value.

$Ba_2MgSi_2O_7$:Eu^{2+} has a broad absorption band ranging from UV (about 300 nm) to blue (about 430 nm) (Fig. 29). The phosphor is, therefore, able to efficiently absorb a wide range of wavelengths from UV to near-UV, violet, and blue, and it may be used as an excitation source for other phosphors. In addition, $Ba_2MgSi_2O_7$:Eu^{2+} has broad emission spectrum in the green from 450 nm to 600 nm. Application of $Ba_2MgSi_2O_7$:Eu^{2+} as a green phosphor for white LEDs can be expected, leading to a white light with a high CRI. The emission intensities at 100 and 150°C are 85% and 75% of that at 25°C, respectively.

4.1.2.4 $Ba_9Sc_2Si_6O_{24}$:Eu^{2+} Phosphor

The crystal structure of $Ba_9Sc_2Si_6O_{24}$ was first determined by Wang et al. (1994) from single crystal XRD. $Ba_9Sc_2Si_6O_{24}$ has a rhombohedral structure with space group of $R\overline{3}$, $a = 0.9872$ nm, and $c = 2.1937$ nm (Fig. 30). The structure is built of ScO$_6$ octahedra and SiO$_4$ tetrahedra corner sharing each other. Ba^{2+} ions are in three independent sites, BaO$_9$ (M1), BaO$_{10}$ (M2), and BaO$_{12}$ (M3) polyhedra. The average Ba–O bond distances are 0.2899,
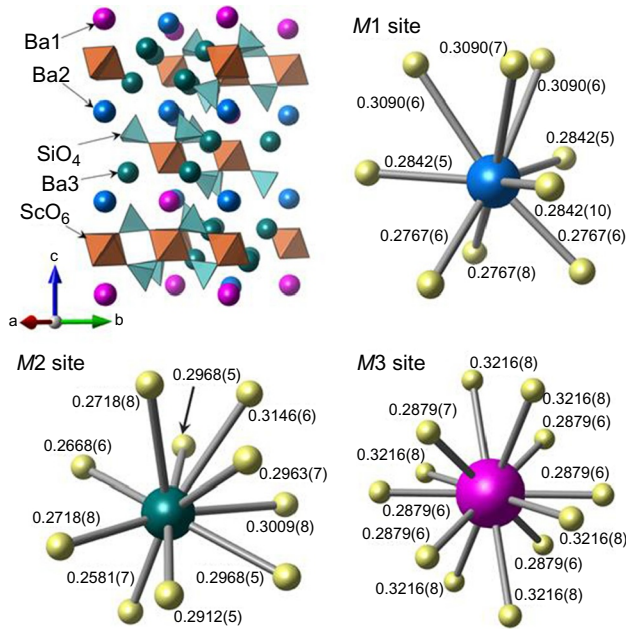
FIG. 30 Crystal structure of $Ba_9Sc_2(SiO_4)_6$. The unit of bond distance is nm. *Pictures were drawn based on the structure data obtained from the database (ICSD #75175).*

0.2903, and 0.3047 nm for $M1$, $M2$, and $M3$, respectively. The $M1$ and $M3$ sites are located between SiO_4–ScO_6–SiO_4 bilayers, and the $M2$ site is surrounded by ScO_6 and SiO_4.

The luminescence properties of $Ba_9Sc_2Si_6O_{24}$:Eu^{2+} (Fig. 31) were first reported by Toda et al. (2006) and then in more details by Nakano et al. (2009). The excitation spectrum consists of three broad bands ranging from 280 to 480 nm with maxima at around 340, 380, and 440 nm. A weak absorption band at 340 nm corresponds to the CT transition from the oxygen 2p orbital (usually forming the valence band) to the 5d orbital of Eu^{2+}, and the two strong and broad bands at 380 and 440 nm belong to allowed 4f–5d transitions of Eu^{2+}. Under 440 nm excitation, $Ba_9Sc_2Si_6O_{24}$:Eu^{2+} exhibits a broad green emission peaking at around 510 nm. The emission intensity of the phosphor is comparable to that of a commercial YAG:Ce^{3+} phosphor. At 100°C, the emission intensity is 75% of that at 25°C (Toda et al., 2006). The internal quantum efficiency under excitation at 350 nm is 47% (Bian et al. 2012).

4.1.3 Red-Emitting Phosphors
4.1.3.1 Ca_2SiO_4:Eu^{2+} Phosphors
In the series of the alkaline-earth orthosilicate phosphors AE_2SiO_4 (AE = alkaline earth), Ca_2SiO_4:Eu^{2+} has been recently reported as a red-emitting phosphor
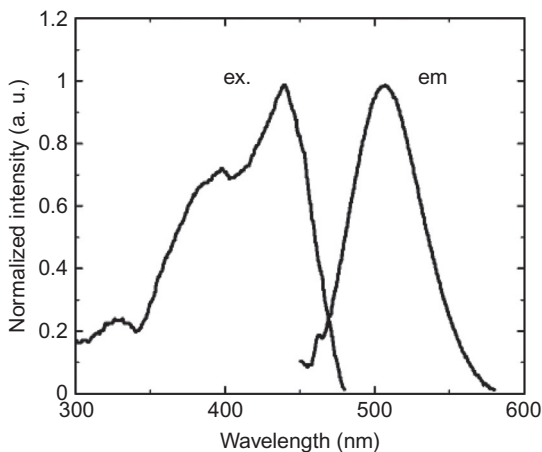
FIG. 31 Photoluminescence excitation and emission spectra of the $Ba_9Sc_2Si_6O_{24}$:Eu^{2+}. *Redrawn from Nakano, T., Kawakami, Y., Uematsu, K., Ishigaki, T., Toda, K., Sato, M., 2009. Novel Ba–Sc–Si–oxide and oxynitride phosphors for white LED. J. Lumin. 129, 1654–1657.*

for white LEDs by Kakihana's group (Sato et al., 2014; Tezuka et al., 2013). Ca_2SiO_4:Eu^{2+} is well known as a green-emitting phosphor excitable with near-UV light (Choi and Hong, 2009; Kim et al., 2005a,b; Luo et al., 2012). Ca_2SiO_4 has five different morphologies, γ-phase, β-phase, α'_L-phase, α'_H-phase, and α-phase (Smith et al., 1965; Yamnova et al., 2011), as summarized in Table 2. Among them, the γ-Ca_2SiO_4 phase with space group *Pcmn* is generally stable at room temperature, and the metastable β-phase can be stabilized at room temperature with addition of various dopants (Kim and Hong, 2004; Lai et al., 1992). Therefore, almost all of the reported Eu^{2+}-activated Ca_2SiO_4 phosphors have a stabilized monoclinic β-phase structure with space group $P2_1/n$. The phosphors show a broad green emission band with a peak at around 502 nm (Choi and Hong, 2009; Luo et al., 2012). In the meantime, Kakihana's group recently reported that the emission band of Eu^{2+}-activated Ca_2SiO_4 shifts to a longer wavelength upon increasing the Eu^{2+} content (Sato et al., 2014). $Ca_{2-x}Eu_xSiO_4$ undergoes a phase transformation from β-phase to α'_L-phase when the Eu^{2+} content is in the range between $x=0.1$ and 0.2. Fig. 32 shows the excitation and emission spectra of the α'_L-phase phosphor with $x=0.2$ and 0.8. The phosphor with $x=0.2$ exhibits two broad green–yellow emission bands with maxima at 560 and 620 nm under excitation at 450 nm. Furthermore, the emission bands shift to longer wavelengths with increasing Eu^{2+} content. The phosphor with $x=0.8$ has a broad red emission band with a peak at 650 nm, which is similar to that of $CaAlSiN_3$:Eu^{2+}. The emission band shift from green–yellow to deep-red is dependent on which sites the emission ion prefers among several acceptable sites. It is well known that alkaline-earth orthosilicate phosphors AE_2SiO_4 have two independent

TABLE 2 Structure Data of Polymorphs of Ca_2SiO_4

	Crystal System	Space Group	Multiplicity of Ca Sites	References
γ-Ca_2SiO_4	Orthorhombic	$Pbnm$	2	della Giusta et al. (1990)
β-Ca_2SiO_4	Monoclinic	$P2_1/n$	2	Toraya and Yamazaki (2002)
α'_L-Ca_2SiO_4	Orthorhombic	$Pna2_1$	6	Mumme et al. (1996)
α'_H-Ca_2SiO_4	Orthorhombic	$Pnma$	2	Mumme et al. (1995)
α-Ca_2SiO_4	Hexagonal	$P\overline{3}m$	3	Eysel and Hahn (1970)
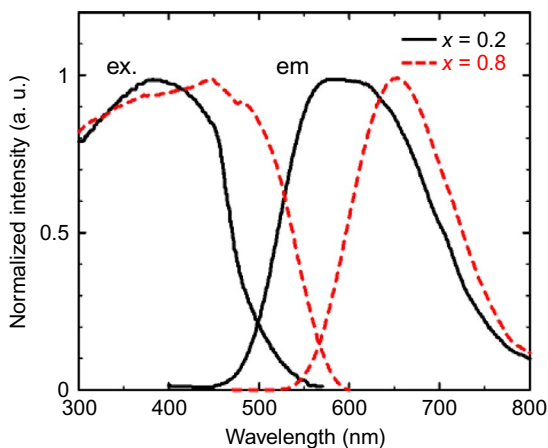
FIG. 32 Excitation and emission spectra of α'_L-$(Ca_{1-x}Eu_x)_2SiO_4$ ($x=0.2$ and 0.8). *Redrawn from Sato, Y., Kato, H., Kobayashi, M., Masaki, T., Yoon, D. H., Kakihana, M., 2014. Tailoring of deep-red luminescence in Ca_2SiO_4:Eu^{2+}. Angew. Chem. Int. Ed. 53, 7756–7759.*

AE sites with different coordination numbers. For instance for $AE=$ Ca, there is a Ca1 site with AEO_{10} and a Ca2 site with AEO_9. In this case, the Eu^{2+} ions preferentially occupy initially the Ca1 sites, and begin to occupy the Ca2 sites when the Eu^{2+} concentration exceeds a critical value, consequently, resulting in shifting the emission band to longer wavelength. The method of customizing the luminescence color by controlling the site selection of the emitting ion is known as crystal-site engineering approach (Noguchi et al., 1996).

4.1.3.2   Olivine-Type NaMgPO$_4$:Eu^{2+} Phosphors

Phosphate compounds have also been considered as excellent host materials of phosphors for white LEDs due to their low material cost, excellent thermal and hydrolytic stabilities, and charge stabilization (Tang et al., 2007; Wu and Wang, 2007; Wu et al., 2006, 2007a,b). Recently, a red-emitting phosphate phosphor excitable by a blue light, olivine-type NaMgPO$_4$:Eu^{2+}, was reported by Kim et al. (2013a). NaMgPO$_4$ has an orthorhombic structure with space group *Pnma*, $a = 1.03701(8)$ nm, $b = 0.61729(5)$ nm, $c = 0.49347(4)$ nm, and $V = 0.31284(4)$ nm^3. The structure is built up of PO$_4$ tetrahedra and MgO$_6$ octahedra that connect each other by corner sharing and edge sharing, forming a 3D framework defining channels along the *b*-axis where Na$^+$ ions can be located, as illustrated in Fig. 33. From the viewpoint of ionic radius, it is reasonable to take into account that Eu^{2+} ions substitute the Na$^+$ sites in NaMgPO$_4$:Eu^{2+}. The average Na–O bond distance in NaO$_6$ is 0.2360 nm.

Fig. 34 shows the excitation and emission spectra of (Na$_{0.975}$Eu$_{0.025}$)MgPO$_4$ (Kim et al., 2013a). The phosphor exhibits a strong broad red emission band centered at 628 nm under excitation at 450 nm. In addition, the excitation spectrum consists of a broad band covering the region from UV to visible, indicating that the phosphor is suitable as wavelength converter excited by any wavelength in this range. The internal quantum efficiency of NaMgPO$_4$:Eu^{2+} at an excitation wavelength of 450 nm is 81%. The phosphor also has excellent thermal stability with respect to temperature quenching as shown in Fig. 35 where the emission intensities are normalized with respect to the value at 25°C. With increasing temperature up to 150°C, the emission intensity of NaMgPO$_4$:Eu^{2+} decreases to 86%.

FIG. 33 Crystal structure of olivine-type NaMgPO$_4$. The unit of bond distance is nm. *Pictures were drawn based on the structural data obtained from Kim, S.W., Hasegawa, T., Ishigaki, T., Uematsu, K., Toda, K., Sato, M., 2013. Efficient red emission of blue-light excitable new structure type NaMgPO$_4$:Eu^{2+} phosphor. ECS Solid State Lett. 2, R49–R51.*
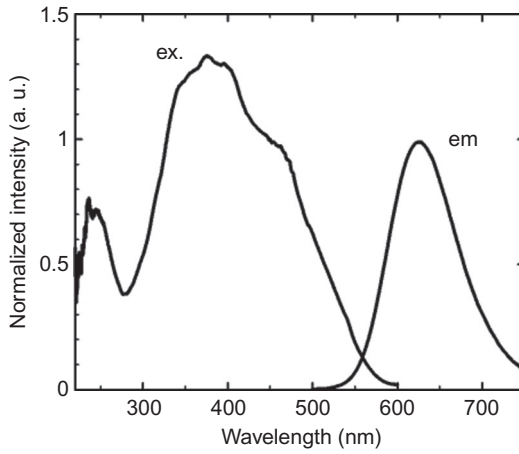
FIG. 34 Excitation and emission spectra of olivine-type NaMgPO$_4$:Eu^{2+}. *Redrawn from Kim, S.W., Hasegawa, T., Ishigaki, T., Uematsu, K., Toda, K., Sato, M., 2013a. Efficient red emission of blue-light excitable new structure type NaMgPO$_4$:Eu^{2+} phosphor. ECS Solid State Lett. 2, R49–R51.*
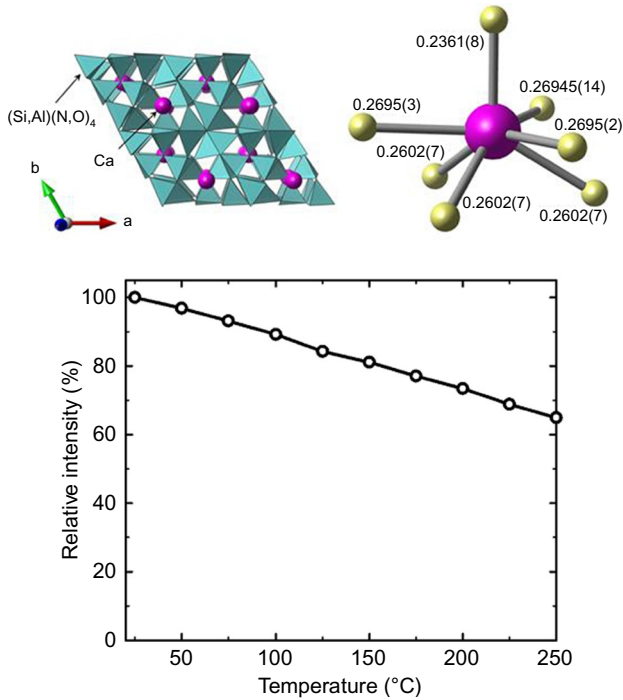
FIG. 35 Temperature dependence of emission intensity of olivine-type NaMgPO$_4$:Eu^{2+}. *Redrawn from Kim, S.W., Hasegawa, T., Ishigaki, T., Uematsu, K., Toda, K., Sato, M., 2013a. Efficient red emission of blue-light excitable new structure type NaMgPO$_4$:Eu^{2+} phosphor. ECS Solid State Lett. 2, R49–R51.*

4.2   (Oxy)nitrides

There are little practical phosphors among nitride and oxynitride materials except those for LED phosphors. Red-emitting ability of excitation and emission wavelengths is sometimes desired in order to change their color chromaticity. This can be achieved by partially or fully substituting nitride ions for oxide ions, bringing about an increase in covalent bond character. (Oxy)nitride phosphors can be classified into two groups, nitridosilicates and nitridoaluminosilicates, the frameworks of which are composed of $Si(N,O)_4$ and $Al(N,O)_4$ tetrahedral units, respectively. Many nitrides are easily hydrolyzed by air moisture and, therefore, chemically stable nitrides and oxynitrides are rare.

4.2.1   Yellow-Emitting Phosphors

4.2.1.1   Ca-α-SiAlON:Eu^{2+} Phosphors

The name SiAlON is given to ceramics composed of the elements Si, Al, O, and N. They have two morphologies, α- and β-SiAlONs, which are solid solutions based upon structure modifications of α- and β-Si_3N_4, respectively (Xie and Hirosaki, 2007; Xie et al., 2010). The general formula of α-SiAlON can be given as $M_xSi_{12-(m+n)}Al_{m+n}O_nN_{16-n}$ ($x=m/v$, where v is the electric valence of metal M) and β-SiAlON can be described by $Si_{6-z}Al_zO_zN_{8-z}$. Both materials have turned out as excellent host materials for Eu^{2+}- or Ce^{3+}-activated phosphors for white LEDs with high luminescence efficiency under blue light excitation (Gan et al., 2013; Xie and Hirosaki, 2007; Xie et al., 2010). Among them, Eu^{2+}-activated Ca-α-SiAlON is one of the yellow-emitting phosphors used in white LEDs (Xie et al., 2004a). The crystal structure of Ca-α-SiAlON with space group $P3_1c$ is shown in Fig. 36. Although it is similar to that of α-Si_3N_4, the unit cell volume is much larger owing to the incorporation of Al, O, and Ca (Jack and Wilson, 1972; Petzow and Herrmann, 2002). Namely, the structure of Ca-α-SiAlON is built up of $(Si,Al)N_4$ tetrahedra to form a 3D framework with corner sharing of tetrahedra. Ca^{2+} ions occupy interstitial sites and have sevenfold anion (N/O) coordination (Izumi et al., 1982) and the average Ca/Eu–N bond distance is 0.2612 nm.
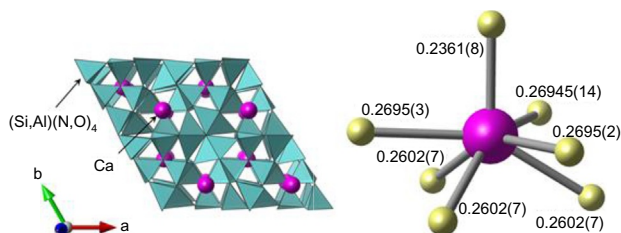
FIG. 36   Crystal structure of Ca-α-SiAlON. The unit of bond distance is nm. *Pictures were drawn based on the structure data obtained from the database (ICSD #163203).*
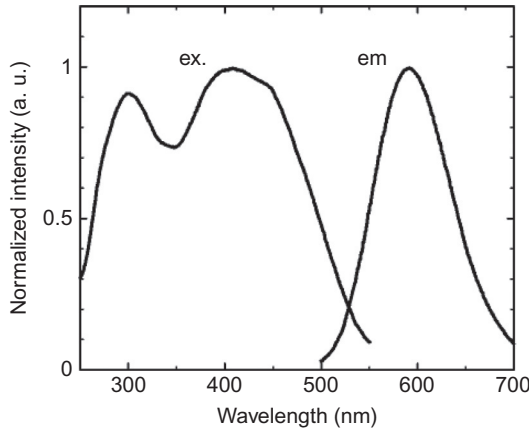
FIG. 37 Excitation and emission spectra of Eu^{2+}-activated Ca-α-SiAlON phosphor. *Redrawn from Xie, R.J., Hirosaki, N., Sakuma, K., Yamamoto, Y., Mitomo, M., 2004. Eu^{2+}-doped Ca-alpha-SiAlON: a yellow phosphor for white light-emitting diodes. Appl. Phys. Lett. 84, 5404.*

The excitation spectrum of Eu^{2+}-activated Ca-α-SiAlON consists of two broad bands covering the region from UV to visible (Fig. 37), indicating that the phosphor is suitable as color converter excitable by any wavelength in this range emitted from a primary light source. The phosphor has a broad yellow emission band ranging from 500 to 700 nm with a maximum at 581 nm, which is longer than that of YAG:Ce^{3+}, meaning that high CRI can be produced by combining Eu^{2+}-activated Ca-α-SiAlON phosphor with a blue-LED chip. In addition, much efforts have recently been devoted to improve the emission color of this phosphor by substituting Ca^{2+} for other metal ions such as Li^+, Mg^{2+}, and Y^{3+}. The position of the emission band can be adjusted by tailoring the composition of the host or by changing the values of *m* and *n* in the chemical formula (Sakuma et al., 2007a,b; Xie et al., 2006a,b). Furthermore, Eu^{2+}-activated Ca-α-SiAlON has an excellent thermal stability against temperature quenching, and the emission intensity of the phosphor at 150°C (~90% of the initial value at 25°C) is much higher than that of YAG:Ce^{3+} phosphor (~87% of the initial value at 25°C) as shown in Fig. 38. This is the typical and the most important feature of (oxy)nitride phosphors.

4.2.1.2   CaAlSiN$_3$:Ce^{3+} Phosphors

CaAlSiN$_3$ is a famous host material used in white LEDs. In particular, Eu^{2+}-activated CaAlSiN$_3$ is one of the best commercial red-emitting phosphors. Detailed discussion of its photoluminescence properties will be given in Section 4.2.1.3. Here, we mainly discuss the Ce^{3+}-activated CaAlSiN$_3$ phosphors emitting yellow light. CaAlSiN$_3$ has an orthorhombic structure with space group *Cmc*2$_1$ (Fig. 39), isostructural with ASi_2N_3 (A=Li and Na)
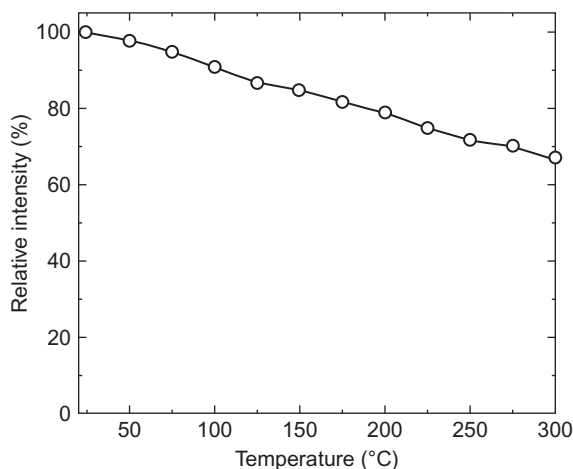
FIG. 38 Temperature dependence of emission intensity of the Eu^{2+}-activated Ca-α-SiAlON. *Redrawn from Xie, R.J., Hirosaki, N., Sakuma, K., Yamamoto, Y., Mitomo, M., 2004. Eu^{2+}-doped Ca-alpha-SiAlON: a yellow phosphor for white light-emitting diodes. Appl. Phys. Lett. 84, 5404.*
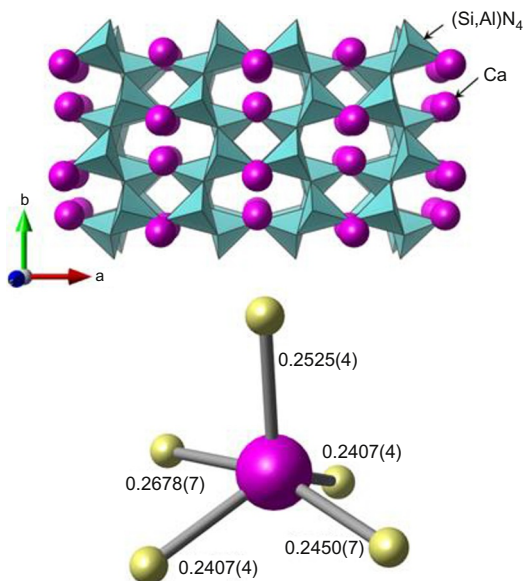
FIG. 39 Crystal structure of $CaAlSiN_3$. The unit of bond distance is nm. *Pictures were drawn based on the structure data obtained from the database (ICSD #161796).*

(Uheda et al., 2006a). Si^{4+} and Al^{3+} ions are distributed randomly at the 8b site have fourfold nitrogen coordination, forming MN_4 ($M = Si^{4+}$ and Al^{3+}) tetrahedra corner sharing each other so that they build a 3D framework. The Ca^{2+} ions occupy sites located in the channels along the *c*-axis and have fivefold nitrogen coordination to form square pyramids. The average Ca–N bond distance is 0.2493 nm.

The luminescence properties of $CaAlSiN_3:Ce^{3+}$ phosphors were first reported by Li et al. (2008a). The excitation spectrum of $CaAlSiN_3:Ce^{3+}$ covers the wide spectral range from 250 to 550 nm and has a strong optical absorption maximum in the blue region (Fig. 40). The phosphor exhibits a broad, asymmetrical yellow emission band peaking at 570 nm. The emission band is composed of two components with maxima at around 556 and 618 nm, whose profile can be fitted by two typical Gaussian functions. The two bands are ascribed to transitions from the 5d excited state to the doublet ground state ($^2F_{7/2}$ and $^2F_{5/2}$) of Ce^{3+}, and the energy difference between the two emission bands corresponds to about 1800 cm^{-1}, similar to that of the theoretical energy difference between $^2F_{7/2}$ and $^2F_{5/2}$ (2000 cm^{-1}; Blasse and Grabmaier, 1994). Optimization of the Ce^{3+} content yields the highest emission intensity for the composition $(Ca_{0.9}Ce_{0.1})AlSiN_3$, which has an external quantum efficiency of 54% at an excitation wavelength of 450 nm. In addition, $CaAlSiN_3:Ce^{3+}$ shows an excellent thermal stability against temperature quenching. At 150°C, the emission intensity of the phosphor is quenched by only 10% with respect to that at 25°C.
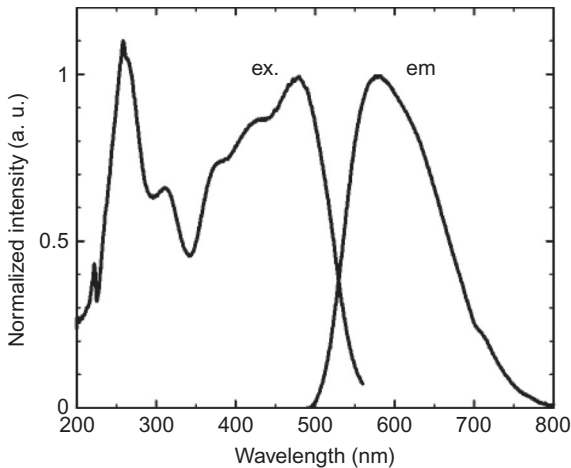
FIG. 40 Excitation and emission spectra of $CaAlSiN_3:Ce^{3+}$. *Redrawn from Li, J., Watanabe, T., Sakamoto, N., Wada, H., Setoyama, T., Yoshimura, M. 2008a. Synthesis of a multinary nitride, Eu-doped CaAlSiN₃ from alloy at low temperatures. Chem. Mater. 20, 2095–2105.*

4.2.1.3 La$_3$Si$_6$N$_{11}$:Ce^{3+} Phosphors

La$_3$Si$_6$N$_{11}$:Ce^{3+} is one of the recently synthesized yellow-emitting nitride phosphors excitable by blue LEDs (George et al., 2013; Seto et al., 2009; Suehiro et al., 2011). The detailed crystallographic data of La$_3$Si$_6$N$_{11}$ are reported by Yamane et al. (2014) and show isostructurality with R_3Si$_6$N$_{11}$ (R=Ce, Pr, Nd, and Sm) (Gaudé et al., 1983; Lauterbach and Schnick, 2000; Schlieper and Schnick, 1995, 1996; Woike and Jeitschko, 1995). Ln$_3$Si$_6$N$_{11}$ has a tetragonal lattice with space group $P4bm$ (no. 100), a=1.0189 nm, c=0.4837 nm, and V=0.5022 nm^3 (Woike and Jeitschko, 1995; Yamane et al., 2014). Both La^{3+} and Si^{4+} ions occupy two crystallographically independent sites (Fig. 41). La1 and La2 are located at the 4c and 2a sites, respectively, while Si1 and Si2 are located at 8d and 4c sites, respectively. The SiN$_4$ tetrahedra form two types of rings, Si$_4$N$_4$ and Si$_8$N$_8$; La1 is surrounded by the Si$_4$N$_4$ ring while La2 is captured in the Si$_8$N$_8$ ring. Both La ions have eightfold nitrogen coordination. The SiN$_4$ tetrahedra are corner sharing each other, providing a 3D network.

Three broad bands with maxima at 350, 385, and 455 nm are observed in the excitation spectrum of La$_3$Si$_6$N$_{11}$:Ce^{3+} (Fig. 42). Because there are two independent sites available for Ce^{3+}, the bands are attributable to the transitions from 4f^1 (^{2}F$_{5/2}$) ground states of Ce^{3+} to various 5d crystal-field levels defined by the chemical environments around Ce^{3+} (Seto et al., 2009; Suehiro et al., 2011). The emission spectrum shows an asymmetric broad
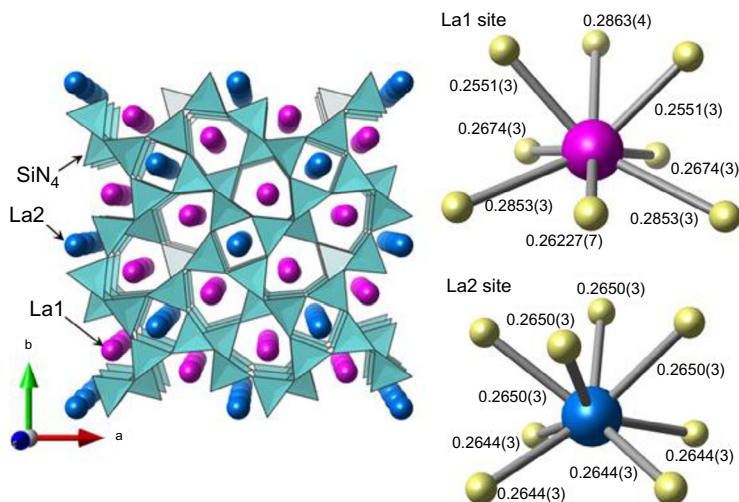
FIG. 41 Crystal structure of La$_3$Si$_6$N$_{11}$. The unit of bond distance is nm. *Pictures were drawn based on the structure data obtained from the database (ICSD #401679).*
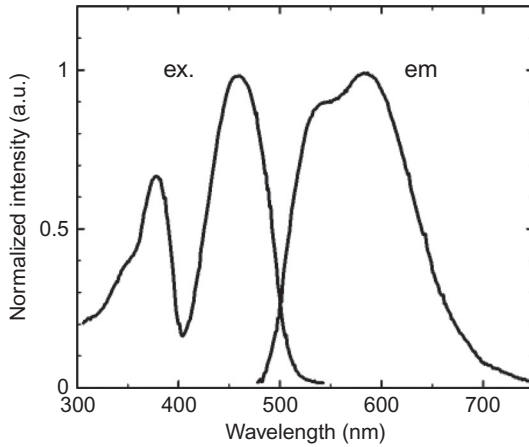
FIG. 42 Excitation and emission spectra of $La_3Si_6N_{11}$:Ce^{3+}. *Redrawn from Seto, T., Kijima, N., Hirosaki, N., 2009. A new yellow phosphor $La_3Si_6N_{11}$:Ce^{3+} for white LEDs. ECS Trans. 25, 247–252.*

reddish–yellow emission band with peaks at 525 and 595 nm. The external quantum efficiency of the phosphor is 42% under an excitation at 450 nm. With increasing temperature up to 150°C, the emission intensity decreases by about 28% with respect to that at 25°C, owing to thermal quenching; this is a little less than for YAG:Ce^{3+}. Then, the thermal stability against temperature quenching is lower compared with another yellow-emitting (oxy)nitride phosphors such as Ca-α-SiAlON:Eu^{2+} and CaAlSiN$_3$:Ce^{3+}.

4.2.2 Blue-Emitting Phosphors

4.2.2.1 $Y_2Si_3O_3N_4$:Ce^{3+} Phosphors

The crystal structure and luminescence properties of the Y–Si–O–N quaternary system have been studied (Ching et al., 2004; Deng et al., 2011; Katharine and Derek, 2001; Lu et al., 2010, 2011; van Krevel et al., 1998, 2000, 2001; Wang and Werner, 1997; Xu et al., 2005; Yang et al., 2015). Among these quaternary materials, Ce^{3+}-activated $Y_2Si_3O_3N_4$ is known to exhibit a blue emission under near-UV excitation (Lu et al., 2011; van Krevel et al., 1998, 2000). Fig. 43 illustrates the crystal structure of $Y_2Si_3O_3N_4$ that crystallizes in an N-melilite-type tetragonal structure with space group $P\bar{4}2_1m$, $a = 0.7614$ nm, $c = 0.4915$ nm, and $V = 0.2849$ nm^3 (Lu et al., 2011). The Y^{3+} ions occupy a crystallographic site and adopt eightfold coordination being bound to four oxygen and four nitrogen atoms; the average Y–N/O bond distance amounts to 0.2514 nm (van Krevel et al., 2000).

The optimum concentration of Ce^{3+} in $Y_2Si_3O_3N_4$:Ce^{3+} was found to be $(Y_{0.98}Eu_{0.02})_2Si_3O_3N_4$ (Lu et al., 2011). This phosphor shows two broad
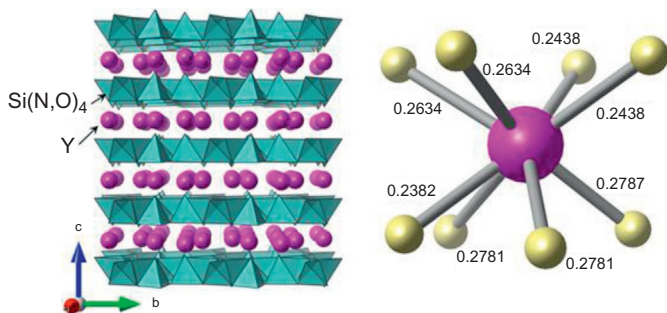
FIG. 43   Crystal structure of $Y_2Si_3O_3N_4$. The unit of bond distance is nm. *Pictures were drawn based on the structure data obtained from the database (ICSD #34583).*
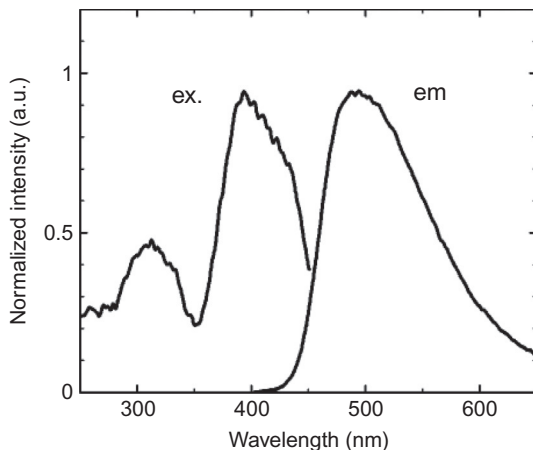
FIG. 44   Excitation and emission spectra of $(Y_{0.98}Ce_{0.02})_2Si_3O_3N_4$. *Redrawn from Lu, F.C., Chen, X.Y., Wang, M.W., Liu, Q.L., 2011. Crystal structure and photoluminescence of $(Y_{1-x}Ce_x)_2Si_3O_3N_4$. J. Lumin. 131, 336–341.*

excitation bands at 310 and 390 nm with a shoulder at around 430 nm (Fig. 44). Upon excitation at 390 nm, a single intense and broad blue emission is observed at 485 nm. The phosphor has a relatively small Stokes shift, approximately 4200 cm^{-1}. The emission intensity at 485 nm gradually decreases with increasing temperature. The relative emission intensity at 150°C is 43% of that at room temperature.

4.2.3   Green-Emitting Phosphors

4.2.3.1   β-SiAlON:Eu²⁺ Phosphors

As mentioned in Section 4.2.1.1, SiAlON materials have two different structural types, α and β (Hirosaki et al., 2005; Xie and Hirosaki, 2007; Xie et al., 2010). Among them, β-type SiAlON is a solid solution of β-Si_3N_4 and
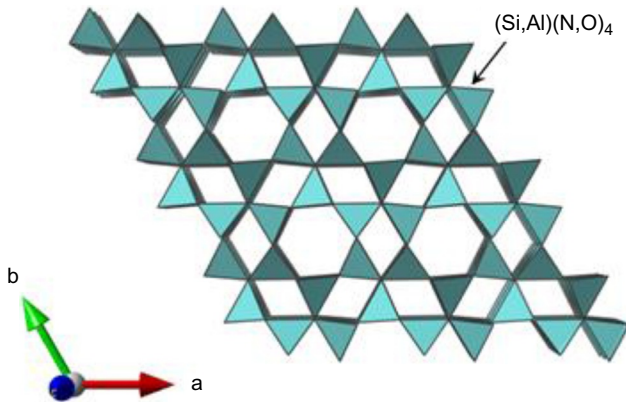
FIG. 45 Crystal structure of β-SiAlON. The unit of bond distance is nm. *Picture was drawn based on the structure data obtained from the database (ICSD #8263).*

Al_2O_3, in which a Si–N pair is replaced by a pair with an equivalent charge, such as Al–O; it is then described by the general formula $Si_{6-z}Al_zO_zN_{8-z}$. β-SiAlON has a hexagonal crystal structure with space group $P6_3$ or $P6_3/m$ (Jack and Wilson, 1972; Oyama and Kamigaito, 1971). This structure is shown in Fig. 45. The phosphor β-SiAlON is known to form a 3D network of corner-sharing (Si,Al)(O,N)$_4$ tetrahedra with infinite channels parallel to the *c*-direction (Kimoto et al., 2009). Xie et al. (2007) investigated in detail the effect of the material composition (*z* value in $Si_{6-z}Al_zO_zN_{8-z}$) and Eu^{2+} content on its luminescence properties. The samples with lower *z* values showed a relatively high solubility of Eu^{2+} without structural change as well as high phase purity, fine particle size, and little particle aggregation. The highest green emission intensity was obtained for $Si_{5.5}Al_{0.5}O_{0.5}N_{7.5}:Eu^{2+}_{0.03}$. The excitation spectrum monitored at 536 nm consists of a broad absorption band extending from 250 to 530 nm (Fig. 46), in which two distinguishable peaks appear at around 303 and 400 nm accompanied with a shoulder at 480 nm, showing strong optical absorption from near-UV (400–420 nm) to blue (420–470 nm) lights available from LEDs. The emission spectrum under excitation at 450 nm exhibits a single broad band with a maximum at 536 nm. The FWHM value is approximately 55 nm, which is smaller than that of the conventional green-emitting Ba-rich $(Ba,Sr)_2SiO_4:Eu^{2+}$ (~65 nm) and $SrSi_2O_2N_2:Eu^{2+}$ (~82 nm) phosphors (Kim et al., 2005a,b; Li et al., 2005; Mueller-Mach et al., 2005), indicating higher color purity of β-SiAlON:Eu^{2+}. In addition, the phosphor shows low thermal quenching. With increasing temperature up to 150°C, the emission intensity decreases by only 12–14% without any emission band shift (Chung and Ryu, 2012; Xie et al., 2007). A white LED for a back-lighting unit combined with a blue LED, a commercial CASN $(CaAlSiN_3:Eu^{2+})$ phosphor, and β-SiAlON:Eu^{2+} shows a high-CRI white light (Chung and Ryu, 2012). The color gamut of the white LED is 102% of National
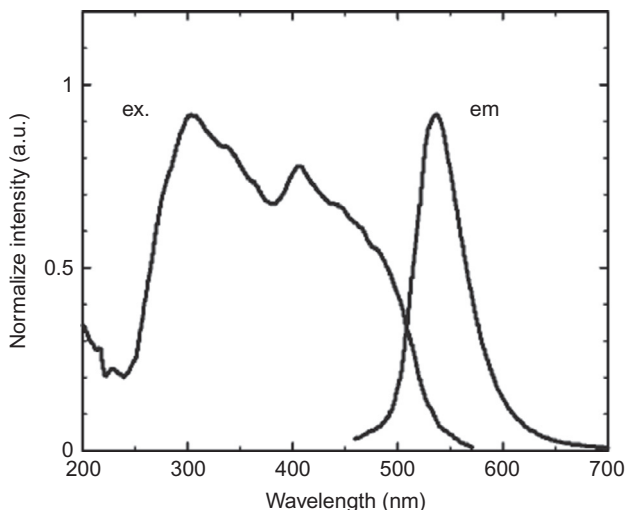
FIG. 46   Excitation and emission spectra of β-SiAlON:Eu^{2+}. *Redrawn from Xie, R.J., Hirosaki, N., Kimura, N., Sakuma, K., Mitomo, M., 2007. 2-Phosphor-converted white light-emitting diodes using oxynitride/nitride phosphors. Appl. Phys. Lett. 90, 1101–1103.*

Television System Committee (NTSC), which is higher than that of the white LED for a back-light unit using Ba-rich $(Ba,Sr)_2SiO_4:Eu^{2+}$ (96% of NTSC).

4.2.3.2 $AESi_2O_2N_2:Eu^{2+}$ (AE = Ca, Sr, and Ba) Phosphors

$AESi_2O_2N_2:Eu^{2+}$ (AE = Ca, Sr, and Ba) have been considered to be among the most promising candidates for green-emitting phosphors for white LEDs. Li et al. (2005) reported the luminescence properties and the crystal structure of the $AESi_2O_2N_2:Eu^{2+}$ (AE = Ca, Sr, and Ba) phosphors synthesized by a conventional solid-state reaction with a $AECO_3$ (AE = Ca, Sr, and Ba)– Eu_2O_3–SiO_2–Si_3N_4 system. Thereafter, Schnick's group (Kechele et al., 2009a) investigated the crystal structure of $AESi_2O_2N_2$ (AE = Ca, Sr, and Ba) in detail and they derived the different crystal structures from that reported by Li et al. (2005). Regarding the crystal structures of $AESi_2O_2N_2$ (AE = Ca, Sr, and Ba), there are some contradictions in the literature, probably due to differences in the estimation of order/disorder between oxygen and nitrogen sites and the existence of impurity phases (mainly Si_3N_4) (Kechele et al., 2009a,b). On the basis of the most reliable crystallographic data reported, the structural features could be summarized as follows: $CaSi_2O_2N_2$ has a monoclinic structure with space group $P2_1$ (Höppe et al., 2004), $SrSi_2O_2N_2$ has a triclinic structure with space group $P1$ (Oeckler et al., 2007), and $BaSi_2O_2N_2$ has an orthorhombic structure with space group $Pbcn$ (Kechele et al., 2009a,b). The crystallographic data of $AESi_2O_2N_2$ (AE = Ca, Sr, and Ba) are summarized in Table 3, and the crystal structures are shown in Fig. 47.

TABLE 3 Structure Data of $AE\mathrm{Si_2O_2N_2}$ ($AE = \mathrm{Ca}$, Sr, and Ba)

	CaSi$_2$O$_2$N$_2$ (Höppe et al., 2004)	SrSi$_2$O$_2$N$_2$ (Oeckler et al., 2007)	BaSi$_2$O$_2$N$_2$ (Kechele et al., 2009a,b)
Crystal System	*Monoclinic*	*Triclinic*	*Orthorhombic*
Space group	$P2_1$ (No. 4)	$P1$ (No. 1)	$Pbcn$ (No. 62)
a (nm)	0.7344(2)	0.708021(14)	1.43902(3)
b (nm)	1.3656(3)	0.723058(17)	0.53433(1)
c (nm)	1.0483(3)	0.725535(12)	0.483254(6)
α (°)	90	88.7669(24)	90
β (°)	102.04(2)	84.7333(11)	90
γ (°)	90	75.9047(20)	90
V (nm^3)	1.0282	0.35872	0.37158
Z	12	4	4
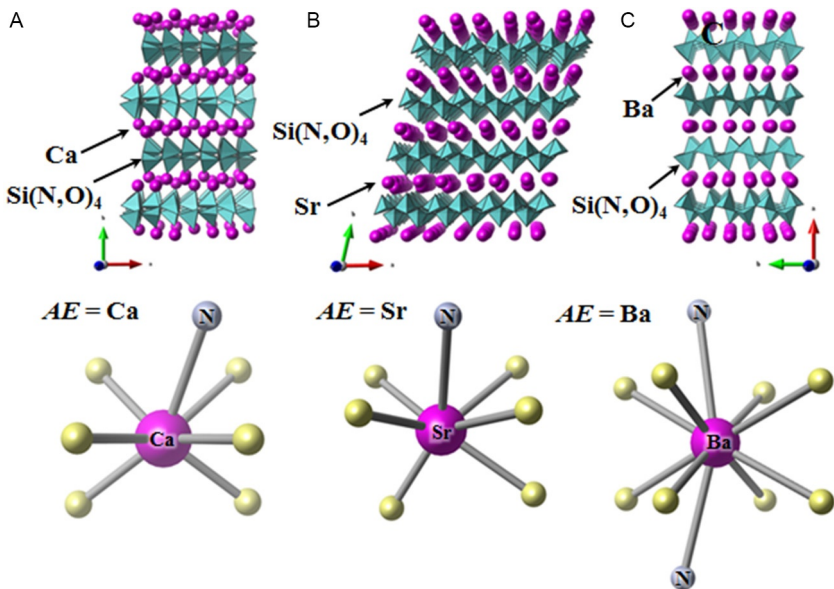
FIG. 47 Crystal structures of $AE\mathrm{Si_2O_2N_2}$ ($AE =$ (A) Ca, (B) Sr, and (C) Ba). The unit of bond distance is nm. *Pictures were drawn based on the structure data obtained from the database (ICSD #413882 (AE=Ca), #172877 (AE=Sr), #173758 (AE=Ba)).*

Although the structure types are different from each other, these materials have a similar layered structure, in which AE layers are separated by highly condensed $(Si_2O_2N_2)^{2-}$ layers. The $(Si_2O_2N_2)^{2-}$ layers are built up of corner-sharing $SiON_3$ tetrahedra in which all nitrogen atoms are shared between three neighboring tetrahedra, while each oxygen atom is terminally bonded to the tetrahedra. The $SrSi_2O_2N_2$ and $BaSi_2O_2N_2$ compounds have a similar an up/down sequence of the $SiON_3$ motifs and, however, the silicate layers are shifted toward each other in $SrSi_2O_2N_2$ (Kechele et al., 2009a,b; Seibald et al., 2011). In $BaSi_2O_2N_2$, Ba^{2+} ions adopt eightfold oxygen coordination in the form of a cuboid that is additionally capped by two nitrogen ions. In $SrSi_2O_2N_2$, Sr^{2+} ions adopt sixfold oxygen coordination in the form of a distorted trigonal prism—leading to the shift of the silicate layer, as in $BaSi_2O_2N_2$—and are additionally capped by one nitrogen atom. $CaSi_2O_2N_2$ has similar crystallographic environments around Ca^{2+} ions to that of $SrSi_2O_2N_2$, but the up/down sequence of $SiON_3$ tetrahedra is different (Kechele et al., 2009a,b; Zeuner et al., 2011).

As shown in Fig. 48, the excitation spectra of $AESi_2O_2N_2{:}Eu^{2+}$ (AE=Ca, Sr, and Ba) have strong broad bands attributed to the crystal-field splitting of 5d of the excited $4f^65d^1$ configuration of Eu^{2+} (Bachmann et al., 2009b; Gu et al., 2010; Li et al., 2015b). These phosphors can be efficiently excited by near-UV or blue light. The emission bands show apparent red shifts in the order $BaSi_2O_2N_2{:}Eu^{2+} < SrSi_2O_2N_2{:}Eu^{2+} < CaSi_2O_2N_2{:}Eu^{2+}$, due to the increase in crystal-field strength around Eu^{2+}. $BaSi_2O_2N_2{:}Eu^{2+}$ shows an extremely blue–green emission band peaking at 494 nm, suggesting a higher symmetry around Ba sites than those of Sr and Ca sites. $SrSi_2O_2N_2{:}Eu^{2+}$ exhibits a broad green emission peak at 537 nm. $CaSi_2O_2N_2{:}Eu^{2+}$ shows a broad
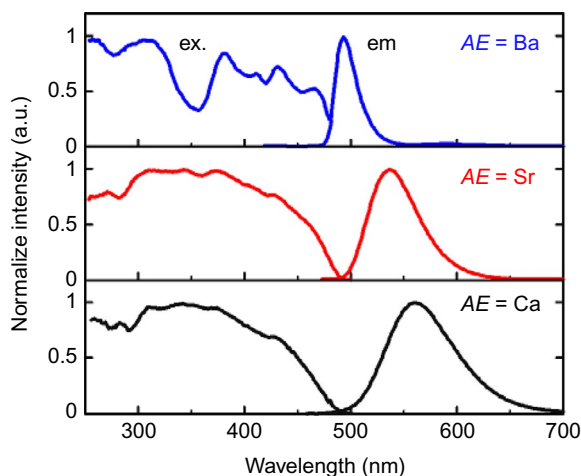
FIG. 48 Excitation and emission spectra of $AESi_2O_2N_2{:}Eu^{2+}$ (AE=Ca, Sr, Ba). *Redrawn from Bachmann, V., Ronda, C., Oeckler, O., Schnick, W., Meijerink, A., 2009. Color point tuning for $(Sr,Ca,Ba)Si_2O_2N_2{:}Eu^{2+}$ for white light LEDs. Chem. Mater. 21, 316–325.*

TABLE 4 Photoluminescence Data of $AESi_2O_2N_2:Eu^{2+}$ (AE = Ca, Sr, Ba) Phosphors (Li, et al., 2005)

AE	Excitation Band (nm)	Emission Band (nm)	Absorption Edge[a] (nm)	Stokes Shift (cm^{-1})	QE (ex.)[b] (%)
Ca	259, 341, 395, 436	560	~280	~5100	72
Sr	260, 341, 387, 440	530–570	~270	~3900–5200	69
Ba	264, 327, 406, 480	499	~240	~1700	41

[a]$AESi_2O_2N_2$ host material.
[b]External quantum efficiency.

yellow emission band with a maximum at 560 nm (Bachmann et al., 2009b). Under excitation at 450 nm, the external quantum efficiencies of these phosphors are 72%, 69%, and 41% for $CaSi_2O_2N_2:Eu^{2+}$, $SrSi_2O_2N_2:Eu^{2+}$, and $BaSi_2O_2N_2:Eu^{2+}$, respectively (Gu et al., 2010). The detailed photoluminescence data of $AESi_2O_2N_2:Eu^{2+}$ (AE = Ca, Sr, and Ba) are summarized in Table 4 (Li et al., 2015a,b). In the case of $SrSi_2O_2N_2:Eu^{2+}$, the emission intensity measured at 150°C is ≥80% of that at room temperature. The excellent luminescence efficiencies of $AESi_2O_2N_2:Eu^{2+}$ (AE = Ca, Sr, and Ba) make them very suitable for use in near-UV or blue-LED-based white LEDs as a conversion phosphor.

4.2.3.3 $Y_4Si_2O_7N_2:Ce^{3+}$ Phosphors

The host phase of $Y_4Si_2O_7N_2:Ce^{3+}$ phosphors is a compound existing in the Y–Si–O–N quaternary system. $Y_4Si_2O_7N_2$ has a crystal structure different from N-melilite type $Y_2Si_3O_3N_4$ (described in Section 4.2.2) as shown in Fig. 49. $Y_4Si_2O_7N_2$ crystallize in a monoclinic structure with space group $P2_1/c$ (so-called J-phase) (MacKenzie et al., 1996). In Table 5 are summarized the crystallographic data of N-melilite $Y_2Si_3O_3N_4$ and J-phase $Y_4Si_2O_7N_2$. In $Y_4Si_2O_7N_2$, two Si(O/N)$_4$ tetrahedra are coupled by corner sharing (nitrogen atom) to form $Si_2O_5N_2$ di-tetrahedral units, running along the a-axis. The Y^{3+} ions have four independent sites with different crystallographic environments, giving one kind of Y(O/N)$_6$ and three kinds of Y(O/N)$_7$ motifs (MacKenzie et al., 1996; Wu et al., 2014; Xia and Wu, 2013). The coordination environment and Y–(O/N) bond distance data of each Y(O/N)$_n$ polyhedra are given in Table 6 (Wu et al., 2014). The Y(O/N)$_n$ polyhedra are linked by sharing edges between them and further linking with $Si_2O_5N_2$ ditetrahedral units is achieved by sharing an O/N atom.
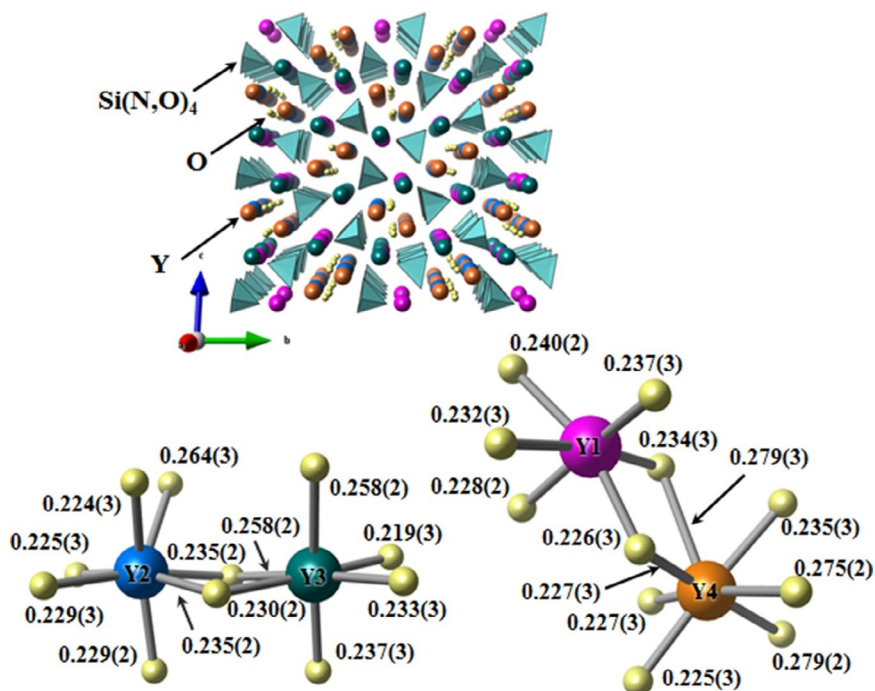
FIG. 49   Crystal structure of $Y_4Si_2O_7N_2$. The unit of bond distance is nm. *Pictures were drawn based on the structure data obtained from the database (ICSD #247785).*

TABLE 5 Structure Data of $Y_2Si_3O_3N_4$ and J-Phase $Y_4Si_2O_7N_2$ (MacKenzie et al., 1996)

Crystal System	$Y_2Si_3O_3N_4$	$Y_4Si_2O_7N_2$
	Tetragonal	*Monoclinic*
Space group	$P\overline{4}2_1m$	$P2_1/c$
a (nm)	0.73083(1)	0.75601(2)
b (nm)	0.73083(1)	1.04411(3)
c (nm)	0.49113(1)	1.07626(3)
α (°)	90	90
β (°)	90	110.042(2)
γ (°)	90	90

TABLE 6 Y–N/O Bond Distance (nm) in $Y_4Si_2O_7N_2$ (Lu et al., 2010)

Y1	Distance	Y2	Distance	Y3	Distance	Y4	Distance
Y1–N1	0.23293(2)	Y2–O2/N3	0.26965(3)	Y3–O1/N2	0.23130(4)	Y4–N1	0.24839(2)
Y1–O1/N1	0.27709(3)	Y2–O4/N5	0.23091(3)	Y3–O2/N3	0.22731(4)	Y4–O1/N2	0.23179(4)
Y1–O3/N4	0.24219(3)	Y2–O5/N6	0.22848(3)	Y3–O3/N4	0.22634(3)	Y4–O2/N3	0.23866(4)
Y1–O5/N6	0.26959(3)	Y2–O6/N7	0.23022(3)	Y3–O4/N5	0.23379(3)	Y4–O3/N4	0.25917(3)
Y1–O7	0.23168(5)	Y2–O7	0.22724(4)	Y3–O5/N6	0.23656(3)	Y4–O4/N5	0.25996(3)
Y1–O8	0.22438(3)	Y2–O7	0.23018(5)	Y3–O7	0.22245(4)	Y4–O6/N7	0.23012(2)
Y1–O8	0.22654(4)	Y2–O8	0.21622(3)	–	–	Y4–O8	0.22889(3)
Average	0.24348(9)	Average	0.23327(4)	Average	0.22962(8)	Average	0.24242(8)
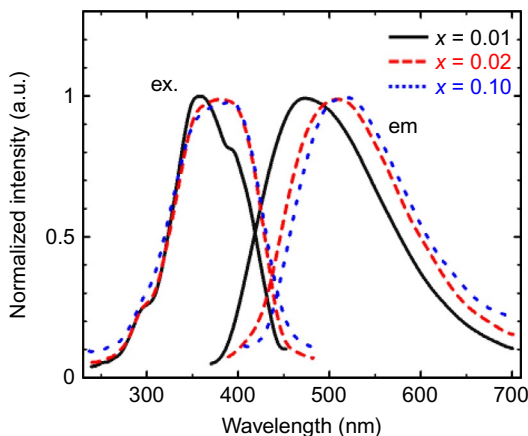
FIG. 50   Excitation and emission spectra of $(Y_{1-x}Ce_x)_4Si_2O_7N_2$ ($x=0.01$, 0.02 and 0.10). *Redrawn from Wu, Q., Yang, Z., Zhao, Z., Que, M., Wang, X., Wang, Y., 2014. Synthesis, crystal structure and luminescence properties of a $Y_4Si_2O_7N_2$:Ce^{3+} phosphor for near-UV white LEDs. J. Mater. Chem. C 2, 4967–4973.*

Fig. 50 shows excitation and emission spectra of $(Y_{1-x}Ce_x)_4Si_2O_7N_2$:$Ce^{3+}$ ($x=0.001$, 0.02, and 0.10). The excitation spectrum of the phosphor with $x=0.001$ shows a broad absorption band ranging from 280 to 425 nm with the largest optical absorption at 355 nm. With increasing Ce^{3+} concentration, the absorption intensity in the near-UV region around 400 nm increases and, in correlation with this, the emission color also shifts from blue to green, suggesting that this red shift is correlated with the population of the four crystallographically independent Y sites available for Ce^{3+}. The phosphor with $x=0.10$ exhibits a broad green emission with a maximum at 515 nm under 398 nm excitation. Under the same excitation the $Y_4Si_2O_7N_2$:Ce^{3+} ($x=0.02$) phosphor has quantum efficiency of about 47%. With increasing temperature up to 200°C, the emission intensity gradually decreases. The relative emission intensity measured at 200°C is approximately 10% of that at room temperature (Wu et al., 2014). The isostructural Ce^{3+}-activated $Lu_4Si_2O_7N_2$ phosphors show much higher green emission intensity, about 180% that of $Y_4Si_2O_7N_2$:Ce^{3+} (Xu et al., 2009).

Besides $Y_4Si_2O_7N_2$ and $Y_2Si_3O_3N_4$, $Y_6Si_3O_9N_4$ and $Y_5(SiO_4)_3N$, two of the members of the Y–Si–O–N quaternary system are also suitable host materials. The Ce^{3+}-activated $Y_6Si_3O_9N_4$ and $Y_5(SiO_4)_3N$ phosphors exhibit a blue or green emission under a near-UV excitation (Deng et al., 2011; van Krevel et al., 1998).

4.2.4   Red-Emitting Phosphors
4.2.4.1   CaAlSiN₃:Eu²⁺ Phosphors

As pointed out in Section 4.2.1, $CaAlSiN_3$:Eu^{2+} (CASN) is one of the notorious commercial red-emitting nitride phosphors for blue LEDs. The luminescence

properties of CASN were first reported by Uheda et al. (2006a,b). Thereafter, this phosphor has been investigated by many researchers whose goals were to enhance the luminescence efficiency and to improvement the synthesis for producing single phase CASN. This phosphor is generally prepared by a solid-state reaction method using a mixture of powder Si_3N_4, Ca_3N_2, and Eu_2O_3 or EuN at high temperatures, over 1600°C, and high pressures, about 0.5–0.9 MPa, in a nitrogen atmosphere. As described earlier, the Ce^{3+} activator substitutes Ca^{2+} sites where Ca^{2+} adopt fivefold nitrogen coordination to form a square pyramid with short Ca–N bond distances. A large crystal-field splitting of the d levels should then be observed when the activator ion substitutes the site which features a narrow space, because of large columbic interaction caused by shorter metal–anion distances and smaller coordination number. The large crystal-field splitting usually results in longer wavelengths of both excitation and emission, as shown in Fig. 6.

The excitation spectrum of CASN shows an extremely broad band covering the spectral region from 250 to 600 nm and having strong optical absorption in the visible (Fig. 51). Under blue light excitation ($\lambda_{ex}=450$ nm), CASN presents a broad deep-red emission with a peak at 655 nm and a FWHM value of 93 nm. The highest emission intensity is obtained for $Ca_{0.99}Eu_{0.01}AlSiN_3$ which exhibits an external quantum efficiency of 70% ($\lambda_{ex}=450$ nm). In addition, the phosphor shows a small Stokes shift of 2200 cm^{-1}. In general, small Stokes shifts contribute to suppressing thermal quenching and to high conversion efficiency (Dorenbos, 2003).

Temperature dependence of the emission intensity of CASN is presented in Fig. 52, normalized with respect to the value at 25°C. CASN has an excellent thermal stability against temperature quenching. When temperature increased
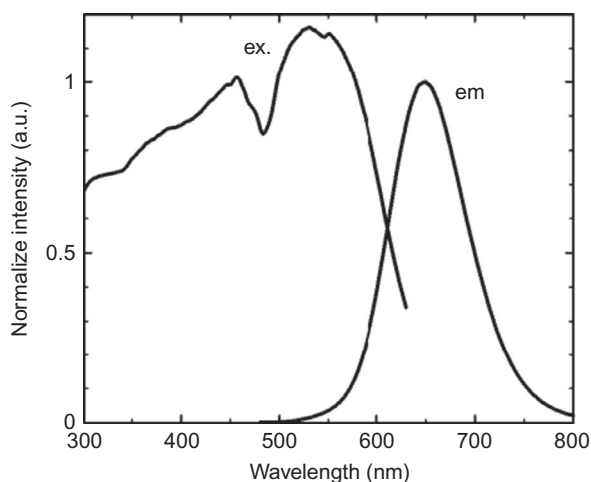
FIG. 51 Excitation and emission spectra of CaAlSiN$_3$:Eu^{2+} (CASN). *Data were collected from a phosphor synthesized by the authors.*
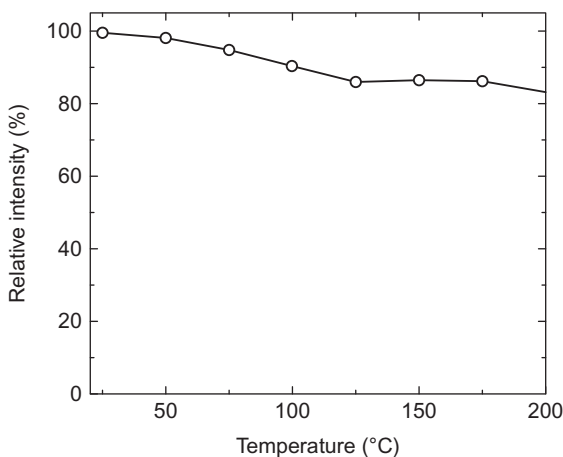
FIG. 52   Temperature dependence of the emission intensity of $CaAlSiN_3:Eu^{2+}$ (CASN). *Redrawn from Piao, X., Machida, K., Horikawa, T., Hanzawa, H., Shimomura, Y., Kijima, N. 2007. Preparation of $CaAlSiN_3:Eu^{2+}$ phosphors by the self-propagating high-temperature synthesis and their luminescent properties. Chem. Mater. 19, 4592–4599.*

up to 150°C, the emission intensity of CASN decreases to 89% of that at room temperature (25°C) (Xie et al., 2006a,b, 2007, 2010). At the same time, fluctuation of the emission band position is very small, actually negligible.

Besides blue light absorption, CASN has a strong optical absorption in green region, leading to a reduction in the CRI of white LEDs combining a blue LED with green and red phosphors. In addition, the emission band of CASN located in the deep-red region (655 nm) is also responsible for the reduction of the luminescence efficiency of white LEDs. To solve these problems, several approaches, such as the formation of solid solutions of $CaAlSiN_3$–$SrAlSiN_3$ or $CaAlSiN_3$–Si_2N_2O and the use of alloy precursors in the synthesis, have been reported (Mikami et al., 2008, 2009a,b; Piao et al., 2007a; Watanabe and Kijima, 2009; Watanabe et al., 2008a,b). Among them, the formation of $CaAlSiN_3$–$SrAlSiN_3$ solid solution is the most promising approach to improve the luminescence of CASN without loss of quantum yield. Since the ionic radius of Sr^{2+} (0.118 nm for sixfold coordination) is larger than that of Ca^{2+} (0.100 nm) (Shannon, 1976), partial substitution of Sr^{2+} for Ca^{2+} results in the reduction of the crystal-field strength around Eu^{2+}, contributing to blue shifts in excitation and emission bands. The emission band of $Sr_xCa_{1-x}AlSiN_3:Eu^{2+}$ effectively shifts to a shorter wavelength with increasing Sr^{2+} content (Fig. 53). Particularly, $Sr_{0.8}Ca_{0.2}AlSiN_3:Eu^{2+}$ shows a highly pure red emission with peaking at 630 nm under excitation at 450 nm. Furthermore, the decrease in the emission intensity by thermal quenching is also successfully minimized to only 10% at 150°C.
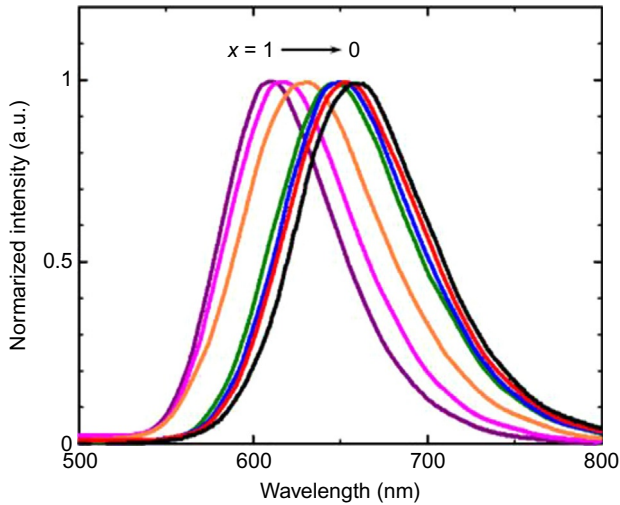
FIG. 53 Excitation and emission spectra of $Sr_xCa_{1-x}AlSiN_3$. *Redrawn from Watanabe, H., Kijima, N., 2009. Crystal structure and luminescence properties of $Sr_xCa_{1-x}AlSiN_3:Eu^{2+}$ mixed nitride phosphors. J. Alloy Compd. 475, 434–439.*

4.2.4.2 $AE_2Si_5N_8:Eu^{2+}$ ($AE = Ca$, Sr, and Ba) Phosphors

$AE_2Si_5N_8:Eu^{2+}$, so-called 2–5–8 phosphors, have been usually used in blue-LED-based white LEDs as a highly efficient conversion red-emitting phosphors (Höppe et al., 2000; Li et al., 2006a; Suehiro et al., 2013; Xie et al., 2006a,b,c, 2007, 2010; Zeuner et al., 2009). Schnick's group first reported the crystal structure of $AE_2Si_5N_8$ ($AE =$ Ca, Sr, and Ba) by single crystal structure determination (Höppe et al., 2004; Schlieper et al., 1995). Table 7 summarizes the corresponding crystal data. $Ca_2Si_5N_8$ has a monoclinic structure with space group Cc, whereas both $Sr_2Si_5N_8$ and $Ba_2Si_5N_8$ have an orthorhombic structure with space group $Pmn2_1$. Although $AE_2Si_5N_8$ have different crystal structures, the local structure is quite similar; the coordination polyhedron of Si is a SiN_4 tetrahedron corner shared with other tetrahedra, providing a 3D framework. Half of the nitride ions are bonded to two Si neighbors while the other half have three Si neighbors (Fig. 54). The coordination numbers of Sr^{2+} (Ba^{2+}) ions are 8 and 9, respectively, while that of Ca^{2+} is 7 (Piao et al., 2006; Schlieper et al., 1995).

Interestingly, the unit cell volume of $Ca_2Si_5N_8$ remains almost constant even when the Eu^{2+} content goes up to 7 mol% ($x = 0.14$ in $Ca_{2-x}Eu_xSi_5N_8$) (Li et al., 2006a). This indicates that the $Ca_2Si_5N_8$ framework is quite rigid and robust. On the other hand, the cell volume of Sr and Ba derivatives decreases linearly with increasing Eu^{2+} content in $AE_{2-x}Eu_xSi_5N_8$ ($AE =$ Sr and Ba, $0.02 \leq x \leq 2.0$) although the lattice shrinkage for $Ba_2Si_5N_8$ is

TABLE 7 Structure Data of $AE_2Si_5N_8$ (AE = Ca, Sr, and Ba)

	$Ca_2Si_5N_8$ (Schlieper and Schnick, 1995)	$Sr_2Si_5N_8$ (Schlieper et al., 1995)	$Ba_2Si_5N_8$ (Schlieper et al., 1995)
Crystal System	*Monoclinic*	*Orthorhombic*	*Orthorhombic*
Space group	*Cc*	*Pmn2$_1$*	*Pmn2$_1$*
a (nm)	1.4352(3)	0.5710(1)	0.5783(1)
b (nm)	0.5610(1)	0.6822(1)	0.6959(1)
c (nm)	0.9689(2)	0.9341(2)	0.9391(2)
α (°)	90.0	90.0	90.0
β (°)	112.06(3)	90.0	90.0
γ (°)	90.0	90.0	90.0
V (nm^3)	0.723	0.36387	0.37793
Z	4	2	2

significantly larger than that for $Sr_2Si_5N_8$. The formation of an all-proportional solid solution between $AE_2Si_5N_8$ (AE = Sr and Ba) and $Eu_2Si_5N_8$ is possible, indicating that $Eu_2Si_5N_8$ is also isostructural.

Emission spectra of $AE_{2-x}Eu_xSi_5N_8$ (AE = Ca, Sr, and Ba; x = 0.02) are shown in Fig. 55, and excitation and emission spectra of $Sr_{0.98}Eu_{0.02}Si_5N_8$ are shown in Fig. 56. The excitation spectrum consists of a broad band ranging from 220 to 600 nm. Although the peak positions in excitation spectra of $Ca_2Si_5N_8$:Eu^{2+} and $Ba_2Si_5N_8$:Eu^{2+} are different from $Sr_2Si_5N_8$:Eu^{2+}, both phosphors have a strong broad optical absorption in the near-UV and blue region. A common feature for the three phosphors is the broad red emission band peaking at around 605, 610, and 574 nm for Ca, Sr, and Ba, respectively (Li et al., 2006a). As the Eu^{2+} content increases from x = 0.02 to 2.00, the emission color of the phosphors vary from yellow to deep-red (from 590 to 680 nm) in the case of $Sr_2Si_5N_8$:Eu^{2+} and from green to deep-red (from 560 to 680 nm) in the case of $Ca_2Si_5N_8$:Eu^{2+}. Under excitation at 465 nm, the emission intensity of the phosphors increases in the order $Ca_2Si_5N_8$:Eu^{2+} < $Ba_2Si_5N_8$:Eu^{2+} < $Sr_2Si_5N_8$:Eu^{2+}. When $Sr_2Si_5N_8$:Eu^{2+} is excited at 450 nm, the external quantum efficiency is ~64%. As shown in Fig. 57, the $Sr_2Si_5N_8$:Eu^{2+} phosphor exhibits a thermal quenching behavior similar to that of CASN. The emission intensity of the phosphor measured at 150°C is 86–90% of that at 25°C.
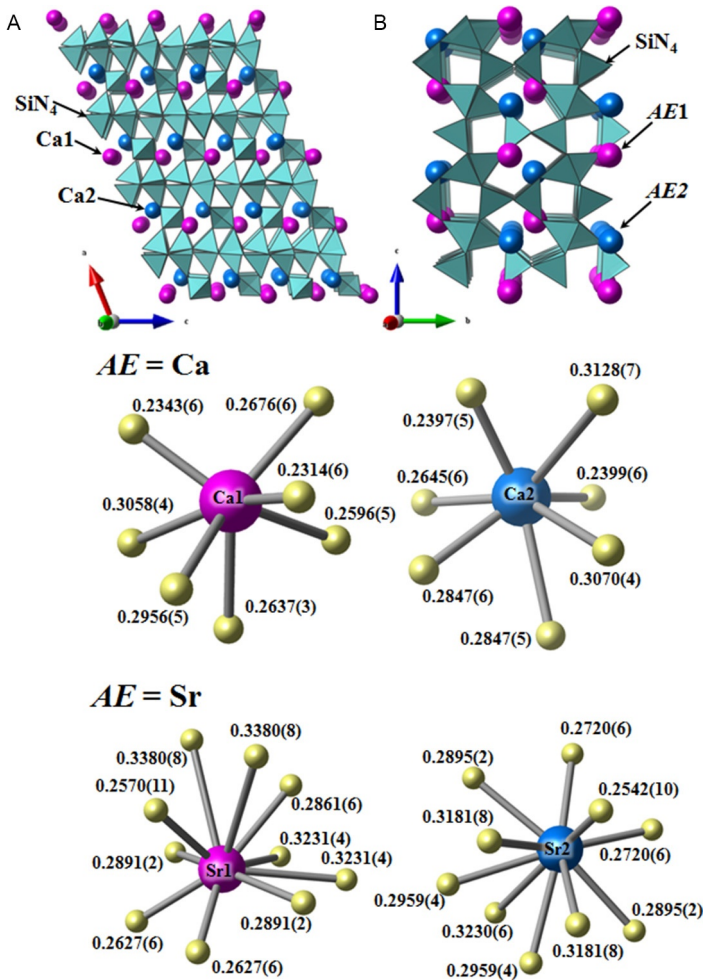
FIG. 54 Crystal structure of $AE_2Si_5N_8$ ($AE=$(A) Ca and (B) Sr(Ba)). The unit of bond distance is nm. *Pictures were drawn based on the structure data obtained from the database (ICSD #79070 (AE=Ca), #401500 (AE=Sr)).*

4.2.4.3 SrAlSi$_4$N$_7$:Eu^{2+} Phosphors

Hecht et al. (2009) first reported red-emitting SrAlSi$_4$N$_7$:Eu^{2+} phosphors. Ruan et al. (2011) investigated their luminescent properties in detail and Ruan et al. (2013) recently reported novel Ce^{3+}-activated yellow emission phosphors based on SrAlSi$_4$N$_7$.

In spite of the fact that the chemical formula of SrAlSi$_4$N$_7$ is the same as that of well-known compounds AERSi$_4$N$_7$ ($AE=$Sr and Ba, $R=$Yb and Y) (Fang et al., 2003; Huppertz and Schnick, 1997), it has a completely different
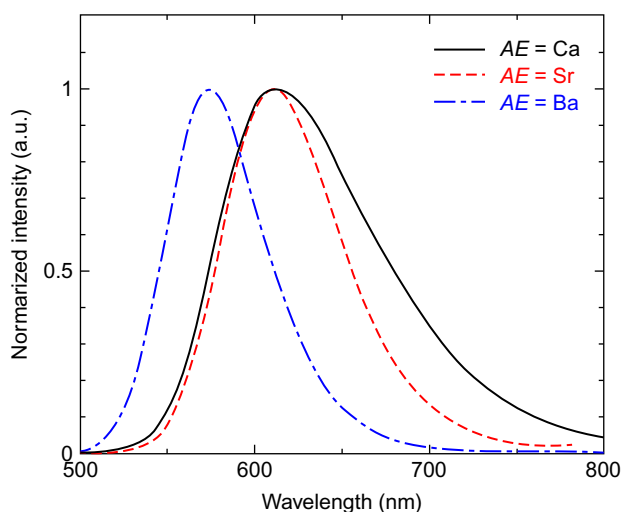
FIG. 55 Emission spectra of $AE_{1.98}Eu_{0.02}Si_5N_8$ ($AE=$Ca, Sr, and Ba). The unit of bond distance is nm. *Redrawn from Li, Y.Q., van Steen, J.E.J., van Krevel, J.W.H., Botty, G., Delsing, A.C.A., DiSalvo, F.J., de With, G., Hintzen, H.T. 2006. Luminescence properties of red-emitting $M_2Si_5N_8{:}Eu^{2+}$ (M=Ca, Sr, Ba) LED conversion phosphors. J. Alloys Compd. 417, 273–279.*
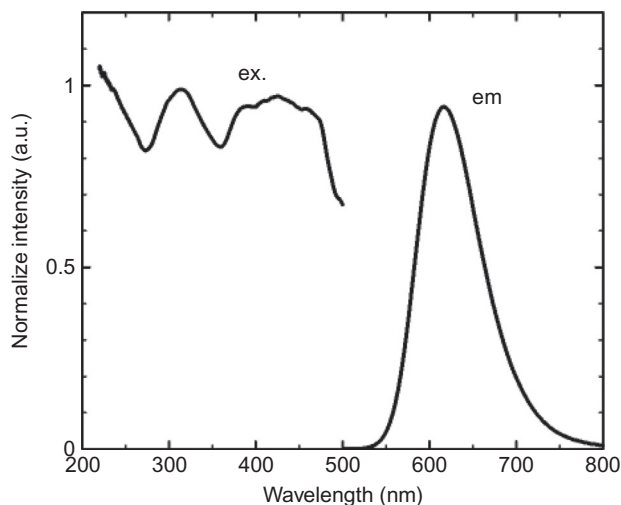
FIG. 56 Excitation and emission spectra of $(Sr_{0.98}Eu_{0.02})_2Si_5N_8$. *Data were collected from a phosphor synthesized by the authors.*

crystal structure. The structure of $SrAlSi_4N_7$ is shown in Fig. 58, and the crystallographic data are summarized in Table 8. $SrAlSi_4N_7$ has an ortho-rhombic structure with space group of $Pna2_1$, $a=1.1742$ nm, $b=2.1391$ nm, $c=0.4966$ nm, and $V=1.2472$ nm^3 (Hecht et al., 2009). The structure is
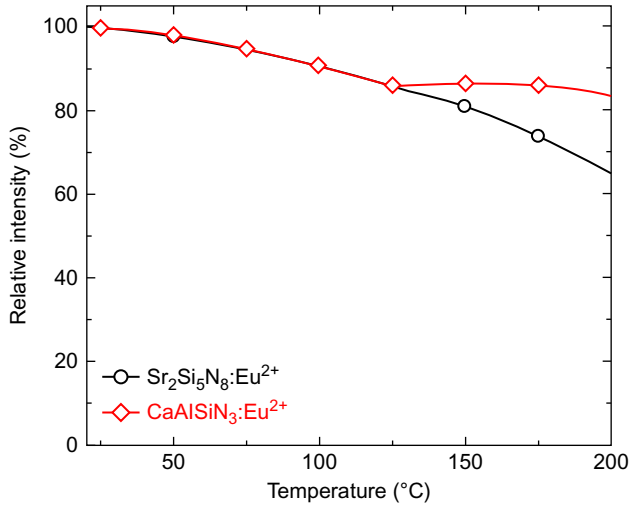
FIG. 57 Temperature dependence of the emission intensity of the $Sr_2Si_5N_8$:Eu^{2+} and CASN:Eu^{2+}. *Redrawn from Xie, R.-J., Hirosaki, N. 2007. Silicon-based oxynitride and nitride phosphors for white LEDs—a review. Sci. Technol. Adv. Mater. 8, 588–600.*
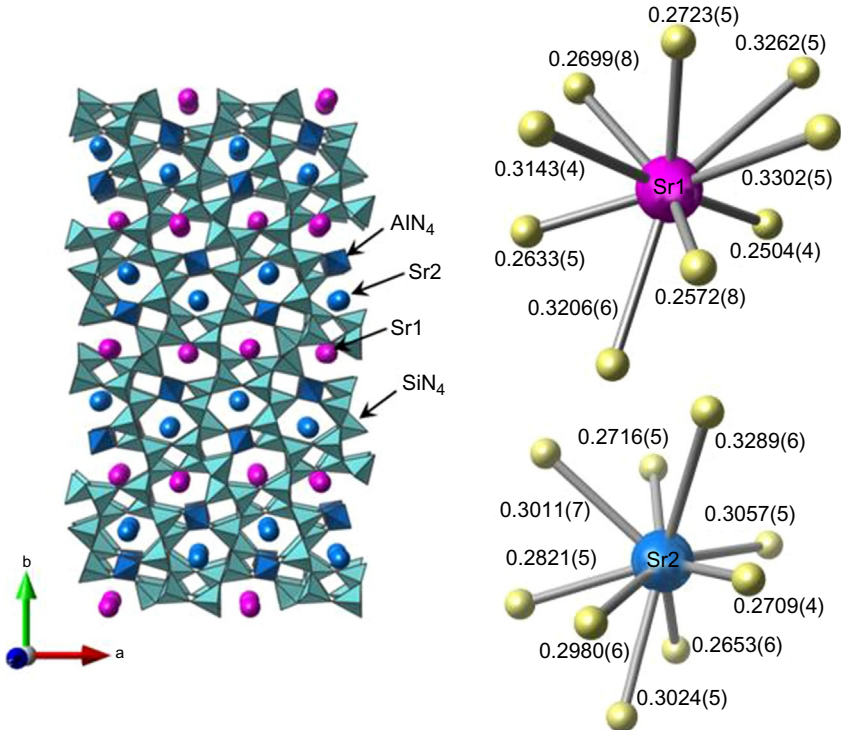
FIG. 58 Crystal structure of $SrAlSi_4N_7$. The unit of bond distance is nm. *Pictures were drawn based on the structure data obtained from the database (ICSD #163667).*

TABLE 8 Structure Data of SrAlSi$_4$N$_7$ (Hecht et al., 2009)

Crystal System	Orthorhombic
Space group	$Pna2_1$
a (nm)	1.1742(2)
b (nm)	2.1391(4)
c (nm)	0.4966(1)
V (nm^3)	1.24733
Z	8
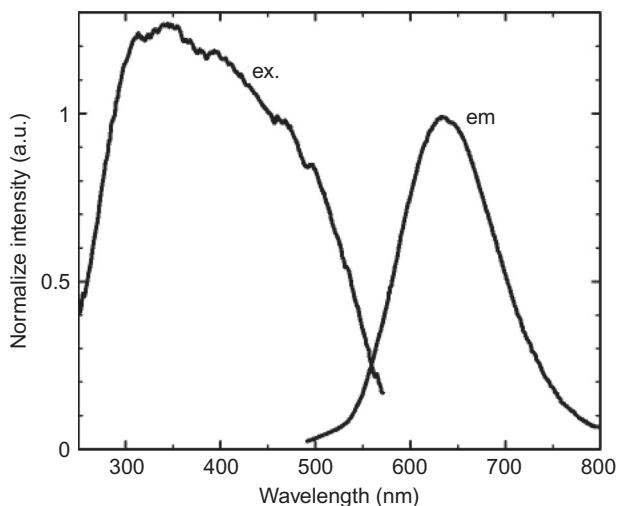
FIG. 59 Excitation and emission spectra of Sr$_{0.97}$Eu$_{0.03}$AlSi$_4$N$_7$. *Redrawn from Ruan, J., Xie, R.J., Hirosaki, N., Takeda, T., 2011. Nitrogen gas pressure synthesis and photoluminescent properties of orange-red SrAlSi$_4$N$_7$:Eu^{2+} phosphors for white light-emitting diodes. J. Am. Ceram. Soc. 94, 536–542.*

composed of SiN$_4$ and AlN$_4$ tetrahedra, linked by corners- and edge sharing each other, to form a highly condensed 3D network. In addition, infinite chains built only by AlN$_4$ tetrahedra edge sharing themselves are formed in parallel to the c-axis. The Sr^{2+} ions occupy the two independent sites and form SrN$_6$ octahedra and SrN$_8$ dodecahedra. The Sr–N bond distance in the SrN$_6$ octahedra varies from 0.2504 to 0.3143 nm, and that in the SrN$_8$ dodecahedra varies from 0.2653 to 0.3057 nm.

Fig. 59 shows the excitation and emission spectra of Sr$_{0.97}$Eu$_{0.03}$AlSi$_4$N$_7$, which exhibits the highest emission intensity under excitation at 450 nm

(Ruan et al., 2011). $SrAlSi_4N_7:Eu^{2+}$ phosphors have a strong absorption band ranging from the UV to the visible, efficiently excitable by a blue light. A broad red emission band with a peak at 625 nm can be seen, and the external quantum efficiency is ∼49% under excitation at 460 nm. At 150°C, the emission intensity under excitation at 460 nm is ∼83% of that at room temperature.

4.3 Sulfides and Oxysulfides

(Oxy)sulfide phosphors have been used in electro- and cathode luminescence. There consist in blue-light excitable materials such as $AES:Eu^{2+}$ (AE = Ca and Sr) and $AEGa_2S_4:Eu^{2+}$ (AE = Ca and Sr) with strong covalent character of the sulfide ions. Since most of the sulfide phosphors have poor chemical stability with respect to humidity, protection of the phosphor particles by a coating layer is required.

4.3.1 $AES:Eu^{2+}$ (AE = Ca and Sr) Phosphors

Rare earth-doped alkaline-earth sulfide materials are well-known phosphors for electroluminescent and cathodoluminescent displays as well as for electron trapping optical memory materials (Ando and Ono, 1990; Choi et al., 1998; Kato and Okamoto, 1983; Pham-Thi and Ravaux, 1991; Wu et al., 2002). Among the alkaline-earth sulfide phosphors, CaS- and SrS-based phosphors have attracted great attention due to their potential for applications in displays (Collins and Ling, 1993; Kravets, 2001; Pham-Thi and Ravaux, 1991). In particular, Eu^{2+}-activated AES (AE = Ca and Sr) have recently been reconsidered to be one of the promising red phosphor candidates for white LEDs (Guo et al., 2006; Hu et al., 2005; Kim et al., 2006; Yang et al., 2014a,b). They have a well-known cubic rock-salt structure with space group $Fm3m$ (a = 0.5695 nm for CaS and a = 0.6020 nm for SrS). The Ca^{2+} and Sr^{2+} ions form $(Ca/Sr)S_6$ octahedra where the Ca–S and Sr–S bond distances are 0.2845 and 0.2900 nm, respectively.

Both $CaS:Eu^{2+}$ and $SrS:Eu^{2+}$ have a broad optical absorption band in the visible ranging from 400 to 600 nm and exhibit a broad red emission peaking at 610 nm in $SrS:Eu^{2+}$ and at 650 nm in $CaS:Eu^{2+}$ (Hu et al., 2005), as shown in Fig. 60. An all-proportional solid solution can be formed between CaS and SrS, making it possible to tune the emission color via controlling the Ca/Sr ratio. Unfortunately, $(Ca,Sr)S:Eu^{2+}$ phosphors are known to exhibit large thermal quenching. Actually, with increasing temperature up to 150°C, the emission intensity of $SrS:Eu^{2+}$ decreases by more than 40% of that at room temperature (Kuo et al., 2010b). Recently, Yang et al. (2014a,b) succeeded to improve considerably the thermal quenching resistance of $CaS:Eu^{2+}$ by doping it with small amounts of Mg and Ga. At 150°C, the emission intensity of $Ca_{0.89}Mg_{0.01}Ga_{0.1}S:Eu^{2+}$ reaches 75% of that measured at room temperature. The Mg and Ga doping also results in significant enhancement of the emission intensity at room temperature.
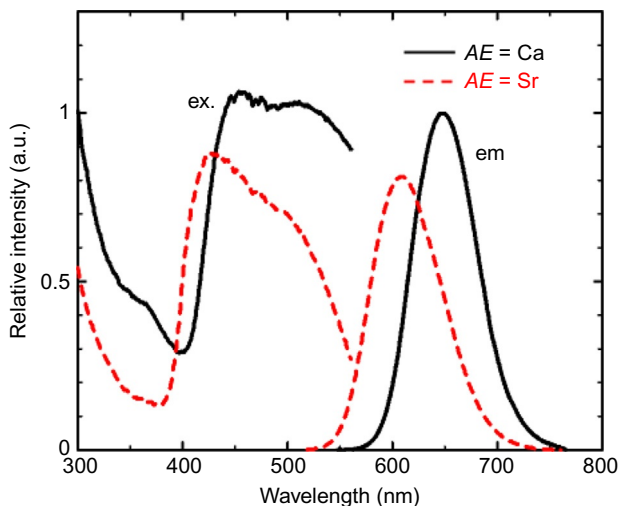
FIG. 60 Excitation and emission spectra of AES (AE=Ca and Sr). *Redrawn from Hu, Y., Zhuang, W., Ye, H., Zhang, S., Fang, Y., Huang, X. 2005. Preparation and luminescent properties of (Ca$_{1-x}$,Sr$_x$)S:Eu^{2+} red-emitting phosphor for white LED. J. Lumin. 111, 139–145.*

4.3.2 $Sr_8Al_{12}O_{24}S_2$:Eu^{2+} Phosphors

The crystal structures of the alkaline-earth oxysulfide compounds $AE_8Al_{12}O_{24}S_2$ (AE=Ca and Sr) have been determined (Brenchley and Weller, 1992). Fig. 61 shows the structure of $Sr_8Al_{12}O_{24}S_2$ which is cubic with space group $I\bar{4}3m$ and a=0.9257 nm.

$Sr_8Al_{12}O_{24}S_2$:Eu^{2+} exhibits a broad excitation band from 400 to 500 nm with a maximum at 450 nm and, under excitation at 450 nm, it exhibits a broad reddish–yellow emission with a maximum at 605 nm (Kuo et al., 2010a,b) (Fig. 62). The broad excitation band well matches with the emission spectral range of a blue-LED chip. The emission intensity measured at 150°C is approximately 70% of that at 25°C. The emission intensity of $Sr_8Al_{12}O_{24}S_2$:Eu^{2+} is successfully enhanced by Er^{3+} codoping (Dong et al., 2012).

4.3.3 $AEGa_2S_4$:Eu^{2+} (AE=Alkaline Earth) Phosphors

Rare earth-doped alkaline-earth thiogallates, $AEGa_2S_4$, have been investigated extensively and used as a green phosphors in field emission displays (FEDs) and thin-film electroluminescent (TFEL) devices from a long time (Bayramov et al., 2003; Ko et al., 2008; Peters and Baglio, 1972; Souriau et al., 2000). Recently, Eu^{2+}-activated $AEGa_2S_4$ are considered to be the most promising candidates for white LEDs as green or yellow phosphors (Huh et al., 2003; Jiang et al., 2000; Joos et al., 2012; Kim et al., 2005d, 2015a; Zhang et al., 2007b).

The crystal structure of $AEGa_2S_4$ is orthorhombic with space group $Fddd$ (Peters and Baglio, 1972). On the other hand, $BaGa_2S_4$ has a crystal structure
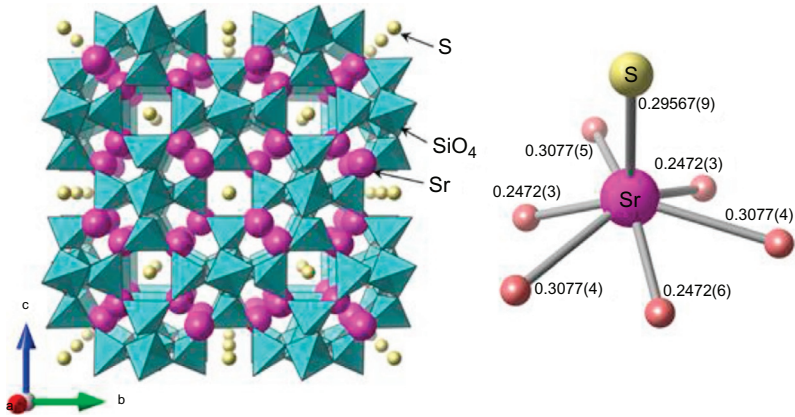
FIG. 61 Crystal structure of $Sr_8Al_{12}O_{24}S_2$. The unit of bond distance is nm. *Pictures were drawn based on the structure data obtained from the database (ICSD #67590).*
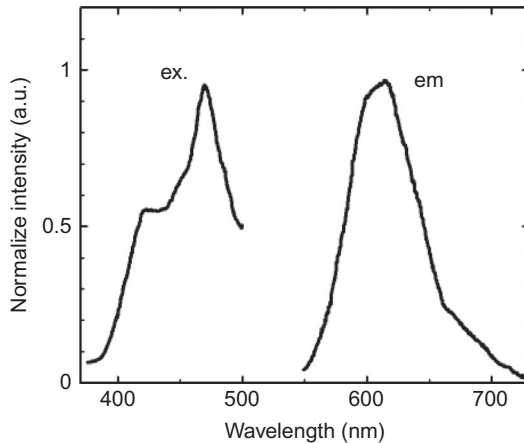
FIG. 62 Excitation and emission spectra of $Sr_8Al_{12}O_{24}S_2:Eu^{2+}$. *Redrawn from Dong, K., Li, Z., Xiao, S., Xiang, Z., Zhang, X., Yang, X., Jin, X., 2012. Yellowish-orange luminescence in $Sr_8Al_{12}O_{24}S_2:Eu^{2+}$ phosphor. J. Alloys Compd. 543, 105–108.*

different from those of $CaGa_2S_4$ and $SrGa_2S_4$: it crystallizes in the cubic space group $Pa\overline{3}$. The detail crystallographic data of $AEGa_2S_4$ are summarized in Table 9. The crystal structure of $SrGa_2S_4$ is shown in Fig. 63. The Sr^{2+} ions occupy square antiprismatic sites formed by eight S^{2-} ions, forming a SrS_8 dodecahedron (Eisenmann et al., 1983). The Sr^{2+} ions are located in three different sites; 8a, 8b, and 16c. The Ga^{3+} ions form GaS_4 tetrahedra.

The excitation spectra of $CSGa_2S_4:Eu^{2+}$ (CS = Ca and Sr) show a broad band extending from 300 to 500 nm (Fig. 64). The broad excitation bands are well matched with the emission spectra of blue-LED chips. $BaGa_2S_4:Eu^{2+}$

TABLE 9 Structure Data of $AEGa_2S_4$ (AE = Alkaline Earth)
(Peters and Baglio, 1972)

	$CaGa_2S_4$	$Sr_2Ga_2S_4$	$Ba_2Ga_2S_4$
Crystal system	Orthorhombic	Orthorhombic	Cubic
Space group	Fddd	Fddd	$Pa\bar{3}$
a (nm)	2.0122(6)	2.0932(6)	1.2660(4)
b (nm)	2.0090(6)	2.0549(6)	1.2660(4)
c (nm)	1.2133(4)	1.2227(4)	1.2660(4)
V (nm^3)	4.90478	5.25922	2.02909
Z	32	32	12
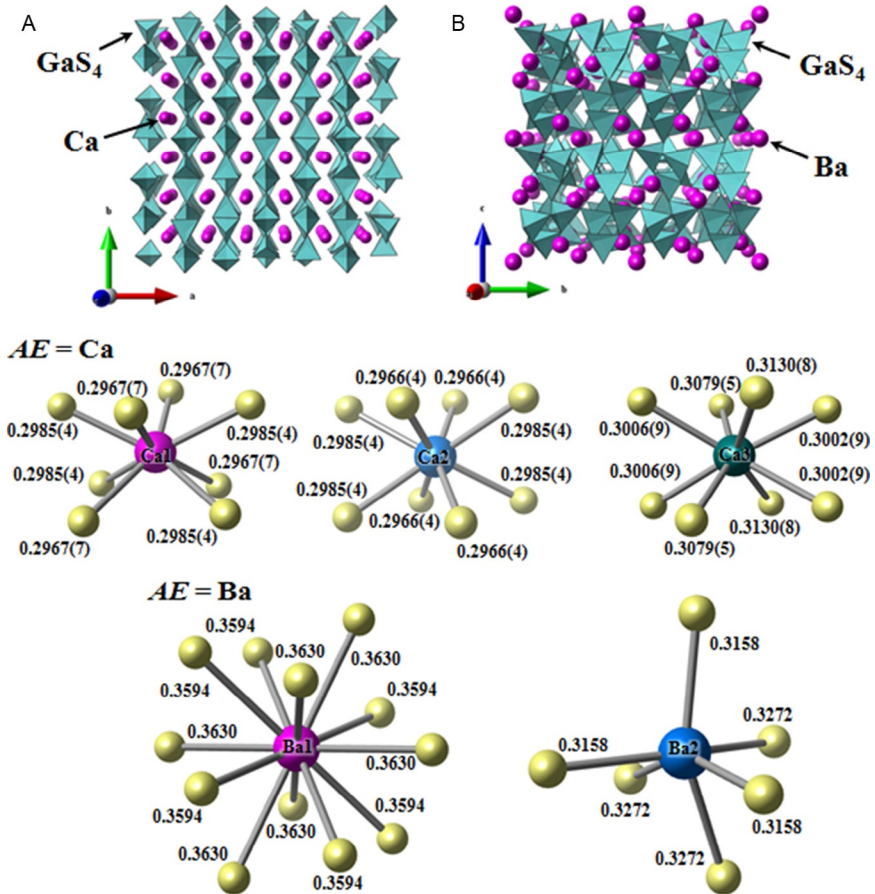
FIG. 63 Crystal structures of $AEGa_2S_4$ (AE = (A) Ca and (B) Ba). The unit of bond distance is nm. *Pictures were drawn based on the structure data obtained from the database (ICSD #46017 (AE=Ca), #22036 (AE=Ba)).*
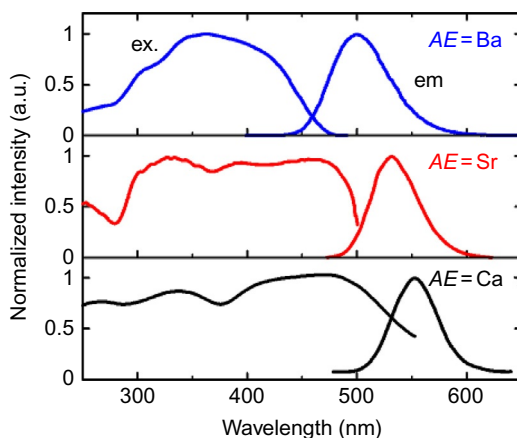
FIG. 64 Excitation and emission spectra of $AEGa_2S_4:Eu^{2+}$ ($AE=$ alkaline earth). *Redrawn from Do, Y.R., Bae, J.W., Kim, Y., Yang, H.G., 2000. Preparation and optical properties of SrGa_2S_4:Eu phosphor. Bull. Korean Chem. Soc. 21, 295–299; Guo, C., Zhang, C., Lü, Y., Tang, Q., Su, Q., 2004. Luminescent properties of Eu^{2+} and Ho^{3+} co-doped CaGa_2S_4 phosphor. Phys. Stat. Sol. 201, 1588–1593; Yoo, H.S., Im, W.B., Vaidyanathan, S., Park, B.J., Jeon, D.Y., 2008. Effects of Eu^{2+} concentration variation and Ce^{3+} codoping on photoluminescence properties of BaGa_2S_4:Eu^{2+} phosphor. J. Electrochem. Soc. 155, J66–J70.*

presents a blue–green emission band centered at 498 nm. $CaGe_2S_4:Eu^{2+}$ and $SrGa_2S_4:Eu^{2+}$ exhibit a green emission (530 nm) and a yellow emission (550 nm), respectively (Ko et al., 2008). The internal quantum efficiency of $SrGa_2S_4:Eu^{2+}$ is 71% under excitation at 460 nm (Hidaka and Takizawa, 2008). Kim et al. (2015a,b) reported the $SrGa_2S_4:Eu^{2+}$ phosphor embedded in glass materials for white LEDs. Thermal stability of the phosphor against temperature quenching is effectively enhanced. The emission intensity measured at 150°C is ∼89% of that at 25°C, which is higher by 5% than that of the powdered $SrGa_2S_4:Eu^{2+}$ phosphor. Recently, a novel Eu^{2+}-activated $CaGa_2S_4$ phosphor with monoclinic morphology was shown to exhibit higher emission intensity compared to the orthorhombic phase $CaGa_2S_4:Eu^{2+}$ phosphor (Suzuki et al., 2012).

4.4 Oxyhalides

Oxyhalide phosphors activated with rare earth ions have been used in X-ray intensifier screens and similar radiographic devices. At present, there are few practical oxyhalide phosphors for white LEDs.

4.4.1 Oxychlorides

4.4.1.1 $Ca_8Mg(SiO_4)_4Cl_2:Eu^{2+}$ Phosphors

Calcium magnesium chlorosilicate with composition $Ca_8Mg(SiO_4)_4Cl_2$ is one of the good phosphor host materials having large chemical and thermal
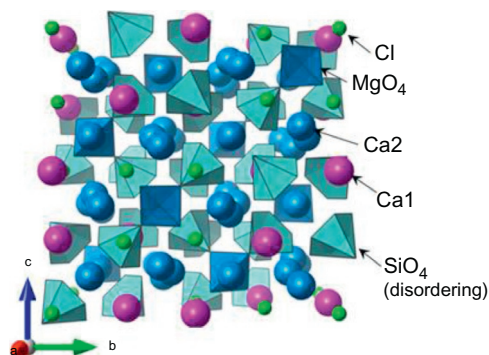
FIG. 65   Crystal structures of $Ca_8Mg(SiO_4)_4Cl_2$. *Picture was drawn based on the structure data obtained from the database (ICSD #68243).*

stability; in particular, Eu^{2+}-activated $Ca_8Mg(SiO_4)_4Cl_2$ have been demonstrated to be high efficient green-emitting phosphors for near-UV and blue-LED-based white LEDs (Guo et al., 2011a; Koo et al., 2008; Li et al., 2013; Lin et al., 2002; Zhang and Liu, 1992). The structure of $Ca_8Mg(SiO_4)_4Cl_2$ is cubic with space group $Fd\bar{3}m$ and $a = 1.506$ nm. There are three kinds of cation sites with different crystallographic environments: two Ca^{2+} sites (Ca1 and Ca2) and one Mg^{2+} site (Fig. 65). The site for Ca1 (C_{2v} symmetry) adopts six-fold oxygen coordination with additional capping by the next nearest six Cl^- at a distance of approximately 0.5 nm. Whereas, the site of Ca2 (C_1 symmetry) adopts eightfold coordination with six oxygen and two chlorine. The site ratio of Ca1:Ca2 in the structure is 1:3. In addition, Mg^{2+} occupies a tetrahedral position with four O^{2-} at the identical distance of 0.186 nm.

The excitation spectrum of the phosphor involves a broad absorption band from 280 to 480 nm, covering near-UV and blue light region (Fig. 66). In the emission spectrum under excitation at 330 nm, there are obviously two emission bands with peaks at 425 and 503 nm. In view of the crystal-field strength of each Ca^{2+} site, the emission bands at around 425 and 505 nm originate from Eu^{2+} substituting for Ca1 and Ca2 site, respectively (Lei et al., 2010; Wang et al., 2007; Zhang and Liu, 1992). When excited at 440 nm, the intensity of the green emission (503 nm) measured at 150°C is 64% of that measured at 25°C (Li et al., 2013).

4.4.1.2 $Sr_3Al_2O_5Cl_2$:Eu^{2+} Phosphors

Detailed crystallographic data for $Sr_3Al_2O_5Cl_2$ are only available from the study by Leib and Müller-Buschbaum (1986). According to this study, $Sr_3Al_2O_5Cl_2$ crystallizes in an orthorhombic structure with space group $P2_12_12_1$, $a = b = c = 0.9422$ nm and $V = 0.8364$ nm^3. Surprisingly, the lattice parameters apparently belong to a cubic system in spite of the orthorhombic system reported. The reported space group seems to be wrong, and the cubic space
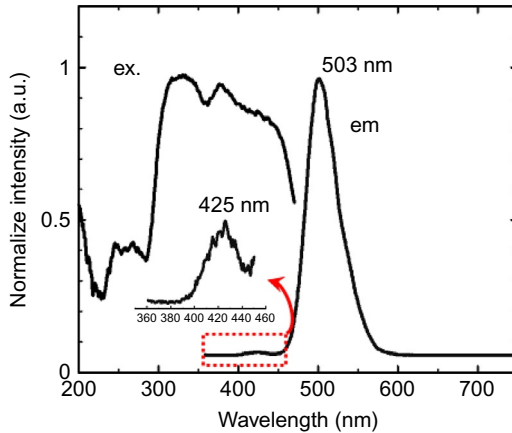
FIG. 66 Excitation and emission spectra of $Ca_8Mg(SiO_4)_4Cl_2:Eu^{2+}$. *Redrawn from Wang, J., Zhang, M., Zhang, Q., Ding, W., Su, Q., 2007. The photoluminescence and thermoluminescence properties of novel green long-lasting phosphorescence materials $Ca_8Mg (SiO_4)_4Cl_2:Eu^{2+},Nd^{3+}$. Appl. Phys. B 87, 249–254. The emission spectrum was obtained by exciting at 330 nm.*

group $P2_13$, which is a super groups of $P2_12_12_1$, is probably the correct space group. Anyway, the crystal structure of $Sr_3Al_2O_5Cl_2$ based on the reported data is shown in Fig. 67. There are three independent Sr^{2+} sites. All Sr^{2+} ions have ninefold coordination with five oxygen and four chlorine atoms, and there are little differences among the Sr–O distances in the three Sr^{2+} site, as summarized in Table 10 (Leib and Müller-Buschbaum, 1986, 1988).

$Sr_3Al_2O_5Cl_2:Eu^{2+}$ shows intense optical absorption in near-UV region and exhibits a broad red emission band centered at ∼620 nm with FWHM of approximately 160 nm due to a typical $4f^65d^1 \rightarrow 4f^7$ transition of Eu^{2+} (Chen et al., 2015a; Dutczak et al., 2013; Zhang et al., 2009a) (Fig. 68). With increasing temperature, the emission intensity decreases rapidly. At 150°C, the emission intensity is down to 27% of the initial value at 25°C (Dutczak et al., 2013). The CRI of the white LEDs combining an InGaN-based blue-LED chip with the $Sr_3Al_2O_5Cl_2:Eu^{2+}$ phosphor is 66, and the luminous efficacies of the fabricated devices are approximately 1.2–2.2 lm/W (Zhang et al., 2009a,b,c).

4.4.1.3 (Ca,Sr)$_7$(SiO$_3$)$_6$Cl$_2$:Eu^{2+} Phosphors

The crystal structure and photoluminescence properties of $(Ca,Sr)_7(SiO_3)_6Cl_2$: Eu^{2+} (Cl_MS:Eu^{2+}) are reported by Daicho et al. (2012). The crystallographic data were determined using synchrotron radiation diffraction data obtained from a Cl_MS single crystal. The structure of $(Ca,Sr)_7(SiO_3)_6Cl_2$ is shown in Fig. 69. In the structure, there are three crystallographically independent cation sites, denoted by $M1$, $M2$, and $M3$, where $M1$ is fully occupied by Ca^{2+}, $M2$ is fully occupied by Sr^{2+}, and $M3$ is disordered in the ratio of
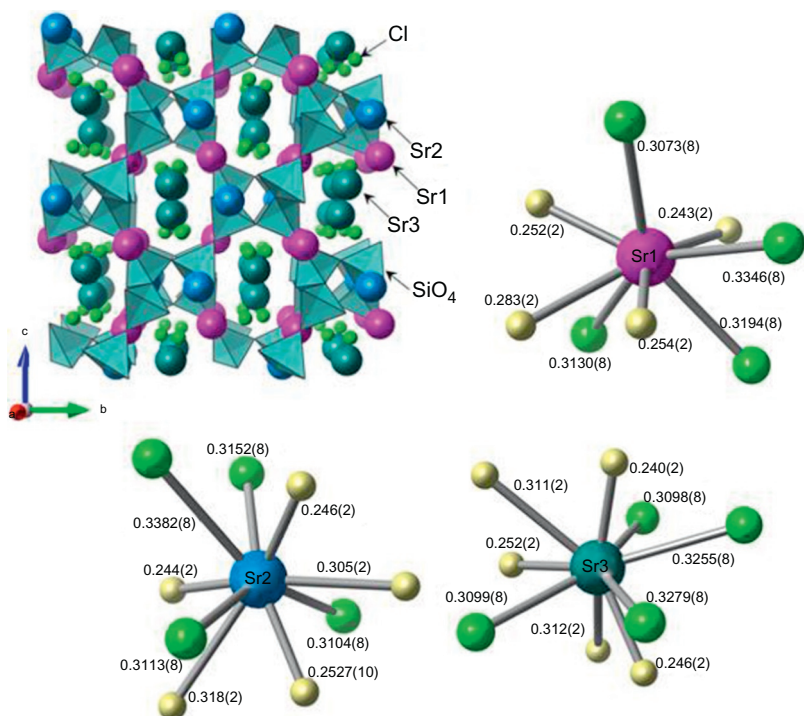
FIG. 67 Crystal structures of $Sr_3Al_2O_5Cl_2$. The unit of bond distance is nm. *Pictures were drawn based on the structure data obtained from the database (ICSD #68365).*

TABLE 10 Sr–O/Cl Bond Distance (nm) in $Sr_3Al_2O_5Cl_2$ (Leib and Müller-Buschbaum, 1986)

Sr1	Distance	Sr2	Distance	Sr3	Distance
Sr1-O2	0.2433	Sr2-O1	0.2437	Sr3-O1	0.2401
Sr1-O3	0.2523	Sr2-O2	0.2461	Sr3-O2	0.2459
Sr1-O1	0.2545	Sr2-O4	0.2527	Sr3-O5	0.2520
Sr1-O4	0.2833	Sr2-O5	0.3048	Sr3-O3	0.3111
Sr1-O4	0.3398	Sr2-O5	0.3181	Sr3-O3	0.3120
Sr1-Cl1	0.3073	Sr2-Cl1	0.3104	Sr3-Cl1	0.3098
Sr1-Cl2	0.3130	Sr2-Cl2	0.3113	Sr3-Cl2	0.3099
Sr1-Cl1	0.3194	Sr2-Cl2	0.3152	Sr3-Cl2	0.3255
Sr1-Cl2	0.3346	Sr2-Cl1	0.3382	Sr3-Cl1	0.3279
Average	0.2942	Average	0.2934	Average	0.2927
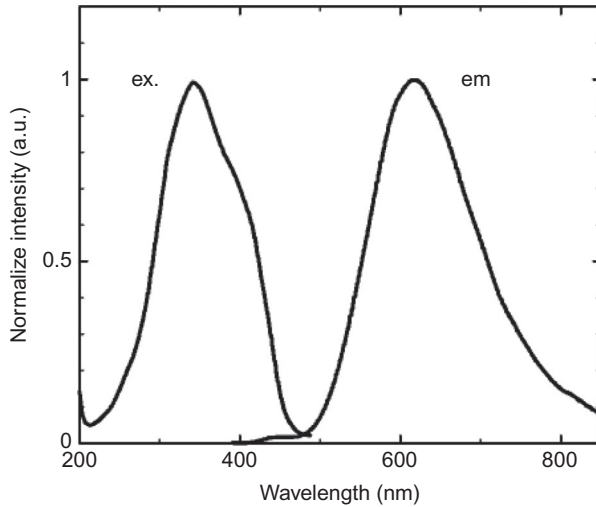
FIG. 68 Excitation and emission spectra of $Sr_3Al_2O_5Cl_2$:Eu^{2+} phosphor. *Redrawn from Zhang, X., Choi, N., Park, K., Kim, J., 2009a. Orange emissive $Sr_3Al_2O_5Cl_2$:Eu^{2+} phosphor for warm-white light-emitting diodes. Solid State Commum. 149, 1017–1020; Zhang, X., Wu, H., Zeng, H., Su, Q., 2007. Luminescent properties of $SrGa_2S_4$:Eu^{2+} and its application in green-LEDs. J. Rare Earth 25, 701–705; Zhang, X., Zhou, F., Shi, J., Gong, M., 2009. $Sr_{3.5}Mg_{0.5}Si_3O_8Cl_4$:$Eu^{2+}$ bluish–green-emitting phosphor for NUV-based LED. Mater. Lett. 63, 852–854.*
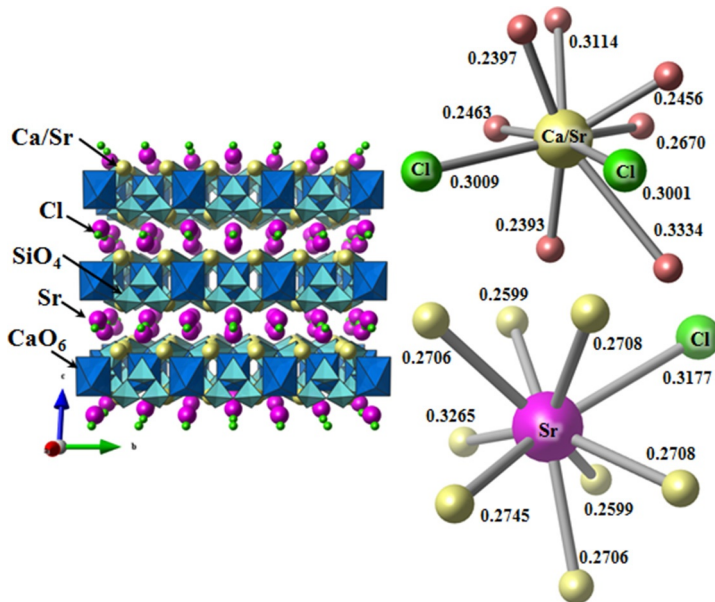
FIG. 69 Crystal structures of $(Ca,Sr)_7(SiO_3)_6Cl_2$. The unit of bond distance is nm. *Pictures were drawn based on the structure data obtained from the database (Daicho et al., 2012).*
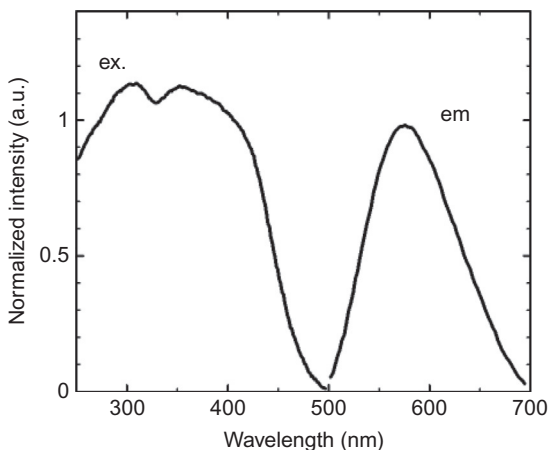
FIG. 70   Excitation and emission spectra of $(Ca,Sr)_7(SiO_3)_6Cl_2:Eu^{2+}$. *Redrawn from Daicho, H., Iwasaki, T., Enomoto, K., Sasaki, Y., Maeno, Y., Shinomiya, Y., Aoyagi, S., Nishibori, E., Sakata, M., Sawa, H., Matsuishi, S., Hosono H., 2012. A novel phosphor for glareless white light-emitting diodes. Nat. Commun. 3, 1132.*

$Ca/Sr = 0.55/0.45$. The $M1$ site (indicated by blue octahedron circle in Fig. 69) adopts sixfold oxygen coordination, forming CaO_6 octahedra that, together with SiO_4 tetrahedra, construct a $Ca(SiO_3)_6$ framework. The $M2$ site (indicated by purple spheres in Fig. 69) adopts eightfold coordination with seven oxygen and one chlorine atoms. The $M3$ site (indicated by yellow spheres in Fig. 69) adopts sevenfold coordination with five oxygen and two chlorine atoms. From Rietveld refinement, it is clear that Eu^{2+} ions substitute both for the $M2$ and $M3$ sites.

Cl_MS:Eu^{2+} shows a strong absorption band in the near-UV region, extending from 370 to 420 nm and exhibits a strong broad emission band peaking at ~580 nm (Fig. 70). The highest emission intensity of the phosphors is obtained for $(Ca_{0.37}Sr_{0.53}Eu_{0.10})_7(SiO_3)_6Cl_2$, the internal quantum efficiency of which is 94% under excitation at 407 nm. Furthermore, Cl_MS:Eu^{2+} has an excellent thermal stability with respect to temperature quenching: the emission intensity measured at 150°C is 94% of that at 25°C.

4.4.2   Oxyfluorides
4.4.2.1 $(Sr,Ba)_3AlO_4F:Ce^{3+}$ Phosphors

$(Sr,Ba)_3AlO_4F$ belongs to the Cs_3CoCl_5-family structure and is isostructual with Ba_3MO_5-type materials (M = tetravalent metal) (Glasser and Glasser, 1965; Drofenik and Golic, 1979; Im et al., 2010, 2011). Fig. 71 shows the crystal structure of $(Sr,Ba)_3AlO_4F$ with space group $I4/mcm$. The Sr and Ba atoms are surrounded by two F and six or eight O atoms, respectively. The
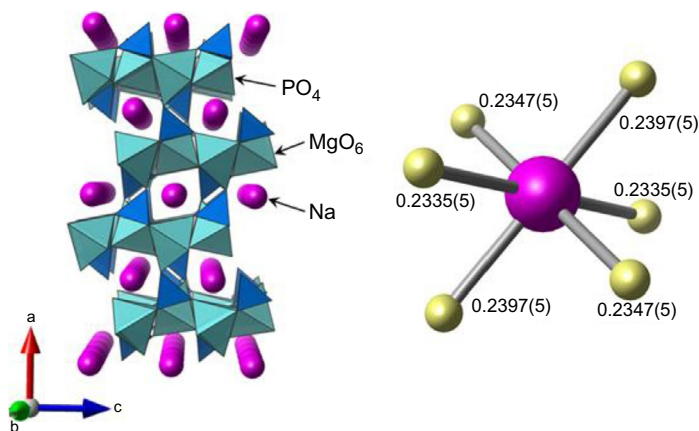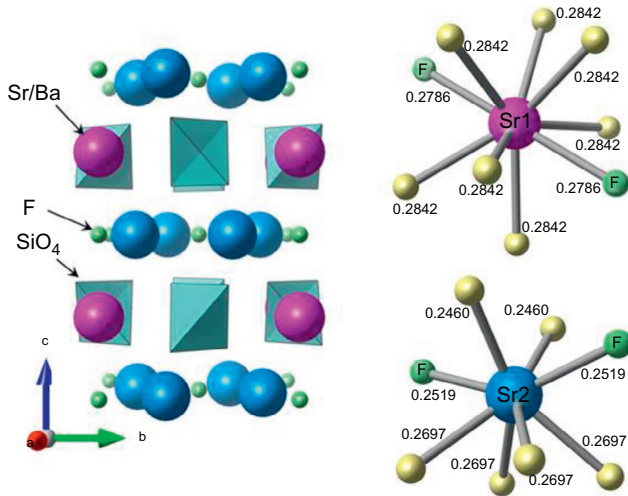
FIG. 71 Crystal structures of $(Sr,Ba)_3AlO_4F$. The unit of bond distance is nm. *Pictures were drawn based on the structure data obtained from the database (ICSD #50736).*

average Sr–F and Sr–O bond distances in the SrO_6F_2 polyhedra are 0.2572 and 0.2638 nm, respectively. The average Ba–F and Ba–O bond distances in the BaO_8F_2 polyhedra are 0.2801 and 0.2891 nm, respectively (Im et al., 2010). The dopant Ce^{3+} ions preferably occupy the Sr^{2+} site because the ionic radius of Eu^{2+} (0.125 and 0.135 nm for 8 and 10 coordination) is similar to that of Sr^{2+} (0.126 nm for 8 coordination), while the ionic radius of Ba^{2+} (0.152 nm for 10 coordination) is much larger than (Shannon, 1976).

The excitation spectrum of $(Sr,Ba)_3AlO_4F:Ce^{3+}$ includes two bands, corresponding to the $4f \rightarrow 5d$ transitions of Ce^{3+}, with the strongest absorption ranging between 380 and 450 nm (Im et al., 2010) (Fig. 72). Under a 400 nm excitation, the emission spectrum exhibits a broad green emission band with maximum at 502 nm. The composition of $Sr_{1.975}BaCe_{0.025}AlO_4F$ gives the highest emission intensity, 1.5 times higher than that of a YAG:Ce^{3+} (P46) phosphor. Furthermore, the quantum efficiency of the phosphor is approximately 95% at room temperature under excitation at 400 nm. However, the emission intensity of $(Sr,Ba)_3AlO_4F:Ce^{3+}$ decreases rapidly with increasing the temperature. At 200°C, the relative emission intensity is down to 50% of that measured at room temperature (25°C). The luminous efficacy of a white LED fabricated by coating a $(Sr,Ba)_3AlO_4F:Ce^{3+}$ phosphor on a 405 nm InGaN chip is 10–15 lm/W and the CRI (R_a) is approximately 62. Denault et al. (2012) have also reported that the luminescence efficiencies of $(Sr,Ba)_3AlO_4F:Ce^{3+}$ are effectively enhanced by doping a small amount of SiO_2 component into the $(Sr,Ba)_3AlO_4F:Ce^{3+}$ lattice, leading to a compound with formula $Sr_2Ba(AlO_4F)_{1-x}(SiO_5)_x:Ce^{3+}$.
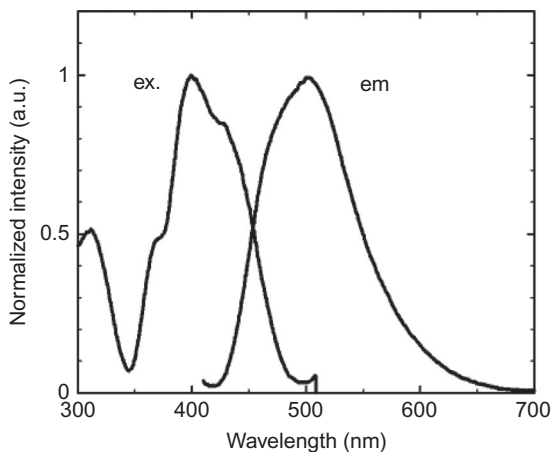
FIG. 72 Excitation and emission spectra of $(Sr,Ba)_3AlO_4F:Ce^{3+}$ at room temperature. *Redrawn from Im, W.B., Brinkley, S., Hu, J., Mikhailovsky, A., Den Baars, S.P., Sechadri, R., 2010. $Sr_{2.975-x}Ba_xCe_{0.025}AlO_4F$: a highly efficient green-emitting oxyfluoride phosphor for solid state white lighting. Chem. Mater. 22, 2842–2849.*

4.5 Energy Transfer Type Phosphors

Energy transfer among the multiple emitting ions in a phosphor is a mean of controlling the emission color. Some pairs of rare earth ions lead to efficient energy transfer, for example, $Ce^{3+} \rightarrow Tb^{3+}$ (green emission) and $Eu^{2+}/Ce^{3+} \rightarrow Mn^{2+}$ (green or red emission). The emission of Tb^{3+} occurs in the green region with sharp lines due to 4f–4f transitions. On the other hand, since the 3d orbitals of Mn^{2+} are themselves outer orbitals, the emission color is strongly dependent on the crystal field of the host crystal. In general, the colors emitted from Mn^{2+} with tetrahedral coordination are greenish and those from Mn^{2+} octahedral coordination are reddish, respectively. Absorption in the visible region by Tb^{3+} and Mn^{2+} is very low due to the forbidden character of 4f–4f and 3d–3d transitions. Therefore, the energy transfer is quite a useful method to improve the absorption of Tb^{3+} and Mn^{2+}.

4.5.1 $Y_2Si_3O_3N_4:Ce^{3+},Tb^{3+}$ Phosphors

$Y_2Si_3O_3N_4:Ce^{3+},Tb^{3+}$ is one of the color-tunable phosphors for white LEDs based on energy transfer from Ce^{3+} to Tb^{3+} (Zhu et al., 2015). Fig. 73 shows the excitation and emission spectra of the material with composition $(Y_{1-x-y}Ce_xTb_y)_2Si_3O_3N_4$ ($x=0, 0.02$ and $y=0, 0.04$). $Y_2Si_3O_3N_4:Ce^{3+}$ exhibits a blue emission with peaking at 480 nm under near-UV excitation (Fig. 73B), while $Y_2Si_3O_3N_4:Tb^{3+}$ exhibits a multipeak excitation band from 250 to 450 nm (Fig. 73A). The energy transfer from Ce^{3+} to Tb^{3+} is known to occur through two different mechanisms: (i) energy transfer from a 5d state of Ce^{3+} to the $^5D_3$ level of Tb^{3+} due to their similar energy (*Resonant energy*
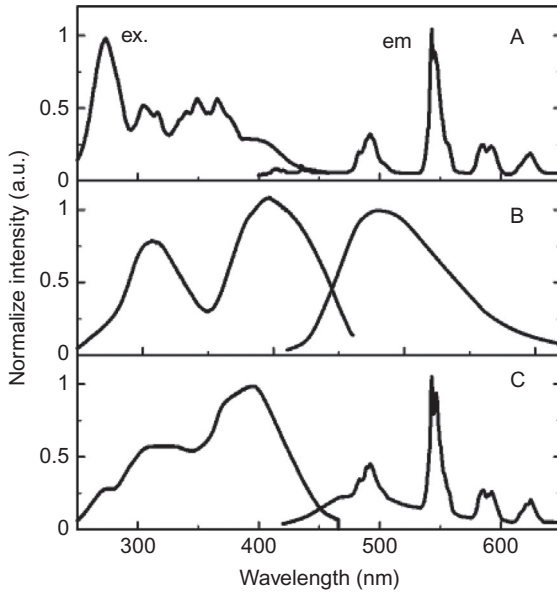
FIG. 73 Excitation and emission spectra of (A) $(Y_{0.96}Tb_{0.04})_2Si_3O_3N_4$, (B) $(Y_{0.98}Ce_{0.02})_2Si_3O_3N_4$, and (C) $(Y_{0.94}Ce_{0.02}Tb_{0.04})_2Si_3O_3N_4$. *Redrawn from Zhu, J., Qin, S., Xia, Z., Liu, Q., 2015. Synthesis and color-tunable emission studies of $Y_2Si_3O_3N_4:Ce^{3+},Tb^{3+}$ phosphors. Ceram. Int. 41, 12633–12637.*

transfer in Section 3.1.3) and (ii) reabsorption by Tb^{3+} 4f–4f transition of Ce^{3+} emission due to the overlap between the emission spectrum of Ce^{3+} (the sensitizer) and the excitation spectrum of Tb^{3+} (*Sensitization of luminescence* in Section 3.1.3). As shown in Fig. 73A and B, this overlap is sizeable. Under 395 nm excitation of Ce^{3+}, the emission spectrum of $Y_2Si_3O_3N_4:Ce^{3+}$, Tb^{3+} exhibits a broad emission centered at 480 nm caused by Ce^{3+} and a narrow green emission at 543 nm from Tb^{3+} (Fig. 73C). With increasing Tb^{3+} concentration, the relative intensity of blue emission due to Ce^{3+} decreases, whereas the relative intensity of green emission due to Tb^{3+} increases remarkably as shown in Fig. 74. The calculated energy transfer efficiency from Ce^{3+} to Tb^{3+} under a near-UV excitation also increases with increasing Tb^{3+} concentration. The highest emission intensity is obtained for $(Y_{0.78}Ce_{0.02}Tb_{0.20})_2Si_3O_3N_4$, with an energy transfer efficiency of ~61%. The CIE chromaticity coordinates of $Y_2Si_3O_3N_4:Ce^{3+},Tb^{3+}$ could be tuned from blue (0.18,0.30) to green (0.34,0.53) when the Tb^{3+} concentration goes up to 20% ($y = 0.20$).

4.5.2 $Ba_3RNa(PO_4)_3F:Eu^{2+},Tb^{3+}$ (R = Rare Earth) Phosphors

$Ba_3RNa(PO_4)_3F:Eu^{2+},Tb^{3+}$, which can be described by the general formula $(Ba_{3-x}Eu_x)_3R_{1-y}Tb_yNa(PO_4)_3F$, are examples of color-tunable phosphors for white LEDs based on energy transfer from Eu^{2+} to Tb^{3+} (Jiao et al., 2013;
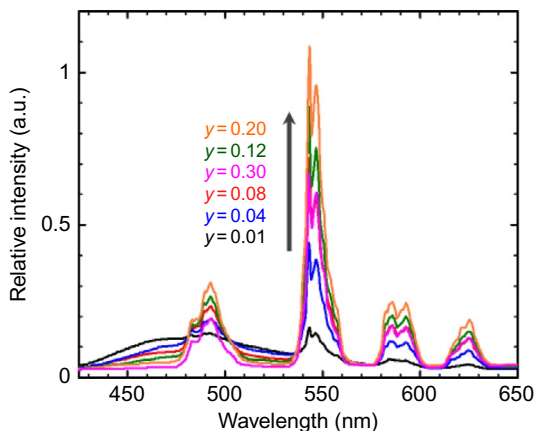
FIG. 74 Dependence of the emission spectra on the $(Y_{0.98-x}Ce_{0.02}Tb_y)_2Si_3O_3N_4$ ($0.01 \leq y \leq 0.30$). *Redrawn from Zhu, J., Qin, S., Xia, Z., Liu, Q., 2015. Synthesis and color-tunable emission studies of $Y_2Si_3O_3N_4:Ce^{3+}\cdot Tb^{3+}$ phosphors. Ceram. Int. 41, 12633–12637.*

Zeng et al., 2015). $Ba_3RNa(PO_4)_3F$ crystallizes in a hexagonal structure with space group $P\bar{6}$ (Fig. 75). There are three kinds of Ba^{2+} sites, denoted Ba1, Ba2, and Ba3, the environments of which are as shown in Fig. 75 (Mathew et al., 1979). Ba1 and Ba2 have both sevenfold coordination with five oxygen and two fluorine atoms, whereas Ba3 has sixfold oxygen coordination. The Ba1 site is occupied by Ba^{2+} and La^{3+}, and Ba2 and Ba3 sites are occupied by Ba^{2+} and Na^+, all the sites being disordered. The average Ba–X bond distances for each Ba site are as follows: Ba1–O is 0.2683 nm, Ba1–F is 0.2436 nm; Ba2–O is 0.2749 nm, Ba2–F is 0.2823 nm; Ba3–O is 0.2550 nm (Jiao et al., 2013).

$Ba_3LaNa(PO_4)_3F:Eu^{2+}$ has two broad excitation band ranging from 330 to 450 nm with a maximum at 400 nm due to Eu^{2+} (Fig. 76), which matches well with the emission of near-UV LED chips (360–410 nm). Under 400 nm excitation, the emission spectrum has an intense blue emission band with a peak at 465 nm attributed to the 5d→4f transition of Eu^{2+}. The highest emission intensity is obtained at a composition of $(Ba_{0.98}Eu_{0.02})_3LaNa(PO_4)_3F$.

Fig. 77A shows the excitation and emission spectra of $Ba_3(La_{0.90}Tb_{0.10})Na(PO_4)_3F$ and $(Ba_{0.99}Eu_{0.01})_3(La_{0.88}Tb_{0.12})Na(PO_4)_3F$. The excitation spectrum of $Ba_3(La_{0.90}Tb_{0.10})Na(PO_4)_3F$ consists of a strong broad band in the range 200–250 nm, which corresponds to the $4f^8 \rightarrow 4f^7 5d^1$ transition of Tb^{3+}. Some small peaks between 280 and 500 nm can be assigned to the 4f–4f transitions. The emission peaks at 490, 543, 581, and 619 nm correspond to the transition from the $^5D_4$ excited level to $^7F_6$, $^7F_5$, $^7F_4$, and $^7F_3$ ground levels of Tb^{3+}, respectively. The three additional peaks observed at 380, 410, and 430 nm are assigned to the $^5D_3 \rightarrow {}^7F_J$ transitions.

M1: Ba and La
M2, M3: Ba and Na
M4: La and Na
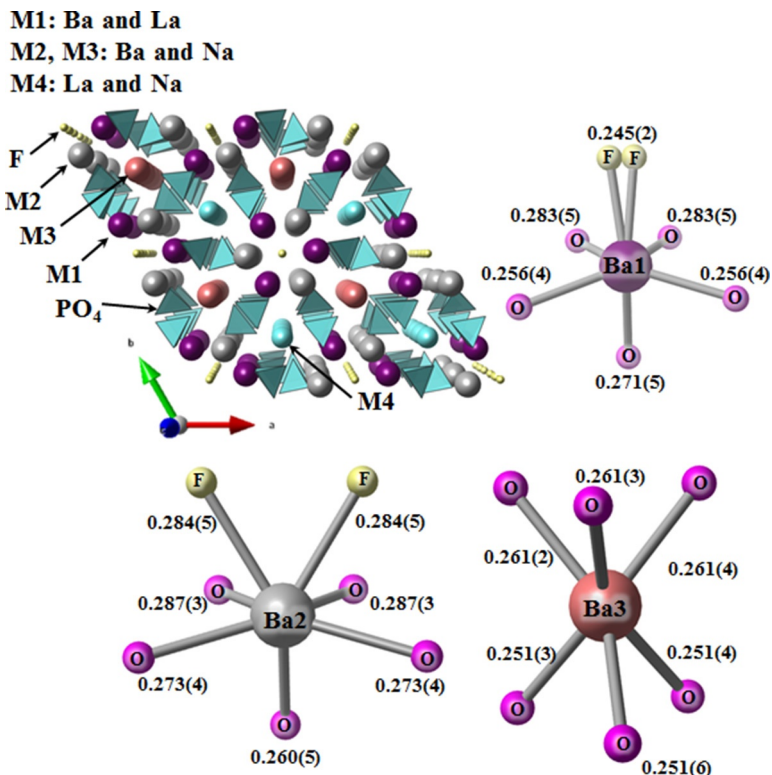
**FIG. 75** Crystal structures of Ba$_3$LaNa(PO$_4$)$_3$F, and coordination environment of three kinds of Ba sites in the structure. The unit of bond distance is nm. *Pictures were drawn based on the structure data obtained from the database (ICSD #10030).*
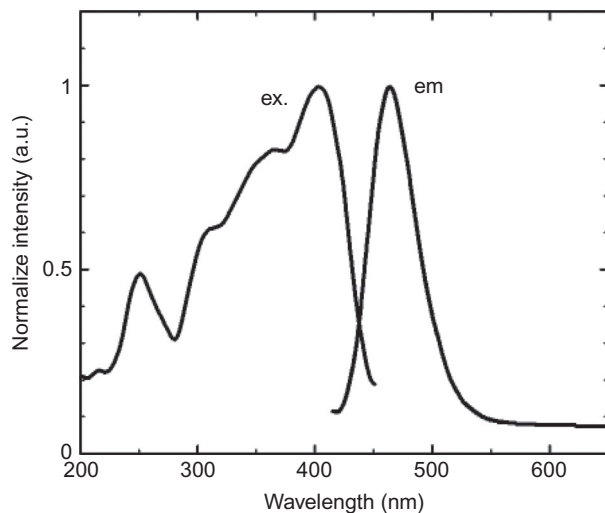
FIG. 76 Excitation and emission spectra of Ba$_3$LaNa(PO$_4$)$_3$F:Eu^{2+}. *Redrawn from Jiao, M., Guo, N., Lü, W., Jia, Y., Lv, W., Zhao, Q., Shao, B., You, H., 2013. Tunable blue-green-emitting Ba$_3$LaNa(PO$_4$)$_3$F:Eu^{2+},Tb^{3+} phosphor with energy transfer for near-UV white LEDs. Inorg. Chem. 52, 10340–10346.*
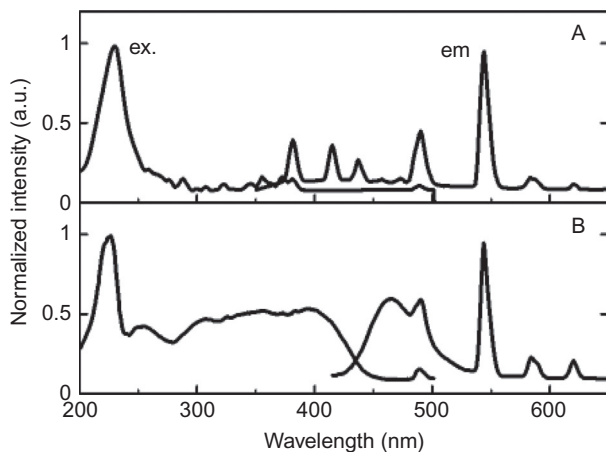
FIG. 77 Excitation and emission spectra of (A) $Ba_3(La_{0.90}Tb_{0.10})Na(PO_4)_3F$ and (B) $(Ba_{0.99}Eu_{0.01})_3(La_{0.88}Tb_{0.12})Na(PO_4)_3F$. *Redrawn from Jiao, M., Guo, N., Lü, W., Jia, Y., Lv, W., Zhao, Q., Shao, B., You, H., 2013. Tunable blue-green-emitting $Ba_3LaNa(PO_4)_3F$:Eu^{2+}, Tb^{3+} phosphor with energy transfer for near-UV white LEDs. Inorg. Chem. 52, 10340–10346.*

In $(Ba_{0.99}Eu_{0.01})_3(La_{0.88}Tb_{0.12})Na(PO_4)_3F$, the broad absorption band extending from 240 to 450 nm mainly consists of contributions from Eu^{2+} (Fig. 77B). Besides, the phosphor shows not only a broad blue emission band (Eu^{2+}) but also an intense green emission (Tb^{3+}). This is a typical example of a Eu^{2+}-to-Tb^{3+} energy transfer. The emission color of $Ba_3LaNa(PO_4)_3F$:Eu^{2+}, Tb^{3+} can be easily modulated from blue to green by adjusting the relative ratio of Eu^{2+}/Tb^{3+} content.

5 SYNTHESIS METHODS OF WHITE LED PHOSPHORS

Typical rare earth-doped phosphors for white LEDs are classified in four groups of compounds: oxides, nitrides (oxynitrides), sulfides (oxysulfides), and halides (oxyhalides). Popular synthesis methods for each group are presented in this section.

It is noteworthy that most phosphors are synthesized by reacting a mixture of raw materials containing the constituting elements of the phosphor at high temperature. The luminescent properties of the phosphors are usually improved by optimizing several parameters such as the reaction temperature and time, mixing ratio, quality and nature of the raw materials, as well as by adding reaction acceleration reagents.

5.1 Oxides

5.1.1 Solid-State Reactions

The solid-state reaction method is the most popular way of synthesizing phosphors not only oxides but also sulfides and (oxy)nitrides. Most of commercially available phosphors are synthesized by this method.

A typical procedure for a solid-state reaction is as follows.

(1) *Mixing of raw materials*: High-purity compounds that contain one or more constituent elements of the phosphor are mixed thoroughly. Reaction accelerators (called "flux" in this field) are often added into the mixture. The raw materials containing the activator elements, the amounts of which are very small, are usually mixed in one of the raw materials for the main components by coprecipitation (Narita, 2006).

(2) *Firing*: The mixture is heated up to high temperatures to react the raw materials efficiently and completely. The temperatures of the reaction are different depending on the phosphors. However, typical oxide phosphors are obtained by heating at 1000–1500°C.

(3) *Postheating process*: The substance obtained by the firing process is the "phosphor." However, it includes by-products, unreacted raw materials, residue of flux, etc. Therefore, the substance undergoes several treatments to purify it. Typical postheating treatments are washing, crashing, and classification, most of which are conducted on a suspension in water. The washing process is meant to dissolve unreacted raw materials, by-products, and/or residue of fluxes by water, acidic solution, or alkali solution. Typically, the fired substance is put into the solution and stirred; in some cases, the solution is also heated. After that, particle size and distribution of the phosphor are adjusted by crashing agglomerated particles and removing particles with unsuitable size. After removing the solvent, the obtained pure phosphor is dried and sieved (Narita, 2006). For example, YAG:Ce^{3+} is obtained by firing a mixture of Y_2O_3, Al_2O_3, CeO_2 at 1400–1500°C (Hoffman, 1977). It is reported that BaF_2 acts as flux reagent (reaction accelerator) for obtaining $Y_3Al_5O_{12}$:Tb^{3+} (Ohno, 1986).

5.1.2 Synthesis via Liquid Phase Precursors

High reaction temperature and long heating time are usually required for the phosphors synthesized by the solid-state reaction method because the reaction among solid-state raw materials proceeds via slow solid-phase diffusion. Therefore, the phosphor particles tend to give hard agglomerates. To overcome the drawbacks of the solid-state reaction, precursor processes, which reduce reaction temperature by using homogenously mixed precursors, are widely investigated not only for phosphors but also for large variety of complex multicomponent oxides (Kakihana, 1996; Kakihana and Yoshimura, 1999). The precursors consist in several types of compounds that include the constituent elements of the phosphors in a homogenously dispersed state. They are usually synthesized via liquid phase process and include organic components.

Many precursors have been examined. Examples are (1) the sol–gel route based upon hydrolysis condensation of metal alkoxides, (2) the gelation route based upon concentration of aqueous solutions involving metal chelates,

often called "chelate gel" or "amorphous chelate" route, and (3) the organic polymeric gel route (Kakihana, 1996). Pechini type in situ polymerizable complex method is explained in detail in a review by Kakihana (1996).

Here, an example of polymerizable complex method is described (Suzuki and Kakihana, 2007; Suzuki et al., 2007). First, aqueous solutions of the constituent metallic elements of the phosphor are prepared; they are often nitrate solutions because these salts are easily soluble. The solutions are then mixed in a ratio corresponding to the composition of the targeted phosphor. Citric acid (CA) is added to the solution that is heated to 80°C to make oxycarboxylate complexes of the metal ions. Then, a glycol (eg, propylene glycol (PG), ethylene glycol) is added and the temperature is raised to 120–150°C in order to promote polyesterification between the CA and the glycol. The obtained transparent resin is a polymeric gel in which the metal elements are dispersed homogeneously. It is heated up to 500°C to remove organic components. After that, it is heated again at higher temperature to obtain a well-crystallized phosphor. In this process, homogeneously reacted phosphors are obtained under relatively mild heating treatment because the metallic components are well dispersed in the precursor mixture and react easily.

The second example described the synthesis of $Sr_2SiO_4:Eu^{2+}$ phosphors by sol–gel process (it is usually called Pechini method) (Han et al., 2012a). A silica sol prepared from tetra-ethoxysilane (TEOS) and a solution of Sr and Eu nitrates are mixed and stirred. Subsequently CA and ethylene glycol are added. Then, polyethylene glycol is added. The mixture is stirred and the pH of the solution is maintained at 4. The mixture is heated at 80°C to hydrolyze it into a sol and then into a gel. The gel is heated to remove organic material and then heated at a higher temperature in a slightly reducing atmosphere to obtain the $Sr_2SiO_4:Eu^{2+}$ phosphor.

Recently, a water-soluble silicon compound (propylene glycol-modified silane; PGMS) that can be used for a precursor of silicate phosphor was synthesized (Suzuki and Kakihana, 2009). The preparation process is as follows: TEOS and PG are mixed and stirred at 80°C for 48 h. After that, a small amount of hydrochloric acid is added and the solution is heated again at 80°C. A transparent solution containing a water-soluble silicon compound (PGMS) is obtained.

The protocol for phosphor synthesis by polymerizable complex method using PGMS is as follows: a PGMS solution, the metal solutions, and CA are mixed, stirred, and heated at 80°C; PG is then added and the solution is heated and stirred at 120°C to promote polyesterification of CA and PG. The obtained polymeric compound is heated to remove organic components and heated again at higher temperature to obtain a crystalline phase of the phosphor. It is reported that $Zn_2SiO_4:Mn^{2+}$ (Takahashi et al., 2009), $(Ca,Ce)_3Sc_2Si_3O_{12}$ (Yamaguchi et al., 2010), $Ca_2SiO_4:Eu^{2+}$ (Luo et al., 2012), $Ba_3Si_6O_{12}N_2:Eu^{2+}$ (Yasushita et al., 2012), and $BaZrSi_3O_9:Eu^{2+}$ (Komukai et al., 2015) are obtained using the PGMS method.

Combustion synthesis is one of the methods for producing nanosized materials (Kopp Alves et al., 2013). In this process, a hydrocarbon is added to a phosphor precursor. Upon heating the hydrocarbon acts as a fuel and the precursor heats up rapidly to yield a small-sized material. Typical hydrocarbons used as fuel are glycine and urea, which are water-soluble carbohydrates. This process is used to obtain LED phosphors such as $Ba_3MgSi_2O_8$:Eu^{2+},Mn^{2+} (Kim et al., 2005e) and YAG:Ce^{3+} (Xia et al., 2005; Yan et al., 2008; Yang et al., 2007).

5.1.3   Synthesis via Aerosol

Solid-state reaction requires processes to adjust the particle size and their distribution because heating causes agglomeration of materials. The aerosol process is proposed to overcome this drawback. Because the raw materials of the phosphors are heated up while they are under the form of an aerosol, agglomeration of the obtained phosphor can be controlled.

Syntheses of spherical phosphors using thermal plasma treatment have been reported (Matsuda et al., 1998). The phosphor powders are introduced in thermal plasma at several thousands of temperature to melt and cooled down during floating to obtain spherical phosphors. The reported phosphors are not used for LEDs but for cathode-ray projection tube displays to improve their resolution and brightness (Hattori, 2001).

An aerosol process using an ultrasonic atomizer and a tubular furnace have been proposed to obtain spherical and nonagglomerated phosphors (Kang et al., 2001; Lenggoro and Okuyama, 2003; Lenggoro et al., 2001). Droplets of a metal solution that contain the raw materials of the phosphor, are introduced in a tubular furnace and heated. During heating, evaporation of the solvent and reaction of the constituents proceed, resulting in the formation of spherical phosphor powders. This process was applied to several types of LED phosphors like garnet YAG:Ce^{3+} (Lee et al., 2009c, 2010a), orthosilicate $(Ba,Sr)_2SiO_4$:Eu^{2+} (Kang et al., 2005; Lee et al., 2010b), and chloroapatite $(Ca,Mg)_5(PO_4)_3Cl$:Eu^{2+} (Wang et al., 2008).

A modification of the aerosol process consists in flame spray pyrolysis. In this procedure, heating of the aerosol is conducted by passing it through a flame generated by burning a fuel (eg, CH_4, H_2) in oxygen/nitrogen mixed gas. Gd_2O_3:Eu^{3+} and $Y_2Si_2O_7$:Eu^{3+} phosphors were prepared by this method (Hasegawa et al., 2013a; Iwako et al., 2010).

5.1.4   Other Synthesis Methods

A novel raw material was proposed recently. Silicon monoxide (SiO) was used for the synthesis of silicate phosphors as a substitute for silicon dioxide (SiO_2) (Ishigaki et al., 2011; Toda, 2012). When a mixture of raw materials of silicate phosphor-containing SiO is heated at 1400–1600°C, SiO sublimates and reacts to give other raw materials more easily in the gas phase. As a result, phosphor synthesis is better promoted and an end-product with better crystallinity is obtained.

Another novel attempt to synthesize phosphors is a rapid heating process using arc imaging furnace (Ishigaki et al., 2010). In this process, a mixture of raw materials is heated up in the furnace at around 2000°C (or more) to be a molten state within around 10 s. After a while, it is quenched and solidified by stopping heating. The cooling rate was estimated as more than 100°C/s. The process is advantageous especially in research activities because of short synthesis time. The synthesis of YAG:Ce^{3+} phosphor with a lens shape by this process was reported (Toda, 2012). The obtained phosphor sample was claimed to be useful for LED color conversion as is, that is without subsequent grinding.

5.2 (Oxy)nitrides

5.2.1 Overview

Most of nitride (oxynitride) phosphors consist of nitride (oxynitride) compounds (host materials) and rare earth activators. The host materials usually include silicon, nitrogen, and alkaline earths or rare earths. Additionally, aluminum and oxygen are occasionally included into them. A nitride phosphor can be synthesized by heating a mixture of nitride raw materials, in the same way as for an oxide phosphor. However, since most of alkaline-earth nitrides and lanthanide nitrides are not stable in an ambient atmosphere, ie, they easily react with water and/or oxygen in air, a variety of synthetic methods other than simple solid-state reaction of nitride raw materials are proposed (Chung et al., 2014; Xie and Hirosaki, 2007; Xie et al., 2010, 2011). Some alternative synthetic methods use oxide or metallic raw materials and conduct nitridation and phosphor synthesis simultaneously.

5.2.2 Synthesis of Nitride Raw Materials

Here, the synthesis methods for nitride compounds, which are important raw materials for nitride phosphors, are described. Although some of the nitride compounds are not easy to handle, they are nevertheless important starting materials.

Three methods are known for synthesizing silicon nitride (Si_3N_4), which is the most important raw material for nitride phosphors (Riley, 2000). The first one is carbothermal reaction. SiO_2 is used as a starting material. It is mixed with carbon (usually graphite) and heated at 1400–1500°C to reduce SiO_2 and obtain Si_3N_4. It is the first industrial manufacturing method of Si_3N_4 and, also, as recently recognized, the cheapest one.

$$3SiO_2 + 6C + 2N_2 \rightarrow \alpha\text{-}Si_3N_4 + 6CO \ (\text{at } 1450-1500°C)$$

The second method, direct nitridation of silicon powder, was the first large-scale production method of Si_3N_4 used in the 1960s.

$$3Si + 2N_2 \rightarrow \alpha\text{-}Si_3N_4 \ (\text{at } 1300-1400°C)$$

The last synthetic method is called diimide route, which is known to be advantageous to produce high-purity material. First, silicon diimide $Si(NH)_2$ is obtained by reaction between $SiCl_4$ and NH_3. Decomposition of $Si(NH)_2$ by heating produces amorphous Si_3N_4. Another heating is required to obtain crystalline Si_3N_4.

$$SiCl_4(l) + 6NH_3(g) \rightarrow Si(NH)_2(s) + 4NH_4Cl(s) \ (\text{at } 0°C)$$

$$3Si(NH)_2 \rightarrow Si_3N_4(\text{amorph}) + N_2(g) + 3H_2(g) \ (\text{at } 1000°C)$$
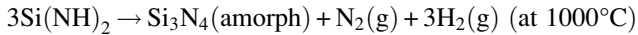
Aluminum nitride (AlN) is synthesized by either direct nitridation of metallic aluminum or carbothermal reaction (Ramisetty et al, 2014). Direct nitridation of metallic aluminum is a self-sustaining reaction, beginning from ignition of aluminum fine powder in a nitrogen-containing atmosphere. This synthetic method is advantageous with respect to low energy consumption. But the obtained material agglomerates substantially and must be ground mechanically into a fine powder.

$$2Al(s/l) + N_2(g) \rightarrow 2AlN(s) + \text{heat}$$
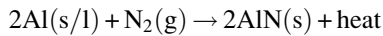
Carbothermal reaction is conducted as follows: powders of Al_2O_3 and carbon are mixed and heated at 1400–1800°C.

$$Al_2O_3(s) + 3C(s) + N_2(g) + \text{heat} \rightarrow 2AlN(s) + 3CO(g)$$
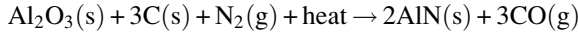
This method produces high-quality materials, whereas manufacturing cost and environmental load is high because a lot of carbon-containing by-product (CO and CO_2) are generated.

Alkaline-earth nitrides are obtained by heating alkaline-earth metals in a nitrogen-containing atmosphere. Alternatively they can also be synthesized by reaction with NH_3, but in this case, small amount of hydrides are generated as by-products (Ehrich, 1963).

Lanthanide nitrides are also obtained by reacting metallic lanthanides and N_2 or NH_3 (Kieffer et al., 1972). Carbothermal reaction of lanthanide oxides does not yield lanthanide nitrides, but lanthanide carbides. The nitrides can then be obtained by reacting the carbides with NH_3 (Nakagawa et al., 1997). It is reported that lanthanide nitrides can also be synthesized by the reaction of lanthanide chlorides and lithium azide (Li_3N) (Fitzmaurice et al., 1994).

5.2.3 Solid-State Reaction of Nitride Raw Materials

Most common synthetic methods of (oxy)nitride phosphors are also solid-state reactions. Rare earth-activated α-sialon phosphor, one of the oldest (oxy) nitride phosphors, was synthesized as follows: A mixture of α-Si_3N_4, γ-Al_2O_3, AlN, (Y_2O_3, $CaCO_3$, or Ca_3N_2), and (Tb_4O_7, CeO_2, or Eu_2O_3) was introduced into a molybdenum crucible and heated at 1700°C for 2 h in a 5% H_2+95% N_2 atmosphere (van Krevel et al., 2002). Xie et al. (2004a)

synthesized the same phosphor as follows: a mixture of α-Si_3N_4, AlN, CaO, and Eu_2O_3 was put into a boron nitride crucible and heated in pressurized nitrogen atmosphere using a resistance heating furnace.

Solid-state reaction processes are applied to produce many commercially available phosphors: eg, $Sr_2Si_5N_8$:Eu^{2+} (Li et al., 2006a,b), $CaAlSiN_3$:Eu^{2+} (Uheda et al., 2006a,b), or β-SiAlON:Eu^{2+} (Hirosaki et al., 2005) for instance. The raw materials for alkaline-earth-containing nitride phosphors, eg, $Sr_2Si_5N_8$:Eu^{2+} and $CaAlSiN_3$:Eu^{2+}, are usually handled in a glove box filled with inert gas because unstable alkaline-earth nitrides (ie, Sr_3N_2 or Ca_3N_2) are used as raw materials. On the other hand, the raw materials for some oxygen-containing nitride phosphors (called oxynitride phosphors) can be handled in air because they do not contain unstable alkaline-earth nitrides. For example, $SrSi_2O_2N_2$:Eu^{2+} can be synthesized from a mixture of $SrCO_3$, SiO_2, Si_3N_4, and Eu_2O_3, without using Sr_3N_2 (Li et al., 2005).

$$2SrCO_3 + SiO_2 + Si_3N_4 \rightarrow 2SrSi_2O_2N_2 + 2CO_2$$
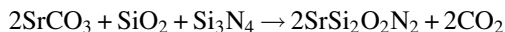
As for the $SrSi_2O_2N_2$:Eu^{2+} phosphor, a two-step synthesis was reported to improve the luminescence properties of the phosphor, ie, $(Sr,Eu)_2SiO_4$ was synthesized first and then reacted with Si_3N_4 to obtain the targeted phosphor (Yun et al., 2007).

It has been proposed that compounds other than nitrides can be used as the raw materials. For example, calcium cyanamide ($CaCN_2$) is used to synthesize the $CaSrSi_5N_8$:Eu^{2+} phosphor (Piao et al., 2008), ie, a mixture of $CaCN_2$, $SrCO_3$, Si_3N_4, and Eu_2O_3 is put into a boron nitride crucible and heated at 1823 K.

5.2.4 Gas Phase Reduction and Nitridation

The gas phase reduction and nitridation method is a synthetic process in which nitridation of easily available raw materials other than nitrides (eg, oxides) and synthesis of the phosphor are conducted simultaneously by the effect of reactive flowing gases. For example, europium-activated Ca-α'-SiAlON was synthesized by the following procedure (Suehiro et al., 2005): Ca–Al–Si–Eu mixed oxide, which is prepared by coprecipitation using CA, was placed in a tubular furnace and heated at 1350–1500°C under a flow of NH_3 and CH_4 gas mixture. Another example is the synthesis of $LaSi_3N_5$:Eu^{2+} phosphor. A mixture of La_2O_3, CeO_2, and SiO_2 was heated twice at 1350 and 1450°C under a flow of NH_3 and CH_4 gas mixture (Suehiro et al., 2009). In these reactions, NH_3 and methane react with the oxide raw materials, reducing and nitridating them to yield the desired phosphors. Using this method, nitride phosphors can be synthesized from easily available oxides and/or carbonates without expensive nitride raw materials.

5.2.5 Carbothermal Reduction and Nitridation

Another synthetic method for obtaining nitride phosphors by simultaneously conducting reduction and nitridation during heating is the carbothermal

reaction. Carbon powder instead of the mixture of hydrocarbon and ammonia is used as reducing reagent. It is advantageous from the viewpoint of process handling, since hazardous and flammable gases are not required. On the other hand, black-colored residual carbon may spoil the luminescent property of the obtained phosphors. Therefore, it is indispensable to optimize heating conditions to reduce carbon residues. This method was reported to be applied to $Sr_2Si_5N_8$:Eu^{2+} (Piao et al., 2006), α-SiAlON (Zhang et al., 2007a), and $SrYSi_4N_7$:Eu^{2+} (Kurushima et al., 2010) phosphors.

5.2.6 Synthesis from Metallic Raw Materials

An alternative synthesis of nitride phosphors uses metallic or intermetallic raw materials (alloys). Nitridation of the raw materials and phosphor synthesis are conducted simultaneously, similarly as in the gas phase reduction and carbothermal methods. It is called self-propagating high-temperature synthesis in the case that heat generated by nitridation is used to raise temperature of the raw materials. Leading attempts to obtain nitride phosphors from metallic raw materials are described later.

A nitride phosphor $(Sr,Ca)AlSiN_3$:Eu^{2+} was synthesized from the intermetallic raw material $(Sr,Ca,Eu)AlSi$ by heating it in nitrogen gas at high pressure (190 MPa) (Watanabe et al., 2008a). The same synthetic route was applied for $CaAlSiN_3$:Eu^{3+}, but was conducted in atmospheric pressure (Piao et al., 2007a; Yang et al., 2012). Another nitride phosphor, $Ba_2Si_5N_8$:Eu^{2+}, was synthesized by heating a metallic mixture prepared by arc melting of Ba, Eu, and Si in a nitrogen gas flow at 1350–1450°C (Piao et al., 2007b). Synthesis of a $LaSi_3N_5$:Ce^{3+} phosphor was conducted by heating a mixture of LaSi, CeSi, and Si_3N_4 in nitrogen at 1873 K (Cai et al., 2009).

The so-called combustion synthesis was also applied in the synthesis of nitride phosphors. For instance, $LaSi_3N_5$:Eu^{2+} was obtained by reacting LaSi, Si, Si_3N_4, and Eu_2O_3 with the following protocol: a mixture of the above-mentioned raw materials, carbon powder, and titanium metal powder was ignited by electric current in a sealed pressure-resistant container filled with nitrogen gas. Once ignited, the combustion reaction proceeded rapidly and completed within a few minutes (Zhou et al., 2011). The carbon and titanium acted as igniter. Generated heat by nitridation of LaSi, and Si heated up the raw materials mixture itself and promoted the reaction between the raw materials.

A similar procedure was applied for $Ca_2Si_5N_8$:Eu^{2+} (Chung and Chou, 2013) and $CaAlSiN_3$:Eu^{2+} (Chung and Huang, 2014). The synthesis of the two phosphors was conducted as follows: Ca, Si, Al, Eu_2O_3, Si_3N_4, NaN_3, and NH_4Cl were mixed and pressed into cylindrical compact pellets. Igniting reagents (eg, mixture of Mg and Fe_3O_4) were filled around the pellets and ignited by an electric heating coil placed near the compact.

Another synthetic method of nitride phosphors from alloys uses supercritical ammonia, ie, nitridation is conducted not by high-temperature nitrogen

gas but by supercritical ammonia. Synthesis of CaAlSiN$_3$:Eu^{2+} was reported as follows: a CaAlSi alloy containing the Eu activator was dissolved in liquid ammonia together with reaction promoter compounds (eg, sodium amide, sodium azide) and heated in a pressure-resistant vessel at 500–800°C (Li et al., 2008a). The authors claimed that synthetic reaction of CaAlSiN$_3$ is promoted by sodium ammonometallates generated as intermediates during the reaction.

5.3   Sulfides

Some sulfide compounds are being tested as host materials of phosphors for LEDs. Most of the sulfide phosphors can be synthesized by solid-state reaction methods. Since the sulfide phosphors have long and rich history as commercial phosphors for cathode-ray tubes and electroluminescence devices, a lot of synthesis methods have been reported. Judging from the aim of this review article, the focus of this chapter will be put not on the full picture of synthesis of sulfide phosphors, but only on the sulfide phosphors useful for LED color conversion. The phosphors mentioned in this chapter include alkaline-earth sulfides, alkaline-earth thiogallates, and alkaline-earth thiosilicates. The coating methods to improve durability of the sulfide phosphors are also presented.

5.3.1   Solid-State Synthesis of Sulfide Phosphors

The most popular synthetic method of sulfide phosphors is solid-state reaction in a hydrogen sulfide (H$_2$S) gas flow (Chartier et al., 2005; Peters and Baglio, 1972; Smet et al., 2008). If all the raw materials needed are sulfides, then the phosphor can be synthesized without H$_2$S in a neutral atmosphere, eg, N$_2$ or Ar. However, the use of sulfidizing reagents improves the quality of the phosphor by preventing oxidation.

Because handling H$_2$S is difficult, many other sulfidizing reagents have been tested. Typical ones are sodium sulfide (Na$_2$S) and carbon disulfide (CS$_2$). The former is typically synthesized from a mixture of sulfur and sodium carbonate (Na$_2$CO$_3$), and the latter is synthesized from a mixture of sulfur and carbon.

Following are examples of synthetic procedures for typical sulfide phosphors for LED color conversion. A strontium thiogallate phosphor (SrGa$_2$S$_4$: Eu^{2+}) was prepared by heating presynthesized sulfide raw materials in H$_2$S gas flow at 900–1000°C (Peters and Baglio, 1972). The same phosphor was synthesized by heating oxide and carbonate raw materials (SrCO$_3$, Ga$_2$O$_3$, and Eu$_2$O$_3$) in H$_2$S gas flow (Chartier et al., 2005). Alternative preparations used sulfidizing organometallic compounds (Jiang et al., 2000) or precursors prepared by liquid phase process (Lee et al., 2009a,b). The phosphor can also be synthesized by the reaction of metal halides and Na$_2$S as sulfidizing reagent (Sastry et al., 1999).

Alkaline-earth sulfides phosphors, $(Ca,Sr)S:Eu^{2+}$, are synthesized simply by heating a mixture of commercially available sulfides and activator compounds in a reducing atmosphere (Hu et al., 2005). Recently, the so-called solvothermal method was applied to alkaline-earth sulfide phosphors. Sulfur, calcium chloride (or strontium chloride), and ethylenediamine $(NH_2CH_2CH_2NH_2)$ solvent were put into a Teflon-lined autoclave and heated to 170–220°C for 12 h (Wang et al., 2002). The obtained materials were nanocrystalline CaS (or SrS) phosphors. Van Haecke et al. conducted similar experiments (Poelman et al., 2009; Van Haecke et al., 2007). The mixtures of $CaCl_2$ (or $SrCl_2$), $EuCl_3$, S, and ethylenediamine were heated at 200°C for 12 h and single crystals of $CaS:Eu^{2+}$ (or $SrS:Eu^{2+}$) phosphors were obtained.

One of the typical methods for synthesizing thiosilicate phosphors is as follows. A mixture of CaS, Si, and activator compounds (EuS or CeF_3) was heated in H_2S gas flow to obtain $Ca_2SiS_4:Eu$ (or Ce) (Smet et al., 2008). In this process, sulfidization of one of the raw materials (Si) and the phosphor synthesis are conducted simultaneously.

5.3.2 Treatments to Improve the Durability of Sulfide Phosphors

Sulfide phosphors have been used for cathode-ray tubes and have also attracted much attention as phosphors for electroluminescent (EL) devices before the advent of LEDs. As for EL phosphors, the durability of sulfide phosphors was not sufficient and a lot of research to improve the problem has therefore been conducted. Some examples of these attempts are described in this section.

Coating treatments are the most popular ways to improve the durability of phosphors. Sol–gel processes are among the most used procedures to create an oxide coating on the phosphor particles. Widespread oxide coating materials have been examined as protective coatings for sulfide phosphors. Silicon oxide (SiO_2) and titanium oxide (TiO_2) were applied to $Ca_{0.8}Sr_{0.2}S:Eu^{2+}$, Tm^{3+} phosphors (Guo et al., 2003). Aluminum oxide (Al_2O_3) was used for $CaS:Eu^{2+}$ phosphor (Avci et al., 2011). A composite coating of SiO_2 and methyl methacrylate (MMA) has also been tested for the same phosphor (Park et al., 2008; Yoo and Kim, 2009).

Another coating method, atomic layer deposition of Al_2O_3 was reported to improve the durability of the $CaS:Eu^{2+}$ phosphor under 80°C and 80% relative humidity (Avci et al., 2009).

5.4 Halides

Most oxyhalide phosphors are synthesized by solid-state reaction similarly to oxide phosphors. The only difference is that the mixture of raw materials contains halide compounds instead of oxides. In this section, the synthesis of two of the well-known halogen-containing phosphors used for LEDs is described.

The chlorophosphate phosphor $Sr_5(PO_4)_3Cl:Eu^{2+}$ was synthesized by heating a mixture of $SrHPO_4$, $SrCO_3$, $SrCl_2$, and Eu_2O_3 at 1000–1200°C in a slightly reducing atmosphere (Kamiya and Mizuno, 2006). The fluorogermanate phosphor $3.5MgO·0.5MgF_2·GeO_2:Mn^{4+}$ was prepared by heating a mixture of MgO, MgF_2, GeO_2, and $MnCO_3$ at 1100°C in air (Okamoto and Yamamoto, 2010).

6 IMPLEMENTING PHOSPHORS IN WHITE LED LAMPS

This section deals with implementation of phosphors in LED lighting devices. Recent progresses, eg, remote phosphor and wafer-level packaging (WLP), are highlighted.

6.1 Conventional LED Packaging

Typical components of a surface mount device (SMD) white-LED package are illustrated in Fig. 78. Phosphors are mixed in the encapsulant, a sealing resin—typically, silicone or an epoxy resin—that is topping a blue-emitting LED chip. Most encapsulants used for LEDs are thermosetting resins. The mixture of resin and phosphor is poured into LED packages using a dispenser and heated to harden the resin.

6.2 Improvements for Conventional Dispensing Process

As described earlier, application of phosphor-containing resin into LED packages is usually conducted using a dispenser. However, it is difficult for common dispensers to pour a precisely constant volume of resin. As a result, the color coordinates of the LEDs may fluctuate. Improved processes have been proposed to overcome this drawback.

An improvement of conventional dispensing process has been proposed that reduces the angular distributions of CCT by adjusting the slanting angle of the reflector cup of the package. In this way, the contact angle
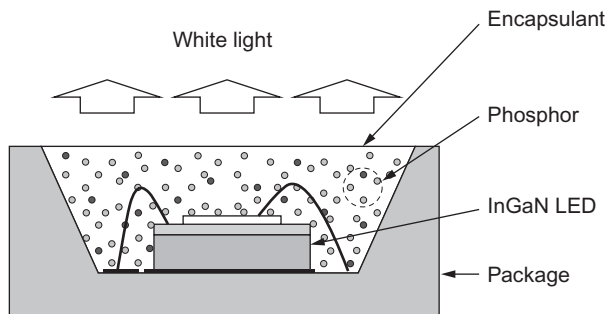
FIG. 78   Typical components of a surface mount device (SMD) type white LED package.
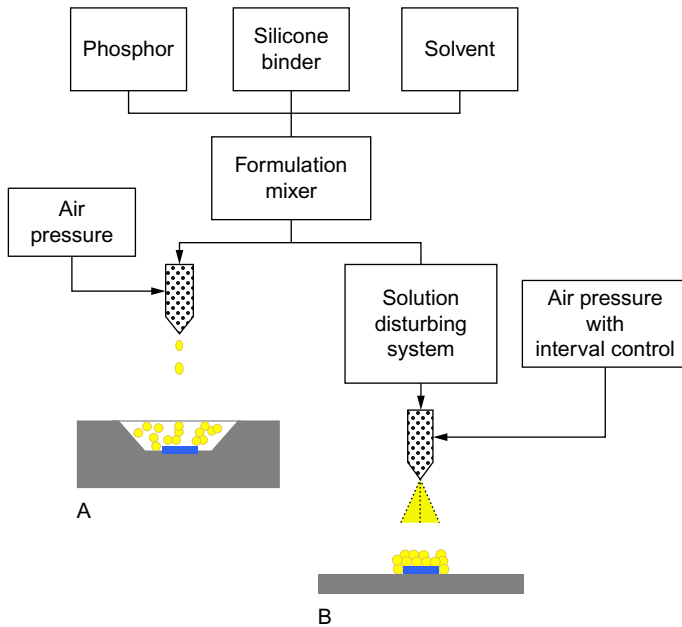
FIG. 79 Schematic diagram of the phosphor coating process. (A) Conventional dispensing and (B) pulsed spray. *Reproduced with permission from Huang, H.-T., Tsai, C.-C., Huang, Y.-P., 2010. Conformal phosphor coating using pulsed spray to reduce color deviation of white LEDs. Opt. Exp. 18 Suppl. 2, A201–A206.* © 2010 OSA Publishing.

between the resin and the reflector is the same as the slanting angle (Zheng et al., 2013).

Alternatively, a pulsed-spray process was examined for application of phosphor-containing resin into LED packages (Huang et al., 2010). The process is presented in Fig. 79. The uniformity of color coordinates obtained by this method was better compared to the conventional dispensing process, in particular, the angular distributions of the color coordinates were more stable.

6.3 Chip-on-Board

Because high light flux is presently required for lighting devices, chip-on-board (COB) type LEDs have been spreading in the market instead of devices including plenty of SMD packages. A typical structure of COB is illustrated in Fig. 80. The structure of the COB involves many LED chips that are mounted directly on a thermal conductive substrate, eg, aluminum or copper. Then, the whole LED chips are covered with an encapsulant doped with the phosphors (Administrator_of_LED_NEWS.ORG, 2013; Keeping, 2014). Using the COB technique avoids mounting SMD packages on the substrate. It is favorable not only from the viewpoint of the production cost but also from the heat
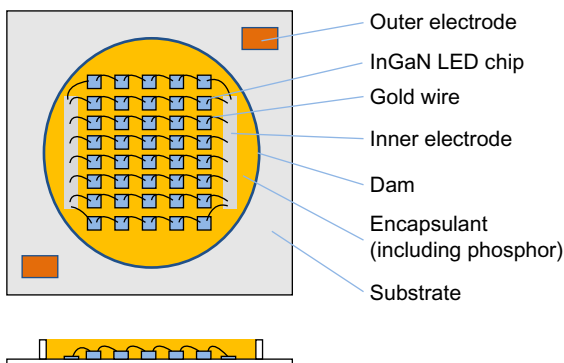
FIG. 80   Schematic view of a typical chip-on-board (COB) type LED.
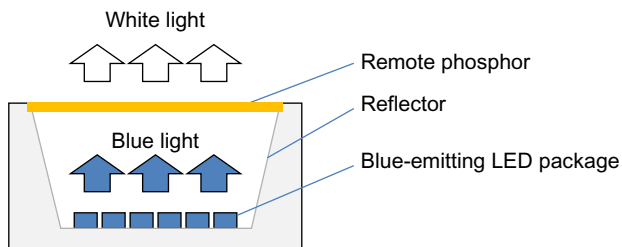
FIG. 81   Cross-sectional view of a typical remote phosphor type LED module.

dissipation of the device because the LED chips contact directly to the substrate and the thermal resistance is reduced by omitting the package of SMD.

6.4   Remote Phosphor

The "Remote phosphor" concept is a LED packaging technology in which phosphors are applied or mixed in glass or resin and the latter is positioned away from the blue-LED chip (Dal Lago et al., 2012). A typical structure of the remote phosphor type LED module is shown in Fig. 81.

Kim et al. (2005c) reported the improvement of conversion efficiency of blue-LED light to yellow light by a remote phosphor. They compared the light output of a phosphor-converted InGaN LED with different configurations of the YAG:Ce^{3+} phosphor. The light output of the remote configuration in which the phosphor-containing resin was laid over a layer of encapsulant without phosphor was larger than that of conventional configuration with a single phosphor-containing encapsulant. Their comparisons both by experiment and ray-tracing simulation revealed that the light output of the remote configuration is ∼15% larger than that of conventional configuration. Yu et al. (2010) also claimed from ray-tracing simulation that the light output of LEDs with a phosphor layer away from the LED chip is higher than that

of a conventional LED with the phosphor dispersed in encapsulant. The phosphor configuration in the latter work was not exactly the same as the so-called remote phosphor, but they indicated logically that separation of the phosphor from LED chips may improve light-conversion efficiency.

Meanwhile, Leung (2014) pointed out that the increase in manufacturing cost of remote phosphor does not balance the gain of light output. He claimed that a downlight module with increased number of conventional white LED packages is cheaper than a downlight using a remote phosphor with the same output.

There are many types of remote phosphor components. Typical ones are plate-shaped polycarbonate (Meneghini et al., 2013), polyethylene terephthalate (PET) (Huang et al., 2011a), or glass on which phosphors are applied with some binder. Phosphor-containing resins or glasses with a variety of shapes (plate, sphere, dome, etc.) have also been widely examined (Conner, 2012; Intematix, 2014; Schiel, 2012). A heat-resistant flexible fluorocarbon polymer-containing phosphor was also proposed as a remote phosphor (Huang et al., 2014).

Many phosphor-containing glasses applicable to the remote-phosphor technology have also been studied. For instance, a composite glass (called "glass ceramics") was produced by annealing a Ce-containing SiO_2–Al_2O_3–Y_2O_3 glass (Fujita et al., 2008) leading to the deposition of crystals of YAG:Ce^{3+} phosphor. Another example is a phosphor-containing glass composite, which was obtained by heating a pressed mixture of glass powder and phosphors to a temperature above the glass transition temperature T_g (Fujita et al., 2013). The composite showed no degradation under 121°C, 95% relative humidity, and 2 atm (so-called highly accelerated stress test conditions, HAST) for 300 h. On the other hand, a silicone resin composite of the same condition showed apparent degradation. A last example is a phosphor-doped glass obtained by mixing a SiO_2–Na_2O–Al_2O_3–Ca_2O glass powder with the phosphor (Tsai et al., 2013). The glass showed better stability in light output during the thermal aging test than a phosphor-mixed silicone resin.

Electrophoretic deposition (EPD) is another process tested for application of phosphors on glass plates. The EPD process results in high particle densities, but adhesion is usually low. To remedy this problem, a photochemical reaction was applied to the EPD process (Yum et al., 2003). A mixed solution of polyvinyl alcohol and ammonium dichromate ((NH_4)$_2$$Cr_2O_7$) was deposited on the phosphor layer made by EPD. Then, UV light was irradiated on it to improve the adhesion. Another way of improving the adhesion was proposed (Kitabatake et al., 2012). First, the surface of a phosphor powder was coated with SiO_2 synthesized from TEOS. The coated phosphor was then deposited on a glass plate by EPD and a SiO_2 sol was applied on the phosphor layer to fill up the space between phosphors. Finally, the plate was heated to 773 K to convert the SiO_2 sol to SiO_2 glass and fill up the space to improve the adhesion of phosphors.

6.5 Technologies for Wafer-Level Packaging

The so-called WLP technology has being recently applied to the fabrication of LEDs (Uhrmann et al., 2011). WLP is a semiconductor process in which formation of electric circuits is conducted on the semiconductor wafer, instead of circuit patterning on a substrate. In the WLP in LED fabrication, the phosphor-containing resin is directly applied to the LED wafer or a phosphor-containing tape or sheet is put onto the LED wafer before it is separated into individual LED chips. The LEDs are ordinarily produced in flip chip (or controlled collapse chip connection) process because the phosphor layer prevents circuit interconnection by wire bonding process. Uhrmann et al. (2011) examined phosphor application of WLP by spray coating. The process prevented sedimentation of phosphor particles and improved the uniformity of color coordinates of the LEDs.

Sintered ceramic plates of phosphors are one of the common forms of phosphors at WLP (Raukas et al., 2012). The advantages of ceramic plates compared to other application methods using resins have been claimed to be higher thermal conductivity, good durability, and lower activator concentration. The latter can be brought by higher density of phosphors in ceramic plates. Low activator concentration is advantageous because it reduces thermal quenching of the phosphor. On the other hand, several drawbacks are pointed out: higher manufacturing cost, limited number of materials available under the form of ceramic plates, difficulty in mixing two or more phosphors into a single component. Owing to the drawbacks, ceramic phosphor plates have not been so popular in commercial application. However, they have been utilized in some special applications requiring high durability and high operating temperature like the headlight of automobiles to increase the light output. As another example of ceramic plate phosphors, it was reported that $(Ba,Sr)_2Si_5N_8:Eu^{2+}$ phosphor was used to make amber color LEDs (Mueller-Mach et al., 2009).

7 TABULATION OF LUMINESCENCE DATA OF PHOSPHORS FOR WHITE LEDs

Reliable luminescence data found in the literature are listed in Table 11 as a useful information on phosphors for the readers.

8 CONCLUDING REMARKS

Among the devices shown in Fig. 3, type (A) that is a white LED combining by a blue light-emitting InGaN LED chip and a yellow-emitting phosphor is currently believed to be the most reliable SSL device from the viewpoint of cost and performance. This is because yellow-emitting $YAG:Ce^{3+}$ has an excellent external quantum efficiency (>99% in manufacture goods) as well

TABLE 11 Luminescence Data of Phosphor Materials for White-LED

Host	Dopant	Conc. (mol%)	λ_{ex} (nm)	λ_{em} (nm)	$T_{1/2}$ (K)	QE (in/ex)	References
Oxide							
$(Ba,Sr)_2SiO_4$	Eu^{2+}	2	395	512	–	78%/–	[1,2]
$(Ba,Sr)_3SiO_5$	Eu^{2+}	4	460	580	400	73%/–	[3]
$(Ba,Sr)_{10}(PO_4)_4(SiO_4)_2$	Eu^{2+}	75	430	507	–	–/–	[1]
$Ba_2MgSi_2O_7$	Eu^{2+}	7	395	505	–	92%/–	[4,5]
Ba_2SiO_4	Eu^{2+}	1	365	503	<500	–/–	[6]
$Ba_2ZnSi_2O_7$	Eu^{2+}	5	413	503	–	–/–	[7]
$Ba_9Sc_2Si_6O_{24}$	Eu^{2+}	5	450	508	–	–/–	[8]
$BaSiO_3$	Eu^{2+}	1	363	555	–	–/–	[9]
$Ca_{1.65}Sr_{0.35}SiO_4$	Eu^{2+}	0.2	375	515	–	<52%/–	[10]
$Ca_2Al_2SiO_7$	Eu^{2+}	3	365	510	–	–/–	[11]
$\alpha'_L\text{-}Ca_2SiO_4$	Eu^{2+}	40	450	653	–	21%/–	[12]
$\gamma\text{-}Ca_2SiO_4$	Ce^{3+}	0.5	445	575	–	28%/–	[13]
$Ca_2Y_2Si_2O_9$	Eu^{2+}	1	335	496	–	–/–	[14]
$Ca_3Sc_2Si_3O_{12}$	Ce^{3+}	3	450	505	–	41%/–	[15-17]
$Ca_3Si_2O_7$	Eu^{2+}	1	460	603	–	–/–	[18]
$Ca_5(PO_4)_2SiO_4$	Eu^{2+}	5	365	530	–	–/–	[19]

TABLE 11 Luminescence Data of Phosphor Materials for White-LED—Cont'd

Host	Dopant	Conc. (mol%)	λ_{ex} (nm)	λ_{em} (nm)	$T_{1/2}$ (K)	QE (in/ex)	References
$K_4CaSi_3O_9$	Eu^{2+}	3	355	525	–	40%/–	[20]
$CaSiO_3$	Eu^{2+}	1	343	440	–	–/–	[9]
α'-$CaSrSiO_4$	Eu^{2+}	5	460	600	–	68%/56%	[21]
$KBaScSi_3O_9$	Eu^{2+}	6	405	521	–	–/–	[22]
Li_2SrSiO_4	Eu^{2+}	0.5	450	562	–	–/–	[23]
$Li_4SrCa(SiO_4)_2$	Ce^{3+}	3	360	420	–	97%/66%	[24]
$Na_{0.34}Ca_{0.66}Al_{1.66}Si_{2.34}O_8$	Ce^{3+}	0.5	335	414	–	–/–	[25]
$NaAlSiO_4$	Eu^{2+}	10	400	551	–	–/–	[26]
$NaBaScSi_2O_7$	Eu^{2+}	10	365	501	–	65%/–	[27]
$RbBaScSi_3O_9$	Eu^{2+}	10	450	500	–	–/–	[28]
$Sr_2Al_2SiO_7$	Eu^{2+}	10.4	343	490	–	–/–	[29]
$Sr_2MgSi_2O_7$	Eu^{2+}	6	395	470	305	–/–	[30]
Sr_2MgSiO_5	Eu^{2+}	2	369	462	–	–/–	[31]
$Sr_3MgSi_2O_8$	Eu^{2+}	1.5	400	461	–	79%/70%	[32]
Sr_3SiO_5	Eu^{2+}	3	400	580	–	82%/–	[33,34]
$SrSiO_3$	Eu^{2+}	1	365	505	–	40%/–	[9,35]
$Y_2Si_2O_7$	Ce^{3+}	1	350	410	–	71%/–	[36]

$BaAl_2O_4$	Eu^{2+}	5	340	499	–	–/–	[37]
$BaMgAl_{10}O_{17}$	Eu^{2+}	11.6	375	450	–	92%/–	[38]
$Ca(Y,Pr)Al_3O_7$	Ce^{3+}	5	450	490	–	–/–	[39]
$GdSr_2AlO_5$	Ce^{3+}	5	442	565	–	–/–	[40]
$LaSr_2AlO_5$	Ce^{3+}	3	445	556	225	42%/–	[41,42]
$Lu_3(Al,Sc)_5O_{12}$	Ce^{3+}	3	445	508	–	–/–	[43]
$Lu_3Al_5O_{12}$	Ce^{3+}	6	450	508	–	<100%/–	[44,45]
Sr_2ScAlO_5	Eu^{2+}	5	450	620	–	48%/–	[46]
$Sr_3Al_2O_6$	Ce^{3+}	1.3	395	460	–	–/–	[47]
$Sr_6Y_2Al_4O_{15}$	Ce^{3+}	20	460	600	–	–/–	[48]
$SrAl_2O_4$	Eu^{2+}	5	340	521	–	–/–	[37,49]
$Tb_3Al_5O_{12}$	Ce^{3+}	6	464	563	–	76%/–	[50,51]
$Y_3Al_3Ga_2O_{12}$	Ce^{3+}	0.7	440	509	–	–/–	[52]
$Y_3Al_4GaO_{12}$	Ce^{3+}	0.7	450	519	–	–/–	[53]
$Y_3Al_5O_{12}$	Ce^{3+}	3	450	545	–	75%/–	[42,54]
$(Ba,Sr)_6BP_5O_{20}$	Eu^{2+}	3	365	480	–	–/–	[2]
$Ba_2Mg(PO_4)_2$	Eu^{2+}	4	380	456	–	–/–	[55]
$Ba_7Zr(PO_4)_6$	Eu^{2+}	3	370	585	–	40%/–	[56]
$Ca_3(PO_4)_2$	Eu^{2+}	1.5	340	480	–	60%/42%	[57]

Continued

TABLE 11 Luminescence Data of Phosphor Materials for White-LED—Cont'd

Host	Dopant	Conc. (mol%)	λ_{ex} (nm)	λ_{em} (nm)	$T_{1/2}$ (K)	QE (in/ex)	References
$Ca_4(PO_4)_2O$	Eu^{2+}	1.25	460	665	–	–/–	[58]
$CsMgPO_4$	Eu^{2+}	4	410	630	–	10%/–	[59]
$LiCaPO_4$	Eu^{2+}	0.1	400	470	–	58–70%/–	[60,61]
$LiSrPO_4$	Eu^{2+}	3	400	445	–	52%/–	[62,63]
$NaBaPO_4$	Eu^{2+}	5.0	355	470	550	39%/–	[64]
$NaMgPO_4$	Eu^{2+}	2.5	450	628	–	81%/–	[65]
$NaSrPO_4$	Eu^{2+}	0.4	380	451	–	42%/–	[66]
$Rb_2CaP_2O_7$	Eu^{2+}	0.6	347	610	–	–/–	[67]
$Sr_3Gd(PO_4)_3$	Eu^{2+}	1	355	500	–	–/–	[68]
$Sr_4(PO_4)_2O$	Eu^{2+}	0.5	465	680	–	–/–	[69]
$Sr_8MgSc(PO_4)_7$	Eu^{2+}	1	400	600	–	21%/–	[70]
$Ca_7Si_2P_2O_{16}$	Eu^{2+}	5	395	525,650	–	–/–	[71]
$Li_6Gd(BO_3)_3$	Ce^{3+}	5	350	420	–	–/–	[72]
$LiCaBO_3$	Ce^{3+}	3	365	428	–	–/–	[73]
$LiSrBO_3$	Eu^{2+}	3	460	618	–	18%/–	[74]
$NaCaBO_3$	Ce^{3+}	1	347	421	–	75%/–	[75]
$NaSr_4(BO_3)_3$	Ce^{3+}	3	340	425	–	–/–	[76]

$Sr_3B_2O_6$	Eu^{2+}	7	375	585	–	–/–	[77]
$Ca_2LaZr_2Ga_3O_{12}$	Ce^{3+}	6	430	515	–	35%/–	[78]
Ca_2GeO_4	Ce^{3+}	0.5	369	489	–	23%/–	[13]
$Ca_3Lu_2Ge_3O_{12}$	Ce^{3+}	2	421	507	–	14%/10%	[79]
$Ca_3Y_2Ge_3O_{12}$	Ce^{3+}	2	425	517	–	14%/9%	[79]
$Lu_2CaMg_2(Si,Ge)_3O_{12}$	Ce^{3+}	6	470	605	–	–/–	[80]
$Sr_3Y_2Ge_3O_{12}$	Ce^{3+}	2	433	531	–	20%/11%	[79]
$Ba_3Sc_4O_9$	Ce^{3+}	0.1	437	583	–	40%/–	[81]
$CaSc_2O_4$	Ce^{3+}	1	450	510	–	–/44%	[82,83]
(Oxy)nitride							
$(Sr,Ca)AlSiN_3$	Eu^{2+}	0.8	455	628	–	70%/>80%	[84,85]
$Ba[Mg_3SiN_4]$	Eu^{2+}	0.5	465	670	–	32%/–	[86]
$Ba_2AlSi_5N_9$	Eu^{2+}	2	450	584	–	–/22.3%	[87]
$Ba_2Si_5N_8$	Eu^{2+}	2	460	580	–	79%/–	[88,89]
$Ba_2Si_5N_8$	Ce^{3+}	2	405	565	–	–/–	[90]
$Ba_3Si_6O_{12}N_2$	Eu^{2+}	20	450	526	–	–/–	[91]
$Ba_3Si_6O_9N_4$	Eu^{2+}	1	400	487	–	–/–	[92,93]
$BaSiN_2$	Eu^{2+}	2	400	606	–	40%/–	[94]
$BaSi_2O_2N_2$	Eu^{2+}	5	450	495	600	71%/–	[95,96]

TABLE 11 Luminescence Data of Phosphor Materials for White-LED—Cont'd

Host	Dopant	Conc. (mol%)	λ_{ex} (nm)	λ_{em} (nm)	$T_{1/2}$ (K)	QE (in/ex)	References
$Ca_2Si_5N_8$	Eu^{2+}	1.4	460	610	–	45%/–	[88,97]
$Ca_2Si_5N_8$	Ce^{3+}	2	395	470	–	–/–	[90,98]
$Ca_3Si_2O_4N_2$	Eu^{2+}	1	380	510	–	24%/17%	[99]
$CaAlSiN_3$	Eu^{2+}	1.6	460	660	–	83%/70%	[100]
$CaAlSiN_3$	Ce^{3+}	10	460	575	–	71%/50%	[101]
$CaSi_2O_2N_2$	Eu^{2+}	2	400	560	440	76%/–	[95,96]
$CaSiN_2$	Ce^{3+}	3	535	625	–	–/40%	[102]
$La_3Si_6N_{11}$	Ce^{3+}	10	460	595	–	–/42%	[103]
$LaAl(Si,Al)_6(N,O)_{10}$	Ce^{3+}	2.75	380	496	–	45%/–	[104,105]
$LaSi_3(N,O)_5$	Eu^{2+}	10	380	545	–	–/–	[106]
$LaSi_3N_5$	Ce^{3+}	10	360	440	–	42%/67%	[107]
$LaSrSiO_3N$	Eu^{2+}	1	400	640	–	–/–	[108]
$Sr_2Si_5N_8$	Eu^{2+}	2	450	620	–	87%/71%	[88]
$Sr_2Si_5N_8$	Ce^{3+}	0.1	397	560	–	–/–	[90]
$SrAlSi_4N_7$	Eu^{2+}	2	450	635	–	>53%/–	[109]
$SrAlSi_4N_7$	Ce^{3+}	3	450	570	–	33%/–	[110]
$SrAlSiN_3$	Eu^{2+}	1	455	610	–	–/–	[111]

$SrSi_2O_2N_2$	Eu^{2+}	5	380	537	600	91%/–	[95,96,112]
$Sr_3Si_2O_4N_2$	Eu^{2+}	2.5	460	600	–	–/–	[113]
$SrSi_6N_8$	$Eu^{2}+$	3	370	450	–	44%/–	[114]
$SrSiN_2$	Eu^{2+}	2	400	674	–	25%/–	[94]
$Y_2Si_3O_3N_4$	Ce^{3+}	5	390	500	–	–/–	[115]
$Y_4Si_2O_7N_2$	Ce^{3+}	5	390	500	–	–/–	[115]
YSi_3N_5	Ce^{3+}	2	374	552	–	–/–	[116]
$YSiO_2N$	Ce^{3+}	5	375	440	–	–/–	[115]
$Ba_5Si_{11}Al_7N_{25}$	Eu^{2+}	5	405	568	–	–/–	[117]
$BaSi_4Al_3N_9$	Eu^{2+}	5	365	500	–	–/–	[117]
$Ca[LiAl_3N_4]$	Eu^{2+}	5	470	668	–	–/–	[118]
$Sr[LiAl_3N_4]$	Eu^{2+}	0.4	440	654	–	76%/52%	[119]
$Sr_3Si_{13}Al_3O_2N_{21}$	Eu^{2+}	8	365	515	–	75%/67%	[120]
Ca-α-SiAlON	Eu^{2+}	7.5	450	590	–	56%/75%	[121]
Li-α-SiAlON	Eu^{2+}		450	570	–	–/–	[122]
Sr-α-SiAlON	Eu^{2+}	2	400	575	–	–/–	[123]
Y-α-SiAlON	Eu^{2+}	5	589.5	610.6	–	17%/12%	[124]
β-SiAlON	Eu^{2+}	1.8	450	535	–	70%/61%	[125,126]
$Ba_3Ga_3N_5$	Eu^{2+}	2	365	638	–	–/–	[127]
$Sr_3B_2(O,N)_6$	Eu^{2+}		450	614	–	–/–	[128]

Continued

TABLE 11 Luminescence Data of Phosphor Materials for White-LED—Cont'd

Host	Dopant	Conc. (mol%)	λ_{ex} (nm)	λ_{em} (nm)	$T_{1/2}$ (K)	QE (in/ex)	References
(Oxy)sulfide							
Ba_2SiS_4	Ce^{3+}	1	405	435	–	36%/–	[129]
$SrSi_2S_5$	Eu^{2+}	5	400	490	–	–/–	[130]
CaS	Eu^{2+}	0.16	460	647	–	53%/–	[131]
SrS	Eu^{2+}	0.16	460	609	–	61%/–	[131]
$CaLaGa_3S_6O$	Ce^{3+}	10	398	442	–	–/–	[132]
$CaLaGa_3S_7$	Eu^{2+}	15	460	554	–	–/–	[133]
$(Zn_{0.6}Sr_{0.3}Mg_{0.1})_2Ga_2S_5$	Eu^{2+}	20	460	560	–	18%/–	[134]
$SrGa_2S_3Se$	Eu^{2+}	8	450	528	–	–/–	[135]
$Sr_8Al_{12}O_{24}S_2$	Eu^{2+}	8	450	605	–	–/–	[136]
$(Ba,Sr)_4Al_2S_7$	Eu^{2+}	1	450	594	–	45%/–	[137]
CaZnOS	Eu^{2+}	4	460	650	–	36%/–	[138]
CaZnOS	Ce^{3+},Li^+	1	460	503	–	–/–	[139]
$KLuS_2$	Eu^{2+}	0.1	390	520	–	–/–	[140]
Sr_2ZnS_3	Eu^{2+}	1	440	590	–	–/–	[141]
Y_2O_2S	Sm^{3+}	3	412	610	–	–/–	[142]
$YCaF_4S_2$	Ce^{3+}	2	470	590	–	16%/–	[143]

(Oxy)halide

$Sr_3GdNa(PO_4)_3F$	Eu^{2+}	1	390	470	–	–/–	[144]
$(Ca,Sr)_7(SiO_3)_6Cl_2$	Eu^{2+}	4	400	580	–	–/–	[145]
$Ba_5SiO_4Cl_6$	Eu^{2+}	5	370	440	–	–/–	[146]
$\beta\text{-}Ca_3SiO_4Cl_2$	Eu^{2+}	4	450	620	–	70%/–	[147]
$Ca_{10}(Si_2O_7)_3Cl_2$	Eu^{2+}	30	395	508	–	–/–	[148]
$Sr_{3.5}Mg_{0.5}Si_3O_8Cl_4$	Eu^{2+}	8	370	484	–	–/–	[149]
$Ca_8Mg(SiO_4)_4Cl_2$	Eu^{2+}	2	355	505	–	–/–	[150]
$Sr_3Al_2O_5Cl_2$	Eu^{2+}	5	400	620	–	>90%/–	[151]

$T_{1/2}$, Thermal quenching temperature; *QE*, quantum efficiency (internal/external).

[1] Yu et al. (2014); [2] Yuan et al. (2007); [3] Hua et al. (2014); [4] Toda et al. (2006); [5] Zhang et al. (2010a,b); [6] Wang et al. (2009); [7] Yao et al. (2010); [8] Nakano et al. (2009); [9] Cui et al. (2012); [10] Gandhi et al. (2014); [11] Luo and Xia (2014); [12] Sato et al. (2014); [13] Kalaji et al. (2014); [14] Zhang et al. (2012a,b); [15] Liu et al. (2013a); [16] Wu et al. (2013); [17] Suzuki et al. (2008); [18] Qian et al. (2012); [19] Roh et al. (2012); [20] Yuan et al. (2012); [21] Tezuka et al. (2013); [22] Abe et al. (2014a); [23] Saradhi and Varadaraju (2006); [24] Zhang et al. (2015a); [25] Dong et al. (2015); [26] Abe et al. (2014b); [27] Liu et al. (2013b); [28] Abe et al. (2014c); [29] Sahu et al. (2015); [30] Zhang et al. (2010a,b); [31] Chen et al. (2015b); [32] Kim et al. (2015b); [33] Shao et al. (2015); [34] Park et al. (2005); [35] Machida et al. (1982); [36] Sokolnicki (2013); [37] Chung et al. (2011); [38] Kim et al. (2002); [39] Unithrattil et al. (2014); [40] Park et al. (2014); [41] Kim and Jung (2011); [42] Im et al. (2009); [43] Zhou et al. (2015a); [44] Xu et al. (2014); [45] Samoylenko et al. (2015); [46] Zhou et al. (2010); [47] Li et al. (2010a); [48] Kawano et al. (2014); [49] Seo et al. (2014); [50] Nazarov et al. (2006); [51] Zorenko et al. (2009); [52] Yadav et al. (2013); [53] Wu et al. (2014); [54] Ji et al. (2015); [55] Xu et al. (2015); [56] Li et al. (2015a); [57] Zhou et al. (2015b); [58] Deng et al. (2013); [59] Ma et al. (2015); [60] Zhang et al. (2013a); [61] Han et al. (2012b); [62] Chen et al. (2010b); [63] Zhang et al. (2013b); [64] Zhang and Huang (2011); [65] Kim et al. (2013a,b); [66] Bandi et al. (2011); [67] Song et al. (2012); [68] Guo et al. (2012); [69] Komuro et al. (2015); [70] Huang et al. (2011b); [71] Wei et al. (2013); [72] Chen et al. (2015c); [73] Li et al. (2010b); [74] Zhang et al. (2012a,b); [75] Zhang et al. (2014a,b); [76] Guo et al. (2011b); [77] Fan et al. (2013); [78] Zhong et al. (2015); [79] Kalaji et al. (2013); [80] Setlur et al. (2006); [81] Hasegawa et al. (2014); [82] Peng et al. (2011); [83] Zhang et al. (2015b); [84] Watanabe and Kijima (2009); [85] Watanabe et al. (2008a,b); [86] Schmiechen et al. (2015); [87] Kechele et al. (2009a,b); [88] Li et al. (2006a); [89] Zeuner et al. (2008); [90] Li et al. (2006b); [91] Li et al. (2015b); [92] Mikami et al. (2009b); [93] Kim et al. (2013b); [94] Duan et al. (2008); [95] Li et al. (2005); [96] Bachmann et al. (2009b); [97] Chung and Chou (2013); [98] Van den Eeckhout et al. (2011); [99] Chiu et al. (2011); [100] Uheda et al. (2006b); [101] Li et al. (2008c); [102] Le Toquin and Cheetham (2006); [103] Seto et al. (2009); [104] Takahashi et al. (2012); [105] Xie et al. (2010); [106] Uheda et al. (2000); [107] Suehiro et al. (2009a,b); [108] Black et al. (2015); [109] Hecht et al. (2009); [110] Ruan et al. (2013); [111] Watanabe et al. (2008a,b); [112] Song et al. (2009); [113] Wang et al. (2012b); [114] Shioi et al. (2008); [115] van Krevel et al., 1998; [116] Yang et al. (2008); [117] Hirosaki et al. (2014); [118] Pust et al. (2014a); [119] Pust et al. (2014b); [120] Fukuda et al. (2009); [121] Xie et al. (2004a,b); [122] Xie et al. (2006a,b,c); [123] Shioi et al. (2010); [124] Suehiro et al. (2010); [125] Hirosaki et al. (2005); [126] Ryu et al. (2009); [127] Hinte et al. (2012); [128] Jung et al. (2011); [129] Ohashi and Ohmi (2008); [130] Nakamura et al. (2010); [131] Hu et al. (2005); [132] Yu et al. (2008); [133] Yu et al. (2012); [134] Jeong et al. (2012); [135] Yu et al. (2011); [136] Kuo et al. (2010a); [137] Hasegawa et al. (2013b); [138] Kuo et al. (2010b); [139] Zhang et al. (2014a,b); [140] Jarý et al. (2013); [141] Petrykin et al. (2010); [142] Li et al. (2008b); [143] Wu et al. (2012); [144] Jiao et al. (2014); [145] Daicho et al. (2012); [146] Zhang et al. (2009b); [147] Kim et al. (2014); [148] Ding et al. (2007); [149] Zhu et al. (2012); [150] Zhang et al. (2009c); [151] Zhang et al. (2009b).

as high thermal and chemical stability (95% in manufacture goods), meeting the demand for high power output. The phosphors with garnet-type structure involving YAG:Ce^{3+}, TAG:Ce^{3+} (Tb$_3$Al$_5$O$_{12}$:Ce^{3+}), and LuAG:Ce^{3+} have common features that are high chemical stability and high resistance against thermal quenching. In addition, since blue-emitting InGaN LED chips have high emission efficiency, these LEDs can emit a high output of white light. However, the drawback of YAG:Ce^{3+}, weakness of emission intensity in the red spectral region, leads to a white light having a low CRI. Attention is therefore presently focused on BOS:Eu^{2+} (Sr-rich (Ba,Sr)$_2$SiO$_4$:Eu^{2+}) as an alternative for YAG:Ce^{3+} (see Section 4.1.1). Controlling the ratio of Ba/Sr in BOS: Eu^{2+} makes it possible to tune the emission color from green to yellow, while keeping external quantum efficiency high. The drawback of BOS:Eu^{2+}, namely poor chemical stability against humidity is expected to be overcome with the current development in silicon oxide coating methods which have already been applied to sulfide phosphors (see Section 5). However, BOS: Eu^{2+} has another drawback, its relatively large thermal quenching, which hinders the fabrication of high output white LEDs. This can also be solved by applying the remote phosphor technology (see Section 6.4), which stirs great attention as a key technology for phosphors having low thermal stability.

Currently, the preeminence of YAG:Ce^{3+} in white LEDs is expected to continue for a while. To improve their low CRI, other white LEDs are being developed such as near-UV LEDs using RGB phosphors (type (b) in Section 2.2). It is desirable for near-UV LEDs to have an emission wavelength near 405 nm, and then the RGB phosphors need to have a strong absorption at this wavelength. Human vision has low sensitivity at 405 nm, so that white light with a high CRI can be obtained in the near-UV LEDs. At present, near-UV LEDs are, however, inferior to blue LEDs in emission efficiency, resulting in a low luminous efficacy and a short practical lifetime. In addition, blue- and red-emitting phosphors with high performance are not exploited yet, so that actually little commercial white near-UV LEDs are available.

Another promising type of white LEDs is type (c) shown in Fig. 3, a high-efficiency blue LED using RG phosphors. High emission efficiency for both for the LED and the phosphors leads to high-CRI and high-LER white LEDs. Limited to illumination uses, white LEDs combining a blue LED with a yellow-emitting phosphor like YAG:Ce^{3+} and a red-emitting nitride phosphor have already been developed. Important problems that should be solved pertain to difficulties in synthesis and the cost of nitride phosphors. No alternative for high performance nitride phosphors is available yet.

Summarizing the earlier present issues, one can understand that white LEDs based on blue-emitting LEDs are still mainstream of development of SSL devices, but improving their low CRI due to less emission ability in the red spectral region of YAG:Ce^{3+} itself is a priority. Study on development of red-emitting phosphors has been focused on nitride and oxynitride

materials. Nitride ions bring about an increase in covalent bond character due to the nephelauxetic effect of the large negative charge borne by nitride ions. The increased covalent character induces a large crystal-field splitting of 5d orbital, this being the reason for red shift of absorption and emission bands as shown in Fig. 6. Following the discovery of high performance red-emitting phosphors $CaAlSiN_3:Eu^{2+}$ (Uheda et al., 2006a), a number of nitride phosphors have been reported. The attention presently paid to nitride phosphors will continue in the future.

Apart from nitrides, other materials have been investigated as red-emitting phosphors. For instance, $Ca_2SiO_4:Eu^{2+}$ was synthesized by Sato et al. (2014) for the first time by applying a crystal-site engineering approach already known in the field of dielectric ceramics. In this approach, the activator ions are selectively doped in specific sites of the host crystal by carefully controlling the concentration of the ion and of the aliovalent ion. This method allows one to transform green-emitting $Ca_2SiO_4:Eu^{2+}$ into a red-emitting phosphor. The method is worthy of attention as a new synthetic technique for phosphor materials. In addition, red-emitting $NaMgPO_4:Eu^{2+}$ phosphors (Kim et al., 2013a) have been developed on the basis of the concept that large crystal-field splitting of 5d orbital can be obtained by inserting large Eu^{2+} ions in narrow octahedral sites; usually the Eu^{2+} ion prefers eightfold coordination in oxides.

Not mentioned in this review, are the recent advances in rare earth free red-emitting phosphors, $K_2SiF_6:Mn^{4+}$ (Adachi and Takahashi, 2008; Nguyen et al., 2014; Setlur et al., 2010; Sijbom et al., 2016). The phosphors exhibit a narrow emission band in the range 600–650 nm, which has a relatively high luminosity factor; expected use of these phosphors is in white LEDs for display backlighting.

Particle sizes of the phosphors used in white LEDs are generally large, ranging from several to several tens of micrometers, allowing the phosphor to effectively absorb radiations emitted from the LED. Additionally, a smooth flat surface is also required to prevent diffused reflection. The surface morphology of phosphors is influenced by the synthesis procedure. The solid-state reactions by heating raw materials at 1000–1500°C are usually adopted, in general, for oxide phosphors. Fluxes are frequently added into the raw materials in order to control the surface morphology. Synthesis methods via liquid phase precursors are recently the focus of attention since they enable controlling the homogeneity of the dispersed dopants as well as the particle morphology of the phosphors (see Section 5). Silicate phosphors are synthesized generally by using metal silicate raw materials, almost all of them are water insoluble. The synthesis method developed by Suzuki and Kakihana (2009) using water-soluble silicate raw materials leads to the development of high performance phosphors.

There are many difficulties in controlling the surface morphology of nitride phosphors since many nitrides have to be synthesized under severe

conditions, at $\sim$1600°C and under a pressure of $\sim$0.9 MPa in nitrogen atmosphere. A very recent improvement is the successful synthesis of $SrLiAl_3N_4$: Eu^{2+} (Pust et al., 2014b) at only 1000°C and under ambient pressure. There is hope that this unique example will be followed by others since less stringent (and simpler) synthetic conditions are urgently desired for nitride phosphors.

Several new concepts for materials design of phosphors and smart ideas for synthesis routes have been proposed in the past decade. Some of them may grow to a key technology in the coming decades for realizing much higher efficiency and lower cost materials. Nobody may have objection against the final goal, the overwhelming replacement of incandescent lamps and fluorescent lamps by white LEDs. Further efforts must be made to realize this goal.

While writing this review on November, 2014, the Royal Swedish Academy of Sciences announced that the Nobel Prize in Physics 2014 was awarded jointly to Isamu Akasaki, Hiroshi Amano and Shuji Nakamura, *for the invention of efficient blue light-emitting diodes which has enabled bright and energy-saving white light sources*. It should be again noteworthy that the role of rare earth ions, especially Ce^{3+} which emits a complementary color (yellow) of blue light, has central contribution to the development of white LEDs.

ACRONYMS AND ABBREVIATIONS

BOS	$(Ba,Sr)_2SiO_4:Eu^{2+}$
CA	citric acid
CASN	$CaAlSiN_3:Eu^{2+}$
CCT	correlated color temperature
CIE	Commission Internationale de l'Éclairage
COB	chip-on-board
CRI	color rendering index
EPD	electrophoretic deposition
FED	field emission display
FWHM	full width at half maximum
HAST	highly accelerated stress test
ICSD	inorganic crystal structure database
LED	light-emitting diode
LER	luminous efficacy of radiation
NTSC	National Television System Committee
PET	polyethylene terephthalate
PG	propylene glycol
PGMS	propylene glycol-modified silane
RG	red–green
RGB	red–green–blue

SMD   surface mount device
SPD   spectral power distribution
SSL   solid-state lighting
TEOS   tetra-ethoxysilane
UV   ultraviolet
WLP   wafer-level packaging
XRD   X-ray diffraction

REFERENCES

Abe, T., Kim, S.W., Ishigaki, T., Uematsu, K., Toda, K., Sato, M., 2014a. Synthesis of new green-emitting $KBa_{1-x}ScSi_3O_9:Eu_x^{2+}$ phosphors for white LEDs. Opt. Mater. 38, 57–60.

Abe, T., Kim, S.W., Ishigaki, T., Uematsu, K., Sato, M., Masaki, T., Yoon, D.H., Toda, K., 2014b. Synthesis and the luminescent properties of $NaAlSiO_4:Eu^{2+}$ phosphor using SiO powder as a silica source. J. Inf. Disp. 15, 31–35.

Abe, T., Kim, S.W., Ishigaki, T., Uematsu, K., Toda, K., Sato, M., 2014c. A novel bluish green-emitting $RbBaScSi_3O_9:Eu^{2+}$ phosphor for white LEDs. J. Ceram. Process Res. 15, 181–184.

Adachi, S., Takahashi, T., 2008. Direct synthesis and properties of $K_2SiF_6:Mn^{4+}$ phosphor by wet chemical etching of Si wafer. J. Appl. Phys. 104, 023512.

Administrator_of_LED_NEWS.ORG, 2013. What's COB LED? In: LED News.org. Available at: http://www.lednews.org/what-cob-led-chip-on-board-definition/ (accessed December 12, 2015).

Aitasalo, T., Hreniak, D., Hölsä, J., Laamanen, T., Lastusaari, M., Niittykoski, J., Pellé, F., Stręk, W., 2007. Persistent luminescence of $Ba_2MgSi_2O_7:Eu^{2+}$. J. Lumin. 122–123, 110–112.

Amano, H., Sawaki, N., Akasaki, I., Toyoda, Y., 1986. Metalorganic vapor phase epitaxial growth of a high quality GaN film using an AlN buffer layer. Appl. Phys. Lett. 48, 353.

Amano, H., Kito, M., Hiramatsu, K., Akasaki, I., 1989. P-type conduction in Mg-doped GaN treated with low-energy electron beam irradiation (LEEBI). Jpn. J. Appl. Phys. 28, L2112–L2114.

Ando, M., Ono, Y.A., 1990. Role of Eu^{2+} luminescent centers in the electro-optical characteristics of red-emitting CaS:Eu thin-film electroluminescent devices with memory. J. Appl. Phys. 68, 3578.

Avci, N., Musschoot, J., Smet, P.F., Korthout, K., Avci, A., Detavernier, C., Poelman, D., 2009. Microencapsulation of moisture-sensitive $CaS:Eu^{2+}$ particles with aluminum oxide. J. Electrochem. Soc. 156, J333–J337.

Avci, N., Cimieri, I., Smet, P.F., Poelman, D., 2011. Stability improvement of moisture sensitive $CaS:Eu^{2+}$ micro-particles by coating with sol–gel alumina. Opt. Mater. 33, 1032–1035.

Bachmann, V., Ronda, C., Meijerink, A., 2009a. Temperature quenching of yellow Ce^{3+} luminescence in YAG:Ce. Chem. Mater. 21, 2077–2084.

Bachmann, V., Ronda, C., Oeckler, O., Schnick, W., Meijerink, A., 2009b. Color point tuning for $(Sr, Ca, Ba)Si_2O_2N_2:Eu^{2+}$ for white light LEDs. Chem. Mater. 21, 316–325.

Bian, L., Wang, T., Liu, S., Yang, S., Liu, Q., 2012. The crystal structure and luminescence of phosphor $Ba_9Sc_2Si_6O_{24}:Eu^{2+},Mn^{2+}$ for white light emitting diode. Mater. Res. Bull. 64, 279–282.

Bandi, V.R., Jeong, J., Shin, H.J., Jang, K., Lee, H.S., Yi, S.S., Jeong, J.H., 2011. Thermally stable blue-emitting $NaSrPO_4:Eu^{2+}$ phosphor for near UV white LEDs. Opt. Commun. 284, 4504–4507.

Barbier, J., Hyde, B.G., 1985. The structures of the polymorphs of dicalcium silicate, Ca_2SiO_4. Acta Cryst. B 41, 383–390.

Barry, T.L., 1968. Fluorescence of Eu^{2+}-activated phases in binary alkaline earth orthosilicate systems. J. Electrochem. Soc. 115, 1181–1184.

Bayramov, A., Najafov, H., Kato, A., Yamazaki, M., Fujiki, K., Nazri, M., Iida, S., 2003. Feasibility of TFEL application of Ce-doped $CaGa_2S_4$ and $SrGa_2S_4$ films prepared by flash evaporation method. J. Phys. Chem. Solids 64, 1821–1824.

Black, A.P., Denault, K.A., Oró-Solé, J., Goñi, A.R., Fuertes, A., 2015. Red luminescence and ferromagnetism in europium oxynitridosilicates with a β-K_2SO_4 structure. Chem. Commun. 51, 2166–2169.

Blasse, G., Grabmaier, B.C., 1994. Energy Transfer. Luminescent Materials. Springer-Verlag, Berlin, pp. 97–107.

Blasse, G., Wanmaker, W.L., Vrugt, J.W., 1968a. Some new classes of efficient Eu^{2+}-activated phosphors. J. Electrochem. Soc. 115, 673.

Blasse, G., Wanmaker, W.L., Vrugt, J.W., Bril, A., 1968b. Fluorescence of Eu^{2+} activated silicates. Philips Res. Rep. 23, 189.

Brenchley, M.E., Weller, M.T., 1992. Synthesis and structure of sulfide aluminate sodalities. J. Mater. Chem. 2, 1003–1005.

Brill, M.H., 1998. How the CIE 1931 color-matching functions were derived from Wright–Guild data. Color Res. Appl. 23, 259.

Cai, L.Y., Wei, X.D., Li, H., Liu, Q.L., 2009. Synthesis, structure and luminescence of $LaSi_3N_5$: Ce^{3+} phosphor. J. Lumin. 129, 165–168.

Catti, M., Gazzoni, G., Ivaldi, G., 1983. Structures of twinned β-Sr_2SiO_4 and of α'-$Sr_{1.9}Ba_{0.1}SiO_4$. Acta Cryst. C 39, 29–34.

Chartier, C., Barthou, C., Benalloul, P., Frigerio, J.M., 2005. Photoluminescence of Eu^{2+} in $SrGa_2S_4$. J. Lumin. 111, 147–158.

Chen, L., Lin, C.C., Yeh, C.W., Liu, R.S., 2010a. Light Converting Inorganic Phosphors for White Light-Emitting Diodes. Materials 3, 2172–2195.

Chen, Y., Wang, J., Zhang, X., Zhang, G., Gong, M., Su, Q., 2010b. An intense green emitting $LiSrPO_4$:Eu^{2+},Tb^{3+} for phosphor-converted LED. Sens. Actuators B Chem. 148, 259–263.

Chen, L., Luo, A., Jiang, Y., Liu, F., Deng, X., Xue, S., Chen, X., Zhang, Y., 2013. Suppressing the phase transformation and enhancing the orange luminescence of $(Sr, Ba)_3SiO_5$:Eu^{2+} for application in white LEDs. Mater. Lett. 106, 428–431.

Chen, R., Hu, Y., Wu, H., Jin, Y., Mou, Z., Zhang, S., 2015a. Luminescent properties of blue green $Sr_3Al_2O_5Cl_2$:Pr^{3+} and orange red $Sr_3Al_2O_5Cl_2$:Eu^{2+}, Pr^{3+} afterglow phosphor. Radiat. Meas. 80, 38–45.

Chen, Z., Zhang, J.H., Chen, S., Lin, M.Y., He, C.Q., Xu, G.D., Wang, M.M., Yu, X.F., Zou, J.Q., Guo, K., 2015b. Preparation and luminescence property of Eu^{2+}, Mn^{2+} co-doped silicates phosphors for white LED. J. Alloys Compd. 632, 756–759.

Chen, P., Mo, F., Xia, S., Wang, G., Guan, A., Zhou, L., 2015c. Luminescence and energy transfer of color-tunable $Li_6Gd(BO_3)_3$:Ce^{3+},Tb^{3+} phosphor. Spectrochim. Acta A 149, 682–686.

Chenavas, J., Joubert, J.C., Merezio, M., 1978. On the crystal symmetry of the garnet structure. J. Less-Common Metals 62, 373–380.

Ching, W.Y., Quyang, L.Z., Yao, H.Z., Xu, Y.N., 2004. Electronic structure and bonding in the Y–Si–O–N quaternary crystals. Phys. Rev. B 70, 085105.

Chiu, Y.C., Huang, C.H., Lee, T.J., Liu, W.R., Yeh, Y.T., Jang, S.M., Liu, R.S., 2011. Eu^{2+}-activated silicon-oxynitride $Ca_3Si_2O_4N_2$: a green-emitting phosphor for white LEDs. Opt. Express 19, A331–A339.

Choi, S.W., Hong, S.H., 2009. Characterization of Ca_2SiO_4:Eu^{2+} phosphors synthesized by polymeric precursor process. J. Am. Ceram. Soc. 92, 2025–2028.

Choi, H., Kim, C.H., Pyun, C.H., Kim, S.J., 1998. Valencies of Eu in CaS:Eu, La. J. Solid State Chem. 138, 149–153.

Chung, S.-L., Chou, W.-C., 2013. Combustion synthesis of $Ca_2Si_5N_8:Eu^{2+}$ phosphors and their luminescent properties. J. Am. Ceram. Soc. 96 (7), 2086–2092.

Chung, S.-L., Huang, S.-C., 2014. Combustion synthesis and photoluminescence properties of red-emitting $CaAlSiN_3:Eu^{2+}$ phosphor for white-LEDs. Materials 7, 7828–7842.

Chung, J.H., Ryu, J.H., 2012. Photoluminescence and LED application of β-SiAlON:Eu^{2+} green phosphor. Ceram. Int. 38, 4601–4606.

Chung, W., Yu, H.J., Park, S.H., Chun, B.H., Kim, J., Kim, S.H., 2011. Spray pyrolysis synthesis of $MAl_2O_4:Eu^{2+}$ (M = Ba, Sr) phosphor for UV LED excitation. J. Cryst. Growth 326, 73–76.

Chung, S.-L., Huang, S.-C., Chou, W.-C., Tangguh, W.W., 2014. Phosphors based on nitridosilicates: synthesis methods and luminescent properties. Curr. Opin. Chem. Eng. 3, 62–67.

Collins, B.T., Ling, M., 1993. Synthesis and cathodoluminescence of orange-yellow- to red-emitting $Ca_{1-x}Mg_xS:Mn$ phosphors. J. Electrochem. Soc. 140, 1752–1755.

Conner, M., 2012. Remote Phosphors: Philips LED Bulb, Tear-down Part II | EDN. EDN network. Available at: http://www.edn.com/electronics-blogs/readerschoice/4311242/Remote-Phosphors-Philips-LED-bulb-Tear-down-Part-II (accessed December 14, 2015).

Cui, Z., Jia, G., Deng, D., Hua, Y., Zhao, S., Huang, L., Wang, H., Ma, H., Xu, S., 2012. Synthesis and luminescence properties of glass ceramics containing $MSiO_3:Eu^{2+}$ (M = Ca, Sr, Ba) phosphors for white LED. J. Lumin. 132, 153–160.

Daicho, H., Iwasaki, T., Enomoto, K., Sasaki, Y., Maeno, Y., Shinomiya, Y., Aoyagi, S., Nishibori, E., Sakata, M., Sawa, H., Matsuishi, S., Hosono, H., 2012. A novel phosphor for glareless white light-emitting diodes. Nat. Commun. 3, 1132.

Dal Lago, M., Meneghini, M., Trivellin, N., Mura, G., Vanzi, M., Meneghesso, G., Zanoni, E., 2012. Phosphors for LED-based light sources: thermal properties and reliability issues. Microelectron. Reliab. 52, 2164–2167.

Davis, W., Ohno, Y., 2005. Toward an improved color rendering metric. In: Proceedings of the SPIE Fifth International Conference on Solid State Lighting, SPIE, p. 59411G.

della Giusta, A., Ottonello, G., Secco, L., 1990. Precision estimates of interatomic distances using site occupancies, ionization potentials and polarizability in Pbnm silicate olivines. Acta Cryst. B 46, 160–165.

Denault, K.A., George, N.C., Paden, S.R., Brinkley, S., Mikhailovsky, A.A., Neuefeind, J., DenBaars, S.P., Seshadri, R., 2012. A green-yellow emitting oxyfluoride solid solution phosphor $Sr_2Ba(AlO_4F)_{1-x}(SiO_5)_x:Ce^{3+}$ for thermally stable, high color rendition solid state white lighting. J. Mater. Chem. 22, 18204–18213.

Deng, D., Xu, S., Su, X., Wang, Q., Li, Y., Li, G., Hua, Y., Huang, L., Zhao, S., Wang, H., Li, C., 2011. Long wavelength Ce^{3+} emission in $Y_6Si_3O_9N_4$ phosphors for white-emitting diodes. Mater. Lett. 65, 1176–1178.

Deng, D., Yu, H., Li, Y., Hua, Y., Jia, G., Zhao, S., Wang, H., Huang, L., Li, Y., Li, C., Xu, S., 2013. $Ca_4(PO_4)_2O:Eu^{2+}$ red-emitting phosphor for solid-state lighting: structure, luminescent properties and white light emitting diode application. J. Mater. Chem. C 1, 3194–3199.

Ding, W., Wang, J., Zhang, M., Zhang, Q., Su, Q., 2007. Luminescence properties of new $Ca_{10}(Si_2O_7)_3Cl_2:Eu^{2+}$ phosphor. Chem. Phys. Lett. 435, 301–305.

Dong, Y., Zhou, G., Xu, J., Zhao, G., Su, F., Su, L., Zhang, G., Zhang, D., Li, H., Si, J., 2006. Luminescence studies of Ce:YAG using vacuum ultraviolet synchrotron radiation. Mater. Res. Bull. 41, 1959–1963.

Dong, K., Li, Z., Xiao, S., Xiang, Z., Zhang, X., Yang, X., Jin, X., 2012. Yellowish-orange luminescence in $Sr_8Al_{12}O_{24}S_2$:Eu^{2+} phosphor. J. Alloys Compd. 543, 105–108.

Dong, J., Wang, L., Cui, C., Tian, Y., Huang, P., 2015. Luminescence properties of Ce^{3+}-doped and Ce^{3+}–Tb^{3+} co-doped $Na_{0.34}Ca_{0.66}Al_{1.66}Si_{2.34}O_8$ phosphor for UV-LED. Ceram. Int. 41, 1341–1346.

Dorenbos, P., 2003. Energy of the first $4f^7 \rightarrow 4f^65d$ transition of Eu^{2+} in inorganic compounds. J. Lumin. 104, 239–260.

Dorenbos, P., 2006. Lanthanides level locations and its impact on phosphor performance. In: Yen, W.M., Shionoya, S., Yamamoto, H. (Eds.), Fundamentals of luminescence, Phosphor Handbook, second ed., vol. 2(11). CRC Press, New York, pp. 139–154.

Drofenik, M., Golic, L., 1979. Refinement of the Sr_2EuFeO_5 and Sr_2EuAlO_5 structures. Acta Cryst. B 35, 1059.

Duan, C.J., Wang, X.J., Otten, W.M., Delsing, A.C.A., Zhao, J.T., Hintzen, H.T., 2008. Preparation, electronic structure, and photoluminescence properties of Eu^{2+}- and Ce^{3+}/Li^+-activated alkaline earth silicon nitride $MSiN_2$ (M = Sr, Ba). Chem. Mater. 20, 1597.

Dutczak, D., Ronda, C., Meijerink, A., Jüstel, T., 2013. Red luminescence and persistent luminescence of $Sr_3Al_2O_5Cl_2$:Eu^{2+}, Dy^{3+}. J. Lumin. 141, 150.

Ehrich, P., 1963. Alkaline earth metals. In: Brauer, G. (Ed.), Handbook of Preparative Inorganic Chemistry, second ed. Academic Press, New York, pp. 887–949 (Section 17).

Eisenmann, B., Jakowski, M., Klee, W., Schaefer, H., 1983. Luminescence and structural properties of $BaGa_2S_4$ and $BaAl_2S_4$. Rev. Chim. Miner. 20, 255.

Eysel, W., Hahn, T., 1970. Crystal chemistry and structure of Na_2SO_4(I) and its solid solutions. Z. Krist-New Cryst. St. 131, 322.

Fairman, H.S., Brill, M.H., Hemmendinger, H., 1977. How the CIE 1931 color-matching functions were derived from Wright–Guild data. Color. Res. Appl. 22, 11–23.

Fan, L., Zhao, X., Zhang, S., Ding, Y., Li, Z., Zou, Z., 2013. Enhanced luminescence intensity of $Sr_3B_2O_6$:Eu^{2+} phosphor prepared by sol–gel method. J. Alloys Compd. 579, 432–437.

Fang, C.M., Li, Y.Q., Hintzen, H.T., de With, G., 2003. Crystal and electronic structure of the novel nitrides $MYSi_4N_7$ (M = Sr, Ba) with peculiar NSi_4 coordination. J. Mater. Chem. 12, 1480–1483.

Feldmann, C., Jüstel, T., Ronda, C.R., Schmidt, P.J., 2003. Inorganic luminescent materials: 100 years of research and application. Adv. Funct. Mater. 13, 511–516.

Fields, J.M., Dear, P.S., Brown, J.J., 1972. Phase equilibria in the system BaO–SrO–SiO_2. J. Am. Ceram. Soc. 55, 585–588.

Fitzmaurice, J.C., Hector, A., Rowley, A.T., Parkin, I.P., 1994. Rapid, low energy synthesis of lanthanide nitrides. Polyhedron 13, 235–240.

Fujita, S., Sakamoto, A., Tanabe, S., 2008. Luminescence characteristics of YAG glass–ceramic phosphor for white LED. IEEE J. Sel. Top. Quantum Electron. 14, 1387–1391.

Fujita, N., Iwao, M., Fujita, S., Ohji, M., 2013. Wavelength conversion material "phosphor-glass composites" for high power solid-state lighting. In: Proc. Int. Display Workshops 2013, pp. 775–778.

Fukuda, Y., Ishida, K., Mitsuishi, I., Nunoue, S., 2009. Luminescence properties of Eu^{2+}-doped green-emitting Sr-sialon phosphor and its application to white light-emitting diodes. Appl. Phys. Express 2, 012401.

Gan, L., Mao, Z.Y., Wang, Y.F., Xu, F.F., Zhu, Y.C., Huang, Q., Liu, X.J., 2013. Photoluminescence properties of Ca–α-SiAlON:Ce^{3+} phosphors as function of composition and microstructure. Ceram. Int. 39, 8319.

Gandhi, S., Thandavan, K., Kwon, B.J., Woo, H.J., Jang, K., Shin, D.S., 2014. Solvothermal synthesis of red and green emitting $Ca_{1.65}Sr_{0.35}SiO_4:Eu^{3+}$ and $Ca_{1.65}Sr_{0.35}SiO_4:Eu^{2+}$ phosphors for solid-state lighting applications. Ceram. Int. 40, 5245.

Gaudé, J., Lange, J., Louër, D., 1983. $Sm_3Si_6N_{11}$, un nouveau nitrure double de silicium et de terre rare. Rev. Chim. Miner. 20, 523–527.

George, N.C., Birkel, A., Brgoch, J., Hong, B.C., Mikhailovsky, A.A., Page, K., Llobet, A., Seshadri, R., 2013. Average and local structural origins of the optical properties of the nitride phosphor $La_{3-x}Ce_xSi_6N_{11}$ ($0 < x \leq 3$). Inorg. Chem. 52, 13730–13741.

Glasser, L.S.D., Glasser, F.P., 1965. Silicates M_3SiO_5. I. Sr_3SiO_5. Acta Cryst. 18, 453.

Goldberg, P., 1966. Luminescence of Inorganic Solids. Academy Press, New York, p. 765.

Gong, Y., Wang, Y., Jiang, Z., Xu, X., Li, Y., 2009. Luminescent properties of long lasting phosphor $Ca_2MgSi_2O_7:Eu^{2+}$. Mater. Res. Bull. 44, 1916–1919.

Gu, Y., Zhang, Q., Li, Y., Wang, H., 2010. Nitridation from core-shell oxides for tunable luminescence of $BaSi_2O_2N_2:Eu^{2+}$ LED phosphors. J. Mater. Chem. 20, 6050–6056.

Guo, C., Chu, B., Wu, M., Su, Q., 2003. Oxide coating for alkaline earth sulfide based phosphor. J. Lumin. 105, 121–126.

Guo, C., Huang, D., Su, Q., 2006. Methods to improve the fluorescence intensity of $CaS:Eu^{2+}$ red-emitting phosphor for white LED. Mater. Sci. Eng. B 130, 189–193.

Guo, C., Li, M., Xu, Y., Li, T., Ren, Z., Bai, J., 2011a. A potential green-emitting phosphor Ca_8Mg $(SiO_4)_4Cl_2:Eu^{2+}$ for white light emitting diodes prepared by sol–gel method. Appl. Surf. Sci. 257, 8836–8839.

Guo, C., Ding, X., Seo, H.J., Ren, Z., Bai, J., 2011b. Double emitting phosphor $NaSr_4(BO_3)_3:Ce^{3+}$, Tb^{3+} for near-UV light-emitting diodes. Opt. Laser Technol. 43, 1351–1354.

Guo, N., Zheng, Y., Jia, Y., Qiao, H., You, H., 2012. A tunable warm-white-light $Sr_3Gd(PO_4)_3$: Eu^{2+}, Mn^{2+} phosphor system for LED-based solid-state lighting. New J. Chem. 36, 168–172.

Haferkorn, B., Meyer, G., 1998. Li_2EuSiO_4, ein Europium (II)-dilithosilicat:Eu $[(Li_2Si)\,O_4]$. Z. Anorg. Allg. Chem. 624, 1079–1081.

Han, J.K., Hannah, M.E., Piquette, A., Hirata, G.A., Talbot, J.B., Mishra, K.C., McKittrick, J., 2012a. Structure dependent luminescence characterization of green–yellow emitting $Sr_2SiO_4:Eu^{2+}$ phosphors for near UV LEDs. J. Lumin. 132, 106–109.

Han, J.K., Hannah, M.E., Piquette, A., Talbot, J.B., Mishra, K.C., McKittrick, J., 2012b. Sol-gel synthesis of single phase, high quantum efficiency $LiCaPO_4:Eu^{2+}$ phosphors. ECS J. Solid State Sci. Technol. 1, R37–R40.

Hasegawa, H., Ueda, T., Yokomori, T., 2013a. $Y_2Si_2O_7:Eu/SiO_2$ core shell phosphor particles prepared by flame spray pyrolysis. Proc. Combust. Inst. 34, 2155–2162.

Hasegawa, T., Kato, H., Takatsuka, Y., Kobayashi, M., Yamane, H., Kakihana, M., 2013b. Orange emission from $(Ba_{1-x}Sr_x)_4Al_2S_7:Eu^{2+}$ thioaluminate phosphors with visible light excitation. ECS J. Solid State Sci. Technol. 2, R3107–R3111.

Hasegawa, T., Kim, S.W., Ishigaki, T., Uematsu, K., Takaba, H., Toda, K., Sato, M., 2014. Novel reddish yellow-emitting Ce^{3+}-doped $Ba_3Sc_4O_9$ phosphors for blue-light-based white LEDs. Chem. Lett. 43, 828–830.

Hattori, H., 2001. New projection tubes using spherical phosphors and an electron gun having an impregnated cathode. J. Soc. Inf. Disp. 9, 251–255.

He, H., Fu, R., Cao, Y., Song, X., Pan, Z., Zhao, X., Xiao, Q., Li, R., 2010. $Ce^{3+} \rightarrow Eu^{2+}$ energy transfer mechanism in the $Li_2SrSiO_4:Eu^{2+}$, Ce^{3+} phosphor. Opt. Mater. 32, 632–636.

Hecht, C., Stadler, F., Schmidt, P.J., Auf der Günne, J.S., Baumann, V., Schnick, W., 2009. $SrAlSi_4N_7:Eu^{2+}$—a nitridoalumosilicate phosphor for warm white light (pc)LEDs with edge-sharing tetrahedra. Chem. Mater. 21, 1595–1601.

Henderson, B., Imbush, G.G., 1989. Optical Spectroscopy of Inorganic Solids. Clarendon, Oxford.

Hidaka, C., Takizawa, T., 2008. Optical properties of $Sr_{1-x}Eu_xGa_2S_4$ mixed compounds. J. Phys. Chem. Solids 69, 358–361.

Hinte, F., Hummel, F., Schmidt, P.J., Wiechert, D., Schnick, W., 2012. $Ba_3Ga_3N_5$—a novel host lattice for Eu^{2+}-doped luminescent materials with unexpected nitridogallate substructure. Chem. Mater. 24, 402–407.

Hirosaki, N., Xie, R.-J., Kimoto, K., Sekiguchi, T., Yamamoto, Y., Suehiro, T., Mitomo, M., 2005. Characterization and properties of green-emitting β-SiAlON:Eu^{2+} powder phosphors for white light-emitting diodes. Appl. Phys. Lett. 86, 211905.

Hirosaki, N., Takeda, T., Funahashi, S., Xie, R.J., 2014. Discovery of new nitridosilicate phosphors for solid state lighting by the single-particle-diagnosis approach. Chem. Mater. 26, 4280–4288.

Hoffman, M.V., 1977. Improved color rendition in high pressure mercury vapor lamps. J. Illuminating Eng. Soc. 6, 89–91.

Holonyak, N., Bevacqua, S.F., 1962. Coherent (visible) light emission from $Ga(As_{1-x}P_x)$ junctions. Appl. Phys. Lett. 1, 82.

Höppe, H.A., Lutz, H., Morys, P., Schnick, W., Seilmeier, A., 2000. Luminescence in Eu^{2+}-doped $Ba_2Si_5N_8$: fluorescence, thermoluminescence, and upconversion. J. Phys. Chem. Solids 61, 2001–2006.

Höppe, H.A., Stadler, F., Oeckler, O., Schnick, W., 2004. $Ca[Si_2O_2N_2]$—a novel layer silicate. Angew. Chem. 116, 5656–5659.

Hu, Y., Zhuang, W., Ye, H., Zhang, S., Fang, Y., Huang, X., 2005. Preparation and luminescent properties of $(Ca_{1-x},Sr_x)S$:Eu^{2+} red-emitting phosphor for white LED. J. Lumin. 111, 139–145.

Hua, Y., Ma, H., Deng, D., Zhao, S., Huang, L., Wang, H., Xu, S., 2014. Enhanced photoluminescence properties of orange emitting $Sr_{2.96-x}Ba_xSiO_5$:Eu^{2+} phosphors synthesized with Sr_2SiO_4 as precursor. J. Lumin. 148, 39–43.

Huang, H.-T., Tsai, C.-C., Huang, Y.-P., 2010. Conformal phosphor coating using pulsed spray to reduce color deviation of white LEDs. Opt. Express 18 (Suppl. 2), A201–A206.

Huang, H.-T., Huang, Y.-P., Tsai, C.-C., 2011a. Planar lighting system using array of blue LEDs to excite yellow remote phosphor film. J. Disp. Technol. 7, 44–51.

Huang, C.H., Chen, Y.C., Chen, T.M., Chan, T.S., Sheu, H.S., 2011b. Near UV-pumped yellow-emitting $Sr_8MgSc(PO_4)_7$:Eu^{2+} phosphor for white-light LEDs with excellent color rendering index. J. Mater. Chem. 21, 5645–5649.

Huang, K.-C., Lu, W.-J., Liao, K.-Y., Tsai, T.-C., Lai, T.-H., Sheu, G.-J., Li, Y.-L., 2014. White LED featuring remote phosphor with poly(vinylidene fluoride-co-hexafluoropropylene). Mater. Lett. 122, 265–268.

Huh, Y.D., Shim, J.H., Kim, Y., Do, Y.R., 2003. Optical properties of three-band white light emitting diodes. J. Electrochem. Soc. 150, H57–H60.

Huppertz, H., Schnick, W., 1997. Synthesis, crystal structure, and properties of the nitridosilicates $SrYbSi_4N_7$ and $BaYbSi_4N_7$. Z. Anorg. Allg. Chem. 623, 212–217.

ICSD, Inorganic Crystal Structure Database, 2015. Fachinformationszentrum Karlsruhe, Germany, and the National Institute of Standards and Technology (NIST), USA.

Im, W.B., Fellows, N.N., DenBaars, S.P., Seshadri, R., Kim, Y.I., 2009. $LaSr_2AlO_5$, a versatile host compound for ce^{3+}-based yellow phosphors: structural tuning of optical properties and use in solid-state white lighting. Chem. Mater. 21, 2957–2966.

Im, W.B., Brinkley, S., Hu, J., Mikhailovsky, A., Den Baars, S.P., Sechadri, R., 2010. $Sr_{2.975-x}Ba_xCe_{0.025}AlO_4F$: a highly efficient green-emitting oxyfluoride phosphor for solid state white lighting. Chem. Mater. 22, 2842–2849.

Im, W.B., George, N., Kurzman, J., Brinkley, S., Mikhailovsky, A., Hu, J., Chmelka, B.F., Den Baars, S.P., Sechadri, R., 2011. Efficient and color-tunable oxyfluoride solid solution phosphors for solid-state white lighting. Adv. Mater. 23, 2300–2305.

Intematix, 2014. Intematix—ChromaLitTM remote phosphor. Available at: http://www.intematix. com/products/chromalit (accessed December 14, 2015).

Ishigaki, T., Yoshimura, M., Matsushita, N., Uematsu, K., Toda, K., Sato, M., 2010. Melt synthesis of Eu-doped oxide phosphors using arc-imaging furnace. J. Eur. Ceram. Soc. 30, 165–169.

Ishigaki, T., Toda, K., Sakamoto, T., Uematsu, K., Sato, M., 2011. Crystal growth of silicate phosphors from the vapor phase. IEICE Trans. Electron. E94-C, 1745–1748.

Iwako, Y., Akimoto, Y., Omiya, M., Ueda, T., Yokomori, T., 2010. Photoluminescence of cubic and monoclinic Gd_2O_3:Eu phosphors prepared by flame spray pyrolysis. J. Lumin. 130, 1470–1474.

Izumi, F., Mitomo, M., Suzuki, J., 1982. Structure refinement of yttrium α-sialon from X-ray powder profile data. J. Mater. Sci. Lett. 1, 533–535.

Jack, K.H., Wilson, W.I., 1972. Ceramics based on the Si-Al-O-N and related systems. Nat. Phys. Sci. 238, 28–29.

Jacobs, R.R., Krupke, W.F., Weber, M.F., 1978. Measurement of excited-state-absorption loss for Ce^{3+} in $Y_3Al_5O_{12}$ and implications for tunable 5d→4f rare-earth lasers. Appl. Phys. Lett. 33, 410.

Jang, H.S., Jeon, D.Y., 2007a. Yellow-emitting Sr_3SiO_5:Ce^{3+},Li^+ phosphor for white-light-emitting diodes and yellow-light-emitting diodes. Appl. Phys. Lett. 90, 041906.

Jang, H.S., Jeon, D.Y., 2007b. White light emission from blue and near ultraviolet light-emitting diodes precoated with a Sr_3SiO_5:Ce^{3+},Li^+ phosphor. Opt. Lett. 32, 3444–3446.

Jang, H.S., Yang, H., Kim, S.W., Han, J.Y., Lee, S.G., Jeon, D.Y., 2008. White light-emitting diodes with excellent color rendering based on organically capped CdSe quantum dots and Sr_3SiO_5:Ce^{3+},Li^+ phosphors. Adv. Mater. 20, 2696–2702.

Jang, H.S., Kwon, B.H., Yang, H., Jeon, D.Y., 2009a. Bright three-band white light generated from CdSe/ZnSe quantum dot-assisted Sr_3SiO_5:Ce^{3+},Li^+-based white light-emitting diode with high color rendering index. Appl. Phys. Lett. 95, 161901.

Jang, H.S., Won, Y.H., Vaidyanathan, S., Kim, D.H., Jeon, D.Y., 2009b. Emission band change of $(Sr_{1−x}M_x)_3SiO_5$:Eu^{2+} (M=Ca, Ba) phosphor for white light sources using blue/near-ultraviolet LEDs. J. Electrochem. Soc. 156, J138–J142.

Jarý, V., Havlák, L., Bárta, J., Mihóková, E., Jarý, V., Havlák, L., Bárta, J., Mihóková, E., Nikl, M., 2013. Optical properties of Eu^{2+}-doped $KLuS_2$ phosphor. Chem. Phys. Lett. 574, 61–65.

Jee, S.D., Park, J.K., Lee, S.H., 2006. Photoluminescence properties of Eu^{2+}-activated Sr_3SiO_5 phosphors. J. Mater. Sci. 41, 3139–3141.

Jeong, Y.K., Cho, D.H., Kim, K.B., Kang, J.G., 2012. Highly luminescent $(Zn_{0.6}Sr_{0.3}Mg_{0.1})_2Ga_2S_5$:$Eu^{2+}$ green phosphors for a white light-emitting diode. Bull. Korean Chem. Soc. 33, 2523–2528.

Ji, E.K., Song, Y.H., Lee, M.J., Yoon, D.H., 2015. Thermally stable phosphor-in-glass for enhancement of characteristic in high power LED applications. Mater. Lett. 157, 89–92.

Jiang, Y.D., Villalobos, G., Souriau, J.C., Paris, H., Summers, C.J., Wang, Z.L., 2000. Synthesis and properties of green phosphor $SrGa_2S_4$:Eu^{2+} for field emission displays by an environmentally clean technique. Solid State Commun. 113, 475–478.

Jiao, M., Guo, N., Lü, W., Jia, Y., Lv, W., Zhao, Q., Shao, B., You, H., 2013. Tunable blue-green-emitting $Ba_3LaNa(PO_4)_3F$:Eu^{2+},Tb^{3+} phosphor with energy transfer for near-UV white LEDs. Inorg. Chem. 52, 10340–10346.

Jiao, M., Jia, Y., Lü, W., Lv, W., Zhao, Q., Shao, B., You, H., 2014. $Sr_3GdNa(PO_4)_3F:Eu^{2+},Mn^{2+}$: a potential color tunable phosphor for white LEDs. J. Mater. Chem. C 2, 90–97.

Joos, J.J., Meert, K.W., Parmentier, A.B., Poelman, D., Smet, P.F., 2012. Thermal quenching and luminescence lifetime of saturated green $Sr_{1-x}Eu_xGa_2S_4$ phosphors. Opt. Mater. 34, 1902–1907.

Jung, S.H., Kang, D.S., Jeon, D.Y., 2011. Effect of substitution of nitrogen ions to red-emitting $Sr_3B2O_{6-3/2x}N_x:Eu^{2+}$ oxy-nitride phosphor for the application to white LED. J. Cryst. Growth 326, 116–119.

Kakihana, M., 1996. Invited review "sol–gel" preparation of high temperature superconducting oxides. J. Sol–Gel Sci. Technol. 6, 7–55.

Kakihana, M., Yoshimura, M., 1999. Synthesis and characteristics of complex multicomponent oxides prepared by polymer complex method. Bull. Chem. Soc. Jpn. 72, 1427–1443.

Kalaji, A., Saines, P.J., George, N.C., Cheetham, A.K., 2013. Photoluminescence of cerium-doped $(Ca_{1-x}Sr_x)_3RE_2Ge_3O_{12}$ garnet phosphors for solid state lighting: relating structure to emission. Chem. Phys. Lett. 586, 91–96.

Kalaji, A., Mikami, M., Cheetham, A.K., 2014. Ce^{3+}-activated γ-Ca_2SiO_4 and other olivine-type $ABXO_4$ phosphors for solid-state lighting. Chem. Mater. 26, 3966–3975.

Kamiya, S., Mizuno, H., 2006. Phosphors for Lamps. In: Yen, W.M., Shionoya, S. (Eds.), Phosphor Handbook, second ed. CRC Press, New York, pp. 451–494 (Chapter 5, Section 6).

Kang, Y.C., Lenggoro, I.W., Park, S.B., Okuyama, K., 2001. One-step synthesis of the green phosphor Ce-Tb-Mg-Al-O system with spherical particle shape and fine size. Appl. Phys. A 72, 103–105.

Kang, H.S., Kang, Y.C., Jung, K.Y., Park, S.B., 2005. Eu-doped barium strontium silicate phosphor particles prepared from spray solution containing NH_4Cl flux by spray pyrolysis. Mater. Sci. Eng. B 121, 81–85.

Kang, E.H., Choi, S.W., Chung, S.E., Jang, J., Kwon, S., Hong, S.H., 2011. Photoluminescence characteristics of $Sr_3SiO_5:Eu^{2+}$ yellow phosphors synthesized by solid-state method and pechini process. J. Electrochem. Soc. 158, J330–J333.

Kanke, Y., Navrotsky, A., 1998. A calorimetric study of the lanthanide aluminum oxides and the lanthanide gallium oxides: stability of the perovskites and the garnets. J. Solid State Chem. 141, 424–436.

Katharine, L., Derek, P.H., 2001. The crystal structure of $Y_3Si_5N_9O$ and revision of the compositions of some high nitrogen-containing M–Si–O–N (M=Y, La) phases. J. Mater. Chem. 11, 507–512.

Kato, K., Okamoto, F., 1983. Preparation and cathodoluminescence of CaS:Eu and $Ca_{1-x}Sr_xS$:Eu phosphors. Jpn. J. Appl. Phys. 22, 76–78.

Kawano, Y., Kim, S.W., Ishigaki, T., Uematsu, K., Toda, K., Takaba, H., Sato, M., 2014. Site engineering concept of Ce^{3+}-activated novel orange-red emission oxide phosphors. Opt. Mater. Express 4, 1770–1774.

Kechele, J.A., Hecht, C., Oeckler, O., auf der Günne, J.S., Schmidt, P.J., Schnick, W., 2009a. $Ba_2AlSi_5N_9$—a new host lattice for Eu^{2+}-doped luminescent materials comprising a nitridoalumosilicate framework with corner- and edge-sharing tetrahedra. Chem. Mater. 21, 1288–1295.

Kechele, J.A., Oeckler, O., Stadler, F., Schnick, W., 2009b. Structure elucidation of $BaSi_2O_2N_2$— a host lattice for rare-earth doped luminescent materials in phosphor-converted (pc)-LEDs. Solid State Sci. 11, 537–543.

Keeping, S., 2014. The rise of chip-on-board LED modules | DigiKey. Available at: http://www.digikey.com/en/articles/techzone/2014/mar/the-rise-of-chip-on-board-led-modules (accessed March 31, 2015).

Kieffer, R., Ettmayer, P., Pajakoff, S., 1972. Ueber mononitride und stickstoffreichere nitride der seltenerdmetalle (Mitt. I). Monatshefte für Chemie 103, 1285–1298.

Kim, Y.M., Hong, S.H., 2004. Influence of minor ions on the stability and hydration rates of β-dicalcium silicate. J. Am. Ceram. Soc. 87, 900–905.

Kim, J.H., Jung, K.Y., 2011. Preparation and luminescence characterization of fine-sized LaSr$_2$AlO$_5$:Ce phosphor prepared by spray pyrolysis. J. Lumin. 131, 1487–1491.

Kim, K.B., Kim, Y.I., Chun, H.G., Cho, T.Y., Jung, J.S., Kang, J.G., 2002. Structural and optical properties of BaMgAl$_{10}$O$_{17}$:Eu^{2+} phosphor. Chem. Mater. 14, 5045–5052.

Kim, J.S., Jeon, P.E., Choi, J.C., Park, H.L., 2005a. Emission color variation of M$_2$SiO$_4$:Eu^{2+} (M = Ba, Sr, Ca) phosphors for light-emitting diode. Solid State Commun. 133, 187–190.

Kim, J.S., Park, Y.H., Kim, S.M., Choi, J.C., Park, H.L., 2005b. Temperature-dependent emission spectra of M$_2$SiO$_4$:Eu^{2+} (M = Ca, Sr, Ba) phosphors for green and greenish white LEDs. Solid State Commun. 133, 445–448.

Kim, J.K., Luo, H., Schubert, E.F., Cho, J., Sone, C., Park, Y., 2005c. Strongly enhanced phosphor efficiency in GaInN white light-emitting diodes using remote phosphor configuration and diffuse reflector cup. Jpn. J. Appl. Phys. 44, L649–L651.

Kim, J.M., Kim, K.N., Park, S.H., Park, J.K., Kim, C.H., Jang, H.G., 2005d. Synthesis and luminescent characteristics of CaGa$_2$S$_4$:Eu^{2+} yellow phosphor for light emitting diode. J. Korean Chem. Soc. 49, 201–207.

Kim, J.S., Mho, S.W., Park, Y.H., Choi, J.C., Park, H.L., Kim, G.S., 2005e. White-light-emitting Eu^{2+} and Mn^{2+}-codoped silicate phosphors synthesized through combustion process. Solid State Commun. 136, 504–507.

Kim, K.N., Kim, J.M., Choi, K.J., Park, J.K., Kim, C.H., 2006. Synthesis, characterization, and luminescent properties of CaS:Eu phosphor. J. Am. Ceram. Soc. 89, 3413–3416.

Kim, J.M., Park, S.J., Kim, K.H., Choi, H.W., 2012. The luminescence properties of M$_2$MgSi$_2$O$_7$:Eu^{2+} (M = Sr, Ba) nano phosphor in ultraviolet light emitting diodes. Ceram. Int. 38S, S571–S575.

Kim, S.W., Hasegawa, T., Ishigaki, T., Uematsu, K., Toda, K., Sato, M., 2013a. Efficient Red Emission of Blue-Light Excitable New Structure Type NaMgPO$_4$:Eu^{2+} Phosphor. ECS Solid State Lett. 2, R49–R51.

Kim, H.G., Kang, E.H., Kim, B.H., Hong, S.H., 2013b. Preparation and luminescence properties of Ba$_3$Si$_6$O$_9$N$_4$:Eu^{2+} phosphor. Opt. Mater. 35, 1279–1282.

Kim, T.G., Kim, T., Kim, J., Kim, S.J., Im, S.J., 2014. Interplay between crystal structure and photoluminescence properties of β-Ca$_3$SiO$_4$Cl$_2$:Eu^{2+}. J. Phys. Chem. C 118, 12428–12435.

Kim, Y.H., Arunkumar, P., Im, W.I., 2015a. Facile fabrication of moisture resistance and thermally stable SrGa$_2$S$_4$:Eu^{2+} phosphor-in-glass microcubes for white LED. Ceram. Int. 41, 5200–5204.

Kim, Y.H., Arunkumar, P., Park, S.H., Yoon, H.S., Im, W.B., 2015b. Tuning the diurnal natural daylight with phosphor converted white LED—advent of new phosphor blend composition. Mater. Sci. Eng. 193, 4–12.

Kimoto, K., Xie, R.J., Matsui, Y., Ishizuka, K., Hirosaki, N., 2009. Direct observation of single dopant atom in light-emitting phosphor of β-SiAlON:Eu^{2+}. Appl. Phys. Lett. 94, 041908.

Kitabatake, T., Uchikoshi, T., Munakata, F., Sakka, Y., Hirosaki, N., 2012. Optical and adhesive properties of composite silica-impregnated Ca-α-SiAlON:Eu^{2+} phosphor films prepared on silica glass substrates. J. Eur. Ceram. Soc. 32, 1365–1369.

Ko, K.Y., Huh, Y.D., Do, Y.R., 2008. Cathodoluminescence and longevity properties of potential Sr$_{1-x}$M$_x$Ga$_2$S$_4$:Eu (M = Ba or Ca) green phosphors for field emission displays. Bull. Korean Chem. Soc. 29, 822–826.

Komeno, A., Uematsu, K., Toda, K., Sato, M., 2006. VUV properties of Eu-doped alkaline earth magnesium silicate. J. Alloy Compd. 408–412, 871–874.

Komukai, T., Takatsuka, Y., Kato, H., Kakihana, M., 2015. Luminescence properties of BaZr-Si$_3$O$_9$:Eu synthesized by an aqueous solution method. J. Lumin. 158, 328–332.

Komuro, N., Mikami, M., Saines, P.J., Akimoto, K., Cheetham, A.K., 2015. Deep red emission in Eu^{2+}-activated Sr$_4$(PO$_4$)$_2$O phosphors for blue-pumped white LEDs. J. Chem. Mater. C 3, 7356–7362.

Koo, H.Y., Hong, S.K., Han, J.M., Kang, Y.C., 2008. Eu-doped Ca$_8$Mg(SiO$_4$)$_4$Cl$_2$ phosphor particles prepared by spray pyrolysis from the colloidal spray solution containing ammonium chloride. J. Alloy Compd. 457, 429–434.

Kopp Alves, A., Bergmann, C.P., Berutti, F.A., 2013. Combustion synthesis. In: Novel Synthesis and Characterization of Nanostructured Materials. Springer, Berlin, New York, pp. 11–22 (Chapter 2).

Krames, M.R., Shchekin, O.B., Mueller-Mach, R., Mueller, G.O., Zhou, L., Harbers, G., Craford, M.G., 2007. Status and future of high-power light-emitting diodes for solid-state lighting. J. Disp. Technol. 3, 160–175.

Kravets, V.G., 2001. Using electron trapping materials for optical memory. Opt. Mater. 16, 369–375.

Kulshreshtha, C., Sharma, A.K., Shon, K.S., 2009. Effect of local structures on the luminescence of Li$_2$(Sr,Ca,Ba)SiO$_4$:Eu^{2+}. J. Electrochem. Soc. 156, J52–J56.

Kuo, T.W., Huang, C.H., Chen, T.M., 2010a. Novel yellowish-orange Sr$_8$Al$_{12}$O$_{24}$S$_2$:Eu^{2+} phosphor for application in blue light-emitting diode based white LED. Opt. Express 18, A231–A236.

Kuo, T.W., Liu, W.R., Chen, T.M., 2010b. High color rendering white light-emitting-diode illuminator using the red-emitting Eu^{2+}-activated CaZnOS phosphors excited by blue LED. Opt. Express 18, 8187–8189.

Kurushima, T., Gundiah, G., Shimomura, Y., Mikami, M., Kijima, N., Cheetham, A.K., 2010. Synthesis of Eu^{2+}-activated MYSi$_4$N$_7$ (M$=$Ca, Sr, Ba) and SrYSi$_{4−x}$Al$_x$N$_{7−x}$O$_x$ (x$=$0–1) green phosphors by carbothermal reduction and nitridation. J. Electrochem. Soc. 157, J64–J68.

Lai, G.C., Nojiri, T., Nakano, K., 1992. Studies of the stability of β-Ca$_2$SiO$_4$ doped by minor ions. Cem. Concr. Res. 22, 743–754.

Lauterbach, R., Schnick, W., 2000. Nd$_3$Si$_5$AlON$_{10}$—Synthese, Kristallstruktur und Eigenschaften eines Sialonsim La$_3$Si$_6$N$_{11}$-Strukturtyp. Z. Anorg. Allg. Chem. 626, 56–61.

Le Toquin, R., Cheetham, A.K., 2006. Red-emitting cerium-based phosphor materials for solid-state lighting applications. Chem. Phys. Lett. 423, 352–356.

Lee, C., Petrykin, V., Kakihana, M., 2009a. Synthesis of SrGa$_2$S$_4$:Mn,Ce and SrGa$_2$S$_4$:Mn,La phosphors by sulfurization of oxide precursors prepared by an amorphous metal complex method and a micro-gel freezing drying process. J. Ceram. Soc. Jpn. 117, 377–380.

Lee, C.-W., Petrykin, V., Kakihana, M., 2009b. Synthesis and effect of Sr substitution on fluorescence of new Ba$_{2−x}$Sr$_x$ZnS$_3$:Eu^{2+} red phosphor: considerable enhancement of emission intensity. J. Cryst. Growth 311, 647–650.

Lee, S.H., Jung, D.S., Han, J.M., Young Koo, H., Kang, Y.C., 2009c. Fine-sized Y$_3$Al$_5$O$_{12}$:Ce phosphor powders prepared by spray pyrolysis from the spray solution with barium fluoride flux. J. Alloys Compd. 477, 776–779.

Lee, S.H., Koo, H.Y., Lee, S.M., Kang, Y.C., 2010a. Characteristics of Y$_3$Al$_5$O$_{12}$:Ce phosphor powders prepared by spray pyrolysis from ethylenediaminetetraacetic acid solution. Ceram. Int. 36, 611–615.

Lee, S.H., Koo, H.Y., Lee, S.Y., Lee, M.-J., Kang, Y.C., 2010b. Effect of BaF_2 as the source of Ba component and flux material in the preparation of $Ba_{1.1}Sr_{0.88}SiO_4$:$Eu_{0.02}$ phosphor by spray pyrolysis. Ceram. Int. 36, 339–343.

Lei, B., Sha, L., Zhang, H., Liu, Y., Man, S., Yue, S., 2010. Preparation and luminescence properties of green-light-emitting afterglow phosphor $Ca_8Mg(SiO_4)_4Cl_2$:Eu^{2+}. Solid State Sci. 12, 2177–2181.

Leib, W., Müller-Buschbaum, H., 1986. Aluminum strontium chloride oxide ($Sr_3Al_2O_5Cl_2$) an oxohaloaluminate with $Ba_3Fe_2O_5Cl_2$-structure. Rev. Chim. Miner. 23, 760–765.

Leib, W., Müller-Buschbaum, H., 1988. Synthese und Kristallstruktur von $Sr_3Ga_2O_5Cl_2$ und $Sr_3Fe_{1.18}Al_{0.82}O_5Cl_2$. Monatshefte für Chemie 119, 157–164.

Lenggoro, I.W., Okuyama, K., 2003. Preparation of fine phosphor and luminescence micro/nanoparticles using spray pyrolysis. In: Nalwa, H.S., Rohwer, L.S. (Eds.), Handbook of Luminescence, Display Materials, and Devices, vol. 2. American Scientific Publishers, Stevenson Ranch, CA, pp. 327–359.

Lenggoro, I.W., Xia, B., Mizushima, H., Okuyama, K., Kijima, N., 2001. Synthesis of $LaPO_4$:Ce,Tb phosphor particles by spray pyrolysis. Mater. Lett. 50, 92–96.

Leung, M., 2014. White LED and remote phosphor comparison. Available at: http://www.cree.com/∼/media/Files/Cree/LED%20Components%20and%20Modules/XLamp/White%20Papers/Remote%20Phosphor.pdf (accessed March 30, 2015).

Levshov, S.M., Berezovskaya, I.V., Efryushina, N.P., Zadneprovskii, B.I., Dotsenko, V.P., 2011. Synthesis and luminescence properties of Eu^{2+}-doped Li_2SrSiO_4. Inorg. Mater. 47, 285–289.

Li, Y.Q., Delsing, A.C.A., de With, G., Hintzen, H.T., 2005. Luminescence properties of Eu^{2+}-activated alkaline-earth silicon-oxynitride $MSi_2O_{2−δ}N_{2+2/3δ}$ (M=Ca, Sr, Ba): a promising class of novel LED Conversion phosphors. Chem. Mater. 17, 3242–3248.

Li, Y.Q., van Steen, J.E.J., van Krevel, J.W.H., Botty, G., Delsing, A.C.A., DiSalvo, F.J., de With, G., Hintzen, H.T., 2006a. Luminescence properties of red-emitting $M_2Si_5N_8$:Eu^{2+} (M=Ca, Sr, Ba) LED conversion phosphors. J. Alloys Compd. 417, 273–279.

Li, Y.Q., de With, G., Hintzen, H.T., 2006b. Luminescence properties of Ce^{3+}-activated alkaline earth silicon nitride $M_2Si_5N_8$ (M=Ca, Sr, Ba) materials. J. Lumin. 116, 107–116.

Li, J., Watanabe, T., Sakamoto, N., Wada, H., Setoyama, T., Yoshimura, M., 2008a. Synthesis of a multinary nitride, Eu-doped $CaAlSiN_3$ from alloy at low temperatures. Chem. Mater. 20, 2095–2105.

Li, X., Yang, Z., Guan, L., Guo, Q., Liu, C., Li, P., 2008b. Fabrication and luminescence properties of red emitting phosphor Y_2O_2S:Sm^{3+} for white LED by combustion method. J. Alloys Compd. 464, 565–568.

Li, Y.Q., Hirosaki, N., Xie, R.J., Takeda, T., Mitomo, M., 2008c. Yellow-orange-emitting CaAlSiN$_3$:Ce^{3+} phosphor: structure, photoluminescence, and application in white LEDs. Chem. Mater. 20, 6704–6714.

Li, G., Lai, Y., Cui, T., Yu, H., Liu, D., Gan, S., 2010a. Luminescence properties and charge compensation of $Sr_3Al_2O_6$ doped with Ce^{3+} and alkali metal ions. Mater. Chem. Phys. 124, 1094–1099.

Li, P., Wang, Z., Yang, Z., Guo, Q., Li, X., 2010b. Luminescent characteristics of $LiCaBO_3$:M (M=Eu^{3+}, Sm^{3+}, Tb^{3+}, Ce^{3+}, Dy^{3+}) phosphor for white LED. J. Lumin. 130, 222–225.

Li, J., Zhang, H., Lei, B., Qin, J., Liu, Y., Xiao, Y., Zheng, M., Sha, L., 2013. Luminescent properties of green long-lasting $Ca_8Mg(SiO_4)_4Cl_2$:Eu^{2+}, from Ca_2SiO_4:Eu^{3+} and $MgCl_2$ at low temperature. Physica B 430, 31–35.

Li, C., Dai, J., Deng, D., Shen, C., Xu, S., 2015a. Synthesis, luminescent properties and white light emitting diode application of $Ba_7Zr(PO_4)_6$:Eu^{2+} yellow-emitting phosphor. Physica B 475, 105–109.

Li, C., Chen, H., Xu, S., 2015b. $Ba_3Si_6O_{12}N_2$:Eu^{2+} green-emitting phosphor for white light emitting diodes: luminescent properties optimization and crystal structure analysis. Optik 126, 499–502.

Lin, H., Liu, X.R., Pun, E.Y.B., 2002. Sensitized luminescence and energy transfer in Ce^{3+} and Eu^{2+} codoped calcium magnesium chlorosilicate. Opt. Mater. 18, 397–401.

Lin, Y., Nan, C.W., Zhou, X., Wu, J., Wang, H., Chen, D., Xu, S., 2003. Preparation and characterization of long afterglow $M_2MgSi_2O_7$-based (M: Ca, Sr, Ba) photoluminescent phosphors. Mater. Chem. Phys. 82, 860–863.

Liu, G.K., Jacquier, B., 2005. Spectroscopic Properties of Rare Earths in Optical Materials. Springer Verlag, Berlin.

Liu, Y., Zhang, X., Hao, Z., Luo, Y., Wang, X., Ma, L., Zhang, J., 2013a. Luminescence and energy transfer in $Ca_3Sc_2Si_3O_{12}$:Ce^{3+},Mn^{2+} white LED phosphors. J. Lumin. 133, 21–24.

Liu, C., Xia, Z., Lian, Z., Zhou, J., Yan, Q., 2013b. Structure and luminescence properties of green-emitting $NaBaScSi_2O_7$:Eu^{2+} phosphors for near-UV-pumped light emitting diodes. J. Mater. Chem. C 1, 7139–7147.

Lu, F.C., Song, X.P., Liu, Q.L., 2010. Crystal structure and photoluminescence properties of $(Y_{1-x}Ce_x)_4Si_2O_7N_2$. Opt. Mater. 33, 91–98.

Lu, F.C., Chen, X.Y., Wang, M.W., Liu, Q.L., 2011. Crystal structure and photoluminescence of $(Y_{1-x}Ce_x)_2Si_3O_3N_4$. J. Lumin. 131, 336–341.

Luo, Y., Xia, Z., 2014. Effect of partial nitridation on the structure and luminescence properties of melilite-type $Ca_2Al_2SiO_7$:Eu^{2+} phosphor. Opt. Mater. 36, 1874–1878.

Luo, Y.Y., Jo, D.S., Senthil, K., Tezuka, S., Kakihana, M., Toda, K., Masaki, T., Yoon, D.H., 2012. Synthesis of high efficient Ca_2SiO_4:Eu^{2+} green emitting phosphor by a liquid phase precursor method. J. Solid State Chem. 189, 68–74.

Ma, B., Huang, Z., Fang, M., Liu, Y., Wu, X., 2015. Structural and luminescence properties of red-emitting $Cs_{1-x}MgPO_4$:xEu^{2+} phosphors for near-UV-pumped light emitting diodes. RSC Adv. 5, 9933–9938.

Machida, K., Adachi, G., Shiokawa, J., Shimada, M., Koizumi, M., Suito, K., Onodera, A., 1982. High-pressure synthesis, crystal structures, and luminescence properties of europium(II) metasilicate and europium(II)-activated calcium and strontium metasilicates. Inorg. Chem. 21, 1512–1519.

MacKenzie, K.J.D., Gainsford, G.J., Ryan, M.J., 1996. Rietveld refinement of the crystal structures of the yttrium silicon oxynitrides $Y_2Si_3N_4O_3$ (N-melilite) and $Y_4Si_2O_7N_2$ (J-phase). J. Eur. Ceram. Soc. 16, 553–560.

Mathew, M., Mayer, I., Dickens, B., Schroeder, L., 1979. Substitution in barium-fluoride apatite: the crystal structures of $Ba_{10}(PO_4)_6F_2$, $Ba_6La_2Na_2(PO_4)_6F_2$ and $Ba_4Nd_3Na_3(PO_4)_6F_2$. J. Solid State Chem. 28, 79–95.

Matsuda, N., Tamatani, M., Okumura, M., Albessard, A.K., Inoue, Y., Kawasaki, K., 1998. Preparation of spherical phosphors by thermal-plasma treatment. J. Soc. Inf. Disp. 6, 159–161.

Meagher, E.P., 1975. The crystal structures of pyrope and grossularite at elevated temperatures. Am. Miner. 60, 218–228.

Meneghini, M., Dal Lago, M., Trivellin, N., Meneghesso, G., Zanoni, E., 2013. Thermally activated degradation of remote phosphors for application in LED lighting. IEEE Trans. Device Mater. Reliab. 13, 316–318.

Mikami, M., Watanabe, H., Uheda, K., Kijima, N., 2008. Nitridoaluminosilicate $CaAlSiN_3$ and its derivatives—theory and experiment. Mater. Res. Soc. Symp. Proc. 1040. Q10.

Mikami, M., Watanabe, H., Uheda, K., Shimooka, S., Shimomura, Y., Kurushima, T., Kijima, N., 2009a. New phosphors for white LEDs: material design concepts. Mater. Sci. Eng. 1, 012002.

Mikami, M., Shimooka, S., Uheda, K., Imura, H., Kijima, N., 2009b. New green phosphor $Ba_3Si_6O_{12}N_2$:Eu for white LED: crystal structure and optical properties. Key Eng. Mater. 403, 11–14.

Miyakawa, T., Dexter, D.L., 1970. Phonon sidebands, multiphonon relaxation of excited states, and phonon-assisted energy transfer between ions in solids. Phys. Rev. B 1, 2961–2969.

Mueller-Mach, R., Mueller, G.O., Krames, M.R., Hoppe, H.A., Stadler, F., Schick, W., Juestel, T., Schmidt, P., 2005. Highly efficient all-nitride phosphor-converted white light emitting diode. Phys. Status Solidi A 202, 1727–1732.

Mueller-Mach, R., Mueller, G.O., Krames, M.R., Shchekin, O.B., Schmidt, P.J., Bechtel, H., Chen, C.-H., Steigelmann, O., 2009. All-nitride monochromatic amber-emitting phosphor-converted light-emitting diodes. Phys. Status Solidi (RRL) 3, 215–217.

Mumme, W.G., Hill, R.J., Bushnell, G.W., Segnit, E.R., 1995. Rietveld crystal structure refinements, crystal chemistry and calculated powder diffraction data for the polymorphs of dicalcium silicate and related phases. Neues Jahrbuch für Mineralogie—Abhandlungen 169, 35–68.

Mumme, W.G., Cranswick, L., Chakoumakos, B., 1996. Rietveld crystal structure refinements from high temperature neutron powder diffraction data for the polymorphs of dicalcium silicate. Neues Jahrbuch für Mineralogie—Abhandlungen 170, 171–188.

Nakagawa, T., Matsuoka, H., Sawa, M., Idehara, K., Katsura, M., 1997. Preparation of lanthanide nitrides by carbothermic reduction using ammonia. J. Nucl. Mater. 247, 147–150.

Nakamura, S., Fasol, G., 1997. The Blue Laser Diode, first ed. Springer-Verlag, Heidelberg.

Nakamura, S., Mukai, T., Senoh, M., 1994. Candela-class high-brightness InGaN/AlGaN double-heterostructure blue-light-emitting diodes. Appl. Phys. Lett. 64, 1687.

Nakamura, M., Kato, H., Takatsuka, Y., Petrykin, V., Tezuka, S., Kakihana, M., 2010. Synthesis and luminescence properties of a Cyan-blue thiosilicate-based phosphor $SrSi_2S_5$:Eu^{2+}. J. Inf. Disp. 11, 135–139.

Nakano, T., Kawakami, Y., Uematsu, K., Ishigaki, T., Toda, K., Sato, M., 2009. Novel Ba–Sc–Si-oxide and oxynitride phosphors for white LED. J. Lumin. 129, 1654–1657.

Nakazawa, E., 2006. Fundamentals of luminescence. In: Yen, W.M., Shionoya, S., Yamamoto, H. (Eds.), Transient characteristics of luminescence, Phosphor Handbook, second ed., vol. 2(7), CRC Press, New York, pp. 83–97.

Nakazawa, E., Shionoya, S., 1967. Energy transfer between trivalent Rare earth ions in inorganic solids. J. Chem. Phys. 47, 3211–3219.

Nakazawa, E., Shionoya, S., 1970. Relaxation between excited levels of Tb^{3+} ion due to resonance energy transfer. J. Phys. Soc. Jpn. 28, 1260–1265.

Narita, K., 2006. Methods of Phosphor Synthesis and Related Technology. In: Yen, W.M., Shionoya, S., Yamamoto, H. (Eds.), Phosphor Handbook, second ed., CRC Press, New York, pp. 341–354 (Chapter 4, Section 1).

Nazarov, M., Yoon, C., Kwak, C.H., Sohn, J.R., 2006. Quantum efficiency of Yttrium and Terbium garnets. Moldavian J. Phys. Sci. 5 (N1), 42–49.

Nguyen, H.D., Lin, C.C., Fang, M.H., Liu, R.S., 2014. Synthesis of Na_2SiF_6:Mn^{4+} red phosphors for white LED applications by co-precipitation. J. Mater. Chem. C 2, 10268–10272.

Noguchi, T., Hase, T., Miyasaka, Y., 1996. Analysis of the dependence of ferroelectric properties of strontium bismuth tantalate (SBT) thin films on the composition and process temperature. Jpn. J. Appl. Phys. 35, 4900–4904.

Oeckler, O., Stadler, F., Rosenthal, T., Schnick, W., 2007. Real structure of $SrSi_2O_2N_2$. Solid State Sci. 9, 205–212.

Ohashi, T., Ohmi, K., 2008. Improvement in luminescent characteristics by Al CODOPING in Ba_2SiS_4:Ce blue phosphor for white LEDs. J. Light. Vis. Environ. 32, 139–142.

Ohno, K., 1986. Effect of BaF_2 on the synthesis of the single-phase cubic $Y_3Al_5O_{12}$:Tb. J. Electrochem. Soc. 133, 638–643.

Ohno, Y., 2004. Color rendering and luminous efficacy of white LED spectra. Proc. SPIE 5530, 88–98.

Okamoto, S., Yamamoto, H., 2010. Luminescent-efficiency improvement by alkaline-earth fluorides partially replacing MgO in $3.5MgO \cdot 0.5MgF_2 \cdot GeO_2$:$Mn^{4+}$ deep-red phosphors for light emitting diodes. J. Electrochem. Soc. 157, J59–J63.

Oyama, Y., Kamigaito, O., 1971. Solid solubility of some oxides in Si_3N_4. Jpn. J. Appl. Phys. 10, 1637.

Pardha Saradhi, M., Varadaraju, U.V., 2006. Photoluminescence studies on Eu^{2+}-activated Li_2SrSiO_4 a potential orange-yellow phosphor for solid-state lighting. Chem. Mater. 18, 5267–5272.

Park, J.K., Kim, C.H., Park, S.H., Park, H.D., Choi, S.Y., 2004. Application of strontium silicate yellow phosphor for white light-emitting diodes. Appl. Phys. Lett. 84, 1647–1649.

Park, J.K., Choi, K.J., Kim, K.N., Kim, C.H., 2005. Investigation of strontium silicate yellow phosphors for white light emitting diodes from a combinatorial chemistry. Appl. Phys. Lett. 87, 031108.

Park, J.K., Choi, K.J., Yeon, J.H., Lee, S.J., Kim, C.H., 2006. Embodiment of the warm white-light-emitting diodes by using a Ba^{2+} codoped Sr_3SiO_5:Eu phosphor. Appl. Phys. Lett. 88, 043511.

Park, I.W., Kim, J.H., Yoo, J.S., Shin, H.H., Kim, C.K., Choi, C.K., 2008. Longevity improvement of CaS:Eu phosphor using polymer binder coating for white LED application. J. Electrochem. Soc. 155, J132–J135.

Park, J.Y., Lee, J.H., Raju, G.S.R., Moon, B.K., Jeong, J.H., Choi, B.C., Kim, J.H., 2014. Synthesis and luminescent characteristics of yellow emitting $GdSr_2AlO_5$:Ce^{3+} phosphor for blue light based white LED. Ceram. Int. 40, 5693–5698.

Pavese, A., Artioli, G., Prencipe, M., 1995. X-ray single-crystal diffraction study of pyrope in the temperature range 30-973 K. Am. Miner. 80, 457–464.

Peijzel, P.S., Meijerink, A., Wegh, R.T., Reid, M.F., Burdick, G.W., 2005. A complete $4f^n$ energy level diagram for all trivalent lanthanide ions. J. Solid State Chem. 178, 448–453.

Peng, W.F., Zou, S.Y., Liu, G.X., Xiao, Q.L., Zhang, R.J., Xie, L.J., Liu, Y.L., 2011. Combustion synthesis of $CaSc_2O_4$:Ce^{3+} nano-phosphors in a closed system. J. Alloys Compd. 509, 6673–6676.

Peters, T.E., Baglio, J.A., 1972. Luminescence and structural properties of thiogallate phosphors Ce^{3+} and Eu^{2+}-activated phosphors. Part I. J. Electrochem. Soc. 119, 230–236.

Petrykin, V., Okube, M., Yamane, H., Sasaki, S., Kakihana, M., 2010. Sr_2ZnS_3: crystal structure and fluorescent properties of a New Eu(II)-activated yellow emission phosphor. Chem. Mater. 22, 5800–5802.

Petzow, G., Herrmann, M., 2002. Silicon nitride ceramics. Struct. Bond. (Berlin) 102, 47–167.

Pham-Thi, M., Ravaux, G., 1991. Calcium sulfide phosphors prepared by the flux method: I. Growth parameters and luminescent efficiency. J. Electrochem. Soc. 138, 1103–1106.

Phillips, J.M., 2006. Chair, Research Needs for Solid-State Lighting: Report of the basic energy sciences workshop on solid-state lighting, 2006. U.S. Department of Energy, Office of Basic Energy Sciences, p. 169. Available at: http://www.usdoe.gov/bes/reports/files/SSL_rpt.pdf (accessed December 14, 2015).

Piao, X., Horikawa, T., Hanzawa, H., Machida, K., 2006. Characterization and luminescence properties of $Sr_2Si_5N_8$:Eu^{2+} phosphor for white light-emitting-diode illumination. Appl. Phys. Lett. 88, 161908.

Piao, X., Machida, K., Horikawa, T., Hanzawa, H., Shimomura, Y., Kijima, N., 2007a. Preparation of $CaAlSiN^3$:Eu^{2+} phosphors by the self-propagating high-temperature synthesis and their luminescent properties. Chem. Mater. 19, 4592–4599.

Piao, X., Machida, K., Horikawa, T., Hanzawa, H., 2007b. Self-propagating high temperature synthesis of yellow-emitting $Ba_2Si_5N_8$:Eu^{2+} phosphors for white light-emitting diodes. J. Electrochem. Soc. 91 (4), 041908.

Piao, X., Machida, K., Horikawa, T., Hanzawa, H., 2008. Synthesis of nitridosilicate $CaSr_{1-x}$ $Eu_xSi_5N_8$ (x = 0–1) phosphor by calcium cyanamide reduction for white light-emitting diode applications. J. Electrochem. Soc. 155, J17–J22.

Podhorodecki, A., Gluchowski, P., Zatryb, G., Syperek, M., Misiewicz, J., Lojkowski, W., Strek, W., 2011. Influence of pressure-induced transition from nanocrystals to nanoceramic form on optical properties of Ce-doped $Y_3Al_5O_{12}$. J. Am. Ceram. Soc. 94, 2135–2140.

Poelman, D., Van Haecke, J.E., Smet, P.F., 2009. Advances in sulfide phosphors for displays and lighting. J. Mater. Sci. Mater. Electron. 20, 134–138.

Pust, P., Wochnik, A.S., Baumann, E., Schmidt, P.J., Wiechert, D., Scheu, C., Schnick, W., 2014a. $Ca[LiAl_3N_4]$:Eu^{2+}—a narrow-band red-emitting nitridolithoaluminate. Chem. Mater. 26, 3544–3549.

Pust, P., Weiler, V., Hecht, C., Tücks, A., Wochnik, A.S., Henß, A.-K., Wiechert, D., Scheu, C., Schmidt, P.J., Schnick, W., 2014b. Narrow-band red-emitting $Sr[LiAl_3N_4]$:Eu^{2+} as a next-generation LED-phosphor material. Nat. Mater. 13, 891–896.

Qian, F., Fu, R., Agathopoulos, S., Gu, X., Song, X., 2012. Synthesis and luminescence properties of a broad-band red phosphor $Ca_3Si_2O_7$:Eu^{2+} for warm white light-emitting diodes. J. Lumin. 132, 71–75.

Ramisetty, M., Sastri, S., Kashalikar, U., 2014. Manufacturing of aluminum nitride powder for advanced applications. Am. Ceram. Soc. Bull. 93, 28–31.

Raukas, M., Kelso, J., Zheng, Y., Bergenek, K., Eisert, D., Linkov, A., Jermann, F., 2012. Ceramic phosphors for light conversion in LEDs. ECS J. Solid State Sci. Technol. 2, R3168–R3176.

Riley, F.L., 2000. Silicon nitride and related materials. J. Am. Ceram. Soc. 83, 245–265.

Roh, H.S., Hur, S., Song, H.J., Park, I.J., Yim, D.K., Kim, D.W., Hong, K.S., 2012. Luminescence properties of $Ca_5(PO_4)_2SiO_4$:Eu^{2+} green phosphor for near UV-based white LED. Mater. Lett. 70, 37–39.

Ruan, J., Xie, R.J., Hirosaki, N., Takeda, T., 2011. Nitrogen gas pressure synthesis and photoluminescent properties of orange-red $SrAlSi_4N_7$:Eu^{2+} phosphors for white light-emitting diodes. J. Am. Ceram. Soc. 94, 536–542.

Ruan, J., Xie, R.J., Funahashi, S., Tanaka, Y., Takeda, T., Suehiro, T., Hirosaki, N., Li, Y.Q., 2013. A novel yellow-emitting $SrAlSi_4N_7$:Ce^{3+} phosphor for solid state lighting: synthesis, electronic structure and photoluminescence properties. J. Solid State Chem. 208, 50–57.

Ryu, J.H., Won, H.S., Park, Y., Kim, S.H., Song, W.Y., Suzuki, H., Yoon, C., 2009. Synthesis of Eu_x $Si_{6-z}Al_zO_zN_{8-z}$ green phosphor and its luminescent properties. Appl. Phys. A 95, 747–752.

Sahu, I.P., Bisen, D.P., Brahme, N., Tamrakar, R.K., 2015. Luminescence enhancement of bluish-green $Sr_2Al_2SiO_7$:Eu^{2+} phosphor by dysprosium co-doping. J. Lumin. 167, 278–288.

Sakuma, K., Hirosaki, N., Xie, R.J., Yamamoto, Y., Suehiro, T., 2007a. Luminescence properties of (Ca, Y)-α-SiAlON:Eu phosphors. Mater. Lett. 61, 547–550.

Sakuma, K., Xie, R.J., Hirodaki, N., 2007b. Red-shift of emission wavelength caused by reabsorption mechanism of europium activated Ca-α-SiAlON ceramic phosphors. J. Lumin. 126, 843–852.

Samoylenko, S.A., Tret'yak, E.V., Shevchenko, G.P., Kichanov, S.E., Kozlenko, D.P., Malashkevich, G.E., Stupak, A.P., Savenko, B.N., 2015. Crystal structure and optical properties of $Lu_3Al_5O_{12}$:Ce^{3+} obtained by a colloidal chemical synthesis method. J. Appl. Spectrosc. 81, 1048–1055.

Saradhi, M.P., Varadaraju, U.V., 2006. Photoluminescence studies on Eu^{2+}-activated Li_2SrSiO_4—a potential orange-yellow phosphor for solid-state lighting. Chem. Mater. 18, 5267–5272.

Sastry, T.S.R., Bacalski, C.F., McKittrick, J., 1999. Preparation of green-emitting $Sr_{1-x}Eu_xGa_2S_4$ phosphors by a solid-state rapid metathesis reaction. J. Electrochem. Soc. 146, 4316–4319.

Sato, Y., Kato, H., Kobayashi, M., Masaki, T., Yoon, D.H., Kakihana, M., 2014. Tailoring of deep-red luminescence in Ca_2SiO_4:Eu^{2+}. Angew. Chem. Int. Ed. 53, 7756–7759.

Schanda, J.E., 2007. Colorimetry: Understanding the CIE System. Wiley, Hoboken.

Schiel, M., 2012. Remote-phosphor technology can deliver a more uniform and attractive light output from LED lamps. Available at: http://www.ledsmagazine.com/articles/print/volume-9/issue-9/features/remote-phosphor-technology-can-deliver-a-more-uniform-and-attractive-light-output-from-led-lamps-mag.html (Accessed March 30, 2015; MAGAZINE).

Schlieper, T., Schnick, W., 1995. Nitrido-silicate. III. Hochtemperatur-Synthese, Kristallstruktur und magnetische Eigenschaften von $Ce_3[Si_6N_{11}]$. Z. Anorg. Allg. Chem. 621, 1535–1538.

Schlieper, T., Schnick, W., 1996. Crystal structure of tripraseodymium hexasiliconundecanitride, $Pr_3Si_6N_{11}$. Z. Kristallogr. 211, 254.

Schlieper, T., Milius, W., Schnick, W., 1995. Nitrido-silicate. II [1]. Hochtemperatur-Synthesen und Kristallstrukturen von $Sr_2Si_5N_8$ und $Ba_2Si_5N_8$. Z. Anorg. Allg. Chem. 621, 1380–1384.

Schmiechen, S., Strobel, P., Hecht, C., Reith, T., Siegert, M., Schmidt, P.J., Huppertz, P., Wiechert, D., Schnick, W., 2015. Nitridomagnesosilicate $Ba[Mg_3SiN_4]$:Eu^{2+} and structure–property relations of similar narrow-band red nitride phosphors. Chem. Mater. 27, 1780–1785.

Seibald, M., Oeckler, O., Celinski, V.R., Schmidt, P.J., Tücks, A., Schnick, W., 2011. Real structure and diffuse scattering of $Sr_{0.5}Ba_{0.5}Si_2O_2N_2$:$Eu^{2+}$—a highly efficient yellow phosphor for pc-LEDs. Solid State Sci. 13, 1769–1778.

Seo, Y.W., Moon, B.K., Choi, B.C., Jeong, J.H., Shim, K.S., 2014. Effects of flux concentration on the structural and luminescent properties of Eu^{2+}-doped $SrAl_2O_4$. J. Korean Phys. Soc. 65, 1619–1623.

Setlur, A.A., Heward, W.J., Gao, Y., Srivastava, A.M., Chandran, R.G., Shankar, M.V., 2006. Crystal chemistry and luminescence of Ce^{3+}-doped $Lu_2CaMg_2(Si,Ge)_3O_{12}$ and its use in LED based lighting. Chem. Mater. 18, 3314–3322.

Setlur, A.A., Radkov, E.V., Henderson, C.S., Her, J.-H., Srivastava, A.M., Karkada, N., Satya Kishore, M., Prasanth Kumar, N., Aesram, D., Deshpande, A., Kolodin, B., Grigorov, L.S., Happek, U., 2010. Energy-efficient, high-color-rendering LED lamps using oxyfluoride and fluoride phosphors. Chem. Mater. 22, 4076–4082.

Seto, T., Kijima, N., Hirosaki, N., 2009. A new yellow phosphor $La_3Si_6N_{11}$:Ce^{3+} for white LEDs. ECS Trans. 25, 247–252.

Shannon, R.D., 1976. Revised effective ionic radii and systematic studies of interatomic distances in halides and chalcogenides. Acta Cryst. A 32, 751–767.

Shao, Q., Lin, H., Dong, Y., Fu, Y., Liang, C., He, J., Jiang, J., 2015. Thermostability and photostability of Sr_3SiO_5:Eu^{2+} phosphors for white LED applications. J. Solid State Chem. 225, 72–77.

Sheu, J.K., Chang, S.J., Kuo, C.H., Su, Y.K., Wu, L.W., Lin, Y.C., Lai, W.C., Tsai, J.M., Chi, G.C., Wu, R.K., 2003. White-light emission from near UV InGaN-GaN LED chip precoated with blue/green/red phosphors. IEEE Photonic Technol. Lett. 15, 18–20.

Shimizu, M., Kimata, M., Iida, I., 1995. Crystal structure of $Ba_2MgSi_2O_7$ melilite: the longest tetrahedral Mg–O distance. Neues Jahrbuch für Mineralogie Monatshefte 1995 (1), 39–47.

Shimizu, Y., Sakano, K., Noguchi, Y., Moriguchi, T., 2003. Light emitting device with blue light LED and phosphor components. U.S. Patent 6614179.

Shimomura, Y., Honma, T., Shigeiwa, M., Akai, T., Okamoto, K., Kijima, N., 2007a. Photoluminescence and crystal structure of green-emitting $Ca_3Sc_2Si_3O_{12}$:Ce^{3+} phosphor for white light emitting diodes. J. Electrochem. Soc. 154, J35–J38.

Shimomura, Y., Kurushima, T., Kijima, N., 2007b. Photoluminescence and crystal structure of green-emitting phosphor $CaSc_2O_4$:Ce^{3+}. J. Electrochem. Soc. 154, J234–J238.

Shioi, K., Hirosaki, N., Xie, R.J., Takeda, T., Li, Y., 2008. Luminescence properties of $SrSi_6N_8$: Eu^{2+}. J. Mater. Sci. 43, 5659–5661.

Shioi, K., Hirosaki, N., Xie, R.J., Takeda, T., Li, Y.Q., Matsushita, Y., 2010. Synthesis, crystal structure, and photoluminescence of Sr-α-SiAlON:Eu^{2+}. J. Am. Ceram. Soc. 93, 465–469.

Shur, M.S., Zukauskas, A., 2005. Solid-state lighting: toward superior illumination. Proc. IEEE 93, 1691–1703.

Sijbom, H.F., Joos, J.J., Martin, L.I.D.J., Van den Eeckhout, K., Poelman, D., Smet, P.F., 2016. Luminescent behavior of the K_2SiF_6:Mn^{4+} red phosphor at high fluxes and at the microscopic level. ECS J. Solid State Sci. Technol. 5, R3040–R3048.

Smet, P.F., Korthout, K., Van Haecke, J.E., Poelman, D., 2008. Using rare earth doped thiosilicate phosphors in white light emitting LEDs: towards low colour temperature and high colour rendering. Mater. Sci. Eng. B 146, 264–268.

Smith, D.K., Majumdar, A., Ordway, F., 1965. The crystal structure of γ-dicalcium silicate. Acta Cryst. 18, 787–795.

Sokolnicki, J., 2013. Rare earths (Ce, Eu, Tb) doped $Y_2Si_2O_7$ phosphors for white LED. J. Lumin. 134, 600–606.

Song, X., He, H., Fu, R., Wang, D., Zhao, X., Pan, Z., 2009. Photoluminescent properties of $SrSi_2O_2N_2$:Eu^{2+} phosphor: concentration related quenching and red shift behaviour. J. Phys. D 42, 065409.

Song, H.J., Yim, D.K., Cho, I.S., Roh, H.S., Kim, J.S., Kim, D.W., Hong, K.S., 2012. Luminescent properties of phosphor converted LED using an orange-emitting $Rb_2CaP_2O_7$:Eu^{2+} phosphor. Mater. Res. Bull. 47, 4522–4526.

Souriau, J.C., Jiang, Y.D., Penczek, J., Paris, H.G., Summers, C.J., 2000. Cathodoluminescent properties of coated $SrGa_2S_4$:Eu^{2+} and ZnS: Ag, Cl phosphors for field emission display applications. Mater. Sci. Eng. B 76, 165–168.

Spitsyn, V.I., Kovba, L.M., Peromova, M.V., Yidinskaya, I.V., Prokof'eva, I.G., 1968. A contribution to enquiry about double oxides of barium and rare earth elements. Dokl. Akad. Nauk SSSR 180, 879.

Steigerwald, D.A., Bhat, J.C., Collins, D., Fletcher, R.M., Holcomb, M.O., Ludowise, M.J., Martin, P.S., Rudaz, S.L., 2002. Illumination with solid state lighting technology. IEEE J. Sel. Top. Quantum Electron. 8, 310–320.

Suehiro, T., Hirosaki, N., Xie, R.-J., Mitomo, M., 2005. Powder synthesis of Ca-α'-SiAlON as a host material for phosphors. Chem. Mater. 17, 308–314.

Suehiro, T., Hirosaki, N., Xie, R.J., Sato, T., 2009. Blue-emitting $LaSi_3N_5$:Ce^{3+} fine powder phosphor for UV-converting white light-emitting diodes. Appl. Phys. Lett. 95, 051903.

Suehiro, T., Onuma, H., Hirosaki, N., Xie, R.J., Sato, T., Miyamoto, A., 2010. Powder synthesis of Y-α-SiAlON and its potential as a phosphor host. J. Phys. Chem. C 114, 1337–1342.

Suehiro, T., Hirosaki, N., Xie, R.J., 2011. Synthesis and photoluminescent properties of (La, Ca)$_3$Si$_6$N$_{11}$:Ce^{3+} fine powder phosphors for solid-state lighting. ACS Appl. Mater. Interfaces 3, 811–816.

Suehiro, T., Xie, R.J., Hirosaki, N., 2013. Facile synthesis of (Sr, Ca)$_2$Si$_5$N$_8$:Eu^{2+}-based red-emitting phosphor for solid-state lighting. Ind. Eng. Chem. Res. 52, 7453–7456.

Sun, X., Zhang, J., Zhang, X., Luo, Y., Wang, X.J., 2008. Long lasting yellow phosphorescence and photostimulated luminescence in Sr$_3$SiO$_5$:Eu^{2+} and Sr$_3$SiO$_5$:Eu^{2+}, Dy^{3+} phosphors. J. Phys. D Appl. Phys. 41, 195414.

Suzuki, Y., Kakihana, M., 2007. Parallel synthetic exploration of Tm^{3+}-doped alkaline-earth gallate phosphors by use of polymerizable complex method. J. Ceram. Soc. Jpn. 115, 612–614.

Suzuki, Y., Kakihana, M., 2009. Preparation of water soluble silicon compound and its application for synthesis of (Y, Ce, Gd)$_2$SiO$_5$ blue emission phosphor. J. Ceram. Soc. Jpn. 117, 330–334.

Suzuki, Y., Kakihana, M., Shimomura, Y., Kijima, N., 2007. Synthesis of Ca$_3$Sc$_2$Si$_3$O$_{12}$:Ce^{3+} using polymerizable complex method. J. Jpn. Soc. Powder Powder Metall. 54, 44–47.

Suzuki, Y., Kakihana, M., Shimomura, Y., Kijima, N., 2008. Synthesis of Ca$_3$Sc$_2$Si$_3$O$_{12}$:Ce^{3+} phosphor by hydrothermal Si alkoxide gelation. J. Mater. Sci. 43, 2213–2216.

Suzuki, A., Takizawa, T., Hidaka, C., Shigetaka, N., Kitajima, I., 2012. A novel monoclinic phase of impurity-doped CaGa$_2$S$_4$ as a phosphor with high emission intensity. Acta Cryst. E 68, i42.

Takahashi, N., Suzuki, Y., Kakihana, M., 2009. Synthesis of Zn$_2$SiO$_4$:Mn^{2+} green emission phosphor by hydrothermal gelation method using a novel water soluble silicon compound. J. Ceram. Soc. Jpn. 117, 313–315.

Takahashi, K., Harada, M., Yoshimura, K., Fukunaga, H., Tomomura, Y., Hirosaki, N., Xie, R.J., 2012. Improved photoluminescence of Ce^{3+} activated LaAl(Si$_{6−z}$Al$_z$)(N$_{10−z}$O$_z$)(z∼1) blue oxynitride phosphors by calcium co-doping. ECS J. Solid State Sci. Technol. 1, R109–R112.

Tam, T.T.H., Du, N.V., Kien, N.D.T., Thang, C.X., Cuong, N.D., Huy, P.T., 2014. Co-precipitation synthesis and optical properties of green-emitting Ba$_2$MgSi$_2$O$_7$:Eu^{2+} phosphor. J. Lumin. 147, 358–362.

Tamaki, H., Murazaki, Y., 2007. Phosphors for lamps. In: Yen, W.M., Shionoya, S., Yamamoto, H. (Eds.), Phosphors for white light-emitting diodes, Phosphor Handbook, second ed. vol. 5(9), CRC Press, New York, pp. 533–543.

Tang, Y.S., Hu, S.F., Lin, C.C., Bagkar, N.C., Liu, R.S., 2007. Thermally stable luminescence of KSrPO$_4$:Eu^{2+} phosphor for white light UV light-emitting diodes. Appl. Phys. Lett. 90, 151108.

Tezuka, S., Sato, Y., Komukai, T., Takatsuka, Y., Kato, H., Kakihana, M., 2013. Eu^{2+}-activated CaSrSiO$_4$: a new red-emitting oxide phosphor for white-light-emitting diodes. Appl. Phys. Express 6, 072101.

Toda, K., 2012. New processing of LED phosphors. Trans. Electr. Electron. Mater. 13, 225–228.

Toda, K., Kawakami, Y., Kousaka, S., Ito, Y., Komeno, A., Uematsu, K., Sato, M., 2006. New silicate phosphors for a white LED. IEICE Trans. Electron. E89-C, 1406–1412.

Toraya, H., Yamazaki, S., 2002. Simulated annealing structure solution of a new phase of dicalcium silicate Ca$_2$SiO$_4$ and the mechanism of structural changes from-dicalcium silicate hydrate to L'-dicalcium silicate via the new phase. Acta Cryst. B 58, 613–621.

Tsai, C.-C., Cheng, W.-C., Chang, J.-K., Chen, L.-Y., Chen, J.-H., Hsu, Y.-C., Cheng, W.-H., 2013. Ultra-high thermal-stable glass phosphor layer for phosphor-converted white light-emitting diodes. J. Disp. Technol. 9, 427–432.

Uheda, K., Takizawa, H., Endo, T., Yamane, H., Shimada, M., Wang, C.M., Mitomo, M., 2000. Synthesis and luminescent property of Eu^{3+}-doped $LaSi_3N_5$ phosphor. J. Lumin. 87, 967–969.

Uheda, K., Hirosaki, N., Yamamoto, H., 2006a. Host lattice materials in the system Ca_3N_2-AlN-Si_3N_4 for white light emitting diode. Phys. Status Solidi A 203, 2712–2717.

Uheda, K., Hirosaki, N., Yamamoto, Y., Naito, A., Nakajima, T., Yamamoto, H., 2006b. Luminescence properties of a red phosphor, $CaAlSiN_3:Eu^{2+}$, for white light-emitting diodes. Electrochem. Solid-State Lett. 9, H22–H25.

Uhrmann, T., Matthias, T., Lindner, P., 2011. Silicon-based wafer-level packaging for cost reduction of high brightness LEDs. In: Proc. IEEE 61st Electron. Comp. Technol. Conf. (ECTC), pp. 1622–1625.

Unithrattil, S., Lee, K.H., Chung, W.J., Im, W.B., 2014. Full-color-emitting $CaYAl_3O_7:Pr^{3+},Ce^{3+}$ phosphor for near-UV LED-based white light. J. Lumin. 152, 176–181.

Van den Eeckhout, K., Smet, P.F., Poelman, D., 2011. Luminescent afterglow behavior in the $M_2Si_5N_8$:Eu family (M=Ca, Sr, Ba). Materials 4, 980–990.

Van Haecke, J.E., Smet, P.F., De Keyser, K., Poelman, D., 2007. Single crystal CaS:Eu and SrS:Eu luminescent particles obtained by solvothermal synthesis. J. Electrochem. Soc. 154, J278–J282.

van Krevel, J.W.H., Hintzen, H.T., Metselaar, R., Meijerink, A., 1998. Long wavelength Ce^{3+} emission in Y–Si–O–N materials. J. Alloy Compd. 268, 272–277.

van Krevel, J.W.H., Hintzen, H.T., Metselaar, R., 2000. On the Ce^{3+} luminescence in the melilite-type oxide nitride compound $Y_2Si_{3-x}Al_xO_{3+x}N_{4-x}$. Mater. Res. Bull. 35, 747–754.

van Krevel, J.W.H., Hintzen, H.T., Metselaar, R., Gendre, L.L., Marchand, R., 2001. Oxidation resistance of Ln–Si–O–N powders (Ln=Y, Gd and La). Solid State Sci. 3, 49–56.

Van Krevel, J.W.H., van Rutten, J.W.T., Mandal, H., Hintzen, H.T., Metselaar, R., 2002. Luminescence properties of terbium-, cerium-, or europium-doped α-sialon materials. J. Solid State Chem. 165, 19–24.

Wang, L.H., Schneemeyer, L.F., Cava, R.J., Siegrist, T., 1994. A new barium scandium silicate: $Ba_9Sc_2(SiO_4)_6$. J. Solid State Chem. 113, 211–214.

Wang, P.L., Werner, P.E., 1997. Study on the structures of N-containing melilite $Y_2Si_3O_3N_4$ and $Nd_2Si_{2.5}Al_{0.5}O_{3.5}N_{3.5}$. J. Mater. Sci. 32, 1925–1929.

Wang, C., Tang, K., Yang, Q., An, C., Hai, B., Shen, G., Qian, Y., 2002. Blue-light emission of nanocrystalline CaS and SrS synthesized via a solvothermal route. Chem. Phys. Lett. 351, 385–390.

Wang, J., Zhang, M., Zhang, Q., Ding, W., Su, Q., 2007. The photoluminescence and thermoluminescence properties of novel green long-lasting phosphorescence materials $Ca_8Mg(SiO_4)_4Cl_2:Eu^{2+}, Nd^{3+}$. Appl. Phys. B 87, 249–254.

Wang, W.-N., Iskandar, F., Okuyama, K., Shinomiya, Y., 2008. Rapid synthesis of non-aggregated fine chloroapatite blue phosphor powders with high quantum efficiency. Adv. Mater. 20, 3422–3426.

Wang, Z.J., Yang, Z.P., Guo, Q.L., Li, P.L., Fu, G.S., 2009. Luminescence characteristics of Eu^{2+} activated Ca_2SiO_4, Sr_2SiO_4 and Ba_2SiO_4 phosphors for white LEDs. Chin. Phys. B 18, 2068–2071.

Wang, Z., Yang, B., Li, P., Yang, Z., Guo, Q., 2012a. Energy transfer between activators at different crystallographic sites in $Sr_3SiO_5:Eu^{2+}$. Physica B 407, 1282–1286.

Wang, X.M., Wang, C.H., Kuang, X.J., Zou, R.Q., Wang, Y.X., Jing, X.P., 2012b. Promising oxonitridosilicate phosphor host $Sr_3Si_2O_4N_2$: synthesis, structure, and luminescence properties activated by Eu^{2+} and Ce^{3+}/Li^+ for pc-LEDs. Inorg. Chem. 51, 3540–3547.

Watanabe, H., Kijima, N., 2009. Crystal structure and luminescence properties of $Sr_xCa_{1-x}AlSiN_3:Eu^{2+}$ mixed nitride phosphors. J. Alloy Compd. 475, 434–439.

Watanabe, H., Yamane, H., Kijima, N., 2008a. Crystal structure and luminescence of $Sr_{0.99}Eu_{0.01}AlSiN_3$. J. Solid State Chem. 181, 1848–1852.

Watanabe, H., Wada, H., Seki, K., Itou, M., Kijima, N., 2008b. Synthetic method and luminescence properties of $Sr_xCa_{1-x}AlSiN_3:Eu^{2+}$ mixed nitride phosphors. J. Electrochem. Soc. 155, F31–F36.

Wei, D., Huang, Y., Seo, H.J., 2013. Novel yellowish-green emitting luminescence in $Ca_7Si_2P_2O_{16}:Eu^{2+}$ phosphor. Mater. Res. Bull. 48, 3614–3619.

Woike, M., Jeitschko, W., 1995. Preparation and crystal structure of the nitridosilicates $Ln_3Si_6N_{11}$ (Ln = La, Ce, Pr, Nd, Sm) and $LnSi_3N_5$ (Ln = Ce, Pr, Nd). Inorg. Chem. 34, 5105–5108.

Wu, C., Wang, Y., 2007. Hydrothermal synthesis and luminescent properties of $(La, Gd)PO_4:Tb$ phosphors under VUV excitation. Mater. Lett. 61, 2416–2418.

Wu, J., Newman, D., Viney, I.V.F., 2002. Study on relationship of luminescence in CaS:Eu, Sm and dopants concentration. J. Lumin. 99, 237–245.

Wu, Z.C., Shi, J.X., Wang, J., Gong, M.L., Su, Q., 2006. A novel blue-emitting phosphor $LiSrPO_4:Eu^{2+}$ for white LEDs. J. Solid State Chem. 179, 2356–2360.

Wu, J.L., Gundiah, G., Cheetham, A.K., 2007a. Structure–property correlations in Ce-doped garnet phosphors for use in solid state lighting. Chem. Phys. Lett. 441, 250–254.

Wu, Z.C., Shi, J.X., Gong, M.L., 2007b. Nanosized $LiSrPO_4:Eu^{2+}$ phosphor with blue-emission synthesized by the sol–gel method. Mater. Chem. Phys. 103, 415–418.

Wu, H., Hu, Y., Zeng, B., Mou, Z., Deng, L., 2011. Tunable luminescent properties by adjusting the Sr/Ba ratio in $Sr_{1.97-x}Ba_xMgSi_2O_7:Eu^{2+}_{0.01}$, $Dy^{3+}_{0.02}$ phosphors. J. Phys. Chem. Solids 72, 1284–1289.

Wu, Y.C., Chen, Y.C., Chen, T.M., Lee, C.S., Chen, K.J., Kuo, H.C., 2012. Crystal structure characterization, optical and photoluminescent properties of tunable yellow-to orange-emitting $Y_2(Ca, Sr)F_4S_2:Ce^{3+}$ phosphors for solid-state lighting. J. Mater. Chem. 22, 8048–8056.

Wu, Y.F., Chan, Y.H., Nien, Y.T., Chen, I.G., 2013. Crystal structure and optical performance of Al^{3+} and Ce^{3+} codoped $Ca_3Sc_2Si_3O_{12}$ green phosphors for white LEDs. J. Am. Ceram. Soc. 96, 234–240.

Wu, Q., Yang, Z., Zhao, Z., Que, M., Wang, X., Wang, Y., 2014. Synthesis, crystal structure and luminescence properties of a $Y_4Si_2O_7N_2:Ce^{3+}$ phosphor for near-UV white LEDs. J. Mater. Chem. C 2, 4967–4973.

Xia, Z., Wu, W., 2013. Preparation and luminescence properties of Ce^{3+} and Ce^{3+}/Tb^{3+}-activated $Y_4Si_2O_7N_2$ phosphors. Dalton Trans. 42, 12989–12997.

Xia, G., Zhou, S., Zhang, J., Xu, J., 2005. Structural and optical properties of YAG:Ce^{3+} phosphors by sol–gel combustion method. J. Cryst. Growth 279, 357–362.

Xie, R.-J., Hirosaki, N., 2007. Silicon-based oxynitride and nitride phosphors for white LEDs—a review. Sci. Technol. Adv. Mater. 8, 588–600.

Xie, R.J., Hirosaki, N., Sakuma, K., Yamamoto, Y., Mitomo, M., 2004a. Eu^{2+}-doped Ca-alpha-SiAlON: a yellow phosphor for white light-emitting diodes. Appl. Phys. Lett. 84, 5404.

Xie, R.-J., Mitomo, M., Uheda, K., Xu, F.-F., Akimune, Y., 2004b. Preparation and luminescence spectra of calcium- and rare-earth (R = Eu, Tb, and Pr)-codoped α-SiAlON ceramics. J. Am. Ceram. Soc. 85, 1229–1234.

Xie, R.J., Hirosaki, N., Mitomo, M., Takahashi, K., Sakuma, K., 2006a. Highly efficient white-light-emitting diodes fabricated with short-wavelength yellow oxynitride phosphors. Appl. Phys. Lett. 88, 101104.

Xie, R.J., Hirosaki, N., Mitomo, M., Sakuma, K., Kimura, N., 2006b. Wavelength-tunable and thermally stable Li-alpha-sialon: Eu^{2+} oxynitride phosphors for white light-emitting diodes. Appl. Phys. Lett. 89, 241103.

Xie, R.J., Hirosaki, N., Suehiro, T., Xu, F.F., Mitomo, M., 2006c. A simple, efficient synthetic route to $Sr_2Si_5N_8$:Eu^{2+}-based red phosphors for white light-emitting diodes. Chem. Mater. 18, 5578–5583.

Xie, R.J., Hirosaki, N., Kimura, N., Sakuma, K., Mitomo, M., 2007. 2-Phosphor-converted white light-emitting diodes using oxynitride/nitride phosphors. Appl. Phys. Lett. 90, 1101–1103.

Xie, R.-J., Hirosaki, N., Li, Y., Takeda, T., 2010. Rare-earth activated nitride phosphors: synthesis, luminescence and applications. Materials 3, 3777–3793 (191101).

Xie, R.J., Li, Y.Q., Hirosaki, N., Yamamoto, H., 2011. Nitride Phosphors and Solid-State Lighting. CRC Press, New York, pp. 77–83.

Xu, Y.N., Rulis, P., Ching, W.Y., 2005. Electronic structure and bonding in quaternary crystal $Y_3Si_5N_9O$. Phys. Rev. B 72, 113101.

Xu, X., Cai, C., Hao, L., Wang, Y., Li, Q., 2009. The photoluminescence of Ce-doped $Lu_4Si_2O_7N_2$ green phosphors. Mater. Chem. Phys. 118, 270–272.

Xu, J., Chen, W., Zeng, R., Peng, D., 2014. A carbon-free sol–gel method for preparation of $Lu_3Al_5O_{12}$:Ce^{3+} phosphors for potential applications in laser scintillators and LEDs. Mater. Lett. 133, 1–4.

Xu, S., Tang, K., Zhu, D., Han, T., 2015. Luminescence properties and energy transfer of Ba_2Mg $(PO_4)_2$:Eu^{2+}, Mn^{2+} phosphor synthesized by co-precipitation method. Opt. Mater. 42, 106–110.

Yadav, P.J., Joshi, C.P., Moharil, S.V., 2013. Two phosphor converted white LED with improved CRI. J. Lumin. 136, 1–4.

Yamada, N., Shionoya, S., Kushida, T., 1972. Phonon-assisted energy transfer between trivalent rare earth ions. J. Phys. Soc. Jpn. 32, 1577–1586.

Yamaguchi, T., Suzuki, Y., Kakihana, M., 2010. Low temperature synthesis of $(Ca, Ce)_3Sc_2$ Si_3O_{12} phosphor by hydrothermal gelation method using novel water soluble silicon compound. J. Jpn. Soc. Powder Powder Metall. 57, 706–710.

Yamamoto, H., 2006. Fundamentals of luminescence. In: Yen, W.M., Shionoya, S., Yamamoto, H. (Eds.), Luminescence of a localized centers, Phosphor Handbook, second ed. vol. 2(3), CRC Press, New York (Chapter 2, Section 3).

Yamane, H., Naqura, T., Miyazaki, T., 2014. $La_3Si_6N_{11}$. Acta Crystal. E 70, i23–i24.

Yamnova, N.A., Zubkova, N.V., Eremin, N.N., Zadov, A.E., Gazeev, V.M., 2011. Crystal structure of larnite β-Ca_2SiO_4 and specific features of polymorphic transitions in dicalcium orthosilicate. Cryst. Rep. 56, 210–220.

Yan, X., Zheng, S., Yu, R., Cai, J., Xu, Z., Liu, C., Luo, X., 2008. Preparation of YAG:Ce^{3+} phosphor by sol-gel low temperature combustion method and its luminescent properties. Trans. Nonferrous Met. Soc. China 18, 648–653.

Yang, Z., Li, X., Yang, Y., Li, X., 2007. The influence of different conditions on the luminescent properties of YAG:Ce phosphor formed by combustion. J. Lumin. 122–123, 707–709.

Yang, H., Liu, Y., Ye, S., Qiu, J., 2008. Purple-to-yellow tunable luminescence of Ce^{3+} doped yttrium–silicon–oxide–nitride phosphors. Chem. Phys. Lett. 451, 218–221.

Yang, J., Wang, T., Chen, D., Chen, G., Liu, Q., 2012. An investigation of Eu^{2+}-doped $CaAlSiN_3$ fabricated by an alloy-nitridation method. Mater. Sci. Eng. B 177, 1596–1604.

Yang, H.K., Noh, H.M., Moon, B.K., Jeong, J.H., Yi, S.S., 2014a. Luminescence investigations of Sr_3SiO_5:Eu^{2+} orange–yellow phosphor for UV-based white LED. Ceram. Int. 40, 12503–12508.

Yang, L., Zhang, N., Zhang, R., Wen, B., Li, H., Bian, X., 2014b. A CaS:Eu based red-emitting phosphor with significantly improved thermal quenching resistance for LED lighting applications. Mater. Lett. 129, 134–136.

Yang, J., Feng, J., Zhao, M., Ren, X., Pan, W., 2015. Electronic structure, mechanical properties and anisotropy of thermal conductivity of Y–Si–O–N quaternary crystals. Comput. Mater. Sci. 109, 231–239.

Yao, S.S., Li, Y.Y., Xue, L.H., Yan, Y.W., You, Y., 2010. Luminescence studies on $Ba_2ZnSi_2O_7$: Eu^{2+} phosphors. Luminescence 25, 399–402.

Yasushita, C., Kato, H., Kakihana, M., 2012. Synthesis of an oxynitride-based green phosphor $Ba_3Si_6O_{12}N_2$:Eu^{2+} via an aqueous-solution process, using propylene-glycol-modified silane. J. Inf. Disp. 13, 107–111.

Yoo, S.H., Kim, C.K., 2009. Nanocomposite encapsulation of CuS:Eu light-emitting diode phosphors for the enhancement of the stability against moisture. J. Electrochem. Soc. 156, J170–J173.

Yu, R., Wang, J., Zhang, M., Zhang, J., Yuan, H., Su, Q., 2008. A new blue-emitting phosphor of Ce^{3+}-activated $CaLaGa_3S_6O$ for white-light-emitting diodes. Chem. Phys. Lett. 453, 197–201.

Yu, R., Jin, S., Cen, S., Liang, P., 2010. Effect of the phosphor geometry on the luminous flux of phosphor-converted light-emitting diodes. IEEE Photon. Technol. Lett. 22, 1765–1767.

Yu, H.J., Chung, W., Park, S.H., Kim, J., Kim, S.H., 2011. Luminous properties of $SrGa_2S_3Se$ phosphors doped with Eu^{2+} for LEDs application. Mater. Lett. 65, 474–476.

Yu, R., Li, H., Ma, H., Wang, C., Wang, H., Moon, B.K., Jeong, J.H., 2012. Photoluminescence properties of a new Eu^{2+}-activated $CaLaGa_3S_7$ yellowish-green phosphor for white LED applications. J. Lumin. 132, 2783–2787.

Yu, J., Gong, W., Zhang, Y., Ning, G., 2014. White-light-emitting diode using a single-phase full-color $(Ba, Sr)_{10}(PO_4)_4(SiO_4)_2$:$Eu^{2+}$ phosphor. J. Lumin. 147, 250–252.

Yuan, S.L., Chen, X.L., Zhu, C.F., Yang, Y.X., Chen, G.R., 2007. Eu^{2+}, Mn^{2+} co-doped (Sr, $Ba)_6BP_5O_{20}$—a novel phosphor for white-LED. Opt. Mater. 30, 192–194.

Yuan, B., Wang, X., Tsuboi, T., Huang, Y., Seo, H.J., 2012. A new yellowish-green-emitting phosphor:Eu^{2+}-doped $K_4CaSi_3O_9$. J. Alloys Compd. 512, 144–148.

Yum, J., Seo, S.-Y., Lee, S., Sung, Y.-E., 2003. $Y_3Al_5O_{12}$:$Ce_{0.05}$ phosphor coatings on gallium nitride for white light emitting diodes. J. Electrochem. Soc. 150, H47–H52.

Yun, B.-G., Miyamoto, Y., Yamamoto, H., 2007. Luminescence properties of $(Sr_{1-u}Ba_u)Si_2O_2N_2$: Eu^{2+}, yellow or orange phosphors for white LEDs, synthesized with $(Sr_{1-u}Ba_u)_2SiO_4$:Eu^{2+} as a precursor. J. Electrochem. Soc. 154, J320–J325.

Zeng, C., Liu, H., Hu, Y., Liao, L., Mei, L., 2015. Color-tunable properties and energy transfer in $Ba_3GdNa(PO_4)_3F$:Eu^{2+},Tb^{3+} phosphor pumped for *n*-UV *w*-LEDs. Opt. Laser Technol. 74, 6–10.

Zeuner, M., Hintze, F., Schnick, W., 2008. Low temperature precursor route for highly efficient spherically shaped LED-phosphors $M_2Si_5N_8$:Eu^{2+} (M=Eu, Sr, Ba). Chem. Mater. 21, 336–342.

Zeuner, M., Schmidt, P.J., Schnick, W., 2009. One-pot synthesis of single-source precursors for nanocrystalline led phosphors $M_2Si_5N_8$:Eu^{2+} (M=Sr, Ba). Chem. Mater. 21, 2467–2473.

Zeuner, M., Pagano, S., Schnick, W., 2011. Nitridosilicates and oxonitridosilicates: from ceramic materials to structural and functional diversity. Angew. Chem. Int. Ed. 50, 7754–7775.

Zhang, S., Huang, Y., 2011. The luminescence characterization and thermal stability of Eu^{2+} ions-doped $NaBaPO_4$ phosphor. J. Am. Ceram. Soc. 94, 2987–2992.

Zhang, X., Liu, X., 1992. Luminescence properties and energy transfer of Eu^{2+} doped Ca_8Mg $(SiO_4)_4C_{l2}$ phosphors. J. Electrochem. Soc. 139, 622–625.

Zhang, H., Horikawa, T., Hanzawa, H., Hamaguchi, A., Machida, K., 2007a. Photoluminescence properties of α-SiAlON:Eu^{2+} prepared by carbothermal reduction and nitridation method. J. Electrochem. Soc. 154, J59–J61.

Zhang, X., Wu, H., Zeng, H., Su, Q., 2007b. Luminescent properties of $SrGa_2S_4:Eu^{2+}$ and its application in green-LEDs. J. Rare Earth 25, 701–705.

Zhang, X., Choi, N., Park, K., Kim, J., 2009a. Orange emissive $Sr_3Al_2O_5Cl_2:Eu^{2+}$ phosphor for warm-white light-emitting diodes. Solid State Commun. 149, 1017–1020.

Zhang, X., Wang, X., Huang, J., Shi, J., Gong, M., 2009b. Near UV-based LED fabricated with $Ba_5SiO_4(F,Cl)_6:Eu^{2+}$ as blue- and green-emitting phosphor. Opt. Mater. 32, 75–78.

Zhang, X., Zhou, F., Shi, J., Gong, M., 2009c. $Sr_{3.5}Mg_{0.5}Si_3O_8Cl_4:Eu^{2+}$ bluish–green-emitting phosphor for NUV-based LED. Mater. Lett. 63, 852–854.

Zhang, X., Tang, X., Zhang, J., Wang, H., Shi, J., Gong, M., 2010a. Luminescent properties of $Sr_2MgSi_2O_7:Eu^{2+}$ as blue phosphor for NUV light-emitting diodes. Powder Technol. 204, 263–267.

Zhang, X., Zhang, J., Wang, R., Gong, M., 2010b. Photo-physical behaviors of efficient green phosphor $Ba_2MgSi_2O_7:Eu^{2+}$ and its application in light-emitting diodes. J. Am. Ceram. Soc. 93, 1368–1371.

Zhang, Z.J., Delsing, A.C.A., Notten, P.H.L., Zhao, J.T., Hintzen, H.T., 2012a. Photolumines-cence properties of Eu^{2+}-activated $Ca_2Y_2Si_2O_9$ phosphor. Mater. Res. Bull. 47, 2040–2044.

Zhang, J., Zhang, X., Gong, M., Shi, J., Yu, L., Rong, C., Lian, S., 2012b. $LiSrBO_3:Eu^{2+}$: a novel broad-band red phosphor under the excitation of a blue light. Mater. Lett. 79, 100–102.

Zhang, X., Chen, Y., Zhou, L., Gong, M., 2013a. NUV chip based white LED using thermal stable Eu^{2+}-activated phosphate and borate phosphor. Mater. Lett. 93, 390–392.

Zhang, X., Mo, F., Zhou, L., Gong, M., 2013b. Properties–structure relationship research on $LiCaPO_4:Eu^{2+}$ as blue phosphor for NUV LED application. J. Alloy Compd. 575, 314–318.

Zhang, X., Song, J., Zhou, C., Zhou, L., Gong, M., 2014a. High efficiency and broadband blue-emitting $NaCaBO_3:Ce^{3+}$ phosphor for NUV light-emitting diodes. J. Lumin. 149, 69–74.

Zhang, Z.J., Feng, A., Sun, X.Y., Guo, K., Man, Z.Y., Zhao, J.T., 2014b. Preparation, electronic structure and luminescence properties of Ce^{3+}-activated CaZnOS under UV and X-ray exci-tation. J. Alloys Compd. 592, 73–79.

Zhang, J., Zhang, W., Qiu, Z., Zhou, W., Yu, L., Li, Z., Lian, S., 2015a. $Li_4SrCa(SiO_4)_2:Ce^{3+}$, a highly efficient near-UV and blue emitting orthosilicate phosphor. J. Alloys Compd. 646, 315–320.

Zhang, Q., Ni, H., Wang, L., Xiao, F., 2015b. Effects of BaF_2 flux on the synthesis of green emit-ting phosphor $CaSc_2O_4:Ce^{3+}$. ECS J. Solid State Sci. Technol. 4, R23–R26.

Zheng, H., Ma, J., Luo, X., 2013. Conformal phosphor distribution for white lighting emitting diode packaging by conventional dispensing coating method with structure control. IEEE T. Comp. Pack. Man 3, 417–421.

Zhong, J., Zhuang, W., Xing, X., Liu, R., Li, Y., Liu, Y., Hu, Y., 2015. Synthesis, crystal struc-tures, and photoluminescence properties of Ce^{3+}-doped $Ca_2LaZr_2Ga_3O_{12}$: new garnet green-emitting phosphors for white LEDs. J. Phys. Chem. C 119, 5562–5569.

Zhou, T.L., Song, Z., Song, X.P., Bian, L., Liu, Q.L., 2010. A red oxide phosphor, $Sr_2ScAlO_5:Eu^{2+}$ with perovskite-type structure, for white light-emitting diodes. Chin. Phys. B 19, 127808.

Zhou, Y., Yoshizawa, Y., Hirao, K., Lenčéš, Z., Šajgalík, P., 2011. Combustion synthesis of $LaSi_3N_5:Eu^{2+}$ phosphor powders. J. Eur. Ceram. Soc. 31, 151–157.

Zhou, W., Ma, X., Zhang, M., Luo, Y., Xia, Z., 2015a. Synthesis and photoluminescence proper-ties of green-emitting $Lu_3(Al,Sc)_5O_{12}:Ce^{3+}$ phosphor. Ceram. Int. 41, 7140–7145.

Zhou, W., Han, J., Zhang, X., Qiu, Z., Xie, Q., Liang, H., Lian, S., Wang, J., 2015b. Synthesis and photoluminescence properties of a cyan-emitting phosphor $Ca_3(PO_4)_2:Eu^{2+}$ for white light-emitting diodes. Opt. Mater. 39, 173–177.

Zhu, G., Wang, Y., Ci, Z., Liu, B., Shi, Y., Xin, S., 2012. $Ca_8Mg(SiO_4)_4Cl_2:Ce^{3+},Tb^{3+}$: a potential single-phased phosphor for white-light-emitting diodes. J. Lumin. 132, 531–536.

Zhu, J., Qin, S., Xia, Z., Liu, Q., 2015. Synthesis and color-tunable emission studies of $Y_2Si_3O_3N_4:Ce^{3+},Tb^{3+}$ phosphors. Ceram. Int. 41, 12633–12637.

Zorenko, Y., Gorbenko, V., Voznyak, T., Zorenko, T., Kuklinski, B., Turos Matysyak, R., Grinberg, M., 2009. Luminescence properties of phosphors based on $Tb_3Al_5O_{12}$ (TbAG) terbium-aluminum garnet. Opt. Spectrosc. 106, 365–374.

Chapter 279

REE Mineralogy and Resources

M. Hoshino[*,1], **K. Sanematsu**[*] **and Y. Watanabe**[†]

[*]*Mineral Resource Research Group, National Institute of Advanced Industrial Science and Technology, Tsukuba, Japan*
[†]*Akita University, Mining Museum of Akita University, Akita, Japan*
[1]*Corresponding author: e-mail: hoshino-m@aist.go.jp*

Chapter Outline

1 INTRODUCTION

1.1 Rare Earth Elements

Rare earth elements (REEs) represent the group of 17 elements comprising 15 lanthanides, plus yttrium (Y) and scandium (Sc) (Table 1). Among the REEs, yttrium was discovered first in 1794 by a Finish chemist, Johan Gadolin who isolated an oxide and called it "yttria," in a mineral collected from a quarry near the village of Ytterby in Sweden. It turned out to be a

129

TABLE 1 Names and Symbols of the Rare Earth Elements

Atomic Number	Symbol	Name	Ionic Radii (Å) (Coordination VIII)
21	Sc	Scandium	Sc^{3+}: 0.87
39	Y	Yttrium	Y^{3+}: 1.02
57	La	Lanthanum	La^{3+}: 1.16
58	Ce	Cerium	Ce^{3+}: 1.14, Ce^{4+}: 0.87
59	Pr	Praseodymium	Pr^{3+}: 1.13
60	Nd	Neodymium	Nd^{3+}: 1.11
61	Pm	Promethium	
62	Sm	Samarium	Sm^{3+}: 1.08
63	Eu	Europium	Eu^{2+}: 1.25, Eu^{3+}: 1.07
64	Gd	Gadolinium	Gd^{3+}: 1.05
65	Tb	Terbium	Tb^{3+}: 1.04
66	Dy	Dysprosium	Dy^{3+}: 1.03
67	Ho	Holmium	Ho^{3+}: 1.02
68	Er	Erbium	Er^{3+}: 1.00
69	Tm	Thulium	Tm^{3+}: 0.99
70	Yb	Ytterbium	Yb^{3+}: 0.99
71	Lu	Lutetium	Lu^{3+}: 0.98

Data source for ionic radii (Shannon, R.D., 1976. Revised effective ionic radii and systematic studies of interatomic distances in halides and chalcogenides. Acta Crystallogr. A32, 751–767).

mixture of several oxides of rare earths, including yttrium oxide. The first individual REE to be isolated was cerium (Jöns Jacob Berzelius and Wilhelm Hisinger, 1803). Most other REEs were isolated individually in the 19th century, and the last naturally occurring one—Lu—was isolated in 1907. It took over 150 years from to first REE to the final discovery of promethium in 1947. Because promethium is a radioactive element, formed from decays of unstable isotopes of europium and uranium, with the longest half-life of 17.7 years for ^{145}Pm, the element does not occur in the Earth's crust in detectable concentrations. For this reason, promethium is excluded from the consideration in this review.

REEs never occur individually but collectively they are found in various minerals in the Earth's crust. This is a natural verification that these elements

partition similarly in melts, fluids, and minerals on the earth. Exceptions are cerium (Ce) and europium (Eu), which may take different valence states (Ce^{4+} and Eu^{2+}) depending on the oxidation state of the melts or fluids in addition to trivalence typical of REEs. Thus, this characteristic is used to assess relative redox conditions in some mineral or rock systems (Henderson, 1996) and affects the concentration of REEs in minerals and ores in natural environments. Scandium is usually found separately from other rare earths and, therefore, like promethium is not considered in this review.

The ionic radii of trivalent REE ions are about 1 Å, which are compatible to those of Ca^{2+}, Na^+, Th^{4+}, etc., and are significantly larger than those of other trivalent ions such as B^{3+}, Al^{3+}, and Fe^{3+} (Miyawaki and Nakai, 1996). Ionic radii of the trivalent REE ions are systematically reduced from La to Lu with increasing atomic number. Slight differences of the ionic radii of REE ions (Table 1) also affect the partitioning of REEs into the minerals. The ionic radius of Y^{3+} is similar to the heavy REE ions, resulting in the similarity of chemical behavior of yttrium with the REEs with larger atomic numbers.

The REEs are electropositive so their compounds are generally ionic. From a mineralogical standpoint, these compounds are oxides, halides, carbonates, phosphates, and silicates. Because REE ionic radii are relatively large, substitution reactions usually involve large cations such as calcium or strontium even though some additional charge balancing is often necessary.

The REEs are transition metals. In the transition metals, the s orbital of the outermost shell is filled before filling of the lower electron shells is complete. In atoms of the period six transition elements, the 6s orbital is filled before the 5d and 4f orbitals. In the lanthanides, it is the 4f orbitals that are being filled, so the configuration of the valence electrons is similar in all the REEs, hence all exhibit similar chemical behavior.

Because of high ionic charges and large radii, REEs behave as incompatible elements in magma, so that the REEs are more concentrated in the melt, whereas compatible elements such as iron and magnesium are more incorporated into minerals in the early stages of fractional crystallization. This geochemical behavior leads to enrichment of REEs in felsic igneous rocks formed from the residual melt in the later stages of fractional crystallization. The degree of incompatibility varies; lighter REEs are more incompatible than the heavier ones.

REEs are commonly classified into light and heavy groups, with scandium unclassified (Henderson, 1996). The grouping differs with different study scopes such as electron configuration, mineralogy, chemical behavior, etc. For example, Ni et al. (1995) classified the REEs into "cerium-group" type (La-Gd), yttrium-group type (Tb-Lu and Y) on the basis of the partitioning of REEs in monazite (La-Gd) and xenotime (Tb-Lu and Y). In this review, we classify them into light rare earth elements (LREEs: La-Eu) and heavy rare earth elements (HREEs: Gd-Lu and Y), because Gd is selectively

incorporated into HREE minerals like xenotime. We also note that "light" and "heavy" are most commonly and properly used with "lanthanides," and strictly speaking a "heavy rare earth" is inaccurate for Y, which is lighter than any of the lanthanides.

The subject of this review is REE mineralogy and resources, of which major REE minerals are monazite and xenotime in addition to bastnäsite. Later, REE concentrations and contents correspond to total of La to Lu and Y. REO (total REE oxides) refers to the total of La to Lu and Y oxides in rocks and ores, including divalent and tetravalent, while REE_2O_3 represents the total of trivalent La-Lu and Y oxides in REE minerals.

Geochemically, REEs are more abundant in the Earth's crust than the underlying mantle and more common in the upper continental crust than the lower crust. The abundance of REEs in the continental crust varies from 43 (Ce) to 0.3 ppm (Tm, Lu), and light REEs (93 ppm) are more abundant than the heavy ones (32 ppm) (Rudnick and Gao, 2003). They reported that REEs (147 ppm in total) are more abundant than copper (27 ppm), tin (1.7 ppm), and molybdenum (0.8 ppm) in the continental crust. This is because the incompatible REEs are concentrated in partial melts that have crystallized to form the continental crust, and light REEs are larger in ion radius than the heavy ones (Table 1), characterizing more incompatible nature of LREEs than HREEs.

1.2 Applications and Mining History of REEs

Historically, the utilization of REEs started from LREEs such as lanthanum and cerium, and it has expanded to heavier REEs such as praseodymium, neodymium, samarium, terbium, and dysprosium, although the applications of the heaviest group elements such as holmium, erbium, thulium, ytterbium, and lutetium have not been well developed yet.

Industrial application of REEs started with artificial lighting using gas mantles containing thorium and cerium oxides in the late 19th century. In the early 20th century, iron–cerium alloy found common use in lighter flints (Table 2). However, the demand for REEs was quite limited until the mid-20th century when reliable technologies for REE separation were developed and the properties of individual elements were investigated.

During the early half of the 20th century, REEs were produced mainly from monazite in placer deposits, particularly those of the southeastern United States and Brazil (Castor and Hedrick, 2006). A phosphate vein deposit, Steenkampskraal in South Africa, also produced monazite for the thorium-based nuclear power reactors operating in the mid-20th century, and REEs were recovered as the by-product of thorium. However, by the late 1960s, these reactors were decommissioned as uranium reactors were built, and the demand for thorium declined (Blench, 2010).

With declining interest in thorium as a potential nuclear fuel and increased concern over the disposal of radioactive thorium, bastnäsite came to displace

TABLE 2 Major Application of Rare Earth Elements in the Industry

Product	Element	Property Development	Widespread Application
Yttrium-stabilized zirconia	Y	1897	1984 Ceramic knife
Lighter flint	Ce	1903	1975 Disposable lighter
Metallurgy	La, Ce	1927	1970 Desulfurization of steel
Polishing	Ce	1943	1970s Mechanical polishing 1990s Chemical mechanical polishing
FCC catalyst	Ce	1955	1970 Petroleum refining
Phosphors	Y, Eu	1964	Late 1960s Color television
$SmCo_5$ magnet	Sm	1965	1970s Motor, speaker
Hydrogen absorbing alloy	La	1968	1997 Nickel–metal hydride battery in hybrid vehicles
Sm_2Co_{17} magnet	Sm	1975	1970s Motor, speaker
NdFeB magnet	Nd, Dy, Tb	1983	1980s Computer, magnetic resonance imaging 1990s Voice coil motor, factory automation machinery 2000s Automobile, wind turbine
SmFeN magnet	Sm	1990	2000s Motor, computer

monazite in the production of the REEs due to its much lower thorium content (Fig. 1). Between 1965 and 1985, most of the world's REEs came from bastnäsite found in the Mountain Pass carbonatite deposit, United States. The increased REE production from bastnäsite lowered REE prices significantly and promoted a variety of modern applications of REEs (Table 2).

The REEs have been applied in various fields such as fluid catalytic cracking (FCC) catalysts for petroleum refining, high-index and colored glasses, desulfurizers in steel production, and polishing materials for glass products and electrical components. Cerium and lanthanum are the elements that are mainly used for these applications. Some other elements such as europium, yttrium, and terbium were used to produce phosphors for fluorescent and cathode ray tubes, and samarium for SmCo magnets (Table 2).
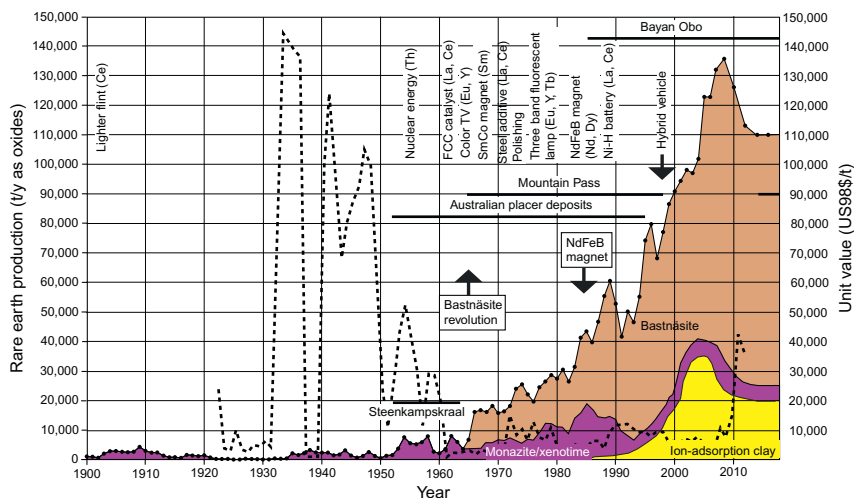
FIG. 1 Historical change of the production amount of REO from bastnäsite, phosphates (monazite and xenotime), and ion-adsorption clays, with unit value (shown in *thick broken line*) (USD/kg), based on the data by U.S. Geological Survey (2015). The value is normalized to the US dollars in 1998. The operation period of some important mines and years when important REE-based products and technologies have been commercialized are also shown.

A new and substantial demand for the REEs came about from the permanent magnet industry when neodymium–iron–boron (NdFeB) magnet was discovered and commercialized in 1985. Because NdFeB magnets surpass SmCo magnets in energy product and have lower cost, they are now commonly used in motors, factory machinery, generators, voice coil motor, magnetic resonance imaging, and others. Dysprosium and terbium are used as additives to NdFeB magnets to improve their heat resistance, and the motors with such heat resistive NdFeB magnets have been installed in hybrid and electric vehicles as well as wind turbines (Minowa, 2008). The NdFeB magnet market has been rapidly growing because these new generation vehicles and wind turbines help to reduce CO_2 emissions. In 2010, the demand for the production of permanent magnets has reached 33,250 tons REO, which corresponded to 27% total share of the world's REE consumption (Roskill Information Services Ltd, 2011).

Robust demand for HREEs (Dy and Tb) urged the mining sector to seek new REE sources in addition to bastnäsite in carbonatite, which dominates in LREEs. Ion-adsorption type deposits were discovered in early 1970s in the Jiangxi province in China, which was followed by the discoveries in the Guangdong, Guangxi, and Hunan provinces in a couple of years. Because some of the ion-adsorption type deposits are enriched in HREEs, these new deposits began production in 1985, when the demand for HREEs to make high-grade NdFeB magnets commenced in Japan (Fig. 1). Since then, the

ion-adsorption type deposits have become the exclusive source of HREEs in the world. The production of REEs from this deposit type increased exponentially due to the strong demand of HREEs, attaining more than 35,000 tons per year in 2005.

1.3 Present Situation of REE Supply and Demand

During the 1980s, China emerged as a major producer of REE raw materials, while the Australian and US market shares decreased dramatically. Since 1998, more than 90% of the world's REE production has come from China, and most of this production is from the Bayan Obo deposit in Inner Mongolia, in which REE minerals are bastnäsite and monazite. In addition to the production from Bayan Obo, a part of REEs have been produced from other carbonatite deposits (Maonuiping and Weishan) as well as ion-adsorption type deposits in southern China.

However, strengthened control on REE production by the Chinese government reduced the amount approximately to 90,000 tons per year in recent years. Especially, the production from ion-adsorption type deposits has been reduced to conserve domestic resources in China. This reduced REE production by China affected the world REE production which is limited to 110,000 tons per year in recent years (Fig. 1; U.S. Geological Survey, 2015). The Chinese government also reduced the exported amounts of REEs from 50,000 tons in 2009 to 30,000 tons in 2010. This reduction reduced the availability of REEs in the countries outside China, resulting in the soaring REE prices in 2011–2012 (Fig. 2). At the same time, this reduction promoted REE exploration projects outside China, many of them targeting HREE resources.

To satisfy the demand for REEs outside China, production of bastnäsite was revived at the Mountain Pass Mine in the United States and started anew at the Mount Weld carbonatite deposit in Australia in 2013. The production from these projects was 4800 and 6600 tons in 2014, respectively. Mountain Pass operation was put on hold in the late 2015 due to the unfavorable economics as a result of steady decline of REE prices (Fig. 2).

Because of the unstable prices and supply of dysprosium and terbium, the magnet industry of Japan, the second NdFeB magnet producer in the world after China, has reduced the amounts of dysprosium used in the magnets and developed dysprosium-free magnets, and the demand of HREEs outside China has decreased.

1.4 What Will be the Next Source of REEs?

Recent increase of the demand for REEs, especially dysprosium and terbium used in the permanent magnet industry is modifying a concept of the REE mineralogy and resources. This is amplified by the REE supply restrictions
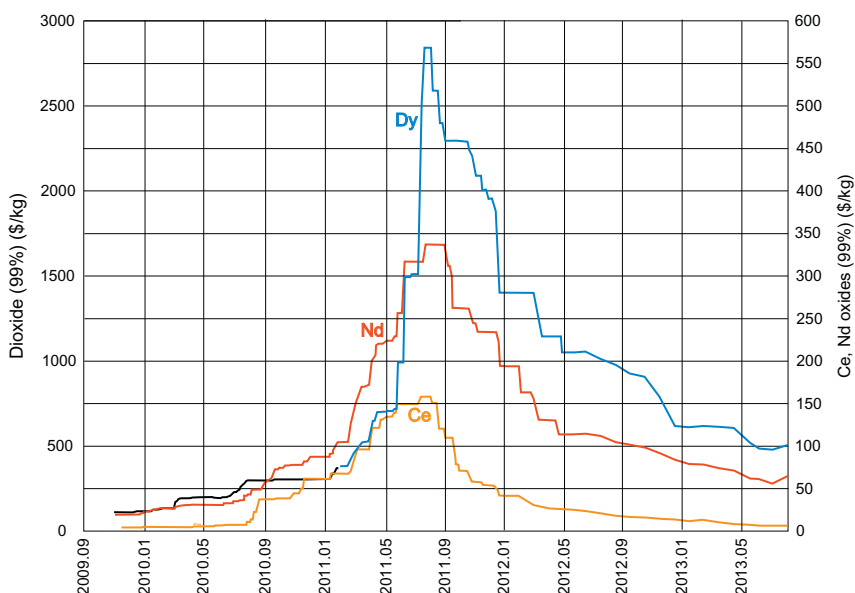
FIG. 2 Prices of dysprosium, cerium, and neodymium oxides outside China from 2009 to 2013. *Data source is Metal-Pages.*

outside of China. Bastnäsite from carbonatite deposits remains the dominant source of LREEs. Exploration has been extended worldwide to secure the supply of REEs, especially the heavy ones. In recent years, various attempts are made to produce HREEs from unconventional sources, such as peralkaline igneous rocks, which have not been regarded as a REE source except the Lovozero deposit in Kola Peninsula, Russia, where LREEs have been produced from loparite as a by-product of niobium (Lippmaa et al., 2006). Therefore, this paper reviews the potential sources of REEs, especially HREEs (ion-adsorption types and apatite deposits), which are regarded as the most critical group of elements for the future green technologies (European Commission, 2010; U.S. Department of Energy, 2011).

2 GEOCHEMISTRY OF REEs

2.1 Mineral–Melt Partition Coefficients of REEs

The behavior of REEs is heavily dependent on the partitioning of REEs between immiscible melts, between minerals and melts, between melts and fluids, and between minerals and fluids. This partitioning is determined by the partitioning coefficients (D), represented as

$$D_i^{\alpha-\beta} = C_i^{\alpha}/C_i^{\beta}$$

where C is concentration, subscript i refers to an element and superscripts α and β refer to α- and β-phases, respectively. The partitioning coefficients are related to the pressure, temperature, chemical composition, and oxygen fugacity of the melts or fluids. These coefficients have been estimated by numerous experiments, chemical analyses of natural materials, and theoretical calculations.

Although the partitioning coefficients of the REEs are affected by various factors mentioned earlier, it is useful to compare the coefficients of representative minerals in the igneous rocks (for example, basalt) for understanding of the behavior of the REEs. White (2013) compiled the mineral–melt partition coefficients of REEs for mafic magmas, based on the data assembled in Geochemical Earth Reference Model (GERM, www.earthref.org/GERM; Fig. 3). These results show that the coefficients of clinopyroxene, garnet, plagioclase, and amphibole are much higher than those of olivine and spinel, and the minerals with the high partitioning coefficients control the concentration of REEs. Although olivine is the most abundant mineral in the upper mantle, the partitioning of REEs is not significantly affected because of its low coefficients. Among REEs, europium is highly partitioned to plagioclase because divalent (Eu^{2+}) europium in relatively reducing conditions substitutes for Ca^{2+} in
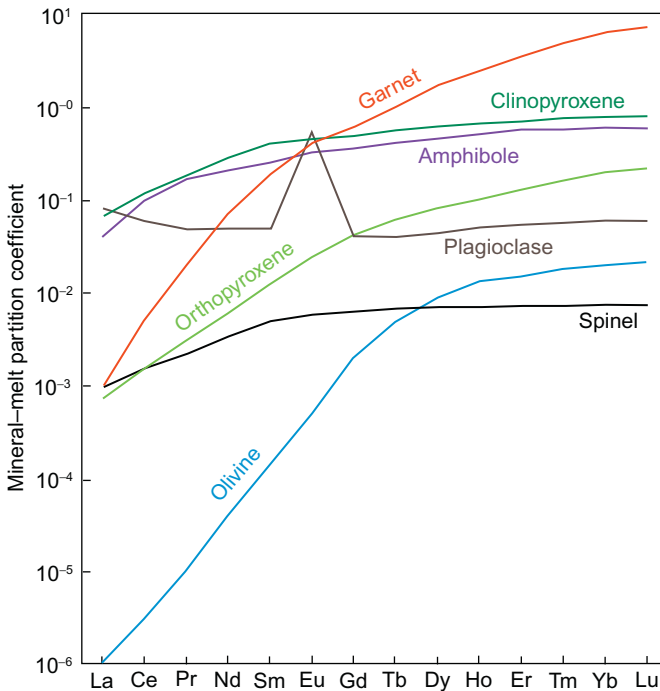
FIG. 3 REE mineral-melt partition coefficients for mafic magmas after White (2013).

plagioclase, and HREEs are highly partitioned to garnet due to the similarity of ionic size, which is the main cause of HREE depletion in the magmas such as carbonatites that principally form at the garnet-stable field (Harrison, 1981).

2.2 Concentration of REEs in the Earth

2.2.1 Bulk Silicic Earth

Chondrites constitute primitive meteorites, which represent chemical properties of the solar nebula, the cloud of gas and dust from which the solar system formed. Chondrites are classified into carbonaceous chondrites, ordinary chondrites, and enstatite chondrites. Ordinary chondrites are composed of olivine, orthopyroxene, and lesser amounts of nitrogen–iron alloy, while enstatite chondrites are highly reduced, with iron metal and enstatite. Those chondrite classes may have undergone thermal and impact influence in the host stars (Van Schmus and Wood, 1967).

In contrast, carbonaceous chondrites are enriched in the abundances of carbon, sulfur, water, and other volatile compounds than the other chondrite classes. This indicates the most primitive chemical characteristic among the classes of chondrites mentioned earlier. Thus, one of the subclasses of carbonaceous chondrites, represented by Carbonaceous Ivuna (CI) chondrite, has been regarded to represent the chemical composition of the solar system. This is supported by the fact that the composition of CI chondrites is most similar to that of the sun determined by spectrographically except noncondensing elements and lithium (White, 2013). The chemical composition of the CI chondrite shows that the abundance of REEs in the earth follows Oddo–Harkins effect that the elements with even atomic number are more stable and abundant than the neighboring elements of the odd atomic number, and the lighter REEs are more abundant than the heavier ones (Table 3 and Fig. 4).

2.2.2 Mantle

The chemical composition of the mantle is assumed by modifying the composition of CI chondrites, on the basis of the correlation with elements in peridotites, which are dominated in the mantle. Abundances of the refractory lithophile elements including REEs in the primitive mantle are enhanced relative to CI chondrite (Table 3), because volatile and siderophile elements and some oxygen were removed to the core (eg, McDonough and Sun, 1995). HREEs mainly condensed first in aluminate hibonite ($CaAl_{12}O_{19}$) with lithophile elements such as Th and U, when it formed from high-temperature gas of solar composition. Somewhat less refractory elements (V, Nb, Ta, LREEs, Sr, and Ba) condensed to calcium titanates such as perovskite when they became present as an additional host. Europium, the most volatile element in this group, condensed when feldspar became stable (Lodders, 2003).

TABLE 3 Rare Earth Compositions in the Mantle and Crusts (ppm)

	CI Chondrite (Lodders and Fegley, 1998)	Primitive Mantle (Lyubetskaya and Korenaga, 2007)	Oceanic Crust (White and Klein, 2013)	Lower Continental Crust (Rudnick and Gao, 2003)	Middle Continental Crust (Rudnick and Gao, 2003)	Upper Continental Crust (Rudnick and Gao, 2003)	Continental Crust (Rudnick and Gao, 2003)
La	0.235	0.508	2.13	8	24	31	20
Ce	0.620	1.340	5.81	20	53	63	43
Pr	0.094	0.203	0.94	2.4	5.8	7.1	4.9
Nd	0.460	0.994	4.90	11	25	27	20
Sm	0.150	0.324	1.70	2.8	4.6	4.7	3.9
Eu	0.057	0.123	0.62	1.1	1.4	1.0	1.1
Gd	0.200	0.432	2.25	3.1	4.0	4.0	3.7
Tb	0.037	0.080	0.43	0.5	0.7	0.7	0.6
Dy	0.250	0.540	2.84	3.1	3.8	3.9	3.6
Ho	0.056	0.121	0.63	0.7	0.82	0.83	0.77
Er	0.160	0.346	1.85	1.9	2.3	2.3	2.1
Tm	0.025	0.054	0.28	0.24	0.32	0.30	0.28
Yb	0.160	0.346	1.85	1.5	2.2	2.0	1.9
Lu	0.025	0.054	0.28	0.25	0.4	0.31	0.30
Y	1.56	3.37	18.1	16	20	21	19
Sc	5.90	12.7	36.2	31	19	14	21.9
Total	9.99	21.54	80.81	104	167	183	147
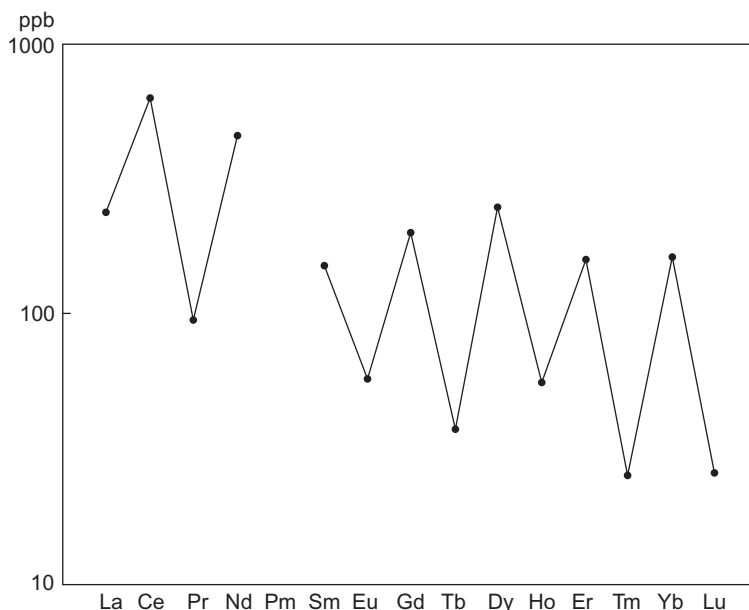
FIG. 4 Abundance of lanthanides in CI chondrite. *After Lodders, K., Fegley, B., 1998. The Planetary Scientist's Companion. Oxford University Press, New York.*
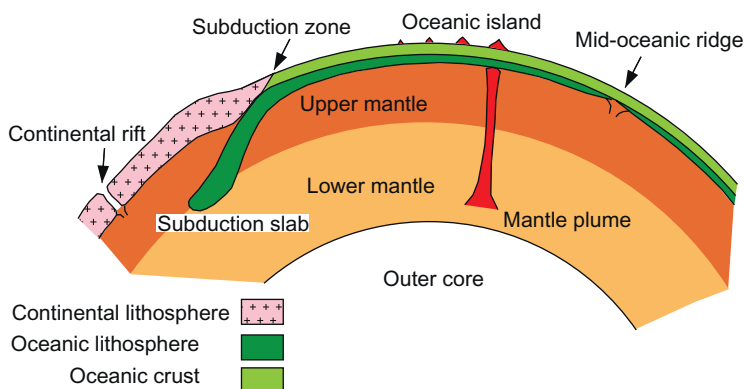
FIG. 5 Major sites of magma generation.

Isotopic variations (^{87}Sr/^{86}Sr, ^{143}Nd/^{144}Nd, ^{206}Pb/^{204}Pb) in basalt, which are the product of partial melting of the mantle, clearly show that the chemical composition of the present-day mantle is heterogeneous. Such isotopic variations are conspicuous among the basalts erupted at mid-oceanic ridge basalt (MORB) and those erupted on oceanic island basalts (OIB) (Fig. 5). MORB is enriched in ^{143}Nd/^{144}Nd and depleted in ^{87}Sr/^{86}Sr, while OIB are depleted

in $^{143}Nd/^{144}Nd$ and enriched in $^{87}Sr/^{86}Sr$, compared to the bulk silicic earth. These results show that the source for MORB is relatively depleted in incompatible elements. This means that the source mantle of most MORB has experienced depletion in incompatible elements while the source of OIB has experienced enrichment in incompatible elements, compared to the estimated composition of the primitive mantle (White, 2013).

Thus, there is a clear difference in the REE composition between MORB and OIB; MORB is depleted in LREEs but OIB is enriched in them (Fig. 6). The depletion of incompatible elements including LREEs in MORB is explained by extraction of partial melts from previously depleted MORB mantle, which have formed oceanic crust and more importantly continental crust that are enriched in incompatible elements (Saunders et al., 1988; Table 3).

The enrichment of LREEs in OIB is interpreted by its smaller degree of partial melting, which is suggested by alkaline elements rich compositions
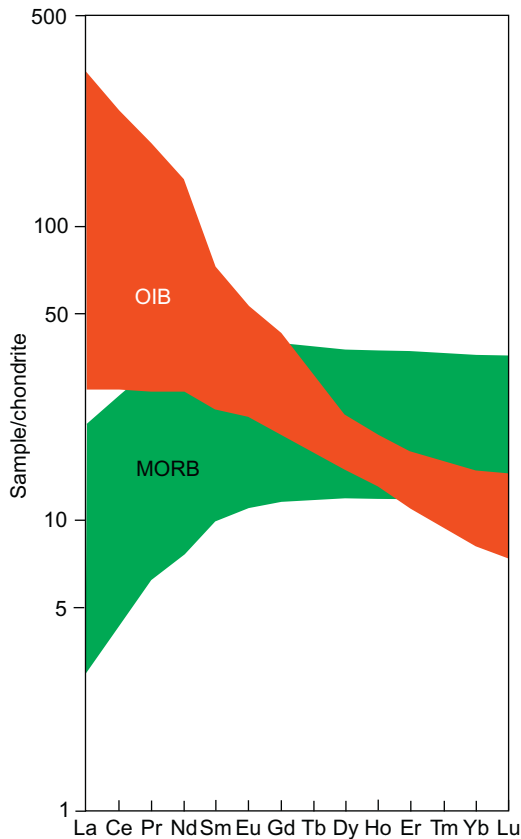
FIG. 6 Chondrite-normalized REE patterns of mid-oceanic ridge basalt (MORB) and oceanic island basalt (OIB) (White, 2013).

of the OIB. In addition to this, however, the composition of the source mantle is assumed to be heterogeneous and distinct, and this heterogeneity may derive from the depth of the mantle; MORB are derived from the shallow mantle, and OIB are derived from deep the mantle (Fig. 5; White, 2013).

2.2.3 The Crust

The Earth's crust is the largest reservoir of REEs (Table 3) although the crust represents only a small fraction of mass (about 0.5%) of the Earth. The crust is composed of oceanic and continental crust. The oceanic crust is created by the magmatism at mid-oceanic ridges and basaltic in composition. The continental crust is much thicker and on average andesitic in composition.

The composition of the oceanic crust is estimated by the compositions and mineral assemblages of MORB (Table 3). It is remarkably uniform throughout the oceanic basins. The composition of the continental crust, on the other hand, is extremely heterogeneous, and it is difficult to estimate the average composition. Estimates of crustal composition have been based on the compositions of the rocks taken over a large area, or the compositions of the glacial clays and/or loess that are regarded as well-mixed products of rocks in a wide area and time span. The most recent comprehensive study by Rudnick and Gao (2003) indicates that the upper and middle crusts are more enriched in REEs than the lower crust, and the upper crust is characterized by a negative Eu anomaly and middle and lower crust by slightly positive Eu anomaly (Fig. 7).
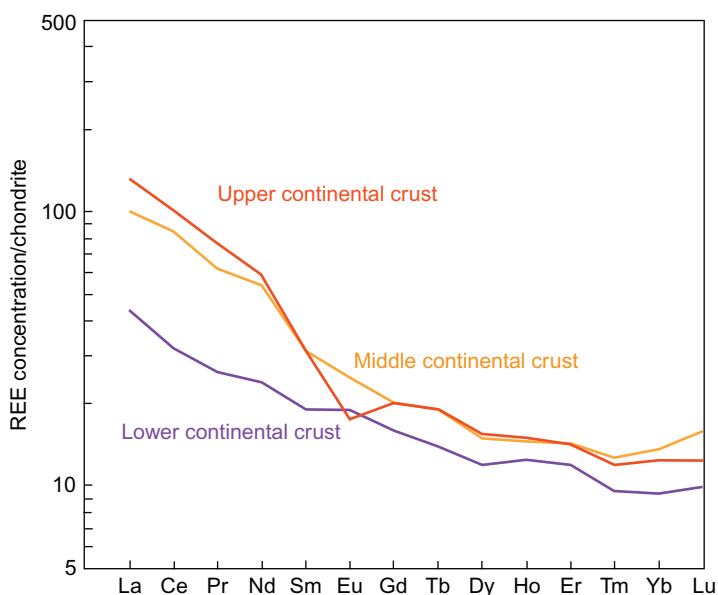
FIG. 7 Comparison of chondrite-normalized REE patterns in upper, middle, and lower crust (Rudnick and Gao, 2003).
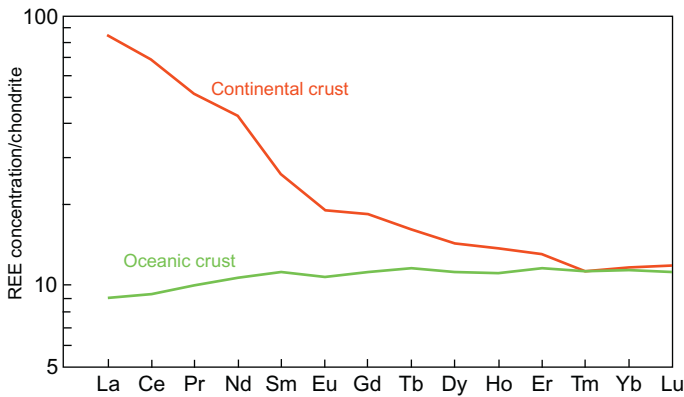
FIG. 8   Comparison of chondrite-normalized REE patterns of the total oceanic crust (White and Klein, 2013) and continental crust (Rudnick and Gao, 2003).

The comparison of the chondrite-normalized REE patterns in the whole continental and oceanic crusts shows that both are enriched in all REEs relative to primitive mantle as well as CI chondrite, and the continental crust is enriched in LREEs relative to the HREEs. In contrast, the oceanic crust is somewhat enriched in HREEs (Fig. 8). The oceanic crust is produced through comparatively large extents of melting of the upper mantle that has already been depleted in incompatible elements through previous episodes of melting. The strong enrichment of LREEs in the continental crust suggests that relatively small degree of partial melting of primitive mantle material has been important in its evolution (Hofmann, 2005; White, 2013).

2.3   Rare Earth Partitioning to Melts

In addition to MORB and OIB, there are two more important tectonic settings for the generation of magmas: subduction zones and continental rift zones (Fig. 5). This section describes the partitioning of REEs to melts along the subduction zones and continental rift zones.

2.3.1   Subduction Zones

Generation of magmas along the subduction zones is ascribed to the partial melting of mantle peridotite under hydrous condition. This hydrous condition is realized by the supply of aqueous fluids from subduction slab, which is metamorphosed and dehydrated when it descends beneath the continental or island arc margin. Aqueous fluids exsolved from the slab, which have been subducted to about 100–120 km depth beneath the mantle wedge below the magmatic arc, ascend into the mantle wedge asthenosphere, of which medium part attains temperatures of more than 1400°C. This addition of fluids to

the mantle peridotites decreases the solidus temperature of the peridotites, resulting in the partial melting (Tatsumi et al., 1983). The site of this partial melting becomes deeper toward the backarc, and the chemical compositions of primitive magmas change laterally from tholeiitic basalt to alkaline olivine basalt through high-alumina basalt toward the backarc (Kuno, 1959).

REE compositions of the subduction-related arc magmas are generally consistent with the magmas generated by partial melting of peridotite, whereas a variation is present between the basalts on the volcanic front and those on the backarc. The backarc basalts are more alkaline in composition, more enriched in LREEs, and more depleted in HREEs than those on the volcanic front (Fig. 9). This difference is explained as that the primitive alkali basalts on the backarc form by a lower degree of partial melting (<10%) at a deeper level (50–80 km) than high-alumina basalts and tholeiitic basalts, which form by as much as 15–25% melting of mantle peridotite at a shallower level (40 km) (Kushiro, 2007; Tatsumi et al., 1983).

The major volcanic rocks in the magmatic belts above the subduction zones are calc-alkaline rocks. Calc-alkaline rocks (mainly basaltic andesites and andesites) are characterized by relatively low FeO/MgO ratio and greater enrichment in alkali elements than tholeiitic basalts. The calc-alkaline magma can be produced in several different ways: crystal fractionation, crystal assimilation, and magma mixing, the last of which has recently been regarded the major process (Tatsumi and Takahashi, 2006; Winter, 2010). Many calc-alkaline rocks represent mixing of mantle-derived mafic magmas with dacitic or rhyolitic melts produced by partial melting of the crust due to thermal input form the rising mafic magma (Tatsumi and Takahashi, 2006), and final fractionation of the calc-alkaline magma toward dacites and rhyolites occurs at shallow levels. The REE concentrations and chondrite-normalized REE patterns of calc-alkaline rocks are variable, but the abundance of REEs increases with fractionation (Fig. 10). The progressive enrichment in LREEs from low-K to high-K andesites may reflect lower degree of partial melting of the parent rocks.

Arc-magmatism sometimes includes high-Mg andesite, which cannot be formed by low-pressure fractional crystallization or partial melting of basalts, because these processes lower the magnesium contents. Adakites are high-Mg andesites with high alkalis, Ni, Sr, and Cr and low Nb, Ti, and HREEs (Fig. 11). The depletion of HREEs implies that garnet was a fractionating phase. Partial melting of an eclogitic slab is a mechanism to form adakite, as well as partial melting of eclogite or garnet amphibolite of the deep arc or continental crust (Winter, 2010). Such magmatism occurs where a hot spreading ridge and/or young oceanic lithosphere is subducting (eg, Miocene-Quaternary Southwest Japan arc where the Miocene Shikoku basin has been subducting), or where subarc crust is extremely thickened by the contraction tectonics, represented by the region of "flat-slab subduction" in Central Volcanic Zone in the Chilean Andes.
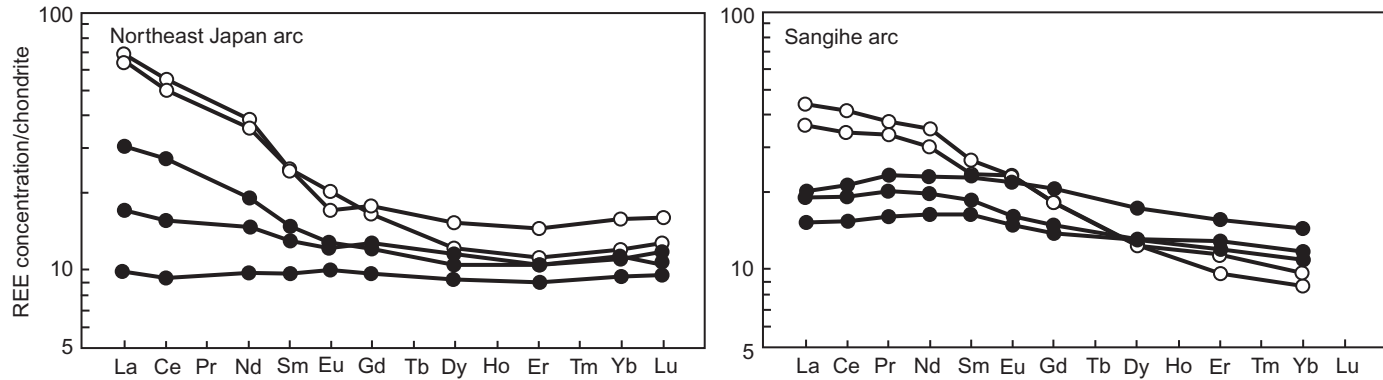
FIG. 9 Chondrite-normalized REE patterns of the primitive basalts across the Northeast Japan arc and Sangihe arc. *Solid circles*: basalts on the volcanic front, *open circles*: basalts on the backarc. *After Tatsumi, M., 1995. Subduction Zone Magmatism: A Contribution to whole Mantle Dunamics. University of Tokyo Press, Tokyo, 186p (in Japanese).*
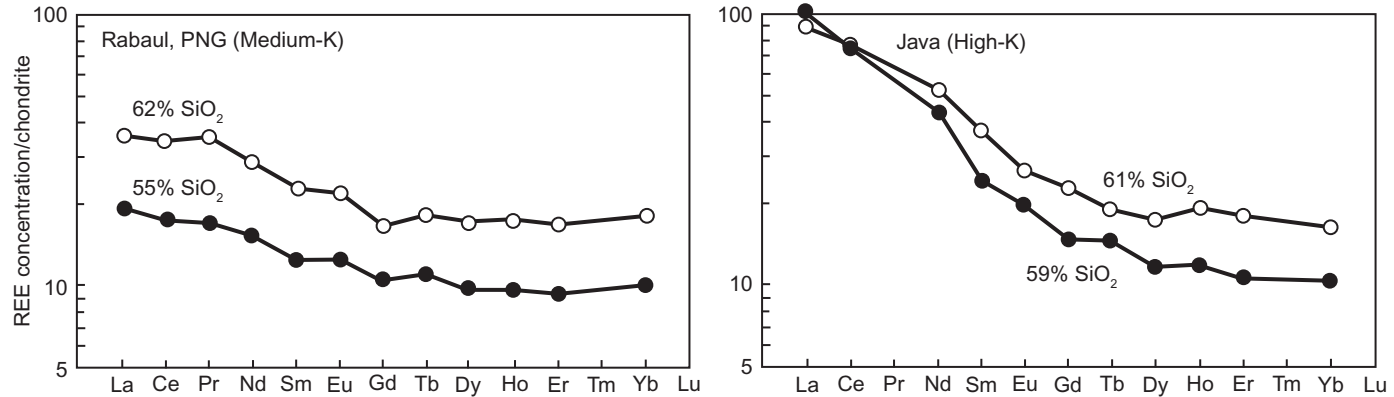
FIG. 10 Chondrite-normalized REE patterns of the medium-K and high-K calc-alkaline and sites. *After Gill, J., 1981. Orogenic Andesites and Plate Tectonics. Springer-Velag, Berlin, 390p.*
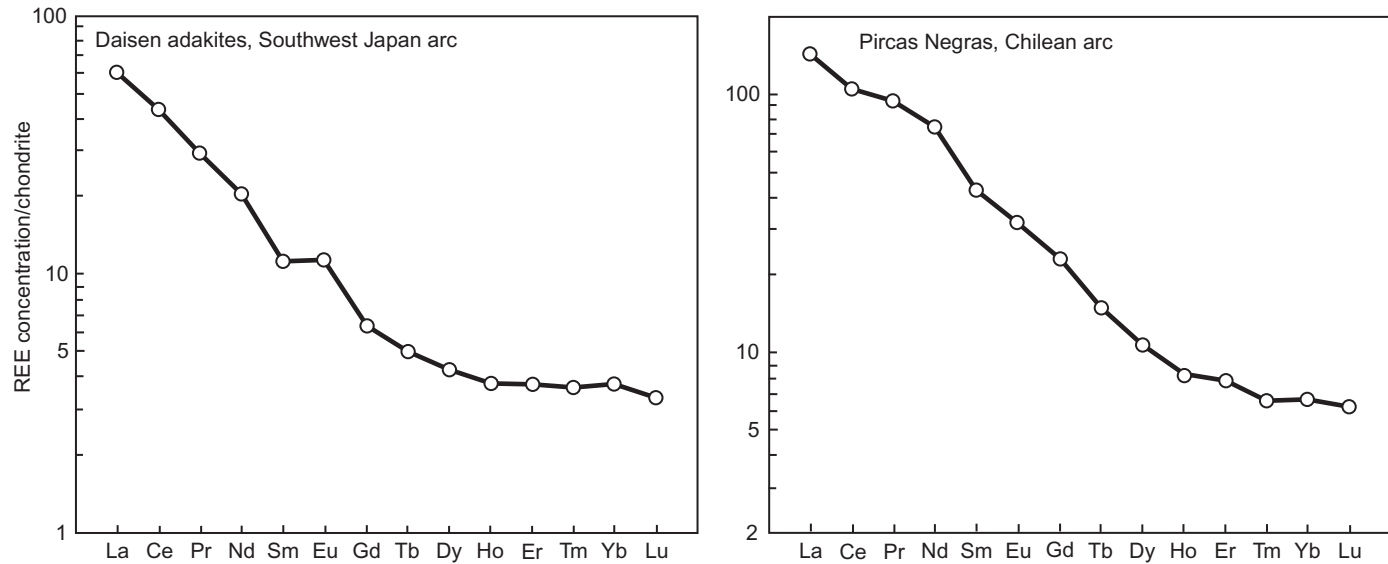
FIG. 11 Chondrite-normalized REE patterns of the Daisen (Southwest Japan arc; Tokunaga et al., 2010) and Pircas Negras (Central Chilean arc; Goss et al., 2013) adakites. The *plots* are the average of original data.

Granitoid is the broad term for felsic plutonic rocks, including granite, granodiorite, and tonalite. Granitoids occur in a large volume in the magmatic arcs along the subduction zones. The major process that forms granitoid magma is believed to be melting of lower crustal materials by mafic magma accumulation at the base of the crust, and chemical compositions, especially trace elements concentrations, are reflected by the compositions of the source materials (Winter, 2010). Thus, granitoids in the subduction zones are classified into igneous-type (I-type) and sedimentary-type (S-type), which are produced by partial melting of a mafic mantle-derived igneous source material and by partial melting of peraluminous sedimentary source rocks, respectively (Chappell and White, 1974). Another classification proposed by Ishihara (1977) is based on oxidation state of the granitoid magmas: magnetite (oxidized) series and ilmenite (reduced) series. The major reason of the different oxidation state of granitoid magmas is the absence or presence of carbon, which can reduce the magmas, in the source materials. Because carbon is commonly included in sedimentary rocks, this classification is somewhat similar to the classification by Chappell and White (1974), although I- and S-types do not directly correspond to magnetite-series and ilmenite-series, respectively. All of the S-type granitoids are included in ilmenite-series, whereas I-type include both magnetite-series and ilmenite-series granitoids.

REEs in any type of the granitoids are mostly contained in the accessory REE minerals such as allanite, monazite, and xenotime, in addition to Ca-bearing minerals, in which REEs occur as isomorphous admixture. Principal among these minerals are garnet, epidote, apatite, titanite, and fluorite (Bea, 1996; Rapp and Watson, 1986). In allanite- or monazite-bearing granitoids, the bulk of the whole-rock REEs (up to 90%) is concentrated in two or three accessory minerals, allanite and monazite and either titanite, zircon, or fluorite, and apatite (Bea, 1996; Gavrilova and Turanskaya, 1958; Gromet and Silver, 1983; Lyakhovich, 1967).

The Mesozoic western Japan arc is the type locality of the magnetite-series and ilmenite-series granitoids, where three zones of granitoids are present from the north to south: Sanin (I-type magnetite-series), Sanyo (I-type ilmenite-series), and Ryoke (I- and S-types ilmenite-series) belts (Fig. 12A). The comparison of chondrite-normalized REE patterns of these granitoids shows that primitive granitoids of these three belts have a similar LREE-enriched pattern with a minor europium negative anomaly, but different fractionation patterns are observed between the magnetite-series and ilmenite-series granitoids (Fig. 12B–D).

The magnetite-series granitoids in the Sanin belt show depletion of both LREEs and HREEs with significant depletion of europium during the fractionation. This depletion is explained by the fractionation of plagioclase for europium and the precipitation of titanite as well as apatite mainly for LREEs, because P_2O_5 and TiO_2 concentration of the Shirakawa granitoids decreases significantly from the primitive ($SiO_2 = 69.31$ wt.%) parts (P_2O_5: 0.12 wt.%;
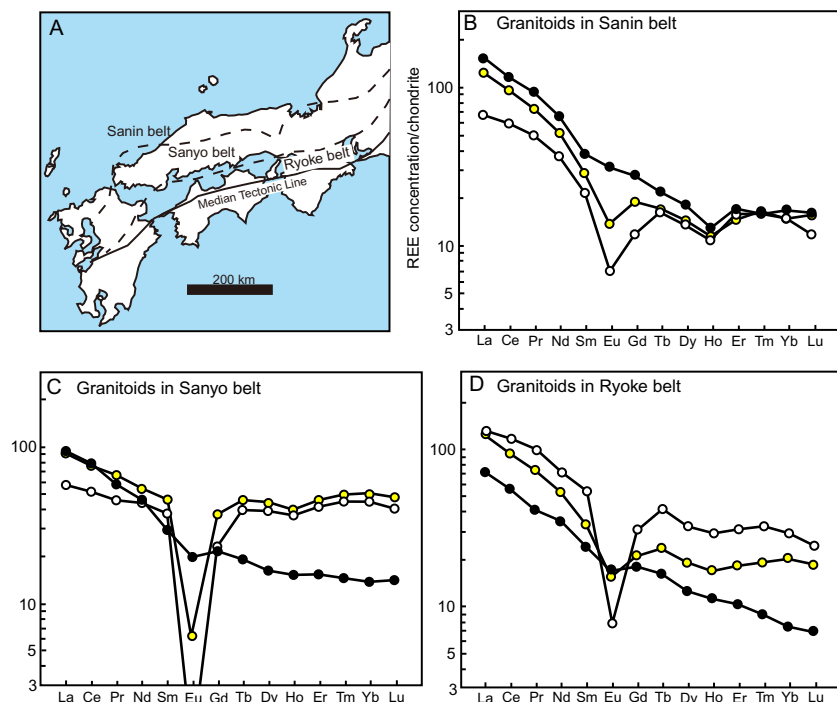
FIG. 12 (A) Map showing the distribution of the Sanin, Sanyo, and Ryoke belts in the southwestern Japan arc and the locations of the granitoids analyzed. (B) Chondrite-normalized patterns of granitoids in the Sanin belt. (C) Chondrite-normalized REE patterns of granitoids in the Sanyo belt. (D) Chondrite-normalized REE patterns of granitoids in the Ryoke belt. *Solid, gray*, and *open circles* represent the least fractionated, averaged, and most fractionated granitoids in each belt. *Data are taken from Ishihara, S., Murakami, H., 2006. Fractionated ilmenite-series granites in southwest Japan: source magma for REE-Sn-W mineralization. Resour. Geol. 56, 245–256; Ishihara, S., Wu, C., 2001. Genesis of Late Cretaceous-Paleogene granitoids with contrasting chemical trends in the Chubu district, central Japan. Bull. Geol. Surv. Jpn 52, 471–491.*

TiO_2: 0.43 wt.%) to fractionated ($SiO_2 = 77.34$ wt.%) parts (P_2O_5: 0.01 wt.%; TiO_2: 0.05 wt.%) (Fig. 12B). In contrast, the ilmenite-series Ryoke granitoids show enrichment in REEs (Fig. 12D), especially HREEs in addition to the depletion of europium, although the P_2O_5 and TiO_2 contents decrease from the less fractionated granitoids (P_2O_5: 0.23 wt.%; TiO_2: 0.71 wt.%) to fractionated granitoids (P_2O_5: 0.02 wt.%; TiO_2: 0.10 wt.%), similar to that of the magnetite-series granitoids. Titanite is stable in the oxidized felsic magma but not in the reduced magma, because in the reduced condition, ilmenite becomes stable instead of titanite (Wones, 1989). The titanite/silicate melt partition coefficients of REEs are much higher (0.3–1; Prowatke and Klemme, 2006) than those of ilmenite, and thus, REEs are incorporated into titanite in the magnetite-series granitoids. However, in the reduced magmas,

REEs, especially HREEs are not incorporated in the accessory minerals significantly, resulting in the enrichment in the fractionated melt. Because the granitoids in the Ryoke belt have been deeply eroded and only relatively deeper portions are exposed on the surface, such enrichment is not clear. However, in the Sanyo belt, where highly fractionated ilmenite-series I-type granitoids are exposed, the granitoids are highly enriched in HREEs in addition to strong negative europium anomalies (Fig. 12C). Thus, oxidation state of granitoid melts affects REE concentration by the presence or absence of highly REE partitioned accessory minerals although the REE concentrations and compositions of the primitive oxidized and reduced granitoid magmas are not significantly different.

2.3.2 Continental Rift Zone

The magmatism of the continental rift zones is characterized by the occurrence of kimberlite and carbonatite in addition to alkali basalt. These three rock types commonly occur together, forming an igneous complex. Because of the incompatible characteristic of REEs, they are concentrated more in the magmas formed by low degree of partial melting such as peralkaline and carbonatite magmas.

Carbonatites are defined as igneous rocks composed of more than 50 modal percent primary carbonate and containing less than 20 wt.% SiO_2 (Le Maitre, 2002). Carbonatites are known to range in age from the Archean to the Recent, with an increasing abundance toward more recent time (Rukhlov and Bell, 2010). Carbonatite magmatism has been almost exclusively restricted to the continental environments characterized by thickened lithosphere and relatively stable cratons of Archean age. Especially, carbonatites cluster in large igneous provinces such as 66 Ma Deccan flood basalt province, 130 Ma Paraná-Etendeka, 250 Ma Siberian province, and 370 Ma Kola alkaline province (Ernst and Bell, 2010). Most carbonatites are associated with prominent geological structures such as rift systems or grabens, major faults, large-scale uplifts, and cratonic domains (Rukhlov and Bell, 2010).

Carbonatite magmas are able to form by direct melting of a carbonate-bearing mantle source, by immiscible separation from a carbonated silicate melt, and by crystal fractionation of a carbonated alkali silicate melt (Halama et al., 2005), among which the mantle-source carbonatites are most dominant. The models of carbonatite magma generation from mantle source are debatable; it forms by sublithospheric source (Bell and Tilton, 2002; Nelson et al., 1988) or by metasomatized lithosphere with mantle materials (Bell and Simonetti, 2010; Chakhmouradian, 2006). Whichever the origin, it is accepted that carbonatite magmas form at pressures exceeding 1.9 GPa in the garnet- and amphibole-stable fields (Fig. 13). Primary carbonatite melts can generate near the solidus greater than 70 km from dolomitic or carbonated amphibole lherzolite by very low degree of partial melting. This is consistent with LREE
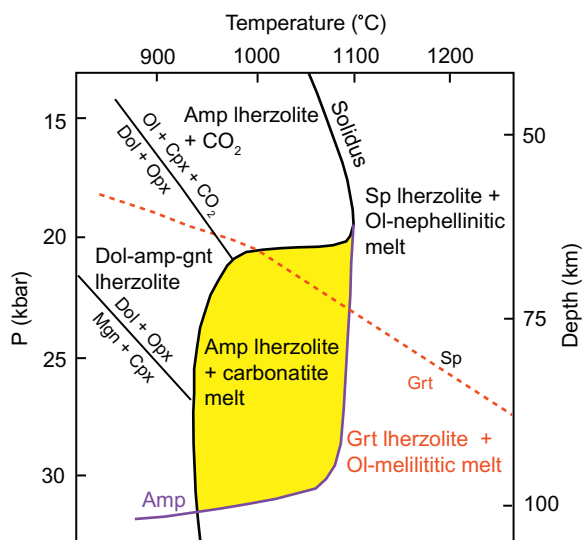
FIG. 13 Phase relationships in metasomatized lherzolitic mantle modified from Wallace and Green (1988) and Chakhmouradian (2006). *Gray area* shows where carbonatite magmas are in equilibrium with amphibole lherzolite. *Broken line* separates the stability fields of spinel and garnet. *Solid thin lines* show the stability fields of other minerals. *Gray line* shows amphibole stability field. Abbreviations: *Amp*: amphibole, *Cpx*: clinopyroxene, *Dol*: dolomite, *Grt*: garnet, *Mgn*: magnetite, *Ol*: olivine, *Opx*: orthopyroxene, *Sp*: spinel.

enrichment in carbonatites (Table 4 and Fig. 14), because the partition coefficients between carbonatite melt and garnet are low (<0.3) for LREEs but high (0.3–10) for HREEs based on the melting experiment of garnet lherzolite (Dasgupta et al., 2009). Carbonatites are known to contain the highest amounts of REEs (~500 to >10,000 ppm; Table 4) of any igneous rocks, although only a few carbonatites attain minable level of REE concentration (>4 wt.%).

Carbonatites are classified into calcite-carbonatite, dolomite-carbonatite, ferro-carbonatite, and natro-carbonatite, based on the most abundant carbonate minerals (Woolley and Kempe, 1989). In these carbonatites, REEs reside mainly in the Ca-bearing phases, ie, carbonates, apatite, Ca-Nb-oxides, and Ca-silicates, where they substitute with Sr^{2+} for Ca^{2+}. Specific REE minerals such as ancylite, bastnäsite, britholite, monazite, parisite, etc., are either rare or volumetrically insignificant accessory phases (Hornig-Kjarsgaard, 1998). Carbonatites are generally show systematic enrichment form Lu to La with some exceptions that show Ce-negative anomalies. It is evident that the concentration and relative enrichment of the REEs in most carbonatites is controlled by carbonate phases and apatite because of their high modal amounts and moderate REE abundances. Rare earth rich accessories such as perovskite and pyrochlore influence the bulk-rock REE pattern only if they occur in sufficient amounts (Hornig-Kjarsgaard, 1998).

Kimberlite is a complex group of hybrid volatile-rich (dominantly CO_2), potassic, or ultrapotassic rocks with a fine-grained matrix and macrocrysts

TABLE 4 Representative Rare Earth Compositions of Kimberlite, Carbonatite, and Alkaline Basalt

	Kimberlite, South Africa[1]	Calcite Carbonatite[2]	Dolomite Carbonatite[3]	Ferro-Carbonatite[4]	Alkaline Basalt, Southern Kenya[5]	Ijolite, Spitskop, South Africa[6]	Nepheline Syenite, Kovdor, Russia[7]
La	156	608	746	2666	70	19.8	52.1
Ce	317	1687	2183	5125	141	46.3	88.7
Pr	36	218	560	550	16	6.1	8.40
Nd	134	883	634	1618	63	26	27.3
Sm	19	130	45	128	12	5.3	3.99
Eu	4.9	39	12	34	3.6	1.7	0.78
Gd	12	105	–	130	9.7	5.6	2.84
Tb	1	9	5	16	1.3		0.39
Dy	5	34	–	52	6.9	4.6	2.16
Ho	1	6	–	6		0.9	0.44
Er	2	4	–	17	2.7	2.1	1.26
Tm	0.2	1	–	2			0.19
Yb	0.9	5	10	16	1.7	1.3	1.22
Lu	0.1	1	0			0.2	0.18
Y	20	119	61	204	34		12.5
Sc	19	7	14	10	26		10.7
Total	728	3856	4270	10,574	388	120	213

Data sources: 1, Le Roex, A.P., Bell, D.R., Davis, P., 2003. Petrogenesis of group I kimberlites from Kimbery, South Africa: evidence from bulk-rock geochemistry. J. Petrol. 44, 2261–2286; 2–4, Winter, J.D., 2010. Principles of Igneous and Metamorphic Petrology, second ed. Prentice Hall, New York, 720p; 5, Späth, A., Le Roex, A.P., Opiyo-Akech, N., 2001. Plume-lithosphere interaction and the origin of continental rift-related alkaline volcanism-the Chyulu Hills volcanic province, southern Kenya. J. Petrol. 42, 765–787; 6, Harmer, R.E., 1999. The petrogenetic association of carbonatite and alkaline magmatism: constraints from the Spitskop Complex, South Africa. J. Petrol. 40, 525–548; 7, Arzamastsev, A.A., Bea, F., Glaznev, V.N., Arzamastseva, L.V., Montero, P., 2001. Kola alkaline province in the Paleozoic: evaluation of primary mantle magma composition and magma generation conditions. Russ. J. Earth Sci. 3, 1–32.
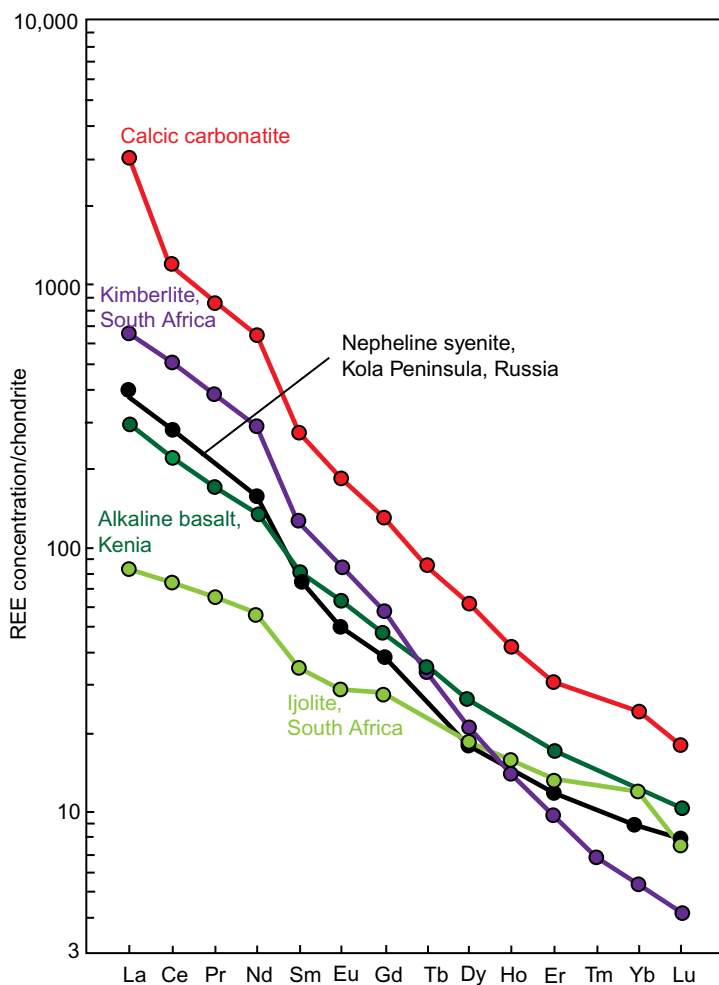
FIG. 14 Chondrite-normalized REE patterns of the igneous rocks in the continental rifting setting. *Data sources are kimberlite (Le Roex, A.P., Bell, D.R., Davis, P., 2003. Petrogenesis of group I kimberlites from Kimbery, South Africa: evidence from bulk-rock geochemistry. J. Petrol. 44, 2261–2286), calcic carbonatite (Hornig-Kjarsgaard, I., 1998. Rare earth elements in Sövitic carbonatites and their mineral phases. J. Petrol. 39, 2105–2121), alkali basalt (Späth, A., Le Roex, A.P., Opiyo-Akech, N., 2001. Plume-lithosphere interaction and the origin of continental rift-related alkaline volcanism-the Chyulu Hills volcanic province, southern Kenya. J. Petrol. 42, 765–787), and ijolite and nepheline syenite (Downes, H., Balaganskaya, E., Beard, A., Liferovich, R., Demaiffe, D., 2005. Petrogenetic processes in the ultramafic, alkaline and carbonatitic magmatism in the Kola Alkaline Province: a review. Lithos 85, 48–75).*

of olivine and several of the following: ilmenite, garnet, diopside, phlogopite, enstatite, and chromite. Many kimberlites contain diamond and coesite, which indicate a deep mantle origin. Kimberlite occurs mainly at continental rift zones and some clusters along transform fault zones similar to carbonatite.

Kimberlite is thought to form at depth less than 300 km, and CO_2-rich kimberlite and carbonatite may be produced by partial melting of carbonated lherzolite. Although kimberlite geochemistry is complex and because of its hybrid nature, it is difficult to determine the compositions of original melt, like carbonatite, kimberlite is enriched in LREEs, suggesting garnet was a residual phase in their source regions (Table 4 and Fig. 14) (Winter, 2010).

Alkaline rocks occur not only in the rift zones, but also in other tectonic settings such as continental and oceanic intraplate settings and subduction zones, particularly in backarc setting or in the waning stages of magmatic activity (Winter, 2010). Alkaline rocks are deficient in SiO_2, with respect to Na_2O, K_2O, and CaO to the extent that they become undersaturated in SiO_2. On the other hand, some rocks may be deficient in Al_2O_3 so that Al_2O_3 may not be able to accommodate the alkalis in normative feldspars. Such rocks are called peralkaline and may be either silica undersaturated or silica oversaturated.

In the continental rift zones, high volume and short duration alkaline magmatism are recognized. These zones are characterized by ascending asthenospheric mantle, which form various types of alkaline magmas in addition to tholeiitic magmas at shallow depths (as shallow as 50 km) by partial melting at the beginning of the rifting (Winter, 2010). The primitive alkali basalt magmas are generally interpreted to form by small degree (1–3%) of batch melting of a source mantle at the base of continental lithosphere that is scarce in garnet, resulting in a slightly more enrichment of HREEs compared with carbonatite and kimberlite (Fig. 14).

Large peralkaline plutonic complexes cluster in the older-age eroded continental rift zones, represented by Kola Peninsula in Russia, Northern South Africa, and northeastern Canada (Ernst and Bell, 2010). These peralkaline complexes are heavily differentiated and commonly include carbonatite units (eg, Downes et al., 2005; Ernst and Bell, 2010; Féménias et al., 2005; Harmer, 1999). The origin of the nepheline syenite, major constituent of these peralkaline complexes, is interpreted as the result of fractional crystallization from alkaline ultramafic magmas. Such nepheline syenite at Kola Peninsula, Russia, has LREE-enriched patterns, which are similar to those of carbonatite, kimberlite, and alkali basalt in the same region, although total concentration of REE of nepheline syenite is quite variable because of extensive fractional crystallization and accumulation of the magma (Downes et al., 2005).

2.4 Magmatic Crystallization and REE Enrichment

The REE concentrations of the primitive magmas for various rock types are not high enough to reach typical ore grades that are found in economical mineral deposits, even in the case of carbonatites which commonly contain up to a few thousand ppm of REEs. The magmatic processes subsequent to melt formation, ie, (1) accumulation, (2) immiscibility, and (3) fractional crystallization are important to increase REE concentration to the economic grades.

2.4.1 Accumulation

Concentration of REEs in the cumulates is found in large peralkaline igneous complexes such as the Khibina and Lovozero complexes in Kola Peninsula of Russia, and the Ilímaussaq complex in southern Greenland.

Kola Peninsula includes more than 20 main alkaline rock complexes, ages of which cluster between 360 and 390 Ma (Downes et al., 2005). The Khibina complex is a cylindrical shape body about 30 km in diameter, and it has a concentric zonal structure formed by successive phases of intrusion including nepheline syenite, ijolite, and carbonatite. The ijolite unit contains an apatite-rich layer that is composed of magnetite, titanite, and apatite in the hanging wall of an intrusion. This layer partly attains more that 80% apatite in volume, forming high-grade apatite ores in the complex. Because the apatite typically contains up to 5 wt.% REEs as oxides (Belousova et al., 2002; Sha and Chappell, 1999), the apatite ores are regarded as a potential REE resource (Zaitsev and Kogarko, 2012). This apatite concentration is interpreted as that apatite crystallized from silicate magma and accumulated in the upper part of the magma chamber due to crystal sorting in the convecting melt (Kogarko and Khapaev, 1987).

Lovozero is another large cylindrical complex located east of the Khibina complex. This complex is about 26 km in diameter and is divided into three units: phase I nepheline syenite, phase II layered nepheline syenite, and phase III eudialyte-bearing nepheline syenite. The phase II unit is composed of repeating layers, each of which has a basal apatite–loparite-enriched part and an upper alkali feldspar and nepheline rich part (Féménias et al., 2005). This segregation is ascribed to the different specific gravity among the constituent minerals: loparite (4.6–4.9), apatite (3.2), and nepheline (2.7), forming a cumulus layer of heavy minerals at the base of the magma chamber (Kogarko et al., 2002; Fig. 15). Because loparite at Lovozero contains 28–35 wt.% REEs as oxides (Kogarko et al., 2002), REEs are produced as by-product of niobium in loparite mined from the loparite-enriched layers of the complex (Hedrick et al., 1997) (Fig. 15).

The Ilímaussaq complex in Greenland is northwesterly elongated peralkaline body, 17 km × 7 km in size, which was associated with continental rifting between 1350 and 1140 Ma (Upton et al., 2003) and is one of the highly evolved and silica undersaturated peralkaline intrusions. The body is divided into a lower part of kakortokites and lujavrites and upper naujaite part (Pfaff et al., 2008). The lowermost kakortokites, 200 m thick, include 29 units (8 m thick on average) composed of a set of black-colored arfvedsonite-rich layer, red-colored eudialyite-rich layer, and white-colored K-feldspar and nepheline rich layer. Pfaff et al. (2008) interpreted the layers formed by different mineral abundance in each unit is as a result of their different specific gravities. Among these minerals, eudialyte contains 2.5–6.8 wt.% REO, and thus eudialyte-rich layers and/or units are concentrated in REEs.
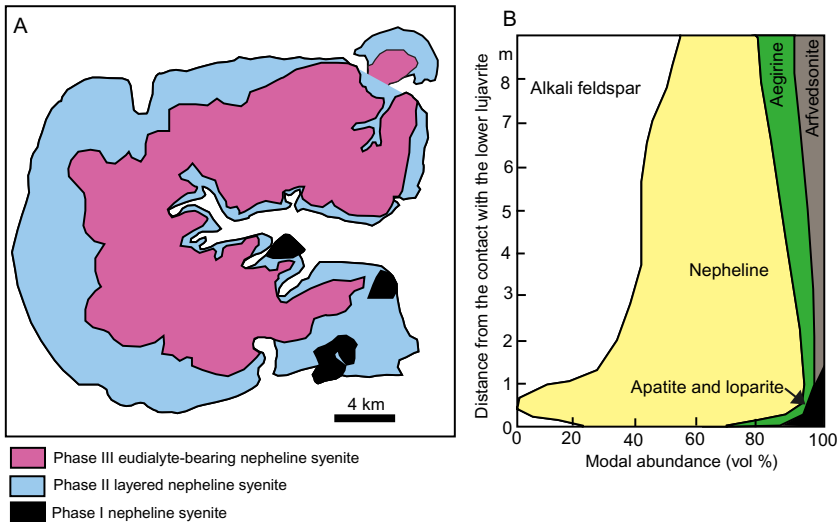
FIG. 15 Simplified geological map of the Lovozero peralkaline complex (A) and constituent mineral abundance of a unit in the Phase II layered nepheline syenite (B). *After Féménias, O., Coussaert, N., Brassinnes, S., Demaiffe, D., 2005. Emplacement processes and cooling history of layered cyclic unit II-7 from the Lovozero alkaline massif (Kola Peninsula, Russia). Lithos 83, 371–393.*

2.4.2 Immiscibility

There is a long-standing debate about whether carbonatite magmas are products of liquid immiscibility or are derived directly from melting of the mantle. However, many recent experimental studies have demonstrated that carbonatite melts can form from carbonated lherzolite at moderate or high pressures. Although several studies suggest that carbonatite melts form by immiscibility from silicate melts (eg, Demény et al., 2004; Halama et al., 2005; Krasnova et al., 2004), most of the carbonatites are considered to be a product of direct melting of lithospheric mantle composed of garnet lherzolite that is metasomatized by volatile-rich melts/fluids of a sublithospheric source (Bell and Simonetti, 2010).

2.4.3 Fractional Crystallization

Because of incompatible characteristics of REEs, fractional crystallization may increase concentration of REEs in the melts which form late-stage REE-enriched rocks (eg, granites). However, the process of REE enrichment is not simple, because REE distribution is controlled by a variety of REE-bearing rock-forming minerals. Carbonatites, the major source of REE resources, are believed to be enriched in REEs during the fractional crystallization. When carbonatites crystallize, REE-bearing phosphate minerals, including apatite and monazite, precipitate earlier than REE-bearing carbonate (calcite) and REE carbonate

(bastnäsite) (Xu et al., 2010). Balance between carbonate (calcite) and phosphate (apatite) results in the concentration of heavy or light REEs in the residual melt. Xu et al. (2010) discussed this enrichment process in the Miaoya deposit in central China. Their results show that due to extremely low partitioning of LREEs to calcite, even though apatite and monazite precipitated early in the evolution, REEs, especially LREEs, were enriched to an economical grade of 1.72 wt.% REO in the fractionated carbonatites, and were finally incorporated in REE fluorocarbonates such as bastnäsite-(Ce) and synchysite-(Ce).

The abundance of REEs of peraluminous melts is low and consequently the abundances of REEs in peraluminous granites and pegmatites are low, but their solubilities greatly increase with increasing peralkalinity of the melts. This leads to high concentration of high-field strength elements (HFSE) in peralkaline granites by extreme fractionation of peralkaline magma. Such examples are observed at Khaldzan Buregtey deposit in Mongolia (Kovalenko et al., 1995) and Nechalacho (Thor Lake) deposit in Canada (Sheard et al., 2012), although subsequent hydrothermal processes played a major role for the concentration of REE in these deposits (Salvi and Williams-Jones, 2005).

2.5 Partitioning to Fluids

For many years, REEs were considered to be immobile in hydrothermal fluids. This idea is supported by very low concentration of REEs in low temperature hot spring water (van Middlesworth and Wood, 1998). However, it has become apparent that REEs can be concentrated to ore grades by hydrothermal processes (Migdisov and Williams-Jones, 2014; Samson and Wood, 2005; Williams-Jones et al., 2012). Recent studies of REE mineralization associated with carbonatites and peralkaline igneous complexes have revealed that the REE mineralization in these igneous complexes is exclusively related to hydrothermal activities that followed magmatic processes (eg, Migdisov and Williams-Jones, 2014; Sheard et al., 2012; Wall et al., 2008; Williams-Jones et al., 2012). The only apparent exception is the Mountain Pass deposit in the United States, which is assumed to have formed by fractional crystallization of carbonatite magma without significant hydrothermal alteration (Castor, 2008a). This section reviews the recent studies on the complexation of REEs, and REE partitioning between fluids and melts.

2.5.1 Complexation of REEs

Except under very acidic conditions, simple hydrated trivalent ions are not capable of transporting significant quantities of the REEs. Rather, the formation of strong aqueous complexes is required. Because aqueous REE^{3+} ions are "hard" in the sense of Pearson (1963), they form stronger complexes with "hard" ligands such as F^-, SO_4^{2-}, CO_3^{2-}, PO_4^{3-}, and OH^- than with "soft" ligands (eg, HS^-, CN^-, Br^-, and I^-). The "borderline" ligand Cl^- forms comparatively weak

complexes with the REEs at low temperatures ($<200°C$), but the stability of such complexes increases dramatically with increasing temperature.

Samson and Wood (2005) summarized the experimental results on the complexation of the REE as follows: (1) complexation of the REE by chloride is weak at standard conditions, even at high chloride concentrations, but increases significantly as temperature increases above $200°C$; (2) important species identified are $REECl^{2+}$, $REECl_2^{+}$, and possibly $REECl_3^{0}$, with the latter complexes, those with higher chloride ligand numbers, becoming relatively more important with increasing chloride concentration and temperature; and (3) the stability constants do not vary as a function of atomic number between 200 and $300°C$.

Several authors have considered that fluoride complexes played a major role for transportation of REEs, because of abundant presence of fluorine in REE deposits as well as "hard" characteristic of fluorine with the trivalent REE ions (eg, Agangi et al., 2010; Smith and Henderson, 2000; Williams-Jones et al., 2000). However, the presence of large amounts of fluoride-bearing minerals such as fluorite and fluorapatite in a deposit does not necessarily mean that the activity of free fluoride ion was sufficiently high to stabilize fluoride complexes of REEs. The activity of free fluoride may be maintained at relatively low value by the low solubility of minerals such as fluorite and topaz, binding of fluoride in complexes with H^{+}, Al^{3+}, Li^{+}, Fe^{3+}, Si^{4+}, Na^{+}, etc., and preferential partitioning of fluoride into silicate melts compared to aqueous fluids (Samson and Wood, 2005).

2.5.2 Aqueous Fluid–Silicate Melt Partitioning of REEs in Granites

Partitioning of the REEs between aqueous chloride brines and silicate melts has been described using the distribution coefficient, $K_d(i)$, defined as:

$$K_d(i) = C_i^f / C_i^m,$$

where C_i^f and C_i^m are the concentrations of element i in the aqueous fluid and the melt, respectively. Samson and Wood (2005) summarized the partitioning as: (1) REEs partition preferentially into the silicate melt relative to the aqueous phase (ie, $K_d < 1$), except for the LREEs at the highest aqueous chloride concentrations, (2) REEs partition increasingly into the aqueous phase with increasing chloride concentration, (3) K_d values for the LREEs are higher than those for the HREEs, (4) at low salinity, Eu shows an anomalously high preference for the aqueous fluid relative to the other REEs, (5) K_d may increase with increasing temperature and decreasing pressure, and (6) partitioning of REEs between aqueous fluid and silicate melt is relatively unaffected by the presence of fluoride. Samson and Wood (2005) concluded that the most important fluids are the moderate to high salinity (>10 wt.%) and high-temperature fluids for the Olympic Dam and Pea Ridge deposits, by the review of the fluids responsible for high-grade REE mineralization.

2.5.3 Aqueous Fluid–Silicate Melt Partitioning of REEs in Carbonatites

In carbonatites, REE mineralization is mostly related to late-stage hydrothermal activity. Studies of fluid inclusions in apatite indicate the predominance of aqueous, alkali-carbonate–chloride-bearing brines in the late magmatic phases in carbonatite intrusions (Rankin, 2005). The aqueous fluids associated with carbonatites have variable salt contents, ranging from 1 to over 50 wt.% dissolved solids, and K:Na ratios between 0.1 and 0.6. Sulfate and fluoride contents may also be high as suggested by the common occurrence of sulfate- and fluoride-bearing daughter minerals. Associated assemblages of CO_2-rich inclusions are interpreted as trapped portion of an immiscible CO_2-rich fluid originated from an original carbonated alkaline–chloride brine. Besides Na and K, the main components of the aqueous portions of carbonatitic fluids are Ca and Fe, which range between 2 and 20 wt.%, and levels of Sr, Ba, and REEs can be as high as several wt.% (Table 5). This indicates the importance and potential of carbonatitic fluids in the REE-Ba-Sr-F mineralization associated with carbonatites (Rankin, 2005). Xie et al. (2009) discussed that in most of the REE-mineralized carbonatites, REE mineralization was caused by the aqueous CO_2 emission process that may have been caused by a fast decrease in fluid pressure found at the Maoniuping deposit in China.

Based on the fluid inclusion chemistry (Fig. 16), Bühn and Rankin (1999) show the decreasing tendency of elements to partition into the associated fluid phase as $Cl = Na > K > (Cs, Rb, Pb, Cu, Zn) > U = Th > Ti > Y = Ba > F = Mg > REEs = Sr > Mn = Fe$ (Nb). Although REEs, Sr, and Ba do not appear to fractionate preferentially into the fluid, the high concentrations of these elements in carbonatites imply that the expelled fluids will be similarly enriched in these metals as is evident form the strong REE enrichment observed in some fenites (Morogan, 1989) and late-stage veins (Heinrich et al., 2003). Preferential partitioning during fluid–melt fractionation within the REEs is not observed, and LREE enrichment of the parent carbonatite magma is succeeded by similar enrichments in the associated magmatic fluid (Rankin, 2005), although significant REE fractionation between fluids and hydrothermal minerals is observed (Heinrich et al., 2003).

The qualitative retention series mentioned earlier may explain the behavior of elements during migration of a carbonatite fluid and its progressive interaction with country rocks (Bühn and Rankin, 1999). The least-soluble elements (Ca, Nb, REEs, Ba, Sr, F) are likely to precipitate first, whereas the more soluble elements (Na, Cl, K) are retained in a residual aqueous brine to permeate further into country rocks, forming zones of fenitization.

2.5.4 Transportation and Deposition of REEs in Hydrothermal System

Recent interesting experiments conducted at McGill University by the group led by Migdisov and Williams-Jones have evaluated the speciation of REEs

TABLE 5 Estimated Compositions of Carbonatitic Fluids Associated with the Kalkfeld and Okorusu Carbonatites in Namibia

	Kalkfeld			Okorusu		
Sample No.	*KF113*	*KF153*	*KF155*	*OK10c1*	*OK10c2*	*OK10c3*
Na_2O (%)	21	20	18	21	21	22
CaO (%)	16	14	13	5	5	6
K_2O (%)	7	8	11	8	9	7
FeO (total) (%)	4	3	4	4	3	3
MgO (%)	1	2	2	0.4	0.3	0.2
TiO_2 (%)	1	1	1			
MnO (%)	0.6	0.6	0.7	0.4	0.2	0.2
CO_2 (%)	20	20	20	20	20	20
H_2O (%)	20	20	20	20	20	20
Cl (%)	5	0.7	6.7	10	11	12
F (%)	0.6	1.2	0.5	3.4	2.9	2.9
Sr (ppm)	11,000	33,000	11,000	13,000	10,000	12,000
Ba (ppm)	3800	8500	4200	35,000	28,600	35,100
REE (ppm)	10,200	22,500	12,300	26,000	37,700	27,100
Zr (ppm)		480		120	160	130
Nb (ppm)	190	260				
Th (ppm)	400	1600	400	400	400	500
U (ppm)	50	130	110	10	10	20

After Bühn, B., Rankin, A.H., 1999. Composition of natural, volatile-rich Na-Ca-REE-Sr carbonatitic fluids trapped in fluid inclusions. Geochim. Cosmochim. Acta 63, 3781–3797; Bühn, B., Rankin, A.H., Schneider, J., Dulski, P., 2002. The nature of orthomagmatic, carbonatitic fluids precipitating REE, Sr-rich fluorite: fluid-inclusion evidence from the Okorusu fluorite deposit, Namibia. Chem. Geol. 186, 75–98.

as a function of pH and temperature (eg, Migdisov and Williams-Jones, 2007, 2014; Migdisov et al., 2009), and the results are summarized in Williams-Jones et al. (2012) as follows.

Although the fluorine activities in the REE-mineralizing hydrothermal fluids are not well known, based on the compilation of the salinities in the fluids in major REE deposits, Williams-Jones et al. (2012) estimated dominant REE aqueous species for an ore fluid that contains 10 wt.% NaCl, 500 ppm F, and 200 ppm Nd. The estimation based on experimental data by Migdisov et al. (2009) shows that at 200°C, NdF^{2+} is the dominant dissolved
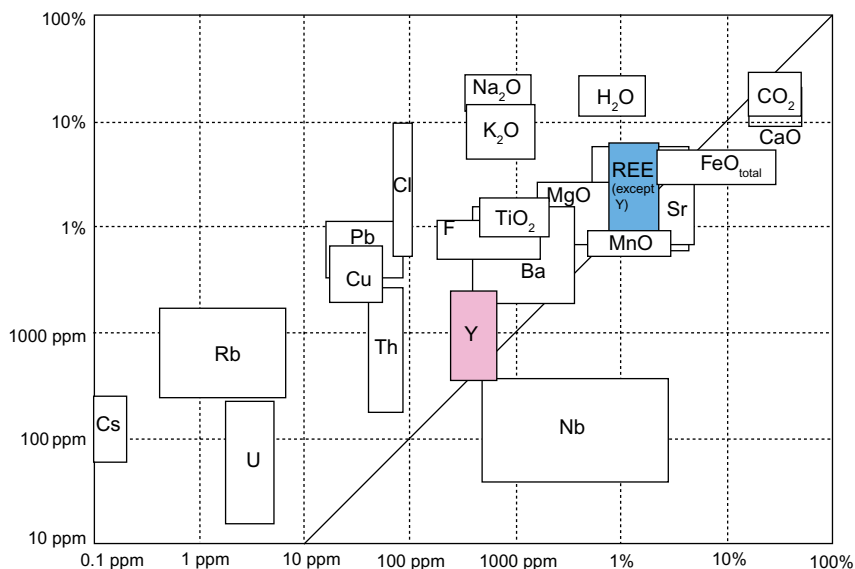
FIG. 16 Comparison between the compositions of the trapped carbonatitic fluid and the Kalkfed carbonatite. The *squares* show the measurement error margins. *Elements* below the *dividing line* are refractory and were retained in the Kalkfed carbonatite. *After Bühn, B., Rankin, A.H., 1999. Composition of natural, volatile-rich Na-Ca-REE-Sr carbonatitic fluids trapped in fluid inclusions. Geochim. Cosmochim. Acta 63, 3781–3797.*
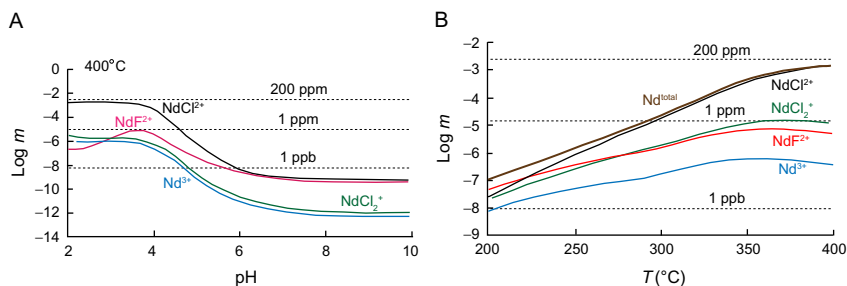
FIG. 17 Concentration of aqueous Nd species (log molality), as a function of pH at 400°C (A) and as a function of temperature at pH 3 (B). The fluid contained 10 wt.% NaCl, 500 ppm fluorite, and 200 ppm Nd. *After Williams-Jones, A.E., Migdisov, A.A., Samson, I.M., 2012. Hydrothermal mobilisation of the rare earth elements: a tale of "ceria" and "yttria". Elements 8, 355–360.*

species for pH values above 3 and that $NdCl^{2+}$ becomes important at this pH at higher temperature (Fig. 17B). At 400°C, $NdCl^{2+}$ is the dominant species for pH values below 7 (Fig. 17A). This estimation indicates that rare earth chloride minerals are relatively soluble at higher temperatures, but REE fluorides are extremely insoluble even at high temperature. This means that the amount of REEs that can be transported as fluoride complexes is limited.

For example, at pH 3 and $t=400°C$ dissolved Nd, 200 ppm in concentration, mainly occurs as $NdCl^{2+}$ (Fig. 17A). At the pH 5, however, the Nd solubility decreases to less than 1 ppm, because HF dissociation makes more fluoride ions available, resulting in precipitation of fluocerite-(Nd) (NdF_3). Decrease of temperature also promotes HF dissociation, reducing NdF_3 solubility (Fig. 17B). Thus despite the high stability of REE fluoride complexes, fluorine acts a binding ligand that promotes precipitation of REE minerals such as fluocerite-(Ce) and more importantly bastnäsite-(Ce). Phosphate complex is also not able to become the major REE transporter because of the very low solubility of monazite-(Ce). Therefore, chloride species are expected to transport the REEs in most hydrothermal systems. The deposition of the REEs as bastnäsite-(Ce) is shown by the reaction:

$$REECl^{2+} + HF + HCO_3^- = REECO_3F(bastnäsite) + 2H^+ + Cl^-$$

Increase of pH and/or HCO_3^- activity or decrease in Cl^- activity will lead to deposition of bastnäsite. At Bayan Obo, the host for the REE mineralization is dolomite. Reaction of the ore fluid with dolomite provides a very effective mechanism for ore deposition because of the reaction:

$$2H^+ + CaMg(CO_3)_2 = Ca^{2+} + Mg^{2+} + 2HCO_3^-,$$
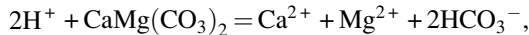
which leads to sharp increases in both pH and HCO_3^- activity. This explains the intimate association of bastnäsite-(Ce) with fluorite in the deposit. Like REE fluorides, fluorite is extremely insoluble, and thus any free fluorine will deposit as fluorite when calcium becomes available (Williams-Jones et al., 2012).

2.6 Transportation and Deposition of REEs in Submarine Hydrothermal System

2.6.1 Concentrations and Compositions of REEs in Submarine Hydrothermal Systems

Submarine hydrothermal fluids at mid-oceanic ridges have been recognized as an important source of several elements in the oceans. Studies hydrothermal fluids from the Pacific vent sites have shown that they are enriched in REEs relative to seawater concentrations by as much as 10–100 times with significant positive Eu anomalies, several thousand times higher than seawater (Michard, 1989; Fig. 18). Hydrothermal plumes from the venting sites rise and mix with ambient seawater, until neutral buoyancy is achieved after which the plume disperses laterally.

Studies of REEs in seafloor vent fluids have focused mostly on basalt-hosted hydrothermal systems along mid-oceanic ridges where fluids have remarkably uniform chondrite-normalized REE patterns characterized by LREE enrichment and large-positive Eu anomalies (Klinkhammer et al., 1994; Michard, 1989; Michard et al., 1983). Mitra et al. (1994) reported that the endmember hydrothermal fluids from sulfide-rich black smokers are
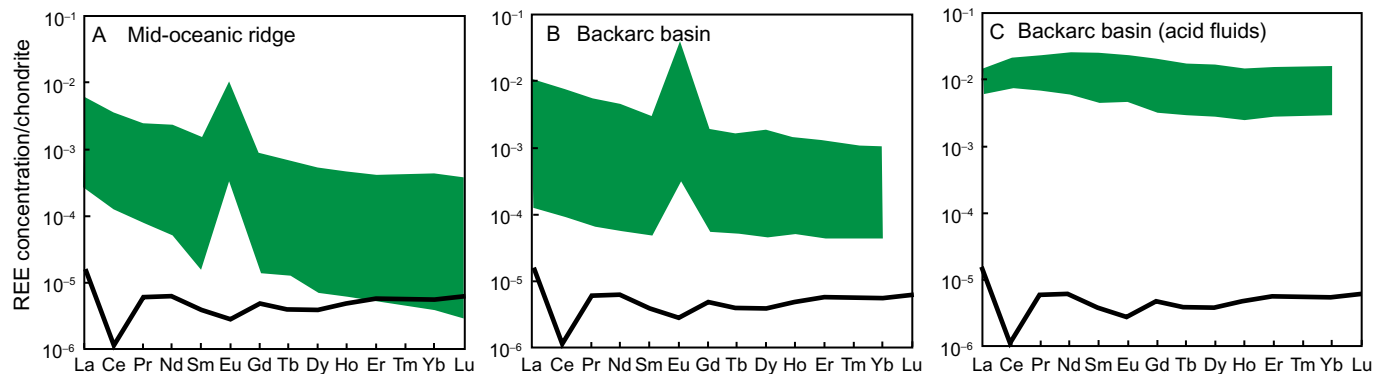
FIG. 18 Chondrite-normalized REE patterns of hydrothermal fluids in comparison with the pattern of present seawater. (A) Mid-oceanic ridge fluids. (B) Backarc basin fluids at PACMANUS, eastern Manus Basin. (C) Backarc basin acid fluids at DESMOS and SuSu Knolls, eastern Manus Basin. *Panel A: Data from Michard, A., Albarede, F., Michard, G., Minster, J.F., Charlou, J.L., 1983. Rare-earth elements and uranium in high-temperature solutions from the East Pacific Rise hydrothermal vent filed (13°N). Nature 303, 795–797; Michard, A., 1989. Rare earth element systematics in hydrothermal fluids. Geochim. Cosmochim. Acta 53, 745–750; Klinkhammer, G.P., Elderfied, H., Edomond, J.M., Mitra, A., 1994. Geochemical implications of rare earth element patterns in hydrothermal fluids from mid-ocean ridges. Geochim. Cosmochim. Acta 58, 5105–5113; Mitra, A., Elderfield, H., Greaves, M.J., 1994. Rare earth elements in submarine hydrothermal fluids and plumes from the Mid-Atlantic Ridge. Mar. Geol. 46, 217–235. Panel B: Data from Craddock, P.R., Bach, W., Seewald, J.S., Rouxel, O.J., Reeves, E., Tivey, M.K., 2010. Rare earth element abundances in hydrothermal fluids from the Manus Basin, Papua New Guinea: indicators of sub-sealoor hydrothermal processes in back-arc basins. Geochim. Cosmochim. Acta 74, 5494–5513. Panel C: Data from Craddock, P.R., Bach, W., Seewald, J.S., Rouxel, O.J., Reeves, E., Tivey, M.K., 2010. Rare earth element abundances in hydrothermal fluids from the Manus Basin, Papua New Guinea: indicators of sub-sealoor hydrothermal processes in back-arc basins. Geochim. Cosmochim. Acta 74, 5494–5513.*

enriched in LREEs by factors of 50–100, 2000–7000 in Eu, and by factors of 5–30 in HREEs compared with seawater. Rare earth enrichments in seafloor hydrothermal fluids relative to ambient seawater reflect removal from crustal rocks during fluid–rock interaction. It has been suggested that plagioclase dissolution controls the distribution of REEs in submarine hydrothermal fluids because the chondrite-normalized REE compositions of mid-oceanic ridge hydrothermal fluids and plagioclase are similar with prominent positive Eu anomaly (Campbell et al., 1988; Klinkhammer et al., 1994).

Laboratory studies, however, suggest that REE compositions of seafloor vent fluids are unrelated to primary rock composition because REE distribution patterns in experimental hydrothermal solutions are different from primary REE compositions of the volcanic rocks or individual minerals with which these fluids have reacted (Allen and Seyfried, 2005; Bach and Irber, 1998). These studies suggest that vent fluid REE compositions reflect solubility control during fluid–rock interaction influenced by aqueous REE speciation, which in turn is strongly influenced by numerous aspects of fluid chemistry such as pH, temperature, and the availability of ligands.

In the backarc spreading centers (eg, Manus Basin), hydrothermal fluids are also enriched in REEs similar to the fluids at mid-oceanic ridges (Fig. 18B). However, the REE compositions of the fluids at the backarc centers are not uniform like those at the mid-oceanic ridges, but are quite various; some enriched in LREEs and some enriched in HREEs (Craddock et al., 2010). In the Manus Basin fluids, aqueous REE compositions are not inherited directly from those of the primary crustal rocks with which hydrothermal fluids interact, but are consistently correlated with differences in fluid pH and ligand (chloride, fluoride, and sulfate) concentrations. For example, hydrothermal fluids from the DESMOS and North Su vents, which are characterized by low pH <1.8 (measured at 25°C) acid-sulfate solutions, show higher concentrations of REEs than those of high-temperature black smoker fluids at Vienna Woods and PACMANUS, but are similar to those of acid-sulfate fluids from continental geothermal environments. These fluids show a flat chondrite-normalized REE pattern (Fig. 18C), which is significantly different from the LREE-enriched pattern with positive Eu anomaly at mid-oceanic ridges and other vents in the backarc setting (Craddock et al., 2010). These data suggest that REE compositions from the vent fluids are fractionated from primary crustal rock REE compositions during fluid–rock interaction owing to differences in aqueous REE solubility, and the elevated REE concentration in the acid-sulfate fluids is ascribed to low pH of the fluids that extracted REE efficiently from the host rocks (Craddock et al., 2010).

Klinkhammer et al. (1983) and Michard et al. (1983) showed that the precipitation of hydrothermal iron oxyhydroxide particles leads to REE scavenging. Mitra et al. (1994) concluded that more than 95% of REE are removed from the fluids by iron oxide particles, on the basis of the hydrothermal fluids from the Trans-Atlantic Geotraverse vent and Snakepit sites of the

Mid-Atlantic Ridge. Craddock et al. (2010) showed that REE concentrations in the submarine hydrothermal fluids are also affected by the precipitation of anhydrite which incorporates REE effectively. Hongo et al. (2007) further discussed that with dilution of the hydrothermal fluids with ambient seawater, europium, and LREEs are removed from the fluids by carbonate- and sulfide-particles in the hydrothermal vents prior to the cerium scavenging by iron and manganese oxide particles in seawater at Yonaguni Knoll IV in the Okinawa Trough.

2.6.2 Deposition of REEs in Submarine Hydrothermal Systems

The geochemical studies of sedimentary rocks formed above the submarine volcanic rocks reveal that stratiform ferromanganese ores that immediately overlay the basaltic layers in Japan are enriched in REEs, in particular, HREEs (Kato et al., 2005). The REE concentration and pattern (which is characterized by a negative Ce anomaly) of these ores are similar to those in the hydrothermal ferromanganese sediments near mid-oceanic spreading centers, and Kato et al. (2005) interpreted that the REE-rich ferromanganese ores were umber deposits that primarily formed by hydrothermal plume fall precipitates that scavenged REE near the hydrothermal sites. Such ferromanganese sediments are now exposed in the accretionary complexes along the subduction zones such as the Mino-Tamba and Shimanoto belts in Japan after diagenetic and/or metamorphic processes, which changed original REE-bearing iron hydroxides to REE minerals such as wakefieldite-(Nd) ($NdVO_4$) (Moriyama et al., 2011) and vanadoallanite-(La) (Nagashima et al., 2013).

The enrichment of REEs in ferromanganese ores (1800 ppm) contrasts with the lower concentrations of REEs in typical manganese ores (60 ppm) and Mn-bearing iron ores (540 ppm) in the Japanese deposits (Watanabe, 2007). This diversified concentrations of REEs lead to a model that the REEs were scavenged by iron oxyhydroxide and/or manganese oxide particles during the oxidation and neutralization process of the hydrothermal plume (Bau and Koschinsky, 2009) because the partition coefficients of REEs to iron oxyhydroxide increase with increasing pH (Bau, 1999).

Rare earth concentrations have been also discovered in nonferruginous deep-sea sediments. Kato et al. (2011) found that submarine sediments near the mid-oceanic ridge in the Pacific contain a few thousands ppm of REEs. These sediments are enriched in HREEs and they concluded that the deposition of the REEs is related to the hydrothermal activity at the mid-oceanic ridge, and the main hosts for the REEs are phillipsite in addition to iron oxyhydroxide. In contrast, Kon et al. (2014) found that majority of the REEs in the deep-sea mud, collected from off Minami-Torishima Island of Japan is included in biogenic apatite. Their study result is consistent with a previous study which has found that REEs are contained in biogenic phosphate phases of fish teeth in deep-sea sediments of the central Pacific

(Toyoda and Tokonami, 1990). Extraction experiments targeting REEs from the pelagic sediments in different sampling sites of the Pacific indicate that phosphate phases are high in REEs and are characterized by a negative Ce anomaly (Toyoda and Masuda, 1991; Toyoda et al., 1990). More detailed studies are necessary to determine the origin of the REEs in such sea mud.

2.7 Weathering

Weathering is one of the important processes that concentrates and/or fractionates REEs. This process particularly effective for carbonatite deposits, because high concentrations of REEs, which may reach 10–25 wt.%, are expected for laterites that are developed above the carbonatites and alkaline complexes (Morteani and Preinfalk, 1996). The high REE concentrations result from the high concentrations in carbonatites and from a significant amount of carbonates which can dissolve in acidic water during weathering. Another important process is the adsorption of REEs on clays during weathering of granite to form ion-adsorption type deposits. This process will be described in detail in Section 4.

2.7.1 Lateritic Profile and Behavior of REEs

Laterites are near-surface weathering products, which are strongly enriched in Fe_2O_3 and Al_2O_3, and depleted in SiO_2 (Bárdossy and Aleva, 1990). They can be distinguished from the underlying rocks, saprolites, which are more enriched in SiO_2 and preserve original rock textures. Laterites are generally distributed in near-equatorial belts characterized by the present tropical climate. Bauxites are included in laterites, which are or will become economically minable, containing not less than 45–50% Al_2O_3 and not more than 20% Fe_2O_3 and 3–5% SiO_2 (Valeton, 1972).

In saprolites, original rock textures are largely preserved, but most weatherable minerals such as mafic silicates and feldspars are altered to clay minerals such as smectites and kaolinite and other weathering products including amorphous materials. Quartz and other less weatherable minerals such as Fe oxides and Ti oxides are largely preserved. The upper pedolith is composed of clay zone, ferruginous zone, laterite, and soil in ascending order. In the clay zone, textures of the original rock are overprinted by homogeneous masses of clays, typically dominated by kaolin-group minerals. The ferruginous zone is formed of various concentrations of ferric iron oxides and hydroxides near the water table, and this zone may be cemented by precipitation of silica and iron hydroxide minerals to form a duricrust that is resistant to further erosion. The laterite is loose Fe-rich subsoil rock formed as a result of residual enrichment and precipitation of iron hydroxide and oxide minerals from iron-derived deeper in the profile. This horizon can be composed largely of pisolites, gravel-sized subspherical accretionary concentrations (Ridley, 2013).

Bauxite deposits, composed of mixtures of fine-grained aluminum hydroxide minerals (gibbsite, boehmite, and diaspore), occur between the duricrust and clay zones on the Al-rich protoliths such as sedimentary rocks, alkali basalt, and syenite. Quartz-free alkaline rocks such as nepheline syenite are preferable for high-grade bauxite formation (Bárdossy and Aleva, 1990) because occurrence of quartz, which is one of the most abundant and weathering-resistant minerals, strongly influences the Al_2O_3 content of bauxite. Ni-Co laterite deposits form mainly in the saprolite and clay (smectite-rich) zones on the silica-poor ultramafic rocks. Generally REE concentrations in the regolith profiles including bauxite and Ni-Co laterite deposits are limited to a few thousands ppm, and majority of REEs appear to occur as supergene aluminous phosphate minerals such as florencite-(Ce) (Braun et al., 1993, 1998; Dill, 2001; Sanematsu et al., 2011). The behaviors and concentrations of REEs in bauxite are further described in Section 4.1.8.

2.7.2 Weathering of Carbonatites

Carbonatites are the major source of REEs, although the REE concentrations (about 0.2 wt.% REO) of the majority of the carbonatites are far below the present-day minable ore grade ($\sim$4 wt.% REO). However, some of the carbonatites are upgraded by weathering, because dominant constituent minerals of carbonatites are calcite and dolomite, which are subject to dissolution in acidic water near the surface. The best examples are Mount Weld in Australia, Araxá in Brazil, and Zandkopsdrift in South Africa.

The Mount Weld carbonatite in Western Australia is a cylindrical intrusion, 3.6 km in diameter, intruding into basaltic rocks of Archean age (Duncan and Willett, 1990). The carbonatite is about 2.06 Ga in age, consists mainly of calcium carbonatite, with subordinate amounts of phosphorite and glimmerite. The major REE mineral in the carbonatite is apatite, associated with minor monazite and synchysite (Willett et al., 1989). This carbonatite is covered by 40 m thick regolith, which was formed during the Mesozoic and is composed of a lower residual zone with abundant relict igneous minerals (apatite, magnetite, ilmenite, pyrochlore, monazite, and silicates) and an upper supergene zone of insoluble aluminous oxides, clays, aluminum phosphate minerals (goyazite, gorceixite, and florencite), secondary phosphate minerals (monazite and churchite), REE oxides (cerianite), manganiferous wad, and ferric iron oxides with absorbed niobium, tantalum, titanium, vanadium, yttrium, and chromium (Duncan and Willett, 1990).

The rare earth concentration at Mount Weld is less than 0.2 wt.% REO in the fresh carbonatite, but it reaches 4.5 wt.% in the regolith (Lottermoser, 1990). Lottermoser (1990) interpreted this concentration by two mineralization stages: (1) dissolution of carbonate minerals by circulation of groundwater and formation of residual apatite concentration and (2) apatite dissolution followed by aluminophosphate precipitation over the horizon of residual and secondary apatite, by the circulation of acid solutions near the paleosurface. Similar

process is found in Araxá carbonatite in Brazil, where magmatic REE minerals (apatite, monazite) are replaced by gorceixite and secondary apatite in the regolith, of which REE concentration is ~5.8 wt.%, much higher that the concentration (0.7–1 wt.%) of the fresh carbonatite (Morteani and Preinfalk, 1996).

3 RARE EARTH MINERALOGY

3.1 Variation of REE Minerals Associated with Their Crystal Chemistry

There are more than 200 minerals that contain essential or significant REE concentrations which occur as a variety of compounds such as silicates, fluorocarbonates, fluorides, oxides, and phosphates (Table 6). They are included in igneous, metamorphic, and sedimentary rocks as accessory minerals. Some of carbonatites and alkaline rocks contain a major amounts of REE minerals and form REE ores (Fig. 19). REEs are divided into LREEs and HREEs by the difference of geochemical properties as previously discussed, and this leads to the two contrasting type REE minerals and deposits: LREE-rich type and HREE-rich type. There is no REE deposit producing well-balanced LREEs and HREEs, making it more difficult to develop the REE deposits. Fig. 20 shows production of REE by operation, country, and ore type in 2014 (Roskill Information Services Ltd, 2015).

REE minerals frequently contain as many as 10 different rare earths as major elements and have complex chemical compositions because REEs are chemically similar. Geochemical behavior of REEs is similar to actinides, such as Th and U, so many of REE minerals contain Th and U as essential components (Table 6). A variety of chemical compositions of REE minerals are related to not only the chemical behavior but also properties of REE minerals having many isostructural minerals. Especially important among REE minerals are zircon structure (tetragonal, $a = 6.604$, $c = 5.979$, $I4_1/amd$, Hazen and Finger, 1979), monazite structure (monoclinic, $P2_1/n$, $a = 6.7902$, $b = 7.0203$, $c = 6.4674$ Å, $\beta = 103.38$ degree, Ni et al., 1995) and fergusonite structure (tetragonal $a = 5.16$, $c = 10.89$, $I4_1/a$, Komkov, 1959) (Fig. 21). Their chemical formulae can be generalized as ABO_4 (Table 7). In the case of monazite, A and B correspond to LREEs and phosphorus (P), respectively. Existence of radioactive elements such as U and Th in REE minerals (Table 6), which is becoming a problematic issue for the development of REE deposits, is related to the fact that many REE minerals of ABO_4 type are isostructural with Th or U minerals such as thorite and coffinite (Table 7). Later, we review a variety of minerals that have zircon and monazite structures.

3.1.1 ABO$_4$ Minerals with Zircon Structure

Zircon-structure minerals are zircon ($ZrSiO_4$), thorite ($ThSiO_4$), coffinite ($USiO_4$), xenotime ($HREEPO_4$), and a few other listed in Table 7. These

TABLE 6 Rare Earth Elements, Thorium, and Uranium Content of Representative REE-Bearing Minerals

Name	Chemical Formula	REE_2O_3 (wt.%)	$HREE_2O_3$ ratio (%)	ThO_2 (wt.%)	UO_2 (wt.%)	Representative Deposits and Prospects	References
Silicate							
Allanite–REE-rich epidote	$(LREE,Ca)_2Al_2Fe^{2+}Si_3O_{12}(OH)$	3–51	1–35	Bdl.-3.6	Bdl.	Hoidas Lake, Canada (GWM), Benjamin River, Canada (GWM)	Hoshino et al. (2006, 2007), Halpin (2010), and Roskill Information Services Ltd (2015)
Britholite-(Ce)	$(Ca,LREE)_5(SiO_4,PO_4)_3(OH,F)$	27–62	0–10	Bdl.-21	Bdl.-3.5	Kipawa, Canada (Matamec)	Anthony et al. (1995), Della-Ventura et al. (1999), Petrella et al. (2014), and Roskill Information Services Ltd (2015)
Cerite	$(LREE,Ca)_9(Mg,Fe)$ $(SiO_4)_6(SiO_3OH)(OH)_3$	61–66	0	Bdl.	Bdl.	–	Anthony et al. (1995) and Förster (2000)
Steenstrupine	$Na_{14}LREE_6Mn_2Fe_2(Zr,Th)$ $(Si_6O_{18})_2(PO_4)_7 \cdot 3H_2O$	29–35	0–6	0.4–5.1	Bdl.-0.3	Kvanefjeld, Greenland (GME)	Khomyakov and Sørensen (2001) and Roskill Information Services Ltd (2015)
Britholite-(Y)	$(Ca,HREE)_5(SiO_4,$ $PO_4)_3(OH,F)$	44–61	55–90	Bdl.-1.6	Bdl.-0.7	Kipawa, Canada (Matamec)	Anthony et al. (1995), Pekov et al. (2011), and Roskill Information Services Ltd (2015)

Gadolinite	$Be_2Fe^{2+}HREE_2Si_2O_{10}$	41–55	92–100	Bdl.-0.9	Bdl.	–	Anthony et al. (1995) and Demartin et al. (1993)
Kainosite	$Ca_2HREE_2Si_4O_{12}(CO_3)\cdot H_2O$	37–39	97–98	Bdl.	Bdl.	–	Anthony et al. (1995)
Thalenite	$HREE_3Si_3O_{10}(F,OH)$	55–64	100	Bdl.	Bdl.	–	Anthony et al. (1995)
Thortveitite	$(HREE)_2Si_2O_7$	2–30	100	Bdl.	Bdl.	–	Gramaccioli et al. (2000)
Yttrialite	$(HREE,Th)_2Si_2O_7$	51–56	94	6–12′	0.8–3	–	Anthony et al. (1995)
[a]Zircon	$(Zr,HREE)SiO_4$	Bdl.-20	30–100	Bdl.-19.3	Bdl.-14.8	Nechalacho, Canada (Avalon)	Hoshino et al. (2010, 2013) and Breiter et al. (2006, 2009)
Mosandrite	$(Ca, Na, REE)_{12}(Ti,Zr)_2Si_7O_{31}H_6F_4$	17–33	11–55	Bdl.-1.1	Bdl.	Kipawa, Canada (Matamec)	Bellezza et al. (2009), Sokolova, and Cámara (2008), Hoshino (unpublished data), and Roskill Information Services Ltd (2015)
Eudialyte	$Na_{15}(Ca,REE)_6(Fe, Mn)_3Zr_3(Si,Nb)$ $Si_{25}O_{73}(OH,Cl,H_2O)_5$	1–10′	25–54	Bdl.	Bdl.	Kipawa, Canada (Matamec)	Anthony et al. (1995), Hoshino (unpublished data), and Roskill Information Services Ltd (2015)
Oxide							
Cerianite	$(LREE,Th)O_2$	83–96	0–24	Bdl.-8	Bdl.-0.1	–	Anthony et al. (1997), Pan and Stauffer (2000), and Zaitsev et al. (2011)
Loparite	$(LREE,Na,Ca)(Ti,Nb)O_3$	7–36	0	0.4–1.2	Bdl.-0.3	Lovozersky Russia (SMW)	Kogarko et al. (2002)

Continued

TABLE 6 Rare Earth Elements, Thorium, and Uranium Content of Representative REE-Bearing Minerals—Cont'd

Name	Chemical Formula	REE$_2$O$_3$ (wt.%)	HREE$_2$O$_3$ ratio (%)	ThO$_2$ (wt.%)	UO$_2$ (wt.%)	Representative Deposits and Prospects	References
Pyrochlore group	(Na,Ca,LREE)$_2$Nb$_2$O$_6$F	Bdl.-19	0	Bdl.-22	Bdl.-25	–	Zurevinski and Mitchell (2004)
Euxenite group	(HREE,Ca,U,Th)(Nb,Ta,Ti)$_2$O$_6$	1–30'	59–100	Bdl.-4.1	Bdl.-37	–	Aurisicchio et al. (2001, 2002) and Škoda and Novák (2007)
[a]Fergusonite-fergusonite-beta	(HREE)NbO$_4$	41–46	77–100	Bdl.-1.7	Bdl.-1.1	Nechalacho, Canada (Avalon)	Anthony et al. (1997), Hoshino et al. (2013), Petrella et al. (2014), and Roskill Information Services Ltd (2015)
[a]Samarskite	(HREE,Fe,U,Th,Ca)(Nb,Ta,Ti)O$_4$	4–24'	76–98	3–11'	10–32	–	Anthony et al. (1997) and Simmons et al. (2006)
Aeschynite	(REE,Ca,Fe,Th)(Ti,Nb)$_2$(O,OH)$_6$	16–37	18–100	0.6–15.8	Bdl.-10.1	–	Anthony et al. (1997), Aurisicchio et al. (2001), and Bonazzi and Menchetti (1999)
Brannerite	(U,Ca,REE)(Ti,Fe)$_2$O$_6$	0–4	100	Bdl.-4.1	41–63	–	Anthony et al. (1997)
Fluorocarbonate and fluoride							
Ancylite	Sr(LREE)(CO$_3$)$_2$OH·H$_2$O	42–64	0–2	Bdl.-0.61	Bdl.		Anthony et al. (2003), Bulakh et al. (1998), and Pekov et al. (1997)

Bastnasite	$(LREE)CO_3F$	70–77	0–3	Bdl.-0.3	Bdl.	Mountain Pass, United States (Molycorp), Baiyun Obo, China	Anthony et al. (2003), Hoshino et al. (2013), Taylor and Pollard (1996), and Roskill Information Services Ltd (2015)
Parisite	$(LREE)_2Ca(CO_3)_3F_2$	55–62	0–3	Bdl.-1.3	Bdl.	Mountain Pass, United States (Molycorp), Baiyun Obo, China	Hoshino et al. (2013), Taylor and Pollard (1996), and Roskill Information Services Ltd (2015)
Synchysite	$(LREE)\ Ca(CO_3)_2F$	50–55	0–9	Bdl.-0.8	Bdl.	Mountain Pass, United States (Molycorp), Baiyun Obo, China	Anthony et al. (2003), Förster (2000), Hoshino et al. (2013), and Roskill Information Services Ltd (2015)
Huanghoite	$BaLREE(CO_3)_2F$	38–42	0–1	Bdl.-0.5	Bdl.-0.1	–	Anthony et al. (2003) and Yang et al. (2000)
Fluocerite	$(LREE)F_3$	70–83	0–1	Bdl.-1.6	Bdl.		Anthony et al. (1997) and Roskill Information Services Ltd (2015)
Fluorite-yttrofluorite-tveitite	$(Ca,HREE)F_2-Ca_{1-X}HREE_XF_{2+X}$ $(X<0.3)$	Bdl.-39 (as REE)	73–100	Bdl.	Bdl.	–	Pekov et al. (2009)
Waimirite	$(HREE)F_3$	65–66 (as REE)	96–100	Bdl.	Bdl.	Jabal Tawlah, Saudi Arabia	Atencio et al. (2015) and Watanabe et al. (2014)

TABLE 6 Rare Earth Elements, Thorium, and Uranium Content of Representative REE-Bearing Minerals—Cont'd

Name	Chemical Formula	REE$_2$O$_3$ (wt.%)	HREE$_2$O$_3$ ratio (%)	ThO$_2$ (wt.%)	UO$_2$ (wt.%)	Representative Deposits and Prospects	References
Phosphate							
Apatite group	(Ca,REE)$_5$(PO$_4$)$_3$(F,OH)	Bdl.-21	0–47	Bdl.-0.3	Bdl.-0.3	Nolans Bore, Australia (Arafura), Hoidas Lake, Canada (GWM), Blockspruit, South Africa, Benjamin River, Canada	Hoshino et al. (2015) and Roskill Information Services Ltd (2015)
Belovite	(Sr,Na,LREE)$_5$(PO$_4$)$_3$(F,OH)	21–24	0	Bdl.-0.5	Bdl.		Anthony et al. (2000)
Florencite-REE-rich goyazite	LREEAl$_3$(PO$_4$)$_2$(OH)$_6$	10–33	0	Bdl.-1.4	Bdl.	–	Roskill Information Services Ltd (2015), Wall and Mariano (1996), and Anthony et al. (2000)
[a]Monazite	(LREE,Th)PO$_4$	35–71	1–17′	Bdl.-28	Bdl.-6.5	Mt Weld, Australia (Lynas), Steenkampskraal, South Africa (GWM/Rareco), Zandkopsdrift, South Africa (Frontier Minerals)	Förster (1998), Hoshino et al. (2012a, 2012b), Roskill Information Services Ltd (2015), and Zhu and O'Nions (1999a)
[a]Xenotime	(HREE)PO$_4$	31–67	92–100	Bdl.-37	Bdl.-1	Ptinga, Brazil (NMT/Mitsubishi)	Förster (2006), Roskill Information Services Ltd (2015), and Wall and Mariano (1996)

[a]APO$_4$ mineral.

FIG. 19 Xenotime ore (*dark brownish crystals*) from Nechalacho alkaline deposit, Canada.
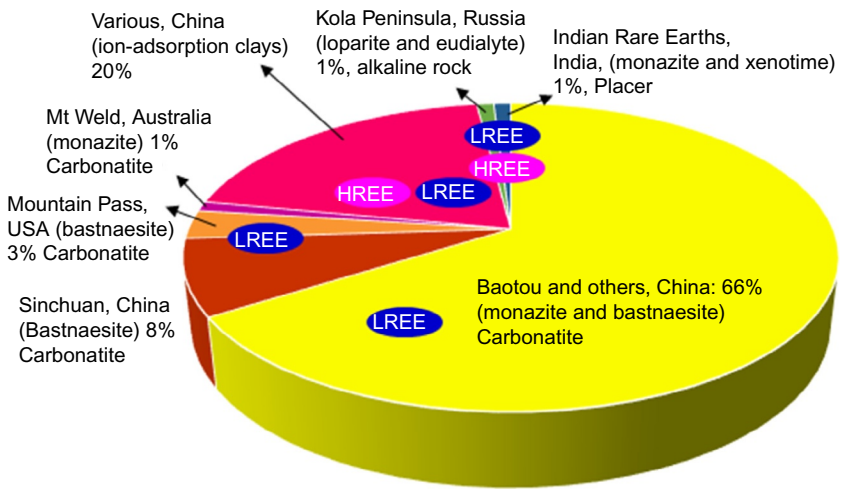
FIG. 20 Production of REEs by operation, country, and ore type, 2014. *Modified Roskill Information Services Ltd., 2015. Rare Earths: Market Outlook to 2020, 15th ed. Roskill, London, 1–337.*

minerals display variable degrees of solid solubility among one another depending on temperature, pressure, and chemical composition of magma and hydrothermal fluid. A fifty percent rule has been adopted for naming the minerals including solid solutions following recommendations by the Commission on New Minerals and Mineral Names (CNMMN) of the International Mineralogical Association. Take olivine as an example, even though it is not a REE mineral: olivine consists of forsterite (Mg_2SiO_4) and fayalite (Fe_2SiO_4); if Mg and Fe are mixed in a certain olivine and iron content is over 50%, the mineral is identified as fayalite (Nickel, 1992).
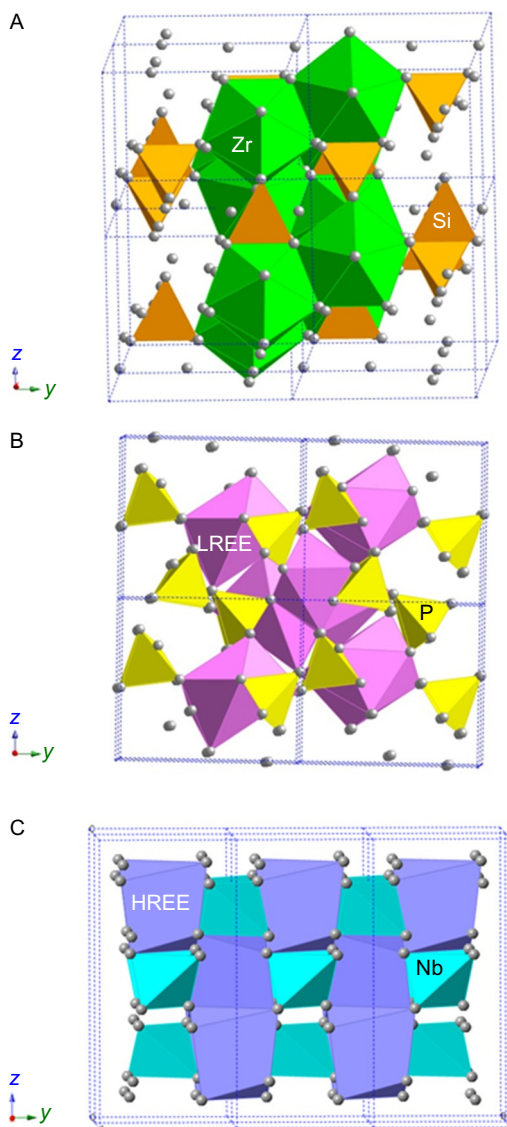
FIG. 21 Crystal structures of ABO$_4$ group minerals: (A) zircon, (B) monazite, and (C) fergusonite.

Table 8 shows chemical compositions of zircon grains from various rocks. Zircon is one of the oldest earth minerals and is a common mineral in meteorite and moon rocks. SiO$_2$ content in the host rocks of zircon grains increases from carbonatite to granitic pegmatite. This is called "mineral fractionation," simply, mafic elements such as magnesium and iron are first removed from magma during crystallization, which leads to silica-rich magma. Zircon

TABLE 7 Isostructures of Monazite, Zircon, and Fergusonite
(Anthony et al., 1995, 1997, 2000, 2003; Finch and Hanchar, 2003)

Monazite (LREEPO$_4$)	
Huttonite ThSiO$_4$	Rooseveltite BiAsO$_4$
Zircon (ZrSiO$_4$)	
Hafnon HfSiO$_4$	Thorite ThSiO$_4$
Coffinite USiO$_4$	Xenotime HREEPO$_4$
Pretulite ScPO$_4$	ChromatiteCaCrO$_4$
Behierite (Ta,Nb)BO$_4$	Wakefieldite YVO$_4$
Dreyerute BiVO$_4$	Chermovite YAsO$_4$
Schiavinatoite (Nb,Ta)BO$_4$	
Fergusonite (HREENbO$_4$)	
Formanite HREETaO$_4$	Stolzite PbWO$_4$
Scheelite CaWO$_4$	Powellite CaMoO4
Wulfenite PbMoO$_4$	

in carbonatite has chemical composition close to the endmember (ZrSiO$_4$), while zircon in granitic pegmatite, strongly fractionated rock, may contain over 15% REE$_2$O$_3$ (especially HREEs). The high amounts of HREEs are preferentially incorporated by xenotime substitution HREE^{3+}+P^{5+} ↔ Zr^{4+}+Si^{4+}, but a continuous solid solution between the endmembers (zircon and xenotime) is unlikely to exist (eg, Förster, 2006). Some zircons contain up to 20 wt.% REE$_2$O$_3$ (Tables 6 and 8; Hoshino et al., 2010). Moreover, some zircons from the granitic pegmatite contains high Th and U contents by thorite (Zr^{4+}↔Th^{4+}) and coffinite substitutions (Zr^{4+}↔U^{4+}). The zircons includes up to 11 wt.% UO$_2$ and a lesser extent ThO$_2$ (up to 7 wt.%) (Table 6; Hoshino et al., 2010). Although zircon grains have a wide variety of the chemical compositions, the four minerals listed in Table 8 are all identified as zircon following the 50% rule. Zircon contains generally less than 1 wt. % REEs and the analyses with significantly higher REE concentrations are attributed to alteration and/or accidental analysis of inclusions (Hoskin and Schaltegger, 2003). However, zircon in silicate rocks contains large amounts of REEs and is one of the valuable REE minerals in Nechalacho alkaline syenite deposit, Canada (Hoshino et al., 2013), and Khaldzan Buregtey alkaline granite deposit, Mongolia (Hoshino, unpublished data). Zircon is known to have variable crystallinity in addition to various chemical compositions

TABLE 8 Chemical Compositions of Zircon Grains from Various Rocks (Hoshino et al., 2010, 2012a)

Occurrence Host Rocks	Malawi Carbonatite[a]	Saigon Alkaline Basalt	Nakano Granite	Oro Granitic Pegmatite
P_2O_5 (wt.%)	–	–	–	1.65
SiO_2	36.4	34.57	33.85	22.66
ZrO_2	63.45	64.6	62.86	39.69
HfO_2	0.81	0.82	2.09	1.94
ThO_2	–	–	–	1.71
UO_2	–	–	–	2.4
Al_2O_3	–	–	–	0.89
Sc_2O_3	–	–	–	0.31
Y_2O_3	–	–	0.25	10.68
Dy_2O_3	–	–	–	1.22
Er_2O3	–	–	–	1.75
$Tm2O_3$	–	–	–	0.51
Yb_2O_3	–	–	–	3.27
Lu_2O_3	–	–	–	0.69
CaO	–	–	–	0.96
FeO	–	–	0.28	0.8
Sum	100.66	99.99	99.33	91.13[b]
Total $HREE_2O_3$	–	–	0.25	18.43

[a]*Hoshino (unpublished data).*
[b]*The low total is due to hydration.*

(Hoshino et al., 2012a). Fig. 22 shows the powder X-ray diffraction (PXRD) patterns of three zircon samples from different localities that suggest various crystallinity of zircon: from high crystallinity to fully amorphous. Because zircon has high density and is resistant to chemical weathering, it is concentrated with other refractory minerals in placer deposits, principally in river and beach sands (Abdel-Rehim, 2005; Orris and Grauch, 2002; Sengupta and Van Gosen, 2016). Leaching experiments using zircon samples with different crystallinity indicate that extraction of HREEs from low crystallinity zircon using dilute hydrochloric acid is much easier compared to the highly crystalline zircon (Hoshino et al., 2012a).
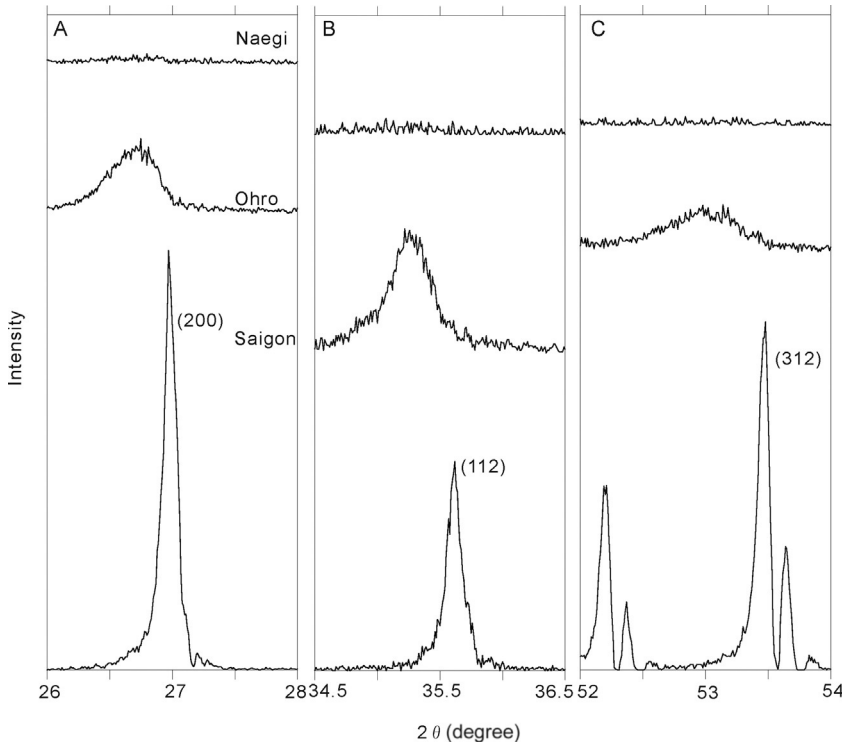
FIG. 22 PXRD patterns of three zircon samples from granitic pegmatites (Naegi, Ohro, and Saigon) representing the 2θ ranges characteristic of radiation damage, from well crystallized to fully amorphous states. (A) Profiles of (200) peak. (B) Profiles of (112) peak. (C) Profiles of (312) peak. *After Hoshino, M., Watanabe, Y., Sanematsu, K., Kon, Y., Shimizu, M., 2012a. Characteristics of zircon suitable for REE extraction. Int. J. Miner. Process. 102–103, 130–135.*

3.1.2 ABO$_4$ Minerals with Monazite Structure

Monazite occurs as accessory minerals in igneous, metamorphic, and sedimentary rocks. In addition, monazite is found throughout the world in placer deposits, beach sands, and is also a component of the ores of the Bayan Obo deposit (Table 6 and Fig. 20). Monazite is a phosphate mineral containing approximately 70% REE oxides. According to dominant REE contents, monazite is divided into monazite-(Ce), monazite-(La), monazite-(Nd), and monazite-(Sm), and the first type is most common in nature. Monazite is isostructural with huttonite (ThSiO$_4$), cheralite (CaTh(PO$_4$)$_2$), gasparite, and roosevelite (Table 7) and displays variable degrees of solid solution among the endmembers (Förster, 2006). Thus, natural monazite often contains thorium (Th) and arsenic (As) as major elements (Hoshino et al., 2012b; Ondrejka et al., 2007). Monazite includes 1–28 wt.% ThO$_2$ and smaller concentrations of UO$_2$ (0–6.5 wt.%) (Table 6; Förster, 1998; Zhu and O'Nions, 1999a). The high Th
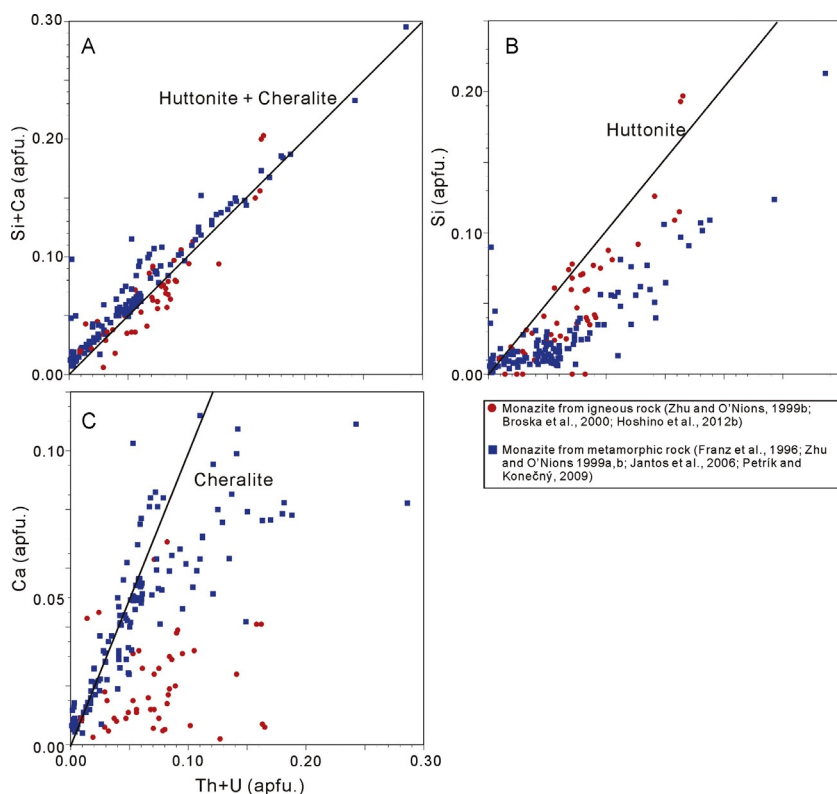
FIG. 23 Plots of monazite from igneous and metamorphic rock illustrating chemical exchanges. (A) (Th+U) vs Si+Ca. (B) (Th+U) vs Si (huttonite exchange). (C) (Th+U) vs Ca (cheralite exchange) (Zhu and O'Nions, 1999b). *From Hoshino, M., Watanabe, Y., Ishihara, S., 2012b. Crystal chemistry of monazite from the granitic rocks of Japan: petrogenetic implications. Can. Mineral. 50, 1331–1346.*

content in monazite, a serious obstacle for development of REE deposits, is preferentially incorporated by huttonite $REE^{3+}+P^{5+} \leftrightarrow (Th, U)^{4+}+Si^{4+}$ or by cheralite substitution $2REE^{3+} \leftrightarrow (Th, U)^{4+}+Ca^{2+}$. Fig. 23 shows plots of Th+U, Ca, and Si for igneous and metamorphic monazite to illustrate the exchange vectors. Fig. 23A shows a correlation between Th+U vs Si+Ca, indicating that nearly all of the Th+U can be accommodated by huttonite and cheralite substitutions. Fig. 23B and C show that the cheralite exchange dominates in metamorphic monazite (Franz et al., 1996; Janots et al., 2006; Petrík and Konečný, 2009; Zhu and O'Nions, 1999a,b), while the huttonite exchange is more common in igneous monazite (Broska et al., 2000; Hoshino et al., 2012b; Zhu and O'Nions, 1999b). In contrast, ThO_2 content of hydrothermal monazite (≤ 1.5 wt.%; eg, Schandl and Gorton, 2004; Sheard et al., 2012) is much lower than that of igneous and metamorphic monazite (1.5–28 wt.%)

(eg, Hoshino et al., 2012b; Zhu and O'Nions, 1999a). These results indicate that Th and U substitution mechanism into monazite changes depending on the origin of the mineral. In nature, isostructural minerals display various coupled substitutions that depend on temperature, pressure, and chemical compositions of magma and hydrothermal fluids, which result in complex chemical compositions of REE minerals.

Not only chemical compositions but also textures may be different in REE minerals. Back scattered electron (BSE) imaging and electron microprobe analysis (EMPA) show complex chemical zoning depending on the difference of the chemical compositions (Fig. 24). The bright zones in the BSE images are rich in heavy element contents, while the dark zones are rich in light elements such as silicon and aluminum. Magmatic REE minerals commonly show oscillatory zoning (Fig. 24A), while metamorphic and hydrothermal minerals have spongy texture and patchy zoning (Fig. 24C–F). Various types of chemical zoning suggest a difference in formation conditions of REE minerals.

REE minerals have various occurrences, chemical compositions, coupled substitutions, and texture, all of which make interpretation difficult. However, if we could interpret the complexity of REE minerals, accurate geological information may result, because to the best of our knowledge no other group of minerals stores an abundance of geological information comparable to REE minerals. A variety of REE minerals is remarkably related to the geologic ages and localities of these minerals, which is discussed in Section 3.2.

3.2 Variation of REE Minerals Associated with the Evolution of Earth

As mentioned earlier, REE minerals are important as geochemical indicators and resources. However, what is a mineral in the first place? A mineral substance is a naturally occurring solid formed by geological processes either on earth or in extraterrestrial bodies (Nickel and Grice, 1998). According to IMA, there are over 4900 known mineral species. Even today, new minerals are being discovered throughout the world, and the number of minerals continues to increase. Did all 4900 minerals known today were present on earth since the time the earth was born? Why is there such a large variety of minerals on earth, ie, over 4900? These questions formulated by Dr. Robert M. Hazen of Geophysical Laboratory of Carnegie Institution for Science represent an attempt to establish a framework of new mineralogy based on "mineral evolution" (Hazen et al., 2008). Here, we follow an outline of "mineral evolution" and the variation of REE minerals associated with earth evolution based on our studies.

About 4.6 billion years have passed since the birth of the earth and Hazen et al. (2008) divided geological events related to "mineral evolution" into 10 events (Table 9). Element abundance by mass of the earth calculated based
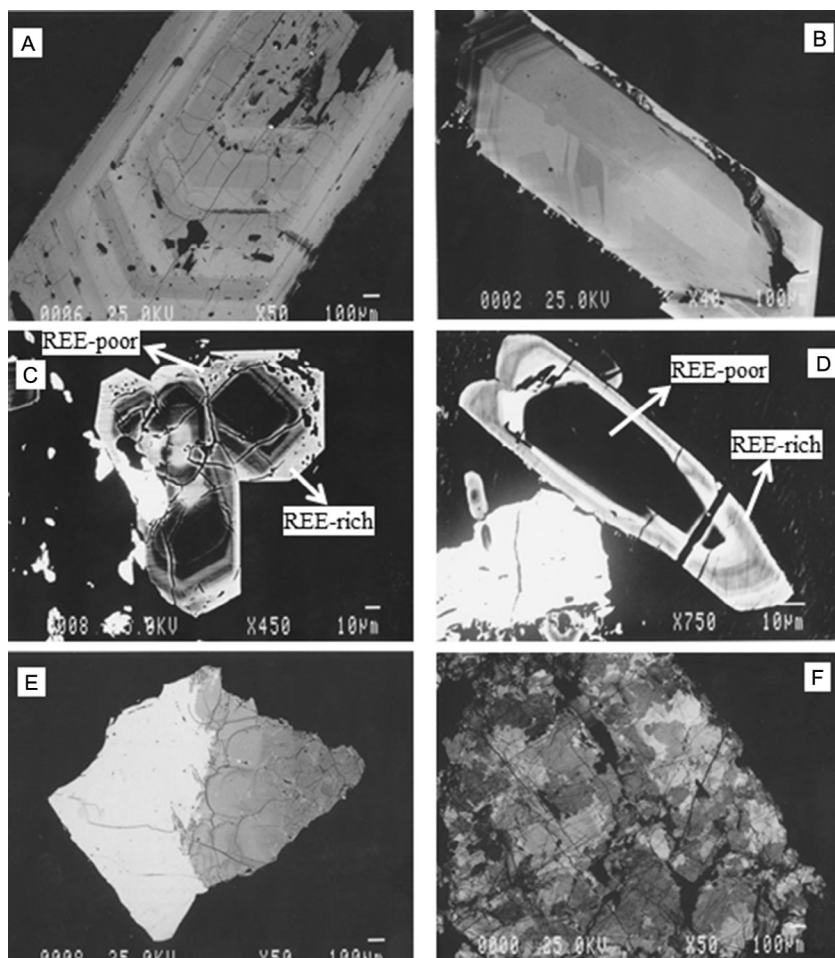
FIG. 24 Back scattered electron images showing chemical zoning of REE minerals. (A) Allanite from Oro granite, Japan with oscillatory zoning, (B) dissakisite from Trimoun talc mine, France with normal zoning, (C) zircon consisting of REE-poor core and REE-rich rim (spongy texture) from Naegi granite, Japan, (D) apatite consisting of REE-poor core and REE-rich rim (spongy texture) from the Dingnan biotite granites, China, (E) allanite from Fukudayama granitic pegmatite, Japan with patchy zoning, and (F) allanite from Itoigawa albite, Japan with patchy zoning. *From Hoshino, M., Kimata, M., Shimizu, M., Nishida, N., Fujiwara, T., 2006. Allanite-(Ce) in granitic rocks from Japan: genetic implications of patterns of REE and Mn enrichment. Can. Mineral. 44, 45–62; Hoshino, M., Kimata, M., Nishida, N., Shimizu, M., 2008. Crystal chemical significance of chemical zoning in dissakisite-(Ce). Phys. Chem. Miner. 35, 59–70; Hoshino, M., Kimata, M., Nishida, N., Shimizu, M., Akasaka, T., 2010. Crystal chemistry of zircon from granitic rocks, Japan: genetic implications of HREE, U and Th enrichment. N. Jb. Miner. Abh. 187, 167–188; Ishihara, S., Hua, R., Hoshino, M., Murakami, H., 2008. REE abundance and REE minerals in granitic rocks in Nanling Range, Jiangxi Province, Southern China, and generation of the REE-rich weathered crust deposits. Resour. Geol. 58, 355–372.*

TABLE 9 Three Eras and Ten Stages of Earth's Mineral Evolution

Era/Stage of Mineral Evolution	Age (Ga)	Cumulative No. of Species
Prenebular "Ur-Minerals"	>4.6	12
Era of planetary accretion (>4.55 Ga)		
(1) Primary chondrite minerals	>4.56	60
(2) Achondrite and planetesimal alteration	>4.56–4.55	250
Era of crust and mantle reworking (4.55–2.5 Ga)		
(3) Igneous rock evolution	4.55–4.0	350–500
(4) Granite and pegmatite formation	4.0–3.5	1000
(5) Plate tectonics	>3.0	1500
Era of biologically mediated mineralogy (>2.5 Ga to present)		
(6) Anoxic biological world	3.9–2.5	1500
(7) Great Oxidation Event	2.5–1.9	>4000
(8) Intermediate ocean	1.9–1.0	>4000
(9) Snowball Earth events	1.0–0.542	>4000
(10) Phanerozoic era of biomineralization	<0.542	4900+

After Hazen, R.M., Ferry, J.M., 2010. Mineral evolution: mineral evolution: mineralogy in the fourth dimension. Elements 6, 9–12.

on the chemical composition of chondrite which is the material of the earth, are 34.6% Fe, 29.5% O, 15.2% Si, 12.7% Mg, 2.4% Ni, 1.9% S, 1.1% Ca, 1.1% Al, 1.1% and others (Mason, 1966). The elemental abundances did not change significantly from birth of the earth to the present time. However, the number of mineral species has increased from 12 to over 4900 species during 4.6 billion years. In the long history of the earth, some geologic events such as granite and pegmatite formation (4.0–3.5 Ga) and "Great Oxidation Event" (1.9–2.5 Ga), ie, Earth's oxidation by the advent of photosynthesis, have substantially increased the number of mineral species (Table 9).

As discussed in Section 1.1, REEs are barely incorporated into minerals and remain in melt during magmatic differentiation because of their large ionic radii and high valences. There is no systematic study about the evolution of REE minerals, particularly on dominant factors for their formation (age, geological event, etc.). However, the detailed mineral

evolution of thorium–uranium, boron–beryllium, mercury, and carbon minerals were reported by Hazen et al. (2009, 2011, 2012, 2013). Thorium and uranium are also incompatible elements as well as REEs. The representative thorium–uranium minerals are thorite and coffinite which are isostructural with zircon and xenotime (Table 7). Many thorium–uranium minerals occur in fractionated silicate rocks such as granite and granitic pegmatites as well as REE minerals (eg, Anthony et al., 1995, 1997, 2000).

In the history of the earth, formation of granite and granitic pegmatites started about 4.0 billion years ago (Table 9), which is one of the big triggers for increasing the number of thorium–uranium mineral species (Hazen et al., 2009). We expect that evolution of REE minerals is also similar to that of thorium–uranium minerals. The crystallization of REE minerals occur in fractionated magma such as granitic magma and occasionally form large REE deposits (Ercit, 2005). Therefore, granite and granitic pegmatite are important research targets for "mineral evolution" of REEs.

Hazen et al. (2008) suggested that chemical compositional ranges of minerals in the same mineral species remarkably expanded from Precambrian eon to Phanerozoic eon. The Japanese islands are situated in subduction-related island arc formed by four tectonic plates. Most of the rocks in the island formed after the Paleozoic era, while rocks occurring in "craton" (the stable interior portion of a continent characteristically composed of ancient crystalline basement rock) like the Canadian Shield mainly emplaced before the Paleozoic era. We compare Japanese minerals with Canadian ones, as a simple example. The gross area of the Japanese island and Canada are $337,930 \, km^2$ (0.25% in the gross area of the world) and $9,984,670 \, km^2$ (6.7%), respectively, and the difference is over 25 times. Mineral species present in the Japanese islands and Canada are 1200 (Kato, 2008) species and 1600 species, respectively (Horváth, 2014). Most of the Canadian basement rocks are Precambrian craton, and they formed before or during the Great Oxidation Event (GOE). In contrast, Japanese basement rocks formed after GOE (after the Paleozoic). GOE is the most important trigger for mineral evolution (Table 9), according to Hazen et al. (2009), mineral species increased from 1500 to >4000 after GOE. Thus mineral species in Japan are so various (c.1200 species), considering its relatively smaller size. The variety of minerals in Japan may be related to complex tectonic setting after the Paleozoic era, which implies that there is a characteristic mineral evolution in subduction-related magmatic arcs like Japan. In the discussion later, we introduce some studies concerning allanite, zircon and monazite, the representative REE minerals occurring in granitic rocks in Japan.

Calc-alkaline granitic rocks in subduction-related magmatic arcs, including the Japanese islands, are classified into magnetite-series (oxidized type) and ilmenite-series (reduced type) based on the presence or absence of magnetite, which reflects the redox state of the granitic magmas (Ishihara, 1977). The oxidation state of the granitic magmas is considered to reflect the source materials

of the magma; an oxidized mafic source for the magnetite-series, and assimilation of organic carbon in the accreted sedimentary rocks in the lower to middle crust (Ishihara and Matsuhisa, 1999) or through subduction processes (Takagi, 2004) for the ilmenite-series. On the other hand, Chappell and White (1974) described two types of granitic suites for the Phaleozoic Lachaln Fold Belt of eastern Australia as follows: I-type granitic rocks derived from source of igneous rocks and containing moderate amount of Al_2O_3 and high amount of Na_2O. Sedimentary-type (S-type) results from the partial melting of metasedimentary source rocks and having high Al_2O_3 but low Na_2O. A serious debate had arisen over the notion that Paleozoic granitic rocks of I- and S-types (Chappell and White, 1974) correspond approximately to Mesozoic–Cenozoic granitic rocks of the magnetite-series and the ilmenite-series, respectively (Whalen and Chappell, 1988), although Ishihara (1981) pointed out that the ilmenite-series granitic rocks from Japan are composed of both I-type and S-type granitic rocks.

The different chemical compositions between the magnetite- and ilmenite-series magmas may cause a slight difference in chemical composition of accessory minerals such as allanite, zircon, and monazite. Hoshino et al. (2006) reported that allanites from granitic rocks in the Japanese island arc are divided into Mn-poor (2 wt.% > MnO, 0.14 apfu > Mn) and Mn-rich (2 wt.% < MnO, 0.14 apfu < Mn) types, and the latter occur in Japanese granitic rocks (Fig. 25). In only this section, we use middle rare earth elements (MREEs: Sm-Dy) for convenience. Mn-poor allanites characteristically occur in magnetite-series granitic rocks and are relatively rich in LREE (La-Nd), whereas Mn-rich allanites occurs in ilmenite-series granitic rocks and exhibit enrichment in MREEs (Fig. 26). The relationship between Mn-rich and Mn-poor allanite-(Ce) is expressed by the coupled substitution $Mn^{2+}+(MREE, HREE)^{3+} \leftrightarrow Ca^{2+}+LREE^{3+}$ (Hoshino et al., 2006). The Mn-rich allanites characteristically occur in Mesozoic ilmenite-series granitic rocks in the Japanese arc and are not observed in granitic rocks in continental margins and intracontinental setting (Hoshino et al., 2006, 2007). This characteristic occurrence of Mn-rich allanite in Mesozoic ilmenite-series granitic rocks is related to sediment composition incorporated during the formation of ilmenite-series granitic magma (Hoshino et al., 2006, 2007).

Zircon from granitic rocks in subduction-related magmatic arcs, eg, Japan, are classified into two types: HREE-U-Th-poor and a HREE-U-Th-rich type (Hoshino et al., 2010). The occurrence of two types of zircon is not related to the difference of ilmenite- and magnetite-series, but the HREE-U-Th-rich zircons characteristically occur in granitic pegmatite. On the Y-Hf diagrams (Fig. 27), zircons in the Paleozoic–Mesozoic granitic rocks from the Japanese arc are compared with zircons in various Precambrian–Mesozoic intracontinental setting. HfO_2 content in zircon from many granitic pegmatites in the intracontinental settings of the Precambrian–Mesozoic era (eg, Černý and Siivola, 1980; Kempe et al., 2004; Lumpkin and Chakoumakos, 1988;
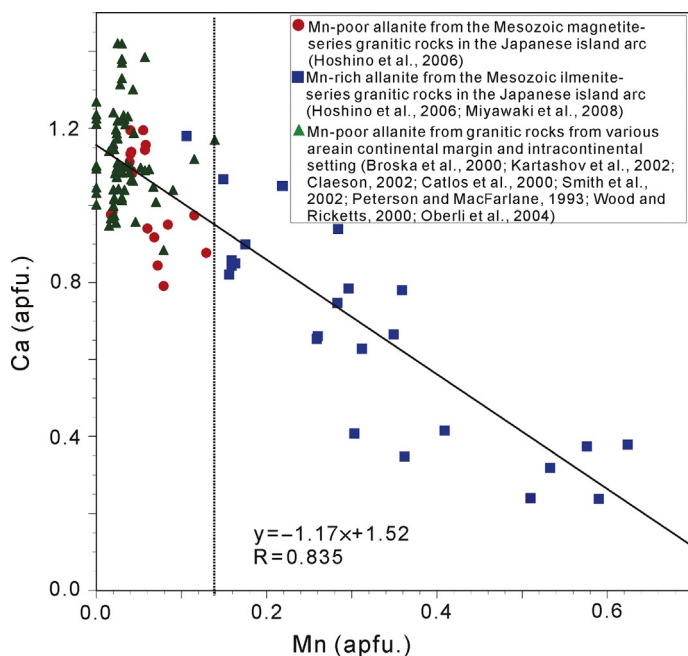
FIG. 25 Plot of Ca vs Mn of the allanite-(Ce) samples, suggesting substitution of Mn for Ca. The *dashed line* shows the boundary between Mn-rich and Mn-poor allanite-(Ce), at 0.14 apfu Mn (Broska et al., 2000; Claeson, 2002; Hoshino et al., 2006; Catlos et al., 2000; Kartashov et al., 2002; Miyawaki et al., 2008; Oberli et al., 2004; Peterson and MacFarlane, 1993; Smith et al., 2002; Wood and Ricketts, 2000). *This plot was modified from Hoshino, M., Kimata, M., Shimizu, M., Nishida, N., Fujiwara, T., 2006. Allanite-(Ce) in granitic rocks from Japan: genetic implications of patterns of REE and Mn enrichment. Can. Mineral. 44, 45–62.*

Van Lichtervelde et al., 2009) is highly variable, while zircon from Japanese granitic rocks has a wide range of Y content. Although hafnian zircons ($HfO_2 > 10$ wt.%) from many granitic pegmatite occur in the intracontinental settings, zircons from the granitic rocks in the Japanese arc always have HfO_2 content less than 10 wt.% (Fig. 27). In subduction-related volcanic rocks, HFSE (Nb, Ta, Zr, and Hf) display a characteristic depletion relative to REEs and large-ion lihophile elements (LILE) (Pearce and Peate, 1995). The average global subducted sediment is enriched in Ba, Mn, and HREEs relative to upper continental crust (Plank and Langmuir, 1998). Therefore, occurrence of Y-rich and Hf-poor zircon may be related to the above subduction magmatism, namely the Japanese island arc.

Hoshino et al. (2012b) reported that monazite from magnetite-series granitic rocks is relatively rich in LREEs, whereas monazite in ilmenite-series granitic rocks exhibits enrichment in MREEs, which is similar to geochemical behavior for allanite from Japanese granitic rocks (Fig. 26). As already mentioned, monazite is isostructural with huttonite and cheralite, so they display variable solid
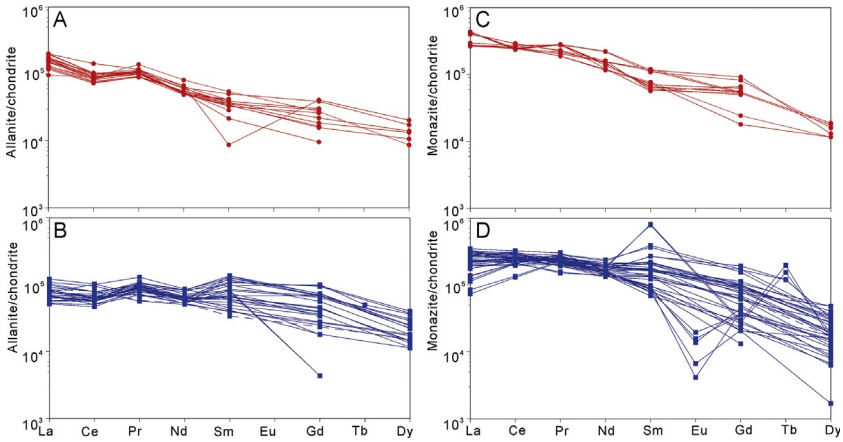
FIG. 26 Plots of chondrite-normalized REE concentration in monazite and allanite. (A) Mn-poor allanite from magnetite-series granitic rocks ((La/Sm)cn: 3.37–6.52). (B) Allanite from ilmenite-series granitic rocks ((La/Sm)cn: 0.43–2.93). (C) Monazite from magnetite-series granitic rocks ((La/Sm)cn: 2.25–7.50). (D) Monazite from ilmenite-series granitic rocks ((La/Sm)cn: 0.09–4.56). *Panel A: Data from Hoshino, M., Kimata, M., Shimizu, M., Nishida, N., Fujiwara, T., 2006. Allanite-(Ce) in granitic rocks from Japan: genetic implications of patterns of REE and Mn enrichment. Can. Mineral. 44, 45–62. Panel B: Data from Suzuki, K., Adachi, M., Yamamoto, K., 1990. Possible effects of grain-boundary REE on the REE distribution in felsic melts derived by partial melting. Geochem. J. 24, 57–74; Hoshino, M., Kimata, M., Shimizu, M., Nishida, N., Fujiwara, T., 2006. Allanite-(Ce) in granitic rocks from Japan: genetic implications of patterns of REE and Mn enrichment. Can. Mineral. 44, 45–62; Miyawaki, R., Yokoyama, K., Matsubara, S., Tsutsumi, Y., Goto, A., 2008. Uedaite-(Ce), a new member of the epidote group with Mn at the A site, from Shodoshima, Kagawa Prefecture, Japan. Eur. J. Mineral. 20, 261–269. Panel C: Data from Hoshino, M., Watanabe, Y., Ishihara, S., 2012b. Crystal chemistry of monazite from the granitic rocks of Japan: petrogenetic implications. Can. Mineral. 50, 1331–1346. Panel D: Data from Suzuki, K., Adachi, M., Yamamoto, K., 1990. Possible effects of grain-boundary REE on the REE distribution in felsic melts derived by partial melting. Geochem. J. 24, 57–74; Hoshino, M., Watanabe, Y., Ishihara, S., 2012b. Crystal chemistry of monazite from the granitic rocks of Japan: petrogenetic implications. Can. Mineral. 50, 1331–1346.*

solutions among the endmembers. In order to clarify the relationship between the monazite and the host granitic rocks, Hoshino et al. (2012b) adopted the ternary system 2REEPO$_4$ (monazite)–CaTh(PO$_4$)$_2$ (cheralite)–2ThSiO$_4$ (huttonite) (Fig. 28). This figure shows that the cheralite component in monazite changes remarkably dependent on the kind of host rock. Monazite grains with high cheralite components occur in highly differentiated S-type granites from intracontinental settings (Broska and Petrík, 2008; Förster, 1998), while the ones from the magnetite-series and ilmenite-series granitic rocks in Japanese island arc contain a relatively low cheralite component (Hoshino et al., 2012b). These results are concordant with the fact that typical S-types in Japanese granitic rocks are scarce (Chappell and White, 1974) and only one-third of the Japanese ilmenite-series granitic rocks are classified partly as S-type (Ishihara, 1981).
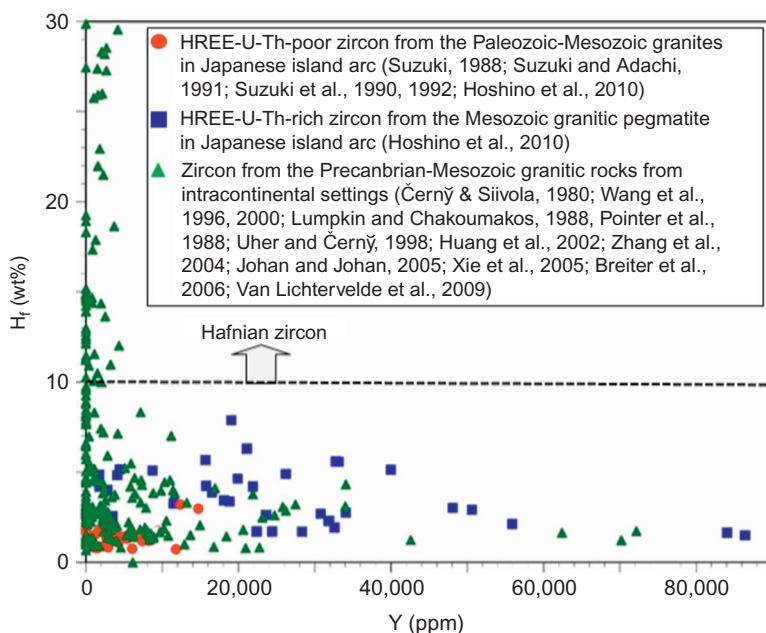
FIG. 27 Plot of Hf (wt.%) vs. Y (ppm) for zircons from granitic rocks in Japanese island arc (the Mesozoic-Paleozoic era) and in intracontinental settings (Mesozoic-Precambrian age). Data from Breiter et al., 2006; Černý and Siivola, 1980; Hoshino et al., 2010; Huang et al., 2002; Johan and Johan, 2005; Lumpkin and Chakoumakos, 1988; Pointer et al., 1988; Suzuki, 1988; Suzuki and Adachi, 1991; Suzuki et al., 1990, 1992; Uher and Černý, 1998; Van Lichtervelde et al., 2009; Wang et al., 1996, 2000; Xie et al., 2005; Zhang et al., 2004.
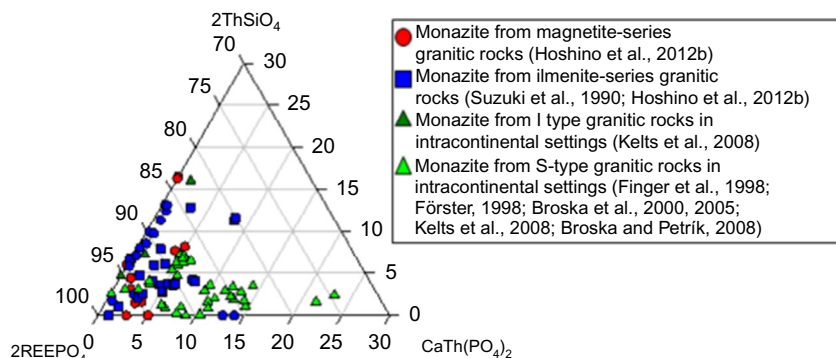
FIG. 28 $2REEPO_4$–$CaTh(PO_4)_2$–$2ThSiO_4$ diagram of monazite from magnetite-series and ilmenite-series granitic rocks in Japanese island arc (the Mesozoic) and I-type and S-type granitic rocks in intracontinental settings (the Paleozoic). In calculating the endmember proportions, the contents of U, Pb, and Fe are included with cheralite molecule. Data from Broska and Petrík, 2008; Broska et al., 2000, 2005; Finger et al., 1998; Förster, 1998; Hoshino et al., 2012b; Kelts et al., 2008; Suzuki et al., 1990. *From Hoshino, M., Watanabe, Y., Ishihara, S., 2012b. Crystal chemistry of monazite from the granitic rocks of Japan: petrogenetic implications. Can. Mineral. 50, 1331–1346.*

This low, but slightly different, cheralite component is characteristic of monazite in the Japanese granitic rocks, suggesting that the huttonite and cheralite components in monazite reflect the source of the granitic magmas.

The REE minerals crystallized in a relatively young geologic setting such as the Japanese arc after a start of mantle convection in the history of earth evolution show the different geochemical trends for those before the Paleozoic era. Further studies are required in order to clarify if similar geochemical trends are observed for REE minerals from other island arcs and continental margins. Understanding the occurrences of a variety of REE minerals in different tectonic settings and different geologic ages will also contribute to effective exploration of REE deposits.

4 INTRODUCTION TO REE DEPOSITS

4.1 Classification of REE Deposits

Rare earth deposits are formed by different geological processes in deep-seated plutonic environment, magmatic–hydrothermal environment, and surface weathering environment. The variable style of mineralization is due to the nature of REE concentration, which can be realized by the divergent processes in magmatic, hydrothermal, weathering, and sedimentary environments. These processes commonly overlap with each other, as exemplified by the magmatic–hydrothermal REE mineralization related to carbonatite intrusions such as the Mount Weld deposit in Australia, in which REEs were concentrated by weathering. This chapter reviews the representative types of REE deposits, which are commonly categorized into carbonatite, peralkaline-rock associated, iron oxide–apatite (IOA), hydrothermal vein, sediment-hosted hydrothermal, ion-adsorption type, and placer deposit (Kanazawa and Kamitani, 2006; Linnen et al., 2014; Long et al., 2010; Wu et al., 1996). In addition to these deposit types, some mining operations try to produce REEs from bauxite and clay deposits as well as sedimentary phosphates (Fig. 29).

Rare earth deposits are also classified in terms of the production style of the ores; main production or by-production, and LREE- and HREE-dominant deposits (Table 10 and Fig. 30). Because of (1) segregation of LREE and HREE groups by the natural magmatic and hydrothermal processes, (2) variable amounts and values of individual REEs, and (3) variable production costs of REE ores, mineable ore grades are significantly different by deposit types, REE mineralogy, and REE compositions in the ores. Thus, the types of REE deposits that actually produced or have been producing the ores are limited.

4.1.1 Carbonatite Deposits

Carbonatite deposits are the most dominant and common REE deposit type. Since the mid-1960s, when the Mountain Pass deposit started production, this
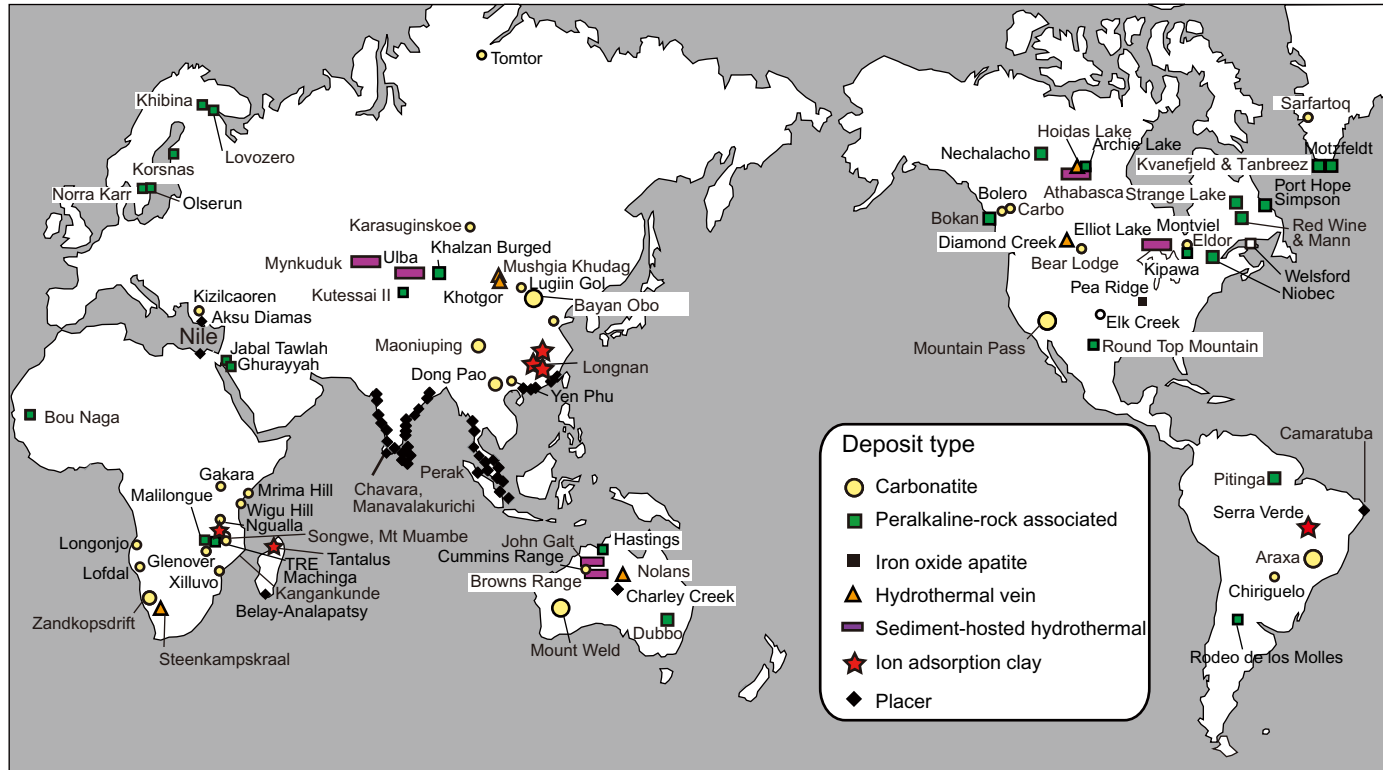
FIG. 29 A map showing the type and distribution of the major REE deposits in the world.

TABLE 10 Classification of Rare Earth Deposits

Deposit Type	Economic Remarks	Mineralogy	Genetic Model	Main or by-Production, or Potential Resource	Representative Deposits
Carbonatite	The bastnäsite-(Ce) ores are high grade (generally >4 wt.% REO), enriched in LREEs. Apatite ores are low in grade (<1.5 wt.%), but relatively enriched in HREEs. Weathering may upgrade the ores, but change mineralogy complex	Bastnäsite-(Ce), Synchysite-(Ce), monazite-(Ce), apatite	Primary magmatic–hydrothermal, but weathering may upgrade the deposits to economic level	Main or by-production of iron, niobium, phosphorus	Bayan Obo (China). Mountain Pass (United States), Mount Weld (Australia), Araxá (Brazil), Catalão (Brazil)
Peralkaline-rock associated	Generally low grade (<2 wt.% REO), some enriched in HREEs. Some associated with nepheline syenite and some with alkaline granite. Complex mineralogy	Loparite, eudialyte, mosandrite, zircon, fergusonite-(Y), xenotime-(Y)	Magmatic and/or hydrothermal	By-production of niobium, zirconium, or main	Lovozero (Russia), Dubbo (Australia), Ilimaussaq (Greenland), Noora Karr (Sweden), Kipawa (Canada), Strange Lake (Canada), Nechalacho (Canada), Bokan (United States)
Iron oxide–apatite	Generally low grade (<2 wt.%) but apatite could be recovered from mine tailing. LREE rich	Apatite	Magmatic or hydrothermal	By-production of iron	Kirunavaara (Sweden), Pea Ridge (United States), Mineville (United States)

TABLE 10 Classification of Rare Earth Deposits—Cont'd

Deposit Type	Economic Remarks	Mineralogy	Genetic Model	Main or by-Production, or Potential Resource	Representative Deposits
Hydrothermal vein	LREE-rich vein phosphate, generally low grade (1–3 wt.%)	Apatite, monazite-(Ce)	Hydrothermal	By-production of phosphurous	Hoidas Lake (Canada), Steenkampskraal (South Africa), Nolans (Australia)
Sediment-hosted hydrothermal	Low grade (<1 wt.%), but HREE rich	Xenotime-(Y)	Hydrothermal	Main	Browns Ranges (Australia)
Ion-adsorption clay	Extremely low grade (0.05–0.2 wt.%), but economic due to low cost of REE extraction. LREE and HREE rich	Halloysite, kaolinite	Weathering	Main	Longnan (China), Serra Verde (Brazil)
Placer	Large in volume. Low grade	Monazite-(Ce), Xenotime-(Y)	Sedimentary	By-production of titanium oxides	Eneabba (Australia), Manavalakuruchi (India)
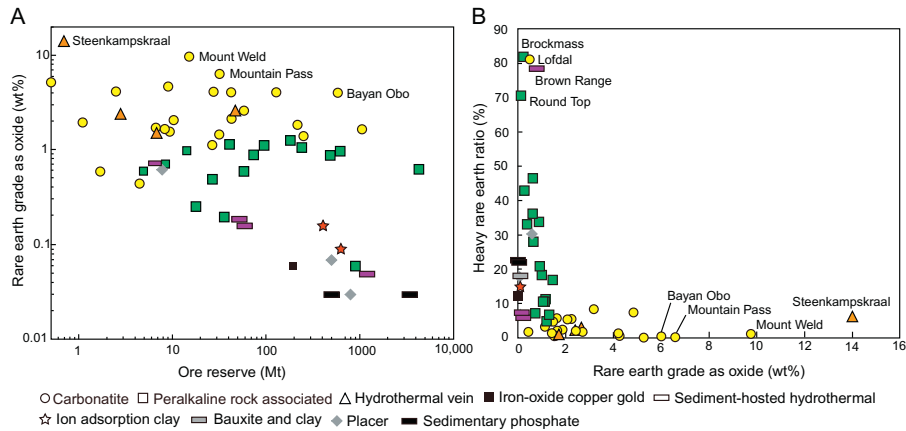
FIG. 30 Diagrams showing the ore reserves and grade of REE ores in the world (A) and the relation between REE grade and HREE ratio (B). *Data are from TMR Advanced Rare Earth Project Index (http://www.techmetalsresearch.com). Data for Bayan Obo are taken from Smith, M.P., Campbell, L.S., Kynicky, J., 2015. A review of the genesis of the world class Bayan Obo Re-REE-Nb deposits, Inner Mongolia, China: multistage processes and outstanding questions. Ore Geol. Rev. 64, 459–476.*

deposit type has been producing the majority of the REE resources in the world. The representative carbonatite deposits are Bayan Obo and Maoniuping in China, Mountain Pass in the United States, Mount Weld in Australia, and Araxá and Catalão in Brazil (Fig. 29). The major REE minerals are bastnäsite-(Ce), synchysite-(Ce), monazite-(Ce), and apatite, but so far bastnäsite-(Ce) ores have been preferentially processed due to the easiness of the REE extraction.

Although carbonatite is magmatic in origin, most of the high-grade ores of this type are formed by subsequent hydrothermal activities (Smith et al., 2015; Wall et al., 2008; Williams-Jones et al., 2012; Xie et al., 2009). Some representative deposits (Bayan Obo, Mountain Pass, Mount Weld) possess large reserves (>1 Mt REO) and relatively high-grade ores (>4 wt.%) that can fully cover the world REE demand, which is 100–200 kt a year. These deposits are enriched in light REEs because of the genetic condition of the carbonatite magmas (low degree of partial melting of garnet-bearing amphibole lherzolite at depth >70 km), although the deposits with apatite ores are relatively enriched in HREEs (Table 11). Exceptions for the LREE-enriched nature in carbonatites are hydrothermal xenotime-(Y)-rich veins associated with carbonatite at Lofdal in Namibia (Wall et al., 2008), and Yen Phu, a small, and highly weathered carbonatite prospect in northern Vietnam, which is composed of goethite-rich ore containing xenotime-(Y), monazite-(Ce), samarskite-(Y), and fergusonite-(Y) above an intrusive xenotime-bearing dolomite-carbonatite body (Watanabe, 2014). Although the genetic conditions of the carbonatite magmas of these deposits have not been clarified, the low grades and enrichment of HREEs in the ores are similar to those of the deposits associated with peralkaline rocks, suggesting that these carbonatite magmas might have formed above the garnet-stable depth in the lithosphere (Fig. 14).

The Bayan Obo deposit in Inner Mongolia of China is the largest and most productive REE deposit in the world (Fig. 31). It has estimated reserves of high-grade ores of 48 Mt at 6 wt.% REO, and lower grade resources of 750 Mt at 4.1 wt.% REO (Smith et al., 2015). The deposit also contains 1500 Mt of iron (at 35 wt.% Fe), and 2.2 Mt of Nb (0.13 wt.% Nb). Despite the large scale of the deposit and abundant scientific research conducted on the deposit, its genesis has been controversial because of the complex nature of the deposit (Wu, 2008).

The Bayan Obo deposit is composed of three major ore bodies: Main, Western, and Eastern ore bodies, which are hosted in the sedimentary dolomite layer of the Proterozoic Bayan Obo Group. In the Main and Eastern ore bodies, the REE mineralization is associated with magnetite–hematite iron ores, whereas in the Western ore body it is hosted in dolomite. The Main and Eastern ore bodies have cores of massive magnetite, which are fringed with banded ores dominated by aegirine–augite, magnetite, fluorite, and hematite (Chao et al., 1992). Based on the published papers, Smith et al. (2015) compiled mineral paragenesis of the deposit, which is separated into five stages: Stage 1

TABLE 11 Reserves, Ore Grades, and Mineralogy of Some Carbonatite Deposits

Type	Deposit Name	Tonnage (Mt)	Ore Grade (REO) %	HREEs %	Main Mineralogy
Carbonate rich	Mountain Pass (United States)	13.6	8.24	0.3	Bastnäsite-(Ce)
	Dong Pao (Vietnam)	N.A.	5.2	1.0	Bastnäsite-(Ce)
	Kizilcaören (Turkey)	N.A.	3.7	1.4	Bastnäsite-(Ce)
	Bear Lodge (United States)	57.9	2.7	2.1	Bastnäsite-(Ce)
Phosphate rich	Glenover (South Africa)	10.4	2.1	4.0	Apatite
	Zandkopsdrift (South Africa)	42.5	2.2	5.8	Florencite, gorceixite, goyazite from apatite
	Mount Weld (Australia)	14.9	9.7	7.5	Florencite, gorceixite, goyazite from apatite
	Yen Phu (Vietnam)	N.A.	0.78	39.0	Xenotime-(Y)
	Lofdal (Namibia)	1.7	0.59	80.2	Xenotime-(Y)

Tonnage and ore grade data from TMR Advanced Rare Earth Project Index (http://www.techmetalsresearch.com).

(magnetite–ferroan dolomite–monazite), Stage 2 (magnetite–monazite–apatite–bastnäsite), Stage 3 (magnetite–monazite–apatite–bastnäsite aegirine–calcite–fluorite), Stage 4 (fluorite–amphibole–phlogopite–parisite), and Stage 5 (biotite–barite–huanghoite–sulfides). They interpret that the Bayan Obo mineralization started by metasomatism (Stages 1 and 2) which was caused by infiltration of carbonatitic melts or fluids into host dolomite at around 1.3 Ga, followed by several stages of metamorphism and deformation with remobilization of REEs (Stages 3–5) culminating in 400–430 Ma. Williams-Jones et al. (2012) explained that the main mechanism of the REE precipitation at Bayan Obo was sharp increase of pH and HCO_3^- activity by the reaction of the hydrothermal fluids with host dolomite.
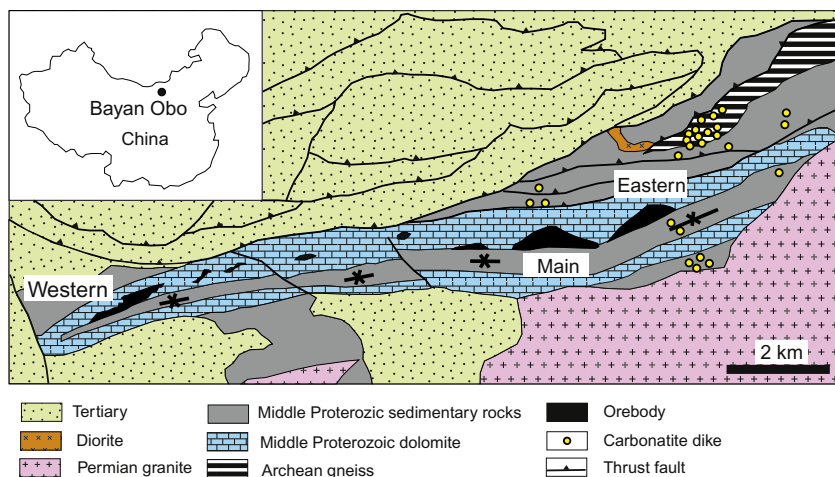
FIG. 31 Geological map of the Bayan Obo area. *After Smith, M.P., Wu, C., 2000. The geology and genesis of the Bayan Obo Fe-REE-Nb deposit: a review. In: Porter, T.M. (Ed.), Hydrothermal Iron Oxide Copper-Gold & Related Deposits: A Global Perspective, vol. 1, PGC Publishing, Adelaide, pp. 271–281.*

The Maoniuping carbonatite in Sichuan province of China forms a dike swarm present in quartz syenite intruding in the Mesozoic Mianxi alkaline granite. The carbonatite dikes are up to 400 m long and 90–200 m thick with 24–40 Ma radiometric ages (Xie et al., 2009). Fenitization is well developed around the carbonatite. The carbonatite dikes comprise mainly calcite (50–90%), aegirine, barite, fluorite, and bastnäsite-(Ce), with other REE minerals such as chevkinite-(Ce), parisite-(Ce), cerianite, titanite, britholite-(Ce), aeschynite-(Ce), and monazite-(Ce) (Yang and Wooley, 2006). Estimated REE reverses of the deposit are 1.2 Mt REO with an average grade of 2.89 wt.% (Xie et al., 2009).

Rare earth mineralization at Maoniuping occurs as veins hosted in quartz syenite and carbonatite. Four main mineralization stages are recognized: (1) carbonatite stage, (2) pegmatite stage, (3) barite-bastnäsite stage, and (4) calcite stage. Xie et al. (2009) interpreted the mineralization of the deposit based on melt and fluid inclusion study as that ore-forming fluids resulted from the unmixing of carbonatite melt and carbonatitic fluid. Initial ore-forming fluids were high-temperature (600–850°C), high-pressure (>350 MPa), and high-density supercritical magmatic fluids, characterized by SO_4-rich and multicomponent composition (eg, K, Na, Ca, Ba, Sr, and REEs). These fluids evolved to aqueous-rich fluid at low temperature though a CO_2-rich fluid at high to medium temperature, which was responsible for REE precipitation. The main mechanism for REE precipitation was phase separation of CO_2 and aqueous fluids resulting from a decrease of temperature and pressure.
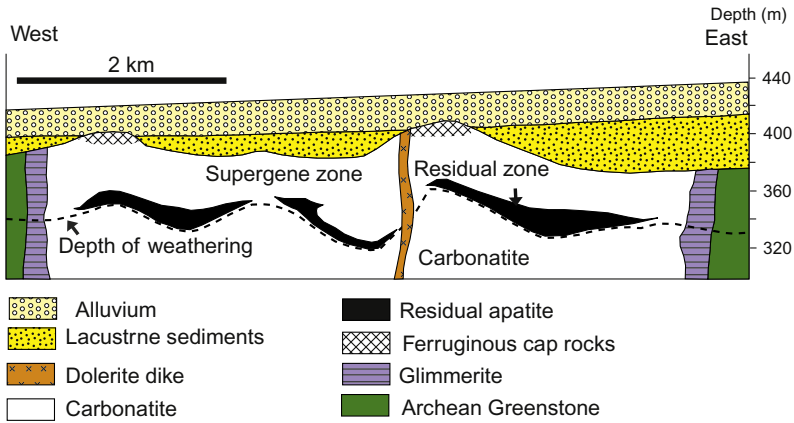
FIG. 32 Schematic cross section of the Mount Weld carbonatite. *After Lottermoser, B.G., 1990. Rare-earth element mineralisation within the Mr. Weld carbonatite laterite, Western Australia. Lithos, 151–167.*

Some of the carbonatites (Mount Weld, Araxá, Zandkopsdrift) have elevated REE grades due to weathering. The Mount Weld carbonatite is covered by 40 m thick regolith, which was formed during the Mesozoic and is composed of a lower residual zone with abundant relict igneous minerals (apatite, magnetite, ilmenite, pyrochlore, monazite, and silicates) and an upper supergene zone of insoluble aluminous oxides, clays, aluminum phosphate, and phosphate minerals (Fig. 32). The REE concentration is less than 0.2 wt.% REO in the fresh carbonatite, but 4.5 wt.% in the regolith (Lottermoser, 1990). Although higher ore grades are preferable for mining, these carbonatite ores have difficulty in mineral concentration and REE extraction, because of the complex and highly refractory nature of the secondary REE mineralogy, represented by aluminum phosphate minerals (crandallite, florencite-(Ce)), and minute mineral size. In addition to this, abundant presence of iron oxides (goethite and hematite) in the weathered ores disturbs selective flotation of REE minerals. Therefore, special care is necessary to produce high-grade ore concentration from the weathered carbonatite ores, which were successfully achieved at Mount Weld by optimizing conditions such as flotation pH, modulus of sodium silicate, etc. (Qi et al., 1992).

4.1.2 Peralkaline Rock-Associated Deposits

There are a variety of the REE deposits associated with peralkaline rocks, which are largely classified into the deposits associated with nepheline syenites, alkaline granites, and alkaline volcanic rocks. Because the REE deposits associated with peralkaline rocks are always lower in grade (<2 wt.% REO) than the carbonatite deposits, so far no project has been successfully developed except the Lovozero deposit in Kola Peninsula of Russia, where

1500–2500 tons of REO have been produced as by-product of niobium from loparite annually (Zaitsev and Kogarko, 2012). Nevertheless, many of the deposits of this group are enriched in more valuable HREEs (Fig. 30), inheriting from the composition of the REEs of alkaline magmas, and hence a number of projects aim to produce HREEs in the world (Fig. 29).

The deposits associated with nepheline syenites are further classified into the deposits formed by the magmatic process and hydrothermal process. The deposits formed by plutonic process are represented by those (Kvanefjeld, Zone 3, Sørensen, and Tanbreez) associated with the Ilímaussaq complex in Greenland, Kipawa in Quebec State of Canada, Norra Kärr in Sweden, in addition to the Lovozero deposit. The major REE minerals of these deposits are loparite (Lovozero), steenstrupine $[Na_{14}Ce_6Mn_2Fe_2(Zr,Th,U)$ $(PO_4)_7Si_{12}O_{36}(OH)_{23}H_2O]$ (Ilímaussaq) and eudialyte $[Na_{15}Ca_6(Fe^{2+},Mn^{2+})_3Zr_3$ $(Si,Nb)(Si_{25}O_{73})(O,OH,H_2O)_3(Cl,OH)_2]$ (Ilímaussaq, Norra Kärr, Kipawa), and mosandrite $[(H_3O^+,Na,Ca)_3Ca_3REE(Ti,Zr)(Si_2O_7)(O,OH,F)_4$ (Kipawa) which are unconventional for the production of REEs except loparite. Accumulation of these REE minerals in the magma chambers is an important mechanism for mineral concentration at Lovozero and a part of Ilímaussaq complexes. Among these, the REE reserves of the deposits in the Ilímaussaq complex amounts to 38.3 Mt REO, which exceeds the total reserves of the Bayan Obo deposit in China.

The deposits formed by hydrothermal process are represented by the Nechalacho deposit in Northwest Territories of Canada, which hosts 4.2 Mt REO with an average grade of 1.37 wt.% REO. The rare earth mineralization of the Nechalacho deposit is hosted in the metasomatized zone situated at the uppermost part of the 2.1 Ga Thor Lake syenite intruding in the 2.2 Ga Grace Lake granite (Sheard et al., 2012). The metasomatized zone includes lower and upper mineralized zones, with intercalation of magnetite and sodic–potassic altered syenite layers (Hoshino et al., 2013). These lower and upper mineralized zones possibly represent original eudialyte cumulate layers and zircon cumulate layers, which are completely metasomatized with secondary zircons and fergusonite-(Y) in addition to REE fluorocarbonates such as bastnäsite-(Ce), parisite-(Ce), and synchysite-(Ce) (Hoshino et al., 2013; Sheard et al., 2012). The major REE ore minerals at Nechalacho are zircon and fergusontite-(Y), both of which are enriched in HREEs.

The deposits associated with alkaline granites are represented by Strange Lake in Canada, Bokan in the United States, Khaldzan Buregtey in Mongolia, Pitinga in Brazil, and Jabal Tawlah in Saudi Arabia. The mineralization of all these deposits is related to the metasomatism and subsequent hydrothermal activities. The major REE minerals of these deposits are xenotime-(Y) (Bokan, Pitinga, Jabal Tawlah), zirconium silicates (zircon, elipdite) (Khaldzan Buregtey), and waimirite-(Y) and Nb-oxides (Jabal Tawlah). Those of the Strange Lake deposit are more complex: pyrochlore, monazite-(Ce), bastnäsite-(Ce), gadolinite-(Y) $[Y_2Fe^{2+}Be_2Si_2O_{10}]$, gerenite-(Y) $[(Ca,Na)_2$

(Y,REE)$_3$Si$_6$O$_{18}$2H$_2$O], kainosite-(Y) [Ca$_2$(Y,Ce)$_2$Si$_4$O$_{12}$(CO$_3$)H$_2$O], etc. (Kerr and Rafuse, 2012).

The Strange Lake deposit is hosted by the 1.2 Ga Strange Lake peralkaline granite, a cylindrical body about 6 km in diameter, which intruded in Archean basement rocks in northeastern Canada. The rare earth mineralization was found at Main zone and B zone, which are hosted in subsolvus granite, containing discrete K-feldspar and albite crystals, that fringes the fresh less evolved hypersolvus granite core. The main zone consists of lower grade part where REE-bearing minerals are disseminated in the subsolvus granite, and higher grade pegmatite and aplite lens enriched in Zr, Nb, and REEs. The B zone is similar to the high-grade part of the Main zone with pervasive alteration with hematite (Kerr and Rafuse, 2012). Salvi and Williams-Jones (1996) interpreted that the REE mineralization at Strange Lake, which is enriched in Ca-silicates, occurred at low temperature ($\leq$200°C) condition by the introduction of Ca-rich meteoric or formation water subsequent to high temperature ($\geq$350°C) alteration attributed to Ca-free magmatic fluids.

The rare earth deposits associated with alkaline volcanic rocks are Dubbo in Australia and Round Top in the United States. The Dubbo deposit is composed of the Jurassic Toongi trachyte plug, 800 m $\times$ 400 m in size, which intruded in the basement sedimentary and volcanic rocks. This trachyte is disseminated with zirconosilicates (eudialyte and armstrogite), natroniobite, and calcian bastnäsite. Because trachyte is enriched in zirconium (1.96 wt.% ZrO$_2$), REEs are planned to be recovered as by-product (Verbaan et al., 2015). The Round Top deposit in western Texas, United States, is located in the southern extension of the Basin and Range region. This deposit is hosted by 36 Ma peraluminous rhyolite laccolith, 2 km $\times$ 1.5 km in size, with hydrothermal alteration. The rhyolite is heavily enriched in incompatible elements, with hydrothermal zircon, bastnäsite-(Ce), columbite, xenotime-(Y), etc. (Price et al., 1990; Rubin et al., 1989).

4.1.3 IOA Deposits

IOA deposits, represented by Kiirunavaara in Sweden, are an important source of iron. This deposit type is characterized by the variable concentrations of magnetite, fluorapatite, and actinolite, and is found in northern Sweden, Missouri in the United States, Benjamin River in Canada, Chile and central Iran. The genesis of the deposits has been debatable: direct crystallization of immiscible Fe-rich melt that separated from a parent silicate magma (Jonsson et al., 2013; Naslund et al., 2002), or deposition of iron oxides from hydrothermal fluids either magmatic or crustal origin (Hildebrand, 1986; Nabatian et al., 2014; Nold et al., 2013), or mixture of the two processes (Nold et al., 2013).

Whichever the origin, it has been well known that apatite associated with iron oxides of this deposit type generally contain 200–7000 ppm of REEs (Frietsch and Perdahl, 1995), some are significantly enriched in REEs,

eg, >11 wt.% REO at Mineville, United States. The Pea Ridge iron deposit in Missouri, United States, contains an unexploited high-grade REE resource in breccia pipes associated with 1.5 Ga granite and syenite. Bulk samples of REE-rich breccia, which contains monazite and xenotime in addition to apatite, contain approximately 12% REO which may become a good REE resource (Castor, 2008b).

4.1.4 Hydrothermal Vein Deposits

Rare earth bearing hydrothermal phosphate veins have been found in several places in the world. They are Steenkampskraal in South Africa, Hoidas Lake in Canada, Nolans in Australia, and Mushgai Khudag in Mongolia. Among these, the Steenkampskraal deposit once produced REEs as by-product of thorium from monazite (total production was 50,000 tons of monazite concentrate averaging 45 wt.% REO; Andreoli et al., 1994). These deposits are composed of phosphate vein which mainly contain apatite, except for the monazite-dominated veins at Steenkampskraal. The apatite of these deposits generally contain up to 3 wt.% REO. Thus, the REO grades of the ores are generally 1–3 wt.%, and REE are mostly included in apatite and associated monazite. The sources of hydrothermal fluids for these veins have not been well studied yet, except the Steenkampskraal and Hoidas Lake deposits, which are described later.

The Steenkampskraal deposit in western South Africa is composed of a monazite–apatite vein hosted by 1.2–1.1 Ga quartz diorite and tonalite of the Roodewal suite in the metamorphic rocks of granulite facies. The vein is about 290 m long and up to 4 m wide. It contains zircon, monazite, apatite, and sulfides (pyrite, chalcopyrite, and galena) in addition to magnetite, ilmenite, and quartz. Those minerals are completely recrystallized and/or sheared by the subsequent metamorphic and deformation events (Andreoli et al., 1994). Andreoli et al. (1994) proposed a model that the monazite–apatite vein at Steenkampskraal formed by the fluid exsolved from the host igneous rocks when they crystallized.

The Hoidas Lake deposit in northern Saskatchewan, Canada, is a structurally controlled vein deposit with allanite-(Ce) and fluorapatite as the main REE carriers. The mineralized veins cut Archean and Paleoproterozoic gneiss and include hyalophane-bearing pegmatitic dikes, REE-mineralized veins with allanite, diopside, hornblende, hyalophane, and titanite, and late breccia veins that contain several stages of apatite. Detailed fluid inclusion study indicates that the Hoidas Lake mineralization involved two fluid types with early carbonic fluid followed by a mixed Na-Ca-K-rich saline aqueous fluid, the latter of which is attributed to exsolution from an evolving alkaline melt. The temperature of the mineralized fluids is estimated to be 310°C. The similarity of the fluids with above characteristics to those of the fluids related to carbonatitic or alkaline magmas suggests that the Hoidas Lake veins are distal pegmatitic part of the carbonatitic or alkaline magmatic system (Pandur et al., 2014, 2015).

4.1.5   Sediment-Hosted Hydrothermal Deposits

This deposit type is typically associated with unconformity-related uranium mineralization, which is found in the Athabasca basin, Saskatchewan, Canada, and Gordon Downs region in Western Australia.

The Athabasca basin in Saskatchewan, Canada, 350 km × 200 km in size, hosts the largest uranium resources in the world. The uranium deposits in the basin, which are categorized to unconformity-associated deposits, are distributed along the margin of the basin near the unconformity between the Proterozoic basin-fill sedimentary rocks and the basement gneiss (Jefferson et al., 2007). In this basin, there are some REE prospects which are characterized by the presence of xenotime with goyazite, hematite, and clay minerals disseminated in sandstone. Such REE mineralization, ie, at Maw Zone, apparently formed from the similar saline oxidizing basin fluids that were responsible for hydrothermal alteration and uranium mineralization (Quirt et al., 1991).

In the Brown Ranges prospect in Western Australia, xenotime-(Y) and subordinate florencite-(Ce) are disseminated and/or included in quartz veinlets with REE-bearing zircon, goyazite, and hematite, forming several ore bodies a few hundred meters in size sporadically distributed in the Archean to Paleoproterozoic metasedimentary rocks. Detectable uranium and thorium are found in xenotime-(Y) (Cook et al., 2013). Vallini et al. (2007) proposed that the xenotime mineralization at the Killi Hills prospect, 60 km south of Browns Ranges, is related to an unconformity between the Killi Formation and the overlying Cardiner Sandstone and have formed from fluids released during diagenesis of the later. However, the REE mineralization at Browns Ranges is clearly ascribed to percolation of a volatile-rich, acidic fluid, possibly granite-derived, through permeable arkose units. Late hematite may suggest mixing with meteoric water and subsequent oxidation (Cook et al., 2013).

4.1.6   Ion-Adsorption Type Deposits

Ion-adsorption type deposits are formed by weathering of igneous rocks (typically granites) that contain certain REE-bearing minerals. Due to surface weathering, REE minerals are decomposed, and ionized REEs are absorbed on clay minerals such as halloysite and kaolinite. The absorbed REEs are recovered by a dilute electrolyte solution such as ammonium sulfate solution and precipitated by oxalic acid solution. Because the mining and recovery processes are simple and inexpensive, REEs are commercially produced from extremely low grade (typically up to 2000 ppm REE) weathered clay in southern China. On the other hand, developing of ion-adsorption type deposits includes environmental issues related to in situ leaching, large leach residue, overexploitation, and environmental restoration costs (Ding, 2012; Yang et al., 2013).

Although ion-adsorption type deposits were developed only in southern China (Xie et al., 2016), several projects have been also known in the

countries outside China in the recent years (Sanematsu and Watanabe, 2016). The Tantalus REE project in northern Madagascar was established as a result of an exploration program between 2008 and 2014 by Tantalus Rare Earths AG. The ore bodies are hosted in weathered crusts overlying syenite and other smaller intrusive rocks with high REE contents (Ganzeev and Grechishchev, 2003). The Malawi REE project was recently established in the Chambe Basin located northwest of the Mulanje Massif, southern Malawi (Le Couteur, 2011). Kaolinite-bearing weathered crusts developed on syenitic rocks contain ion-exchangeable REEs. The Serra Verde REE project located in Goiás Province of Brazil is currently explored by Mineração Serra Verde. This deposit is believed to have the total mineral resources (measured+indicated+inferred) of 931 Mt at a cutoff grade of 0.12 wt.% REO (data from website of Mineração Serra Verde). The parent rock underlying the ore bodies is the Proterozoic alkaline Serra Dourada Granite, which occurs in an area of 60 km × 10 km. The granite consists of biotite granite and biotite-muscovite granite, which are associated with tin-bearing veins that host monazite and xenotime. The Serra Dourada Granite contains 500–1700 ppm REEs and is rich in HREEs (Marini et al., 1992). Small ion-adsorption type deposits and prospects have been also found in Southeast Asia. In northern Myanmar (Kachin State and Shan State), REEs are intermittently produced from ion-adsorption type deposits developed on granitic rocks. Some ion-adsorption type prospects were found in weathered granites in northern Vietnam (Mentani, 2012) and western Thailand (Sanematsu et al., 2013).

Both alkaline and calc-alkaline granitic rocks can be the parent rocks of ion-adsorption type deposits because fractional crystallization is more important for HREE enrichment than partial melting as previously discussed. Geochemical, mineralogical, and geological characteristics of ion-adsorption type deposits and their parent rocks are discussed in Section 4.2.

4.1.7 Placer Deposits

Most placer deposits with significant amounts of REE minerals are Tertiary or Quaternary deposits derived from source areas that include granitic rocks or high-grade metamorphic rocks. However, paleoplacer deposits (eg, Olserum in Germany) that are as old as Precambrian contain REE resources. Most of the commercial deposits are in sands of marine origin along or near present coastlines and consist of titanium mineral placers with by-product zircon and monazite (Castor and Hedrick, 2006; Table 12). However, due to high thorium content, monazite is not recovered from beach heavy sands, with a few exceptions. These major deposits are located in Western Australia, India, South Africa, and Madagascar, which once formed a part of the Pangea (Fig. 33).

Among the placer deposits in the world, the Eneabba deposit in Western Australia is the largest. The heavy minerals of the deposit comprise about

TABLE 12 Major Monazite-Bearing Placer Deposits in the World

Deposit Name	Country	Type	Major Mineral	Weight (Mt)	Rare Earth Oxide (Mt)
Eneabba	Australia	Beach	Monazite	43	25.8
Manavalakuruchi	India	Beach	Monazite	2.6	1.42
Richard Bay	South Africa	Beach	Monazite	1.15	0.65
Fort Dauphine	Madagascar	Beach	Monazite	0.89	0.54
WIM150	Australia	Beach	Monazite, xenotime	0.75	0.45
Tolagnaro	Madagascar	Beach	Monazite	0.72	0.43
Ranchi-Purulia	India	Fluvial	Monazite	0.27	0.16
Oak Grove	United States	Fluvial	Monazite	0.27	0.16
Camaratuba	Brazil	Beach	Monazite	0.24	0.15
Nile Delta	Egypt	Beach	Monazite	0.22	0.13
Jurien Bay	Australia	Beach	Monazite	0.18	0.11
Chavara	India	Beach	Monazite	0.18	0.10

Data source: Orris, G.J., Grauch, R.I., 2002. Rare earth element mines, deposits, and occurrences. U.S. Geological Survey Open File Report 02-189, 78p.

6% of the sand mined, and monazite makes up 0.5–7.0% of the heavy minerals (Shepherd, 1990). In addition to Australia, by-product monazite has been recovered from beach sands in Brazil, India, Malaysia, Thailand, and Vietnam. The valuable REE minerals are generally confined to monazite and a lesser amount of xenotime because of the abundance of these minerals in placer deposits (Castor and Hedrick, 2006; Jackson and Christiansen, 1993; Sengupta and Van Gosen, 2016) and of the established beneficiation and metallurgical technique (Gupta and Krishnamurthy, 2005; Jordens et al., 2013). In Malaysia, 571 tons of monazite and 208 tons of xenotime were produced in 2011 (Minerals and Geoscience Department Malaysia, 2012).

4.1.8 Other Deposits

Some bauxite deposits developed on carbonate rocks and syenite have been known to contain some elevated amounts of REEs (up to 2000 ppm approximately) (Boulangé and Colin, 1994; Calagari and Abedini, 2007; Eliopoulos et al., 2014; Karadağ et al., 2009; Mordberg et al., 2000). Because the REE
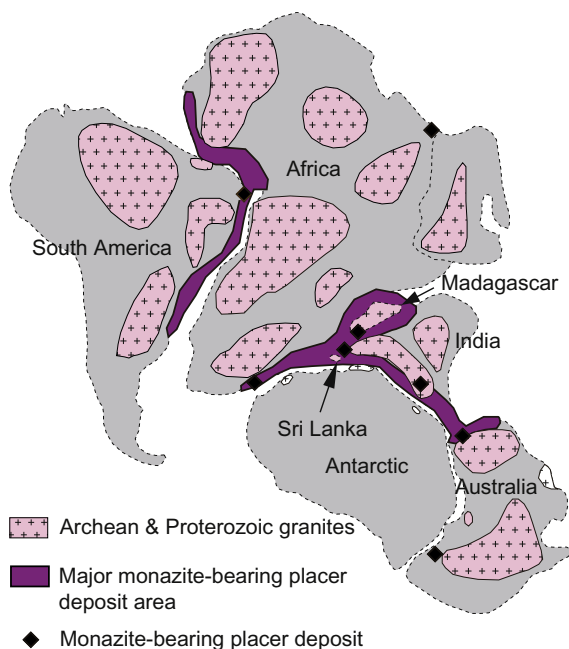
FIG. 33 Location of the continents in the late Paleozoic and the distribution of the Archean and Proterozoic granite with major monazite-bearing placer deposits *After Watanabe, Y., 2010. Rare earth. Shigen Chishitsu 60, 103–122 (in Japanese).*

concentration in bauxite has a positive correlation with phosphorous and titanium contents, it is assumed that the REEs are included in titanium minerals and aluminum phosphate minerals such as crandallite and florencite-(Ce) (Wagh and Pinnock, 1987). Where carbonate rocks dominate, bauxite ores contain parisite-(Ce) at the lowest part and churchite-(Y) above it (Wang et al., 2010b). During the process of bauxite production, the residue, called red mud, is separated and disposed in tailing pools. The residues from the bauxite production in Jamaica contain more than two times REEs (2000–3000 ppm), which are in particular, enriched in scandium (150 ppm) than the original bauxite (Wagh and Pinnock, 1987). Thus, there is a potential to produce REEs from red mud as by-product of alumina, which is explored by the Jamaica Bauxite Institute.

A unique project to produce REEs as by-product of high-purity alumina is conducted in Quebec, Canada. This Orbite project aims to produce REEs from homogeneous mudstone of the Cambrian-Ordovician L'Original Formation that contains about 53 wt.% SiO_2, 23 wt.% Al_2O_3, 8.4 wt.% Fe_2O_3, and 500–600 ppm REE. The alumina facility also is expected to be designed to recover 1.2 Mt/y silica, 189,000 t/y of hematite, about 28,000 t/y of magnesium oxide, and about 1000 t/y of other oxides, which include gallium oxide, REE oxides, and scandium oxide (Mobbs, 2014).

4.2 Ion-Adsorption Type Deposits

4.2.1 Characteristics of Ion-Adsorption Type REE Deposits

Minable ion-adsorption type REE deposits are confined almost exclusively to southern China (Xie et al., 2016) in a mild and humid climate although several deposits and prospects are known in Africa, South America, and Southeast Asia (Fig. 34). The first discovery of the ion-adsorption type deposit dates back to 1969 when HREE-rich granites were found in Longnan County of Jiangxi Province (Chen, 1996; Ding, 2012). Over 169 of ion-adsorption type REE deposits have been found in southern China (Chen, 1996; Ding, 2012; Wall, 2014; Wang et al., 2013; Xie et al., 2016; Zhang, 1990), and they are present in Jiangxi, Guangdong, Fujiang, Guangxi (Zhuang Autonomous Region), Hunan, and Yunnan Provinces (Fig. 35) listed in decreasing order of resources (Zhou et al., 2012). Some of the deposits were found in Heinan Province (Yuan et al., 2013). Ore reserves of the ion-adsorption type deposits are classified into large (>0.5 Mt), medium (0.05–0.5 Mt), and small (<0.01 Mt) (Zhu, 1999). Although specific data on the reserves are not available, the total resources of each deposit were reported by Xie et al. (2016). The deposits sizes are generally smaller than other REE deposits associated with carbonatites, peralkaline rocks, and hydrothermal veins which were previously mentioned in Section 4.1.

Ion-adsorption type REE deposits are categorized as weathering deposits; however, this ore formation process contrasts to the other weathering REE deposits such as placer deposits and weathered carbonatite deposits (Lottermoser, 1990; Verplanck et al., 2016), which are called residual deposits. The most significant difference in these deposit types is whether the REEs are adsorbed on the surfaces of weathering products or are incorporated in mineral structures. In residual deposits, REEs are contained in residual minerals such as monazite and zircon which are resistant to chemical weathering. If weathered rocks are mechanically eroded and these residual heavy minerals are selectively concentrated in basin by sedimentation, they may form placer deposits. In ion-adsorption ores, REEs are mostly present in ion-exchangeable phase of weathered granites, and blasting, crushing, grinding, or mineral processing is not needed. REEs are easily extracted by ion exchange using dilute electrolyte solutions such as ammonium sulfate solution at ambient temperature (eg, Chi and Tian, 2009; Chi et al., 2012; Moldoveanu and Papangelakis, 2012, 2013; Tian et al., 2013; Wu et al., 1990) as illustrated in Fig. 36. The schematic of extraction by leaching is suggested by Chi and Tian (2009) as follows:

$$\left[Al_2Si_2O_5(OH)_4\right]_m \bullet nREE_{(s)}^{3+} + 3nNH_4^+{}_{(aq)}$$
$$\Leftrightarrow \left[Al_2Si_2O_5(OH)_4\right]_m \bullet \left(NH^{4+}\right)_{3n(s)}^{3+} + nREE_{(aq)}^{3+}$$
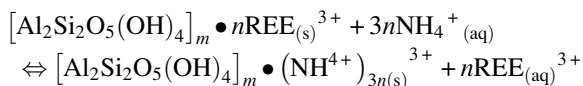
This bulk-leaching process enables mining low-grade ores. In recent years, ion-adsorption ore grades and extraction recoveries have both been decreasing, and therefore, extraction costs become more expensive than before
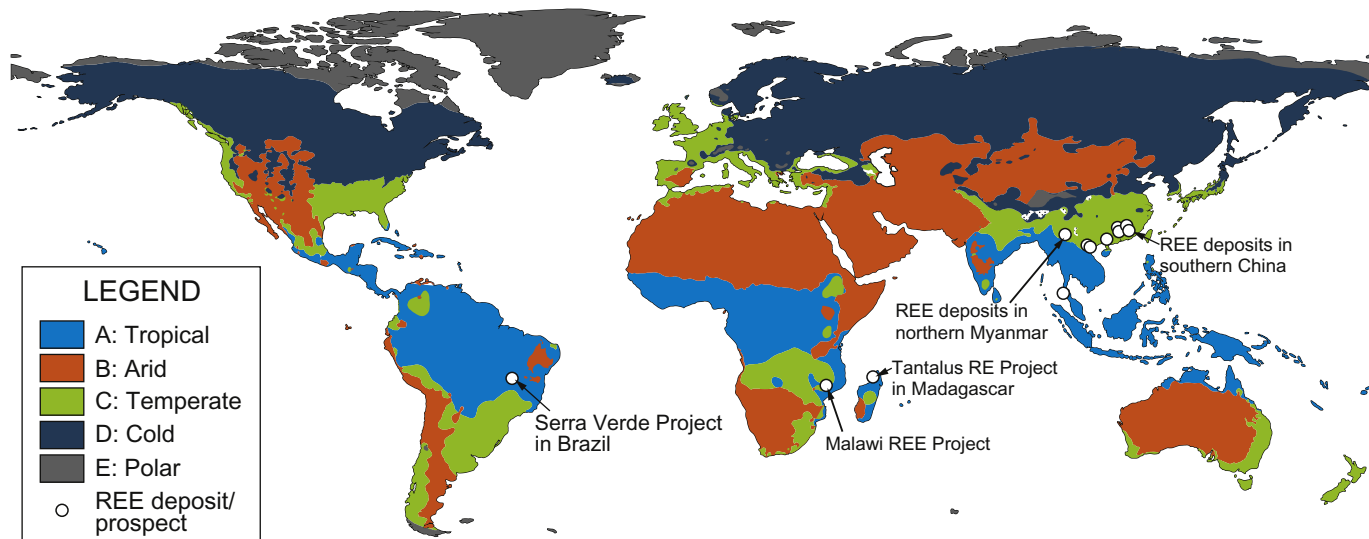
FIG. 34 World map of the Köppen–Geiger climate classification. *Modified after Peel, M.C., Finlayson, B.L., McMahon, T.A., 2007. Updated world map of the Köppen–Geiger climate classification. Hydrol. Earth Syst. Sci. 11, 1633–1644.*
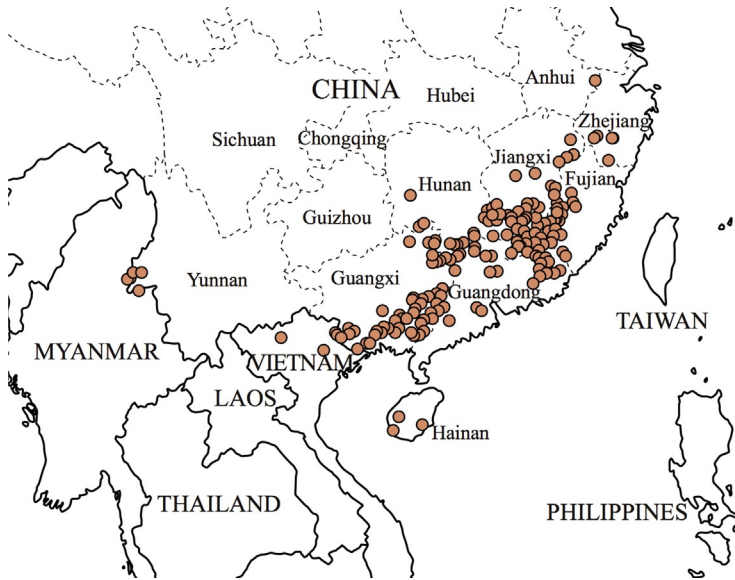
FIG. 35 Distribution map of ion-adsorption type REE deposits and prospects in southern China and neighboring countries (Myanmar and Vietnam). *Modified after Yuan, Z.X., Li, J.K., Wang, D.H., Zheng, Z.C., 2013. Metallogenic Regularity of Rare Earth Deposits in China. Dizhi Publisher, Beijing, 1–116 (in Chinese); Wang, D.H., Zhao, Z., Yu, Y., Zhao, T., Li, J.K., Dai, J.J., Liu, X.X., He, H.H., 2013. Progress, problems and research orientation of ion-adsorption type rare earth resources. Rock Miner. Anal. 32, 796–802 (in Chinese with English abstract); Sanematsu, K., 2015. REE deposits and prospective areas in Southeast Asia. Proceedings of PACRIM 2015 Congress, Hong Kong, China, 671–677.*
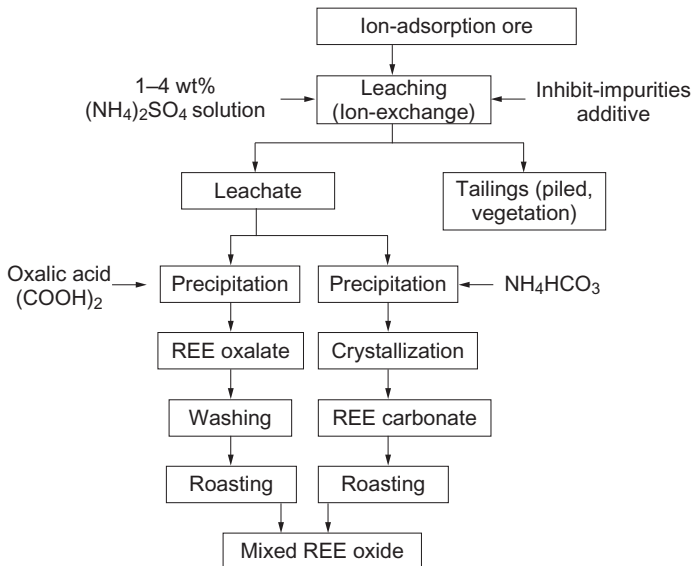
FIG. 36 Simplified flow of REE leaching from ion-adsorption ores. *Partly modified after Chi, R.A., Tian, J., 2009. Weathered Crust Elution-Deposited Rare Earth Ores. Nova Science Publishers, New York. 288 p.*

because more extraction reagent is required (Tian et al., 2013). Ion-adsorption ores generally contain lower amounts of Th and U than REE ores from other deposits. For example, ion-adsorption ores in Dingnan contain 29–37 ppm Th and 2.8–4.7 ppm U (Murakami and Ishihara, 2008). After a reaction with ammonium sulfate solution, 0.03–0.31 ppm Th and 0.25–0.71 ppm U were extracted from these ores (Sanematsu and Kon, 2013). Acidic solution during granite weathering indicates that ion-adsorption ores are not lateritic because the latter are typically formed in alkaline solution. Eventually, major compositions of ion-adsorption ores (high SiO_2 and low Fe_2O_3 and Al_2O_3 contents) do not correspond to lateritic compositions of low SiO_2 and high Fe_2O_3 and Al_2O_3 contents.

Generally, small sizes of ion-adsorption deposits are due to the constraint that ore bodies can only develop near the surface. Thicknesses of the weathering profiles on parent rocks generally range from 6 to 10 m on average, although they can reach up to 30 m (Bao and Zhao, 2008; Chen, 1996, 2013; Li and Li, 2010; Pan, 2011; Tong, 2013; Wang et al., 2013; Wu et al., 1990, 1996; Yang and Xiao, 2011; Yang et al., 1981; Zhang, 1990; Zhu, 1999), and locally up to 60 m (Bao and Zhao, 2008; Huo, 1992; Yang and Xiao, 2011). Parent rocks of ion-adsorption type deposits consist mostly of granitoids with minor felsic volcanic rocks and metamorphic rocks (Chi and Tian, 2009; Huo, 1992; Zhang, 1990).

4.2.2 REE Geochemistry of Parent Granites

Rare earth contents of igneous rocks are generally dependent on both the degree of partial melting and fractional crystallization as previously explained in Section 2. The parent rocks of the deposits consist mainly of biotite granite, muscovite–biotite granite, muscovite granite (eg, Longnan deposits; Fig. 37) and lesser amounts of volcanic rocks such as rhyolite (Heling deposits; Fig. 38). Most REE deposits in the world are typically associated with per-alkaline rocks (eg, Linnen et al., 2014; Wall, 2014); however, ion-adsorption type deposits are sourced from metaluminous and peraluminous rocks, not from peralkaline rocks, based on a molar $Al_2O_3/(Na_2O+K_2O)$ ratio and $Al_2O_3/(CaO+Na_2O+K_2O)$ ratio (aluminum saturation index: ASI) as shown in Fig. 39. These granites show K_2O contents approximately from 4.5% to 7% and Na_2O+K_2O contents from 7.5% to 10% (Bao and Zhao, 2008; Deng, 1988; Feng et al., 2012; Gu et al., 2006; Hua et al., 2007; Huang et al., 1989; Ishihara et al., 2008; Li et al., 2007; Ma et al., 1991; Yang and Xiao, 2011; Yang et al., 1981; Yu et al., 2004; Zhang, 1990), classified as calc-alkaline and alkali granites (Fig. 40A and B). Based on the classification of granitoid-series (Ishihara, 1977), the parent granites are primarily classified into ilmenite-series with some exceptions of magnetite-series granitoids in Dajishan and Qinghu (Table 13).
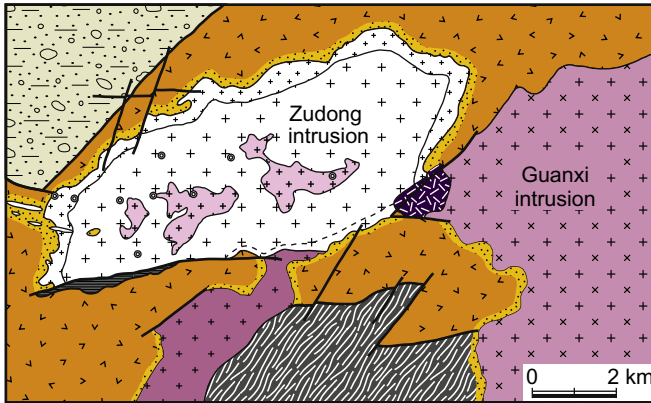
LEGEND
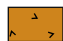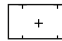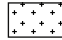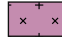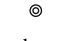
Zudong biotite granite		Lower Jurassic volcanic rocks	
Zudong muscovite granite		Lower Triassic clastic rocks	
Zudong fine-grained muscovite granite		Permian coal measures	
Guanxi Bt granite		Sinian-Cambrian metarmophic rocks	
Granophyre		Hornfels	
Bankeng granite		Pegmatite vein	
		Drill hole	

FIG. 37 Geologic map of the HREE-rich Longnan deposits in southern China. *Partly modified from Huang, D.H., Wu, C.G., Han, J.Z., 1989. REE geochemistry and mineralization characteristics of the Zudong and Guanxi Granites, Jiangxi Province. Acta Geol. Sin. 2, 139–157.*

The HREE-rich Longnan deposits, located in Longnan County in Jiangxi Province, are underlain by the Zudong and Guangxi granite intrusions (Fig. 37). The Zudong intrusion consists of the main body of muscovite granite underlying the HREE-rich ion-adsorption ore body (Fig. 41A), whereas the Guanxi intrusion consists mainly of biotite granite underlying another ore body (Fig. 41C; Huang et al., 1989). A zircon U-Pb age and whole-rock Rb-Sr age of the Zudong intrusion give 124 and 148 Ma, respectively, and those of the Guanxi intrusion give 170 and 176 Ma, respectively (Huang et al., 1989). A recent study reported 168 Ma as a zircon U-Pb age of the Zudong muscovite granite (Zhao et al., 2014). These biotite and muscovite granites mostly show high SiO_2 contents of 72–76%, low P_2O_5 contents of <0.06% and ASI below ~1.1 (Bao and Zhao, 2008; Wu et al., 1990; Yang et al., 1981; Zhang, 1990; Fig. 40). Previous works reported that REE contents of the Zudong muscovite granite range from 195 to 342 ppm and those of biotite granite range from 150 to 288 ppm (Bao and Zhao, 2008; Huang et al., 1989; Wu et al., 1990,
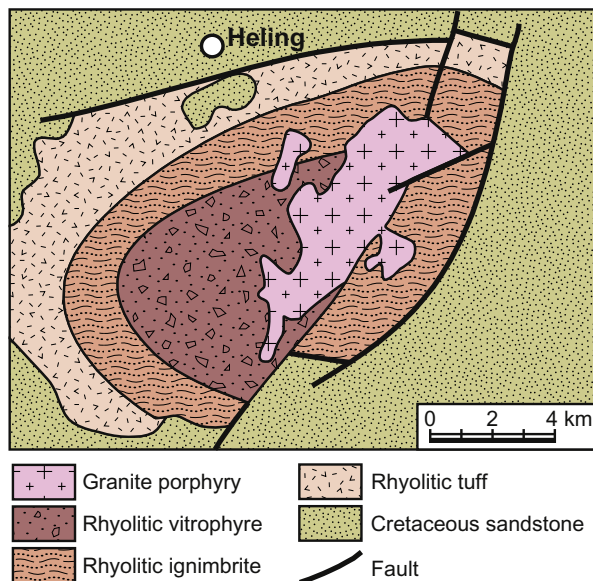
FIG. 38 Geologic map of the LREE-rich Heling deposits in southern China. *Partly modified from Zhang, Z.H., 1990. A study on weathering crust ion adsorption type REE deposit, South China. Contrib. Geol. Miner. Resour. Res. 5, 57–71 (in Chinese with English abstract); Zhang, F.R., Ye, B.G., 1995. The lithofacies of Hululian volcanic dome, Xunwu County, Jiangxi. Geol. Jiangxi 9, 45–51 (inChinese with English abstract); Bao, Z., Zhao, Z., 2008. Geochemistry of mineralization with exchangeable REY in the weathering crusts of granitic rocks in South China. Ore Geol. Rev. 33, 519–535.*

1993b). Huang et al. (1989) documented a different suite of accessory minerals of muscovite granite and biotite granite of the Zudong intrusion in Longnan. In their work, the muscovite granite underlying most of the HREE-rich ion-adsorption ore bodies contains abundant fluorite, and synchysite-(Y), and subordinate zircon, xenotime, monazite, gadolinite, aeschynite-(Y), pyrochlore, topaz, and columbite with lesser amounts of fergusonite, grossular, apatite, ilmenite, and magnetite (Table 13). In contrast, biotite granite of the Zudong intrusion, underlying the moderately HREE-rich ore bodies (Fig. 41B), contains zircon, xenotime, monazite, apatite, and lesser amounts of HREE-bearing minerals relative to the muscovite granite.

Another good example of HREE-rich deposits is Zhaibeiding which is located in Ruyuan County, Guangdong Province. The Zhaibeiding granites consist of differentiated muscovite granite and biotite granite similar to the Longnan deposits and a U-Pb zircon age is 144.8 Ma (Ma et al., 1991; Wu et al., 1993b). These granites typically show high SiO_2 contents of ~76.5% and low P_2O_5 contents of ≤0.05% (Ma et al., 1991; Wu et al., 1993b) and contain accessory minerals including garnet, fergusonite, gadolinite, REE fluorocarbonates, tourmaline, fluorite, monazite, samarskite, xenotime, and

FIG. 39 Plots of molar $Al_2O_3/(Na_2O+K_2O)$ vs $Al_2O_3/(CaO+Na_2O+K_2O)$ ratios of parent rocks underlying the ion-adsorption ore bodies in southern China.

pyrite (Wu et al., 1993b; Table 13). The ion-adsorption ores show REE grades from 131 to 589 ppm and La_N/Yb_N ratios from 0.23 to 1.5 (Ma et al., 1991; Wu et al., 1993b), which suggest strong enrichment in HREE (Figs. 40F,G and 41D).

The LREE-rich Heling deposits are located in Xunwu County of Jiangxi Province. A weathering profile is mainly developed on the Heling granite porphyry, which is surrounded by rhyolitic lava and tuff. The granite porphyry has high alkali (Na_2O+K_2O) contents (Bao and Zhao, 2008; Song and Shen, 1986; Yang et al., 1981; Zhang, 1990) compared to calc-alkaline granites in other deposits, suggesting a low degree of partial melting. The REE content of the granite porphyry is 808 ppm, significantly higher than those of calc-alkaline granites associated with other deposits. The Heling granite are enriched in LREEs and depleted in HREEs and are predominantly contained in bastnäsite-(Ce) and apatite with subdominant in zircon, monazite, fergusonite, and synchysite-(Y). The ion-adsorption ores of Heling show high REE grade ranging widely from 510 to 6460 ppm, and high La_N/Yb_N ratios of 42–121 compared to the Longnan ores, because the underlying parent rocks were originally rich in REEs (particularly in LREEs; Fig. 41F).

FIG. 40 Plots of (A) K_2O contents (Rickwood, 1989), (B) Na_2O+K_2O contents (Cox et al., 1979; Miyashiro, 1978; Wilson, 1989), (C) P_2O_5 contents, (D) LREE contents, (E) HREE contents, (F) REE contents, (G) La_N/Yb_N ratios, and (H) Y/Ho ratios vs SiO_2 contents of parent rocks of ion-adsorption deposits in southern China (Bao and Zhao, 2008; Chen and Yu, 1994; Deng, 1988; Hua et al., 2007; Huang, 1989; Huang et al., 1989; Ishihara et al., 2008; Wu et al., 1990, 1993b; Yang et al., 1981; Yuan et al., 1993; Zhang, 1990). Subscript N represents normalization by chondrite values (Sun and McDonough, 1989). The typical HREE-rich deposits are indicated by *colored areas*.

These studies indicate that the parent granites underlying the HREE-rich deposits are confined to strongly differentiated muscovite–biotite granites and muscovite granites characterized by high SiO_2 contents over ~75% and very low P_2O_5 contents of ≲0.02% (Bao and Zhao, 2008; Deng, 1988; Huang et al., 1989; Ma et al., 1991; Sanematsu and Watanabe, 2016; Wu et al., 1992, 1993b; Yang and Xiao, 2011; Yang et al., 1981; Zhang, 1990). Alkali feldspars (albite and K-feldspar) and fine-grained hydrothermal minerals including fluorite and REE fluorocarbonates commonly occur in these granites. The significant enrichment of HREE by magmatic differentiation was also recognized in some I-type granites (Chappell and White, 1974) of high $SiO_2 \gtrsim 75\%$ in the Lachlan Fold Belt of southeastern Australia

TABLE 13 Characteristics of Typical Ion-Adsorption Type REE Deposits in Southern China

Province or Region	Deposits (County/City)	Elevation	REE Grade	Recovery of Ion-Exchangeable REEs	Thickness of Weathered Crusts	Parent Rocks	Accessory Minerals of Parent Rocks	References
Jiangxi Province	Longnan (Longnan County)	300–400 m	143–1228 ppm in Zudong 336–886 ppm in Guanxi	47–~100%	~10 m (Max 30 m)	Zudong Ms granite and Bt granite, and Guanxi Bt granite	Fl, RFC, Zrn, Xen, Mnz, Gdn, Aec, Pcr, Frg, Grt, Apt, Ilm, and Mag	Yang et al. (1981), Huang et al. (1989), Zhang (1990), Wu et al. (1990a, 1993b), and Bao and Zhao (2008)
	Heling (Xunwu County)	250–300 m	1020–1530 ppm (Ave 1350 ppm; Max 6460 ppm) in porphyry 510–1530 ppm (Ave 910 ppm; Max 4900 ppm) in rhyolite	>60%	6–9 m (Max 28 m)	Bt granite porphyry, and rhyolitic lava and tuff	Apt, RFC, Zrn, Mnz, Frg, Tur, and Fl in granite porphyry	Yang et al. (1981), Song and Shen (1982), Zhang (1990), Yu et al. (2004), and Bao and Zhao (2008)
	Dingnan (Dingnan County)	300–800 m	287–651 ppm	>42%	~10 m	(Ms-bearing) Bt granite	Apt, RFC, Mnz, Xen, Thr, and Fl	Zhang (1990), Ishihara et al. (2008), Murakami and Ishihara (2008), and Wang et al. (2013a)
	Dajishan (Quannan County)	350–400 m	311–990 ppm	Unknown	Max 30 m	Wuliting Bt granodiorite	Mag, Ttn, Apt, Py, Zrn, Aln, and Chl	Yang et al. (1999), Qiu et al. (2004), Hua et al. (2007), and Ishihara et al. (2008)

Continued

TABLE 13 Characteristics of Typical Ion-Adsorption Type REE Deposits in Southern China—Cont'd

Province or Region	Deposits (County/City)	Elevation	REE Grade	Recovery of Ion-Exchangeable REEs	Thickness of Weathered Crusts	Parent Rocks	Accessory Minerals of Parent Rocks	References
	Datian (Gan County)	<400 m	Unknown	>60%	Unknown	Datian Ms granite and Bt granite	Apt, Grt, Zrn, Mnz, Xen, Frg, Exn, Fl, Ilm, and Mag(?).	Deng (1988), Zhang (1990), and Wu et al. (1992, 1993b)
	Yangbu (Gan County)	200–300 m	Unknown	Unknown	Ave ~7 m	Yangbu Hlb-bearing Bt granite and porphyry	Apt, Epi, Mag, Zrn, and Ttn.	Zhao et al. (2012)
Guangdong Province	Wujingfu and Wufang (Jiexi and Jiedong Counties)	<100 m	680–1800 ppm	>60%	Unknown	Bt granite	Unknown	Zhang (1990), Lu (2008), and Yang and Xiao (2011)
	Laishi (Xinfeng County)	100–200 m	680–1800 ppm (Ave ~800 ppm)	80–90%	Max 30 m	Fogang (Hlb-bearing) Bt granite	Aln, Ttn, Apt, Zrn, Mnz, Xen, Ilm, Rtl, Mag, and Smk	Huang (1989), Li et al. (2007), Xu et al. (2007), Yang and Xiao (2011), and Xinfeng County (2014)
	Zhaibeiding (Ruyuan County)	<300 m	680–1800 ppm (Ave ~800 ppm)	>70%	Unknown	Ms granite and Bt granite	Grt, Frg, Gdn, RFC, Tur, Fl, Mnz, Smk, Xen, and Py	Ma et al. (1991), Wu et al. (1990b, 1992, 1993b), Yang and Xiao (2011), and Ruyuan Yao Autonomous County (2014)

	Renju (Pingyuan County)	250–400 m	680–1800 ppm (Max ~4100 ppm)	>65%	Unknown	Bt granite, Bt granite porphyry, and intermediate volcanic rock	Ttn, Apt, Zrn, Mnz, Fl, Mag, and Ilm in granite and granite porphyry.	Zhang (1990), Chen and Yu (1994), and Yang and Xiao (2011)
	Xiache (Heping County)	200–300 m	850–1250 ppm (Max ~2800 ppm)	72.6–85.5%	Unknown	Hlb-Bt granite porphyry and partly intermediate volanic rock	Aln, Mnz, Xen, and other accessory minerals	Yang and Xiao (2011) and Deng (2013)
Guangxi Zhuang Autonomous Region	Huashan (Zhongshan County)	Unknown	429–679 ppm	Unknown	Unknown	(Hlb-bearing) Bt granite	Apt, Zrn Aln, Mnz, Xen, and Frg	Zhu et al. (2006), Hua et al. (2007), Bao and Zhao (2008), and Feng et al. (2012)
	Guposhan (Hezhou City)	Unknown	699–1324 ppm	Unknown	Unknown	(Hlb-bearing) Bt granite	Apt, Zrn Aln, Mnz, Xen, Frg, and Gdn	Zhu et al. (2006), Gu et al. (2006), Hua et al. (2007), Bao and Zhao (2008), and Feng et al. (2012)
	Qinghu (Liuchuan County)	20–144 m	640–1700 ppm	57.7%	8.3–22.6 m (Ave 15.1 m)	Hlb-Bt monzonite and partly syenite	Apt, Ttn, Zrn, Aln, Ilm, and Mag	Xu and Yuan (1992), Yuan et al. (1993), and Pan (2011)
	Majigang (Bobai County)	150–200 m	590–2260 ppm (Ave ~1130 ppm)	74.0%	20–30 m (Ave 22 m)	Qtz monzonite porphyry and Px monzonite	Unknown	Pan (2011)

TABLE 13 Characteristics of Typical Ion-Adsorption Type REE Deposits in Southern China—Cont'd

Province or Region	Deposits (County/City)	Elevation	REE Grade	Recovery of Ion-Exchangeable REEs	Thickness of Weathered Crusts	Parent Rocks	Accessory Minerals of Parent Rocks	References
Fujian Province	Chengnan (Ninghua County)	330–410 m	420–1700 ppm (Ave ~840 ppm)	41–72%	0.72–7.45 m (Max 17.3 m)	Bt granite	Unknown	Zhang (1990) and Chen (2013)
	Xiaota (Yong'an City)	<500 m	510–1700 ppm	Unknown	8–20 m (Max 30 m)	Hlb-bearing Bt granite	Apt, Ttn, Aln, Mnz, Xen, and Frg	Tong (2013)
Hunan Province	Guposhan (Jianghua County)	300–700 m	Max 1327 ppm	Unknown	Unknown	Bt granite	Probably same as Guposhan in Guangxi	Luo (2011) and Li and Shen (2013)
Yunnan province	Long'an (Longchuan County)	1000–1100 m (?)	Max ~2900 ppm (Ave ~1100 ppm)	30–40%	4–13 m (Ave 6.6 m)	Granite	Unknown	Li and Li (2010)

Aec=aeschynite, Aln=allanite, Apt=apatite, Bt=biotite, Exn=euxenite, Fl=fluorite, Frg=fergusonite, Gdn=gadolinite, Grt=garnet, Hlb=hornblende, Ilm=ilmenite, Mag=magnetite, Mnz=monazite, Ms=muscovite, Pcr=pyrochlore, Py=pyrite, RFC=REE fluorocarbonates (bastnäsite, parisit, synchysite, etc.), Rtl=rutile, Smk=samarskite, Thr=thorite, Ttn=titanite, Tur=tourmaline, Xen=xenotime, Zrn=zircon.
Modified from Sanematsu, K., Watanabe, Y., 2016. Characteristics and genesis of ion adsorption-type REE deposits. Rev. Econ. Geol. 18, in press.
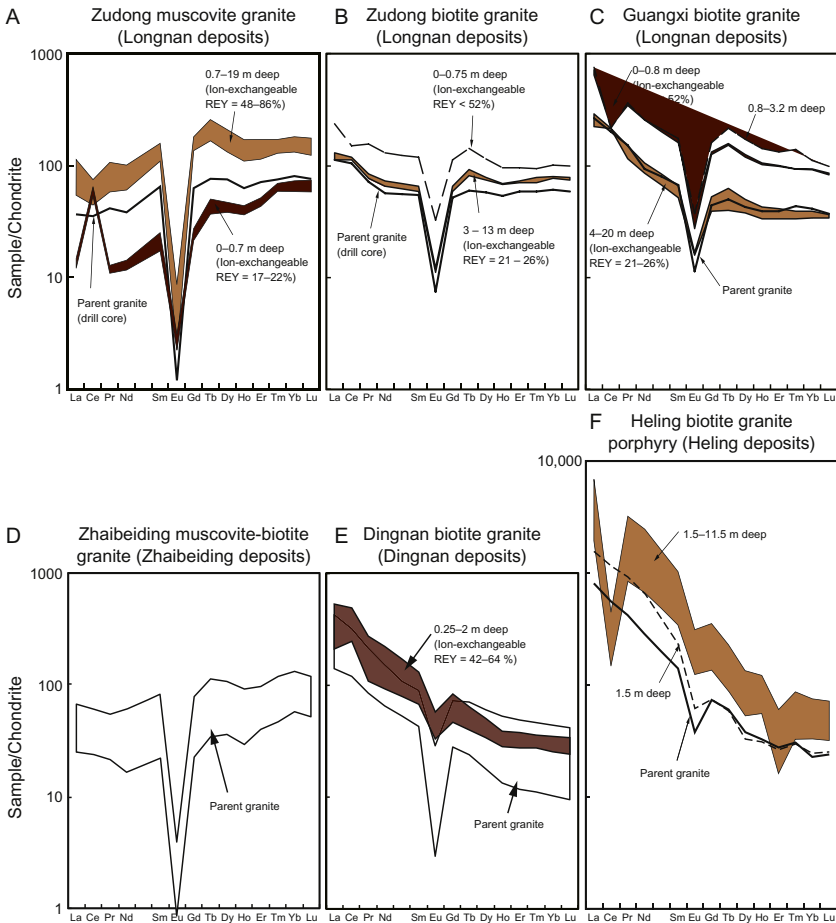
FIG. 41 Chondrite-normalized REE pattern of ion-adsorption ores developed on (A) the Zudong muscovite granite, (B) Zudong biotite granite, (C) Guangxi biotite granite in the Longnan deposits (Wu et al., 1990), on (D) muscovite–biotite granite in the Zhaibeiding deposits (Ma et al., 1991; Wu et al., 1993b), on (E) biotite granite in the Dingnan deposits (Ishihara et al., 2008; Murakami and Ishihara, 2008; Sanematsu et al., 2013), and (F) biotite granite porphyry in the Heling deposits (Bao and Zhao, 2008) in Jiangxi Province, southern China. *Chondrite values are from Sun, S.S., McDonough, W.F., 1989. Chemical and isotopic systematics of oceanic basalts: implications for mantle composition and processes. In Saunders, A.D., Norry, M.J. (Eds.), Magmatism in the Ocean Basins. Geological Society Special Publication, no. 42, pp. 313–345.*

(Chappell, 1999) and in Southwest Japan (Ishihara and Murakami, 2006). The occurrences of hydrothermal minerals are suggested by elevated Y/Ho ratios of whole-rock compositions (Sanematsu and Watanabe, 2016), because fractionation of Y/Ho is controlled by fluids generated from differentiated igneous rocks (Bau, 1996; Bau and Dulski, 1995). For example, the HREE-rich

Zudong, Zhaibeiding, and Datian granites (mostly muscovite-bearing) are characterized by enrichment in HREEs ($La_N/Yb_N = 0.11–1.5$; Fig. 40G), Y/Ho ratios ranging widely from 25 to 47 (Fig. 40H), and occurrences of hydrothermal minerals (Bao and Zhao, 2008; Huang et al., 1989; Wu et al., 1990). In contrast, less fractionated biotite granites tend to show lower Y/Ho ratios 15–31 (Fig. 40H), and they are significantly enriched in LREEs ($La_N/Yb_N = 1.4–70$; Fig. 40G).

4.2.3 REE-Bearing Minerals and Their Susceptibilities to Weathering

In the process of granite weathering elements, including REEs, can be released from the primary magmatic and hydrothermal REE-bearing minerals, and secondary REE-bearing minerals which are formed by alteration and replacement to the primary minerals at ambient temperatures. REE fluorocarbonates dissolve in acidic soil water near the surface, however, other REE-bearing minerals such as phosphates, oxides, and silicates are likely to dissolve more slowly (Sanematsu and Watanabe, 2016).

REE fluorocarbonates in igneous rocks occur along grain boundaries, as veinlets and in cavities, and it has been suggested that they were formed by F- and CO_2-rich fluids in deuteric alteration at the last stage of fractional crystallization (eg, Bea, 1996; Berger et al., 2008; Huang et al., 1989; Ishihara et al., 2008; Maruéjol et al., 1990; Sanematsu et al., 2013). Occurrences of these minerals may be indicated by high Y/Ho ratios as previously explained. In the Longnan deposits, the muscovite granite, which is the main ore body of the HREE-rich Zudong intrusion (Fig. 37), contains abundant F-bearing minerals such as fluorite, synchysite-(Y), and topaz, whereas the biotite granite of the Zudong intrusion only contains some F-bearing minerals such as biotite and apatite (Huang et al., 1989). Wu et al. (1992) studied HREE-rich granites (not all are related to REE deposits) regionally in the Nanling Range and demonstrated relatively high F contents of 340–6700 ppm with a median value of 1400 ppm. The REE fluorocarbonate minerals generally dissolve in acidic soil water during weathering of parent granites (Huang et al., 1989).

Allanite and titanite are considered to be the important REE sources (particularly LREE and HREE sources, respectively) for ion-adsorption ores as well as REE fluorocarbonates (Sanematsu and Watanabe, 2016; Sanematsu et al., 2015, 2016). Allanite and titanite, which are common REE- and REE-bearing minerals in monazite-free granite, contribute significantly to whole-rock REE contents (Bea, 1996; Gromet and Silver, 1983), and they can be precursor minerals of REE fluorocarbonates by hydrothermal alteration. Partition coefficients for REEs between allanite and melt indicate that allanite predominantly incorporates LREEs rather than HREEs (eg, Gieré and Sorensen, 2004), and that titanite is moderately rich in HREEs in contrast to allanite (eg, Prowatke and Klemme, 2005). Modal and EMPA analyses of

Gromet and Silver (1983) indicated that allanite and titanite together account for 80–95% of REEs in monazite-free granodiorite. Bea (1996) analyzed accessory minerals of variable granitoids and crustal protoliths using laser-ablation inductively coupled-plasma mass-spectrometry (LA-ICP-MS) and EMPA, and indicated that strongly peraluminous granites contain monazite, xenotime, apatite, zircon, Th-silicates (thorite and/or huttonite), and pyro-chlore, and that metaluminous and weakly peraluminous granites contain alla-nite, titanite, apatite, zircon, monazite, and Th-silicates. In his study, a percentage of LREEs (except for Eu) of each mineral relative to whole-rock LREE is mostly dominated by monazite in the strongly peraluminous allanite-free granites, and by allanite in the other monazite-free granites. Pre-dominant HREE-bearing minerals are zircon, apatite, and xenotime in the strongly peraluminous allanite-free granites, and are zircon and titanite in the other monazite-free granites. As the quantitative data of Bea (1996) indi-cated, magmatic allanite and monazite rarely coexist in granitoids except in the case of crystallizing before equilibrium of melt (Broska et al., 2000).

Allanite and titanite are the dominant REE-bearing minerals in granitoids, whereas the occurrences of these minerals are not common in strongly differ-entiated granites underlying ion-adsorption ore bodies (Table 13 and Fig. 40). Previous studies in southern China and the following studies suggested that crystallization of allanite and titanite becomes unstable during magmatic differentiation and this is probably due to fluorine in highly differentiated melt. Allanite in granitoids commonly alters to secondary minerals including fluorite and REE fluorocarbonates, such as bastnäsite and synchysite (Bea, 1996; Berger et al., 2008; Caruso and Simmons, 1985; Gieré, 1996; Gieré and Sorensen, 2004; Lira and Ripley, 1990). Titanite is also transformed to secondary minerals including allanite, monazite, xenotime, REE fluorocarbo-nates, anatase, rutile, quartz, calcite, and/or chlorite (Middleton et al., 2013; Pan et al., 1993). Titanite is stable in the oxidized felsic magma, whereas it is unstable in the reduced magma, because in the reduced condition, ilmenite becomes stable instead of titanite (Wones, 1989). An experimental study indi-cates that titanite is unstable in fluorine-rich melts because it reacts with fluo-rine to form fluorite (Price et al., 1999). The reduced residual melt including a certain amount of fluorine may become enriched in HREE progressively by fractional crystallization because titanite, a HREE-bearing mineral, hardly crystallizes and zircon is not common due to shortage of zirconium in melt. Eventually, HREEs are more incorporated into other minerals which probably include synchysite-(Y) and xenotime.

REE-bearing phosphates consisting of apatite, and lesser amounts of mon-azite and xenotime, in granites have an important role in immobilizing REE during weathering (eg, Aide and Aide, 2012; Aubert et al., 2001; Laveuf and Cornu, 2009; Sanematsu et al., 2015; Sanematsu and Watanabe, 2016). Apatite is altered and replaced by secondary REE-bearing phosphate minerals

such as rhabdophane and crandallite group which commonly occur in weathered rocks and soils and these secondary phosphates have an important role in immobilizing REE during weathering (Aubert et al., 2001; Banfield and Eggleton, 1989; Berger et al., 2014; Braun and Pagel, 1994; Braun et al., 1990, 1993; Du et al., 2012; Janots et al., 2015; Köhler et al., 2005; Marques et al., 2004; Oelkers et al., 2008; Sanematsu et al., 2013; Stille et al., 2009; Taunton et al., 2000).

In contrast with apatite, the dissolution rate of monazite at room temperature is much lower than that of apatite, even in acidic ($2 < pH < 6$) conditions (Chaïrat et al., 2007; Guidry and MacKenzie, 2003; Harouiya et al., 2007; Oelkers and Poitrasson, 2002; Oelkers et al., 2008; Valsami-Jones et al., 1998). Monazite occurs in a crystalline state in nature, rather than in a metamict state, even after large radiation doses, because it is relatively easy to anneal the radiation damage at low temperatures over geologic time (Boatner and Sales, 1988; Meldrum et al., 1998, 2000). Relatively few studies have been conducted on radiation damage and annealing of xenotime, however, some old studies indicate that monazite and xenotime are mostly crystalline and are not in a metamict state (Hurley and Fairbairn, 1953; Hutton, 1950; Ueda, 1957). In weathered granites, fine-grained residual monazite commonly occurs with a lesser amount of xenotime. An occurrence of apatite is relatively rare because it dissolves in acidic water or is replaced with secondary phosphates. Huang et al. (1989) indicated that masses of monazite and xenotime were not significantly reduced during weathering of the HREE-rich Zudong intrusion. The low dissolution rate of monazite in soil water and its resistance to weathering accounts for the typical occurrences of monazite in placer-heavy minerals and REE deposits (Hutton, 1950; Jackson and Christiansen, 1993; Kanazawa and Kamitani, 2006; Orris and Grauch, 2002; Roy, 1999; Sengupta and Van Gosen, 2016).

Zircon is resistant to chemical weathering, and residual zircon crystals are commonly found in ion-adsorption ores (Huang et al., 1989; Sanematsu and Kon, 2013). A very common occurrence of zircon in placer sands and sediments reflects the resistance to chemical weathering (eg, Hutton, 1950; Jackson and Christiansen, 1993; Orris and Grauch, 2002). Zircon is commonly found in a moderately to highly metamict state in granites, but its crystallinity can be preserved by annealing of the radiation damage even at relatively low temperatures (Ewing, 1994; Ewing et al., 2003). Nevertheless, the common occurrence of damaged zircon is attributed to an annealing process that is slower in zircon than in monazite at low temperatures (Ewing et al., 2003). Experimental studies suggest that dissolution rate of zircon is generally low and that the dissolution rate of metamict zircon is higher than that of the crystalline zircon at low temperatures (<150°C) (Balan et al., 2001; Ewing, 1999; Ewing et al., 1981; Tole, 1985; Tromans, 2006). These results suggest that REE dissolution from zircon and contribution to ion-adsorption ores is minor or insignificant.

4.2.4 Mobility and Fractionation of REE During Weathering

The degree of weathering, that is influential to REE mobility, is closely associated with the pH of soil and soil water and they were measured at different REE deposits in southern China. The moderately low pH values in the surface soils are attributed to humic substances and to CO_2 in the atmosphere. The pH values of water associated with weathered granites of the Zudong and Guanxi intrusions vary from a moderately low pH of 4.4–5.2 in the surface soil, to a pH of 5.5–6.0 in the strongly weathered zone that includes the ion-adsorption ores, and to a pH of 6.3 in the weakly weathered zone on parent granites (Wu et al., 1990). Similar pH values were reported in other mining sites of Xunwu, Dingnan, and Gan Counties in Jiangxi Province, consisting of 4.13–4.80 in the surface soil, 4.36–4.84 in the strongly weathered zone, and 5.01–5.77 in the moderately weathered zone (Wei et al., 2001). At other mining sites of Guangdong Province, Yang and Xiao (2011) reported similar pH values consisting of 4.8–5.96 in the surface soil, 5.22–6.80 in the strongly weathered zone including ion-adsorption ores, and 6.23–6.48 in the moderately weathered zone on parent rocks. These results suggest that the strongly weathered zone occurs in a pH range between 4 and 6 and the underlying moderately weathered zone occurs in a slightly higher pH range between 4.5 and 6.5, approximately (Sanematsu and Watanabe, 2016). The increase of pH is due to rock-forming minerals or ground water.

Vertical variation of REE contents in a weathering profile is strongly influenced by the degree of weathering which is controlled by the depth from the surface. Soil water is generally acidic at the surface, because of the presence of CO_2 dissolved from the air and/or humic substances (humic and fulvic acids), which are produced by biological degradation of organic matter if the surface is covered by vegetation. Rock-forming minerals and REE-bearing minerals are altered and dissolved by reacting with acidic soil water with the exception of minerals that have very low solubilities. A weathering profile including ion-adsorption type ore bodies has been classified into different zones based on the degree of weathering reflected by constituent minerals, textures, and colors (Wu et al., 1990; Yang et al., 1981; Zhang, 1990). The weathering profile may be classified into the surface soil zone (A), strongly weathered zone (B), moderately weathered zone (C), weakly weathered zone (D), and basement rock (E) from top to bottom (eg, Wu et al., 1990; Zhang, 1990) as shown in Fig. 42. However, the classification criteria are ambiguous and weathered zones may be classified differently by different geologists. REEs are generally concentrated in the moderately weathered zone (C); this zone can be recognized as an ore body if it is thick enough and contains sufficient amount of ion-exchangeable REEs.

Ion-adsorption ores typically show over ~50% of ion-exchangeable REEs which are primarily present on the surface of clays such as kaolinite and halloysite (Bao and Zhao, 2008; Chen, 2013; Chi and Tian, 2009; Chi et al.,
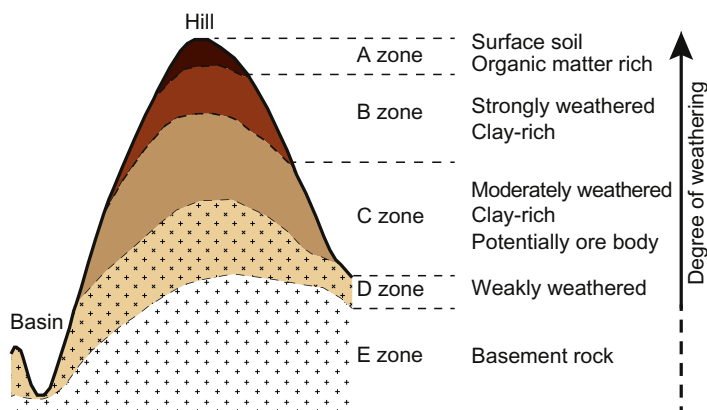
FIG. 42 Schematic model of ion-adsorption ore bodies in southern China. *Modified after Yang, Y.Q., Hu, Z.S., Luo, Z.M., 1981. Geological characteristics of mineralization of rare earth deposits of the ion-adsorption type and their prospecting direction. Bull. Inst. Miner. Depos. Chin. Acad. Geol. Sci. 2, 102–118 (in Chinese with English abstract); Zhang, Z.H., 1990. A study on weathering crust ion adsorption type REE deposit, South China. Contrib. Geol. Miner. Resour. Res. 5, 57–71 (in Chinese with English abstract); Wu, C.Y., Huang, D.H., Guo, Z.G., 1990. REE geochemistry in the weathered crust of granites, Longnan area, Jiangxi Province. Acta Geol. Sin. 3, 193–210.*

2005, 2012; Pan, 2011; Song and Shen, 1986; Tong, 2013; Wu et al., 1990, 1993a,b, 1996; Yang, 1987; Yang et al., 1981; Zhang, 1990). The REE contents of parent rocks range generally from 130 to 810 ppm (Bao and Zhao, 2008; Chen, 2013; Hua et al., 2007; Huang, 1989; Huang et al., 1989; Ishihara et al., 2008; Li and Shen, 2013; Luo, 2011; Ma et al., 1991; Pan, 2011; Wu et al., 1993b; Yang et al., 1999), and the higher REE contents are found in LREE-rich alkaline rocks (Bao and Zhao, 2008; Hua et al., 2007; Huang, et al., 1989). REE grades of ion-adsorption ores range widely from 140 up to 6500 ppm (Bao and Zhao, 2008; Chen, 2013; Hua et al., 2007; Li and Li, 2010; Li and Shen, 2013; Murakami and Ishihara, 2008; Pan, 2011; Tong, 2013; Wu et al., 1990; Yang and Xiao, 2011; Yang et al., 1981, 1999; Zhang, 1990), and they are up to 6 times of the REE contents of parent granites (Bao and Zhao, 2008; Huang et al., 1989; Wu et al., 1990; Yang and Xiao, 2011). The LREE/HREE ratios of the ion-adsorption deposits are variable from HREE-rich deposits (eg, Longnan) to LREE-rich deposits (eg, Heling) (Zhu, 1999). The LREE/HREE ratios of ion-adsorption ores constrained by those of parent granites, ie, HREE-rich ores are derived from HREE-enriched (low LREE/HREE ratio) parent granites.

The REE-enriched zone is typically below the REE-depleted zone (Wu et al., 1990; Yang et al., 1981; Zhang, 1990) because soil water dissolving REE^{3+} ions move downward in a weathering profile. In some weathering profiles (Fig. 40B and C), the REE-enriched zone is found near the surface above the REE-depleted zone because the weathered granite is more or less eroded.

The fractionation between Ce and other REE is commonly recognized in a weathering profile and numerous studies reported positive Ce anomalies in weathered granitic rocks (eg, Banfield and Eggleton, 1989; Huang et al., 1989; Mongelli, 1993). The positive Ce anomaly results from immobilization as CeO_2 by oxidizing from Ce^{3+} to Ce^{4+} near the surface because CeO_2 is hardly soluble compared with other REE^{3+} at 25°C under atmospheric pressure (Brookins, 1988). Sanematsu and Watanabe (2016) proposed that the weathering profile can be simply divided into a REE-leached zone of the upper part of the profile and a REE-accumulation zone in the lower part of the profile unless the contact zone fluctuates dramatically (Fig. 43). REEs, except for Ce, are scavenged from the leached zone, and they are immobilized by incorporating into secondary minerals or by adsorbing onto weathering products in the accumulation zone during weathering. This migration and fractionation of REEs lead to the negative Ce anomaly in the accumulation zone including ion-adsorption ores (eg, Bao and Zhao, 2008; Chi et al., 2005; Sanematsu et al., 2013; Sanematsu and Watanabe, 2016; Wu et al., 1990; Fig. 44). Aggregates of fine-grained CeO_2 commonly occur with feldspars, clays, and Mn oxides in weathered granite, particularly in the REE-leached zone. The significant Ce enrichment in Mn oxides is most likely to result from adsorption and oxidization from Ce^{3+} to Ce^{4+} by δ-MnO_2 (De Carlo et al., 1998; Ohta and Kawabe, 2001).
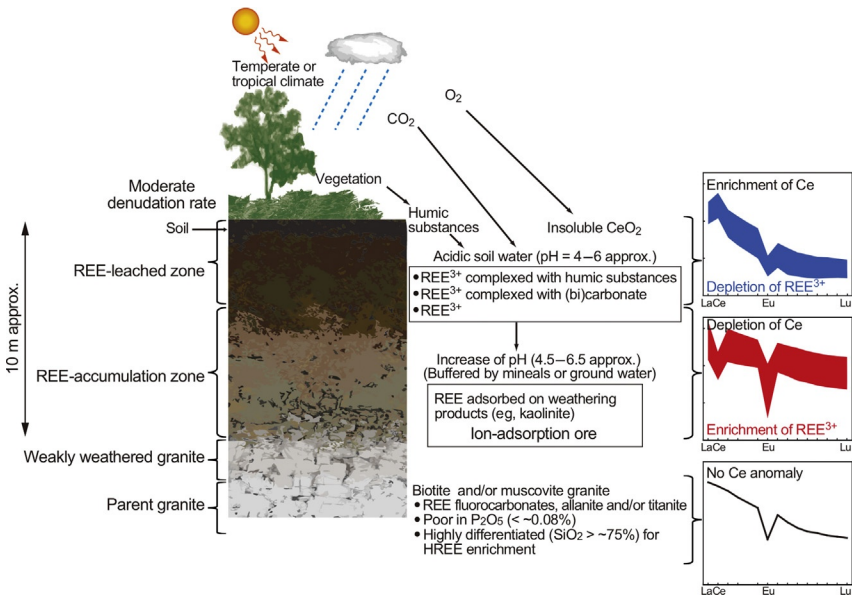
FIG. 43 Schematic model of the genesis of ion-adsorption type REE ore bodies developed on granites (Sanematsu and Watanabe, 2016). *Graphs* show the typical examples of chondrite-normalized REE patterns of the REE-leached zone, REE-accumulation zone (ion-adsorption ores), and parent granite.
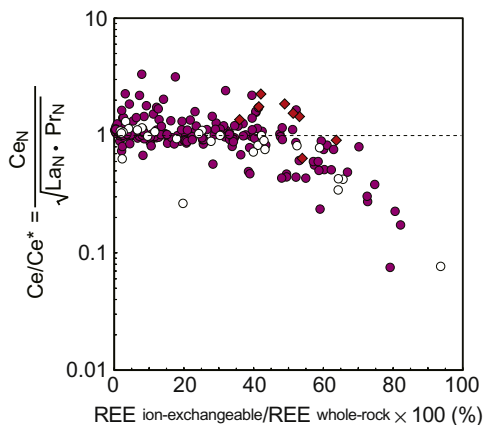
FIG. 44 Plots of Ce anomalies vs PERs (percentages of ion-exchangeable REEs relative to whole-rock REEs) of weathered granites including ion-adsorption ores in southern China (*diamond*) and Thailand (*circle*). *Data from Sanematsu, K., Kon, Y., 2013. Geochemical characteristics determined by multiple extraction from ion-adsorption type REE ores in Dingnan County of Jiangxi Province, South China. Bull. Geol. Surv. Jpn. 64, 313–330; Sanematsu, K., Kon, Y., Imai, A., 2015. Influence of phosphate on mobility and adsorption of REEs during weathering of granites in Thailand. J. Asian Earth Sci. 111, 14–30.*

4.2.5 Complexing of REEs

Mobile elements including REEs in soil water migrate downward from the upper zone to lower zone in a weathering profile of granite. In this process, REEs are mobile in soil water as ions or by forming complexes, and they are subsequently immobilized by adsorption or incorporation into secondary minerals (or leached out from the weathering profile). This REE immobilization is caused by an increase of pH resulting from the contact of low-pH soil water with rock-forming minerals or ground water. Ground-water levels generally decrease in the weathering profile due to uplift of the basement in the temperate areas, but these levels have larger fluctuations in tropical areas due to a change between dry and rainy seasons. This leads to a fluctuation of the contact zone in which REEs are immobilized.

Previous studies including thermodynamic experiments and analyses of natural water suggest that REEs are primarily complexed with carbonate and bicarbonate ions in soil water or ground water at circumneutral pH ($5 \leq \mathrm{pH} \leq 9$), and that the predominant ligand is dependent on pH and the concentration of the species. Experimental and theoretical studies suggested that REEs are dissolved in solution by forming carbonate and bicarbonate complexes ($REECO_3^+$ and $REEHCO_3^{2+}$, respectively) at pH over 5, and free REE^{3+} ions at pH below 5–6 (Cantrell and Byrne, 1987; Liu and Byrne, 1998; Wood, 1990), which is a common value in a weathering profile on granite. REE fluoride complexes such as $REEF^{2+}$ and $REEF_2^+$ may be present,

because F^- is released by degradation of REE fluorocarbonate, fluorite, and biotite. However, the carbonate and bicarbonate complexes or free REE^{3+} are more dominant than fluoride and other inorganic complexes in solutions with pH over 6.5 at low temperature (Cantrell and Byrne, 1987; Wood, 1990). Phosphate complexes of REE^{3+} may be significant in high phosphate concentration at a pH range of 7–9 (Byrne et al., 1991; Lee and Byrne, 1992), though these complexes are insignificant in ground water with low phosphate concentration, and REE–carbonate complexes are predominant at the same pH range (Johannesson et al., 1996). Carbonate and bicarbonate are the most important inorganic ligands for REEs in natural waters, and experimental studies suggest that HREEs are more easily complexed than LREEs (Cantrell and Byrne, 1987; Lee and Byrne, 1993; Pourret et al., 2007a). The stability constant of bicarbonate increases from La to Lu (Cantrell and Byrne, 1987; Lee and Byrne, 1993), suggesting the enrichment in HREEs in CO_2-rich solution. Enrichment in HREEs and/or U was found in CO_2-rich solutions even at low temperatures in carbonaceous metasedimentary rocks (McLennan and Taylor, 1979), in CO_2-rich natural water (Michard et al., 1987), and in weathered schist (Koppi et al., 1996).

Humic substances are critical for leaching and complexing with REEs during granite weathering as well as carbonate and bicarbonate ions. Chen et al. (2001) leached REEs by 0.01 mol/L organic acids from weathered granites in Guangdong Province and results indicated that HREEs are more selectively leached than LREEs by citric and acetic acids compared with those leached by ammonium sulfate solution. Results of thermodynamic studies indicated that amount of REEs complexed with humic acid are strongly dependent on pH (Glaus et al., 2000; Pourret et al., 2007b; Sonke and Salters, 2006; Takahashi et al., 1997, 1999), and the carboxyl of humic acid is the main binding site of REEs (Pourret et al., 2007b; Takahashi et al., 1997). Fulvic acid is also important for complexation with REEs and has similarity with humic acid (Pourret et al., 2007b). Binding between REEs and humic substances becomes more stable with decreasing ionic radii from La to Lu (Sonke and Salters, 2006; Takahashi et al., 1997), and this suggests that HREEs are more strongly bound to humic substances than LREEs.

Fractionation of LREEs/HREEs is influenced by complexation with carbonate ions, bicarbonate ions, and humic substances during weathering, however, this is less significant than the primary fractionation caused by weathering susceptibilities of initial magmatic and hydrothermal minerals (REE fluorocarbonates, allanite, titanite, etc.) as previously explained. Chondrite-normalized REE patterns of ion-adsorption ores typically reflect those of parent granites (Fig. 41) and fractionation of REEs may occur due to dissolution of specific minerals. Ion-adsorption ores can become enriched in HREEs relative to the parent granite in Longnan because of the dissolution of HREE-rich fluorocarbonate of synchysite-(Y) (Bao and Zhao, 2008; Huang et al., 1989; Wu et al., 1990). In contrast, ion-adsorption ores become

enriched in LREEs relative to the parent granite when the dominant REE minerals being leached are LREE-rich fluorocarbonates, as shown by examples of Heling (Bao and Zhao, 2008).

4.2.6 Adsorption of REE on Clays

Adsorption of REE in soil and weathered rocks is dependent on nature of adsorption materials, and the pH and ionic strength of the solution as reviewed by Laveuf and Cornu (2009). Weathered granites contain various fine-grained weathering products (minerals, amorphous materials, and organic matter) that can adsorb REEs. Previous studies on ion-adsorption ores have shown that kaolinite and halloysite (kaolin group) are most likely to adsorb REE^{3+} ions because they are predominant clays in the ores from southern China (Bao and Zhao, 2008; Chi and Tian, 2009; Chi et al., 2012; Murakami and Ishihara, 2008; Wu et al., 1990, 1993a; Yang, 1987) and from Thailand (Imai et al., 2013; Sanematsu et al., 2013, 2015). Kaolinite (or halloysite) has two types of cation exchange resulting from isomorphous substitution of Al^{3+} for Si^{4+} (permanent charge) and basal surface (variable charge). Ferris and Jepson (1975) and Ma and Eggleton (1999) documented that exchangeable cations of kaolinite occur mostly on the edges and on the basal surface of the mineral. In addition, permanent negative charge from the isomorphous substitution is not very significant in exchangeable cations. Cation exchange capacity is similar for kaolinite and halloysite, and tube halloysite may have a higher capacity (Joussein et al., 2005; Ma and Eggleton, 1999). The cation exchange capacities of kaolinite and halloysite increase with decreasing particle size because of the edge and surface effects. This is strongly dependent on the pH of the solution (Joussein et al., 2005; Ma and Eggleton, 1999).

Other clay minerals such as illite, vermiculite, montmollironite, and amorphous materials are also capable of exchanging REEs because they have permanent charge and/or pH-dependent surface charge (variable charge), which can be expressed as the pH of the point of zero charge (PZC). The surface of minerals and amorphous materials are more positively charged below their own PZCs and they are more negatively charged above the PZCs. Generally silicates and silica have higher PZCs and metal oxides have lower PZCs (Kosmulski, 2009, 2011). PZC of kaolinite is less than 3.6 (Kosmulski, 2009, 2011; Schroth and Sposito, 1997), suggesting that kaolinite is negatively charged in ion-adsorption ores with low pH of 4.1–6.0 (Wei et al., 2001; Wu et al., 1990; Yang and Xiao, 2011) and is capable of adsorbing REEs. Although halloysite lacks data for PZC, it is likely similar to the PZC of kaolinite because of the almost same composition and crystal structure. Cation exchange capacities of 2:1 layer clays such as illite and montmorillonite are generally higher than those of kaolinite and halloysite (eg, Carroll, 1959; Laveuf and Cornu, 2009) because they have both permanent and variable charges. Illite, which is also found in ion-adsorption ores, may adsorb REEs

because its PCZ is ~2.5 (Kosmulski, 2009, 2011). On the other hand, the higher PCZ of montmorillonite (7–9; Kosmulski, 2009, 2011) indicates that montmorillonite is unlikely to adsorb REEs at basal surface because of its positive variable charge. In summary, these PZC values suggest that kaolin-group minerals and/or illite are capable of adsorbing REEs in natural soil and ground water.

Phosphate content strongly influences fractions of ion-exchangeable REEs in weathered granites (Sanematsu et al., 2015), because REEs in mineral phases are mostly incorporated in phosphates (eg, monazite, xenotime, rhabdophane, crandallite group) in weathered rocks. Experimental studies indicate that apatite dissolution rate increases with decreasing pH and is higher than dissolution rates of other phosphates such as monazite at ambient temperatures (Chaïrat et al., 2007; Guidry and MacKenzie, 2003; Harouiya et al., 2007; Oelkers et al., 2008; Valsami-Jones et al., 1998). The apatite dissolution is strongly influenced by rhabdophane precipitation and dissolution in acidic water at room temperature (Köhler et al., 2005). These results suggest that dissolution of apatite and immobilization of REEs by both primary phosphates (monazite and xenotime) and secondary phosphates (rhabdophane and crandallite group) during weathering have an important role in controlling REE concentration in soil and ground waters. Sanematsu et al. (2015) analyzed chemical compositions of weathered granites overlying the contrasting (P_2O_5-rich and -poor) granite suites, and they indicate that high percentages of ion-exchangeable REEs are likely derived from P_2O_5-poor granites (Fig. 45).
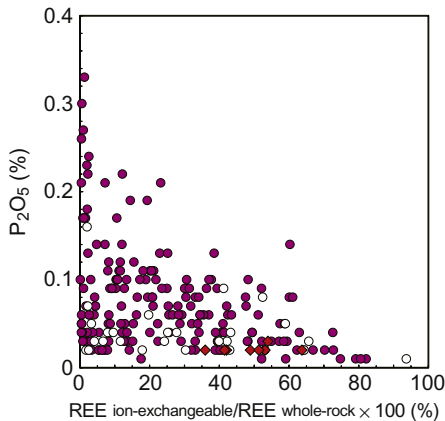
FIG. 45 Plots of P_2O_5 contents vs PERs of weathered granites including ion-adsorption ores in southern China (*diamond*) and Thailand (*circle*). Open circles show hydrothermally altered and weathered granites. *Data from Sanematsu, K., Kon, Y., 2013. Geochemical characteristics determined by multiple extraction from ion-adsorption type REE ores in Dingnan County of Jiangxi Province, South China. Bull. Geol. Surv. Jpn. 64, 313–330; Sanematsu, K., Kon, Y., Imai, A., 2015. Influence of phosphate on mobility and adsorption of REEs during weathering of granites in Thailand. J. Asian Earth Sci. 111, 14–30.*

4.2.7 Denudation or Preservation of Ore Body

Depth of REE ore bodies is variable at different deposits (Figs. 42 and 43), because weathered crusts on granites have been removed by erosion. If a denudation rate is high, an ore body is rarely preserved or crops out on the surface. In contrast, if a denudation rate is low, an ore body is buried deep in a weathering profile. A moderate denudation rate may lead to ore formation in a moderate depth, and this is probably typical in ion-adsorption type deposits in southern China (Bao and Zhao, 2008; Zhang, 1990). The weathered crusts on the Zudong intrusion in the Longnan deposits have a thin REE-leached zone with a positive Ce anomaly up to only 0.7 m deep and a thick REE-accumulation zone (ore body) with a negative Ce anomaly is developed from 0.7 to 19 m deep (Wu et al., 1990). In other deposits of Heiling, Guposhan, and Huashan, the REE-leached zone with a positive Ce anomaly is thin as well (Bao and Zhao, 2008). The thin REE-leached zones suggest that they have been mostly eroded after supplying REEs to the REE-accumulation zone in the lower part of the profile.

Chemical weathering is promoted by the temperate and tropical climate conditions because the chemical weathering rate increases with the increase in annual precipitation and temperature (both are climatic parameters) (Gislason et al., 2009; Oliva et al., 2004; Sanematsu and Watanabe, 2016; Viers et al., 2014; White and Blum, 1995). The ion-adsorption type deposits and prospects were found in the temperate (C) and tropical (A) areas, see Fig. 34 (Köppen, 1936; Peel et al., 2007), because chemical weathering and degradation of REE-bearing minerals are promoted by moderate to high temperatures and high annual precipitation rates. Not only chemical weathering but also moderate mechanical erosion is required to preserve REE ore bodies.

Elevations of granite areas appear to have important roles to preserve the ore bodies as well as climate because they are closely related to denudation (erosion) of weathered rocks (Einsele, 2000). A moderate denudation rate of southern China is preferable for the preservation of weathering profiles including ion-adsorption ore bodies. Ion-adsorption type deposits in southern China were found in low hill areas (Bao and Zhao, 2008), and they are mostly present below an elevation of 550 m (Zhang, 1990). On the other hand, Wang et al. (2013) summarized that the elevation ranges mostly from 160 to 400 m with some exceptions of higher hills in Dingnan (Wang et al., 2013), Guposhan (Li and Shen, 2013), and Long'an as summarized in Table 13. Denudation rate of low hills is compared to that of high mountains (Einsele, 2000; Milliman and Syvitski, 1992), and this likely helps to preserve thick weathering profiles of ion-adsorption ores in southern China (Table 13). Since the denudation rate is controlled by both weathering and transport rates of weathered materials, and thick weathering profiles can be preserved where more weathered rocks can be developed by weathering than can be removed by transport processes (Einsele, 2000). Because the most important transport processes consist of rainfall, surface runoff, and river flow (Einsele, 2000),

thick weathering profiles are likely to be developed in areas with moderate rainfall not to accelerate a transport of weathered materials but to promote chemical weathering. Southern China is located in the areas of temperate climate and the annual temperature is a range of 18–21°C and annual precipitation is a range of 1500–2000 mm on average (Wang et al., 2013). Climates control rainfall and temperature, and they are consistent with denudation rates, which are basically equivalent to annual discharge of suspended sediments from various drainage basins (Einsele, 2000; Milliman and Meade, 1983).

4.2.8 Conclusions

The parent granites for the REE deposits consist mainly of biotite granite and muscovite granite characterized by high SiO_2 content ($SiO_2 \gtrsim 75\%$) and low P_2O_5 contents (<0.08%). The HREE-rich granites are confined to highly differentiated ($SiO_2 \gtrsim 75\%$) muscovite granite and muscovite–biotite granite, which contain fine-grained fluorite and hydrothermal REE minerals formed during deuteric alteration.

The most favorable REE source minerals for formation of ion-adsorption ores are REE fluorocarbonates, synchysite, and bastnäsite, because they release REE^{3+} during weathering and dissolve in low-pH soil water. Allanite and titanite are the subdominant sources of LREEs and HREEs, respectively. In contrast, monazite and xenotime are strongly resistant to chemical weathering. Apatite is altered and replaced by secondary phosphates including rhabdophane and florencite which immobilize REEs during weathering. These results indicate that high P_2O_5 contents in granites are not favorable for ion-adsorption ore formation.

REE-bearing minerals in parent granites are decomposed by acidic soil water and the REEs migrate downward in the weathering profile. The REEs are immobilized by adsorption or incorporation into secondary minerals (mostly phosphates) due to pH increase, which results from the interaction of the soil water with various minerals or higher pH ground water. The REE-leached zone displays a positive Ce anomaly due to the immobile CeO_2, which formed from oxidation of Ce^{3+} to Ce^{4+}. In contrast, the accumulation zone, corresponding to the ion-adsorption ores, exhibits a negative Ce anomaly because the other REE^{3+} are preferentially adsorbed onto weathering products. The weathering profile of the deposits can be divided into a REE-leached zone with positive Ce anomalies in the upper part of the profile and a REE-accumulation zone with negative Ce anomalies in the lower part of the profile.

Many studies suggest that REEs are transported as complexes with carbonate ions, bicarbonate ions, and humic substances and as REE^{3+} ions in soil and ground water. The predominant ligand is dependent on pH and concentration of the species. Previous studies suggest that REEs are most likely to adsorb onto the surface of kaolinite and halloysite in ion-adsorption ores because of their PZCs and abundances of these clays. The fractionation between LREEs and HREEs in ion-adsorption ores is constrained by the weathering

susceptibilities and relative abundances of REE-bearing minerals in parent granites, that is: HREE-rich ion-adsorption ores are derived from HREE-rich granites.

A mild and wet climate (temperate or tropical climate of Köppen–Geiger climate classification), a moderate denudation rate, and a setting of low hills are preferable conditions for both chemical weathering of granite and preservation of thick weathering profiles that may host ion-adsorption ore bodies.

4.3 Introduction to Apatite REE Deposit

Phosphorous is one of the three major nutrients (N, K, P) required by plants and 80–90% of the phosphate mined in the world is used to produce chemical fertilizers. Securing stable supply of phosphate fertilizers is essential to a sustainable food production considering a continuing rapid growth of world population (Van Kauwenbergh et al., 2013). The world resources of phosphate rocks are more than 300 billion tons (U.S. Geological Survey, 2015). Fig. 46 is a distribution map of economic and potentially economic phosphate deposits in the world. "Phosphate rock" is the term generally used in industry to describe mineral assemblages with a high concentration of phosphate minerals, commonly francolite ($Ca_5(PO_4, CO_3)_3(OH, F, Cl)$)—apatite ($Ca_5(PO_4)_3(OH, F, Cl)$) series. There are two main types of phosphate deposits: sedimentary and igneous. The former deposits sometimes are called phosphorite and contain varieties of francolite (CO_2-rich fluorapatite), the latter mainly consists of fluorapatite (F-rich apatite) (Ihlen et al., 2014). Later, we use terms sedimentary and igneous apatite deposit, ore, and rock in sense of phosphate deposit, ore, and rock.

Apatites contain a variety of REEs in concentrations from several thousands of ppm to several wt.%. They are generally enriched in LREEs (eg, Pan and Fleet, 2002; Roeder et al., 1987), however, some apatites are rich in HREEs: apatites in sedimentary phosphate rocks (Emsbo et al., 2015) and deep-sea mud (Kato et al., 2011; Kon et al., 2014), and igneous phosphate rocks (Hoshino et al., 2015; Roeder et al., 1987: apatites containing over 20 wt.% REE_2O_3). In addition, both Th and U contents in apatite are very low in contrast to common REE minerals such as monazite and xenotime, and this may be a big advantage over the other types of REE deposits (eg, alkaline REE deposits). Thus, the extraction of REEs from apatite as by-products in the existing plants for phosphate fertilizer would be highly economically efficient and feasible compared with the development of new REE deposits.

Phosphoric acid for fertilizer is mostly produced from fluorapatite ore (including phosphorite) using sulfuric acid as follows:

$$Ca_5(PO_4)_3F + 5H_2SO_4 + xH_2O \rightarrow 3H_3PO_4 + 5CaSO_4 \cdot x/5H_2O \downarrow + HF \uparrow$$
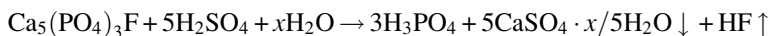
where $x = 0$ for calcium sulfate anhydrate, $x = 0.5$ for hemihydrate, and most commonly $x = 2$ for dihydrate (gypsum) (Peelman et al., 2014; Wang et al., 2010a). This process is also known as the "wet process," and
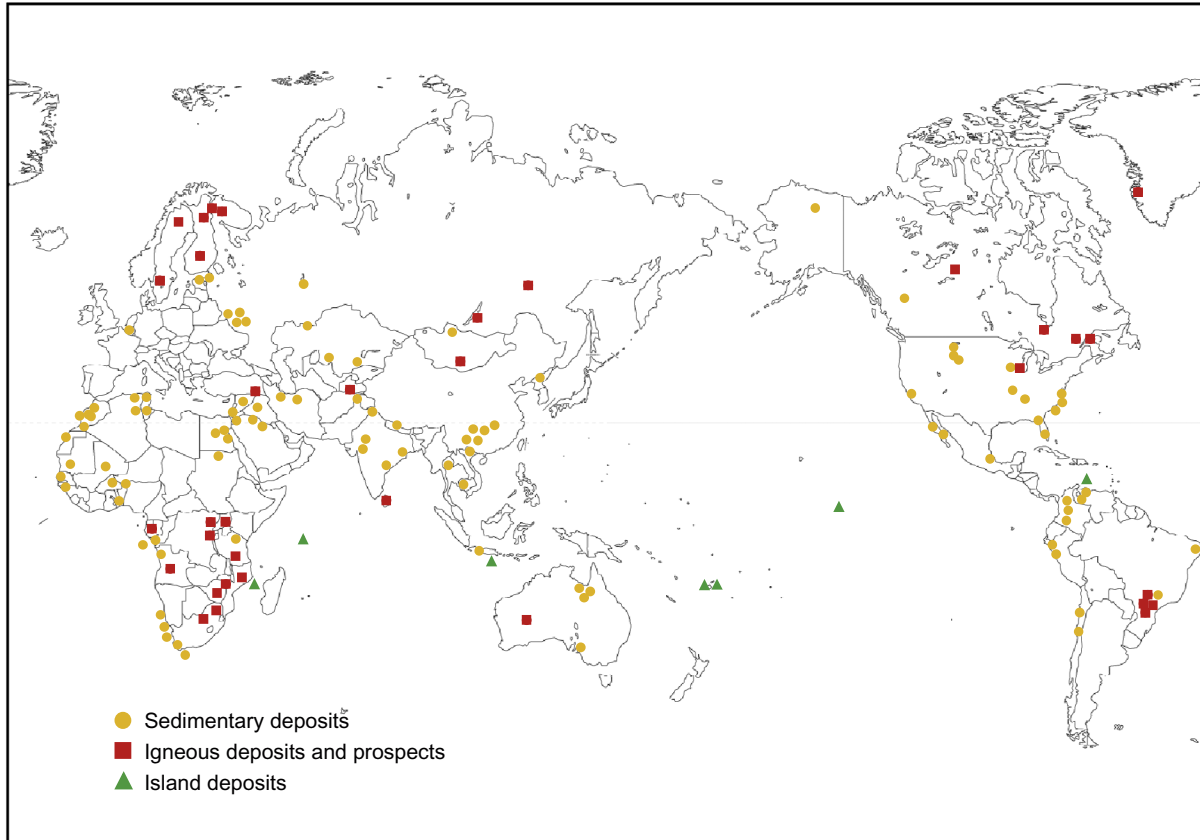
FIG. 46 Distribution map of economic and potentially economic phosphate deposits of the world. *Modified from Van Kauwenbergh, S.J., Stewart, M., Mikkelsen, R., 2013. World reserves of phosphaterock...a dynamic and unfolding story. Better Crops 97, 18–20; Emsbo, P., McLaughlin, P.I., Breit, G.N., du Bray, E.A., Koenig, A.E., 2015. Rare earth elements in sedimentary phosphate deposits: solution to the global REE crisis? Gondwana Res. 27, 776–785.*

gypsum ($CaSO_4 \cdot 2H_2O$) is precipitated as solid residue of this reaction. Gypsum is highly stable and has high partition coefficients for REEs, and thus it is extremely important to study effective methods of REE recovery (eg, solvent extraction, adsorption) in the process of phosphoric acid production from apatite. Many economic igneous phosphate deposits show relatively high REE contents compared to sedimentary phosphate deposits, for example, apatite ores from Khibiny (Kola Peninsula, Russia) and Phalaborwa (South Africa) contains from several thousands to 8000 ppm REEs (Koopman and Witkamp, 2000; Table 14). Although the REE grades are lower than REE ore from Mountain Pass in the United States that contains abundant bastnäsite and monazite (8.9 wt.% of REE_2O_3: Castor, 2008a,b) and than REE-rich alkaline syenite from Nechalacho in Canada that contains zircon and fergusonite as REE host minerals (1.5 wt.% of REE_2O_3: Sheard et al., 2012), REE productions as by-product from apatite ores should be considered due to the earlier mentioned characteristics of apatite.

Apatite crystals show various chemical compositions due to high structural tolerance (Pan and Fleet, 2002), and apatite ore for phosphoric acid production also contains impurities such as Fe, Mg, Si, and Al to some extend (EFMA, 2000). Therefore, studies concerning effective methods for REE recovery form phosphoric acid containing a variety of impurities and low REE contents are extremely important. Although, at the present time, no phosphate deposit producing REEs as by-products of fertilizer production is officially known, recent years have brought some significant progress in this field as mentioned later. In addition, about 80% of the REE in apatite rocks is incorporated into gypsum ($CaSO_4 \cdot 2H_2O$) in the current process for phosphoric acid production from the apatite rocks (Peelman et al., 2014; Zielinski et al., 1993). If REE recovery from the apatite rocks are improved or REEs are recoverable from the residual gypsum, a significant amount of REEs can be produced from the apatite rocks as a by-product of phosphoric acid production.

In Section 4.3.1, we firstly discuss REEs and actinide substitution mechanism of apatite and apatite-group minerals, secondary introduce the classification and variety of apatite deposit types by focusing on REE resource (especially HREEs). We finally present the studies concerning precipitation, solvent extraction and adsorption for REE recovery in the process of phosphoric acid production.

4.3.1 REE and Actinide Crystal Chemistry of Apatite-Group Minerals

The apatite-group minerals of the general formula, $M_{10}(ZO_4)_6X_2$ (M=Ca, Sr, Pb, Na, …, Z=P, As, Si, V, …, and X=F, OH, Cl, …), are remarkably tolerant to structural distortions and chemical substitutions, and consequently, are extremely diverse in chemical composition (eg, Elliott, 1994; Kreidler and Hummel, 1970; McConnell, 1973; Roy et al., 1978). Therefore, many apatite-group minerals occur in nature (Table 15) and more than 100 synthetic

TABLE 14 Summary Data of the Representative Igneous Apatite Deposits and Prospects and Some Phosphorites

Type of Deposit	Subtype	Province	Deposit/ Prospect	Main Commodity	Other REE-Bearing Minerals	Chemical Compositions of Apatite Ores								References
						P_2O_5 (wt.%)	Fe_2O_3	LREEs (ppm)	HREEs (ppm)	LREEs/ HREEs	Dy (ppm)	Th (ppm)	U (ppm)	
Igneous	Carbonatite-pyroxenite	Northeastern Transvaal, South Africa	Phalaborwa	Fluoroapatite		34.18–40.28	9.3–47.51	6463–7528	355–660	16.2–19.7	73.3–82.7	97.2–192	8.84–17.3	EFMA (2000), Ogata et al. (2016), and Watanabe (unpulished data)
	Carbonatite-Laterite	Northeastern Catalo city, Brazile	Catalao	Fluoroapatite	Monazite	2.0–24.9	8.2–77.6	1002–15,630	33.4–639	24.5–62.0	7.8–207.3	10–270	0.1–250	De Oliveira and Imbernon (1998) and Hirano et al. (1990)
	Carbonatite-Laterite	250 km northeast of Kalgoorlie, Westtern Australia	Mt. Weld	Fluoroapatite	Monazite, allanite	1.9–24.7	15.14–66.1	4870–293,073[a]	35–921[b]	27.9–498	–	5–2000	20–1000	Lottermoser (1990)

Continued

TABLE 14 Summary Data of the Representative Igneous Apatite Deposits and Prospects and Some Phosphorites—Cont'd

Type of Deposit	Subtype	Province	Deposit/ Prospect	Main Commodity	Other REE-Bearing Minerals	Chemical Compositions of Apatite Ores								References
						P_2O_5 (wt.%)	Fe_2O_3	LREEs (ppm)	HREEs (ppm)	LREEs/ HREEs	Dy (ppm)	Th (ppm)	U (ppm)	
	Carbonatite-Nepheline syenite	Kola alkalin province, Russia	Khibina, Lesnaya Varaka, Kovdor	Fluoroapatite	Monazite, lueshite, carbocernaite, hydroxyl-bastnäsite, kukharenkoite, anzaite, burbankite, carbocernaite, bastnäsite, synchysite, cordylite, kukharenkoite, ancylite, loparite, britholite, cerite	2.97–10.45	9.30–47.51	152–2403	14.6–144.7	9.2–17.2	1.79–19.6	2.89–53.5	0.23–350	Chakhmouradian and Mitchell (1998) and Zaitsev et al. (2014)
	Cabonatite	The Reynolds Range, 135 km northwest of Alice Springs in Northern Territories, Australia	Nolans	Fluoroapatite	Allanite	28.62–38.37	0.07–2.59	6595–80,653	1670–2612	3.9–31.5	5.1–244	92.4–9836	9.2–1030	Jaireth et al. (2014), Murakami et al. (2011), and Roskill Information Services Ltd (2015)

Nepheline syenite	South Gobi, Mongolia	Mushgai Khudag	Fluoroapatite	Bastnasite, perrierite, parisite, synchysite, monazite	13.33–33.9	1.54–18.55	19,154–122,929	923–3011	16.4–82.4	375–689	8.1–460	23–420	Elsner et al. (2011) and Sanematsu (unpublished data)
IOA mineralization[c] associated with felsic magma	Kiruna area of northern Sweden	Kiirunavaara, Rektron, Henry, Malmberget, Grängesberg	Fluoroapatite	Monazite, allanite	–		1760–5627	469–2530[d]	1.4–4.2	46.7–278	–	–	Frietsch and Perdahl (1995) and Harlov et al. (2002)
IOA mineralization associated with felsic magma	Central Andean Cordillera in the Antogagasta province of northern Chile	EL Laco	Fluoroapatite		–		8806–9033[d]	431–438[e]	20.1–20.9	105	–	–	Rhodes et al. (1999)
IOA mineralization associated with anorogenic rhyolites	95 km southwest of st. Louis, the Pea Ridge Deposit is part of the southeast Missouri Iron Metallogenic Province	Pea Ridge	Fluoroapatite	Monazite, xenotime	29.06[f]	15.73	23,442	1261	18.5	354	129	20.3	Samson and Wood (2005), Whitten and Yancey (1990), and Watanabe (unpublished data)
IOA mineralization associated with gabbro intrution	Approximately 50 km northeast of Bathurst, New Brunswick in Canada	Benjamin River	Fluoroapatite	Allanite	8.48–15.88	12.37–17.44	2052–6734	916–2442	2.5–3.1	96.7–275	32–76.2	4.66–9.45	Hoshino et al. (submitted, unpublished data)

TABLE 14 Summary Data of the Representative Igneous Apatite Deposits and Prospects and Some Phosphorites—Cont'd

Type of Deposit	Subtype	Province	Deposit/ Prospect	Main Commodity	Other REE-Bearing Minerals	Chemical Compositions of Apatite Ores								References
						P_2O_5 (wt.%)	Fe_2O_3	LREEs (ppm)	HREEs (ppm)	LREEs/ HREEs	Dy (ppm)	Th (ppm)	U (ppm)	
	IOA mineralization associated with ferro-edenite and actinolite intrution and their weatherd crust	Bushveld complex, South Africa	Blockspruit	Fluoroapatite	Monazite, xenotime	0.31– 0.84	7.7– 21.1	467– 6398	330– 5282	1.01– 2.44	34– 553	38.5– 553	5– 92.6	Hoshino et al. (2015) and Hoshino (unpublished data)
	Apatite-allanite mineralization associated with lamprophyres and/or carbonatites	The Rae Province in Northen Saskatchewan, Canada	Hoidas Lake	Fluoroapatite	Allanite, monazite	28.42– 38.02	0.08– 0.51	21,210– 37,637	1604– 1843	12.1– 23.4	175– 203	789– 1300	82.2– 140	Halpin (2010) and Hoshino (unpublished data)
Sedimentary	Pelletal phosphorite	Morroco			Francolite	–	33.4	0.2	439	100[d]	4.4	29	–	157	McArthur and Walsh (1984) and EFMA (2000)

	Nodular siliceous phosphorite, platy phosphatised shell debris, subspherical pllets	South Africa		Francolite	–	–	–	39.5–336	12.2–53.9	3.2–6.5	3.4–16	–	–	McArthur and Walsh (1984) and EFMA (2000)
	Phoshorite	Florida, United States		Francolite	–	34.3	1.1	322	62.4[d]	5.2	17	–	85.6	McArthur and Walsh (1984) and EFMA (2000)
	Steinkerns and nodular concretion of phosphorite	New York State, United States		Francolite	–	–	–	2387–2817	583–725[d]	3.8–4.1	160–205	–	–	McArthur and Walsh (1984)

– No data and description.
[a]Only La, Ce, Nd, Sm, Eu.
[b]Only Tb, Yb, Lu.
[c]Similar to Kiruna-type.
[d]Not include Y.
[e]Apatite separated by hand pick and magnetic separation.
[f]Apatite concentrates.

TABLE 15 Representative Apatite-Group Minerals

Mineral Name	Endmember Formula (Reduced)	Space Group	Supergroup Type
Phosphate			
Fluorapatite	$Ca_5(PO_4)_3F$	$P6_3/m$	Apatite
Hydroxyapatite	$Ca_5(PO_4)_3(OH)$	$P2_1/b$	Apatite
Chlorapatite	$Ca_5(PO_4)_3Cl$	$P2_1/b$	Apatite
Alforsite	$Ba_5(PO_4)_3Cl$	$P6_3/m$	Apatite
Pyromorphite	$Pb_5(PO_4)_3Cl$	$P6_3/m$	Apatite
Pieczkaite	$Mn_5(PO_4)_4Cl$	$P6_3/m$	Apatite
Belovite-(La)	$(Sr,Na,La)_5(PO_4)_3(OH)$	$P\bar{3}$	Belovite
Belovite-(Ce)	$(Sr,Na,Ce)_5(PO4)_3(OH)$	$P\bar{3}$	Belovite
Deloneite-(Ce)	$(Na,Ca,Sr,Ce)_5(PO4)_3F$	$P3$	Belovite
Carlgieseckeite-(Nd)	$NaNdCa_3(PO_4)_3F$	$P\bar{3}$	Belovite
Kuannersuite-(Ce)	$NaCeBa_3(PO_4)_3F_{0.5}Cl_{0.5}$	$P\bar{3}$	Belovite
Fluorcaphite	$SrCaCa_3(PO_4)_3F$	$P6_3$	Belovite
Fluorphosphohedyphane	$Ca_2Pb_3(PO_4)_3F$	$P6_3/m$	Hedyphane
Miyahisaite	$(Sr,Ca)_2Ba_3(PO_4)_3F$	$P6_3/m$	Hedyphane
Phosphohedyphane	$Ca_2Pb_3(PO_4)_3Cl$	$P6_3/m$	Hedyphane
Arsenate			
Svabite	$Ca_5(AsO_4)_3F$	$P6_3/m$	Apatite
Johnbaumite	$Ca_5(AsO_4)_3(OH)$	$P6_3/m$	Apatite
Mimetite	$Pb_5(AsO_4)_3Cl$	$P6_3/m$	Apatite
Turneaureite	$Ca_5(AsO_4)_3Cl$	$P6_3/m$	Apatite
Hedyphane	$(Pb,Ca)_5(AsO_4)_3Cl$	$P6_3/m$	Hedyphane
Morelandite	$Ba_5(AsO_4)_3Cl$	$P6_3/m$ or $P6_3$	Hedyphane
Silicate			
Britholite-(Ce)	$(Ce,Ca)_5(SiO_4)_3(OH)$	$P6_3/m$	Britholite
Britholite-(Y)	$(Y,Ca)_5(SiO_4)_3(OH)$	$P6_3/m$	Britholite
Fluorbritholite-(Ce)	$(Ce,Ca)_5(SiO_4)_3F$	$P6_3/m$	Britholite
Fluorbritholite-(Y)	$(Y,Ca)_5(SiO_4)_3F$	$P6_3/m$	Britholite

Continued

TABLE 15 Representative Apatite-Group Minerals—Cont'd

Mineral Name	Endmember Formula (Reduced)	Space Group	Supergroup Type
Fluorcalciobritholite	$(Ca,REE)_5(SiO_4,PO_4)_3F$	$P6_3/m$	Britholite
Chlorellestadite	$Ca_5(SiO_4,SO_3)_3Cl$	$P6_3$ or $P6_3/m$	Ellestadite
Fluorellestadite	$Ca_5(SiO_4,SO_3)_3\,F$	$P6_3/m$	Ellestadite
Hydroxylellestadite	$Ca_5(SiO_4,SO_3)_3(OH)$	$P2_1/m$	Ellestadite
Mattheddleite	$Pb_5(SiO_4,SO_4)_3Cl$	$P6_3/m$	Ellestadite
Borosilicate			
Melanocerite-(Ce)	$Ce_5(Si,B)_3O_{12}(OH,F)\cdot nH_2O$	?	Britholite
Tritomite-(Ce)	$Ce_5(Si,B)_3(O,OH,F)_{13}$	$P6_3/m$	Britholite
Tritomite-(Y)	$Y_5(Si,B)_3(O,OH,F)_{13}$	$P6_3/m$	Britholite
Sulfate			
Aiolosite	$Na_2(Na_2Bi)(SO_4)_3Cl$	$P6_3/m$	Hedyphane
Cesanite	$(Na,Ca)_5(SO_4)_3(OH)$	$P6_3/m$	Hedyphane
Caracolite	$(Na,Pb)_5(SO_4)_3Cl$	$P2_1/m$	Hedyphane
Vanadate			
Vanadinite	$Pb_5(VO_4)_3Cl$	$P6_3/m$	Apatite

After Pan, Y., Fleet, M.E., 2002. Compositions of the Apatite-group minerals: substitution mechanisms and controlling factors. In: Kohn, M.J., Rakovan, J., Hughes, J.M. (Eds.), Phosphates—Geochemical, Geobiological, and Materials Importance, Reviews in Mineralogy and Geochemistry, vol. 48, 13–49; Pekov, I.V., Zubkova, N.V., Husdal, T.A., Kononkova, N.N., Aqakhanov, A.A., Zadov, A.E., Pushcharovsky, D.Y., 2012. Carlgesecieite-(Nd), NaNdCa₃(PO₄)₃F, a new belovite-group mineral species from the Ilímaussaq alkaline complex, south Greenland. Can. Mineral. 50, 571–580; Hughes, J.M., Rakovan, J.F., 2015. Structurally robust, chemically diverse: apatite and apatite supergroup minerals. Elements 11, 165–170.

compounds with apatite structure have been reported (Pan and Fleet, 2002). According to the differences in formation environment of the natural apatite-group minerals, various chemical substitutions occur among them to yield varieties of the chemical compositions in apatite-group minerals. Hence it is fundamentally important to understand the substitution mechanisms and other factors, both intrinsic and extrinsic, that control the compositional variations in the apatite (Pan and Fleet, 2002).

Based on which anion, ie, fluorine, OH⁻, or chlorine is dominant on the halogen site, apatite is, respectively, divided into fluorapatite, hydroxyapatite,

and chlorapatite. Among the three, fluorapatite and oxy are by far the most common in nature. Fluorapatite is ubiquitous accessory phase in igneous, metamorphic, and sedimentary rocks and a major constituent in phosphorites and certain carbonatites and anorthosites (Dymek and Owens, 2001; McConnell, 1973). Of particular importance in biological systems, hydroxy-apatite and fluorapatite (and their carbonate-bearing varieties) are important mineral components of bones, teeth, and fossils (Ivanova et al., 2001; Kon et al., 2014; McConnell, 1973).

It was reported that apatite crystals may incorporate up to 21 wt.% REE_2O_3 (Hoshino et al., 2015; Hughes et al., 1991; Roeder et al., 1987). Four main types of charge-compensating mechanisms have been proposed for the substitution of Ca^{2+} by REE^{3+} (and Y^{3+}) in apatite (Chen et al., 2002a,b; Cherniak, 2000; Comodi et al., 1999; Felsche, 1972; Fleet and Pan, 1995; Ito, 1968; Roeder et al., 1987; Rønsbo, 1989; Serret et al., 2000):

$$REE^{3+} + X^{2-} = Ca^{2+} + F^- \tag{1}$$

$$2REE^{3+} + \square(vacancy) = 3Ca^{2+} \tag{2}$$

$$REE^{3+} + Na+ = 2Ca^{2+} \tag{3}$$

$$REE^{3+} + SiO_4{}^{4-} = Ca^{2+} + PO_4{}^{3-} \tag{4}$$
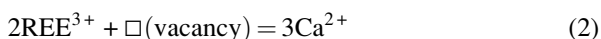
In these coupled substitutions, the mechanisms (1) and (2) are reported only in synthetic compounds with apatite structure and not in natural apatite. On the other hand, (3) and (4) are generally observed in nature. Apatite-group minerals including REEs as major elements are named belovite and britholite (Table 15); the coupled substitutions (3) and (4) are largely responsible for accommodating REEs into belovite and britholite, respectively (Pan and Fleet, 2002). This suggests that the coupled substitution mechanisms between the two minerals and apatite are very important for REE incorporation into natural apatite.

Substitution (3) is well established on the basis of compositional data from natural apatite (eg, Comodi et al., 1999; Peng et al., 1997; Roeder et al., 1987; Rønsbo, 1989; Table 16) and is largely responsible for accommodating REEs into belovites (eg, Pekov et al., 1996; Rakovan and Hughes, 2000). Incorporation of REEs into apatite by (3) results in the apatite coincidentally containing high concentrations of alkaline elements like Na. Therefore, the substitution of (3) is often observed for apatite in alkaline rocks including carbonatites. LREE-rich apatite-group minerals including belovite-(Ce) and belovite-(La) have been reported, no HREE-rich one was found in nature. Therefore, apatites formed as a result of coupled substitution (3) tend to enrich in LREEs. Belovite contains Sr as major element, which indicates that apatites occurring via coupled substitution (3) characteristically show substitution of Sr for Ca. Interestingly, Th content in belovite is below the detection limit by EMPA (eg, Pekov et al., 1996), which results in extremely low Th contents in the apatites occurring as a result of coupled substitution (3).

TABLE 16 Major and Trace Elements Compositions of Apatite from IOA and Carbonatite Deposits and Prospects

Occurrence	HREE-Rich Apatite from Benjamin River IOA Prospect (Hoshino et al., submitted)			HREE-Rich Apatite Blockspruit IOA Prospect (Hoshino et al., 2015; Hoshino, Unpublished Data)		LREE-Rich Apatite Hoidas Lake Deposit (Halpin, 2010)		Apatite Kiirunavaara IOA Deposit (Harlov et al., 2002)		Apatite Se-Chahun IOA Deposit (Bonyadi et al., 2011)		Apatite from Kola Carbonatite-Nepheline (Salmagorskii Complex, Korobeinikov et al., 1998)	
wt.% by EMPA	Dark Zone	Bright Zone	Porous Zone	REE-Poor Apatite (rim)	REE-Rich Apatite (core)	REE-Poor Apatite (no. 3792013)	REE-Rich Apatite (no. 379063)	REE-Poor Apatite (KJU-4)	REE-Rich Apatite (KJU-4)	Dark Zone[a]	Bright Zone[b]	Core	Rim
SiO_2	0.73	1.18	0.28	0.74	6.69	0.23	2.39	0.04	0.17	0.14	0.19	Bdl.	Bdl.
Na_2O	Bdl.	Bdl.	Bdl.	Bdl.	Bdl.	Bdl.	Bdl.	0.04	0.22	Bdl.	0.23	Bdl.	Bdl.
CaO	52.33	51.33	54.00	52.60	40.48	54.42	48.38	55.3	54.2	53.23	51.64	54.95	55.31
SrO	Bdl.	Bdl.	Bdl.	Bdl.	Bdl.	0.70	1.30	0.05	0.04	Bdl.	Bdl.	1.92	1.67
P_2O_5	40.35	39.25	40.88	43.21	29.51	41.61	36.78	42.0	41.6	40.79	40.17	41.64	41.96
As_2O_5	Bdl.	Bdl.	Bdl.	Bdl.	Bdl.	Bdl.	Bdl.	Bdl.	Bdl.	Bdl.	0.03	Bdl.	Bdl.
SO_3	Bdl.	Bdl.	Bdl.	Bdl.	0.02	0.03	0.56	0.01	0.24	Bdl.	0.07	Bdl.	Bdl.
ThO_2	Bdl.	Bdl.	Bdl.	Bdl.	0.24	0.11	0.22	Bdl.	Bdl.	Bdl.	Bdl.	Bdl.	Bdl.
UO_2	Bdl.	Bdl.	Bdl.	Bdl.	0.21	Bdl.	Bdl.	Bdl.	Bdl.	Bdl.	Bdl.	Bdl.	Bdl.
K_2O	Bdl.	Bdl.	Bdl.	Bdl.	0.02	Bdl.	Bdl.	Bdl.	Bdl.	Bdl.	Bdl.	Bdl.	Bdl.

TABLE 16 Major and Trace Elements Compositions of Apatite from IOA and Carbonatite Deposits and Prospects—Cont'd

Occurrence	HREE-Rich Apatite from Benjamin River IOA Prospect (Hoshino et al., submitted)			HREE-Rich Apatite Blockspruit IOA Prospect (Hoshino et al., 2015; Hoshino, Unpublished Data)		LREE-Rich Apatite Hoidas Lake Deposit (Halpin, 2010)		Apatite Kiirunavaara IOA Deposit (Harlov et al., 2002)		Apatite Se-Chahun IOA Deposit (Bonyadi et al., 2011)		Apatite from Kola Carbonatite-Nepheline (Salmagorskii Complex, Korobeinikov et al., 1998)	
wt.% by EMPA	Dark Zone	Bright Zone	Porous Zone	REE-Poor Apatite (rim)	REE-Rich Apatite (core)	REE-Poor Apatite (no. 3792013)	REE-Rich Apatite (no. 379063)	REE-Poor Apatite (KJU-4)	REE-Rich Apatite (KJU-4)	Dark Zone	Bright Zone	Core	Rim
FeO	0.09	0.08	0.03	0.10	0.19	Bdl.	Bdl.	0.06	0.05	0.00	0.16	Bdl.	Bdl.
MnO	Bdl.	Bdl.	Bdl.	Bdl.	Bdl.	Bdl.	Bdl.	0.02	0.02	Bdl.	Bdl.	Bdl.	Bdl.
PbO	Bdl.	Bdl.	Bdl.	0.04	0.03	Bdl.	Bdl.	Bdl.	Bdl.	Bdl.	Bdl.	Bdl.	Bdl.
Y_2O_3	0.34	0.52	0.20	1.50	6.61	Bdl.	0.07	0.02	0.06	0.09	0.18	Bdl.	Bdl.
La_2O_3	0.40	0.58	0.08	Bdl.	1.69	0.04	1.23	0.02	0.18	0.02	0.30	Bdl.	Bdl.
Ce_2O_3	0.91	1.37	0.23	0.18	5.21	0.14	3.71	0.03	0.46	0.15	0.69	0.25	0.19
Pr_2O_3	0.10	0.16	0.03	Bdl.	0.57	0.10	0.36	Bdl.	Bdl.	Bdl.	Bdl.	Bdl.	Bdl.
Nd_2O_3	0.45	0.71	0.13	0.26	2.99	0.11	1.39	0.02	0.19	0.03	0.30	Bdl.	Bdl.
Sm_2O_3	0.07	0.13	0.03	0.21	0.5	Bdl.	Bdl.	Bdl.	Bdl.	Bdl.	Bdl.	Bdl.	Bdl.
Gd_2O_3	0.16	0.26	0.07	0.09	0.77	0.04	Bdl.	Bdl.	Bdl.	Bdl.	Bdl.	Bdl.	Bdl.

Tb$_2$O$_3$	Bdl.	Bdl.	Bdl.	0.01	0.05	Bdl.	Bdl.	Bdl.	Bdl.	Bdl.	Bdl.	Bdl.	Bdl.
Dy$_2$O$_3$	0.08	0.13	0.04	0.17	0.83	Bdl.	Bdl.	Bdl.	Bdl.	Bdl.	Bdl.	Bdl.	Bdl.
Ho$_2$O$_3$	0.05	0.06	0.03	Bdl.	0.20	Bdl.	Bdl.	Bdl.	Bdl.	Bdl.	Bdl.	Bdl.	Bdl.
Er$_2$O$_3$	Bdl.	Bdl.	Bdl.	0.13	0.61	Bdl.	Bdl.	Bdl.	Bdl.	Bdl.	Bdl.	Bdl.	Bdl.
Yb$_2$O$_3$	Bdl.	Bdl.	Bdl.	0.07	0.29	Bdl.	Bdl.	Bdl.	Bdl.	Bdl.	Bdl.	Bdl.	Bdl.
F	2.21	2.09	2.28	2.61	2.48	2.65	3.54	3.76	3.55	3.09	2.80	3.23	2.72
Cl	0.70	0.68	0.17	0.02	0.08	0.05	0.30	0.04	0.06	0.37	1.00	0.05	n.d.
	99.01	98.53	98.48	101.95	100.27	100.23	100.23	101.41	101.04	97.92	97.74	102.04	101.85
$\sum$HEE$_2$O$_3$	0.63	0.97	0.34	1.97	9.36	0.04	0.07	0.02	0.06	0.09	0.18	Bdl.	Bdl.
$\sum$REE$_2$O$_3$	2.56	3.92	0.84	2.63	20.3	0.43	6.76	0.09	0.83	0.29	1.47	0.25	0.19
(ppm) by LA-ICP-MS													
Sr	385 (32)[c]	454 (57)	236 (84)		140 (8)			–	–	206	273		
Y	3179 (490)	6041 (1200)	2264 (764)		22,154 (9223)			844	909	806	1037		
La	2568 (616)	4128 (1239)	711 (140)		10,398 (1596)			454	1307	1772	1581		
Ce	8458 (2584)	13,196 (3302)	2216 (467)		28,398 (5331)			1137	2856	4279	4030		
Pr	840 (127)	1267 (202)	279 (62)		3415 (765)			163	377	442	414		
Nd	3370 (712)	5426 (1076)	1139 (220)		13,902 (3327)			670	1407	1571	1469		

TABLE 16 Major and Trace Elements Compositions of Apatite from IOA and Carbonatite Deposits and Prospects—Cont'd

Occurrence	HREE-Rich Apatite from Benjamin River IOA Prospect (Hoshino et al., submitted)			HREE-Rich Apatite Blockspruit IOA Prospect (Hoshino et al., 2015; Hoshino, Unpublished Data)		LREE-Rich Apatite Hoidas Lake Deposit (Halpin, 2010)		Apatite Kiirunavaara IOA Deposit (Harlov et al., 2002)		Apatite Se-Chahun IOA Deposit (Bonyadi et al., 2011)		Apatite from Kola Carbonatite-Nepheline (Salmagorskii Complex, Korobeinikov et al., 1998)	
wt.% by EMPA	*Dark Zone*	*Bright Zone*	*Porous Zone*	*REE-Poor Apatite (rim)*	*REE-Rich Apatite (core)*	*REE-Poor Apatite (no. 3792013)*	*REE-Rich Apatite (no. 379063)*	*REE-Poor Apatite (KJU-4)*	*REE-Rich Apatite (KJU-4)*	*Dark Zone*	*Bright Zone*	*Core*	*Rim*
Sm	667 (109)	1212 (200)	298 (60)		2993 (922)			138	223	229	232		
Eu	46 (12)	70 (17)	16 (4)		155 (28)			19	29	14	21		
Gd	736 (121)	1447 (354)	383 (83)		2857 (916)			164	207	194	213		
Tb	103 (17)	199 (33)	16 (12)		554 (114)			23	27	23	27		
Dy	554 (101)	1121 (292)	382 (60)		3331 (1233)			135	149	129	163		

Ho	113 (17)	230 (48)	83 (16)	837 (167)		28	30	24	32		
Er	278 (48)	560 (120)	210 (44)	2295 (571)		77	83	61	83		
Tm	36 (7)	71 (15)	27 (6)	328 (67)		10	11	7	10		
Yb	200 (35)	383 (89)	145 (39)	1471 (378)		56	61	39	57		
Lu	22 (4)	38 (8)	16 (5)	132 (28)		8	9	5	7		
Th	118 (28)	274 (65)	78 (16)	1202 (426)		–	–	300	806		
U	35 (9)	55 (13)	13 (4)	640 (226)		–	–	4	56		
Total LREE	15,949	25,299	4659	59,261		2581	6199	8307	7746		
Total HREE	4485	10,090	3443	33,959		501	1486	1287	1629		
Total REE	20,434	35,389	8102	93,220		3082	7685	9594	9375		
LREE/HREE	3.56	2.51	1.35	1.75		5.15	4.17	6.46	4.76		

Bdl: below detection limit. n.d.: not determined. –: no data.
[a]Dark zone for EMPA: average of data from X 205–2 to To22-a-1 of Table 3 in Bonyadi et al. (2011). Dark zone for LA-ICP-MS: average of data from 105–140 to 280–315 of Table 4 in Bonyadi et al. (2011).
[b]Bright zone for EMPA: average of data from X205-2 to To22-10 of Table 3 in Bonyadi et al. (2011). Bright zone for LA-ICP-MS: average of data from 315–350 to 560–595 of Table 4 in Bonyadi et al. (2011).
[c]Number in parentheses is standard deviation.

Substitution (4) is also well documented in natural REE-bearing apatites (Comodi et al., 1999; Roeder et al., 1987; Rønsbo, 1989) and is supported by a complete solid solution between hydroxyapatite and britholite-(Y) (Ito, 1968; Khudolozhkin et al., 1973). This substitution leads to the endmember $Ca_4REE_6(SiO_4)_6F_2$, which has been synthesized for compositions involving La, Ce, Nd, and Y (Ito, 1968; Mayer et al., 1974). As mentioned earlier, belovite is only LREE type of La- and Ce-type, but Ce- and Y-type for britholite have been reported. Therefore, there are both LREE-rich and HREE-rich types of apatite formed via substitution (4). Britholite typically occurs in alkaline rocks and pegmatite in the metamict state. It has been reported that britholite contains up to 21 wt.% ThO_2 and 3.5 wt.% UO_2 (Table 6). Compositional data (Baumer et al., 1983; Hughson and Sen Gupta, 1964) have shown that Th^{4+} ions substitute for Ca^{2+} via:

$$Th^{4+} + \square(vacancy) = 2Ca^{2+} \tag{5}$$
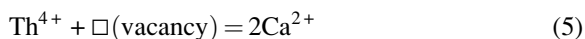
Similarly, Clarke and Altschuler (1958) suggested that U in apatite is mainly tetravalent and that U^{4+} ions occupy the Ca sites via a similar substitution (Baumer et al., 1983):

$$U^{4+} + \square(vacancy) = 2Ca^{2+} \tag{6}$$
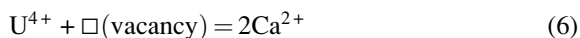
Therefore, apatite with britholite substitution (4) contains relatively high Th contents compared to apatite with belovite substitution (3), but U is below detection limit by EMPA (Table 16).

Incorporation of REEs into natural apatite is caused by belovite-type and/or britholite-type substitution (Pan and Fleet, 2002) and may be related to the alkalinity and the silica saturation in melt (Roeder et al., 1987; Watson and Green, 1981). Britholite substitution is important for HREE, Th, and U incorporation into apatite.

4.3.2 Apatite REE Deposits

Most of phosphate fertilizers are produced from apatite ores. As mentioned earlier, apatite deposits are divided into S- and I-types which are distributed all over the world (Fig. 46). Sedimentary apatite deposits are exploited to produce more than 80% of the total world production of apatite rocks (Ihlen et al., 2014; Van Kauwenbergh et al., 2013). Sedimentary phosphate deposits occurred throughout the long geological time scale from Precambrian to Recent, but most of them are located in the great Cenozoic deposits of North Africa including Morocco, Tunisia, and Algeria (Van Kauwenbergh, 2010), and the United States and southeast Atlantic (Emsbo et al., 2015, 2016; Manheim and Gulbrandsen, 1979; Van Kauwenbergh, 2010). Most sedimentary phosphorite deposits were apparently formed in continental and ocean basin margins (Fig. 46). Their phosphorous were mainly derived from deep oceanic source associated with upwelling currents of cold, nutrient-rich waters

(Manheim and Gulbrandsen, 1979; Trappe, 1998). Some sedimentary phosphorite deposits are biogenic and are derived mainly from excrement of seabirds (guano: island deposits in Fig. 46). Most of the world's guano deposits have been already mined out, and the current resource is much smaller than that of the other sedimentary phosphate deposits. Igneous apatite deposits are often associated with carbonatites and/or alkalic (silica deficient) intrusions which generally occurred in Paleozoic age (Notholt, 1979). Igneous apatite rocks are mainly exploited in Russia, the Republic of South Africa, Brazil, Sweden, Finland, and Zimbabwe (Fig. 46). Commercial apatite ores vary in grade from over 37% P_2O_5 to less than 25% P_2O_5 (Van Kauwenbergh, 2010). Although present resources of apatite rock are large, the general high demand has over the years lead to a progressive depletion of high-grade ores and ores of good quality with few contaminants. The economic grade of a sizable igneous apatite deposit is now 4–5 wt.% P_2O_5 (Ihlen et al., 2014). The igneous ores are generally lower grade in terms of phosphate content compared to sedimentary ones, but give higher quality beneficiation products with low contents of unwanted impurities (eg, Cd, As, U, Th, Mg, and Al).

Depending on their origin (igneous or sedimentary), apatite rocks have different mineralogical, textural, and chemical characteristics (Van Kauwenbergh, 2010). As mentioned earlier, one of the significant differences is the variety of apatite-group minerals occurring from each origin: francolite predominates in sedimentary apatite rocks, while fluorapatite predominates in igneous apatite rocks. Francolite is defined as apatite that contains significant CO_2 with >1% fluorine (McConnell, 1938) and contains CO_2 up to 7 wt.% (Van Kauwenbergh, 2010). On the other hand, the fluorapatite associated with igneous source rocks forms at the various stages such as primary magmatic and hydrothermal stages (eg, Ihlen et al., 2014).

As mentioned earlier, apatite contains a variety of REE concentrations (several thousand ppm to several wt.%), due to substitution of REEs for Ca in the apatite structure. REE extraction from apatite rocks as by-product of phosphoric acid production would be economically efficient because of the high cost for development of new REE deposits. From this perspective, recently, several evaluations on REE resource potential of apatite rocks are published. For example, Ihlen et al. (2014) investigated the REE resource potential of various apatite deposits in Norway. REE contents in sedimentary phosphate rocks are several ppm at most and those in igneous apatite ores are up to 30% (Table 14), but size of deposits for the former is much larger than the latter. Thus, both types of the apatite deposits are well worth studying as new REE resources for the future.

Table 16 shows the variation in chemical analyses of REE-rich apatite grains from some igneous phosphate deposits and prospects. These deposits are accompanied by carbonatite, nepheline syenite, and IOA deposits. It is notable that HREE-rich apatite occur in IOA deposits which are corresponding to "Kiruna-type" deposits. The origin of this deposit type has

been a matter of substantial debate for over 100 years, and several fundamentally different modes of formation have been suggested (Jonsson et al., 2013). These include direct magmatic segregation or crystallization, magmatic–hydrothermal replacement, and hydrothermal precipitation in the sense of iron oxide–copper–gold (IOCG-type) deposits (eg, Jonsson et al., 2013). Fig. 47 shows chondrite-normalized REE pattern of apatite ores from various igneous and sedimentary apatite deposits and prospects. Apatite ores from carbonatite and nepheline syenite generally show LREE-rich patterns, while those from the Benjamin River and the Blockspruit IOA prospects show quite HREE-rich patterns (Fig. 47).

In this review, we will discuss the REE potential of igneous apatite referring the case studies in Benjamin River (Canada) and Blockspruit (South Africa)
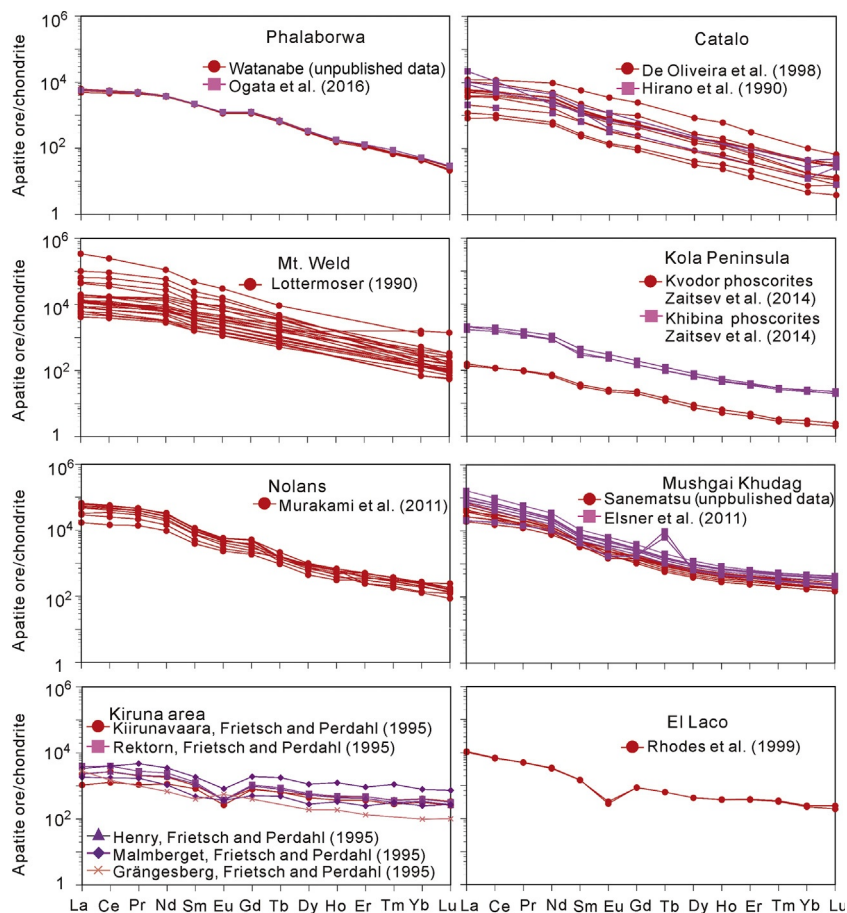
FIG. 47 Chondrite-normalized REE patterns for apatite ores from the representative igneous apatite deposits and phosphorite deposits (sedimentary).
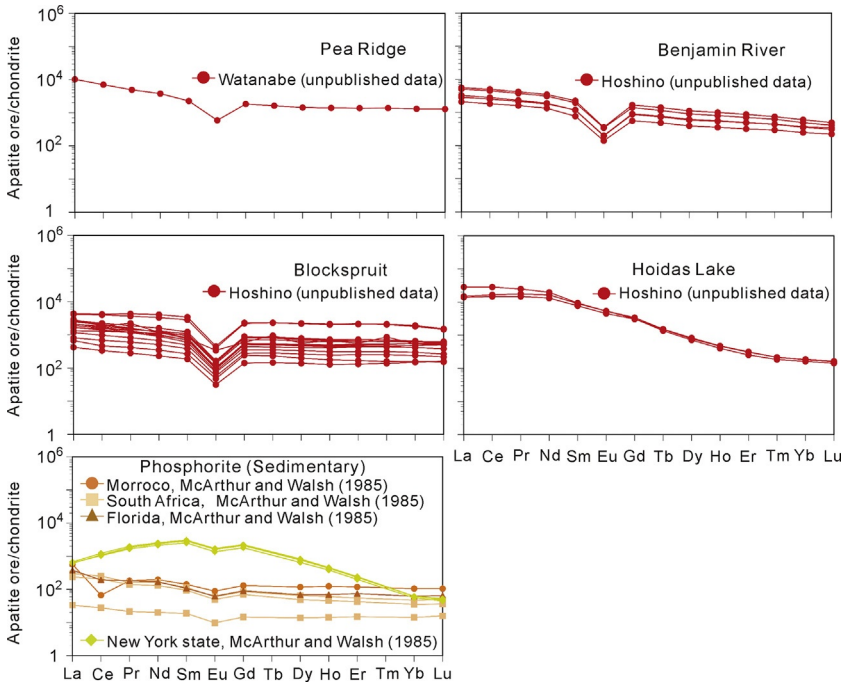
FIG. 47—Cont'd

both of which are HREE-rich IOA prospects. Then the REE potential of sedimentary apatite will be mentioned. Recently, HREE-bearing apatite in deep-sea mud (unsolidified marine sediments) has attracted considerable attention (eg, Kon et al., 2014; Nakamura et al., 2015; Yasukawa et al., 2014). In addition, Emsbo et al. (2015) reported that HREE-bearing apatite in sedimentary apatite deposits (phosphorites) has large potential as a REE resource. We will briefly introduce their and others results concerning such sedimentary apatite in both deep-sea mud and sedimentary apatite deposits.

4.3.2.1 HREE-Rich Apatite Prospects and Deposits: Benjamin River HREE-Rich IOA Prospect, Canada

The Benjamin River IOA prospect is hosted by a gabbro-granite plutonic complex approximately 50 km northwest of Bathurst, New Brunswick in Canada. The prospect area is underlain mainly by Silurian volcanic rocks of the Chaleur Group which are intruded by small gabbro-granite plutonic complexes (Fig. 48). The Chaleur Group in the prospect area is composed of sub-aerial mafic volcanic rocks of the Bryant Point Formation and felsic volcanic rocks of the Benjamin Formation, in which rhyolite is dated as 420.8 ± 0.4 Ma
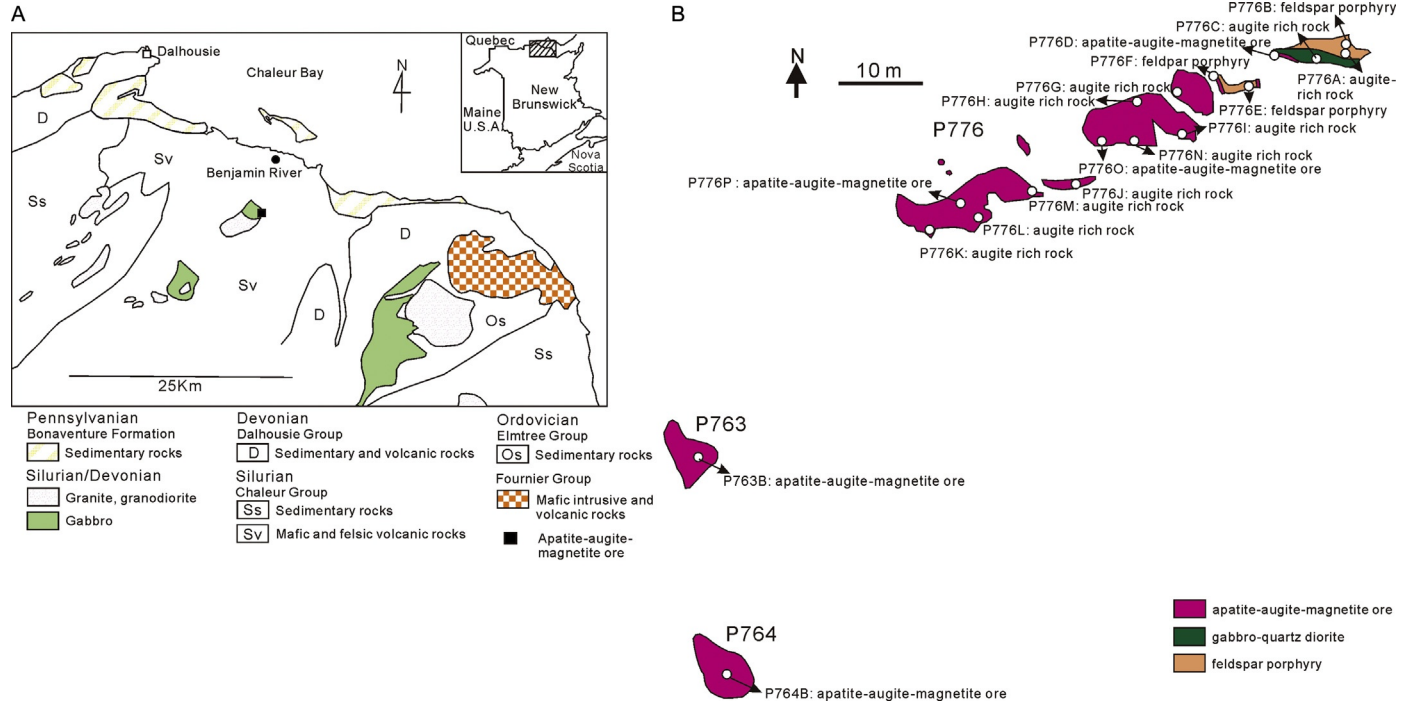
FIG. 48 Regional geology and location of the Benjamin River deposit (A). Route map along the trench at *solid square* in A (B). *Panel A: After Davies, J.L., 1979. Geology map of northern New Brunswick: New Brunswick Department of Natural Resources, Map NR-3; Sinclair, W.D., Kingston, D.M., 1990. Rare-earth-bearing apatite near Benjamin River, northern New Brunswick. Geol. Surv. Can. 90-1B, 95–104. Panel B: From Hoshino, M., Watanabe, Y., Kon, Y. Contribution of apatite to the crystallization of allanite in an Iron-Oxide-Apatite (IOA) prospect, Benjamin River, Canada. Resour. Geol. (submitted).*

by U-Pb zircon method (Wilson and Kamo, 2008). The prospect contains apatite–augite–magnetite ores, gabbro-quartz–diroite and feldspar porphyry. A major lensoidal pegmatite apatite–augite–magnetite ore body, 100 m long and 10–20 m wide in size (Fig. 48), is associated with gabbro-quartz–diroite and feldspar porphyry of the complex. Apatite within the pegmatite ore body (Fig. 48) is heterogeneously distributed and apatite crystals are randomly oriented, although in places, it is concentrated in layers in which apatite crystals are oriented normal to the laying (Sinclair and Kingston, 1990). Apatite is commonly euhedral and deep pink in color, ranging in size up to a few centimeters (Fig. 49). Augite, dark green in color, is interstitial to apatite. Euhedral to subhedral magnetite occurs at a later pargenetic stage and magnetite veins are present in the pegmatite ore body. Relative amounts of these three minerals are variable in outcrops.

Major REE minerals in Benjamin river prospect are apatite and allanite (Hoshino et al., submitted). The Mineral Liberation Analyzer™ (MLA) results show that apatite–augite–magnetite ores contain 16–60% apatite and 0.7–1.7% allanite together with REE-rich epidote in addition to augite (31.7–75.9%) and magnetite (1.4–6.5%). REE-rich apatite in the Benjamin River prospect contains up to 5.24 wt.% REE_2O_3 (1.6 wt.% $HREE_2O_3$) and shows high HREE distribution (Table 16 and Fig. 50; Hoshino et al., submitted). This result is noteworthy, considering that REE contents of apatite grains from general IOA deposits (Kiirunavaara, Se-Chahun) are 9500 ppm at most and very low, especially HREEs (Table 16). Na_2O in apatite from Benjamin River prospect, was observed for the representative other IOA deposits,
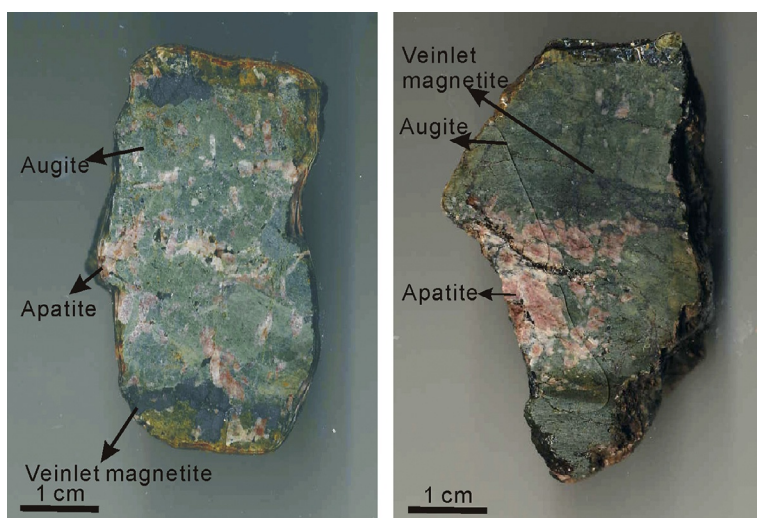
FIG. 49 Photographs of apatite–augite–magnetite ores. *From Hoshino, M., Watanabe, Y., Kon, Y. Contribution of apatite XE "apatite" to the crystal growth of allanite in an iron-oxide-apatite (IOA) prospect, Benjamin River, Canada. Resour. Geol. (submitted).*
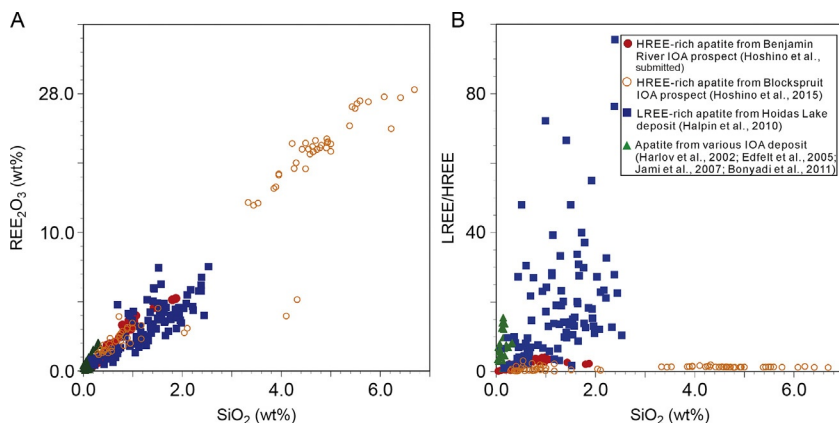
FIG. 50 Plots of SiO_2 vs REE_2O_3 contents (A) and LREE/HREE ratio (B) in apatites in IOA deposits and prospects. LREEs: La-Eu, HREEs: Y, Gd-Lu, REE_2O_3: Y, La-Lu. Data from Bonyadi et al., 2011; Edfelt et al., 2005; Halpin et al., 2010; Harlov et al., 2002; Hoshino et al., 2015; Hoshino et al., submitted; Jami et al., 2007). *From Hoshino, M., Watanabe, Y., Kon, Y. Contribution of apatite XE "apatite" to the crystal growth of allanite in an iron-oxide-apatite (IOA) prospect, Benjamin River, Canada. Resour. Geol. (submitted).*

is below detection limit by EMPA. Benjamin River apatite crystals contain high SiO_2, and REE incorporation into them are accomplished only by britholite substitution, but their Th and U contents are low (Table 16 and Fig. 50). BSE images of Benjamin River apatite crystals show bright, dark, porous zones (Fig. 51), and the last contain very low REE_2O_3 and SiO_2 contents compared to the first two (Table 16). Allanite always occurs near porous zone of apatite, which suggests that allanite grains characteristically occurring in apatite–augite–magnetite ore formed by REEs leached from apatite by hydrothermal fluid in hydrothermal stages. Similar crystallization of REE minerals by remobilization of REEs from apatite are observed in many other IOA deposits, but in monazite form in most of IOA deposits like Kiruna, not in allanite (Hoshino et al., submitted). The stability of allanite and monazite appears to be related to the activity of Ca: allanite forms at high Ca activity, whereas monazite precipitates at lower Ca activity (eg, Casillas et al., 1995; Lee and Dodge, 1964; Snetsinger, 1967). Dominant occurrence of augite at Benjamin River IOA prospect may have been responsible for allanite, but not monazite precipitation, because of high Ca activity in the hydrothermal fluid (Hoshino et al., submitted). Interestingly, hydrothermal monazite and allanite from IOA deposit, which were crystallized by embracing REE leached from apatite, have very low ThO_2 (<0.60 wt.%: Bonyadi et al., 2011; Harlov et al., 2002; Hoshino et al., submitted), although igneous monazite and allanite generally include high ThO_2 contents (Hoshino et al., 2006, 2012b). These findings suggest that IOA deposits have big advantage as research objects for future REE resources.
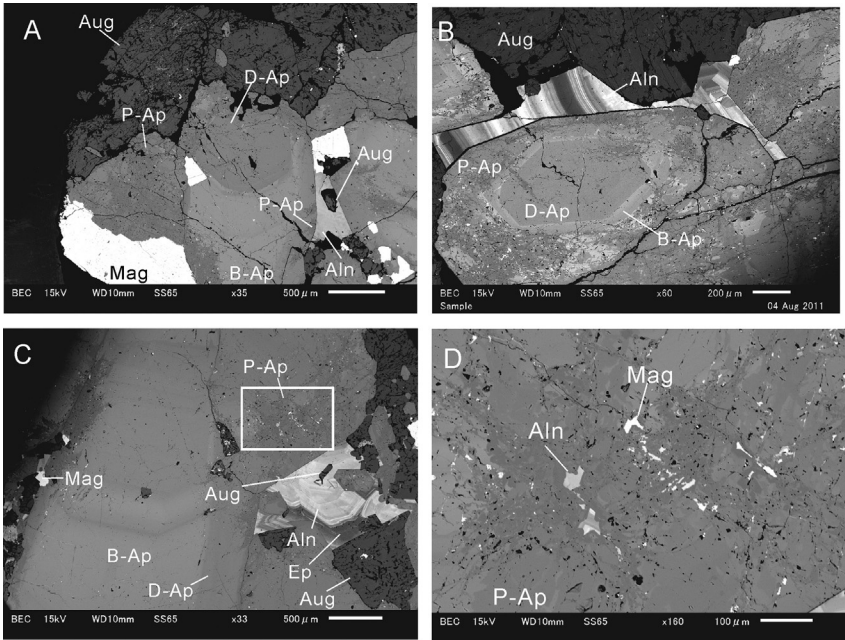
FIG. 51 Electron backscatter images of apatite grains from apatite–augite–magnetite ores (A–C) euhedral apatite consist of *dark*, *bright*, and *porous zones*. *Porous zone* of apatite always accompany allanite. (D) Close up of *white square* in (C). *Porous zone* have allanite and magnetite inclusions. Abbreviations: *B-Ap*: bright zone of apatite, *D-Ap*: dark zone of apatite, *P-Ap*: porous zone of apatite, *Aug*: augite, *Mag*; magnetite, *Aln*: allanite, *Ep*: epidote, *Ab*: albite, *Qz*: quartz. *From Hoshino, M., Watanabe, Y., Kon, Y. Contribution of apatite XE "apatite" to the crystal growth of allanite in an iron-oxide-apatite (IOA) prospect, Benjamin River, Canada. Resour. Geol. (submitted).*

4.3.2.2 HREE-Rich Apatite Prospects and Deposits: The Blockspruit HREE-Rich IOA Prospect, South Africa

The Blockspruit IOA prospect consists of ferro-actinolite intrusive rocks emplaced into the Kenkelbos-type granite of Proterozoic age, Bushveld complex (Fig. 52), (zircon age of Kenkelbos-type granite 2055.32 ± 0.34 Ma (MSWD $=2$, $n=6$)) (Fig. 52). Many fluorite deposits occur in this prospect, which exist as either narrow vertical north-west striking pegmatitic veins or nearly horizontal large sheets. The largest horizontal sheets are the Ysterkop North and South bodies, which measure 1500 and 1000 m^2 in area, respectively, and have been proved by drilling to be in excess of 30 m thick (Crocker et al., 1988). The Ysterkop North and South bodies contain characteristic black boulders of hematite rocks, although these rocks are poorly exposed on surface due to intense weathering and flat topography. The hematitized rocks consist of pegmatitic quartz, fluorite, and ferro-actinolite more or less completely replaced by hematite. HREE-rich ferro-actinolite rocks cropping out are composed of dark green to black ferro-actinolite with pinkish
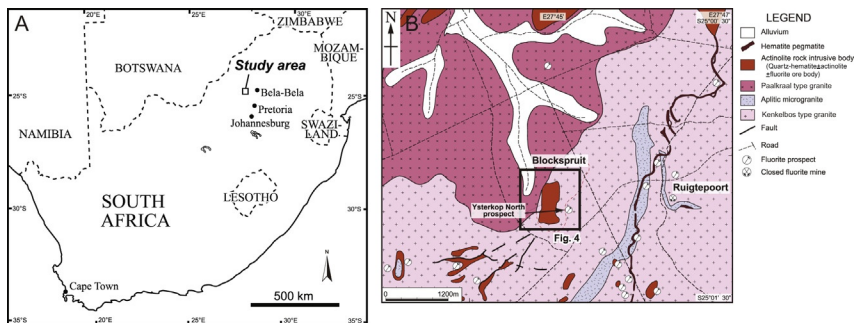
FIG. 52 Locality map of the study area (A). Geological map of the Blockspruit IOA prospect (B). The *red broken line* around the Ysterkop North is the outer limit of the ore body determined by Crocker et al. (2001). *Dense-colored areas* in the center represent occurrence area of silicified and hematitized actinolite rock of the Ysterkop North bodies observed by Horiuchi et al. (2014). *Panel B: Modified from Crocker, I.T., Eales, H.V., Ehlers, D.L., 2001. The fluorite, cassiterite and sulphide deposits associated with the acid rocks of the Bushveld Complex. Memoir 90, Council for Geoscience, Pretoria, South Africa, p. 115.*
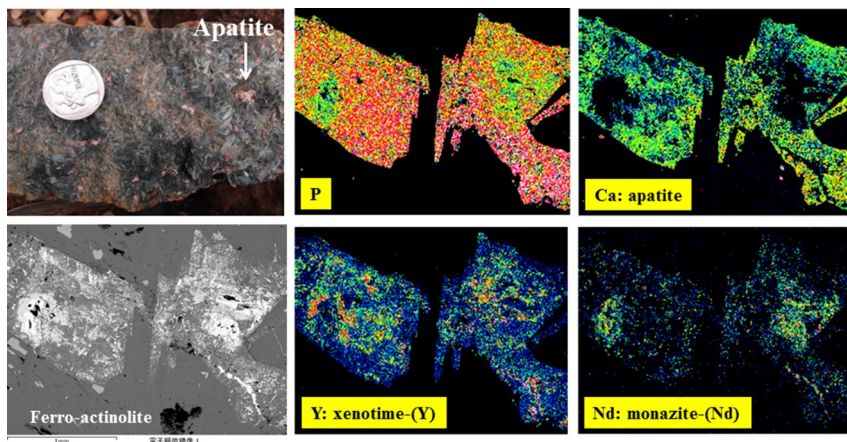
FIG. 53 Hand specimen of HREE-rich ferro-actinolite rock in outcroup and X-ray mapping by SEM-EDS of apatite containing xenotime and monazite inclusions in ferro-actinolite rocks from surface. *Modified from Hoshino, M. Moritz, R., Ovtcharova, M., Watanabe, Y., Spangenberg, J., Putlitz, B., 2015. REE mineralization of the Blockspruit fluorite prospect, Bushveld granitic complex, South Africa: geochemical, mineralogical and fluid inclusion studies. In: Proceedings of the 13th Biennial SGA Meeting, "Mineral Resources in a Sustainable World", 2015, 2, 1513–1516.*

brown intergranular apatite crystals which are commonly replaced by hydro-thermal xenotime and monazite (Fig. 53). Hoshino et al. (2015) sampled 9 drill holes, reaching a depth of 200 m below surface, at the Blockspruit prospect (Fig. 52) in order to understand spatial distribution of HREEs in ferro-actinolite rocks. The results of the drilling project in the area show that the HREE-rich ferro-actinolite rocks intruding into the Kenkelbos-type granite

A   Weathered soils of ferro-actinolite rocks from surface

B   Altered ferro-actinolite rocks from surface

Apatite

C   Fresh ferro-edenite rocks from deep zone

Apatite
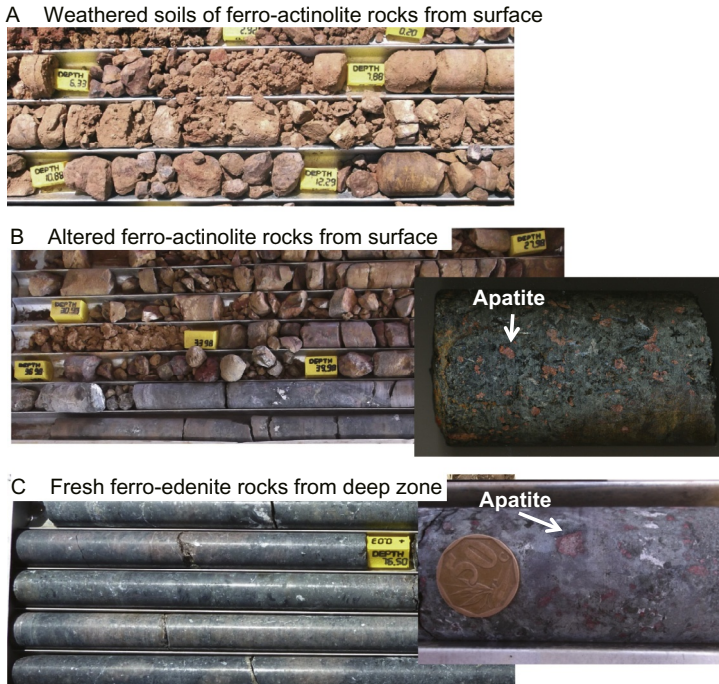
FIG. 54 HREE-rich weathered soils (A), ferro-actinolite (B), and ferro-edenite rocks (C) from drill holes in the Blockspruit prospect (Hoshino et al., 2015).

extend over an area of at least 600 m² and 200 m in depth. The HREE-rich ferro-actinolite rocks are strongly weathered near the surface and form a 30–50-m thick iron oxide rich soil (Fig. 54A). HREE-mineralized ores are divided into three types based on the difference of the depth: (1) weathered soil derived from ferro-actinolite rocks (surface), (2) hydrothermal altered ferro-actinolite rocks (sallow), and (3) fresh ferro-edenite rocks (deep), which suggests that they have different geochemical and mineralogical characteristics. The (1) weathered soil has higher REE contents (5298 ppm REEs; 2308 ppm HREEs) than the nonweathered part of the rock (2 and 3) (2860 ppm REEs; 1063 ppm HREEs) (Fig. 54A–C). REE host minerals in the three types of ores are REE-rich apatite, monazite, and xenotime. We review geochemistry and mineralogy of the three types of HREE-rich ores briefly in this chapter.

The HREE mineralization in surface soil derived from weathered ferro-actinolite rocks were described by Horiuchi et al. (2014) and Hoshino et al. (2015) in detail. As mentioned earlier, in the Blockspruit prospect, HREE-rich ferro-actinolite rocks intrude into granitic rocks, however these rocks are poorly exposed on the surface due to intense weathering and flat topography. Horiuchi et al. (2014) attempted to estimate the potential for HREEs in this

area using termite hills. According to West (1970), the termites forage sands, follow fractures to access moisture, where the main water table depth has been estimated to be 60–90 m, and bring soil from deep zone to surface. These suggest that building materials of termite hills reflect chemical composition of underground rocks and are suitable samples for geochemical survey of hidden rocks. In addition, recent advancements in portable X-ray fluorescence (XRF) spectrometry have enabled rapid semiquantitative field analysis of the chemical compositions of soils and rocks. Although XRF spectrometry is only effective for La, Ce, Nd, and Y in REE analysis, Horiuchi et al. (2014) carried out portable XRF analyses of 200 termite hills at the Blockspruit prospect and created REE anomaly map. Horiuchi et al. (2014) compared the results from portable XRF spectrometry with those from inductively coupled-plasma mass-spectrometry (ICP-MS) carried out in a laboratory and demonstrated that portable XRF data for La and Y are strongly correlated with LREE and HREE contents obtained by ICP-MS, respectively. Their study also showed that the Y-rich areas in elemental distribution map of termite hills correspond to occurrence of HREE-rich ferro-actinolite intrusive rocks (Figs. 52 and 55). There are many IOA prospects similar to the Blockspruit in Bushveld complex, so termite mounds are an effective tool for REE geochemical prospection. The weathered soil of ferro-actinolite rocks contains 5380 ppm REEs (2308 ppm HREEs); tiny monazite and xenotime are responsible for its REE enrichment. Interestingly, monazite-(Ce) is most common in nature, but monazite-(Nd) in commonly occurs in the weathered soil. Thus the weathered soil of ferro-actinolite rocks are enriched in HREEs.
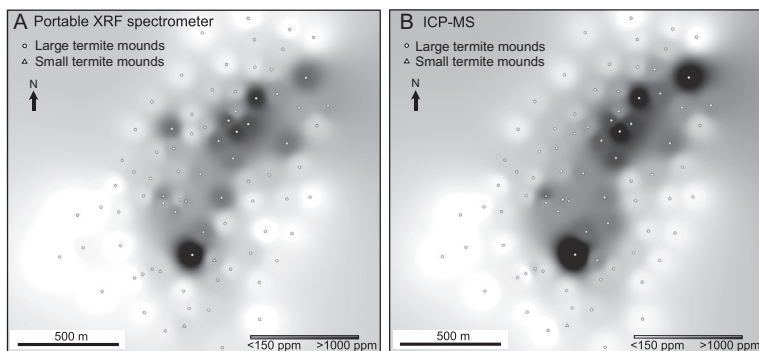
FIG. 55 Geochemical anomaly maps of Y concentration in the survey area (Fig. 52B), measured by portable XRF spectrometer (A) and ICP-MS (B). The Y-rich areas in elemental distribution map of termite hills correspond to occurrence of HREE-rich ferro-actinolite intrusive rock. Maps were made by inverse distance weighting interpolation method, using a distance coefficient (P-value) of 3. *Modified from Horiuchi, Y., Ohno, T., Hoshino, M., Shin, K.-C, Murakami, H., Tsunematsu, M., Watanabe, Y. 2014. Geochemical prospecting for rare earth elements using termite mound materials. Mineral. Deposita 49, 1013–1023.*

Drilling project revealed that there are fresh (deep zone) (Fig. 54C) and hydrothermal altered HREE-rich ferro-actinolite rocks (shallow zone) (Fig. 54B). The former are blackish rocks, the latter are greenish–yellowish rocks, and both of them contain reddish apatite (Fig. 54). Modal abundance of the HREE-rich ferro-actinolite rocks is 80% ferro-actinolite, 12% Fe-oxide, 5% apatite, 0.4% monazite, 0.2% xenotime, 0.3% plagioclase, and 0.3% fluorite. As mentioned earlier, the hydrothermally altered ferro-actinolite rocks from the shallow zone contain REE-poor apatite grains replaced by REE-phosphates such as xenotime-(Y) and monazite-(Nd) (Fig. 53). On the other hand, apatite grains in the fresh ferro-edenite rocks from the deeper zone consist of REE-rich cores (with up to 20.3 wt.% REE_2O_3) and REE-poor rims including REE phosphate inclusions (Table 16 and Fig. 56B). Generally, apatite grains contain 0.5–1 wt.% REE_2O_3 (Preston et al., 1996). Previous studies suggest that some of IOA deposits and prospects such as Kiirunavaara are associated with REE enrichment, but REE content in apatite grains from these deposits is about 9500 ppm (Table 16). Thus REE-rich apatite in ferro-edenite from the Blockspruit prospect probably has the highest REE contents among REE-bearing apatite reported so far (Table 16). The REE-poor rim of apatite from fresh ferro-edenite in deep zone contains small monazite-(Nd) and xenotime-(Y) inclusions (Fig. 56B). This texture is similar to apatite in hydrothermal altered ferro-actinolite rocks (Fig. 56A). These textual observations allow one to distinguish the REE mineralization in the Blockspruit fluorite prospect into the following two stages: (1) the first is related to magmatic ferro-edenite intrusive rocks accompanying REE-rich apatite and (2) the second is related to the decomposition of REE-rich apatite and reprecipitation of monazite-(Nd) and xenotime by hydrothermal alteration. Magmatic ferro-edenite rocks containing HREE-rich apatite intrude into granite. After that, REEs in the magmatic HREE-rich apatite are leached by hydrothermal fluid accompanied by fluorite mineralization and newly precipitate as monazite-(Nd) and xenotime-(Y). Ferro-edenite was also altered to ferro-actinolite during hydrothermal alteration. Monazite and xenotime, generally being heavy minerals resistant to chemical decomposition and erosion, are concentrated with other heavy resistant minerals in placer deposits, principally in river and beach sands (Sengupta and Van Gosen, 2016). On surface, weathering of ferro-actinolite rocks including apatite-bearing monazite and xenotime inclusions progresses, which results in the decomposition of apatite and residues of monazite and xenotime in the weathered soil. It is easy to collect the thick weathered crust near the surface (30–50 m) which does not need to be crushed, and this will be an advantage for the development of the Blockspruit. It is an important key for the development of this prospect whether monazite and xenotime concentrates can be produced or not by mineral processing.

The Na content in HREE-rich apatite from the Blockspruit prospect is below detection limit by EMPA as well as those from Benjamin River prospect, which suggests that REE incorporation into the Blockspruit apatite is achieved
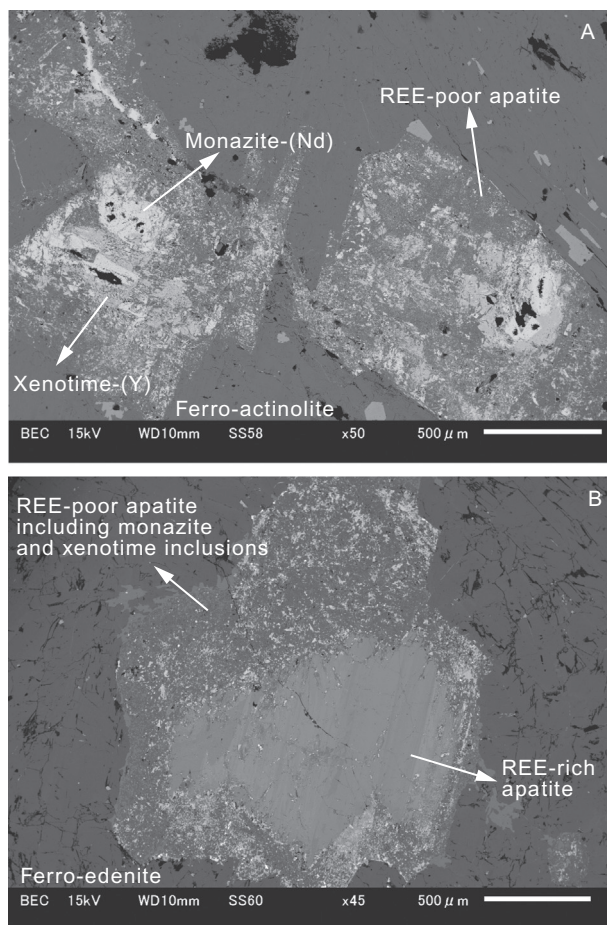
FIG. 56 Back scattered electron (BSE) images of apatite grains in Blockspruit IOA prospect. (A) REE-poor apatite grains replaced by monazite and xenotime in altered ferro-actinolite rock from shallow zones. (B) Apatite grains consisting of a REE-rich core and a REE-poor rim including monazite and xenotime inclusions from the deep zone. *After Hoshino, M. Moritz, R., Ovtcharova, M., Watanabe, Y., Spangenberg, J., Putlitz, B., 2015. REE mineralization of the Blockspruit fluorite prospect, Bushveld granitic complex, South Africa: geochemical, mineralogical and fluid inclusion studies. In: Proceedings of the 13th Biennial SGA Meeting, "Mineral Resources in a Sustainable World", 2015, 2, 1513–1516.*

by only britholite-type substitution (Table 16). Blockspruit REE-rich apatite is highly affected by britholite-type substitution compared with Benjamin River REE-rich apatite, namely has higher REE contents (Fig. 50), so the former has higher Th contents than the latter (Table 16). However, the Th contents are very low compared with other REE minerals like monazite and xenotime and would not be a serious obstacle for REE production from these apatites.

4.3.2.3 REE-Bearing Apatite in Sedimentary Deposits (Phosphorites) and Deep-Sea Mud

In this chapter, several important studies concerning REE-bearing apatite in both sedimentary apatite deposits and deep-sea mud will be introduced. As mentioned earlier, sedimentary phosphate deposits range in age from Precambrian to Recent. Thus, from the geochemical view, REE contents in sedimentary phosphates from worldwide occurrences are used as paleoenvironmental indicators. However, the recent REE crisis has sparked widespread attention, and sedimentary apatite rocks are also likely to become yet another important target for REE exploration. As mentioned earlier, the crystal–chemical characteristics of apatite prefer LREEs to HREEs in most natural environments. Because the current demand for REEs is increasing mainly for HREEs, HREE-rich apatite ores are much more appropriate for exploration and mining. From this perspective, Ihlen et al. (2014) investigated the sedimentary and igneous apatite rocks in Norway and evaluated their REE potential. The igneous apatite rocks contain 3000–10,000 ppm REEs (HREEs: 170–1000 ppm) and may have REE potential. On the other hand, the sedimentary apatite rocks contain very low REE contents, but geochemical data were not shown. Thus, the authors concluded that sedimentary apatite rocks do not have REE potential. Alternatively, Emsbo et al. (2015) analyzed 23 sedimentary apatite deposits (phosphorites) and found some of them contain relatively high concentration of REEs (~5000 ppm) and HREEs (~2000 ppm). Interestingly, their study also showed that REE contents in sedimentary apatite rocks are very heterogeneous over geologic age and sampling location. The geologic process controlling REE contents in sedimentary phosphate deposits are intensely debated and its further understanding is expected to facilitate more efficient exploration for HREE-rich apatite deposits.

Besides these sedimentary apatite rocks, apatite in deep-sea mud is also proposed as HREE resource recently (Kato et al., 2011; Kon et al., 2014; Nakamura et al., 2015; Yasukawa et al., 2014). While their profitable exploitation depends on overcoming the technical and environmental obstacles associated with seafloor mining at depth of 2–6 km (Nakamura et al., 2015), REEs in such deep-sea mud are easily extractable by simple chemical treatments as well. The following paragraph will mention some important characteristics of REE-bearing apatite in deep-sea mud.

The distribution of REEs in the deep-sea unsolidified sediments has been investigated by numerous researchers (eg, Bernat, 1975; Toyoda and Tokonami, 1990). Bernat (1975) made several important observations on average REE contents of separated constituent minerals in the deep-sea unsolidified sediments of the Pacific. Deep-sea mud abundant in HREEs (REEs in the deep-sea mud at numerous sites throughout the eastern South and central North Pacific sea floor) was recently reported by Kato et al. (2011). The HREE-rich deep-sea mud contains low Th and U, which is a big advantage for HREE resource. On the other hand, REE-enriched deep-sea mud with
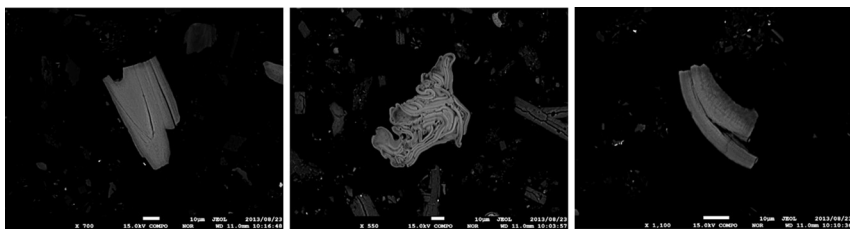
FIG. 57 Back scattered electron images of apatite grains from unsolidified sediments in deep seafloor of Minami-Torishima area. These textures are very different from igneous apatite grains (Figs. 51 and 56) and are probably biological origin like fish bone. *After Kon, Y., Hoshino, M., Sanematsu, K., Morita, S., Tsunematsu, M., Okamoto, N., Yano, N., Tanaka, M., Takagi, T., 2014. Geochemical characteristics of apatite in heavy REE-rich deep-sea mud from Minami-Torishima Area, Southeastern Japan. Resour. Geol. 64, 47–57.*

concentrations exceeding 6500 ppm (0.65%) at around 3 m beneath the sea floor was also found in the Minami-Torishima area at depths of 5600–5800 m (JAMSTEC, 2013). Kon et al. (2014) suggested that REE contents of the deep-sea mud in Minami-Torishima are constrained by the proportion of apatite based on their geochemical and mineralogical investigations. The apatite grains from the deep-sea mud in Minami-Torishima contain up to 21,000 ppm REEs (10,500 ppm HREEs) and have HREE-rich distribution. There is a positive correlation between P_2O_5 and CaO in HREE-rich deep-sea mud. There is a strong positive correlation between relative proportion of apatite and REE content in the HREE-rich deep-sea mud. Kon et al. (2014) reported BSE image of apatite grains from HREE-rich deep-sea mud which are weak for electron beam and porous texture (probably biological origin like fish bone) (Fig. 57). According to Yasukawa et al. (2014), all REEs can be readily leached from the mud by dilute acids, which it is probably due to low crystallinity and porous texture of apatite in HREE-rich deep-sea mud. According to Nakamura et al. (2015), formation of REE-rich muds is strongly related to hydrothermal activity at MORB. However, deposition mechanism of HREE-rich apatite is controversial topic and needs further studies.

4.3.2.4 Summarized Characteristics of HREE-Rich Apatite

Both the Benjamin River and the Blockspruit IOA prospects contain apatite as major REE minerals. REEs leached from apatite form new monazite, xenotime, and allanite. Sodium in apatite grains from both prospects is below detection limit by EMPA, which suggests that REEs in their apatite grains are incorporated only by britholite substitution. The presence of monazite, xenotime, and allanite as a major REE mineral in the Benjamin River and Blockspruit IOA prospects is advantageous for the exploitation because monazite, xenotime, and allanite are higher in REE content than apatite, upgrading the ore. Main minerals in the Benjamin River and the Blockspruit IOA

prospects are augite and ferro-edenite–actinolite which are mafic silicate minerals. Apatite accompanying diopside as main minerals in Hoidas Lake deposits contains high LREE contents, but is not IOA deposit. These suggest that magma crystallizing REE-rich apatite (over several wt.%) and mafic silicate minerals, as main minerals, from the above three prospects, and these deposits have very high silica activity compared to carbonatite, alkaline rocks, and other IOA deposits. As mentioned earlier, incorporation of REEs into apatite is related to silica activity, and the high activity in the above three prospects and deposits may be a major cause of occurrence of apatite having high REE contents. Apatite in the Hoidas Lake deposit have LREE-rich distribution (Table 16 and Fig. 50) and form accompanying lamprophyres and/or carbonatites. Apatite crystallization having LREE-rich distribution from other IOA deposits are also related to intrusions of carbonatite and felsic magma. On the other hand, HREE-rich apatite crystallization in Benjamin River and Blockspruit prospects are accompanied by intrusion of mafic magma like diorite and ferro-edenite magma. These differences of intrusive rocks are related to those of REE distribution (LREE-rich or HREE-rich) (Fig. 50). The Blockspruit and the Benjamin River IOA prospects are promising as HREE resources. In particular, existences of many similar type of prospects in Bushveld complex, South Africa are expected, so further explorations are needed.

Sedimentary apatite rocks generally contain low REE contents compared to igneous ones (Table 14), so in the past it has been thought that their REE economic potentials are low. Recently, some sedimentary apatite rocks having HREE potential were reported by Emsbo et al. (2015). REE contents in sedimentary apatite rocks are quite different based on the difference of occurrence compared to those in igneous apatite rocks. Detailed studies concerning mineralogy of sedimentary apatite rocks are also rare (eg, with respect to REE substitution mechanism). Further studies about the relationships between REE concentration and sedimentary environment (eg, sea composition and age) of sedimentary apatite are needed.

4.3.3 REE Production from Apatite as By-Product of Phosphoric Acid: Leaching Method and Adsorbent for REEs

As mentioned earlier, the largest advantage of apatite as REE resources is in the promising possibility for the production of REEs as a by-product of phosphoric acid production. Although this is not achieved in plant-scale at the present time, recent years have brought significant progress for this topic. In this section, we first describe typical chemical processes for phosphoric acid production from apatite ore concisely, and then introduce several recent investigations aiming the REE production as a by-product of the mineral processing. Particularly, it is notable that Ogata et al. (2014) synthesized a noble adsorbent for selective recovery of REEs (especially HREEs) in solution with considerable impurities. These recent advancements would enable one to make better use of a vast amount of phosphate rocks in the near future.

The main reaction called "wet process" in the phosphoric acid production is as follows (also see Section 4.3):

$$Ca_5(PO_4)_3F + 5H_2SO_4 + xH_2O \rightarrow 3H_3PO_4 + 5CaSO_4 \cdot x/5H_2O \downarrow + HF \uparrow$$
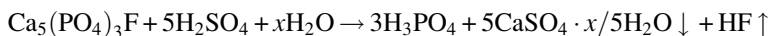
As shown in this chemical equation, (hydrous) calcium sulfate is produced from the reaction and this by-product is called "phosphogypsum" (Zielinski et al., 1993). Phosphogypsum is divided into the following three types according to its hydrous contents: (1) anhydrite, which is corresponding to anhydrous calcium sulfate, $CaSO_4$ ($x=0$ in the above equation); (2) basanite, calcium sulfate hemihydrate, $CaSO_4 \cdot 0.5H_2O$ ($x=0.5$); and (3) gypsum, calcium sulfate dihydrate, $CaSO_4 \cdot 2H_2O$ ($x=2$). Among them, gypsum is the most common by-product of wet process: for example, 5 tons of gypsum formed per ton of P_2O_5 production under typical processing conditions in the current plants. Many treatments for production of high-purity phosphoric acid were proposed. The following five processes are well known: (1) Dihydrate process, (2) Hemihydrate process, (3) Di-Hemihydrate process (double-stage), (4) Hemi-Dihydrate process (single-stage), and (5) Hemi-Dihydrate process (double-stage). Each method has both advantages and disadvantages (see EFMA, 2000 for detail).

Dihydrate process, which is (1) in the earlier mentioned treatments, is most common in the above five processes of phosphorous acid production because of its low cost and simple flow. In this process, gypsum (calcium sulfate dihydrate) is produced as by-product of phosphorous acid and incorporates 80% of REEs into the crystal structure (Zielinski et al., 1993). In some countries, eg, Poland, the dumped gypsum represents the largest national REE resource and thus there have been some attempts to process the copious amount of REE containing gypsum already produced by the industry worldwide (Peelman et al., 2014).

Lokshin et al. (2002), for example, carried out REE leaching experiments of REE-bearing gypsum produced by dihydrate process of apatite ores from Khibiny deposits (REE content: 0.30–0.37 wt.%) using HNO_3. As the result, they succeeded to leach 90% of REE by 10–20% HNO_3. There is also another process that uses NH_4CO_3 for REE-bearing gypsum. In this process, all REEs are incorporated in secondary precipitated $CaCO_3$ and easily leached with HNO_3, in addition, useful $Ca(NO_3)_2$ is produced as a by-product (Habashi, 1985; Peelman et al., 2014). Alternatively, the REE-bearing $CaCO_3$ can be calcined to CaO and leached with NH_4Cl leaving an REE-rich residue (Peelman et al., 2014).

In the view of REE recovery, Di-hemihydrate process, which is (3) in the earlier mentioned treatments, is effective because this selectively produces REE-bearing hemihydrate in the decomposition process of REE-bearing apatite ore and it is easy to leach REEs from hemihydrate using dilute sulfuric acid (Peelman et al., 2014; Zielinski et al., 1993). The differences between

hemihydrate ($CaSO_4 \cdot 0.5H_2O$) and gypsum ($CaSO_4 \cdot 2H_2O$) are water contents, as is evident from chemical formulae.

Zielinski et al. (1993) carried out REE leaching experiments of REE-bearing hemihydrate (0.68 wt.% REEs) produced as a by-product of mineral processing of apatite ore from Kola Peninsula using sulfuric acid on bench scale. This dissolves the hemihydrate and brings the REE into solution. The REE in solution inhibit the reprecipitation of gypsum, allowing for them to be removed through solvent extraction (80–85% REE).

Hydrometallurgical processes, including precipitation, solvent extraction, and adsorption, play main roles in the recovery of the dissolved REEs. Precipitation and solvent extraction are established techniques for metal recovery and are useful especially for large-scale operations at high metal ion concentrations (Roskill, 2015). For REE recovery, solvent extraction is applied commonly. For example, Zielinski et al. (1993) carried out solvent extraction of REEs for hemihydrate cake produced from Kola apatite. In their experiments, the 40 wt.% solution of ROKANOL PIO in kerosene was used as a solvent for REE extraction. ROKANOL PIO is roughly an equimolar mixture of M2EHPA (mono(2-ethylhexyl)phosphoric acid) and D2EHPA (di(2-ethylhexyl) phosphoric acid). REEs in solvent react with $NaSO_4$, after which REEs are recovered in the form of $Na \sim Ln$ double sulfates, which contain 24–25% REEs. The overall REE recovery of the process ranges from 80% to 85%. Advantage of this process does not disturb the phosphoric acid production, and additionally purifies the by-product gypsum so that it can be utilized in the manufacture of building materials. As to other studies, solvent extraction of REEs from apatite has been tested using various solvents, H_2SO_4 with different concentration and several precipitation methods (eg, Jarosiński et al., 1993; Wang et al., 2010a). However, such solvents are generally used for solutions bearing high REE contents.

Adsorption, on the other hand, can be applied to the recovery of metal ions even from low concentration sources with relatively simple processes. Many adsorbents for REEs have been studied, nevertheless, there are no practical adsorbents. Recently, Ogata et al. (2014) synthesized "EDASiDGA" which is a new adsorbent with immobilized diglycol amic acid on the surface of silica gel and easily synthesized at low cost (Fig. 58). EDASiDGA is able to selectively adsorb REEs from a high concentration solution of base metals (eg, Fe, Cu) in a low pH region. It is notable that adsorption ratios of HREEs on EDASiDGA are higher than those of LREEs because HREEs are more valuable (especially Dy) than LREEs. Adsorbed REEs on EDASiDGA are easily leached by 1 M HCl treatment and the EDASiDGA can be used repeatedly. Apatite ores from the representative apatite deposits contain several thousand ppm of REEs (Table 14), which is not high compared with other REE ores including bastnäsite and monazite from carbonatite and alkaline rocks. Apatite generally contains some minor elements such as Fe, Al, and
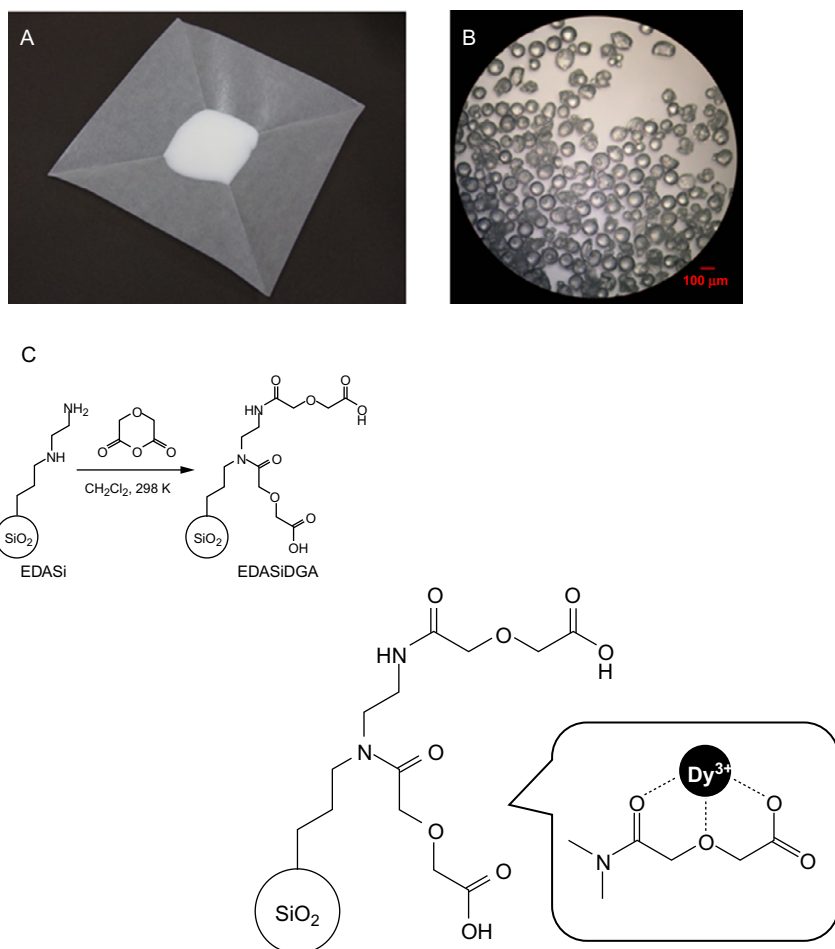
FIG. 58 Photographs of EDASiDGA (A, B). (C) Preparation of an adsorbent and adsorption model of Dy (HREE) by EDASiDGA. *Modified from Ogata, T., Narita, H., Tanaka, M., 2014. Immobilization of diglycol amic acid on silica gel for selective recovery of rare earth elements. Chem. Lett. 43, 1414–1416.*

Mg, so it is very important for adsorbents to capture REEs selectively in such a complex solution.

For apatite ore from Phalaborwa, Ogata et al. (2016) carried out decomposition and REE adsorption experiments using 0.5–6 M H_2SO_4 and EDA-SiDGA on lab-scale. The apatite ores contain about 8000 ppm REEs (Table 14). Gypsum was detected in all of the decomposition experiments (Fig. 59). Leaching ratios for REEs are relatively high in low H_2SO_4 concentration conditions (<2 M H_2SO_4) (Fig. 60). This means that REE leaching from apatite ores by using low concentration H_2SO_4 is possible and the
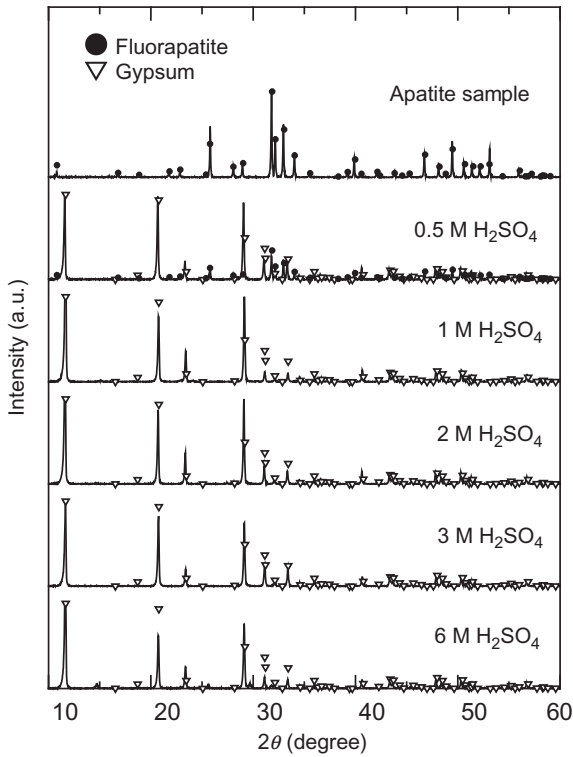
FIG. 59 XRD patterns of the Phalabowra apatite concentrate and the residues obtained from leaching tests at various H_2SO_4 concentrations. *After Ogata, T., Narita, H., Tanaka, M., Hoshino, M., Kon, Y., Watanabe, Y., 2016. Selective recovery of heavy rare earth elements from apatite with an adsorbent bearing immobilized tridentate amido ligands. Sep. Purif. Technol. 159, 157–160.*
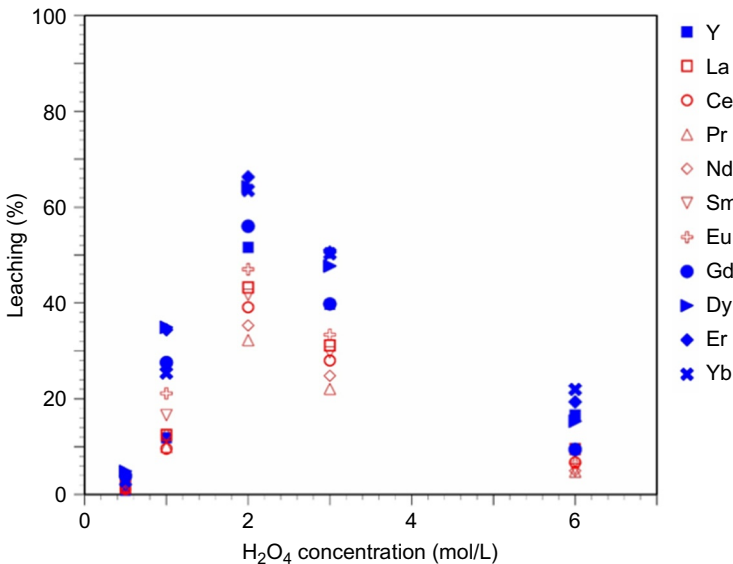
FIG. 60 Effect of H_2SO_4 concentration on REE leaching efficiency for Phalabowra apatite concentrates. *Modified from Ogata, T., Narita, H., Tanaka, M., Hoshino, M., Kon, Y., Watanabe, Y., 2016. Selective recovery of heavy rare earth elements from apatite with an adsorbent bearing immobilized tridentate amido ligands. Sep. Purif. Technol. 159, 157–160.*

leached REEs are retained in solution, not cocrystallizing into gypsum. Ogata et al. (2016) carried out adsorbent experiments for phosphoric acid which is produced from Phalaborwa apatite ores with 2 M H_2SO_4 treatment. The phosphoric acid solution was passed through a column filled with EDASiDGA adsorbent and REEs selectively remained in the column. The REEs in column are easily recovered by low concentration acid treatment like 1 M H_2SO_4. As mentioned earlier, EDASiDGA has high collectivity of MREEs and HREEs, and Ogata et al. (2016) succeeded in increasing Dy concentrations by as much a factor of 24 compared with feed solution after the dissolution of the apatite ore. The described experiments are lab-scale, but their results demonstrate that EDASiDGA is effective for REE recovery from low-grade ores with impurities like Fe. In the future, REE adsorption experiments with EDASiDGA are desperately needed on larger scale with due regard to economic REE production as by-product from apatite ores.

5 SUMMARY

Carbonatites are high in REEs, and most of them are LREE-dominant type, because carbonatite magmas form by low degree of partial melting of garnet-bearing source mantle. In contrast, alkaline rocks are low in REEs, but some are rich in HREEs, due to higher degree of partial melting of the garnet-free magma sources. This indicates that HREE-dominant REE-rich deposits are uncommonly formed by magmatism.

Ion-adsorption type deposits consist of LREE- and HREE-dominant types and are constrained by the degree of partial melting and magmatic differentiation. The formation of HREE-dominant ion-adsorption type deposits is related to the heavily differentiated and reduced granite.

As established by geoscience, it is inevitable that LREEs are mainly produced from carbonatites and HREEs are dominantly extracted from ion-adsorption type deposits underlain by HREE-rich granites. However, REE grades of ion-adsorption type deposits are low and almost all of the minable deposits have been found in southern China. In view of the future of REE supply (considering both feasibility and sustainability), one of the most promising sources of REEs is apatite ores that are mined for fertilizer production, because apatite ores are sufficient in reserves and contain enough amounts of the whole REEs that can cover the world demand.

ABBREVIATIONS

ASI	aluminum saturation index
BSE	back scattered electron
CI	Carbonaceous Ivuna
CNMMN	Commission on New Minerals and Mineral Names
EMPA	electron microprobe analysis
FCC	fluid catalytic cracking
HFSE	high-field strength elements
HREEs	heavy rare earth elements
ICP-MS	inductively coupled-plasma mass-spectrometry
IOA	iron oxide–apatite
I-type	igneous-type
LA-ICP-MS	laser-ablation inductively coupled-plasma mass-spectrometry
LREEs	light rare earth elements
MORB	mid-oceanic ridge basalt
M2EHPA	mono(2-ethylhexyl)phosphoric acid
NdFeB	neodymium–iron–boron
OIB	oceanic island basalt
PXRD	powder X-ray diffraction
PZC	point of zero charge
REEs	rare earth elements
REO	total REE oxides
S-type	sedimentary-type
XRF	X-ray fluorescence

REFERENCES

Abdel-Rehim, A.M., 2005. A new technique for extracting zircon XE "zircon" ium from Egyptian zircon concentrate. Int. J. Miner. Process. 76, 234–243.

Agangi, A., Kamenetsky, V.S., McPhie, J., 2010. The role of fluorine in the concentration and transport of lithophile trace elements in felsic magmas: insights from the Gawler Range Volcanics, South Australia. Chem. Geol. 273, 314–325.

Aide, M.T., Aide, C., 2012. Rare earth elements: their importance in understanding soil genesis. ISRN Soil Sci. 2012. Article ID 783876, 11p.

Allen, D.E., Seyfried Jr., W.E., 2005. REE controls in ultramafic hosted MOR hydrothermal systems: an experimental study at elevated temperature and pressure. Geochim. Cosmochim. Acta 69, 675–683.

Andreoli, M.A.G., Smith, C.B., Watkeys, M., Moore, J.M., Ashwal, L.D., Hart, R.J., 1994. The geology of the Steenkampskraal monazite deposit, South Africa: implicatins for REE-Th-Cu mineralization in charnockite-granulite terranes. Econ. Geol. 89, 994–1016.

Anthony, J.W., Bideaux, R.A., Bladh, K.W., Nichols, M.C., 1995. Handbook of Mineralogy. Silica, Silicates, vol. II Mineralogical Society of America, Chantilly, VA, pp. 1–904.

Anthony, J.W., Bideaux, R.A., Bladh, K.W., Nichols, M.C., 1997. Handbook of Mineralogy. Halides, Hydroxides, Oxides, vol. III Mineralogical Society of America, Chantilly, VA, pp. 1–628.

Anthony, J.W., Bideaux, R.A., Bladh, K.W., Nichols, M.C., 2000. Handbook of Mineralogy. Arsenates, Phosphates, Vanadates, vol. IV Mineralogical Society of America, Chantilly, VA, pp. 1–680.

Anthony, J.W., Bideaux, R.A., Bladh, K.W., Nichols, M.C., 2003. Handbook of Mineralogy. Borates, Carbonates, Sulfate, vol. V. Mineralogical Society of America, Chantilly, VA, pp. 1–813.

Atencio, D., Bastos Neto, A.C., Pereira, V.P., Ferron, J.T.M.M., Hoshino, M., Moriyama, T., Watanabe, Y., Miyawaki, R., Coutinho, J.M.V., Andrade, M.B., Domanik, K., Chukanov, N.V., Momma, K., Hirano, K., Tsunematsu, M., 2015. Waimirite-(Y), orthorhombic YF3, a new mineral from the Pitinga mine, Presidente Figueiredo, Amazonas, Brazil and from Jabal Tawlah, Saudi Arabia: description and crystal structure. Mineral. Mag. 79, 767–780.

Aubert, D., Stille, P., Probst, A., 2001. REE fractionation during granite weathering and removal by waters and suspended loads: Sr and Nd isotopic evidence. Geochim. Cosmochim. Acta 65, 387–406.

Aurisicchio, C., De Vito, C., Ferrini, V., Orlandi, P., 2001. Nb-Ta oxide minerals from miarolitic pegmatites of the Baveno pink granite, NW Italy. Mineral. Mag. 65, 509–522.

Aurisicchio, C., De Vito, C., Ferrini, V., Orlandi, P., 2002. Nb and Ta oxide minerals in the Fonte Del Prete granitic pegmatite dike, island of Elba, Italy. Can. Mineral. 40, 799–814.

Bach, W., Irber, W., 1998. Rare earth element mobility in the oceanic lower sheeted dyke complex: evidence from geochemical data and leaching experiments. Chem. Geol. 151, 309–326.

Balan, E., Neuville, D.R., Trocellier, P., Fritsch, E., Muller, J.P., Calas, G., 2001. Metamictization and chemical durability of detrital zircon. Am. Mineral. 86, 1025–1033.

Banfield, J.F., Eggleton, R.A., 1989. Apatite replacement and rare earth mobilization, fractionation, and fixation during weathering. Clay Clay Miner. 37, 113–127.

Bao, Z., Zhao, Z., 2008. Geochemistry of mineralization with exchangeable REY in the weathering crusts of granitic rocks in South China. Ore Geol. Rev. 33, 519–535.

Bárdossy, G., Aleva, G.J.J., 1990. Lateritic Bauxites. Developments in Economic Geology, vol. 27 Elsevier, Amsterdam/Oxford/New York/Tokyo. 624p.

Bau, M., 1996. Controls on the fractionation of isovalent trace elements in magmatic and aqueous systems: evidence from Y/Ho, Zr/Hf and lanthanide tetrad effect. Contrib. Mineral. Petrol. 123, 323–333.

Bau, M., 1999. Scavenging of dissolved yttrium and rare earths by precipitating iron oxyhydroxide: experimental evidence for Ce oxidation, Y-Ho fractionation, and lanthanide tetrad effct. Geochim. Cosmochim. Acta 63, 67–77.

Bau, M., Dulski, P., 1995. Comparative study of yttrium and rare-earth element behaviours in fluorine-rich hydrothermal fluids. Contrib. Mineral. Petrol. 119, 213–223.

Bau, M., Koschinsky, A., 2009. Oxidative scavenging of cerium on hydrous Fe oxide: evidence from the distribution of rare earth elements an yttrium between Fe oxides and Mn oxides in hydrogenetic ferromanganese crusts. Geochem. J. 43, 37–47.

Baumer, A., Caruba, R., Bizouard, H., Peckett, A., 1983. Chlorapatite de synthèsis: substitution et inclusions de Mn, Ce, U et Th en traces. Can. Mineral. 21, 567–573.

Bea, F., 1996. Residence of REE, Y, Th and U in granites and crustal protoliths: implication for the chemistry of crustal melts. J. Petrol. 37, 521–552.

Bell, K., Simonetti, A., 2010. Source of parental melts to carbonatites-critical isotopic constraints. Mineral. Petrol. 98, 77–89.

Bell, K., Tilton, G.R., 2002. Probing the mantle: the story from carbonatites. EOS Trans. 83, 273–277.

Bellezza, M., Merlino, S., Perchiazzi, N., 2009. Mosandrite: structural and crystal–chemical relationships with rinnite. Can. Mineral. 47, 897–908.

Belousova, E.A., Griffin, W.L., O'Reilly, S.Y., Fisher, N.I., 2002. Apatite as an indicator mineral for mineral exploration: trace-element compositions and their relationship to host rock type. J. Geochem. Explor. 76, 45–69.

Berger, A., Gnos, E., Janots, E., Fernandez, A., Giese, J., 2008. Formation and composition of rhabdophane, bastnäsite and hydrated thorium minerals during alteration: implications for geochronology and low-temperature processes. Chem. Geol. 254, 238–248.

Berger, A., Janots, E., Gnos, E., Frei, R., Bernier, F., 2014. Rare earth element mineralogy and geochemistry in a laterite profile from Madagascar. Appl. Geochem. 41, 218–228.

Bernat, M., 1975. Les isotopes de l'uranium et du thorium et les terres rares dans l'environnement marin. Cah. ORSTOM Ser. Geol. 7, 65–83 (in French).

Blench, T.A., 2010. The Steenkampskraal rare earths and thrium project in South Africa. In: Thorium and Rare Earths Conference, The Southern African Institute of Mining and Metallurgy, pp. 45–57.

Boatner, L.A., Sales, B.C., 1988. Monazite. In: Lutze, W., Ewing, R.C. (Eds.), Radioactive Waste Forms for the Future. North Holland, New York, pp. 495–564.

Bonazzi, P., Menchetti, S., 1999. Crystal chemistry of aeschynite-(Y) from the Western Alps: residual electron density on difference-Fourier map. Eur. J. Mineral. 11, 1043–1049.

Bonyadi, Z., Davidson, G.J., Mehrabi, B., Meffre, S., Ghazban, F., 2011. Significance of apatite REE depletion and monazite inclusions in the brecciated Se-Chahun iron oxide-apatite deposit, Bafq district, Iran: insights from paragenesis and geochemistry. Chem. Geol. 281, 253–269.

Boulangé, B., Colin, F., 1994. Rare earth element mobility during conversion of nepheline syenite into lateritic bauxite at Passa Quatro, Minais Gerais, Brazil. Appl. Geochem. 9, 701–711.

Braun, J.J., Pagel, M., 1994. Geochemical and mineralogical behavior of REE, Th and U in the Akongo lateritic profile (SW Cameroon). Catena 21, 173–177.

Braun, J.J., Pagel, M., Muller, J.P., Bilong, P., Michard, A., Guillet, B., 1990. Cerium anomalies in lateritic profiles. Geochim. Cosmochim. Acta 54, 781–795.

Braun, J.J., Pagel, M., Herbillon, A., Rosin, C., 1993. Mobilization and redistribution of REEs XE "REEs" and thorium in a syenitic lateritic profile: a mass balance study. Geochim. Cosmochim. Acta 57, 4419–4434.

Braun, J.J., Viers, J., Dupré, B., Polve, M., Ndam, J., Muller, J.P., 1998. Solid/liquid REE fractionation in the lateritic system of Goyoum, East Cameroon: the implication for the present dynamics of the soil covers of the humid tropical regions. Geochim. Cosmochim. Acta 62, 273–299.

Breiter, K., Förster, H.-J., Škoda, R., 2006. Extreme P-, Bi-, Nb-, Sc-, U- and F-rich zircon from fractionated perphosphorous granites: the peraluminous Podlesí granite system, Czech Republic. Lithos 88, 15–34.

Breiter, K., Čopjaková, R., Škoda, R., 2009. The involvement of F, CO_2, and As in the alteration of Zr–Th–REE-bearing accessory minerals in the Hora Svaté Kateřiny A-type Granite, Czech Republic. Can. Mineral. 47, 1375–1398.

Brookins, D.G., 1988. Eh-pH Diagrams for Geochemistry. Springer-Verlag, New York. 176p.

Broska, I., Petrík, I., 2008. Genesis and stability of accessory phosphates in silicic magmatic rocks: a Western Carpathian case study. Mineralogia 39, 53–65.

Broska, I., Petrík, I., Williams, C.T., 2000. Coexisting monazite and allanite in peraluminous granitoids of the Tribeč Mountains, western Carpathians. Am. Mineral. 85, 22–32.

Broska, I., Williams, C.T., Janák, M., Nagy, G., 2005. Alteration and breakdown of xenotime-(Y) and monazite-(Ce) in granitic rocks of the Western Carpathians, Slovakia. Lithos 82, 71–83.

Bühn, B., Rankin, A.H., 1999. Composition of natural, volatile-rich Na-Ca-REE-Sr carbonatitic fluids trapped in fluid inclusions. Geochim. Cosmochim. Acta 63, 3781–3797.

Bulakh, A.G., Le Bas, M.J., Wall, F., Zaitsev, A.N., 1998. Ancylite-bearing carbonatites of the Seblyavr massif, Kola Peninsula, Russia. N. Jb. Miner. Mh., 4, 171–192.

Byrne, R.H., Lee, J.H., Bingler, L.S., 1991. Rare earth element complexation by PO_4^{3-} ions in aqueous solution. Geochim. Cosmochim. Acta 55, 2729–2735.

Calagari, A.A., Abedini, A., 2007. Geochemical investigations on Permo-Triassic bauxite horizon at Kanisheeteh, east of Bukan, West-Azarbaidjan, Iran. J. Geochem. Explor. 94, 1–18.

Campbell, A.C., Palmer, M.R., Klinkhammer, G.P., Bowers, T.S., Edmond, J.M., Lawrence, J.R., Casey, J.F., Thompson, G., Humphris, S.E., Rona, P., 1988. Chemistry of hot springs on the Mid-Atlantic Ridge. Nature 335, 514–519.

Cantrell, K.J., Byrne, R.H., 1987. Rare earth element complexation by carbonate and oxalate ions. Geochim. Cosmochim. Acta 51, 597–605.

Carroll, D., 1959. Ion exchange in clays and other minerals. Geol. Soc. Am. Bull. 70, 749–779.

Caruso, L., Simmons, G., 1985. Uranium and microcracks in a 1,000-meter core, Redstone, New Hampshire. Contrib. Mineral. Petrol. 90, 1–17.

Casillas, R., Nagy, G., Pantó, G., Brändle, J., Fórizs, I., 1995. Occurrence of Th, U, Y, Zr, and REE-bearing accessory minerals in late-Variscan granitic rocks from the Sierra de Guadarrama (Spain). Eur. J. Mineral. 7, 989–1006.

Castor, S.B., 2008a. The Mountain Pass rare-earth carbonatite and associated ultrapotassic rocks, California. Can. Mineral. 46, 779–806.

Castor, S.B., 2008b. Rare earth deposits of North America. Resour. Geol. 58, 337–347.

Castor, S.B., Hedrick, J.B., 2006. Rare earth elements. In: Kogel, J.E., Trivedi, N.C., Barker, J.M., Krukowski, S.T. (Eds.), Industrial Mineral and Rocks, seventh ed. Society for Mining, Metallurgy, and Exploration, Inc, Littleton, pp. 769–792.

Catlos, E.J., Sorensen, S.S., Harrison, T.M., 2000. Th–Pb ion-microprobe dating of allanite. Am. Mineral. 85, 633–648.

Černý, P., Siivola, J., 1980. The tanco pegmatite at Bernic Lake, Manitoba. XII. Hafnian zircon. Can. Mineral. 18, 313–321.

Chaïrat, C., Schott, J., Oelkers, E.H., Lartigue, J.-E., Harouiya, N., 2007. Kinetics and mechanism of natural fluorapatite dissolution at 25°C and pH from 3 to 12. Geochim. Cosmochim. Acta 71, 5901–5912.

Chakhmouradian, A.R., 2006. High-field-strength elements in carbonatitic rocks: geochemistry, crystal chemistry and significance for constraining the sources of carbonatites. Chem. Geol. 235, 138–160.

Chakhmouradian, A., Mitchell, R.H., 1998. Lueshite, pyrochlore and monazite-(Ce) from apatite-dolomite carbonatite, Lesnaya Varaka complex, Kola Peninsula, Russia. Mineral. Mag. 62, 769–782.

Chao, E.C.T., Back, J.M., Minkin, J.A., 1992. Host-rock controlled epigenetic, hydrothermal metasomatic origin of the Bayan Obo REE-Fe-Nb ore deposit, Inner Mongolia, P.R.C. Appl. Geochem. 7, 443–458.

Chappell, B.W., 1999. Aluminium saturation in I- and S-type granites and the characterization of fractionated haplogranites. Lithos 46, 535–551.

Chappell, B.W., White, A.J.R., 1974. Two contrasting granite types. Pac. Geol. 8, 173–174.

Chen, D., 1996. The Discovery History of Mineral Deposits of Jiangxi Province, China. Geological Publishing House, Beijing. 245p (in Chinese with English summary).

Chen, R.G., 2013. Characteristics and regularity analysis of the Chengnan rare earth ores in Ninghua County, Fujian Province. J. Yangtze Univ. (Nat. Sci. Ed.) 10, 65–67 (in Chinese).

Chen, B.H., Yu, S.J., 1994. The geological and geochemical characteristics of Late Yanshanian granites in Renju-Huangshe area, Pingyuan Guangdong. J. Zhongshan Univ. 33, 130–133 (in Chinese with English abstract).

Chen, B.H., Wu, F.H., Liu, F.F., 2001. Experimental study on the effects of organic acids on the dissolution of REE in the weathering crust of granite. Chin. J. Geochem. 20, 144–151.

Chen, N., Pan, Y., Weil, J.A., 2002a. Electron paramagnetic resonance spectroscopic study of synthetic fluorapatite: part I. Local structural environment and substitution mechanism of Gd at the Ca2 site. Am. Mineral. 87, 37–46.

Chen, N., Pan, Y., Weil, J.A., Nilges, M.J., 2002b. Electron paramagnetic resonance spectroscopic study of synthetic fluorapatite: part II. Gd3+ at the Ca1 site, with a neighboring Ca2 vacancy. Am. Mineral. 87, 47–55.

Cherniak, D.J., 2000. Rare earth element diffusion in apatite. Geochim. Cosmochim. Acta 64, 3871–3885.

Chi, R.A., Tian, J., 2009. Weathered Crust Elution-Deposited Rare Earth Ores. Nova Science Publishers, New York. 288p.

Chi, R.A., Tian, J., Li, Z.J., Peng, C., Wu, Y.X., Li, S.R., Wang, C.W., Zhou, Z.A., 2005. Existing state and partitioning of rare earth on weathered ores. J. Rare Earths 23, 756–759.

Chi, R.A., Tian, J., Luo, X.P., Xu, Z.G., He, Z.Y., 2012. The basic research on the weathered crust elution-deposited rare earths ores. Nonferrous Met. Sci. Eng. 3, 1–14 (in Chinese with English abstract).

Claeson, D.T., 2002. Stability of REE-bearing minerals in a metaluminous leucotonalite from the Eriksberg gabbro, Transscandinavian Igneous Belt, Sweden. Neues Jahrb. Mineral. Abh. 177, 277–291.

Clarke, R.S., Altschuler, Z.S., 1958. Determination of the oxidation state of uranium in apatite and phosphorite deposits. Geochim. Cosmochim. Acta 13, 127–142.

Comodi, P., Liu, Y., Stoppa, F., Woolley, A.R., 1999. A multi-method analysis of Si-, S- and REE-rich apatite from a new kind of kalsilite-bearing leucitite (Abruzzi, Italy). Mineral. Mag. 63, 661–672.

Cook, N.J., Ciobanu, C.L., O'Rielly, D., Wilson, R., Das, K., Wade, B., 2013. Mineral chemistry of rare earth element (REE) mineralization, Browns Ranges, Western Australia. Lithos 172–173, 192–213.

Cox, K.G., Bell, J.D., Pankhurst, R.J., 1979. The Interpretation of Igneous Rocks. George Allen and Unwin, London. 450p.

Craddock, P.R., Bach, W., Seewald, J.S., Rouxel, O.J., Reeves, E., Tivey, M.K., 2010. Rare earth element abundances in hydrothermal fluids from the Manus Basin. Papua New Guinea: indicators of sub-sealoor hydrothermal processes in back-arc basins. Geochim. Cosmochim. Acta 74, 5494–5513.

Crocker, I.T., Martini, J.E.J., Söhnge, A.P.G., 1988. The Fluorspar Deposits of the Republics of South Africa and Bophuthatswana. Handbook 11, Department of Mineral and Energy Affairs of Republic of South Africa, Pretoria, South Africa. 172pp.

Crocker, I.T., Eales, H.V., Ehlers, D.L., 2001. The fluorite, cassiterite and sulphide deposits associated with the acid rocks of the Bushveld Complex. Memoir 90, Council for Geoscience, Pretoria, South Africa. 115pp.

Dasgupta, R., Hirschmann, M.M., McDonough, W.F., Spiegelman, M., Withers, A.C., 2009. Trace element partitioning between garnet lherzolite and carbonatite at 6.6 and 8.6 GPa with applications to the geochemistry of the mantle and of mantle-derived melts. Chem. Geol. 262, 57–77.

De Carlo, E.H., Wen, X.Y., Irving, M., 1998. The influence of redox reactions on the uptake of dissolved Ce by suspended Fe and Mn oxide particles. Aquat. Geochem. 3, 357–389.

De Oliveira, S.M.B., Imbernon, R.A.L., 1998. Weathering alteration and related REE concentration in the Catalão I carbonatite complex, central Brazil. J. S. Am. Earth Sci. 4, 379–388.

Della-Ventura, G., Williams, C.T., Cabella, R., Oberti, R., Caprilli, E., Bellatreccia, F., 1999. Britholite-hellandite intergrowths and associated REE-minerals from the alkali-syenitic ejecta of the Vico volcanic complex (Latium, Italy): petrological implications bearing on REE mobility in volcanic systems. Eur. J. Mineral. 11, 843–854.

Demartin, F., Pilati, T., Diella, V., Gentile, P., Gramaccioli, C.M., 1993. A crystal chemical investigation of alpine gadolinite. Can. Mineral. 30, 127–136.

Demény, A., Vennemann, T.W., Hegner, E., Nagym, G., Milton, J.A., Embey-Isztin, A., Homonnay, Z., Dobosi, G., 2004. Trace element and C-O-Sr-Nd isotope evidence for subduction-related carbonate-silicate melts in mantle xenoliths (Pannonian Basin, Hungary). Lithos 75, 89–113.

Deng, Z.C., 1988. Characteristics and genesis of the Datian HREE granite, southern Jiangxi. J. Guilin Coll. Geol. 8, 39–48 (in Chinese with English abstract).

Deng, J., 2013. Geological characteristics and metallogenic conditions of the Xiache REE deposits in Heping County, Guangdong Province. Earth 5, 5 (in Chinese).

Dill, H.G., 2001. The geology of aluminium phosphates and sulphates of the alunite group minerals: a review. Earth Sci. Rev. 53, 35–93.

Ding, J.Y., 2012. Historical review of the ionic rare earth mining: in honor of the 60 anniversary of GNMR. Nonferrous Met. Sci. Eng. 3, 14–19 (in Chinese with English abstract).

Downes, H., Balaganskaya, E., Beard, A., Liferovich, R., Demaiffe, D., 2005. Petrogenetic processes in the ultramafic, alkaline and carbonatitic magmatism in the Kola Alkaline Province: a review. Lithos 85, 48–75.

Du, X., Rate, A.W., Gee, M.A.M., 2012. Redistribution and mobilization of titanium, zirconium and thorium in an intensely weathered lateritic profile in Western Australia. Chem. Geol. 330–331, 101–115.

Duncan, R.K., Willett, G.C., 1990. Mount Weld carbonatite. In: Hughes, F.E. (Ed.), Geology of the Mineral Deposits of Australia and Papua New Guinea. The Australasian Institute of Mining and Metallurgy, Melbourne, pp. 591–597.

Dymek, R.F., Owens, B.E., 2001. Petrogenesis of apatite-rich rocks (nelsonites and oxide-apatite gabbronorites) associated with massif anorthosites. Econ. Geol. 96, 797–815.

Edfelt, Å., Armstrong, R.N., Smith, M., Martinsson, O., 2005. Alteration paragenesis and mineral chemistry of the Tjårrojåkka apatite-iron and Cu (−Au) occurrences, Kiruna area, northern Sweden. Miner. Deposita 40, 409–434.

Einsele, G., 2000. Sedimentary Basins: Evolution, Facies, and Sediment Budget, second, completely revised and enlarged ed. Springer, Berlin/Heidelberg/New York/London/Paris/Tokyo/Hong Kong. 792p.

Eliopoulos, D., Economou, G., Tzifas, I., Papatrechas, C., 2014. The potential of rare earth elements in Greece. In: Extended Abstract of ERES2014: 1st European Rare Earth Resources Conference, Milos, 04–07/09/2014, pp. 308–316.

Elliott, J.C., 1994. Structure and Chemistry of the Apatites and Other Calcium Orthophosphates. Elsevier, Amsterdam.

Elsner, H., Buxhholz, P., Schmitz, M., Altangerel, T., 2011. Rare earths. In: Industrial Minerals and Selected Rare Metals in Mongolia, An Investors' Guide. The Government of Mongolia, Ulaanbaatar, pp. 248–265.

Emsbo, P., McLaughlin, P.I., Breit, G.N., du Bray, E.A., Koenig, A.E., 2015. Rare earth elements in sedimentary phosphate deposits: solution to the global REE crisis? Gondwana Res. 27, 776–785.

Emsbo, P., McLaughlin, P.I., du Bray, E.A., Anderson, E.D., Vandenbroucke, T.R.A., Zielinski, R.A., 2016. Rare earth elements in sedimentary phosphorite deposits: A global assessment. Rev. Econ. Geol. 18, 101–113.

Ercit, T.S., 2005. REE-enriched granitic pegmatite. In: Linnen, R.L., Samson, I.M. (Eds.), Rare-Element Geochemistry and Mineral Deposits, vol. 17. Geological Association of Canada, Short Course Notes, St John's, pp. 175–199.

Ernst, R.E., Bell, K., 2010. Large igneous province (LIPs) and carbonatite XE "carbonatite"s. Mineral. Petrol. 98, 55–76.

European Commission, 2010. Critical Raw Materials for the EU. European Commission Enterprise and Industry, Brussels, Belgium, 85p.

European Fertilizers Manufacturers Association (EFMA), 2000. Best available techniques for pollution prevention and control in the european fertilizer industry: booklet no. 4 of 8: production of phosphoric acid. EFMA, Brussels, pp. 1–44.

Ewing, R.C., 1994. The metamict state: 1993—the centennial. Nucl. Instrum. Methods Phys. Res. B91, 22–29.

Ewing, R.C., 1999. Nuclear waste forms for actinides. Proc. Natl. Acad. Sci. 96, 3432–3439.

Ewing, R.C., Haaker, R.F., Lutze, W., 1981. Leachability of zircon as a function of alpha dose. MRS Proc. 11, 389.

Ewing, R.C., Meldrum, A., Wang, L., Weber, W.J., Corrales, L.R., 2003. Radiation effects in zircon. In: Hanchar, J.M., Hoskin, P.W.O. (Eds.), vol. 53. Rev. Mineral. Geochem., Washington, DC, pp. 387–425.

Felsche, F., 1972. Rare earth silicates with apatite structure. J. Solid State Chem. 5, 266–275.

Féménias, O., Coussaert, N., Brassinnes, S., Demaiffe, D., 2005. Emplacement processes and cooling history of layered cyclic unit II-7 from the Lovozero alkaline massif (Kola Peninsula, Russia). Lithos 83, 371–393.

Feng, Z.H., Wang, C.Z., Zhang, M.H., Liang, J.C., 2012. Unusually dumbbell-shaped Guposhan-Huashan twin granite plutons in Nanling Range of south China: discussion on their incremental emplacement and growth mechanism. J. Asia Earth Sci. 48, 9–23.

Ferris, A.P., Jepson, W.B., 1975. The exchange capacities of kaolinite and the preparation of homoionic clays. J. Colloid Interface Sci. 51, 245–259.

Finch, R.J., Hanchar, J.M., 2003. The composition of zircon and igneous and metamorphic petrogenesis. In: Hanchar, J.M., Hoskin, P.W.O. (Eds.), Zircon, vol. 53. Rev. Mineral. Geochem., Washington, DC, pp. 1–25

Finger, F., Broska, I., Roberts, M.P., Schermaier, A., 1998. Replacement of primary monazite by apatite-allanite-epidote coronas in an amphibolite facies granite gneiss from the eastern Alps. Am. Mineral. 83, 248–258.

Fleet, M.E., Pan, Y., 1995. Site preference of rare earth elements in fluorapatite. Am. Mineral. 80, 329–335.

Förster, H.-J., 1998. The chemical composition of REE-Y-Th-U-rich accessory minerals in peraluminous granites of the Erzgebirge-Fichtelgebirge region, Germany, part I: the monazite XE "monazite" -(Ce)-brabantite solid solution series. Am. Mineral. 83, 259–272.

Förster, H.-J., 2000. Cerite-(Ce) and thorian synchysite XE "synchysite"-(Ce) from the Niederbobritzsch granite, Erzgebirge, Germany: implications for the differential mobility of the LREE and Th during alteration. Can. Mineral. 38, 67–79.

Förster, H.-J., 2006. Composition and origin of intermediate solid solutions in the system thorite-xenotime-zircon-coffinite. Lithos 88, 35–55.

Franz, G., Andrehs, G., Rhede, D., 1996. Crystal chemistry of monazite and xenotime from Saxothuringian–Moldanubian metapelites, NE Bavaria, Germany. Eur. J. Mineral. 8, 1097–1108.

Frietsch, R., Perdahl, J.-A., 1995. Rare earth elements in apatite and magnetite in Kiruna-type iron ores and some other iron ore types. Ore Geol. Rev. 9, 489–510.

Ganzeev, A.A., Grechishchev, O.K., 2003. A new genetic type of rare-metal alkali granites of Madagascar. Geol. Geofiz. 44, 539–553.

Gavrilova, L.K., Turanskaya, R.V., 1958. Distribution of rare-earths in rock-forming and accessory minerals of certain granites. Geochemistry 2, 163–169.

Gieré, R., 1996. Formation of rare earth minerals in hydrothermal systems. In: Jones, A.P., Williams, C.T., Wall, F. (Eds.), Rare Earth Minerals: Chemistry, Origin and Ore Deposits. Mineralogical Society Series, vol. 7. Chapman & Hall, London, pp. 105–150.

Gieré, R., Sorensen, S.S., 2004. Allanite and other REE-rich epidote-group minerals. In: Liebscher, A., Franz, G. (Eds.), Epidote. vol. 56. Rev. Mineral. Geochem., Washington, DC, pp. 431–493.

Gislason, S.R., Oelkers, E.H., Eiriksdottir, E.S., Kardjilov, M.I., Gisladottir, G., Sigfusson, B., Snorrason, A., Elefsen, S., Hardardottir, J., Torssander, P., Oskarsson, N., 2009. Direct evidence of the feedback between climate and weathering. Earth Planet. Sci. Lett. 277, 213–222.

Glaus, M.A., Hummel, W., Van Loon, L.R., 2000. Trace metal-humate interactions. I. Experimental determination of conditional stability constants. Appl. Geochem. 15, 953–973.

Goss, A.R., Kay, S.M., Mpodozis, C., 2013. Andean adakite-like high-Mg andesites on the northern margin of the Chilean-Pampean Flat-slab (27–28.5°S) associated with frontal arc migration and fore-arc subduction erosion. J. Petrol. 54, 2193–2234.

Gramaccioli, C.M., Diella, V., Demartin, F., Orlandi, P., Campostrini, I., 2000. Cesian bazzite and thortveitite from Cuasso al Monte, Varese, Italy: a comparison with the material from Baveno, and inferred origin. Can. Mineral. 38, 1409–1418.

Gromet, L.P., Silver, L.T., 1983. Rare earth element distributions among minerals in a granodiorite and their petrogenetic implications. Geochim. Cosmochim. Acta 47, 925–939.

Gu, S.Y., Hua, R.M., Qi, H.W., 2006. Geochemistry and petrogenesis of the Yanshanian Huashan-Guposhan granites in Guanxi. Acta Petrol. Mineral. 25, 97–109 (in Chinese with English abstract).

Guidry, M.W., MacKenzie, F.T., 2003. Experimental study of igneous and sedimentary apatite dissolution: control of pH, distance from equilibrium, and temperature on dissolution rates. Geochim. Cosmochim. Acta 67, 2949–2963.

Gupta, C.K., Krishnamurthy, N., 2005. Extractive Metallurgy of Rare Earths. CRC Press, Boca Raton, FL. 508p.

Habashi, F., 1985. The recovery of the lanthanides from phosphate rock. J. Chem. Technol. Biotechnol. 35A, 5–14.

Halama, R., Vennemann, T., Siebel, W., Markl, G., 2005. The Grønnedal-Ika carbonatite-syenite complex, South Greenlan: carbonatite formation by liquid immiscibility. J. Petrol. 46, 191–217.

Halpin, K.M., 2010. The characteristics and origin of the Hoidas Lake REE deposit. MSc thesis, University of Saskatchewan, Saskatoon, Canada.

Harlov, D.E., Andersson, U.B., Förster, H.J., Nyström, J.O., 2002. Apatite-monazite relations in the Kiirunavaara magnetite-apatite ore, northern Sweden. Chem. Geol. 191, 47–72.

Harmer, R.E., 1999. The petrogenetic association of carbonatite and alkaline magmatism: constraints from the Spitskop Complex, South Africa. J. Petrol. 40, 525–548.

Harouiya, N., Chaïrat, C., Köhler, S.J., Gout, R., Oelkers, E.H., 2007. The dissolution kinetics and apparent solubility of natural apatite in closed reactors at temperatures from 5 to 50°C and pH from 1 to 6. Chem. Geol. 244, 554–568.

Harrison, W.J., 1981. Partitioning of REE between minerals and coexisting melts during partial melting of a garnet lherzolite. Am. Mineral. 66, 242–259.

Hazen, R.M., Finger, L.W., 1979. Crystal structure and compressibility of zircon at high pressure. Am. Mineral. 64, 196–201.

Hazen, R.M., Papineau, D., Bleeker, W., Downs, R.T., Ferry, J.M., McCoy, T.J., Sverjensky, D.A., Yang, H., 2008. Mineral evolution. Am. Mineral. 93, 1693–1720.

Hazen, R.M., Ewing, R.C., Sverjensky, D.A., 2009. Evolution of uranium and thorium minerals. Am. Mineral. 94, 1293–1311.

Hazen, R.M., Bekker, A., Bish, D.L., Bleeker, W., Downs, R.T., Farquhar, J., Ferry, J.M., Grew, E.S., Knoll, A.H., Papineau, D., Ralph, J.P., Sverjensky, D.A., Valley, J.W., 2011. Needs and opportunities in mineral evolution research. Am. Mineral. 96, 953–963.

Hazen, R.M., Golden, J., Downs, R.T., Hysted, G., Grew, E.S., Azzolini, D., Sverjensky, D.A., 2012. Mercury (Hg) mineral evolution: a mineralogical record of supercontinent assembly, changing ocean geochemistry, and the emerging terrestrial biosphere. Am. Mineral. 97, 1013–1042.

Hazen, R.M., Downs, R.T., Kah, L., Sverjensky, D., 2013. Carbon mineral evolution. In: Hazen, R.M., Jones, A.P., Baross, J.A. (Eds.), Carbon in Earth. vol. 75. Rev. Mineral. Geochem., Washington, DC, pp. 79–107.

Hedrick, J.B., Sinha, S.P., Kosynkin, V.D., 1997. Loparite, a rare-earth ore (Ce, Na, Sr, Ca)(Ti, Nb, Ta, Fe^{+3})O_3. J. Alloys Compd. 250, 467–470.

Heinrich, C.A., Pettke, T., Halter, W.E., Aigner-Torres, M., Audétat, A., Günther, D., Hattendorf, B., Bleiner, D., Guillong, M., Horn, I., 2003. Quantitative multi-element analysis of minerals, fluid and melt inclusions by laser-ablation inductively-coupled-plasma mass-spectrometry. Geochim. Cosmochim. Acta 67, 3473–3497.

Henderson, P., 1996. The rare earth elements: introduction and review. In: Jones, A.P., Wall, F., Williams, C.T. (Eds.), Rare Earth Minerals. The Mineralogical Society Series, vol. 7. Chapman & Hall, London, pp. 1–19.

Hildebrand, R.S., 1986. Kiruna-type deposits: their origin and relationship to intermediate subvolcanic plutons in the Great Bear Magmatic Zone, northwest Canada. Econ. Geol. 81, 640–659.

Hirano, H., Kamitani, M., Sato, T., Sudo, S., 1990. Niobium mineralization of Catalao I carbonatite complex, Goias, Brazil. Bull. Geol. Surv. Jpn. 41, 577–594.

Hofmann, A.W., 2005. Sampling mantle heterogeneity through oceanic basalts: isotopes and trace elements. In: Carson, R.W. (Ed.), The Mantle and Core. Treatise of Geochemistry, vol. 2. Elsevier, Amsterdam, pp. 61–101.

Hongo, Y., Obata, H., Gamo, T., Nawaseama, M., Ishibashi, J., Konno, U., Saegusa, S., Ohkubo, S., Tsunogai, U., 2007. Rare earth elements in the hydrothermal system at Okinawa Trough back-arc basin. Geochem. J. 41, 1–15.

Horiuchi, Y., Ohno, T., Hoshino, M., Shin, K.-C., Murakami, H., Tsunematsu, M., Watanabe, Y., 2014. Geochemical prospecting for rare earth elements using termite mound materials. Mineral. Deposita 49, 1013–1023.

Hornig-Kjarsgaard, I., 1998. Rare earth elements in Sövitic carbonatites and their mineral phases. J. Petrol. 39, 2105–2121.

Horváth, L., 2014. Catalogue of mineral species occurring in Canada. http://www.mineralogicalassociation.ca/doc/catcanmin.pdf#search='Catalogue+of+mineral+species+occurring+in+canada'.

Hoshino, M., Watanabe, Y., Kon, Y. Contribution of apatite to the crystallization of allanite in an Iron-Oxide-Apatite (IOA) prospect, Benjamin River, Canada. Resour. Geol. (submitted).

Hoshino, M., Kimata, M., Shimizu, M., Nishida, N., Fujiwara, T., 2006. Allanite-(Ce) in granitic rocks from Japan: genetic implications of patterns of REE and Mn enrichment. Can. Mineral. 44, 45–62.

Hoshino, M., Kimata, M., Arakawa, Y., Shimizu, M., Nishida, N., Nakai, S., 2007. Allanite-(Ce) as an indicator of the origin of granitic rocks in Japan: importance of Sr-Nd isotopic and chemical composition. Can. Mineral. 45, 1329–1336.

Hoshino, M., Kimata, M., Nishida, N., Shimizu, M., Akasaka, T., 2010. Crystal chemistry of zircon from granitic rocks, Japan: genetic implications of HREE, U and Th enrichment. N. Jb. Mineral. (Abh.) 187, 167–188.

Hoshino, M., Watanabe, Y., Sanematsu, K., Kon, Y., Shimizu, M., 2012a. Characteristics of zircon suitable for REE extraction. Int. J. Miner. Process. 102–103, 130–135.

Hoshino, M., Watanabe, Y., Ishihara, S., 2012b. Crystal chemistry of monazite from the granitic rocks of Japan: petrogenetic implications. Can. Mineral. 50, 1331–1346.

Hoshino, M., Watanabe, Y., Murakami, H., Kon, Y., Tsunematsu, M., 2013. Formation process of zircon associated with REE-fluorocarbonate and niobium minerals in the Nechalacho REE deposit, Thor Lake, Canada. Resour. Geol. 63, 1–26.

Hoshino, M., Moritz, R., Ovtcharova, M., Watanabe, Y., Spangenberg, J., Putlitz, B., 2015. REE mineralization of the Blockspruit fluorite prospect, Bushveld granitic complex, South Africa: geochemical, mineralogical and fluid inclusion studies. In: Proceedings of the 13th Biennial SGA Meeting, "Mineral Resources in a Sustainable World", 2015, 2, pp. 1513–1516.

Hoskin, P.W.O., Schaltegger, U., 2003. The composition of zircon and igneous and metamorphic petrogenesis. In: Hanchar, J.M., Hoskin, P.W.O. (Eds.), Zircon, vol. 53. Rev. Mineral. Geochem., Washington, DC, pp. 27–62.

Hua, R.M., Zhang, W.L., Gu, S.Y., Chen, P.R., 2007. Comparison between REE granite and W–Sn granite in the Nanling region, South China, and their mineralizations. Acta Petrol. Sin. 23, 2321–2328 (in Chinese with English abstract).

Huang, W.H., 1989. Geochemical characteristics of the Laishi REE deposits in Xinfeng County, Guangdong Province. Geol. Nonferrous Met.Guangdong Province 2, 26–37 (in Chinese).

Huang, D.H., Wu, C.G., Han, J.Z., 1989. REE geochemistry and mineralization characteristics of the Zudong and Guanxi Granites, Jiangxi Province. Acta Geol. Sin. 2, 139–157.

Huang, X.L., Wang, R.C., Chen, X.M., Hu, H., Liu, C.S., 2002. Vertical variations in the mineralogy of the Yichun topaz-lepidolite granite, Jiangxi Province, southern China. Can. Mineral. 40, 1047–1068.

Hughes, J.M., Cameron, M., Mariano, A.N., 1991. Rare-earth element ordering and structural variations in natural rare-earth-bearing apatite. Am. Mineral. 76, 1165–1173.

Hughson, M.R., Sen Gupta, J.G., 1964. A thorian intermediate member of the britholite-apatite series. Am. Mineral. 49, 937–951.

Huo, M.Y., 1992. Distribution characteristics of the weathering-crust-type rare-earth resources in Nanling, China. J. Nat. Resour. 7, 64–70 (in Chinese with English abstract).

Hurley, P.M., Fairbairn, H.W., 1953. Radiation damage in zircon, a possible age method. Geol. Soc. Am. Bull. 64, 659–674.

Hutton, C.O., 1950. Studies of heavy detrital minerals. Geol. Soc. Am. Bull. 61, 635–716.

Ihlen, P.M., Schiellerup, H., Gautneb, H., Skå, Ø., 2014. Characterization of apatite resources in Norway and their REE potential—a review. Ore Geol. Rev. 58, 126–147.

Imai, A., Yonezu, K., Sanematsu, K., Ikuno, T., Ishida, S., Watanabe, K., Pisutha-Arnond, V., Nakapadungrat, S., Boosayasak, J., 2013. Rare earth elements in hydrothermally altered granitic rocks in the Ranong and Takua Pa tin-field, southern Thailand. Resour. Geol. 63, 84–98.

Ishihara, S., 1977. The magnetite-series and ilmenite-series granitic rocks. Min. Geol. 27, 293–305.

Ishihara, S., 1981. The granitoid series and mineralization. Econ. Geol., 75th Anniv. 458–484.

Ishihara, S., Matsuhisa, Y., 1999. Oxygen isotopic constraints on the geneses of the Miocene outer zone granitoids in Japan. Lithos 46, 523–534.

Ishihara, S., Murakami, H., 2006. Fractionated ilmenite-series granites in southwest Japan: source magna for REE-Sn-W mineralization. Resour. Geol. 56, 245–256.

Ishihara, S., Hua, R., Hoshino, M., Murakami, H., 2008. REE abundance and REE mineral XE "REE mineral"s in granitic rocks in Nanling range, Jiangxi Province, Southern China, and generation of the REE-rich weathered crust deposits. Resour. Geol. 58, 355–372.

Ito, J., 1968. Silicate apatites and oxyapatites. Am. Mineral. 53, 890–907.

Ivanova, T.I., Frank-Kamenetskaya, O.V., Kol'tsov, V., Ugolkov, L., 2001. Crystal structure of calcium-deficient carbonated hydroxyapatite. Thermal decomposition. J. Solid State Chem. 160, 340–349.

Jackson, W.D., Christiansen, G., 1993. International strategic minerals inventory summary report—rare-earth oxides. U.S. Geological Survey, Reston, VA. Circular 930-N. 68p.

Jaireth, S., Hoatson, D.M., Miezitis, Y., 2014. Geological setting and resources of the major rare-earth-element deposits in Australia. Ore Geol. Rev. 62, 72–128.

Jami, M., Dunlop, A.C., Cohen, D.R., 2007. Fluid inclusion and stable isotope study of the Esfordi apatite-magnetite deposit, central Iran. Econ. Geol. 102, 1111–1128.

JAMSTEC, 2013. Discovery and Distribution of Mud Containing Very High Concentrations of Rare Earth Elements and Yttrium around Minami-Torishima Island. Press Release of JAMSTEC, Yokosuka. (cited 21 Mar. 2013). Available from URL: http://www.jamstec.go.jp/e/about/press_release/20130321/.

Janots, E., Negro, F., Brunet, F., Goffé, B., Engi, M., Bouybaouène, M.L., 2006. Evolution of the REE mineralogy in HP–LT metapelites of the Sebtide complex, Rif, Morocco: monazite stability and geochronology. Lithos 87, 214–234.

Janots, E., Bernier, F., Brunet, F., Muñoz, M., Trcera, N., Berger, A., Lanson, M., 2015. Ce (III) and Ce (IV) (re)distribution and fractionation in a laterite profile from Madagascar: insights from in situ XANES spectroscopy at the Ce L_{III}-edge. Geochim. Cosmochim. Acta 153, 134–148.

Jarosiński, A., Kowalczyk, J., Mazanek, C., 1993. Development of the Polish wasteless technology of apatite phosphogypsum utilization with recovery of rare earths. J. Alloys Compd. 200, 147–150.

Jefferson, C.W., Thomas, D.J., Gandhi, S.S., Ramaekers, P., Delaney, G., Brisbin, D., Cutts, C., uirt, D., Portella, P., Olson, R.A., 2007. Unconformity-associated uranium deposits of the Athabasca Basin, Saskatchewan and Alberta. In: Goodfellow, W.D. (Ed.), Mineral Deposits of Canada: a Synthesis of Major Deposit-Types, District Metallogeny, the Evolution of Geological Provinces, and Exploration Methods. Geological Association of Canada, Mineral Deposits Division, Special Publication No. 5, pp. 273–305.

Johan, Z., Johan, V., 2005. Accessory minerals of the Cinovec (Zinnwald) granite cupola, Czech Republic: indicators of petrogenetic evolution. Mineral. Petrol. 83, 113–150.

Johannesson, K.H., Stetzenbach, K.J., Hodge, V.F., Lyons, W.B., 1996. Rare earth element complexation behavior in circumneutral pH groundwaters: assessing the role of carbonate and phosphate ions. Earth Planet. Sci. Lett. 139, 305–319.

Jonsson, E., Troll, V.R., Högdahl, K., Harris, C., Weis, F., Nilsson, K.P., Skelton, A., 2013. Magmatic origin of giant 'Kiruna-type' apatite XE "apatite"-iron-oxide ores in Central Sweden. Sci. Rep. 3, 1644. http://dx.doi.org/10.1038/srep01644.

Jordens, A., Cheng, Y.P., Waters, K.E., 2013. A review of the beneficiation of rare earth element bearing minerals. Miner. Eng. 41, 97–114.

Joussein, E., Petit, S., Churchman, J., Theng, B., Righi, D., Delvaux, B., 2005. Halloysite clay minerals—a review. Clay Miner. 40, 383–426.

Kanazawa, Y., Kamitani, M., 2006. Rare earth minerals and resources in the world. J. Alloys Compd. 408–412, 1339–1343.

Karadağ, M.M., Küpeli, Ş., Arýk, F., Ayhan, A., Zedef, V., Döyen, A., 2009. Rare earth element (REE) geochemistry and genetic implications of the Mortaş bauxite deposit (Seydişehir/Konya–Southern Turkey). Chem. Erde 69, 143–159.

Kartashov, P.M., Ferraris, G., Ivaldi, G., Sokolova, E., McCammon, C.A., 2002. Ferriallanite-(Ce), $CaCeFe^{3+}AlFe^{2+}(SiO_4)(Si_2O_7)O(OH)$, a new member of the epidote group: description, X-ray and Mössbauer study. Can. Mineral. 2002 (40), 1641–1648.

Kato, A., 2008. Nihonsankoubutsubunruibetsuichiran. Mumeikai, Tokyo, p. 131.

Kato, Y., Fujinaga, K., Nozaki, T., Osawa, H., Nakamura, K., Ono, R., 2005. Rare earth, major and trace elements in the Kunimiyama ferromanganese deposit in the northern Chichibu Belt, central Shikoku, Japan. Resour. Geol. 55, 291–299.

Kato, Y., Fujinaga, K., Nakamura, K., Takaya, Y., Kitamura, K., Ohta, J., Toda, R., Nakashima, T., Iwamori, H., 2011. Deep-sea mud in the Pacific Ocean as a potential resource for rare-earth elements. Nat. Geosci. 4, 535–539.

Kelts, A.B., Ren, M., Anthony, E.Y., 2008. Monazite occurrence, chemistry and chronology in the granitoid rocks of the Lachlan fold Belt, Australia: an electron microprobe study. Am. Mineral. 93, 373–383.

Kempe, U., Gruner, T., Renno, A.D., Wolf, D., René, M., 2004. Discussion on Wang et al. (2000) Chemistry of Hf-rich zircons from the Laoshan I- and A-type granites, Eastern China. Mineral. Mag. 68, 669–675.

Kerr, A., Rafuse, H., 2012. Rare-earth element (REE) geochemistry of the Strange Lake deposits: implications for resource estimation and metallogenic models. In: Curret Research (2012) Newfoundland and Labrador Department of Natural Resources, Geological Survey, Report 12–1, pp. 39–60.

Khomyakov, A.P., Sørensen, H., 2001. Zoning in steen-strupine-(Ce) from the Ilímaussaq alkaline complex, South Greenland: a review and discussion. Geol. Greenland Surv. Bull. 190, 109–118.

Khudolozhkin, V.O., Urusov, V.S., Tobelko, K.I., Vernadskiy, V.I., 1973. Dependence of structural ordering of rare earth atoms in the isomorphous series apatite-britholite (abukumalite) on composition and temperature. Geochem. Int. 10, 1171–1177.

Klinkhammer, G., Elderfield, H., Hudson, A., 1983. Rare earth elements in seawater near hydrothermal vents. Nature 305, 185–188.

Klinkhammer, G.P., Elderfied, H., Edomond, J.M., Mitra, A., 1994. Geochemical implications of rare earth element patterns in hydrothermal fluids from mid-Ocean ridges. Geochim. Cosmochim. Acta 58, 5105–5113.

Kogarko, L.N., Khapaev, V.V., 1987. The modelling of the formation of apatite deposits of the Khibina massif (Kola Peninsula). In: Parsons, I. (Ed.), Origin of Igneous Layering. Reidel Publishing Company, Dordrecht, pp. 589–611.

Kogarko, L.N., Williams, C.T., Woolley, A.R., 2002. Chemical evolution and petrogenetic implications of loparite in the layered, agpaitic Lovozero complex, Kola Peninsula, Russia. Mineral. Petrol. 74, 1–24.

Köhler, S.J., Harouiya, N., Chaïrat, C., Oelkers, E.H., 2005. Experimental studies of REE fractionation during water–mineral interactions: REE release rates during apatite dissolution from pH 2.8 to 9.2. Chem. Geol. 222, 168–182.

Komkov, A.I., 1959. The structure of natural fergusonite, and of a polymorphic modification. Sov. Phys. Crystallogr. 4, 796–800 (translation from Kristallografiya, 4, 836–841).

Kon, Y., Hoshino, M., Sanematsu, K., Morita, S., Tsunematsu, M., Okamoto, N., Yano, N., Tanaka, M., Takagi, T., 2014. Geochemical characteristics of apatite in heavy REE-rich deep-sea mud from Minami-Torishima Area, Southeastern Japan. Resour. Geol. 64, 47–57.

Koopman, C., Witkamp, G.J., 2000. Extraction of lanthanides from the phosphoric acid production process to grain a purified gypsum and a valuable lanthanide by-product. Hydrometallurgy 58, 51–60.

Köppen, W., 1936. Das geographische System der Klimate. In: Köppen, W., Geiger, R. (Eds.), Handbuch der Klimatologie. Gebr. Borntraeger, Berlin, pp. 1–44.

Koppi, A.J., Edis, R., Field, D.J., Geering, H.R., Klessa, D.A., Cockayne, D.J.H., 1996. Rare earth element trends and cerium-uranium-manganese associations in weathered rock from Koongarra, Northern Territory, Australia. Geochim. Cosmochim. Acta 60, 1695–1707.

Korobeinikov, A.N., Mitrofanov, E.P., Gehör, S., Laajoki, K., Pavlov, V.P., Mamontov, V.P., 1998. Geology and copper sulphide mineralization of the Salmagorskii Ring igneous complex, Kola Peninsula, NW Russia. J. Petrol. 39, 2033–2041.

Kosmulski, M., 2009. pH-dependant surface charging and points of zero charge. IV. Update and new approach. J. Colloid Interface Sci. 337, 439–448.

Kosmulski, M., 2011. The pH-dependent surface charging and points of zero charge V. Update. J. Colloid Interface Sci. 353, 1–15.

Kovalenko, V.I., Tsaryeva, G.M., Goreglyad, A.V., Yarmolyuk, V.V., Troitsky, V.A., Hervig, R.L., Farmer, G., 1995. The peralkaline granite-related Khaldzan-Buregtey XE "Khaldzan-Buregtey" rare metal (Zr, Nb, REE) deposit, western Mongolia. Econ. Geol. 90, 530–547.

Krasnova, N.I., Blaganskaya, E.G., Garcia, D., 2004. Kovdor—classic phoscorites and carbonatites. In: Wall, F., Zaitsev, A.N. (Eds.), Phoscorites and Carbonatites from Mantle to Mine: the Key Example of the Kola Alkaline Province. The Mineralogical Society of Great Britain & Ireland, Middlesex, pp. 99–132.

Kreidler, E.R., Hummel, F.A., 1970. The crystal chemistry of apatite: structure fields of fluor- and chlorapatite. Am. Mineral. 55, 170–184.

Kuno, H., 1959. Origin of Cenozoic petrographic provinces of Japan and surrounding areas. Bull. Volcanol. 20 (Sereis II), 37–76.

Kushiro, I., 2007. Origin of magmas in subduction zones: a review of experimental studies. Proc. Jpn. Acad., Ser. B 83, 1–15.

Laveuf, C., Cornu, S., 2009. A review on the potentiality of rare earth elements to trace pedogenetic processes. Geoderma 154, 1–12.

Le Couteur, P.C., 2011. Geological Report on the Chambe Basin Area of Exclusive Prospecting License EPL0325/11 Mulanje Massif, Southern Malawi, East Africa. Micron Geological Ltd, Vancouver. 101p.

Le Maitre, R.W., 2002. Igneous Rocks: A Classification and Glossary of Terms. Cambridge University Press, Cambridge, UK.

Lee, H.G., Byrne, R.H., 1992. Examination of comparative rare earth element complexation behavior using linear free-energy relationships. Geochim. Cosmochim. Acta 56, 1127–1137.

Lee, J.H., Byrne, R.H., 1993. Complexation of trivalent rare earth elements (Ce, Eu, Gd, Tb, Yb) by carbonate ions. Geochim. Cosmochim. Acta 57, 295–302.

Lee, D.E., Dodge, F.C.W., 1964. Accessory minerals in some granitic rocks in California and Nevada as a function of calcium content. Am. Mineral. 49, 1660–1669.

Li, J.Y., Li, Z.P., 2010. The metallogenesis prognosis of REE deposit in Longchuan area, Yunnan. Yunnan Geol. 4, 429–430 (in Chinese).

Li, C.C., Shen, X.K., 2013. Investigation of geological conditions of weathering crust type rare earth deposits in Hunan Province. Geol. Rev. 59, 497–498 (in Chinese).

Li, X.H., Li, Z.X., Li, W.X., Liu, Y., Yuan, C., Wei, G.J., Qi, C.S., 2007. U-Pb zircon XE "zircon", geochemical and Sr-Nd-Hf isotopic constraints on age and origin of Jurassic I- and A-type granites from central Guangdong, SE China: a major igneous event in response to foundering of a subducted flat-slab? Lithos 96, 186–204.

Linnen, R.L., Samson, I.M., Williams-Jones, A.E., Chakhmouradian, A.R., 2014. Geochemistry of the rare-earth element, Nb, Ta, Hf, and Zr deposits. In: Holland, H.D., Turekian, K.K., Scott, S.D. (Eds.), Geochemistry of Mineral Deposits, second ed. Treatise on Geochemistry, vol. 13. Elsevier-Pergamon, Oxford, pp. 543–568.

Lippmaa, E., Maremäe, E., Rummel, A., Trummal, A., 2006. Tantalum, niobium and thorium cake production at the Sillamäe oil shale processing plant. Oil Shale 23, 281–285.

Lira, R., Ripley, E.M., 1990. Fluid inclusion studies of the Rodeo de Los Molles REE and Th deposit, Las Chacras Batholith Central Argentina. Geochim. Cosmochim. Acta 54, 663–671.

Liu, X.W., Byrne, R.H., 1998. Comprehensive investigation of yttrium and rare earth element complexation by carbonate ions using ICP-mass spectrometry. J. Solut. Chem. 27, 803–815.

Lodders, K., 2003. Solar system abundances and condensation temperatures of the elements. Astrophys. J. 591, 1220–1247.

Lodders, K., Fegley, B., 1998. The Planetary Scientist's Companion. Oxford University Press, New York.

Lokshin, E.P., Vershkova, Y.A., Vershkov, A.V., Tareeva, O.A., 2002. Leaching of lanthanides from phosphohemihydrate with nitric acid. Russ. J. Appl. Chem. 75, 1753–1759.

Long, K.R., Van Gosen, B.S., Foley, N.K., Cordier, D., 2010. The principal rare earth elements deposits of the United States—a summary of domestic deposits and a global perspective. U.S. Geological Survey Scientific Investigations Report 2010-5220, 96p.

Lottermoser, B.G., 1990. Rare-earth element mineralisation within the Mr. Weld carbonatite laterite, Western Australia. Lithos 24, 151–167.

Lu, C.B., 2008. Geological characteristics of the Wujingfu REE metallogenic province in Jiexi County, Guangdong Province. West-China Exploration Eng. 20, 86–87 (in Chinese).

Lumpkin, G.R., Chakoumakos, B.C., 1988. Chemistry and radiation effects of thorite-group minerals from the Harding pegmatite, Taos Country, New Mexico. Am. Mineral. 73, 1405–1419.

Luo, X.Y., 2011. Mechanism of REE mineralization and ion-adsorption type ore formation in Hunan Province. Acta Mineral. Sin. 1, 332–333 (in Chinese).

Lyakhovich, V.V., 1967. Distribution of rare-earth elements in allanite and monazite as related to geology of the Mt. Wheeler mine area, Nevada. Geochim. Cosmochim. Acta 7, 691–696.

Lyubetskaya, T., Korenaga, F., 2007. Chemical composition of Earth's primitive mantle and its variance, 1, Method and results. J. Geophys. Res. 112 (B3), B03211. http://dx.doi.org/10.1029/2005JB004223.

Ma, C., Eggleton, R.A., 1999. Cation exchange capacity of kaolinite. Clay Clay Miner. 47, 174–180.

Ma, P.X., Liu, Z.X., Bai, G., 1991. On geochemical features and origin of Zhaibeiding HREE-rich granite in Guangdong. J. Hebei Coll. Geol. 14, 351–360 (in Chinese with English abstract).

Manheim, F.T., Gulbrandsen, R.A., 1979. Marine phosphorites. In: Burns, R.G. (Ed.), Marine Minerals, vol. 6. Rev. Mineral. Chelsea, Michigan, pp. 151–173.

Marini, O.J., Botelho, N.F., Rossi, P., 1992. Elementos terras raras en granitoids da província estanífera de Goiás. Rev. Bras. Geosci. 22, 61–72.

Marques, J.J., Schulze, D.G., Curi, N., Mertzman, S.A., 2004. Trace element geochemistry in Brazilian Cerrado soils. Geoderma 121, 31–43.

Maruéjol, P., Cuney, M., Turpin, L., 1990. Magmatic and hydrothermal REE fractionation in the Xihuashan granites (SE China). Contrib. Mineral. Petrol. 104, 668–680.

Mason, B., 1966. Composition of the Earth. Nature 211, 616–618.

Mayer, I., Roth, R.S., Brown, W.E., 1974. Rare earth substituted fluoride-phosphate apatites. J. Solid State Chem. 11, 33–37.

McArthur, J.M., Walsh, J.N., 1984. Rare-earth geochemistry of phosphorites. Chem. Geol. 47, 191–220.

McConnell, D.A., 1938. Structural investigation of the isomorphism of the apatite group. Am. Mineral. 54, 1379–1391.

McConnell, D., 1973. Apatite. Its Crystal Chemistry, Mineralogy, Utilization, and Geologic and Biologic Occurrences. Springer, New York.

McDonough, W.F., Sun, S.S., 1995. The composition of the Earth. Chem. Geol. 120, 223–253.

McLennan, S.M., Taylor, S.R., 1979. Rare earth element mobility associate with uranium mineralisation. Nature 282, 247–250.

Meldrum, A., Boatner, L.A., Weber, W.J., Ewing, R.C., 1998. Radiation damage in zircon and monazite. Geochim. Cosmochim. Acta 62, 2509–2520.

Meldrum, A., Boatner, L.A., Ewing, R.C., 2000. A comparison of radiation effects in crystalline ABO_4-type phosphates and silicates. Mineral. Mag. 64, 185–194.

Mentani, T., 2012. So-called "ion-adsorption type" REE deposits found in weathered crust of ilmenite-series granite in northern Vietnam. Master's thesis, University of Tokyo. 107p.

Michard, A., 1989. Rare earth element systematics in hydrothermal fluids. Geochim. Cosmochim. Acta 53, 745–750.

Michard, A., Albarede, F., Michard, G., Minster, J.F., Charlou, J.L., 1983. Rare-earth elements and uranium in high-temperature solutions from the East Pacific Rise hydrothermal vent filed (13°N). Nature 303, 795–797.

Michard, A., Beaucaire, C., Michard, G., 1987. Uranium and rare earth elements in CO_2-rich waters from Vals-les-Bains (France). Geochim. Cosmochim. Acta 51, 901–909.

Middleton, A.W., Föster, H.-J., Uysal, I.T., Golding, S.D., Rhede, D., 2013. Accessory phases from the Soultz monzogranite, Soultz-sous-Forêts, France: implications for titanite destabilisation and differential REE, Y and Th mobility in hydrothermal systems. Chem. Geol. 335, 105–117.

Migdisov, A.A., Williams-Jones, A.E., 2007. An experimental study of the solubility and speciation of neodymium (III) fluoride in F-bearing aqueous solutions. Geochim. Cosmochim. Acta 71, 3056–3069.

Migdisov, A.A., Williams-Jones, A.E., 2014. Hydrothermal transport and deposition of the rare earth elements by fluorine-bearing aqueous liquids. Miner. Deposita 49, 987–997.

Migdisov, A.A., Williams-Jones, A.E., Wagner, T., 2009. An experimental study of the solubility and speciation of the Rare Earth Elements (III) in fluoride-and chloride-bearing aqueous solutions at temperatures up to 300°C. Geochim. Cosmochim. Acta 73, 7087–7109.

Milliman, J.D., Meade, R.H., 1983. World-wide delivery of river sediment to the oceans. J. Geol. 91, 1–21.

Milliman, J.D., Syvitski, P.M., 1992. Geomorphic/tectonic control of sediment discharge to the ocean: the importance of small mountainous rivers. J. Geol. 100, 525–544.

Minerals and Geoscience Department Malaysia, 2012. Malaysian Minerals Yearbook 2011. Ministry of Natural Resources and Environment Malaysia, Kuala Lumpur, 114p.

Minowa, T., 2008. Rare earth magnets: conservation of energy and the environment. Resour. Geol. 58, 414–422.

Mitra, A., Elderfield, H., Greaves, M.J., 1994. Rare earth elements in submarine hydrothermal fluids and plumes from the Mid-Atlantic Ridge. Mar. Geol. 46, 217–235.

Miyashiro, A., 1978. Nature of alkali volcanic rock series. Contrib. Mineral. Petrol. 66, 91–104.

Miyawaki, R., Nakai, I., 1996. Crystal chemical aspects of rare earthmineras. In: Jones, A.P., Wall, F., Williams, C.T. (Eds.), Rare Earth Minerals. The Mineralogical Society Series, vol. 7. Chapman and Hall, London, pp. 21–40.

Miyawaki, R., Yokoyama, K., Matsubara, S., Tsutsumi, Y., Goto, A., 2008. Uedaite-(Ce), a new member of the epidote group with Mn at the A site, from Shodoshima, Kagawa Prefecture, Japan. Eur. J. Mineral. 20, 261–269.

Mobbs, P., 2014. The Mineral Industry of Canada. 2012 Minerals Yearbook Canada [Advance Release]. U.S. Geological Survey, 20p.

Moldoveanu, G.A., Papangelakis, V.G., 2012. Recovery of rare earth elements adsorbed on clay minerals: I. Desorption mechanism. Hydrometallurgy 117–118, 71–78.

Moldoveanu, G.A., Papangelakis, V.G., 2013. Recovery of rare earth elements adsorbed on clay minerals: II. Leaching with ammonium sulfate. Hydrometallurgy 131–132, 158–166.

Mongelli, G., 1993. REE and other trace elements in a granitic weathering profile from Serre, southern Italy. Chem. Geol. 103, 17–25.

Mordberg, L.E., Stanley, C.J., Germann, K., 2000. Rare earth element anomalies in crandallite group minerals from the Schugorsk bauxite deposit, Timan, Russia. Eur. J. Mineral. 12, 1229–1243.

Moriyama, T., Miyawaki, R., Yokoyama, K., Matsubara, S., Hirano, H., Murakami, H., Watanabe, Y., 2011. Wakefieldite-(Nd), a new neodymium vanadate mineral in the Arase stratiform ferromanganese deposit, Kochi Prefecture, Japan. Resour. Geol. 61, 101–110.

Morogan, V., 1989. Mass transfer and REE mobility during fenitization at Alnö, Sweden. Contrib. Mineral. Petrol. 103, 25–34.

Morteani, G., Preinfalk, C., 1996. REE distribution and REE carriers in laterites formed on alkaline complexes of Araxá and Catalão (Brazil). In: Jones, A.P., Wall, F., Williams, C.T. (Eds.), Rare Earth Minerals: Chemistry, Origin and Ore Deposits. The Mineralogical Society Series, vol. 7. Chapman & Hall, London, pp. 227–255.

Murakami, H., Ishihara, S., 2008. REE mineralization of weathered crust and clay sediment on granitic rocks in the Sanyo Belt, SW Japan and the southern Jiangxi Province, China. Resour. Geol. 58, 373–401.

Murakami, H., Sato, H., Ishiyama, D., Ishihara, S., 2011. Comparison of analytical methods for acid-resistant high-grade REE ores: a case study of the Nolans Bore REE-P-U deposit, Northern Territory, Australia. Shigenchishitsu 61, 129–137 (In Japanese with English abstract).

Nabatian, G., Ghaderi, M., Corfu, F., Neubauer, F., Bernroider, M., Prokofiev, V., Honarmand, M., 2014. Geology, alteration, age, and origin of iron oxide-apatite deposits in Upper Eocene quartz monzonite, Zanjan district, NW Iran. Miner. Deposita 49, 217–234.

Nagashima, M., Nishido-Hamane, D., Tomita, N., Minakawa, T., Inaba, S., 2013. Vanadoallanite-(La): a new epidote-supergroup mineral from Ise, Mie Prefecture, Japan. Mineral. Mag. 77, 2739–2752.

Nakamura, K., Fujinaga, K., Yasukawa, K., Takaya, Y., Ohta, J., Machida, S., Haraguchi, S., Kato, Y. 2015. REY-rich mud: a deep-sea mineral resource for rare earths and yttrium. In:

Bünzli, J.-C.G., Pecharsky, V.K. (Eds.). Vol. 46, Handbook on the Physics and Chemistry of Rare Earths, 268, 79–127.

Naslund, H.R., Henríquez, F., Nyström, J.O., Vivallo, W., Dobbs, F.M., 2002. Magmatic iron ores and associated mineralization: examples from the Chilean High Andes and Coastal cordillera. In: Porter, T.M. (Ed.), Hydrothermal Iron Oxide Copper-Gold & Related Deposits: A Global Perspective, vol. 2. PGC Publishing, Adelaide, pp. 207–226.

Nelson, D.R., Chivas, A.R., Chappell, B.W., McCulloch, M.T., 1988. Geochemical and isotopic systematics in carbonatites and implications for the evolution of ocean-island sources. Geochim. Cosmochim. Acta 52, 1–17.

Ni, Y., Hughes, J.M., Mariano, A.N., 1995. Crystal chemistry of the monazite and xenotime structures. Am. Mineral. 80, 21–26.

Nickel, E.H., 1992. Solid solutions in mineral nomenclature. Can. Mineral. 30, 231–234.

Nickel, E.H., Grice, J.D., 1998. The IMA commission on new minerals and mineral names: procedures and guidelines on mineral nomenclature, 1998. Can. Mineral. 36, 913–926.

Nold, J.L., Davidson, P., Dudley, M.A., 2013. The pilot knob magnetite deposit in the Proterozoic St. Francois Mountains Terrane, southeast Missouri, USA: a magmatic and hydrothermal replacement iron deposit. Ore Geol. Rev. 53, 446–469.

Notholt, A.J.G., 1979. The economic geology and development of igneous phosphate deposits in Europe and the USSR. Econ. Geol. 74, 339–350.

Oberli, F., Meier, M., Berger, A., Rosenberg, C.L., Gieré, R., 2004. U–Th–Pb and ^{230}Th/^{238}U disequilibrium isotope systematics: precise accessory mineral chronology and melt evolution tracing in the Alpine Bergell intrusion. Geochim. Cosmochim. Acta 68, 2543–2560.

Oelkers, E.H., Poitrasson, F., 2002. An experimental study of the dissolution stoichiometry and rates of a natural monazite as a function of temperature from 50 to 230°C and pH from 1.5 to 10. Chem. Geol. 191, 73–87.

Oelkers, E.H., Valsami-Jones, E., Roncal-Herrero, T., 2008. Phosphate mineral reactivity: from global cycles to sustainable development. Mineral. Mag. 72, 337–340.

Ogata, T., Narita, H., Tanaka, M., 2014. Immobilization of diglycol amic acid on silica gel for selective recovery of rare earth elements. Chem. Lett. 43, 1414–1416.

Ogata, T., Narita, H., Tanaka, M., Hoshino, M., Kon, Y., Watanabe, Y., 2016. Selective recovery of heavy rare earth elements from apatite with an adsorbent bearing immobilized tridentate amido ligands. Sep. Purif. Technol. 159, 157–160.

Ohta, A., Kawabe, I., 2001. REE(III) adsorption onto Mn dioxide (δ-MnO$_2$) and Fe oxyhydroxide: Ce(III) oxidation by δ-MnO$_2$. Geochim. Cosmochim. Acta 65, 695–703.

Oliva, P., Dupré, B., Martin, F., Viers, J., 2004. The role of trace minerals in chemical weathering in a high-elevation granitic watershed (Estibere, France): chemical and mineralogical evidence. Geochim. Cosmochim. Acta 68, 2223–2243.

Ondrejka, M., Uher, P., Pršek, J., Ozdín, D., 2007. Arsenian monazite-(Ce) and xenotime-(Y), REE arsenates and carbonates from the Tisovec-Rejkovo rhyolite, Western Carpathians, Slovakia: composition and substitutions in the (REE, Y)XO$_4$ system (X=P, As, Si, Nb, S). Lithos 95, 116–129.

Orris, G.J., Grauch, R.I., 2002. Rare earth element mines, deposits, and occurrences. U.S. Geological Survey Open File Report 02-189, 78p.

Pan, H., 2011. Characteristics and ore genesis of weathering-crust ion-adsorption type REE deposits in the Yunkai Area, Guangxi Region. Land Resour. South. China 9, 37–40 (in Chinese).

Pan, Y., Fleet, M.E., 2002. Compositions of the apatite-group minerals: substitution mechanisms and controlling factors. In: Kohn, M.J., Rakovan, J., Hughes, J.M. (Eds.), Phosphates—Geochemical,

Geobiological, and Materials Importance. vol. 48. Rev. Mineral. Geochem., Washington, DC, pp. 13–49.

Pan, Y., Stauffer, M.R., 2000. Cerium anomaly and Th/U fractionation in the 1.85 Ga Flin Flon Paleosol: clues from REE- and U-rich accessory minerals and implications for paleoatmospheric reconstruction. Am. Mineral. 85, 898–911.

Pan, Y., Fleet, M.E., MacRae, N., 1993. Late alteration in titanite ($CaTiSiO_5$): redistribution and remobilization of rare earth elements and implications for U/Pb and Th/Pb geochronology and nuclear waste disposal. Geochim. Cosmochim. Acta 57, 355–367.

Pandur, K., Kontak, D.J., Ansdell, K.M., 2014. Hydrothermal evolution in the Hoidas Lake vein-type REE deposit, Saskatchewan, Canada: constraints from fluid inclusion microthermometry an evaporate mound analysis. Can. Mineral. 52, 717–744.

Pandur, K., Ansdell, K.M., Kontak, D.J., 2015. Graphic-textured inclusions in apatite: evidence for pegmatitic growth in a REE-enriched carbonatitic system. Geology 43, 547–550.

Pearce, J.A., Peate, D.W., 1995. Tectonic implications of the composition of volcanic arc Magmas. Annu. Rev. Earth Planet. Sci. 23, 251–285.

Pearson, R.G., 1963. Hard and soft acids and bases. J. Am. Chem. Soc. 85, 3533–3539.

Peel, M.C., Finlayson, B.L., McMahon, T.A., 2007. Updated world map of the Köppen-Geiger climate classification. Hydrol. Earth Syst. Sci. 11, 1633–1644.

Peelman, S., Sun, Z.H.I., Sietsma, J., Yang, Y., 2014. Leaching of rare earth elements: past and present. In: 1st European Rare Earth Resources Conference Proceedings, pp. 446–456.

Pekov, I.V., Kulikova, I.M., Kabalov, Y.K., Yeletskaya, O.V., Chukanov, N.V., Men'shikov, Y.P., Khomyakov, A.P., 1996. Belovite-(La), $Sr_3Na(La, Ce)(PO_4)_3(F, OH)$, a new rare earth mineral in the apatite group. Zap. Vses. Mineral. O-va. 125, 101–109.

Pekov, I.V., Petersen, O.V., Voloshin, A.V., 1997. Calcio-ancylite-(Ce) from Ilímaussaq and Narssârssuk, Greenland, Kola Peninsula and Polar Urals, Russia; ancylite-(Ce)-calcio-ancylite-(Ce) an isomorphous series. N. Jb. Mineral. (Abh.) 171, 309–332.

Pekov, I.V., Chukanov, N.V., Kononkova, N.N., Yakubovich, O.V., Massa, W., Voloshin, A.V., 2009. Tveitite-(Y) and REE-Enriched Fluorite from amazonite pegmatites of the Western Keivy, Kola Peninsula, Russia: genetic crystal chemistry of natural Ca, REE-fluorides. Geol. Ore Deposits 51, 595–607.

Pekov, I.V., Zubkova, N.V., Chukanov, N.V., Husdal, T.A., Zadov, A.E., Pushcharovsky, D.Y., 2011. Fluorbritholite-(Y), $(Y, Ca, Ln)_5[(Si, P)O_4]_3$ F, a new mineral of the britholite group. N. Jb. Mineral. (Abh.) 188, 191–197.

Peng, G.Y., Juhr, J.F., McGee, J.J., 1997. Factors controlling sulfur concentrations in volcanic apatite. Am. Mineral. 82, 1210–1224.

Peterson, R.C., MacFarlane, D.B., 1993. The rare-earth-element chemistry of allanite from the Grenville Province. Can. Mineral. 31, 159–166.

Petrella, L., Williams-Jones, A.E., Goutier, J., Walsh, J., 2014. The nature and origin of the rare earth element mineralization in the misery syenitic intrusion, Northern Quebec, Canada. Econ. Geol. 109, 1643–1666.

Petrík, I., Konečný, P., 2009. Metasomatic replacement of inherited metamorphic monazite in a biotite-garnet granite from the Nízke Tatry Mountains, Western Carpathians, Slovakia: chemical dating and evidence for disequilibrium melting. Am. Mineral. 94, 957–974.

Pfaff, K., Krumrei, T., Marks, M., Wenzel, T., Rudolf, T., Markl, G., 2008. Chemical and physical evolution of the 'lower layered sequence' from the nepheline syenitic Ilímaussaq intrusion, South Greenland: implications for the origin of magmatic layering in peralkaline felsic liquids. Lithos 106, 280–296.

Plank, T., Langmuir, C.H., 1998. The chemical composition of subducting sediment and its consequences for the crust and mantle. Chem. Geol. 145, 325–394.

Pointer, C.M., Ashworth, J.R., Ixer, R.A., 1988. The zircon thorite mineral group in metasomatized granite, Ririwai Nigeria 2. Zoning, alteration and exsolution in zircon. Mineral. Petrol. 39, 21–37.

Pourret, O., Davranche, M., Gruau, G., Dia, A., 2007a. Competition between humic acid and carbonates for rare earth elements complexation. J. Colloid Interface Sci. 305, 25–31.

Pourret, O., Davranche, M., Gruau, G., Dia, A., 2007b. Rare earth elements complexation with humic acid. Chem. Geol. 243, 128–141.

Preston, J.S., Cole, P.M., Craig, W.M., Feather, A.M., 1996. The recovery of rare earth oxides from a phosphoric acid XE "phosphoric acid" by-product XE "by-product". Hydrometallurgy 41, 1–19.

Price, J.G., Rubin, J.N., Henry, C.D., Pinkston, T.L., Weedy, S.W., Koppenaal, D.W., 1990. Rare-metal enriched peraluminous rhyolites in a continental arc, Sierra Blanca area, Trans-Pecos Texas; Chemical modification by vapor-phase crystallization. Geol. Soc. Am. Spec. Pap. 246, 103–120.

Price, J.D., Hogan, J.P., Gilbert, M.C., London, D., Morgan, G.B.V.I., 1999. Experimental study of titanite–fluorite equilibria in the A-type Mount Scott Granite; implications for assessing F contents of felsic magma. Geology 27, 951–954.

Prowatke, S., Klemme, S., 2005. Effect of melt composition on the partitioning of trace elements between titanite and silicate melt. Geochim. Cosmochim. Acta 69, 695–709.

Prowatke, S., Klemme, S., 2006. Rare earth element partitioning between titanite and silicate melts: Henry's law revisited. Geochim. Cosmochim. Acta 70, 4997–5012.

Qi, G.W., Parentich, A., Little, L.H., Warren, L.J., 1992. Selective flotation of apatite from iron oxides. Int. J. Miner. Process. 34, 83–102.

Qiu, J.S., Mcinnes, B., Xu, X.S., Allen, C.M., 2004. Zircon ELA-ICP-MS dating for Wuliting Pluton at Dajishan, southern Jiangxi and new recognition about its relation to tungsten mineralization. Geol. Rev. 50, 125–133 (in Chinese with English abstract).

Quirt, D., Korzer, T., Kyser, T.K., 1991. Tourmaline, phosphate minerals, zircon and pitchblende in the Athabasca Group: Maw Zone and McArthur River Areas, Saskatchewan. Summary of Investigations 1991, Saskatchewan Geological Survey, Saskatchewan Energy Mines, Miscellaneous Report, 91-4, pp. 181–191.

Rakovan, J., Hughes, J.M., 2000. Strontium in the apatite structure: strontian fluorapatite and belovite-(Ce). Can. Mineral. 38, 839–845.

Rankin, A.H., 2005. Carbonatite-associated rare metal deposits: composition and evolution of ore-forming fluids—the fluid inclusion evidence. In: Linnen, R.L., Samson, I.M. (Eds.), Rare-Element Geochemistry and Mineral Deposits, vol. 17. Geological Association of Canada Short Course Notes, pp. 299–314.

Rapp, R.P., Watson, E.B., 1986. Monazite solubility and dissolution kinetics: implications for the thorium and light rare earth chemistry of felsic magmas. Contrib. Mineral. Petrol. 94, 304–316.

Rhodes, A.L., Oreskes, N., Sheets, S., 1999. Geology and rare earth element geochemistry of magnetite deposits at El Laco, Chile. Soc. Econ. Geol. Spec. Pub. 7, 299–332.

Rickwood, P.C., 1989. Boundary lines within petrologic diagrams which use oxides of major and minor elements. Lithos 22, 247–263.

Ridley, J., 2013. Ore Deposit Geology. Cambridge University Press, New York. 398p.

Roeder, P.L., MacArthur, D., Ma, X.P., Palmer, G.R., 1987. Cathodoluminescence and microprobe study of rare-earth elements in apatite. Am. Mineral. 72, 801–811.

Rønsbo, J.G., 1989. Coupled substitution involving REEs and Na and Si in apatites in alkaline rocks from the Illimaussaq intrusions, South Greenland, and the petrological implications. Am. Mineral. 74, 896–901.

Roskill Information Services Ltd, 2011. Rare Earths & Yttrium: Market Outlook to 2015. Roskill Information Services, London. 492p.

Roskill Information Services Ltd, 2015. Rare Earths: Market Outlook to 2020, 15th ed. Roskill, London, pp. 1–337.

Roy, P.S., 1999. Heavy mineral beach placers in southeastern Australia: their nature and genesis. Econ. Geol. 94, 567–588.

Roy, D.M., Drafall, L.E., Roy, R., 1978. Crystal chemistry, crystal growth, and phase equilibria of apatites. In: Alper, A.M. (Ed.), Phase Diagrams: Material Sciences and Technology, vol. 6. Academic Press, New York, pp. 186–239.

Rubin, J.N., Henry, C.D., Price, J.G., 1989. Hydrothermal zircons and zircon overgrowths, Sierra Blanca Peaks, Texas. Am. Mineral. 74, 865–869.

Rudnick, R.L., Gao, S., 2003. Composition of the continental crust. In: Rudnick, R.L. (Ed.), Treatise on Geochemistry. The Crust, vol. 3. Elsevier, Amsterdam, pp. 1–64.

Rukhlov, A.S., Bell, K., 2010. Geochronology of carbonatites from the Canadian and Baltic shields, and the Canadian Cordillera: clues to mantle evolution. Mineral. Petrol. 98, 11–54.

Ruyuan Yao Autonomous County, 2014. General Plan of Mineral Resources in Ruyuan Yao Autonomous County. 75p (in Chinese).

Salvi, S., Williams-Jones, A.E., 1996. The role of hydrothermal processes in concentrating high-field strength elements in the Strange Lake peralkaline complex, northeastern Canada. Geochim. Cosmochim. Acta 60, 1917–1932.

Salvi, S., Williams-Jones, A.E., 2005. Alkaline granite-syenite deposits. In: Linnen, R.L., Samson, I.M. (Eds.), Rare-Element Geochemistry and Mineral Deposits, vol. 17. Geological Association of Canada, Short Course Notes, St John's, pp. 315–341.

Samson, I.M., Wood, S.A., 2005. The rare earth elements: behavior in hydrothermal fluid and concentration in hydrothermal mineral deposits, exclusive of alkaline settings. In: Linnen, R.L., Samson, I.M. (Eds.), Rare-Element Geochemistry and Mineral Deposits, vol. 17. Geological Association of Canada, Short Course Notes, St John's, pp. 269–297.

Sanematsu, K., Kon, Y., 2013. Geochemical characteristics determined by multiple extraction from ion-adsorption type REE ores in Dingnan County of Jiangxi Province, South China. Bull. Geol. Surv. Jpn. 64, 313–330.

Sanematsu, K., Watanabe, Y., 2016. Characteristics and genesis of ion adsorption-type rare earth element deposits. Rev. Econ. Geol. 18, 55–79.

Sanematsu, K., Moriyama, T., Sotouky, L., Watanabe, Y., 2011. Mobility of rare earth elements in basalt-derived laterite at the Bolaven Plateau, southern Laos. Resour. Geol. 61, 140–158.

Sanematsu, K., Kon, Y., Imai, A., Watanabe, K., Watanabe, Y., 2013. Geochemical and mineralogical characteristics of ion-adsorption type REE mineralization in Phuket, Thailand. Mineral. Deposita 48, 437–451.

Sanematsu, K., Kon, Y., Imai, A., 2015. Influence of phosphate on mobility and adsorption of REEs during weathering of granites in Thailand. J. Asian Earth Sci. 111, 14–30.

Sanematsu, K., Ejima, T., Kon, Y., Manaka, T., Zaw, K., Morita, S., Seo, Y., 2016. Fractionation of rare-earth elements during magmatic differentiation and weathering of calc-alkaline granites in southern Myanmar. Min. Mag. 80, 77–102.

Saunders, A.D., Norry, M.J., Tarney, J., 1988. Origin of MORB and chemically-depleted mantle reservoirs: trace element constraints. In: Menzies, M.A., Cox, K.G. (Eds.), Oceanic and Continental Lithosphere: Similarites and Differences. J. Petrol., Spec. vol. 1988, 415–545.

Schandl, E.S., Gorton, M.P., 2004. A textural and geochemical guide to the identification of hydrothermal monazite: criteria for selection of samples for dating epigenetic hydrothermal ore deposits. Econ. Geol. 99, 1027–1035.

Schroth, B.K., Sposito, G., 1997. Surface charge properties of kaolinite. Clay Clay Miner. 45, 85–91.

Sengupta, D., Van Gosen, B.S., 2016. Placer-type rare earth element deposits. Rev. Econ. Geol. 18, 81–100.

Serret, A., Cabañas, M.V., Vallet-Regí, M., 2000. Stabilization of calcium oxyapatites with lanthanum(III)-created anionic vacancies. Chem. Mater. 12, 3836–3841.

Sha, L.K., Chappell, B.W., 1999. Apatite chemical composition, determined by electron micro-probe and laser-ablation inductively coupled plasma mass spectrometry, as a probe into gran-ite petrogenesis. Geochim. Cosmochim. Acta 63, 3861–3881.

Sheard, E.R., Williams-Jones, A.E., Heiligmann, M., Pederson, C., Trueman, D.L., 2012. Controls on the concentration of zirconium, niobium, and the rare earth elements in the Thor Lake rare metal deposit, Northwest Territories, Canada. Econ. Geol. 107, 81–104.

Shepherd, M.S., 1990. Eneabba heavy mineral sand placers. In: Hughes, F.E. (Ed.), Geology and Mineral Deposits of Australia and Papua New Guinea. Australasian Institute of Mining and Metallurgy, Parkville, pp. 1591–1594.

Simmons, W.B., Hanson, S.L., Falster, A.U., 2006. Samarskite-(Yb): a new species of the samar-skite group from the little patsy pegmatite, Jefferson County, Colorado. Can. Mineral. 44, 1119–1125.

Sinclair, W.D., Kingston, D.M., 1990. Rare-earth-bearing apatite near Benjamin River, northern New Brunswick. Geol. Surv. Can. 90 (1B), 95–104.

Škoda, R., Novák, M., 2007. Y, REE, Nb, Ta, Ti-oxide (AB2O6) minerals from REL–REE euxenite-subtype pegmatites of the Třebíč Pluton, Czech Republic; substitutions and fraction-ation trends. Lithos 95, 43–57.

Smith, M.P., Henderson, P., 2000. Preliminary fluid inclusion constraints on fluid evolution in the Bayan Obo Fe-REE-Nb deposit, Inner Mongolia, China. Econ. Geol. 95, 1371–1388.

Smith, M.P., Henderson, P., Jeffries, T., 2002. The formation and alteration of allanite in skarn from the Beinn an Dubhaich granite aureole, Skye. Eur. J. Mineral. 14, 471–486.

Smith, M.P., Campbell, L.S., Kynicky, J., 2015. A review of the genesis of the world class Bayan Obo Re-REE-Nb deposits, Inner Mongolia, China: multistage processes and outstanding questions. Ore Geol. Rev. 64, 459–476.

Snetsinger, K.G., 1967. Accessory minerals in some Sierra Nevada granitic rocks as a function of calcium content. Am. Mineral. 52, 832–842.

Sokolova, E., Cámara, F., 2008. From structure topology to chemical composition. VIII. Titanium silicates: the crystal chemistry of mosandrite from type locality of Låven (Skådön), Lange-sundsfjorden, Larvik, Vestfold, Norway. Mineral. Mag. 72, 887–897.

Song, Y.H., Shen, L.P., 1982. Discussion on clay minerals occurring in the weathered crust of a certain acid volcanic rock in Jiangxi Province and their formation conditions. Acta Mineral. Sin. 3, 207–212 (in Chinese with English abstract).

Song, Y.H., Shen, L.P., 1986. REE geochemistry of the weathered crust of acid volcanic rocks—an experimental study. Geochimica 3, 225–234 (in Chinese with English abstract).

Sonke, J.E., Salters, V.J.M., 2006. Lanthanide-humic substances complexation. I. Experimental evidence for a lanthanide contraction effect. Geochim. Cosmochim. Acta 70, 1495–1506.

Stille, P., Pierret, M.C., Steinmann, M., Chabaux, F., Boutin, R., Aubert, D., Pourcelot, L., Morvan, G., 2009. Impact of atmospheric deposition, biogeochemical cycling and water–mineral interaction on REE fractionation in acidic surface soils and soil water (the Strengbachcase). Chem. Geol. 264, 173–186.

Sun, S.S., McDonough, W.F., 1989. Chemical and isotopic systematics of oceanic basalts: implications for mantle composition and processes. In: Saunders, A.D., Norry, M.J. (Eds.), Magmatism in the Ocean Basins. Geological Society Special Publication no. 42, pp. 313–345.

Suzuki, K., 1988. Heterogeneous distribution of uranium within zircon grains: implications for fission-track dating. J. Geol. Soc. Jpn 94, 1–10.

Suzuki, K., Adachi, M., 1991. Precambrian provenance and Silurian metamorphism of the Tsubonosawa paragneiss in the South Kitakami terrane, Northeast Japan, revealed by the chemical Th-U-Total Pb isochron ages of monazite, zircon and xenotime. Geochem. J. 25, 357–376.

Suzuki, K., Adachi, M., Yamamoto, K., Nakai, Y., 1992. Intragrain distribution of REE and crystallization sequence of accessory minerals in the Cretaceous Busetsu Granite at Okazaki, central Japan. Geochem. J. 26, 383–394.

Takagi, T., 2004. Origin of magnetite- and ilmenite-series granitic rocks in the Japan arc. Am. J. Sci. 304, 169–202.

Takahashi, Y., Minai, Y., Ambe, S., Makide, Y., Ambe, F., Tominaga, T., 1997. Simultaneous determination of stability constants of humate complexes with various metal ions using multitracer technique. Sci. Total Environ. 198, 61–71.

Takahashi, Y., Minai, Y., Ambe, S., Makide, Y., Ambe, F., 1999. Comparison of adsorption behavior of multiple inorganic ions on kaolinite and silica in the presence of humic acid using the multitracer technique. Geochim. Cosmochim. Acta 63, 815–836.

Tatsumi, Y., Takahashi, T., 2006. Operation of subduction factory and production of andesite. J. Mineral. Petrol. Sci. 101, 145–153.

Tatsumi, M., Fukuyama, H., Kushiro, I., 1983. Generation of arc basalt magmas and thermal structure of the mantle wedge in subduction zones. J. Geophys. Res. 88, 5815–5825.

Taunton, A.E., Welch, S.A., Banfield, J.F., 2000. Microbial controls on phosphate and lanthanide distributions during granite weathering and soil formation. Chem. Geol. 169, 371–382.

Taylor, R.P., Pollard, P.J., 1996. Rare earth element mineralization in peralkaline systems: the T-zone REE–Y–Be deposit, Thor Lake, Northwest Territories, Canada. In: Jones, A.P., Wall, F., Williams, C.T. (Eds.), Rare Earth Minerals: Chemistry, Origin and Ore Deposits. The Mineralogical Society Series, vol. 7. Chapman & Hall, London, pp. 167–192.

Tian, J., Tang, X.K., Yin, J.Q., Luo, X.P., Rao, G.H., Jiang, M.T., 2013. Process optimization on leaching of a lean weathered crust elution-deposited rare earth ores. Int. J. Miner. Process. 119, 83–88.

Tokunaga, S., Nakai, S., Orihashi, Y., 2010. Two types of adakites revealed by 238U-230Th disequilibrium from Daisen Volcano, southwestern Japan. Geochem. J. 44, 379–386.

Tole, M.P., 1985. The kinetics of dissolution of zircon (ZrSiO$_4$). Geochim. Cosmochim. Acta 49, 453–458.

Tong, Q.H., 2013. Study on the metallogenic regularity of the Xiaotao ion-adsorption type REE deposits in Fujian Province. Earth 6, 26–27 (in Chinese).

Toyoda, K., Masuda, A., 1991. Chemical leaching of pelagic sediments: identification of the carrier of Ce anomaly. Geochem. J. 25, 95–119.

Toyoda, K., Tokonami, M., 1990. Diffusion of rare-earth elements in fish teeth from deep-sea sediments. Nature 345, 607–609.

Toyoda, K., Nakamura, Y., Masuda, A., 1990. Rare earth elements of Pacific pelagic sediments. Geochim. Cosmochim. Acta 54, 1093–1103.

Trappe, J., 1998. Part III. The processes: phosphogenesis and phosphorite genesis. In: Phanerozoic Phosphorite Depositional Systems. Lecture Notes in Earth Sciences, vol. 76. Springer, pp. 61–214.

Tromans, D., 2006. Solubility of crystalline and metamict zircon: a thermodynamic analysis. J. Nucl. Mater. 357, 221–233.

U.S. Department of Energy, 2011. Critical Material Strategy. U.S. Department of Energy, Washington, 190p.

U.S. Geological Survey, 2015. Mineral Commodity Summaries 2015. U.S. Geological Survey, Reston, 196p.

Ueda, T., 1957. Studies on the metamictization of radioactive minerals. Mem. Coll. Sci. (Univ. Kyoto, Ser. B) 24 (2), 81–120.

Uher, P., Černý, P., 1998. Zircon in hercynian granitic pegmatites of the Western Carpathians, Slovakia. Geol. Carpath. 49, 261–270.

Upton, B.G.L., Emeleus, C.H., Heaman, L.M., Goodenough, K.M., Finch, A.A., 2003. Magmatism of the mid-Proterozoic Gardar Province, South Greenland: chronology, petrogenesis and geological setting. Lithos 68, 43–65.

Valeton, I., 1972. Bauxites, Developments in Soil Science 1. Elsevier, Amsterdam/London/New York. 226p.

Vallini, D.A., Groves, D.I., McNaughton, N.J., Fletcher, I.R., 2007. Uraniferous diagenetic xenotime XE "xenotime" in northern Australia and its relationship to unconformity associated uranium mineralization. Miner. Deposita 42, 51–64.

Valsami-Jones, E., Ragnarsdottir, K.V., Putnis, A., Bosbach, D., Kemp, A.J., Cressey, G., 1998. The dissolution of apatite in the presence of aqueous metal cations at pH 2–7. Chem. Geol. 151, 215–233.

Van Kauwenbergh, S.J., 2010. World Phosphate Rock Reserves and Resources. Technical Bulletin IFDC-T-75 (IFDC, 2010).

Van Kauwenbergh, S.J., Stewart, M., Mikkelsen, R., 2013. World reserves of phosphaterock … a dynamic and unfolding story. Better Crops 97, 18–20.

Van Lichtervelde, M., Melcher, F., Wirth, R., 2009. Magmatic vs. hydrothermal origins for zircon associated with tantalum mineralization in the Tanco pegmatite, Manitoba, Canada. Am. Mineral. 94, 439–450.

van Middlesworth, P.E., Wood, S.A., 1998. The aqueous geochemistry of the rare earth elements and yttrium. Part 7. REE, Th and U contents in thermal springs associated with Idaho batholith. Appl. Geochem. 13, 861–884.

Van Schmus, W.R., Wood, J.A., 1967. A chemical-petrologic classification for the chondritic meteorites. Geochim. Cosmochim. Acta 31, 747–754.

Verbaan, N., Bradley, K., Brown, J., Mackie, S., 2015. A review of hydrometallurgical flowsheets considered in current REE projects. In: Simandl, G.J., Neetz, M. (Eds.), Symposium on critical and strategic materials proceedings, November 13–14, 2015. Ministry of Energy and Mines, British Columbia Geological Survey Paper 2015-3, Victoria, British Columbia, pp. 147–162.

Verplanck, P.L., Mariano, A.N., Mariano, A., 2016. Rare earth element ore geology of carbonatites. Rev. Econ. Geol. 18, 5–32.

Viers, J., Oliva, P., Dandurand, J.-L., Dupré, B., 2014. Chemical weathering rates, CO_2 consumption, and control parameters deduced from the chemical composition of rivers: in Drever, J.I. (ed.). In: Holland, H.D., Turekian, K.K. (Eds.), Surface and Groundwater, Weathering and Soils, second ed. Treatise on Geochemistry, vol. 7. Elsevier–Pergamon, Oxford, pp. 175–194.

Wagh, A.S., Pinnock, W.R., 1987. Occurrence of scandium and rare earth elements in Jamaican bauxite waste. Econ. Geol. 82, 757–761.

Wall, F., 2014. Rare earth elements. In: Gunn, G. (Ed.), Critical Metals Handbook. John Wiley & Sons, Ltd, Chicester, UK, p. 454.

Wall, F., Mariano, A.N., 1996. Rare earth minerals in carbonatites: a discussion centred on the Kangankunde Carbonatite, Malawi. In: Jones, A.P., Williams, C.T., Wall, F. (Eds.), Rare Earth Minerals: Chemistry. Origin and Ore Deposits. Mineralogical Society Series, vol. 7. Chapman & Hall, London, pp. 193–225.

Wall, F., Niku-Paavola, V., Storey, C., Müller, A., Jeffries, T., 2008. Xenotime-(Y) from carbonatite dykes at Lofdal, Namibia: unusually low LREE:HREE ratio in carbonatite, and the first dating of xenotime overgrowths on zircon. Can. Mineral. 46, 861–877.

Wallace, M., Green, D.H., 1988. An experimental determination of primary carbonatite composition. Nature 335, 343–346.

Wang, R.C., Fontan, F., Xu, S.J., Chen, X.M., Monchoux, P., 1996. Hafnian zircon from the apical part of the Suzhou granite, China. Can. Mineral. 34, 1001–1010.

Wang, R.C., Zhao, G.T., Lu, J.J., Chen, X.M., Xu, S.J., Wang, D.Z., 2000. Chemistry of Hf-rich zircons from the Laoshan I- and A-type granites, Eastern China. Mineral. Mag. 64, 867–877.

Wang, L., Long, Z., Huang, X., Yu, Y., Cui, D., Zhang, G., 2010a. Recovery of rare earths from wet-process phosphoric acid. Hydrometallurgy 101, 41–47.

Wang, Q., Deng, J., Liu, X., Zhang, Q., Sun, S., Jiang, C., Zhou, F., 2010b. Discovery of the REE minerals and its geological significance in the Quyang bauxite deposit, West Guangxi, China. J. Asian Earth Sci. 39, 701–712.

Wang, D.H., Zhao, Z., Yu, Y., Zhao, T., Li, J.K., Dai, J.J., Liu, X.X., He, H.H., 2013. Progress, problems and research orientation of ion-adsorption type rare earth resources. Rock Miner. Anal. 32, 796–802 (in Chinese with English abstract).

Watanabe, Y., 2007. Heavy rare earth enriched stratiform manganese ores and its future prospects. Kogyozairyo 55, 58–61 (in Japanese).

Watanabe, Y., 2014. Challenges for the production of heavy rare earth elements from hard rocks. Int. J. Soc. Mater. Eng. Resour. 20, 113–117.

Watanabe, Y., Hoshino, M., Murakami, H., Sanematsu, K., Kon, Y., Horiuchi, Y., 2014. The role of earth science for the supply of rare earth elements. In: 1st European Rare Earth Resources Conference Proceedings, 12–18.

Watson, E.B., Green, T.H., 1981. Apatite/liquid partition coefficients for the rare earth elements and strontium. Earth Planet. Sci. Lett. 56, 405–421.

Wei, Z., Yin, M., Zhang, X., Hong, F., Li, B., Tao, Y., Zhao, G., Yan, C., 2001. Rare earth elements in naturally grown fern Dicranopteris linearis in relation to their variation in soils in South-Jiangxi region. Environ. Pollut. 114, 345–355.

West, W.F., 1970. The Bulawayo symposium papers: no. 2, termite prospecting. Chamb. Mines. J. 12, 32–35.

Whalen, J.B., Chappell, B.W., 1988. Opaque mineralogy and mafic mineral chemistry of I- and S-type granites of the Lachlan Folt Belt, southeast Australia. Am. Mineral. 73, 281–296.

White, W.M., 2013. Geochemistry. Wiley-Blackwell, West Sussex. 660p.

White, A.F., Blum, A.E., 1995. Effects of climate on chemical weathering in watersheds. Geochim. Cosmochim. Acta 59, 1729–1747.

White, W.M., Klein, E.M., 2013. The oceanic crust. Treatise of Geochemistry, second ed. edited.

Whitten, C.W., Yancey, R.J., 1990. Characterization of the rare-earth mineralogy at the Pea Ridge deposit, Missouri. U.S.. Bur. Mines Rep. Invest. 9331, 1–9.

Willett, G.C., Duncan, R.K., Rankin, R.A., 1989. Geology and economic evaluation of the Mt. Weld carbonatite, Laverton, Western Australia. In: Ross, J., et al., (Ed.), Kimberlites and Related Rocks. Their Mantle/Crust Setting, Diamond Exploration, vol. 2. Geological Society of Australia, Special Publication, No. 14, pp. 1215–1235.

Williams-Jones, A.E., Samson, I.M., Olivo, G.R., 2000. The genesis of hydrothermal fluorite-REE deposits in the Gallinas Mountains, New Mexico. Econ. Geol. 95, 327–342.

Williams-Jones, A.E., Migdisov, A.A., Samson, I.M., 2012. Hydrothermal mobilisation of the rare earth elements—a tale of "ceria" and "yttria". Elements 8, 355–360.

Wilson, M., 1989. Igneous Petrogenesis. Unwin, Hyman, London. 466p.

Wilson, R.A., Kamo, S.L., 2008. New U-Pb ages from the Chaleurs and Dalhousie groups: implications for regional correlations and tectonic evolution of northern New Brunswick. In: Martin, G.L. (Ed.), Geological Investigations in New Brunswick for 2007, pp. 55–77. New Brunswick Department of Natural Resources; Minerals, Policy and Planning Division, Mineral Resource Report 2008-1.

Winter, J.D., 2010. Principles of Igneous and Metamorphic Petrology, second ed. Prentice Hall, New York. 720p.

Wones, D.R., 1989. Significance of the assemblage titanite+magnetite+quartz in granitic rocks. Am. Mineral. 74, 744–749.

Wood, S.A., 1990. The aqueous geochemistry of the rare-earth elements and yttrium. 1. Review of available low-temperature data for inorganic complexes and the inorganic REE speciation of natural waters. Chem. Geol. 82, 159–186.

Wood, S.A., Ricketts, A., 2000. Allanite-(Ce) from the Eocene Casto granite, Idaho: response to hydrothermal alteration. Can. Mineral. 38, 81–100.

Woolley, A.R., Kempe, D.R.C., 1989. Carbonatites: nomenclature, average chemical compositions, and element distribution. In: Bell, K. (Ed.), Carbonatites: Genesis and Evolution. Unwin & Hyman, London, pp. 1–14.

Wu, C., 2008. Bayan Obo controversy: carbonatites versus iron oxide-Cu-Au-(REE-U). Resour. Geol. 58, 348–354.

Wu, C.Y., Huang, D.H., Guo, Z.G., 1990. REE geochemistry in the weathered crust of granites, Longnan area, Jiangxi Province. Acta Geol. Sin. 3, 193–210.

Wu, C.Y., Bai, G., Huang, D.H., 1992. Characteristics and significance of HREE-rich granitoids of the Nanling Mountain area. Bull. Chin. Acad. Geol. Sci. 25, 43–58 (in Chinese with English abstract).

Wu, C.Y., Lu, H.L., Xu, L.M., Hou, L., 1993a. A preliminary study on modes of occurrence of rare earth elements in the tropical-subtropical weathering crust of Nanling region. Miner. Deposita 12, 297–307 (in Chinese with English abstract).

Wu, C.Y., Huang, D.H., Yuan, Z.X., Bai, G., Nakajima, T., Ishihara, S., 1993b. Trace elements geochemistry and genetic implications for highly evolved granitic rocks from south China. Resour. Geol. Spec. Issue 16, 9–24.

Wu, C., Yuan, Z., Bai, B., 1996. Rare earth deposits in China. In: Jones, A.P., Wall, F., Williams, C.T. (Eds.), Rare Earth Minerals: Chemistry, Origin and Ore Deposits. The Mineralogical Society Series, vol. 7. Chapman & Hall, London, pp. 281–310.

Xie, L., Wang, R., Chen, X., Qiu, J., Wang, D., 2005. Th-rich zircon from peralka line A-type granite: mineralogical features and petrological implications. Chin. Sci. Bull. 50, 809–817.

Xie, Y., Hou, Z., Yin, S., Dominy, S.C., Xu, J., Tian, S., Xu, W., 2009. Continuous carbonatitic melt-fluid evolution of a REE mineralization system: evidence from inclusions in the Maoniuping REE deposit, Western Sichuan, China. Ore Geol. Rev. 36, 90–105.

Xie, Y., Hou, Z., Goldfarb, R.J., Guo, X., Wang, L., 2016. Rare earth element deposits in China. Rev. Econ. Geol. 18, 115–136.

Xinfeng County, 2014. General Plan of Mineral Resources in Xinfeng County. 85p (in Chinese).

Xu, L.M., Yuan, Z.X., 1992. Zircon U-Pb isotopic age of the Qinghu monzonite in Guangxi and its geological significance. Geol. Guangxi 5, 33–36 (in Chinese).

Xu, X.S., Lu, W.M., He, Z.H., 2007. Age and generation of Fogang granite batholith and Wushi diorite-hornblende gabbro body. Sci. China (Ser. D) 50, 209–220.

Xu, C., Kynicky, J., Chakhmouradian, A.R., Campbell, U.H., Allen, C.M., 2010. Trace-element modeling of the magmatic evolution of rare-earth-rich carbonatite from the Miaoya deposit, Central China. Lithos 118, 145–155.

Yang, Z.M., 1987. A study on clay minerals from the REE-rich weathered crust developed on the Longnan Granite in Jianxi. Acta Geol. Sin. 1, 70–80 (in Chinese with English abstract).

Yang, Z., Wooley, A., 2006. Carbonatites in China: a review. J. Asian Earth Sci. 27, 559–575.

Yang, D.H., Xiao, G.M., 2011. Regional metallogenic regularities of the ion adsorption type of rare-earth deposits in Guangdong Province. Geol. Resour. 20, 462–468 (in Chinese with English abstract).

Yang, Y.Q., Hu, Z.S., Luo, Z.M., 1981. Geological characteristics of mineralization of rare earth deposits of the ion-adsorption type and their prospecting direction. Bull. Inst. Mineral Deposit, Chin. Acad. Geol. Sci. 2, 102–118 (in Chinese with English abstract).

Yang, X.M., Yang, X.Y., Zhang, P.S., Zhan, W.L., Tao, K.J., 1999. Geochemical study of REE from granite weathering crusts in Dajishan of Jiangxi Province. Chin. Rare Earths 20, 1–5 (in Chinese with English abstract).

Yang, X.-M., Yang, X.-Y., Zhang, P.-S., Le Bas, M.J., 2000. Ba-REE fluorcarbonate minerals from a carbonatite dyke at Bayan Obo, Inner Mongolia, North China. Mineral. Petrol. 70, 221–234.

Yang, X.J., Lin, A., Li, X.L., Wu, Y., Zhou, W., Chen, Z., 2013. China's ion-adsorption rare earth resources, mining consequences and preservation. Environ. Dev. 8, 131–136.

Yasukawa, K., Liu, H., Fujinaga, K., Machida, S., Haraguchi, S., Ishii, T., Nakamura, K., Kato, Y., 2014. Geochemistry and mineralogy of REY-rich mud in the eastern Indian Ocean. J. Asian Earth Sci. 93, 25–36.

Yu, B., Xie, J.T., Ji, Z.N., Liu, J., 2004. Study on insitu-leaching methods of the Yanfutang ion-adsorption type REE deposits. Metall. Ore Dressing Abroad 41, 37–40 (in Chinese).

Yuan, Z.X., Wu, C.Y., Xu, L.M., Ni, Y.X., 1993. The distribution of trace elements in granitoids in the Nanling Region of China. Chin. J. Geochem. 12, 193–205.

Yuan, Z.X., Li, J.K., Wang, D.H., Zheng, Z.C., 2013. Metallogenic Regularity of Rare Earth Deposits in China. Dizhi Publisher, Beijing, pp. 1–116 (in Chinese).

Zaitsev, V., Kogarko, L., 2012. Sources and perspectives of REE in the Lovozero massif (Kola Peninsula, Russia). In: Abstract of the European Mineralogical Conference, v. 1.

Zaitsev, A.N., Chakhmouradian, A.R., Siidra, O.I., Spratt, J., Williams, C.T., Stanley, C.J., Petrov, S.V., Britvin, S.N., Polyakova, E.A., 2011. Fluorine-, yttrium- and lanthanide-rich cerianite-(Ce) from carbonatitic rocks of the Kerimasi volcano and surrounding explosion craters, Gregory Rift, northern Tanzania. Mineral. Mag. 75, 2813–2822.

Zaitsev, A.N., Williams, C.T., Jeffries, T.E., Strekopytov, S., Motte, J., Ivashenkova, O.V., Spratt, J., Petrov, S.V., Wall, F., Seltmann, R., Borozdin, A.P., 2014. Rare earth elements in phoscorites and carbonatites of the devonian kola alkaline province, russia: examples from Kovdor, Khibina, Vuoriyarvi and Turiy Mys complexes. Ore Geol. Rev. 61, 204–225.

Zhang, Z.H., 1990. A study on weathering crust ion adsorption type REE deposit, South China. Contrib. Geol. Miner. Resour. Res. 5, 57–71 (in Chinese with English abstract).

Zhang, A.C., Wang, R.C., Hu, H., Zhang, H., Zhu, J.C., Chen, X.M., 2004. Chemical evolution of Nb-Ta oxides and zircon from the Koktokay No. 3 granitic pegmatite, Altai, northwestern China. Mineral. Mag. 68, 739–756.

Zhao, Z., Chen, Z.Y., Chen, Z.H., Hou, K.J., Zhao, Z., Xu, J.X., Zhang, J.J., Zeng, Z.L., 2012. Zircon U-Pb dating, tectonic setting and ore-bearing properties evaluation of the Caledonian Yangbu pluton in South Jiangxi. Rock Miner. Anal. 31, 530–535 (in Chinese with English abstract).

Zhao, Z., Wang, D.H., Chen, Z.Y., Chen, Z.H., Zheng, G.D., Liu, X.X., 2014. Zircon U-Pb Age, Endogenic mineralization and petrogenesis of rare earth ore-bearing granite in Longnan, Jiangxi Province. Acta Geosci. Sin. 35 (6), 719–725 (in Chinese with English abstract).

Zhou, X.W., Wen, D.X., Luo, X.P., 2012. The status quo and development trend of the extraction of ion-adsorbed rare earth in southern China. Nonferrous Met. Sci. Eng. 3, 81–85 (in Chinese with English abstract).

Zhu, X., 1999. Mineral Facts of China. Science Press, Beijing. 665p (in Chinese).

Zhu, X.K., O'Nions, R.K., 1999a. Zonation of monazite in metamorphic rocks and its implications for high temperature thermochronology: a case study from the Lewisian terrain, Earth Planet. Sci. Lett. 171, 209–220.

Zhu, X.K., O'Nions, R.K., 1999b. Monazite chemical composition: some implications for monazite geochronology. Contrib. Mineral. Petrol. 137, 351–363.

Zhu, J.C., Zhang, P.H., Xie, C.F., Zhang, H., Yang, C., 2006. The Huashan–Guposhan A-type granitoid belt in the Western part of the Nanling mountains: petrology, geochemistry and genetic interpretations. Acta Geol. Sin. 80, 529–542 (in Chinese with English abstract).

Zielinski, S., Szczepanik, A., Buca, M., 1993. Recovery of lanthanides from Kola apatite in phosphoric acid manufacture. J. Chem. Technol. Biotechnol. 56, 355–360.

Zurevinski, S.E., Mitchell, R.H., 2004. Extreme compositional variation of pyrochlore-group minerals at the Oka Carbonatite complex, Quebec: evidence of magma mixing? Can. Mineral. 42, 1159–1168.

Chapter 280

Quantum Critical Matter and Phase Transitions in Rare Earths and Actinides

L. Rademaker[1,*] and J.A. Mydosh[1,†]

Kavli Institute for Theoretical Physics, University of California Santa Barbara, CA, United States

†*Kamerlingh Onnes Laboratory and Institute-Lorentz, Leiden University, Leiden, The Netherlands*

1*Corresponding authors: e-mail: louk.rademaker@gmail.com; mydosh@physics.leidenuniv.nl*

Chapter Outline

1 INTRODUCTION

Many compounds based on rare earth and actinide elements, such as Ce(Cu,Au)$_6$ and YbRh$_2$Si$_2$, display unusual electronic and magnetic properties. "Unusual" is used in a strong sense such that standard Fermi liquid (FL) theory is not applicable, and a proper theoretical description is still lacking.

However, driven by a theoretical effort it has been suggested that many properties can be understood within the framework of a "quantum phase transition" (QPT): a second-order phase transition from a magnetically

ordered state at zero temperature to a new quantum phase. Such a zero temperature phase transition leads to a dramatic change of the electronic properties at finite, nonzero temperatures.

There are many good reviews on QPTs, for example, Pfleiderer (2009), Gegenwart et al. (2008), Sachdev (2008), and von Löhneysen et al. (2007). Unlike those reviews we will not be complete in the enumeration of all measured properties of all possible quantum critical compounds. Instead, we want to provide a critical view on QPTs in certain prototype rare earth and actinide-based compounds.

The concept of quantum criticality, which we will discuss in-depth in Section 2, has lead to a surge of novel concepts, most important of them is scaling. Scaling suggests that many measurable quantities, such as the specific heat coefficient, the thermal expansion, and magnetic susceptibility, have simple power-law behavior as a function of temperature, pressure, or magnetic field. Indeed, some materials are fully described the scaling laws as derived by the theory of Hertz, Millis, and Moriya. However, it was soon found that many materials—such as $Ce(Cu,Au)_6$ and $YbRh_2Si_2$—not only violate FL theory, but also Hertz–Millis (HM) theory.

After presenting these compounds, we elaborate in Section 3 on the shortcomings of HM theory and list recent attempts toward better theories. In line with our philosophy, we will review those theories critically: unfortunately, many of them are either based on unquantifiable assumptions or lack a microscopic derivation.

Nonetheless, the conceptual power of quantum criticality still stands, and the novel non-Fermi liquid (NFL) materials Ce-115 and URu_2Si_2 are looked at through quantum critical glasses. By discussing difficulties associated with "hidden" quantum critical points (QCPs), disorder, and material stability we aim to show in Section 4 the challenges and opportunities associated with using concepts from QPTs. Section 5 lists other forms of quantum matter beyond the rare earths and actinides.

2 HISTORICAL BACKGROUND

2.1 Classical Continuous Phase Transitions

This chapter deals with phase transitions of a special kind, namely QCPs. Before delving into that topic, we need to review some general properties of phase transitions. Most phase transitions we encounter in daily life, like the liquid–gas or the freezing transition, are of the first order kind. First order transitions are characterized by a discontinuous change of the material properties and release (or absorb) latent heat.

Second order or continuous phase transitions (CPTs) are more subtle. No latent heat is involved, but the specific heat still displays nonanalytic behavior in the form of a divergence or a kink. In terms of the *reduced temperature*

$t = \dfrac{T - T_c}{T_c}$, where T_c is the transition temperature itself, the specific heat behaves as a power law,

$$C_v \sim |t|^{-\alpha}, \tag{1}$$

where α is the *specific heat critical exponent*. A typical example is shown in Fig. 1, which shows the specific heat around the ferromagnetic transition in EuO.

Any phase transition can be described by an *order parameter*, a quantity that is zero in one phase and nonzero in the other. In a ferromagnet, this would be the net magnetization; in an antiferromagnet, the staggered magnetization; and in a superconductor, the superfluid density. Unlike a first order transition, where the order parameter jumps discontinuously, the order parameter m at a CPT goes to zero in a power-law fashion,

$$m \sim (-t)^{\beta}, \tag{2}$$

for $t < 0$, and where β is the *order parameter critical exponent*.

The key element of a CPT is that at the transition, fluctuations *at all length scales* play an important role. Away from the critical point, fluctuations of the order parameter have a typical finite *correlation length* ξ. This correlation length diverges close to the critical point,

$$\xi \sim |t|^{-\nu} \tag{3}$$
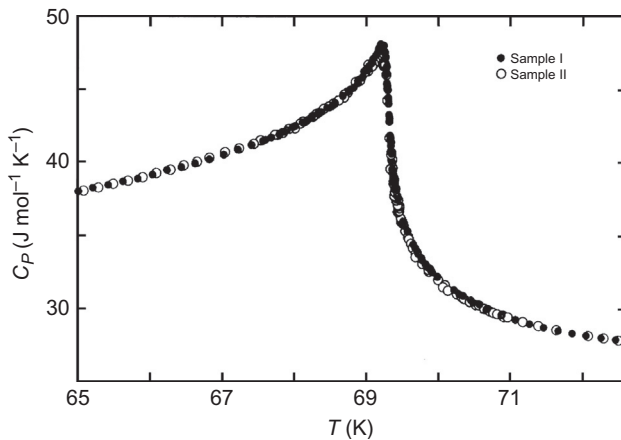
FIG. 1 The specific heat around the ferromagnetic transition in EuO, at $T_c = 69$ K. The critical exponent is $\alpha \approx -0.044$, indicating a near logarithmic divergence. *According to Kornblit, A., Ahlers, G., 1975. Heat capacity of EuO near the Curie temperature. Phys. Rev. B 11 (7), 2678-2688.*

with v the *correlation length critical exponent*. Similarly, the susceptibility associated with the order (eg, the magnetic susceptibility $\chi = \dfrac{\partial M}{\partial H}$ for a ferromagnet) also diverges at the critical point, which defines the *susceptibility exponent*

$$\chi \sim |t|^{-\gamma}. \tag{4}$$

A list of most commonly used exponents is shown in Table 1. All of those exponents are accessible in experiments, for example, table III in Kornblit and Ahlers (1975) includes all the critical exponents for the ferromagnetic transition in EuO.

Because fluctuations at all length scales become equally important, many of the microscopic details of the system become irrelevant. As a result, important physical quantities can be expressed as scaling functions of the diverging correlation length and other macroscopic parameters. For example, for many CPTs the free energy density is just a function of the correlation length itself, $f \sim \xi^{-d}$, where d is the dimensionality of the system. If this is the case, it follows that the specific heat exponent is related to the correlation length exponent by the *hyperscaling relation* $2 - \alpha = vd$. Other such scaling relations, that can be directly derived from the notion of physics-at-all-length-scales, are $2 - \alpha = 2\beta + \gamma$, $2 - \alpha = \beta(\delta + 1)$ and Fishers relation $\gamma = (2 - \eta)v$.

TABLE 1 The Definition of Several Critical Exponents for a Magnetic Material Exhibiting a CPT

Quantity	Exponent	Finite Temperature	Quantum Phase Transition
Order parameter	β	$m \sim (-t)^{\beta}$	$m \sim (g - g_c)^{\beta}$
Specific heat	α	$C \sim |t|^{-\alpha}$	–
Susceptibility	γ	$\chi \sim |t|^{-\gamma}$	$\chi \sim |g - g_c|^{-\gamma}$
Critical isotherm (at $t=0$ or $g=g_c$)	δ	$B \sim |m|^{\delta}$	$B \sim |m|^{\delta}$
Correlation length	v	$\xi \sim |t|^{-v}$	$\xi \sim |g - g_c|^{-v}$
Correlation function (at $t=0$ or $g=g_c$)	η	$G(r) \sim |r|^{-d+2-\eta}$	$G(r) \sim |r|^{-d+2-\eta}$
Dynamics	z	–	$\xi_\tau \sim \xi^{z}$

The first column indicates the physical observable, the second the exponent. The third column indicates how the observable scales near a finite temperature phase transition as a function of the reduced temperature $t = \dfrac{T - T_c}{T_c}$. The fourth column shows how the observable scales near a QPT, as a function of the control parameter $g - g_c$.

These scaling relations highly constrain the possible values the critical exponents can take. In fact, only the symmetry of the order parameter and the dimensionality of the system are relevant in order to determine the critical exponents of a transition. This is the concept of *universality*: every CPT belongs to a universality class (Ising, XY, Heisenberg, etc.) of transitions with the same critical exponents, even though the underlying microscopic physics can be completely different. The beautiful principle of universality has made the study of CPTs among the most popular in modern science.

As early as 1971, Stanley published the first book on phase transitions and critical phenomena (Stanley, 1971), followed by Ma (1976), Goldenfeld (1992), Yeomans (1992), and Herbut (2010). Into the 2000s, a series of multivolume monographs have appeared, edited by Domb and Lebowitz (2001). At the present CPTs are well understood, from both experimental as well as theoretical points of view (Nishimori and Ortiz, 2010). Whenever a new magnetic material is fabricated, one just needs to verify if a CPT occurs and check its universality class. Once that is known, all is known about that particular phase transition.

2.2 Quantum Critical Theory

A QPT is a second order phase transition that occurs at zero temperature, as a function of pressure, magnetic field or any tuning parameter g other than temperature. A standard way of obtaining such a transition is by suppressing the critical temperature of an ordered state—such as a ferromagnet or antiferromagnet—to zero temperature by, for example, pressure. When the pressure exceeds the critical pressure, a quantum disordered regime appears.

Exactly at the critical value of the tuning parameter $g = g_c$, the system develops many unconventional properties. The relevance of QPTs is that for nonzero temperatures close to the critical value g_c the system is still dominated by quantum critical excitations. Thus can arise unconventional specific heat, resistivity, magnetic susceptibility, and so on. This "quantum critical regime," as shown in the typical phase diagram of Fig. 2, is thought to be the key toward understanding many abnormal properties of materials.

In this section, we first provide the traditional theory of how such a quantum critical regime appears. As for all phase transitions, the key lies in the concept of scaling functions and the corresponding exponents close to the transition. In fact, there is an intricate link between QPTs and thermal phase transitions, which becomes clear by considering the example of the Ising model.

Critical exponents for any given model can be computed using the methods of statistical physics. The starting point is to define the microscopic Hamiltonian H relevant for the system under study. For the *Ising model*, a model of interacting spins that can describe (anti)ferromagnetic phase transitions, the Hamiltonian is

$$H = -J \sum_{\langle ij \rangle} S_i^z S_j^z, \tag{5}$$
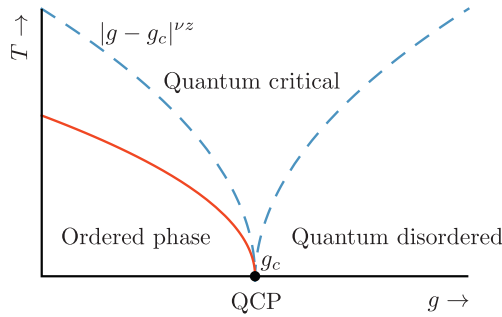
FIG. 2 The typical phase diagram of a quantum phase transition. The horizontal axis represents a tuning parameter g, which can be pressure, magnetic field, or particle density; the vertical axis represents temperature. The high g regime to the right represents the "quantum disordered" phase: a paramagnet or just a regular Fermi liquid. At low g there is an ordered phase, for example, a (anti) ferromagnet. The quantum critical point resides exactly at $T = 0$ where the system goes from the ordered to the disordered phase. At this critical value of $g = g_c$, the nonzero temperature regime is denoted as "quantum critical." In this part of the phase diagram, many properties such as the specific heat or the resistivity are unconventional due to the vicinity of the quantum critical point. Such unconventional behavior is usually referred to as "non-Fermi liquid" behavior.

where S_i^z is the z-component of a classical spin at a lattice site i. For $J > 0$, this model has a ferromagnetic ground state and we therefore expect that below some temperature the system develops spontaneous magnetization.

The Ising model is classical, so that the partition function $\mathcal{Z} = \sum_n e^{-\beta E_n}$, where the sum runs over all possible spin states with energy E_n. Any macroscopic quantities that we are interested in, such as magnetization or specific heat, can be derived from the free energy $\mathcal{F} = -k_B T \log \mathcal{Z}$. In some cases, the partition function and, hence, the free energy can be computed exactly, in most cases, however, we need to resort to an approximation scheme.

The most successful theory is Landau mean field theory: here we assume that spins interact only with the average field of all other spins, given by $m(x)$. A free energy functional can then be written as a function of the magnetization $m(x)$ and temperature T. In general, for a d-dimensional system, we have

$$\mathcal{F}(m,T) = \int d^d x \left(c(\nabla m(x))^2 + a_2(T)m(x)^2 + a_4 m(x)^4 + \cdots \right) \qquad (6)$$

where a_2, a_4, and c are some parameters. For a CPT, Landau showed, we must have $a_2 \sim t$ with t the reduced temperature, a_4 and c are positive definite. The magnetization can be found by minimizing $\mathcal{F}(m, T)$ with respect to the order parameter $m(x)$.

From just these very general considerations, we can compute critical exponents. For example, minimizing the free energy with respect to a homogeneous m gives us the order parameter exponent $\beta = 1/2$. The second derivative $C_V = \dfrac{\partial^2 F}{\partial T^2}$ yields the specific heat exponent $\alpha = 0$. Explicitly writing

out the correlation functions for an inhomogeneous order parameter $m(x)$ yields $\nu = 1/2$ and $\eta = 0$. Finally, an external magnetic field can be included by adding $-h \int d^d x m(x)$ to the free energy, which yields $\delta = 3$ and $\gamma = 1$. (See chapter 4 from Yeomans, 1992 for more details.)

Mean field theory ignores fluctuations, but with increasing dimensionality of the system these fluctuations become less and less relevant. In fact, the mean field exponents become exact in $d > \dfrac{2 - \alpha}{\nu}$ dimensions. This is called the *upper critical dimension*, so that, for example, the Ising model in $d > 4$ dimensions is determined by mean field exponents.

We are now in a position to continue toward quantum systems, where the phase transition does not occur as a function of temperature but at zero temperature due to a change in model parameters. Because in a quantum system the Hamiltonian is an operator the partition function is now given by,

$$\mathcal{Z} = \mathrm{Tr} \exp\left(-\beta \hat{H}\right). \tag{7}$$

The Ising model can be extended to a quantum model, known as the *transverse field Ising model*. The properties of this model are described in detail by Sachdev (2011). It is the prime example of a magnetic system exhibiting a QPT. The Hamiltonian is

$$H_{TFIM} = -Jg \sum_i S_i^x - J \sum_{\langle ij \rangle} S_i^z S_j^z \tag{8}$$

where $J > 0$ is the magnetic exchange coupling between spins, and g is the magnitude of a transversal magnetic field. Now g acts as the tuning parameter that can induce a phase transition between a ferromagnetic phase and a paramagnetic phase. For g≪1 (ferro)magnetic order prevails with two possible ground states,

$$|\psi_0\rangle = \prod_i |\uparrow\rangle_i, \text{ or } \prod_i |\downarrow\rangle_i. \tag{9}$$

Oppositely, for a large transverse field g≫1, the ground state is an uncorrelated ($\langle S_i^z S_j^z \rangle = \delta_{ij}$) paramagnet

$$|\psi_0\rangle = \prod_i |\rightarrow\rangle_i = \prod_i (|\uparrow\rangle_i + |\downarrow\rangle_i)/\sqrt{2}.$$

The paramagnet and the ferromagnet are distinctively different. Therefore, under increase of the transverse field g there will be a QPT from the ferro- to the paramagnet at $g = g_c$.

Suzuki (1976) discovered that the free energy of the d-dimensional quantum Ising model is equivalent to the $(d+1)$-dimensional classical Ising model. Explicitly, the quantum partition function can be rewritten as a Feynman path integral where the inverse temperature $\beta = 1/k_B T$ acts an extra dimension

called imaginary time $\tau \in [0, \beta)$. At zero temperature, the free energy for the d-dimensional quantum Ising model becomes

$$\mathcal{F}(m, g) = \int d^d x d\tau \left\{ c(\partial_\mu m(x, \tau))^2 + a_2(g) m(x, \tau)^2 + a_4 m(x, \tau)^4 + \cdots \right\}, \quad (10)$$

so that the tuning parameter is now g as opposed to T for the classical phase transition.

The parameter $a_2 \sim (g - g_c)$ changes sign when the transverse field is increased. At the transition, not only spatial correlation length diverges, but also the imaginary time correlations ξ_τ. They are related by the dynamical critical exponent z,

$$\xi_\tau \sim \xi^z. \quad (11)$$

It is easy to see that for the Ising model, the dynamical critical exponent is $z = 1$, since x and τ are treated on the same footing.

All other critical exponents can be derived from the critical exponents of the $(d+1)$-dimensional classical Ising model. We have $m \sim (g - g_c)^\beta$ for the order parameter, and similar expressions for the susceptibility exponents and the correlation length exponents. All of those are listed in Table 1. Note that there is not an analogue of the specific heat exponent at zero temperature.

In conclusion, we note that both classical and quantum field theories are described by a free energy functional that depends on the order parameter. The quantum transverse field Ising model in d dimensions is equivalent to the classical Ising model in $(d+1)$ dimensions. This allows us to find the critical exponents associated by the QPT in the quantum Ising model from the classical exponents. In Section 2.4.1, we will discuss Li(HoY)F$_4$, a rare earth material that displays characteristics of a quantum Ising phase transition.

2.3 HM Theories of Itinerant Magnets

In many rare earth materials, the magnetism is not caused by localized spins as described by the Ising model. Instead, it consists of conducting (itinerant) electrons that undergo a spin-density wave (SDW) transition or a superconducting transition. The theory of QPTs in the presence of interacting electrons was pioneered by Hertz (1976), Millis (1993), and Moriya (1985).

Their theory starts with interacting electrons, for which one can write down the partition function at inverse temperature β, defined by Eq. (7). These interacting electrons have an instability toward the formation of some kind of magnetic order. The magnitude of the magnetic order is parametrized by the order parameter field $\Psi(x, \tau)$ where x is the spatial coordinate and τ the imaginary time—the extra dimension as a consequence of quantum physics.

The key assumption in HM theories is that the low-energy physical description of this system can do without referring to electrons. All electronic degrees of freedom can be integrated out and we are left with an effective free

energy (also sometimes called "action") depending on the order parameter field $\Psi(x, \tau)$. For example, for an itinerant ferromagnet this leads to

$$\mathcal{F}[\Psi] = \frac{1}{2}\sum_{q\omega}\left(r_0 + q^2 + \frac{|\omega|}{q}\right)|\Psi(q, \omega)|^2 + \frac{u_0}{4N\beta}\sum_{q_i\omega_i}\Psi_1\Psi_2\Psi_3\Psi_4\delta\left(\sum q\right)\delta\left(\sum \omega\right)$$
(12)

where (q, ω) are momentum and energy, the Fourier transform of (x, τ); r_0 is the tuning parameter that makes the system ferromagnetic or paramagnetic, and u_0 is some effective order parameter interaction. Since this is a low-energy effective field theory, the correct way to study this is through renormalization group theory (Herbut, 2010; Wilson and Kogut, 1974; Yeomans, 1992) —a topic that goes beyond this brief review. Instead, we can infer the most important results from simple scaling arguments.

A scaling argument uses that at the QPT, physical properties are the same at all length scales. Hence, if we multiply the momenta q and the energies ω with some factor, the action Eq. (12) should remain invariant. The difference between the scaling of momenta and energies is characterized by the dynamical critical exponent z, recall Eq. (11). Simple inspection of the ferromagnetic action (12) implies $z = 3$. Similarly, for antiferromagnets we find $z = 2$ (Hertz, 1976).

The upper critical dimension for this model is no longer 4, as was the case for the classical Ising model, but $4 - z$ with z the dynamical critical exponent. This implies that the ferromagnetic QPT in $d > 1$ and the antiferromagnetic QPT in $d > 2$ can be described by mean field exponents!

The scaling arguments can be extended to nonzero temperatures. Whenever the inverse temperature β is smaller than the imaginary time correlation length ξ_τ, one expects that quantum critical fluctuations are dominant. This leads to the famous "quantum critical wedge,"

$$T > (g - g_c)^{\nu z},$$
(13)

the temperature regime where the system can be described as "quantum critical" and standard lore about interacting fermions no longer applies. In this regime, a scaling ansatz for the free energy can be formulated (Zhu et al., 2003),

$$\mathcal{F}(T) \sim \frac{1}{\xi^d \xi_\tau}\tilde{f}(T\xi_\tau) \sim |g - g_c|^{(d+z)\nu}\tilde{f}\left(\frac{T}{|g - g_c|^{\nu z}}\right)$$
(14)

from which we can directly infer that the low-temperature specific heat scales as

$$c_V(T, g = g_c) = -T\frac{\partial^2 \mathcal{F}}{\partial T^2} \sim T^{d/z}.$$
(15)

This is notably different from the standard FL result of a linear specific heat $c_V(T) \sim \gamma T$ where γ is the Sommerfeld coefficient. That is why the system inside the quantum critical wedge is often referred to as a "NFL."

The typical smoking gun for NFL behavior is an unconventional temperature dependence of the resistivity,

$$\rho(T) = \rho_0 + aT^n \tag{16}$$

where $n = 2$ would be for a standard FL. Many materials have n deviating from two—for example, the linear resistivity measured in $YbRh_2Si_2$ (Custers et al., 2003). Within the theoretical framework of HM theory, indeed anomalous exponents were found (Moriya and Takimoto, 1995), for example, $\Delta\rho \sim T^{3/2}$ at a $d = 3$ antiferromagnetic QCP. However, this picture fails when the electron scattering is peaked at "hot spots" on the Fermi surface, that are connected by the antiferromagnetic wavevector $\vec{Q}$. There critical fluctuations lead to a linear T scattering rate, but electrons on the remaining "cold spots" still follow the standard FL lure and the overall resistivity is expected to be $\Delta\rho \sim T^2$ again (Hlubina and Rice, 1995). Disorder can change this picture again (Rosch, 1999, 2000), which makes resistivity a difficult subject matter.

Not all NFL behavior arises due to quantum criticality. To distinguish between NFL behavior due to disorder (Westerkamp et al., 2009) and actual criticality, the Grüneisen ratio Γ was introduced. For any QCP controlled by pressure, the ratio between the thermal expansion $\alpha = -\dfrac{1}{V}\dfrac{\partial S}{\partial p}$ and the specific heat at the critical pressure should diverge (Zhu et al., 2003),

$$\Gamma(T, p = p_c) = \frac{\alpha}{c_V} \sim T^{-1/vz}. \tag{17}$$

The standard theory of HM for a three-dimensional antiferromagnetic QPT gives $z = 2$ and the mean field correlation length exponent $v = 1/2$, hence the Grüneisen ratio should diverge as $1/T$.

A group of cerium-based compounds does seem to exhibit the critical behavior as predicted by HM theory. Most notable is $CeNi_2Ge_2$: at ambient pressure and zero field this material has a critical specific heat $c_V \sim T^{3/2}$ and a Grüneisen ratio $\Gamma \sim T^{-1}$, consistent with the HM predictions, see Fig. 3 (Küchler et al., 2003). The resistivity is found to be $\Delta\rho(T) \sim T^{3/2}$ (Gegenwart et al., 1999). The only suspicious aspect of this material is that it does not have exhibit antiferromagnetism (AFM), only pressure induced superconductivity (SC). However, the isostructural compound $CePd_2Si_2$ does become antiferromagnetic, yet it shows similar high pressure dependent SC. Thus Grosche et al. (2000) have suggested that the critical behavior of $CeNi_2Ge_2$ is related to the high-pressure QCP in $CePd_2Si_2$. Consequently, antiferromagnetic order in $CeNi_2Ge_2$ should exist at "negative" pressures—a challenging concept indeed. Two other related compounds, $CeCu_2Si_2$ and $CeCu_2Ge_2$, seem to have similar HM quantum critical behavior (Stockert et al., 2004), but it appears difficult to consistently synthesize these materials because tiny deviations in their stoichiometry leads to inhomogeneous and competing phases of magnetism and SC (von Löhneysen et al., 2007).
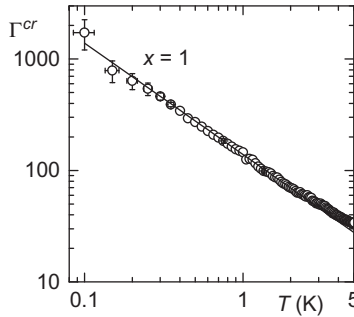
FIG. 3 The critical Grüneisen ratio $\Gamma^{cr} = \alpha^{cr}/c_V^{cr}$ of CeNi$_2$Ge$_2$, on a log–log plot as a function of temperature at ambient pressure and zero field. The noncritical contributions to the specific heat c_V and the thermal expansion α have been subtracted. The solid line represents $\Gamma \sim 1/T$, consistent with Hertz–Millis theory. *From Küuchler, R., Oeschler, N., Gegenwart, P., Cichorek, T., Neumaier, K., Tegus, O., Geibel, C., Mydosh, J.A., Steglich, F., Zhu, L., Si, Q., 2003. Divergence of the Grüneisen ratio at quantum critical points in heavy fermion metals. Phys. Rev. Lett. 91 (6), 0664054.*

As mentioned earlier, the Grüneisen ratio will diverge for *any* QCP, even when it cannot be described by HM theory. For example, in both CeCu$_{6-x}$Au$_x$ (see Section 2.4.2) and YbRh$_2$Si$_2$ (see Section 2.4.3) the Grüneisen ratio diverges, though with a different exponent than is expected from HM theory (Küchler et al., 2003, 2004; Tokiwa et al., 2009).

We have so far only considered static properties. Criticality can also be inferred from dynamical properties, such as the dynamical susceptibility $\chi(k, \omega)$. For example, Sachdev (2011) introduced the scaling function

$$\chi(k,\omega) \sim T^{-(2-\eta)/z} \Phi\left(\frac{k}{T^{1/z}}, \frac{\omega}{T}, \frac{\Delta}{T}\right) \tag{18}$$

where Δ is the gap on either side of the transitions, so $\Delta \to 0$ at the transition.

It is important to note that in numerous rare earth materials unconventional SC is found (for a review, see Pfleiderer, 2009). In a superconductor, electrons are bound together into Cooper pairs. Understanding a superconducting phase thus boils down to finding the "glue," and it has been suggested that quantum critical fluctuations could act as glue (Mathur et al., 1998; Metlitski et al., 2015; Miyake et al., 1986; Scalapino et al., 1986; She and Zaanen, 2009). The QPT associated with the disappearance of magnetism is then obscured by a "superconducting dome." Whereas the idea is appealing, there are as of yet no clear experimental way to discern whether a QCP truly exists below the dome.

Finally, note that in the spin-density wave picture presented in this section, the electrons play a secondary role. This means that throughout the transition, all properties of the electrons themselves such as their effective mass or their Fermi surface shape, can only change continuously (Gegenwart et al., 2008).

In Section 3, we will discuss scenarios inspired by experiments that challenge this notion of electrons as mere bystanders.

2.4 Experiments: Li(Ho,Y)F$_4$, Ce(Cu,Au)$_6$, and YbRh$_2$Si$_2$

2.4.1 Li(HoY)F$_4$

Once the theoretical considerations for quantum criticality in the transverse field Ising model became known, the search began for a real material to display this QPT. The chosen "ideal" compound was pure LiHoF$_4$, a dipolar-coupled insulating ferromagnet with strong Ising anisotropy and small Curie temperature $T_C = 1.53$ K. The first experiments (Bitko et al., 1996) measured ac-magnetic susceptibility down to 0.05 K in $H_\perp$ perpendicular to the Ising axis up to 8 T. The results for both the classical ferromagnetic transition and the QPT (at $T \approx 0$ with critical field $H_\perp^C = 4.93$ T) showed in both cases a mean-field susceptibility divergence, ie, the susceptibility exponent γ was approximately 1. Fig. 4 exhibits the divergences as function of T near $H_\perp^c$ and function of $(H_\perp - H_\perp^C)/H_\perp^C$ at constant T, where we see the near linear dependences.
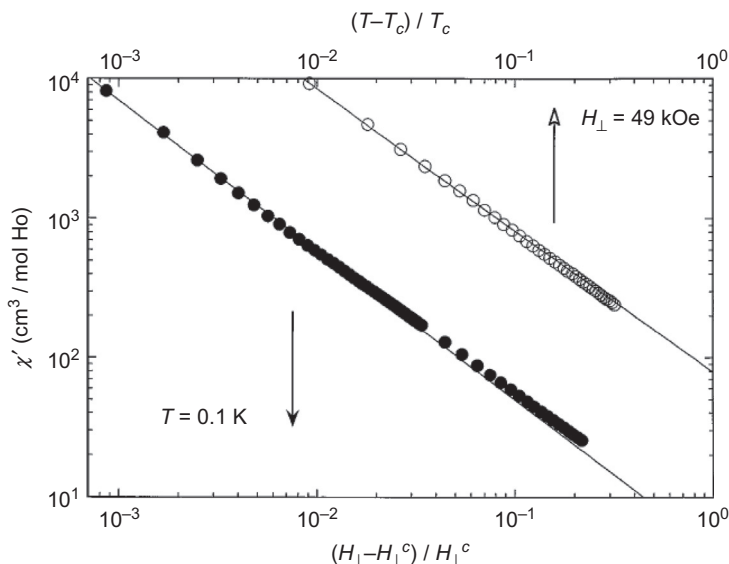
FIG. 4 The divergence of the ac magnetic susceptibility as a function of the reduced critical temperature and applied field $H_\perp$ perpendicular to the Ising axis. T_c has been defined as the lowest temperature of measurement 0.114 K while the extrapolated to $T=0H_\perp$ is 4.93 T. All the susceptibility divergence are mean field like with critical exponent $\gamma = 1$, meaning no difference between the zero field ferromagnetic transition and the field tuned QPT. *According to Bitko, D., Rosenbaum, T.F., Aeppli, G., 1996. Quantum critical behavior for a model magnet. Phys. Rev. Lett. 77 (5), 940.*
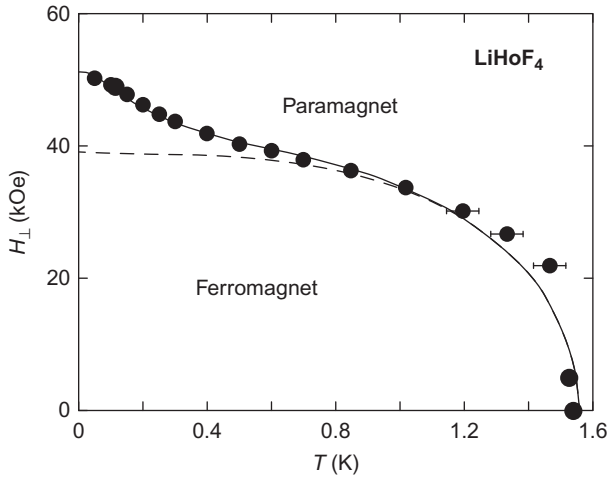
FIG. 5 Experimental phase diagram for LiHoF$_4$ with a ferromagnetic phase up to the Curie temperature, as a function of T_c and applied transverse field $H_\perp$. The dashed line represents the mean-field theory while the solid line and data points include the correction due to the nuclear hyperfine interaction. Here, $H_\perp^c$ is 4.93 T and the lowest measurement temperature is 0.1 K. The divergence of the ac-susceptibility (χ' and χ'') in the given field determines $T_c(H_\perp)$. *According to Bitko, D., Rosenbaum, T.F., Aeppli, G., 1996. Quantum critical behavior for a model magnet. Phys. Rev. Lett. 77 (5), 940.*

Fig. 5 presents the experimental phase diagram (external field $H_\perp$ vs T) of LiHoF$_4$. The low temperature, high-field deviations from the mean field behavior is attributed to nuclear hyperfine interactions of the holium. Inelastic neutron scattering experiments showed that the expected mode-softening at the QPT was perturbed and discontinued by the hyperfine coupling to the nuclear spins that prevented a detailed study of the QPT (Rønnow et al., 2005, 2007).

Early on, experiments of specific heat in $H_\perp$ were performed that spanned the $H_\perp^c$ (Mennenga et al., 1984). However, the then unknown QCP was not reached in temperature and the results merely confirmed the reduced but smeared out in $H_\perp$ specific heat peak of the ferromagnetic transition with an incipient upturn at the lowest temperature. The hyperfine modification to the QPT discouraged further experiments at the QCP and attention then shifted to the diluted Li(Ho$_x$Y$_{1-x}$)F$_4$ and its putative quantum spin-glass (SG) phase transition according to the older work of Wu et al. (1993). However, this left the quantum critical and quantum fluctuation portions of the LiHoF$_4$ phase diagram mostly unexplored.

Even before the interest in the transverse field QPT of Ising LiHoF$_4$ became apparent, the search for a SG state in diluted Li(Y$_{1-x}$Ho$_x$)F$_4$ was underway via ac-susceptibility (Reich et al., 1986). The initial question posed:

can the reduced holmium concentration (eg, $x = 0.167$) and random dipolar interactions create a canonical Ising SG? The efforts are continuing up to the present with the answer still being controversial. Jönsson et al. (2007) claim the absence of a conventional SG transition, based on low temperature SQUID measurements. In contrast (Ancona-Torres et al., 2008) using low field, low-frequency nonlinear susceptibility established the SG transition. Other experiments are divided between a canonical SG phase (Quilliam et al., 2012), and glassy low-temperature dynamics (Rodriguez et al., 2010).

Regardless of the exact SG state, the behavior of diluted $Li(Y_{1-x}Ho_x)F_4$ in a transverse field $H_\perp$ was studied, motivated by theoretical predictions of Read et al. (1995) and Sachdev (2011). Initially, Wu et al. (1993) investigated the nonlinear susceptibility of the $x = 0.167$ compound to low temperatures and high fields, thereby driving the SG temperature $T_SG(H_\perp)$ to near zero as shown in Fig. 6. As 25 mK was approached by varying $H_\perp$, the nonlinear
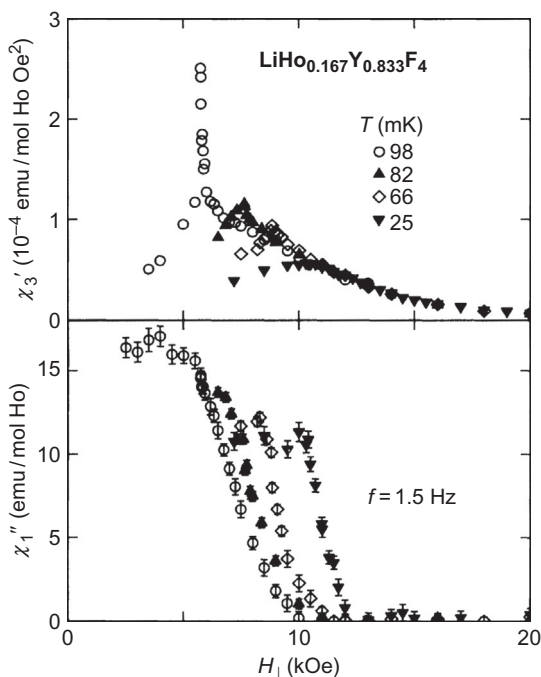
FIG. 6 *Upper panel*: Nonlinear ac-susceptibility as function of $H_\perp$ at various temperatures. Note how the originally sharp classical SG transition is smeared into a broad peak as the QCP is reached. *Lower panel*: Imaginary part (absorption) of the linear ac-susceptibility as above. Note how the absorption decreases as the $H_\perp$ is scanned though the critical temperature both classical and quantum. This behavior indicates dynamical effects around the transitions at the one frequency (1.5 Hz) of measurement. *According to Wu, W., Bitko, D., Rosenbaum, T.F., Aeppli, G., 1993. Quenching of the nonlinear susceptibility at a $T = 0$ spin glass transition. Phys. Rev. Lett. 71 (12), 1919.*

susceptibility became broadened with no sign of the expected QCP divergence and unconventional frequency effects (Kopeć, 1997). Wu et al. (1993) then suggested the disagreements with theory were the result of a first-order quantum SG transition. More recent measurements (Tabei et al., 2006) attribute this lack of QPT behavior to the induced random field Ising features thereby rendering the quantum criticality inaccessible. This conclusion was confirmed by Ancona-Torres et al. (2008) due to the competing effects of quantum entanglement and random fields. Schechter (2008) has demonstrated that a proper treatment of $LiHo_xY_{1-x}F_4$ in a transverse field is the random field-Ising model, not the canonical QPT description introduced in Section 2.2. Additional attempts at finding an Ising SG to confirm the predicted $H_\perp$ behavior remain unclear because of the above complications.

At present, the closest realization of transverse field Ising criticality occurs in columbite $CoNb_2O_6$, a material outside the scope of this review (Coldea et al., 2010; Lee et al., 2010). As for rare earths and actinides, theory still greatly outweighs the "ideal" material experiments.

2.4.2 Ce(Cu,Au)₆

The first heavy-fermion material $CeCu_6$ was originally proposed (von Löhneysen et al., 1994) to show a QCP with combinations of different tuning parameters: Au-dilution, pressure, and magnetic field. This well-studied intermetallic compound was extensively reviewed by von Löhneysen et al. (2007). Here, we briefly summarize the long history of $CeCu_{6-x}Au_x$ and relate the QPT behavior to recently evolving work. Specific heat data are shown in Fig. 7, for various doping x and pressure P.

Pure $CeCu_6$ does not order magnetically down to at least 10 mK. In a good FL, the specific heat C/T should approach a constant as $T \to 0$, hence the slight upturn of C/T in Fig. 7 suggests the presence of spin fluctuations disturbing the FL.

With increasing Au concentration the QCP is reached at $x_c = 0.1$, where the C/T behavior changes to $C/T \sim [\ln(T_o/T)]$. This temperature dependence indicates NFL behavior, an indication of possible quantum criticality. By further increasing the Au concentration x magnetic order is generated. This phase is an incommensurate SDW (Schröder et al., 1994) with small staggered magnetic moments, reaching $\mu \approx 1.2\mu_B$/Ce at $x = 1.0$. The concentration dependence of T_N is shown in the upper panel of Fig. 7. The Nèel temperature T_N begins to decrease above $x = 1.0$ due to the destructive effects of disorder affecting the band structure and Fermi surface of this strongly correlated material. As a function of Au-concentration tuning, we thus have a V-shaped region of quantum criticality just above x_c, as suggested by Fig. 2. Note that the putative FL state for concentrations $x < x_c$ has not been designated.

Another thermodynamic property of $CeCu_{6-x}Au_x$ is the dc bulk magnetic susceptibility χ. Fig. 8 shows $\chi = M/H$ for concentrations $0 \le x \le 0.3$ and the
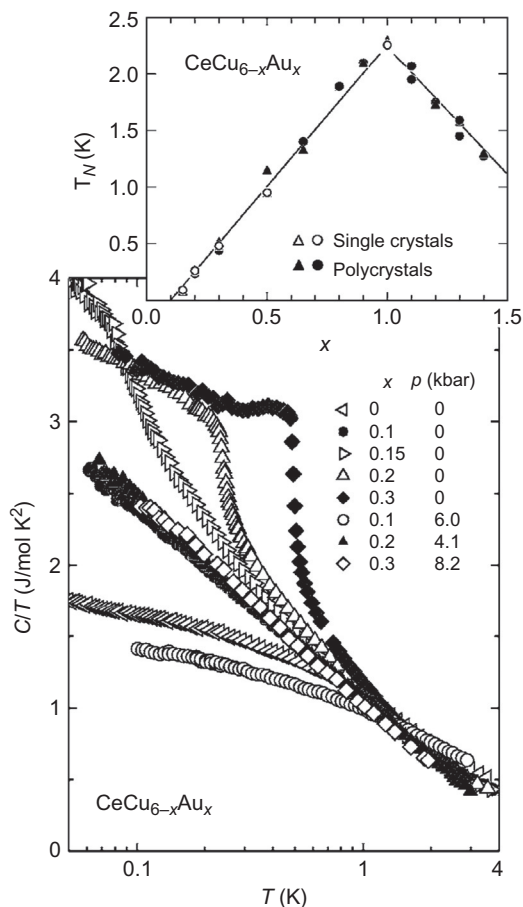
FIG. 7 Specific heat of $CeCu_{6-x}Au_x$ vs log(T) for various tuning parameters Au_x concentration and hydrostatic pressure near the QCP at $x_c = 0.1$. Note the behavior of C/T is logarithmic at x_c signifying the QCP. There are slight deviations from FL behavior ($C/T \approx$ constant) at $x < x_c$; and weak moment, incommensurate antiferromagnetic (SDW-type) order for $x > x_c$. Pressure restores the lower x behavior, ie, removes the AFM-order and generates a return to quantum criticality and FL behavior. The upper panel traces the AFM Nèel temperature as a function of x for single and polycrystal samples. Note how T_N becomes reduced as x increases above 1.0. This illustrates the disorder effects of large gold dilutions probably affecting the band structure and Fermi surface of $CeCu_6$. *According to von Löhneysen, H., Rosch, A., Vojta, M., Wölfle, P., 2007. Fermi-liquid instabilities at magnetic quantum phase transitions. Rev. Mod. Phys. 79 (3), 1015-1075.*

magnetic field H applied along **c**. There is a near constant in T dependence for $x = 0$ and the gradual low temperature upturn at x_c, with the antiferromagnetic order only becoming apparent at $x = 0.3$. The susceptibility behavior at the QCP follows a $\chi = \chi_0 - \delta\sqrt{T}$ dependence. Spin fluctuations seem to be modifying the $x = 0$ FL state where χ should be constant as $T \rightarrow 0$.
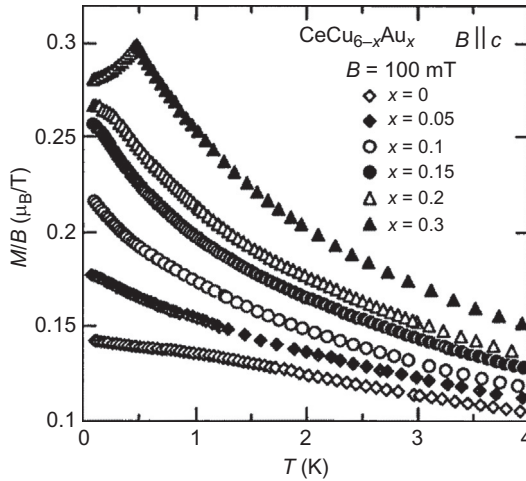
FIG. 8 Magnetic susceptibility, $\chi = M/H$, for various concentrations of CeCu$_{6-x}$Au$_x$ in an easy axis magnetic field of 0.1 T. Note the NFL behavior at $x_c = 0.1$ and the antiferromagnetic peak for $x = 0.3$. *According to* von Löhneysen, H., 1996. *Non-fermi-liquid behaviour in the heavy-fermion system. J. Phys. Condens. Matter 8 (48), 9689.*

Pressure can be used to "retune" the concentration behavior, see Fig. 7. This reversing behavior demonstrates that an increasing Au concentration expands the lattice, whereas pressure P compresses it. Such correspondence is limited to small concentrations and moderate hydrostatic pressures, it breaks down if x or P is too large. Nonetheless, the low temperature specific heat displayed in Fig. 7 established evidence for a QCP where the critical Au concentrations x_c increases with pressure.

Next, consider the all-important resistivity as shown in Fig. 9. At $x = 0$ initial FL behavior is observed, $\rho = \rho_0 + AT^2$. The temperature dependence of the resistivity ρ becomes linear ($\rho = \rho_0 + A'T$) at the critical value $x_c = 0.1$, signaling NFL behavior. For $x = 0.15$, we are already in the magnetically ordered phase, with a dubious suggestion of a "kink" in the resistivity at the spin ordering Nèel temperature T_N. Disturbingly, this magnetic ordering kink is not found at higher gold concentrations, instead there is an enormous increase in the residual resistivity. This transport-property effect clearly establishes the large change in scattering rates with increasing doping, which are mainly related to the Fermi surface and band structures. Note that even at zero doping $x = 0$ there is a rather large residual resistivity!

The SDW, as detected by neutron scattering (Schröder et al., 1994), is a most subtle form of magnetism and the tiny x-disorder is essential to tune it. The mysterious "Kondo hybridization" between the Ce 4f electrons and the conduction electrons compensate the moments, thereby diminish the Ruderman–Kittel–Kasuya–Yosida (RKKY) interaction resulting in this small moment itinerant SDW.
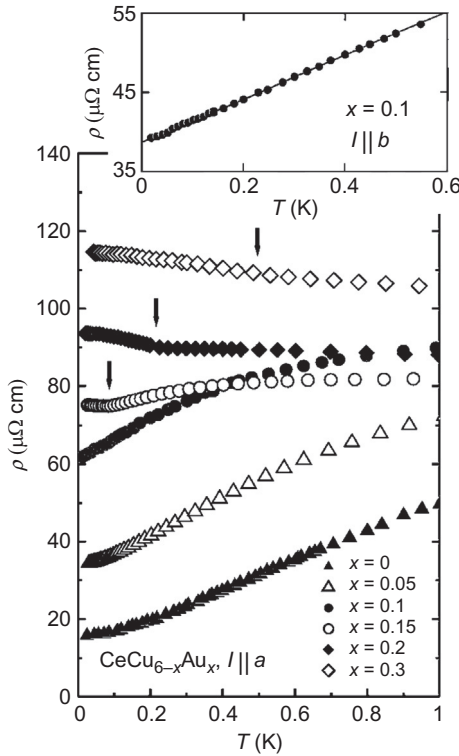
FIG. 9 Electrical resistivity, ρ, of $Ce(Cu_{6-x}Au_x)$ from 0 to 0.3 concentration tuning. The ρ (T) curves illustrate the change of behavior from HFL (T^2) to NFL (T) to a constant resistivity due to the strong disorder of Au_x doping. Here, the antiferromagnetic transition is hardly discernible because of the large disorder scattering. *According to von Löhneysen, H., Rosch, A., Vojta, M., Wölfle, P., 2007. Fermi-liquid instabilities at magnetic quantum phase transitions. Rev. Mod. Phys. 79 (3), 1015-1075.*

Further inelastic neutron scattering probed the critical fluctuations at x_c (Stockert et al., 1998). The spin fluctuations appeared to be highly anisotropic leading to a rod-like formation of excitations in the dynamical structure factor $S(\mathbf{q}, \omega)$. In real space, this corresponds to quasi-2D fluctuations (Rosch et al., 1997). The dynamical structure factor $S(\mathbf{q}=const, \omega)$ resulted in a dynamical scaling of the dynamical susceptibility in ω/T (Schröder et al., 2000). Interestingly, HM theory is incompatible with such ω/T scaling, indicating the need for new theories.

The third way to tune the system is through an external applied magnetic field $\mathbf{H}$. Since Au_x dilution can be reversed with hydrostatic pressure, the field tuning should have similar effects to diminish the AFM and return the compound $CeCu_{6-x}Au_x$ to its QCP at $x_c=0.1$. Such experiments were performed on a single crystal of $CeCu_{5.8}Au_{0.2}$ with $\mathbf{H}$ along its easy axis, measuring

specific heat and resistivity. The field-tuned results could then be compared to Figs. 7–9. However, distinctly different power-law exponents were observed for the field-tuned measurements (von Löhneysen et al., 2001). This behavior is consistent with the HM theories while, in contrast, x and P tuning required a completely different scenario.

Additional field tuning experimental were carried out on silver-doped $CeCu_{6-x}Ag_x$ (Heuser et al., 1998). However, slightly larger $Ag_x(\approx 0.2)$ concentrations are needed to start in the antiferromagnetic phase. Limited measurements were performed only on polycrystalline samples. These authors claim that both doping and field-tuning generate the NFL behavior which is caused by an underlying QCP. One must be careful: NFL properties are not only related to quantum criticality in these strongly correlated intermetallic heavy-fermion compounds. Disorder is also a prime cause of anomalous thermodynamic and transport behavior. Additionally, the magnetic field, as a vector quantity, can induce deviations from T^2 resistivity dependences due to magnetic modes and anisotropic scattering. Similarly, discrepancies can be found in the specific heat. So we must be cautious about claiming NFL behavior is solely related to an underlying QCP.

Therefore, after all is said and measured, a number of open and fundamental queries remain. Why does the field-tuning appear so much different from the pressure or doping-tuned QPT? What is the role of disorder, specifically in terms of destroying the heavy Fermi liquid (HFL) state? How does the Kondo compensation of the local moments exactly work? This last point is related to a more general question on whether the magnetic state is the result of Fermi surface or local moment effects? Then there is, finally, the question of the observed ω/T scaling and the possible two-dimensional spin fluctuations. These ruminations represent our present-day questioning of quantum criticality in $CeCu_{6-x}Au_x$.

2.4.3 $YbRh_2Si_2$

From the opposite end of the lanthanide series, another antiferromagnetic heavy-fermion material was discovered in 2000: $YbRh_2Si_2$ (Trovarelli et al., 2000). This intermetallic compound requires ultra-low temperatures and small magnetic field ($H_c \cong 0.7$ T perpendicular to the easy axis) to reach a QPT, from a very low temperature antiferromagnetic phase ($T_N = 0.07$ K and $10^{-3}\mu_B$ moment). Again, the key signatures of quantum criticality arise through NFL behavior, ie, the unconventional low-T power laws of the resistivity, specific heat and susceptibility. For $YbRh_2Si_2$, the NFL (quantum critical) regime spans the entire temperature-field phase space, above the QCP and even above the antiferromagnetic phase.

Fig. 10 exhibits this phase diagram based on resistivity measurements (Custers et al., 2003). On the left side, the field is applied along the hard direction $H \parallel c$, which requires a field of 0.7 T to reach the QCP. As indicated
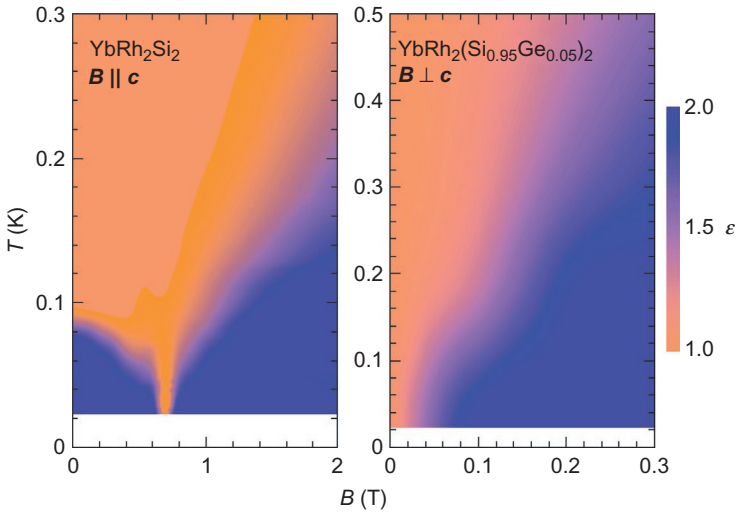
FIG. 10 Temperature vs magnetic field phase diagram of $YbRh_2Si_2$. The color contours illustrate the temperature exponent of the resistivity: red (gray in the print version) equals linear T, blue (dark gray in the print version) quadratic T^2 in the various field tuned regimes. *According to Custers, J., Gegenwart, P., Wilhelm, H., Neumaier, K., Tokiwa, Y., Trovarelli, O., Geibel, C., Steglich, F., Pepin, C., Coleman, P., 2003. The break-up of heavy electrons at a quantum critical point. Nature 424 (6948), 524-527.*

by the resistivity's T-exponent ϵ, there is a large region of NFL behavior throughout most of the phase diagram. The color coding illustrates how the T^ϵ changes from 2 (Fermi-liquid) to 1 (NFL). On the right side, Ge alloying is used to expand the lattice, thus reducing T_N, such that the critical field along the easy axis is reduced to $H_c \cong 0.027$ T. For small concentrations of Ge, here 5%, the lattice disorder and strain are expected to be minimal.

The specific heat, plotted as C/T vs T and $\log T$, is illustrated in Fig. 11 for different applied fields along the easy axis (Oeschler et al., 2008). The enhanced antiferromagnetic peak at T_N is reduced in both temperature and magnitude with applied field H, until it disappears at the QCP, now at $H_c \cong 0.06$ T.

The expected NFL behavior $C/T \sim \log(T_0/T)$, becomes steeper for low temperatures $T < 0.3$ K where it turns into a power-law $C/T \sim T^{-0.3}$. This suggests another entropy contribution, probably from hyperfine interactions resulting from the nuclear magnetism of the Yb nucleus. At larger H-fields, C/T is essentially constant, indicating FL behavior.

The ac susceptibility and magnetization of $YbRh_2Si_2$ show deviations from their high-temperature Curie–Weiss (C-W) behavior. Fig. 12 shows the ac-susceptibility for $YbRh_2Si_2$ at various magnetic fields (Trovarelli et al., 2000). The small peak in zero field followed by flatness denote the tiny moment antiferromagnetic transition. Above the Nèel temperature T_N one
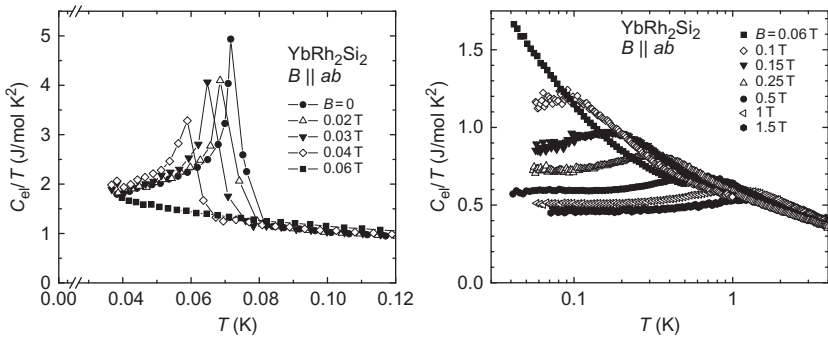
FIG. 11 Specific heat in various magnetic fields for YbRh$_2$Si$_2$, *left*: low fields $H \leq 0.06$ T; *right*: $H \geq 0.06$ $T = H_c$. Note the quenching of antiferromagnetic order (lambda transition) with field and the logarithmic upturn that becomes constant at very large fields. *According to Oeschler, N., Hartmann, S., Pikul, A.P., Krellner, C., Geibel, C., Steglich, F., 2008. Low-temperature specific heat of YbRh2Si2. Phys. B Condens. Matter 403 (5), 1254-1256.*
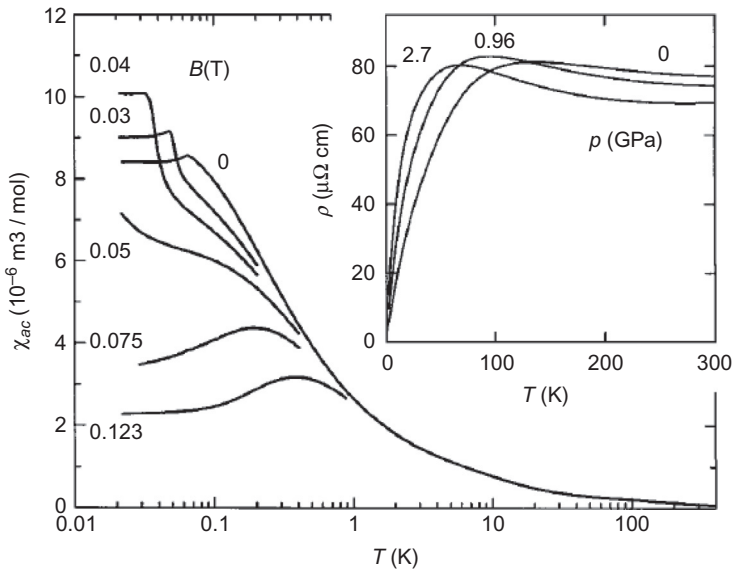
FIG. 12 ac-susceptibility of YbRh$_2$Si$_2$ in small magnetic field approaching the QCP. χ_{ac} gives indications of ferromagnetic freezing in small fields that become smeared out as the eternal field is increased. The inset shows the full $\rho(T)$ behavior with the large high T resistivities and minimum pressure dependences. *According to Trovarelli, O., Geibel, C., Mederle, S., Langhammer, C., Grosche, F.M., Gegenwart, P., Lang, M., Sparn, G., Steglich, F., 2000. YbRh2Si2: pronounced non-Fermi-liquid effects above a low-lying magnetic phase transition. Phys. Rev. Lett. 85 (3), 626.*

can already observe the precursor discrepancy in an upturn away from the C-W form. With increasing field the weak power-law behavior becomes noticeable, eg, at 0.05 T. However, at the lowest temperature there is a stronger increase in χ_{ac} due to the nuclear contribution. The dc-magnetization divided by field, M/H, shows a similar upturn at the critical field H_c that becomes less strong, finally reaching a flat $M/H(T)$ at 0.3 T (Tokiwa et al., 2009). Because a C-W analysis is invalid for this strongly correlated and fluctuating low-temperature regime, highly sophisticated analysis must be used to treat the data and extract physical conclusions (Abrahams and Wölfle, 2012).

Since the Nèel temperature and critical fields are so small it is most difficult to perform microscopic measurements below T_N and around H_c. Therefore most experimental probes at temperatures below 0.07 K are limited to transport or thermodynamic measurements. The Hall effect tuned with the two field directions has been examined in detail by Paschen et al. (2004), which results in the overall phase diagram in Fig. 13 (Gegenwart et al., 2008). The Hall coefficient R_H shows a change at a "crossover" line $T*(H)$ that seems to extrapolate to a sudden jump in R_H at zero temperature. Further experiments tracked the thermopower $S(T, B)$ in the field and temperature region surrounding the QCP (Hartmann et al., 2010). Here, an agreeing crossover feature, namely a change of sign, at the $T*(B)$ line was observed in $S(B)/T$. However, the general behavior of $S(T, B)/T$ is rather complicated with significant scatter thereby preventing a full understanding.
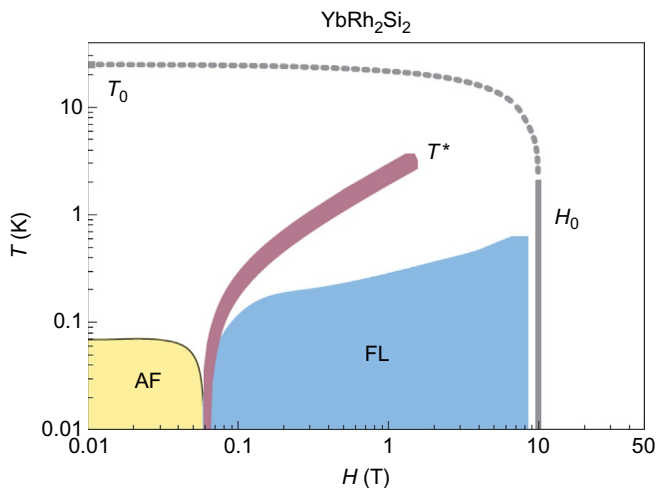
FIG. 13 Extended log$T$(K) vs log$H$(T) phase diagram of YbRh$_2$Si$_2$ as function of magnetic field (in-plane, easy) illustrating the QCP, AFM, NFL, and Lifshitz transition phases. Note the $T*$ line that is used to denote the Kondo breakdown scale, extracted from Hall measurements, and the T_C line illustrating the formation of the HFL. *According to Gegenwart, P., Si, Q., Steglich, F., 2008. Quantum criticality in heavy-fermion metals. Nat. Phys. 4 (3), 186-197.*

Experiments of the Grüneisen ratio $\Gamma = (V_{mol}/\kappa_T)(\alpha_{cr}/C_{cr})$ and magnetic Grüneisen ratio $\Gamma_{mag} = -(dM/dT)/C$, ie, the magnetocaloric effect $(1/T)(dT/dH)$ at constant entropy, were performed by Küchler et al. (2003) and Tokiwa et al. (2009), respectively. Inverse power-law divergences were generally found indicating a QPT as predicted by theory (Zhu et al., 2003), see Section 2.3.

Finally, inelastic neutron scattering (INS) experiments were carried out in magnetic fields down to temperatures of $T \sim 0.1$ K, which is still above T_N, by Stock et al. (2012) to probe the NFL state of $YbSi_2Si_2$. These dynamical resonances detect the spin fluctuations in the meV energy range and their momentum dependence within the Brillouin zone. The zero-field spin fluctuations are incommensurate in the basal plane with ferromagnetic interplane correlations. There is a strong dependence of the fluctuation spectra with temperature due to the competition between ferromagnetic and incommensurate antiferromagnetic components. In large magnetic fields, eg, $H \sim 2 - 10$ T, local moment behavior is field-induced that can be interpreted as localized droplets of Yb^{+3} spins extending on a length scale of $\sim 10 \mathring{A}$. This response indicates a change in behavior for low-field itinerancy, ie, Fermi surface nesting, to Kondo screened local moments (Stock et al., 2012).

A very recent nuclear magnetic resonance (NMR) study of the spin-lattice relaxation time, T_1, of ^{29}Si spanning the QCP (Kambe et al., 2014) has concluded that a coexistence of both HFL and NFL phases exist. These paired states represent an itinerant HFL component degenerate at the QCP with a localized NFL whose ratio $R(T, H) = f_{NFL}/f_{HFL}$ varies with T and H. The description assumes a "two-fluid" scaling relation that nicely fits the data with reasonable scaling exponents. Thus we have a novel interpretation that adds a new element to the quantum critical behavior, yet it leaves the antiferromagnetic state, the putative SDW, unresolved with both quantum critical ferromagnetic and antiferromagnetic fluctuations playing a role (Kambe et al., 2014).

So what then is nature of the antiferromagnetic transition below 0.07 K and how is this state perturbed with tiny fields of ~ 0.06 T to create the QCP? Additional microscopic or local experiments, such as angle-resolved photoemission spectroscopy (ARPES), STM (scanning tunneling microscopy)/STS (scanning tunneling spectroscopy), quantum oscillations, core spectroscopy, etc., are needed to answer this question. Although an enormous amount of effort and manpower resulting in many premier publications have been devoted to $YbRh_2Si_2$ and its QCP, the exact causes and their description have remained incomplete.

Note that there are other ytterbium-based heavy fermion materials that exhibit quantum criticality. A recent example is $YbNi_4(P_{1-x}As_x)_2$, which is an itinerant ferromagnet that can be tuned to criticality by either a magnetic field or arsenic doping. A divergence of the Grüneisen ratio was found, inconsistent with the HM predictions (Steppke et al., 2013).

3 PRESENT THEORIES

3.1 Critique of HM and the Kondo Effect

As discussed in the previous section, both $CeCu_{6-x}Au_x$ and $YbRh_2Si_2$ display features that are incompatible with standard HM theory. This forces us to look at reasons why this itinerant SDW picture should not apply.

The most fundamental critique originates in the microscopic nature of the materials. In addition to the usual set of conduction electrons, the materials discussed in this chapter contain electrons localized in f-orbitals. The interaction between conduction electrons and localized d or f-states was first studied by Kondo (1964), who introduced the model of a single magnetic impurity in a metal,

$$H = \sum_{k\sigma} \epsilon_k c_{k\sigma}^\dagger c_{k\sigma} + J\vec{S} \cdot \vec{s} \tag{19}$$

where $\vec{S}$ is the spin of a localized impurity, k is the electron momentum with dispersion ϵ_k, and $\vec{s} = \sum_{kk'} c_{k\alpha}^\dagger \vec{\sigma}_{\alpha\beta} c_{k'\beta}$ is the total spin of the conduction electrons at the impurity site. At temperatures below the Kondo temperature, $T_K \sim \exp(-1/JN_0)$, where N_0 is the density of states of the conduction electrons at the Fermi level, Kondo showed that the localized spin forms a singlet state with the conduction electrons. This process of Kondo screening effectively delocalizes the initially localized f-electron (Anderson, 1970; Hewson, 1993; Kondo, 1964).

It was expected that Kondo hybridization will also occur in materials that have localized f-electrons in every unit cell. The corresponding Kondo lattice model (Doniach, 1977)

$$H = \sum_{k\sigma} \epsilon_k c_{k\sigma}^\dagger c_{k\sigma} + J\sum_i \vec{S_i} \cdot \vec{s_i} \tag{20}$$

is suggested to be a standard FL below the Kondo coherence temperature T_{coh}. Below this temperature, the f-electrons are hybridized with the conduction electrons, and the effective mass of the new electrons is drastically enhanced: a HFL. The delocalization of the f-electrons implies that the Fermi surface becomes larger than it would be when only the c-electrons would be mobile (Oshikawa, 2000).

Even though the Kondo lattice model has been studied extensively with various methods (such as slave-boson theory Burdin et al., 2000, for further reading see Sec. II.F.2. of von Löhneysen et al., 2007), there is currently no solid understanding of how the hybridization of f- and c-electrons works. This lack of understanding then carries over to the realm of HM theory that requires simple Landau fermi-liquid quasiparticles to start with.

Nevertheless, the notion of a QCP in a Kondo lattice system can be introduced. AFM in the Kondo lattice model can arise from interactions between

the *f*-electrons, mediated by the *c*-electrons (Kasuya, 1956; Ruderman and Kittel, 1954; Yosida, 1957). This RKKY interaction at energy scale $E_{RKKY} \sim J^2 N_0$ competes with the Kondo screening at $T_K \sim \exp(-1/JN_0)$, leading to a QPT as a function of the coupling *J*.

3.2 Kondo Breakdown

A more radical idea involves a breakdown of the Kondo hybridization at the critical point. There are some strong experimental evidences that hint in such a direction, for example, the divergence of the effective mass as exemplified by the diverging specific heat coefficient *C/T* and the existence of *T**-line in YbRh$_2$Si$_2$. Although the idea is certainly appealing, again it seems very difficult to extract quantitative predictions based on the scenario of the Kondo breakdown (Coleman, 1999, 2001, 2015; Coleman et al., 2001; Sengupta, 2000; Si et al., 2001, 2014).

The theories of Kondo breakdown originate from dynamical mean field theory (DMFT) (Georges et al., 1996), a numerical technique where the order parameter is still local in space but can have nonlocal temporal correlations. In addition to the critical fluctuations associated with the antiferromagnetic order, in the Kondo breakdown there are also purely local critical fluctuations associated with the localization of the *f*-electrons.

The most important prediction of the Kondo breakdown scenario is the existence of a large Fermi surface on right side of the transition, encompassing both *f*- and *c*-electrons, whereas on the antiferromagnetic (left) side of the transition the Fermi surface is "small" and only contains *c*-electrons. So far there is no direct experimental evidence, for example, ARPES (Kummer et al., 2015; Paschen et al., 2015), that supports this claim. Indirect evidence, such as the *T** line based on a crossover in the Hall conductivity, can also be explained differently.

Some authors have gone even further by completely discarding the antiferromagnetic transition and focussing on an isolated Kondo breakdown. In this picture, the localized *f*-electrons will form a spin liquid, coexisting with a small Fermi surface metal dubbed *FL** (Senthil et al., 2003, 2004). Antiferromagnetic order would then be an instability of this *FL** phase. The absence of two different transitions suggests this exotic theory is not relevant for experiments.

3.3 Two-Dimensional Physics

A surprising caveat of the Kondo breakdown pictures is that requires the system to be effectively two dimensional (Si et al., 2001). In fact, many features of CeCu$_{6-x}$Au$_x$ such as the logarithmic divergence of the specific heat coefficient can be understood by *d* = 2-dimensional HM theory (Rosch et al., 1997). It is quite puzzling, however, since there is no apparent microscopic reason why these materials would be highly anisotropic.

In addition, later it was found that standard HM theory develops some anomalies in two dimensions that render it incorrect. This originates from the fact that antiferromagnetic fluctuations ($z=2$) in two dimensions have effective dimension $d+z=4$, exactly the upper critical dimension where interactions become marginally relevant. It has been found that one cannot integrate out fermions to arrive at an effective model, as Hertz originally did. Instead, both electrons and critical fluctuations need to be treated at an equal level, which is an ongoing theoretical effort (Abanov and Chubukov, 2000, 2004; Lee, 2009; Metlitski and Sachdev, 2010; Pankov et al., 2004; Varma, 2015).

3.4 Critical Quasiparticles

While Kondo hybridization certainly takes on an important role in many heavy fermion compounds, an alternative approach to the Kondo breakdown picture is to describe the effective mass divergence phenomenologically. The quasiparticle mass enhancement is characterized by the parameter $Z=m/m^*$, and hence experimentally we find $Z \to 0$ at the transition. This would naively imply that the Fermi surface and hence the materials metallic behavior would disappear. Yet, the way around this is via a "critical" Fermi surface (Senthil, 2008) where $Z=0$ but the spectral function still displays some kind of nonanalytic behavior. One can write down phenomenologically the Greens function for the corresponding critical quasiparticles (Abrahams et al., 2014; Vojta et al., 2015; Wölfle and Abrahams, 2011, 2015), from which many critical exponents can be extracted that match experimental results. Nonetheless, a microscopic picture of why quasiparticles would become critical is still lacking.

3.5 Conclusion

The theoretical field seems to be in a state of confusion. At the one hand there are microscopic models based on Kondo physics between f- and c-electrons, but those seem to be nearly impossible to solve rigorously. On the other hand, it is possible to describe a number of experiments by purely phenomenological models. It remains a challenge for the theorists to find a good microscopic basis for their phenomenology. In addition, new experimental results such as ARPES at low temperatures, are then necessary to distinguish between different scenarios of quantum criticality beyond HM.

4 PRESENT MATERIALS AND EXPERIMENTS

There are numerous lanthanide-based heavy-fermion liquids that are claimed to exhibit QPT's. Rather than attempting to catalogue and evaluate these many different materials and their quantum criticality claims, we offer here some overview articles where the reader can find these intermetallic

compounds and extract the experimental details. For up-to-date reference, we refer to the following reviews by Stewart (2001, 2006), Coleman and Schofield (2005), von Löhneysen et al. (2007), Gegenwart et al. (2008), Pfleiderer (2009), Si and Steglich (2010), and Stockert et al. (2011).

In order to create and study a QPT, the general protocol consists of reducing with pressure, magnetic field, frustration and/or dilution the magnetic or superconducting phase to $T = 0$. Here, the a priori question arises, whether such tuning leads to a continuous QPT? The usual justification for a QCP is the appearance of NFL behavior instead of standard FL behavior. However, other types of transitions without these quantum fluctuations could occur, eg, droplets, inhomogenoties, percolation or glassy dynamics (Seo et al., 2014). So additional criteria beyond the NFL effects are needed to characterized the near $T \to 0$ behavior, eg, the use of the Grüuneisen ratio, see Section 2.3.

In both the Cerium-based series, Ce(Co, Rh, Ir)In$_5$ and the uranium compound URu$_2$Si$_2$, distinct NFL behavior has been observed. We will now address the question whether this NFL behavior can be ascribed to a QCP.

4.1 The Cerium Series Ce(Co, Rh, Ir)In$_5$

Let us now focus on an intensely studied Ce-system, viz. Ce(Co, Rh, Ir)In$_5$ where a variety of behavior and tunings have been investigated. CeCoIn$_5$ is a heavy-fermion superconductor with $T_c^S = 2.3$ K that is claimed to be magnetically mediated (Petrovic et al., 2001b). Pressure was then applied to destroy the SC at ≈ 3.5 GPa preceded by an anomalous change in the transport properties at 1.6 GPa where T_c^S reaches a maximum of 2.6 K (Sidorov et al., 2002). However, an anticipated antiferromagnetic phase was only speculated to exist at "negative" pressures. Fig. 14 shows the proposed temperature–pressure phase diagram for CeCoIn$_5$ (Sidorov et al., 2002).

Since pressure tuning did not find the antiferromagnetic order, this then encourages magnetic-field tuning to drive $T_c^S \to 0$, as detected by magnetoresistance measurements. Here, phase diagrams were proposed with a QCP at the destruction of SC, yet before the onset of FL behavior (Paglione et al., 2003). A similar phase diagram was established by Bianchi et al. (2003) from field dependent specific heat and resistivity data, including crossovers from superconducting to NFL to FL behavior. The interpretation of the QCP at 5 T was related to field-tuned antiferromagnetic spin fluctuations. However, the attempt to directly detect signs of AFM failed.

The remaining tuning parameter for CeCoIn$_5$ is doping, and specifically to substitute Cd on the In sites to effectively remove electrons. In the (In$_{1-x}$Cd$_x$)$_5$ experiments, the parameter x refers to the nominal rather than the actual Cd concentration. Indeed AFM order develops with Cd$_x$ for $x > 7.5\%$ as detected via specific heat and resistivity (Pham et al., 2006). In addition of SC being depressed with Cd doping, there seems to exist overlaps
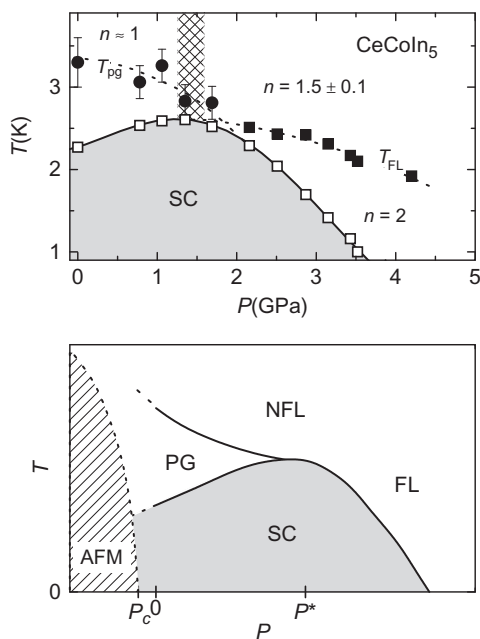
FIG. 14 *Upper panel*: Temperature–pressure phase diagram of CeCoIn$_5$ determined by electrical resistivity. A QCP is expected at $P_{QPT}=3.5$ GPa but it emerges from a FL state instead of an NFL. *Lower panel*: Proposed schematic of various T–P phases. Note that the AFM only appears at negative pressures and the speculations of a pseudogap. *According to Sidorov, V.A., Nicklas, M., Pagliuso, P.G., Sarrao, J.L., Bang, Y., Balatsky, A.V., Thompson, J.D., 2002. Superconductivity and quantum criticality in CeCoIn$_5$. Phys. Rev. Lett. 89 (15), 157004.*

with the antiferromagnetic order, suggesting possible inhomogeneous phases. In order to probe the AFM and SC on a local scale, NMR was employed to study the extent of these phases (Urbano et al., 2007). Here, the results are interpreted in terms of local droplets of magnetism surrounding the Cd impurities. With a sufficient concentration of droplets, that is, cadmium, a percolative transition occurs toward true long-range AFM within the coexistent SC matrix. Further details concerning the dangers of disorder caused by impurity doping is discussed by Seo et al. (2014). Currently their droplet model is probed by nuclear quadrupole resonance (NQR) on a local scale. A cartoon illustration of the pressure dependence of the AFM droplets is shown in Fig. 15. This nucleation interpretation emphasizes the annulling effect of disordered ligand doping on the quantum criticality. For instead of a homogeneous QPT, we now create a freezing of magnetic fluctuations generating an inhomogeneous glassy ground state. In summary: the doped system seems to display not a proper QPT but rather a frozen quantum glass.

Another compound, CeRhIn$_5$, is antiferromagnetic with $T_N \approx 3.8$ K as determined by C/T, χ, and ρ measurements. Neutron scattering has detected
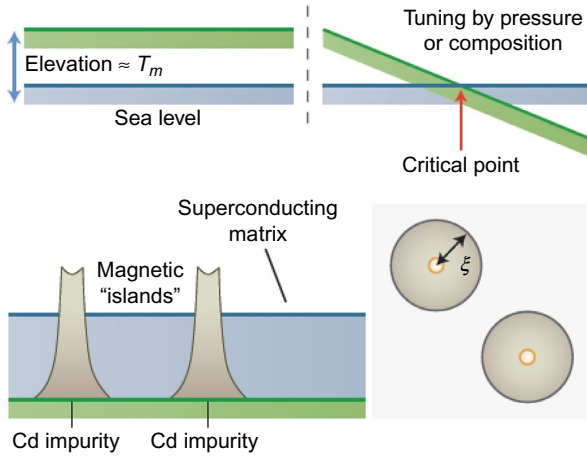
FIG. 15 Cartoon of the Cd doping effect on CeCo$_5$, model of Seo et al. (2014). *Upper left*: The AFM state (green (light gray in the print version)) lies favorable above the SC (sea-level) state. *Upper right*: By tuning the pressure or composition a QCP can be created by reducing the AFM state below the SC state. *Lower left*: Cd doping produces magnetic islands with in the SC matrix. *Lower right*: If the magnetic correlation length exceeds the distance between islands, long-range AFM occurs via percolation. *Cartoon according to Grosche, F.M., 2014. Quantum phase transitions: magnetic islands. Nat. Phys. 10 (2), 94-95.*

an incommensurate spiral magnetic structure with $0.26\mu_B$ Ce-moments (Bao et al., 2000). Under pressure T_N slowly decreases, however, above 1.5 GPa CeRhIn$_5$ becomes superconducting with $T_c^S = 1.9$ K. There exists seemingly a bulk heavy-fermion antiferromagnet to SC crossover (Hegger et al., 2000). Fig. 16 exhibits the resistivity as a function of temperature at different pressures, the $d\rho/dT$ maxima denote the magnetic transition temperature T_N and $\rho = 0$ at $T = 2$ K signals the SC state. Unfortunately, unknown anomalies also exist within the temperature–pressure phase diagram, yet the AFM vanishes at a certain pressure $P_{c1} = 1.77$ GPa when the Nèel temperature equals the superconducting critical temperature, $T_N = T_c^S$. Below P_{c1} there seems a small region of coexistence.

Magnetic field tuning can be combined with pressure tuning, for such systems the specific heat C/T was measured as a function of T, P, and H (Park et al., 2006). The resulting 3D phase diagram is shown in Fig. 17. If we take the $T = 0.65$ K plane to approximate $T = 0$, the data points lying in this plane represent the proposed QCP's. With increasing H and P a line of QCP's separates the antiferromagnetic phase (MO) from a region of coexisting MO and SC. At $H = 0$ a QCP is formed at P_{c1}.

Additional $C/T(T, P)$ measurements were carried out by Knebel et al. (2006) that showed an inhomogeneous SC/AFM state followed, at a higher pressure, by pure SC. With increased H and P a second "tetracritical" quantum point is reached at $P_{c2} = 2.25$ GPa. However, there are little or no
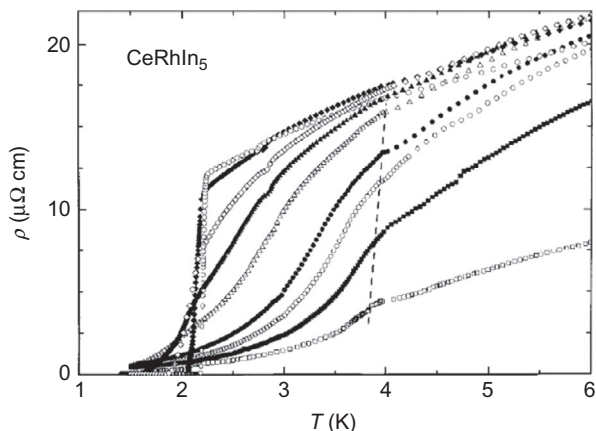
FIG. 16 Pressure induced superconductivity and destruction of antiferromagnetism in CeRhIn$_5$ determined via resistivity with pressure increasing vertically from 0 to 21 kbars. From $d\rho/dT$, the antiferromagnetic transition temperature T_N can be found, and the superconducting transition T_c occurs when $\rho = 0$. *According to Hegger, H., Petrovic, C., Moshopoulou, E.G., Hundley, M.F., Sarrao, J.L., Fisk, Z., Thompson, J.D., 2000. Pressure-induced superconductivity in quasi-2D CeRhIn$_5$. Phys. Rev. Lett. 84 (21), 4986.*
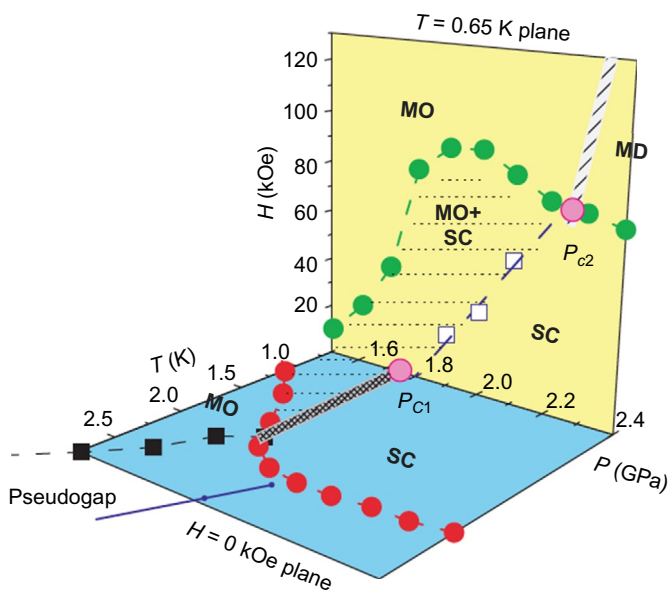

FIG. 17 Magnetic field, temperature, and pressure phase diagram of CeRhIn$_5$. The $T = 0.65$ K plane represents the extrapolated $T = 0$ QCP. Here, lines of phase transitions are expected between magnetically ordered (MO) to coexisting magnetic order with superconductivity (MO+SC) to a superconducting phase (SC), and finally a high field magnetic disordered state (MD). Note the tetracritical point at P_{c2}. *According to Park, T., Ronning, F., Yuan, H.Q., Salamon, M.B., Movshovich, R., Sarrao, J.L., Thompson, J.D., 2006. Hidden magnetism and quantum criticality in the heavy fermion superconductor CeRhIn$_5$. Nature 440 (7080), 65-68.*

experimental data for the temperature dependences, that is, whether there is NFL behavior or if the various coexistence phases are homogeneous or disordered. Nevertheless, Park et al. (2006) attempt to draw similarities with the high-T_c cuprates even though the putative QPT's are undefined. An interesting experiment here is the de Haas–van Alphen studies of the Fermi surface as a function of pressure (Shishido et al., 2005). The authors observed an increase in the cyclotron mass above 1.6 GPa, where SC sets in. Above 2.4 GPa a drastic reconstruction of the Fermi surface occurs that indicates a change from localized to itinerant behavior thereby giving a T_c^S maximum.

Finally and most recently very high magnetic fields (H to 70 T) have been applied to investigate the quantum oscillations, specific heat, and Hall effect of $CeRhIn_5$ (Jiao et al., 2015). These authors observe field-induced modifications of the phase coincident with sharp reconstructions of the Fermi surface (FS) in all the high-field measurements. Especially dramatic are the changes in the quantum oscillation as a function of field H, spanning 10–30 and 45–70 T. Based on the data an experimental phase diagram ($T - H$) may be constructed as shown in Fig. 18—contrast with Fig. 17. Although the lowest temperature of measurement is only $\approx$ 0.4 K, when extrapolated to $T = 0$, two QCPs are proposed: the transition from an AFM with a small Fermi surface (AFM_S) to one with a large Fermi surface (AFM_L) at $\approx$ 30 T; and a transition from an antiferromagnet to a paramagnet (P_L) at $\approx$ 50 T. The authors speculate further with a "schematic" pressure–field phase diagram at $T = 0$ for $CeRhIn_5$. Here, there are intersecting quantum critical lines between SC, AFM_S, AFM_L, and P_L phases as illustrated in the bottom half of Fig. 18. These conjectures of quantum critical lines warrant their experimental proof.

The last in this cerium-troika, $CeIrIn_5$, is a heavy-fermion unconventional superconductor with $T_c^S = 0.4$ K lacking any coexisting magnetic order (Petrovic et al., 2001a). Accordingly, the SC was thought to be mediated by valence fluctuations rather than by spin fluctuations. Thermal conductivity and penetration depth studies indicate a $d_{x^2-y^2}$—type gap symmetry Movshovich et al. (2001) and Vandervelde et al. (2009). Recent doping investigations of Hg and Sn on In sites, and Pt on Ir sites were performed using C(T) and ρ(T) (Shang et al., 2014). The results indicated hole doping via Hg caused AFM while electron doping via Sn or Pt favored a paramagnetic Fermi-liquid. Again the microprobe-determined concentrations are significantly different from the nominal concentrations. So disorder and clustering could be the main cause of the AFM and FL behavior. All of which appears out of a NFL regime. There was no evidence of QPT or QCP for $CeIrIn_5$ or its various doping.

4.2 Hidden Order in URu_2Si_2

There is a particular uranium-based heavy fermion intermetallic compound, URu_2Si_2, that has been studied in-detail regarding a possible QPT. URu_2Si_2
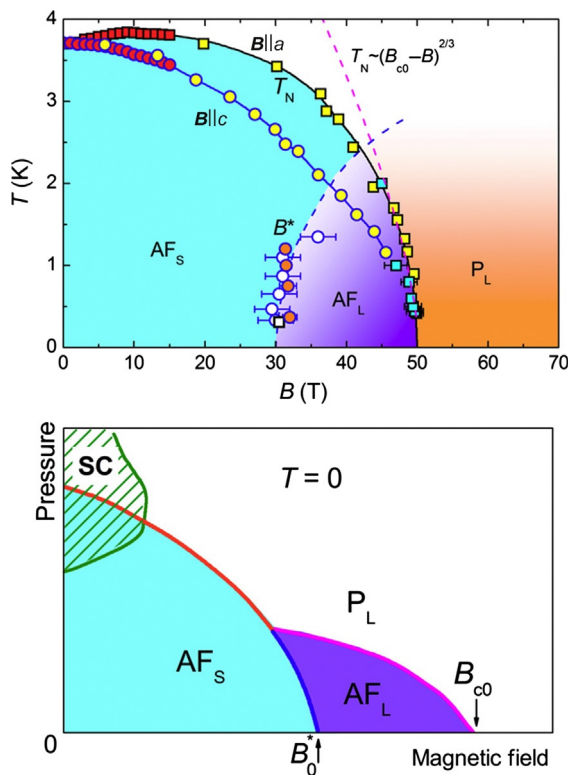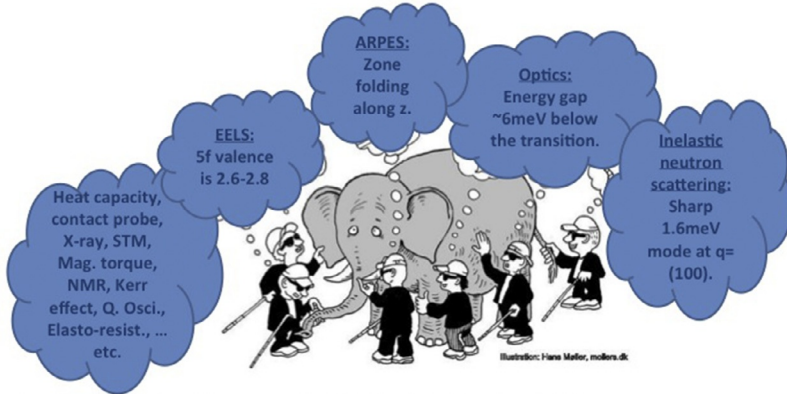
FIG. 18 High field phase diagrams for CeRhIn$_5$. *Upper panel*: Temperature vs field phase diagram down to 0.5 K and up to 50 T, illustrating the change from a small Fermi surface in AFM$_S$ to large Fermi surface in AFM$_L$. P_L represents a large Fermi surface paramagnet. *Lower panel*: Proposed pressure vs field phase diagram at $T = 0$. Note the coexistence of superconductivity (SC) and antiferromagnetism (AFM). *According to Jiao, L., Chen, Y., Kohama, Y., Graf, D., Bauer, E.D., Singleton, J., Zhu, J.X., Weng, Z., Pang, G., Shang, T., et al., 2015. Fermi surface reconstruction and multiple quantum phase transitions in the antiferromagnet CeRhIn$_5$. Proc. Natl. Acad. Sci. 112 (3), 673-678.*

is well-known as the hidden order (HO) material which shows a mysterious CPT at 17.5 K. The origin of this transition is neither magnetic nor structural and still persists after 30 years as unclarified, thus its designation as HO. Only within the HO phase does unconventional SC exists below $T_c = 1.5$ K. Much has been published, both experimentally and theoretically, in relation to the HO state and its formation (Mydosh and Oppeneer, 2011, 2014).

From an experimental point of view, the HO has stimulated the developments of novel methods to detect its origin. In Fig. 19, we show an "elephant" cartoon of these many techniques utilized to characterize the HO. There has been significant progress in developing exotic evaluations of the HO beyond the bulk studies. For the first time, ARPES, STM/STS,

The story of an elephant

ARPES:
Zone
folding
along z.

Optics:
Energy gap
~6meV below
the transition.

EELS:
5f valence
is 2.6-2.8

Inelastic
neutron
scattering:
Sharp
1.6meV
mode at q=
(100).

Heat capacity,
contact probe,
X-ray, STM,
Mag. torque,
NMR, Kerr
effect, Q. Osci.,
Elasto-resist., ...
etc.

Illustration: Hans Møller, mollers.dk

Reviews: Mydosh and Oppeneer *RMP* **83** (2011); *Philos. Mag.* (2014);
Palstra et al. *PRL* **55** (1985); Schlabitz et al. *Z. Phys. B* **62** (1986); Maple et al. *PRL* **56** (1986);
Cooper et al. *PRB* **36** (1987); Bonn et al. *PRL* **61** (1988); Broholm et al. *PRB* **43** (1991);
Jeffries et al. *PRB* **82** (2010); Schmidt et al. *Nature* **465** (2010); Hall et al. *PRB* **86** (2012);
Guo et al. *PRB* **85** (2012); Meng et al. *PRL* **111** (2013); Bareille et al. *Nat. Commun.* **5** (2014)

FIG. 19 Overview cartoon illustrating the many experiments and references on the blind man's elephant searching for the meaning of hidden order in URu_2Si_2. *According to Kung, unpublished.*

magnetic torque, Raman, polar Kerr, cyclotron resonance, elastoresistivity, and core-level spectroscopy have been applied to a heavy fermion system. Furthermore, theorists have proposed more than 30 different models and interpretations to describe the HO. High-ranking multipole orders are a favorite interpretation (Kung et al., 2015; Mydosh and Oppeneer, 2014).

Pressure, magnetic field, and doping have been employed to tune the HO and SC toward quantum criticality. In Fig. 20, we show the 3D phase diagram as a function of T, H, and P, omitting the many different dopings or substitutions that require a 4th dimension. The disordering of the delicate HO state via doping causes a slow crossover to magnetism and HFL behavior. Hence the "puddling" of these inhomogeneous states precludes the formation of continuous and well-defined QCP. Pressure creates a first-order transition toward a long-range antiferromagnetic phase, which has been studied with quantum oscillations and neutron scattering (Hassinger et al., 2010; Villaume et al., 2008). Here, the Fermi surface remains constant with the transition from HO to AFM. Perhaps with negative pressure, we could search for QPT's (Pfleiderer et al., 2006). Therefore, the remaining tuning parameter is magnetic field H along c-axis. Fig. 21 illustrates the high-field tuning of URu_2Si_2 requiring 40 T to complete, a great experimental challenge (Harrison et al., 2003). During the past 25 years, a variety of exotic high field techniques have been developed to study the novel phases originating between 33 and 38 T. Is the destruction of HO at 32 T a QCP? The answer is no, because of its
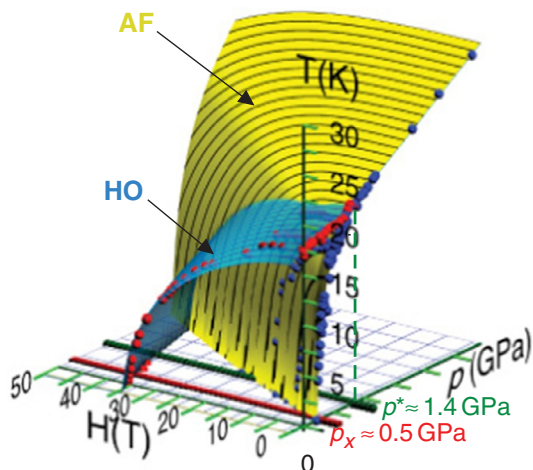
FIG. 20 3D phase diagram of URu_2Si_2 illustrating the different phases (HO, AFM, SC, and HLF) and the possibilities for tuning toward a QCP. Note that the 4th dimension of doping has been omitted. *According to Bourdarot, F., Martin, N., Raymond, S., Regnault, L.P., Aoki, D., Taufour, V., Flouquet, J., 2011. Magnetic properties of URu_2Si_2 under uniaxial stress by neutron scattering. Phys. Rev. B 84 (18), 184430.*
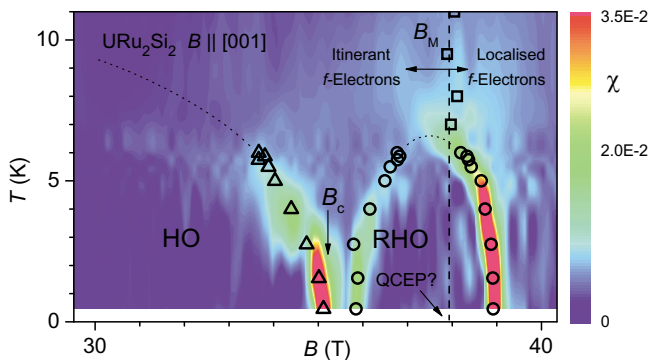

FIG. 21 High magnetic-field phase diagram for URu_2Si_2 showing the destruction of HO and the creation of a then unknown Phase III. Above the dome of III there is a metamagnetic effect in the susceptibility that disappears once the dome is formed. Note the first order transition at the base of the HO and the dome. We now know phase III dome represents a long-range order ferrimagnetic structure. *According to Harrison, N., Jaime, M., Mydosh, J.A., 2003. Reentrant hidden order at a metamagnetic quantum critical end point. Phys. Rev. Lett. 90 (9), 096402.*

first-order nature. Then there is a dome called "Phase III" whose top is second order, but end points first order. An early proposal was an hidden QCP, a metamagnetic end point, extrapolated under the dome to $T=0$—see Fig. 21. Most recently Bragg neutron scattering has been performed in fields up to 40 T, and thus a local magnetic order clarification of Phase III became available. The result is that Phase III is a long-range AFM state, thereby removing the necessity for a quantum critical endpoint (Knafo, 2015). A way of reducing the fields needed for Phase III is to dope Ru sites with a small amount (4%) of Rh (Kuwahara et al., 2013). This leads to a complete destruction of the HO, yet Phase III remains intact. Magnetic Bragg-peaks confirmed the AFM as now found for pure URu_2Si_2 (Kuwahara et al., 2013).

Therefore, with Phase III fully established as long-range AFM, there seems to be no QPT in URu_2Si_2.

5 QUANTUM CRITICALITY BEYOND RARE EARTHS AND ACTINIDES

The concept of quantum criticality extends beyond the rare earth and actinide materials discussed in the previous sections. We wish to provide, for the interested reader, a brief list of other putative QCP's. Much of the proposed quantum critical behavior is spin based, and occurs in magnetic transition metal compounds.

- There has long been the claim of a QCP in the high temperature cuprate superconductors, beneath the superconducting dome. From the theoretical prospective, see Sachdev (2003) and the experimental works of Valla et al. (1999) and Broun (2008). A very recent review of putative QCP's in the copper oxides is by Keimer et al. (2015). Also the more recently discovered pnictides (Fe-based compounds) have been reviewed by Shibauchi et al. (2014) with again evidence for a QCP lying beneath the superconducting dome.
- Bose–Einstein condensation of magnons in quantum magnets offers another route toward QCP via magnetic field tuning. It has been suggested in mainly oxide compounds with $3d$ transition metals, and has been studied intensively during the last twenty or so years with a complete review by Zapf et al. (2014). Here, there is clear evidence, both theoretically and experimentally, of QPTs with surprising behavior at the QCP.
- Low-dimensional spin insulators, ie, Ising and Heisenberg chains and ladders, are tunable with a magnetic field toward a QPT. In this regime, there is a wide variety of quantum behavior, from Luttinger liquids to dimensional crossovers. Accordingly, there are the 1D topics of perturbations of the lattice, various magnetic couplings, Ising or Heisenberg class, spin gaps for integer ($S=1$) and half-integer ($S=1/2$) spins, and different prototypes of QCP's. Complete reviews of 1D quantum magnetism are by Giamarchi (2004) and Mikeska and Kolezhuk (2004). A more recent brief overview of quasi-one-dimensional systems is by Giamarchi (2010).

- Quantum spin liquids are usually created with frustration and can occur without a QPT but they can also be tuned toward a QCP. The spin liquids represent a most unconventional state of matter that are being sought in real systems. For a highly frustrated metallic spin liquid, eg, $Pr_2Ir_2O_7$, a QCP has been proposed from quantum critical scaling of the Grüuneisen ratio Tokiwa et al. (2014). Strong spin–orbit interactions in competition with the magnetic exchange energy form a new tuning parameter. A recent review of the spin liquids is by Balents (2010).
- Metallic $Sr_3Ru_2O_7$ possesses a field-tuned dome-like phase around $H \approx 8$ T. By scanning the field a QCP can be created in two distinct ways: via a metamagnetic transition into the dome extrapolated to $T = 0$; or at the edges of the dome along the $T = 0$ abscissa where there are two putative QCP's denoting the left and right sides of the dome. Very recently a field-tunable antiferromagnetic SDW has been observed in the dome phase (Lester et al., 2015). This would exclude the extrapolated "metamagnetic" QCP and emphasize the dome end points as QCP's.
- Itinerant nearly ferromagnets compounds, eg, $ZrZn_2$ and MnSi can be driven with pressure to a disordered state. However, the putative QCP is of first order. Thus, such transitions do not represent the continuous QPT we studied in this chapter. Only a year ago a new itinerant compound YFe_2Al_{10} (Wu et al., 2014) was proposed to show a continuous QPT without any tuning. This material does not magnetically order down to 0.1 K and an array of bulk measurement and scaling relations at low temperatures offer evidence that YFe_2Al_{10} is special example of a 2D compound where, due to quantum critical fluctuations, its ferromagnetic order is reduced to nearly 0 K. Additional experiments at yet lower temperatures and tuning, for example, (negative) pressure and doping are required to generate the putative ferromagnetic transition at finite temperatures.

We have thus far listed only magnetic or spin-based QPTs. There are also numerous nonmagnetic QPTs, which include the following.

- Quantum ferroelectrics, such as $SrTiO_3$ and $KTaO_3$, exhibit a lattice transition with a ferro-aligned spontaneous electric polarization, **P**. The quantum tuning parameter is the ratio of the a/c lattice constants divided by the Debye wavevector, Λ^2. A recent review of this ferroelectric behavior and more analysis is given by Rowley et al. (2014).
- Conductor–insulator QPTs have been treated for a variety of materials including metal-insulator transitions (MIT) in different dimensions, Anderson localization, superconducting-insulator transitions, etc., by Dobrosavljevic et al. (2012). This is a rather old field of study that has recently been considered from the modern QPT/QCP viewpoint.
- Quantum dots are nanocrystals made of semiconductor materials that are small enough to exhibit quantum mechanical behavior. When formed in

various sizes they emit different colors of light. Now the practical applications are apparent, eg, solar cells, lighting, and TV (LCD) display technologies. Due to nanostructuring lithography, tiny area devices may be formed of a two-dimensional electron gas (2DEG) tuned with superimposed gates and nearby contacts that mimic the bulk Kondo effect. Here, it is required to place an odd number of electrons bearing spin on the dot. For sufficiently small dots, a single electron (spin 1⁄41/2) will generate the Kondo resonance behavior (Rau et al., 2010 and Amasha et al., 2013).

- In ultra-cold gases all thermal fluctuations are frozen out, only remaining are the quantum fluctuations and thus the possibility of QPT/QCP. For example, a QPT has been observed from a superfluid to a Mott insulator (Greiner et al., 2002). While limited in experimental observational techniques, the detectable spatial resolution from a "spread out" coherent gas to localized gas of atoms at each lattice site characterizes the transition. The tuning parameter is the depth of the lattice potential. A review of such many-body cold-gas physics is given by Bloch et al. (2008).

- Two-dimensional superconducting Josephson-junction arrays form a model system with which to study quantum dynamics and QPT. Basically there are two competing energy scales: the Josephson energy associated with the coupling of Cooper pairs between the superconducting islands; and the charging energy necessary to add an extra electron to a neutral island. By tuning these combinations one can generate a superconductor to insulator QPT, along with associated vortex dynamics (Fazio and Van Der Zant, 2001). A magnetic field or disorder can also be used to tune the Josephson array to a QCP. Presently graphene is being overlaid over superconducting discs and gate tuned to reach the QCP (Han et al., 2014).

6 SUMMARY AND CONCLUSIONS

In this chapter, we have introduced quantum criticality and its manifestations of phase transitions in rare earth compounds. These $T = 0$ K phase transitions are created by quantum fluctuations that can be tuned by pressure, doping or disorder, frustration, and magnetic field. The effects of the change of phase reveal themselves at finite temperatures in the basic experimental properties of specific heat, resistivity and magnetic susceptibility. We have summarized the theoretical background and synopsized the latest controversial developments. Rather than focusing on the many materials that are claimed to exhibit QPTs at a QCP, we discuss a few well-studied examples with critique of the experimental shortcomings. Some illustrations of quantum criticality beyond the rare earths are offered in the final section.

Generically speaking there are certain limitations with all the possible tuning methods. However, the disorder or doping randomness as a tuning

parameter creates special difficulties. After all, disorder can fundamentally disturb the basic properties of the material to be tuned. This is particularly true for strongly correlated electron systems. Examples of such are crystal and band-structure changes, the formation of inhomogeneous and nonrandom clusters, unwelcome magnetic behavior, a metal-to-insulator transition, etc. Hence disorder tuning is a delicate procedure and must be carefully controlled via metallurgical and chemical analyses. Although disorder can create NFL behavior, the latter can be taken incorrectly as an indication of a QCP. The prime example here is the $Y_{1-x}U_xPd_3$ pseudobinary alloy, an original NFL without a well-defined ground-state or a QPT (Seaman et al., 1991). Furthermore, magnetic disorder can give rise to a low-temperature SG phase (Mydosh, 2015). This can easily mask the putative QPT by smearing out the QCP into a region of glassy dynamics.

Such effects then pose the question of a percolation transition (Stauffer and Aharony, 1994) caused by lattice or magnetic disorder creating a QPT. Percolation occurs intrinsically from massive disorder and randomness. At the critical percolation concentration, a phase transition occurs at zero temperature, does this percolation transition represent a QPT and is the critical concentration a QCP? At the present stage of experimental investigation, the percolation behavior does not clearly correspond to a QPT, eg, the case of $Pd_{1-x}Ni_x$ (Kalvius et al., 2014). And such a result illustrates the stringent challenge of doping disorder as a tuning parameter for a QPT.

The theoretical situation, on the other hand, is at present confused, even for "clean" transitions tuned by magnetic field or pressure. Sure, there exists the HM theory of itinerant electrons that provides satisfactory answers for a large group of materials, such as $CeNi_2Ge_2$. However, many compounds display clear characteristics that deviate from HM theory, for which only phenomenological theories can currently provide insights. Microscopically, a fundamental unanswered question is the Kondo lattice problem, as well as the theory of quantum critical fluctuations interacting where the electrons cannot be integrated out. Answers to those purely theoretical questions are needed before one can even start to understand specific materials. Luckily, this makes the field of quantum criticality in heavy fermion materials one of the most active and entertaining areas of condensed matter physics.

ACKNOWLEDGMENTS

ABBREVIATIONS

AFM	antiferromagnetism
ARPES	angle-resolved photoemission spectroscopy
CPT	continuous phase transition
DMFT	dynamical mean field theory
FL	Fermi liquid
HFL	heavy Fermi liquid
HM	Hertz–Millis theory
HO	hidden order
NFL	non-Fermi liquid
NMR	nuclear magnetic resonance
RKKY	Ruderman–Kittel–Kasuya–Yosida
SC	superconductivity
SDW	spin-density wave
SG	spin glass
STM	scanning tunneling microscopy
STS	scanning tunneling spectroscopy
QCP	quantum critical point
QPT	quantum phase transition

REFERENCES

Abanov, A., Chubukov, A.V., 2000. Spin-fermion model near the quantum critical point: one-loop renormalization group results. Phys. Rev. Lett. 84 (24), 5608–5611.

Abanov, A., Chubukov, A.V., 2004. Anomalous scaling at the quantum critical point in itinerant antiferromagnets. Phys. Rev. Lett. 93 (25), 255702–255704.

Abrahams, E., Wölfle, P., 2012. Critical quasiparticle theory applied to heavy fermion metals near an antiferromagnetic quantum phase transition. Proc. Natl. Acad. Sci. 109 (9), 3238–3242.

Abrahams, E., Schmalian, J., Wölfle, P., 2014. Strong-coupling theory of heavy-fermion critical-ity. Phys. Rev. B 90 (4), 045105–045109.

Amasha, S., Keller, A.J., Rau, I.G., Carmi, A., Katine, J.A., Shtrikman, H., Oreg, Y., Goldhaber-Gordon, D., 2013. Pseudospin-resolved transport spectroscopy of the kondo effect in a double quantum dot. Phys. Rev. Lett. 110 (4), 046604.

Ancona-Torres, C., Silevitch, D.M., Aeppli, G., Rosenbaum, T.F., 2008. Quantum and classical glass transitions in $LiHo_xY_{1-x}F_4$. Phys. Rev. Lett. 101 (5), 057201.

Anderson, P.W., 1970. A poor man's derivation of scaling laws for the Kondo problem. J. Phys. C: Sol. State Phys. 3 (1), 2436–2441.

Balents, L., 2010. Spin liquids in frustrated magnets. Nature 464 (7286), 199–208.

Bao, W., Pagliuso, P.G., Sarrao, J.L., Thompson, J.D., Fisk, Z., Lynn, J.W., Erwin, R.W., 2000. Incommensurate magnetic structure of $CeRhIn_5$. Phys. Rev. B 62 (22), R14621.

Bianchi, A., Movshovich, R., Vekhter, I., Pagliuso, P.G., Sarrao, J.L., 2003. Avoided antiferro-magnetic order and quantum critical point in $CeCoIn_5$. Phys. Rev. Lett. 91 (25), 257001.

Bitko, D., Rosenbaum, T.F., Aeppli, G., 1996. Quantum critical behavior for a model magnet. Phys. Rev. Lett. 77 (5), 940.

Bloch, I., Dalibard, J., Zwerger, W., 2008. Many-body physics with ultracold gases. Rev. Mod. Phys. 80 (3), 885.

Broun, D.M., 2008. What lies beneath the dome? Nat. Phys. 4 (3), 170–172.

Burdin, S., Georges, A., Grempel, D.R., 2000. Coherence scale of the Kondo lattice. Phys. Rev. Lett. 85 (5), 1048–1051.

Coldea, R., Tennant, D.A., Wheeler, E.M., Wawrzynska, E., 2010. Quantum criticality in an Ising chain: experimental evidence for emergent E8 symmetry. Science 327, 177.

Coleman, P., 1999. Theories of non-Fermi liquid behavior in heavy fermions. Phys. B Condens. Matter 259-61, 353–358.

Coleman, P., 2001. Condensed-matter physics–magnetic spins that last for ever. Nature 413 (6858), 788–789.

Coleman, P., 2015. Heavy fermions and the Kondo Lattice: a 21st century perspective. ArXiv.org, 1509.05769, 1509.05769v1.

Coleman, P., Schofield, A.J., 2005. Quantum criticality. Nature 433 (7023), 226–229.

Coleman, P., Pepin, C., Si, Q., Ramazashvili, R., 2001. How do Fermi liquids get heavy and die? J. Phys. Condens. Matter 13 (35), R723–R738.

Custers, J., Gegenwart, P., Wilhelm, H., Neumaier, K., Tokiwa, Y., Trovarelli, O., Geibel, C., Steglich, F., Pépin, C., Coleman, P., 2003. The break-up of heavy electrons at a quantum critical point. Nature 424 (6948), 524–527.

Dobrosavljevic, V., Trivedi, N., Valles Jr., J.M., 2012. Conductor Insulator Quantum Phase Transitions. Oxford University Press, Oxford, United Kingdom.

Domb, C., Lebowitz, J.L., 2001. Phase Transitions and Critical Phenomena. Academic Press, San Diego, CA, USA.

Doniach, S., 1977. The Kondo lattice and weak antiferromagnetism. Phys. B & C 91, 231–234.

Fazio, R., Van Der Zant, H., 2001. Quantum phase transitions and vortex dynamics in superconducting networks. Phys. Rep. 355 (4), 235–334.

Gegenwart, P., Kromer, F., Lang, M., Sparn, G., Geibel, C., 1999. Non-Fermi-liquid effects at ambient pressure in a stoichiometric heavy-fermion compound with very low disorder: $CeNi_2Ge_2$. Phys. Rev. 82 (6), 1293–1296.

Gegenwart, P., Si, Q., Steglich, F., 2008. Quantum criticality in heavy-fermion metals. Nat. Phys. 4 (3), 186–197.

Georges, A., Kotliar, G., Krauth, W., Rozenberg, M.J., 1996. Dynamical mean-field theory of strongly correlated fermion systems and the limit of infinite dimensions. Rev. Mod. Phys. 68 (1), 13–125.

Giamarchi, T., 2004. Quantum Physics in One Dimension. Oxford University Press, Oxford, UK.

Giamarchi, T., 2010. Quantum phase transitions in Quasi-one-dimensional systems. In: Carr, L.D. (Ed.), Understanding Quantum Phase Transitions. CRC Press, Boca Raton, FL, USA.

Goldenfeld, N., 1992. Lectures on Phase Transitions and the Renormalization Group. Addison-Wesley, Advanced Book Program, Reading, MA.

Greiner, M., Mandel, O., Esslinger, T., Hänsch, T.W., Bloch, I., 2002. Quantum phase transition from a superfluid to a Mott insulator in a gas of ultracold atoms. Nature 415 (6867), 39–44.

Grosche, F.M., Agarwal, P., Julian, S.R., Wilson, N.J., Haselwimmer, R.K.W., Lister, S.J.S., Mathur, N.D., Carter, F.V., Saxena, S.S., Lonzarich, G.G., 2000. Anomalous low temperature states in $CeNi_2Ge_2$ and $CePd_2Si_2$. J. Phys. Condens. Matter 12 (32), L533–L540.

Han, Z., Allain, A., Arjmandi-Tash, H., Tikhonov, K., Feigel'Man, M., Sacépé, B., Bouchiat, V., 2014. Collapse of superconductivity in a hybrid tin-graphene Josephson junction array. Nat. Phys. 10 (5), 380–386.

Harrison, N., Jaime, M., Mydosh, J.A., 2003. Reentrant hidden order at a metamagnetic quantum critical end point. Phys. Rev. Lett. 90 (9), 096402.

Hartmann, S., Oeschler, N., Krellner, C., Geibel, C., Paschen, S., Steglich, F., 2010. Thermopower evidence for an abrupt Fermi surface change at the quantum critical point of $YbRh_2Si_2$. Phys. Rev. Lett. 104 (9), 096401.

Hassinger, E., Knebel, G., Matsuda, T.D., Aoki, D., Taufour, V., Flouquet, J., 2010. Similarity of the Fermi surface in the hidden order state and in the antiferromagnetic state of URu_2Si_2. Phys. Rev. Lett. 105 (21), 216409.

Hegger, H., Petrovic, C., Moshopoulou, E.G., Hundley, M.F., Sarrao, J.L., Fisk, Z., Thompson, J.D., 2000. Pressure-induced superconductivity in quasi-2D $CeRhIn_5$. Phys. Rev. Lett. 84 (21), 4986.

Herbut, I., 2010. A Modern Approach to Critical Phenomena. Cambridge University Press, Cambridge, UK.

Hertz, J.A., 1976. Quantum critical phenomena. Phys. Rev. B 14 (3), 1165–1184.

Heuser, K., Scheidt, E.W., Schreiner, T., Stewart, G.R., 1998. Inducement of non-Fermi-liquid behavior with a magnetic field. Phys. Rev. B 57 (8), R4198.

Hewson, A.C., 1993. The Kondo Problem to Heavy Fermions. Cambridge University Press, Cambridge, UK.

Hlubina, R., Rice, T.M., 1995. Resistivity as a function of temperature for models with hot-spots on the Fermi-surface. Phys. Rev. B 51 (14), 9253–9260.

Jiao, L., Chen, Y., Kohama, Y., Graf, D., Bauer, E.D., Singleton, J., Zhu, J.X., Weng, Z., Pang, G., Shang, T., et al., 2015. Fermi surface reconstruction and multiple quantum phase transitions in the antiferromagnet $CeRhIn_5$. Proc. Natl. Acad. Sci. 112 (3), 673–678.

Jönsson, P.E., Mathieu, R., Wernsdorfer, W., Tkachuk, A.M., Barbara, B., 2007. Absence of conventional spin-glass transition in the Ising dipolar system $LiHo_xY_{1-x}F_4$. Phys. Rev. Lett. 98 (25), 256403.

Kalvius, G.M., Hartmann, O., Wäppling, R., Günther, A., Krimmel, A., Loidl, A., MacLaughlin, D.E., Bernal, O.O., Nieuwenhuys, G.J., Aronson, M.C., et al., 2014. Magnetism of $Pd_{1-x}Ni_x$ alloys near the critical concentration for ferromagnetism. Phys. Rev. B 89 (6), 064418.

Kambe, S., Sakai, H., Tokunaga, Y., Lapertot, G., Matsuda, T.D., Knebel, G., Flouquet, J., Walstedt, R.E., 2014. Degenerate Fermi and non-Fermi liquids near a quantum critical phase transition. Nat. Phys. 10 (11), 840–844.

Kasuya, T., 1956. A theory of metallic ferro- and antiferromagnetism on Zener's model. Prog. Theor. Phys. 16, 45.

Keimer, B., Kivelson, S.A., Norman, M.R., Uchida, S., Zaanen, J., 2015. From quantum matter to high-temperature superconductivity in copper oxides. Nature 518 (7538), 179–186.

Knafo, W., 2015. Private communications.

Knebel, G., Aoki, D., Braithwaite, D., Salce, B., Flouquet, J., 2006. Coexistence of antiferromagnetism and superconductivity in $CeRhIn_5$ under high pressure and magnetic field. Phys. Rev. B 74 (2), 020501.

Kondo, J., 1964. Resistance minimum in dilute magnetic alloys. Prog. Theor. Phys. 32 (1), 37–49.

Kopeć, T.K., 1997. Nonlinear response in quantum spin glasses. Phys. Rev. Lett. 79 (21), 4266.

Kornblit, A., Ahlers, G., 1975. Heat capacity of EuO near the Curie temperature. Phys. Rev. B 11 (7), 2678–2688.

Küchler, R., Oeschler, N., Gegenwart, P., Cichorek, T., Neumaier, K., Tegus, O., Geibel, C., Mydosh, J.A., Steglich, F., Zhu, L., Si, Q., 2003. Divergence of the Grüneisen ratio at quantum critical points in heavy fermion metals. Phys. Rev. Lett. 91 (6), 066405–66414.

Küchler, R., Gegenwart, P., Heuser, K., Scheidt, E.W., Stewart, G.R., Steglich, F., 2004. Grüneisen ratio divergence at the quantum critical point in $CeCu_{6-x}Ag_x$. Phys. Rev. Lett. 93 (9), 096402.

Kummer, K., Patil, S., Chikina, A., Güttler, M., Höppner, M., Generalov, A., Danzenbächer, S., Seiro, S., Hannaske, A., Krellner, C., Kucherenko, Y., Shi, M., Radovic, M., Rienks, E., Zwicknagl, G., Matho, K., Allen, J.W., Laubschat, C., Geibel, C., Vyalikh, D.V., 2015. Temperature-independent Fermi surface in the Kondo lattice $YbRh_2Si_2$. Phys. Rev. X 5 (1), 011028–011029.

Kung, H.H., Baumbach, R.E., Bauer, E.D., Thorsmølle, V.K., Zhang, W.L., Haule, K., Mydosh, J.A., Blumberg, G., 2015. Chirality density wave of the "hidden order" phase in URu_2Si_2. Science 347 (6228), 1339–1342.

Kuwahara, K., Yoshii, S., Nojiri, H., Aoki, D., Knafo, W., Duc, F., Fabrèges, X., Scheerer, G.W., Frings, P., Rikken, G.L.J.A., et al., 2013. Magnetic structure of phase II in $U(Ru_{0.96}Rh_{0.04})_2Si_2$ determined by neutron diffraction under pulsed high magnetic fields. Phys. Rev. Lett. 110 (21), 216406.

Lee, S.S., 2009. Low-energy effective theory of Fermi surface coupled with U(1) gauge field in 2+1dimensions. Phys. Rev. B 80 (16), 165102–165113.

Lee, S., Kaul, R.K., Balents, L., 2010. Interplay of quantum criticality and geometric frustration in columbite. Nat. Phys. 6 (9), 702–706.

Lester, C., Ramos, S., Perry, R.S., Croft, T.P., Bewley, R.I., Guidi, T., Manuel, P., Khalyavin, D.D., Forgan, E.M., Hayden, S.M., 2015. Field-tunable spin-density-wave phases in $Sr_3Ru_2O_7$. Nat. Mater. 14 (4), 373–378.

Ma, S.K., 1976. Modern Theory of Critical Phenomena. Benjamin, Reading, MA, USA.

Mathur, N.D., Grosche, F.M., Julian, S.R., Walker, I.R., 1998. Magnetically mediated superconductivity in heavy fermion compounds. Nature 394 (6688), 39–43.

Mennenga, G., de Jongh, L.J., Huiskamp, W.J., 1984. Field dependent specific heat study of the dipolar Ising ferromagnet $LiHoF_4$. J. Magn. Magn. Mater. 44 (1), 59–76.

Metlitski, M.A., Sachdev, S., 2010. Quantum phase transitions of metals in two spatial dimensions. II. Spin density wave order. Phys. Rev. B 82 (7), 075128.

Metlitski, M.A., Mross, D.F., Sachdev, S., Senthil, T., 2015. Cooper pairing in non-Fermi liquids. Phys. Rev. B 91 (11), 115111–115118.

Mikeska, H., Kolezhuk, A., 2004. One-dimensional magnetism. In: Schollwöck, U., Richter, J., Farnell, D.J., Bishop, R.F. (Eds.), Quantum Magnetism. Springer, Berlin, Germany.

Millis, A.J., 1993. Effect of a Nonzero temperature on quantum critical-points in itinerant fermion systems. Phys. Rev. B 48 (10), 7183–7196.

Miyake, K., Schmitt-Rink, S., Varma, C.M., 1986. Spin-fluctuation-mediated even-parity pairing in heavy-fermion superconductors. Phys. Rev. B 34 (9), 6554–6556.

Moriya, T., 1985. Spin Fluctuations in Itinerant Electron Magnetism. Springer-Verlag, Berlin.

Moriya, T., Takimoto, T., 1995. Anomalous properties around magnetic instability in heavy-electron systems. J. Phys. Soc. Jpn. 64 (3), 960–969.

Movshovich, R., Jaime, M., Thompson, J.D., Petrovic, C., Fisk, Z., Pagliuso, P.G., Sarrao, J.L., 2001. Unconventional superconductivity in $CeIrIn_5$ and $CeCoIn_5$: specific heat and thermal conductivity studies. Phys. Rev. Lett. 86 (22), 5152.

Mydosh, J.A., 2015. Spin glasses: redux: an updated experimental/materials survey. Rep. Prog. Phys. 78 (5), 052501.

Mydosh, J.A., Oppeneer, P.M., 2011. Colloquium: hidden order, superconductivity, and magnetism: the unsolved case of URu_2Si_2. Rev. Mod. Phys. 83 (4), 1301.

Mydosh, J.A., Oppeneer, P.M., 2014. Hidden order behaviour in URu_2Si_2 (a critical review of the status of hidden order in 2014). Phil. Mag. 94 (32-33), 3642–3662.

Nishimori, H., Ortiz, G., 2010. Elements of Phase Transitions and Critical Phenomena. OUP, Oxford.

Oeschler, N., Hartmann, S., Pikul, A.P., Krellner, C., Geibel, C., Steglich, F., 2008. Low-temperature specific heat of $YbRh_2Si_2$. Phys. B Condens. Matter 403 (5), 1254–1256.

Oshikawa, M., 2000. Topological approach to Luttinger's theorem and the Fermi surface of a Kondo lattice. Phys. Rev. Lett. 84 (15), 3370–3373.

Paglione, J., Tanatar, M.A., Hawthorn, D.G., Boaknin, E., Hill, R.W., Ronning, F., Sutherland, M., Taillefer, L., Petrovic, C., Canfield, P.C., 2003. Field-induced quantum critical point in $CeCoIn_5$. Phys. Rev. Lett. 91 (24), 246405.

Pankov, S., Florens, S., Georges, A., Kotliar, G., Sachdev, S., 2004. Non-Fermi-liquid behavior from two-dimensional antiferromagnetic fluctuations: a renormalization-group and large-N analysis. Phys. Rev. B 69 (5), 054426–54512.

Park, T., Ronning, F., Yuan, H.Q., Salamon, M.B., Movshovich, R., Sarrao, J.L., Thompson, J.D., 2006. Hidden magnetism and quantum criticality in the heavy fermion superconductor $CeRhIn_5$. Nature 440 (7080), 65–68.

Paschen, S., Lühmann, T., Wirth, S., Gegenwart, P., Trovarelli, O., Geibel, C., Steglich, F., Coleman, P., Si, Q., 2004. Hall-effect evolution across a heavy-fermion quantum critical point. Nature 432 (7019), 881–885.

Paschen, S., Friedemann, S., Wirth, S., Steglich, F., Kirchner, S., Si, Q., 2015. Kondo destruction in heavy fermion quantum criticality and the photoemission spectrum of $YbRh_2Si_2$. ArXiv. org, cond-mat/1507.06088v1, 1507.06088v1.

Petrovic, C., Movshovich, R., Jaime, M., Pagliuso, P.G., Hundley, M.F., Sarrao, J.L., Fisk, Z., Thompson, J.D., 2001. A new heavy-fermion superconductor $CeIrIn_5$: a relative of the cuprates? Europhys. Lett. 53 (3), 354.

Petrovic, C., Pagliuso, P.G., Hundley, M.F., Movshovich, R., Sarrao, J.L., Thompson, J.D., Fisk, Z., et al., 2001. Heavy-fermion superconductivity in $CeCoIn_5$ at 2.3 K. J. Phys. Condens. Matter 13, L337.

Pfleiderer, C., 2009. Superconducting phases of f-electron compounds. Rev. Mod. Phys. 81 (4), 1551–1624.

Pfleiderer, C., Mydosh, J.A., Vojta, M., 2006. Pressure dependence of the magnetization of URu_2Si_2. Phys. Rev. B 74 (10), 104412.

Pham, L.D., Park, T., Maquilon, S., Thompson, J.D., Fisk, Z., 2006. Reversible tuning of the heavy-fermion ground state in $CeCoIn_5$. Phys. Rev. Lett. 97 (5), 056404.

Quilliam, J.A., Meng, S., Kycia, J.B., et al., 2012. Experimental phase diagram and dynamics of a dilute dipolar-coupled ising system. Phys. Rev. B 85 (18), 184415.

Rau, I., Amasha, S., Oreg, Y., Goldhaber-Gordon, D., 2010. Quantum phase transitions in quantum dots. In: Carr, L.D. (Ed.), Understanding Quantum Phase Transitions. CRC Press, Boca Raton, FL, USA.

Read, N., Sachdev, S., Ye, J., 1995. Landau theory of quantum spin glasses of rotors and Ising spins. Phys. Rev. B 52 (1), 384.

Reich, D.H., Rosenbaum, T.F., Aeppli, G., Guggenheim, H.J., 1986. Ferromagnetism, glassiness, and metastability in a dilute dipolar-coupled magnet. Phys. Rev. B 34 (7), 4956.

Rodriguez, J., Aczel, A.A., Carlo, J.P., Dunsiger, S.R., Macdougall, G.J., Russo, P.L., Savici, A.T., Uemura, Y.J., Wiebe, C.R., Luke, G.M., 2010. Study of the ground state properties of $LiHo_xY_{1-x}F_4$ using muon spin relaxation. Phys. Rev. Lett. 105 (10), 107203.

Rønnow, H.M., Parthasarathy, R., Jensen, J., Aeppli, G., Rosenbaum, T.F., McMorrow, D.F., 2005. Quantum phase transition of a magnet in a spin bath. Science 308 (5720), 389–392.

Rønnow, H.M., Jensen, J., Parthasarathy, R., Aeppli, G., Rosenbaum, T.F., McMorrow, D.F., Kraemer, C., 2007. Magnetic excitations near the quantum phase transition in the Ising ferromagnet LiHoF$_4$. Phys. Rev. B 75 (5), 054426.

Rosch, A., 1999. Interplay of disorder and spin fluctuations in the resistivity near a quantum critical point. Phys. Rev. Lett. 82 (21), 4280–4283.

Rosch, A., 2000. Magnetotransport in nearly antiferromagnetic metals. Phys. Rev. B 62 (8), 4945–4962.

Rosch, A., Schroder, A., Stockert, O., von Löhneysen, H., 1997. Mechanism for the non-Fermi-liquid behavior in CeCu$_{6-x}$Au$_x$. Phys. Rev. Lett. 79 (1), 159–162.

Rowley, S.E., Spalek, L.J., Smith, R.P., Dean, M.P.M., Itoh, M., Scott, J.F., Lonzarich, G.G., Saxena, S.S., 2014. Ferroelectric quantum criticality. Nat. Phys. 10 (5), 367–372.

Ruderman, M.A., Kittel, C., 1954. Indirect exchange coupling of nuclear magnetic moments by conduction electrons. Phys. Rev. 96 (1), 99–102.

Sachdev, S., 2003. Colloquium: order and quantum phase transitions in the cuprate superconductors. Rev. Mod. Phys. 75 (3), 913.

Sachdev, S., 2008. Quantum magnetism and criticality. Nat. Phys. 4 (3), 173–185.

Sachdev, S., 2011. Quantum Phase Transitions. Cambridge University Press, Cambridge, UK.

Scalapino, D.J., Loh Jr., E., Hirsch, J.E., 1986. d-wave pairing near a spin-density-wave instability. Phys. Rev. B 34 (11), 8190–8192.

Schechter, M., 2008. LiHo$_x$Y$_{1-x}$F$_4$ as a random-field Ising ferromagnet. Phys. Rev. B 77 (2), 020401.

Schröder, A., Lynn, J.W., Erwin, R.W., Loewenhaupt, M., von Löhneysen, H., 1994. Magnetic structure of the heavy fermion alloy CeCu$_{5.5}$Au$_{0.5}$. Phys. B Condens. Matter 199, 47–48.

Seaman, C.L., Maple, M.B., Lee, B.W., Ghamaty, S., Torikachvili, M.S., Kang, J.S., Liu, L.Z., Allen, J.W., Cox, D.L., 1991. Evidence for non-Fermi liquid behavior in the Kondo alloy Y$_{1-x}$U$_x$Pd$_3$. Phys. Rev. Lett. 67 (20), 2882.

Schröder, A., Aeppli, G., Coldea, R., Adams, M., Stockert, O., von Löhneysen, H., Bucher, E., Ramazashvili, R., Coleman, P., 2000. Onset of antiferromagnetism in heavy-fermion metals. Nature 407 (6802), 351–355.

Sengupta, A.M., 2000. Spin in a fluctuating field: the Bose (+ Fermi) Kondo models. Phys. Rev. B 61 (6), 4041–4043.

Senthil, T., 2008. Critical Fermi surfaces and non-Fermi liquid metals. Phys. Rev. B 78 (3), 035103–035114.

Senthil, T., Sachdev, S., Vojta, M., 2003. Fractionalized Fermi liquids. Phys. Rev. Lett. 90 (21), 216403–216404.

Senthil, T., Vojta, M., Sachdev, S., 2004. Weak magnetism and non-Fermi liquids near heavy-fermion critical points. Phys. Rev. B 69 (3), 035111–035119.

Seo, S., Lu, X., Zhu, J.X., Urbano, R.R., Curro, N., Bauer, E.D., Sidorov, V.A., Pham, L.D., Park, T., Fisk, Z., et al., 2014. Disorder in quantum critical superconductors. Nat. Phys. 10 (2), 120–125.

Shang, T., Baumbach, R.E., Gofryk, K., Ronning, F., Weng, Z.F., Zhang, J.L., Lu, X., Bauer, E.D., Thompson, J.D., Yuan, H.Q., 2014. CeIrIn$_5$: superconductivity on a magnetic instability. Phys. Rev. B 89 (4), 041101.

She, J.H., Zaanen, J., 2009. BCS superconductivity in quantum critical metals. Phys. Rev. B 80 (18), 184518–184615.

Shibauchi, T., Carrington, A., Matsuda, Y., 2014. A quantum critical point lying beneath the superconducting dome in iron pnictides. Ann. Rev. Condens. Matter Phys. 5, 113–135.

Shishido, H., Settai, R., Harima, H., Ōnuki, Y., 2005. A drastic change of the Fermi surface at a critical pressure in CeRhIn$_5$: dHvA study under pressure. J. Phys. Soc. Jpn. 74 (4), 1103–1106.

Si, Q., Steglich, F., 2010. Heavy fermions and quantum phase transitions. Science 329 (5996), 1161–1166.

Si, Q., Rabello, S., Ingersent, K., Smith, J.L., 2001. Locally critical quantum phase transitions in strongly correlated metals. Nature 413 (6858), 804–808.

Si, Q., Pixley, J.H., Nica, E., Yamamoto, S.J., Goswami, P., Yu, R., Kirchner, S., 2014. Kondo destruction and quantum criticality in Kondo Lattice systems. J. Phys. Soc. Jpn. 83 (6), 061005–061011.

Sidorov, V.A., Nicklas, M., Pagliuso, P.G., Sarrao, J.L., Bang, Y., Balatsky, A.V., Thompson, J.D., 2002. Superconductivity and quantum criticality in CeCoIn$_5$. Phys. Rev. Lett. 89 (15), 157004.

Stanley, H.E., 1971. Introduction to phase transitions and critical phenomena. Oxford University Press, Oxford.

Stauffer, D., Aharony, A., 1994. Introduction to percolation theory. CRC press, London, UK.

Steppke, A., Küchler, R., Lausberg, S., Lengyel, E., Steinke, L., Borth, R., Lühmann, T., Krellner, C., Nicklas, M., Geibel, C., Steglich, F., Brando, M., 2013. Ferromagnetic quantum critical point in the heavy-fermion metal YbNi$_4$(P$_{1-x}$As$_x$)$_2$. Science 339 (6122), 933–936.

Stewart, G.R., 2001. Non-Fermi-liquid behavior in d- and f-electron metals. Rev. Mod. Phys. 73 (4), 797.

Stewart, G.R., 2006. Addendum: non-Fermi-liquid behavior in d- and f-electron metals. Rev. Mod. Phys. 78 (3), 743.

Stock, C., Broholm, C., Demmel, F., Van Duijn, J., Taylor, J.W., Kang, H.J., Hu, R., Petrovic, C., 2012. From incommensurate correlations to mesoscopic spin resonance in YbRh$_2$Si$_2$. Phys. Rev. Lett. 109 (12), 127201.

Stockert, O., von Löhneysen, H., Rosch, A., Pyka, N., Loewenhaupt, M., 1998. Two-dimensional fluctuations at the quantum-critical point of CeCu$_{6-x}$Au$_x$. Phys. Rev. Lett. 80 (25), 5627.

Stockert, O., Faulhaber, E., Zwicknagl, G., Stüßer, N., Jeevan, H.S., Deppe, M., Borth, R., Küchler, R., Loewenhaupt, M., Geibel, C., Steglich, F., 2004. Nature of the APhase in CeCu$_2$Si$_2$. Phys. Rev. Lett. 92 (13), 136401–136404.

Stockert, O., Kirchner, S., Steglich, F., Si, Q., 2011. Superconductivity in Ce-and U-based '122' heavy-fermion compounds. J. Phys. Soc. Jpn. 81 (1), 011001.

Suzuki, M., 1976. Relationship between D-dimensional quantal spin systems and (D+1)-dimensional ising systems–equivalence, critical exponents and systematic approximants of partition-function and spin correlations. Prog. Theor. Phys. 56 (5), 1454–1469.

Tabei, S.M.A., Gingras, M.J.P., Kao, Y.J., Stasiak, P., Fortin, J.Y., 2006. Induced random fields in the LiHo$_x$Y$_{1-x}$F$_4$ quantum Ising magnet in a transverse magnetic field. Phys. Rev. Lett. 97 (23), 237203.

Tokiwa, Y., Radu, T., Geibel, C., Steglich, F., Gegenwart, P., 2009. Divergence of the magnetic Grüneisen ratio at the field-induced quantum critical point in YbRh$_2$Si$_2$. Phys. Rev. Lett. 102 (6), 066401–066404.

Tokiwa, Y., Ishikawa, J.J., Nakatsuji, S., Gegenwart, P., 2014. Quantum criticality in a metallic spin liquid. Nat. Mater. 13 (4), 356–359.

Trovarelli, O., Geibel, C., Mederle, S., Langhammer, C., Grosche, F.M., Gegenwart, P., Lang, M., Sparn, G., Steglich, F., 2000. YbRh$_2$Si$_2$: pronounced non-Fermi-liquid effects above a low-lying magnetic phase transition. Phys. Rev. Lett. 85 (3), 626.

Urbano, R.R., Young, B.L., Curro, N.J., Thompson, J.D., Pham, L.D., Fisk, Z., 2007. Interacting antiferromagnetic droplets in quantum critical $CeCoIn_5$. Phys. Rev. Lett. 99 (14), 146402.

Valla, T., Fedorov, A.V., Johnson, P.D., Wells, B.O., Hulbert, S.L., Li, Q., Gu, G.D., Koshizuka, N., 1999. Evidence for quantum critical behavior in the optimally doped cuprate $Bi_2Sr_2CaCu_2O_{8+\delta}$. Science 285 (5436), 2110–2113.

Vandervelde, D., Yuan, H.Q., Onuki, Y., Salamon, M.B., 2009. Evidence of d-wave pairing symmetry of the gap of the heavy-fermion superconductor $CeIrIn_5$ from magnetic-penetration-depth measurements. Phys. Rev. B 79 (21), 212505.

Varma, C.M., 2015. Quantum criticality in quasi-two dimensional itinerant antiferromagnets. Phys. Rev. Lett. 115, 186405.

Villaume, A., Bourdarot, F., Hassinger, E., Raymond, S., Taufour, V., Aoki, D., Flouquet, J., 2008. SigNature of hidden order in heavy fermion superconductor URu_2Si_2: resonance at the wave vector $Q_0 = (1,0,0)$. Phys. Rev. B 78 (1), 012504.

Vojta, M., Bulla, R., Wölfle, P., 2015. Critical quasiparticles in single-impurity and lattice Kondo models. ArXiv.org, 1507.04595, 1507.04595v1.

von Löhneysen, H., 1996. Non-fermi-liquid behaviour in the heavy-fermion system. J. Phys. Condens. Matter 8 (48), 9689.

von Löhneysen, H., Pietrus, T., Portisch, G., Schlager, H.G., Schröder, A., Sieck, M., Trappmann, T., 1994. Non-Fermi-liquid behavior in a heavy-fermion alloy at a magnetic instability. Phys. Rev. Lett. 72 (20), 3262.

von Löhneysen, H., Pfleiderer, C., Pietrus, T., Stockert, O., Will, B., 2001. Pressure versus magnetic-field tuning of a magnetic quantum phase transition. Phys. Rev. B 63 (13), 134411.

von Löhneysen, H., Rosch, A., Vojta, M., Wölfle, P., 2007. Fermi-liquid instabilities at magnetic quantum phase transitions. Rev. Mod. Phys. 79 (3), 1015–1075.

Westerkamp, T., Deppe, M., Küchler, R., Brando, M., Geibel, C., Gegenwart, P., Pikul, A.P., Steglich, F., 2009. Kondo-Cluster-Glass state near a ferromagnetic quantum phase transition. Phys. Rev. Lett. 102(20). 206404-4.

Wilson, K.G., Kogut, J., 1974. The renormalization group and the ϵ expansion. Phys. Rep. 12 (2), 75–199.

Wölfle, P., Abrahams, E., 2011. Quasiparticles beyond the Fermi liquid and heavy fermion criticality. Phys. Rev. B 84 (4), 041101–041104.

Wölfle, P., Abrahams, E., 2015. Spin-flip scattering of critical quasiparticles and the phase diagram of $YbRh_2Si_2$. ArXiv.org, 1506.08476.

Wu, W., Bitko, D., Rosenbaum, T.F., Aeppli, G., 1993. Quenching of the nonlinear susceptibility at a T= 0 spin glass transition. Phys. Rev. Lett. 71 (12), 1919.

Wu, L.S., Kim, M.S., Park, K., Tsvelik, A.M., Aronson, M.C., 2014. Quantum critical fluctuations in layered YFe_2Al_{10}. Proc. Natl. Acad. Sci. 111 (39), 14088–14093.

Yeomans, J.M., 1992. Statistical Mechanics of Phase Transitions. Oxford Science Publications, Oxford, UK.

Yosida, K., 1957. Magnetic properties of Cu-Mn alloys. Phys. Rev. 106 (5), 893–898.

Zapf, V., Jaime, M., Batista, C.D., 2014. Bose-Einstein condensation in quantum magnets. Rev. Mod. Phys. 86 (2), 563.

Zhu, L., Garst, M., Rosch, A., Si, Q., 2003. Universally diverging Grüneisen parameter and the magnetocaloric effect close to quantum critical points. Phys. Rev. Lett. 91(6). 066404-4.

Chapter 281

Lanthanides in Luminescent Thermometry

C.D.S. Brites*, A. Millán† and L.D. Carlos*,[1]

*CICECO—Aveiro Institute of Materials, University of Aveiro, Aveiro, Portugal
†ICMA—Instituto de Ciencia de Materiales de Aragón, University of Zaragoza, Zaragoza, Spain
[1]Corresponding author: e-mail: lcarlos@ua.pt

Chapter Outline

1 INTRODUCTION

Temperature is a central concept of thermodynamics and statistical mechanics its inverse being defined by the derivative of the body's entropy S with respect to its internal energy U, $T^{-1} = \partial S / \partial U$ (Hartmann, 2006; Reif, 1965). While entropy is a measure of the amount of atomic disorder in a body, temperature describes how strong the intensity of random submicroscopic motions of the body's particle constituents is. Temperature is one of the most important physical variable affecting the dynamics and viability of practically all natural and engineered systems, from atomic through macroscopic levels (Allison and Gillies, 1997; Childs et al., 2000; Jaque et al., 2014b; McCabe and Hernandez, 2010; Okabe et al., 2012).

Temperature measurements rely on repeatable physical manifestations of molecular effects, reporting macroscale changes in the body's heat content, and are crucial in countless technological and industrial developments and in scientific research, accounting presently for ca. ~80% of the sensor market throughout the world. The global market is likely to grow to $6.13 billion in 2020, as recently estimated by Grand View Research (a business consulting firm).[1] The thermal expansion of air, alcohol, or mercury, the ductility and conductivity changes of metals, shifts in infrared reflections, and luminescent intensity variations, for instance, are calibrated to associate molecular level changes with easily interpretable temperature scales (McCabe and Hernandez, 2010). For convenience, the measurement methods can be classified into three categories, depending on the nature of contact which exists between the sensor and the object of analysis (Childs et al., 2000):

- *Invasive*. The monitoring device is in direct contact with the medium of interest, eg, thermistor- or thermocouple-based technologies.
- *Semiinvasive*. The medium of interest is treated in some manner to enable remote observation, eg, imaging of thermally sensitive paints.
- *Noninvasive*. The medium of interest is observed remotely, eg, infrared and luminescence thermography.

Traditional contact thermometers, such as liquid-filled and bimetallic thermometers, thermocouples, pyrometers, and thermistors, are generally not suitable for temperature measurements at scales below 10 μm (Brites et al., 2012; Jaque and Vetrone, 2012; Uchiyama et al., 2006; Wang et al., 2013b). Moreover, contact measurements require, in general, conductive heat transfer and thus need to reach equilibrium between the sensor and the object. This thermal connection disturbs the temperature of the sample during the measurement, especially for small systems (in which the size is small compared to that of the sensor head) (Wang et al., 2013b).

Indeed, current technological demands in areas such as microelectronics, microoptics, photonics, microfluidics, and nanomedicine have reached a point such that the use of contact thermometry is not able to make measurements when spatial resolution decreases to the submicron scale, as, for example, in intracellular temperature fluctuations (Arai et al., 2014, 2015; Chapman et al., 1995; Donner et al., 2012; Gota et al., 2009; Hayashi et al., 2015; Homma et al., 2015; Hu et al., 2015; Huang et al., 2010; Liu et al., 2015; Okabe et al., 2012; Qiao et al., 2014; Suzuki et al., 2007; Uchiyama et al., 2015; Vetrone et al., 2010a; Wang et al., 2011a; Zohar et al., 1998), temperature mapping of microcircuits (Aigouy et al., 2005, 2009; Jung et al., 2011; Kolodner and Tyson, 1983; Liu and Yang, 2007; Liu et al., 2012;

---

1. Temperature sensors market analysis by application (automotive, consumer electronics, environmental, medical, process industries) and segment forecasts to 2020.

Mecklenburg et al., 2015; Saïdi et al., 2011; Shi et al., 2015; Tessier et al., 2007b; Wickberg et al., 2015), and microfluids (Aigouy et al., 2011; Barilero et al., 2009; del Rosal et al., 2014; Feng et al., 2011, 2013; Gosse et al., 2009; Graham et al., 2010; Mao et al., 2002; Samy et al., 2008).

In living organism, for instance, temperature is continuously monitored (Narberhaus et al., 2006) being related to many cellular functions, including gene expression, protein stabilization, enzyme–ligand interactions, and enzyme activity (Hayashi et al., 2015; Jaque et al., 2014a; Somero, 1995; Suzuki et al., 2007; Zohar et al., 1998). Moreover, the expression of heat shock, cold shock, and some virulence genes is coordinated in response to temperature changes (Narberhaus et al., 2006). Intracellular temperature depends on the chemical reactions occurring inside cells (Okabe et al., 2012; Takei et al., 2014; Tsuji et al., 2013), which are accompanied by either heat release or heat absorption, with the concomitant modification of the ambient temperature (Homma et al., 2015; Lowell and Spiegelman, 2000; Qiao et al., 2014). Therefore, the ability to develop an accurate method to glean intracellular temperatures will lead to novel insight about cell pathology and physiology, in turn, contributing to novel theranostic techniques (Hayashi et al., 2015; Ke et al., 2012; Kucsko et al., 2013; Li et al., 2007; Vetrone et al., 2010b). Despite the considerable demand and the large number of papers published on the subject in the past decade (Arai et al., 2014, 2015; Donner et al., 2012; Gota et al., 2009; Hayashi et al., 2015; Homma et al., 2015; Hu et al., 2015; Liu et al., 2015; Okabe et al., 2012; Qiao et al., 2014; Vetrone et al., 2010a), high-resolution intracellular temperature distribution maps within living cells have not yet been recorded being nowadays a tremendous challenge for the scientific community (Jaque et al., 2014a).

In microelectronics, the ongoing miniaturization of circuits and devices and the ever faster switching speeds generate significant thermal gradients at the submicron scale (as, for instance, in the case of the millions of transistors incorporated in modern microprocessors) increasing the importance of localized heating problems (Shi et al., 2015). Steady-state and transient characterization of the temperature distribution with high spatial resolution are, thus, critical for performance and reliability analysis (Asheghi and Yang, 2005; Christofferson et al., 2008), noninvasive off-chip characterization (Mecklenburg et al., 2015; Perpiña et al., 2004; Shi et al., 2015), and for probing and understanding energy dissipation and heat transport (Cahill et al., 2014). Moreover, in order to understand the working of such devices, a theory of statistical mechanics and thermodynamics at the microscopic and mesoscopic scales is required, comprehension of the limitations of the concept of temperature at the submicron scale is a prerequisite for such theory (Kliesch et al., 2014). The pioneer works of Hartmann et al. (Hartmann, 2006; Hartmann et al., 2004) and, more recently, of Kliesch et al. (2014) discuss this topic in terms of a minimal length scale on which the correlations between

parts of a system are small enough to permit the definition of local temperature. However, the results predicted by such theoretical models are hardly comparable to the experimental temperature determination in nanoparticles (NPs).

The limitations of contact thermometers for small systems where the spatial resolution decreases to the submicron scale have spurred the development of new noncontact (semi-invasive and noninvasive) accurate thermometers with micrometric and nanometric spatial resolution, a challenging research topic under constant development in the last five years (Brites et al., 2012; Jaque and Vetrone, 2012; Wang et al., 2013b; Yue and Wang, 2012). High-resolution thermometry noncontact techniques in micrometer/nanometer range have been cataloged in many different manners, as, for instance, depending on whether they make use of electrical or optical signals or are based on near- or far-field applications (Brites et al., 2012). Independently of the classification, what really matters is a precise identification of the advantages and drawbacks of each method, as well as a proper selection according to the required spatial, temporal, and temperature resolutions. Table 1 presents a summary of the current methods for noncontact high-resolution thermal measurements in micrometer/nanometer range, highlighting the advantages and disadvantages of each technique.

Among noninvasive spectroscopic methods for determining temperature, the thermal dependence of phosphor luminescence—band shape, peak energy and intensity, and excited states, lifetimes, and risetimes—is one of the most promising accurate techniques (often referred to as thermographic phosphor thermometry). It works remotely with high-detection relative thermal sensitivity ($>1\% \, \text{K}^{-1}$) and spatial resolution ($<10 \, \mu\text{m}$) in short acquisition times ($<1 \, \text{ms}$), even in biological fluids, strong electromagnetic fields, and fast-moving objects (Brites et al., 2010; Jaque and Vetrone, 2012; Wang et al., 2013b).

Temperature measurements based on intensity changes require ratiometric readout. The intensity ratio between two transitions is not compromised by the well-known disadvantages of experiments based on the intensity of only one transition, such as the critical dependence on variations of the sensor concentration, small material inhomogeneities, and optoelectronic drifts of the excitation source and detectors, and, thus, are much more reliable (Brites et al., 2010; Jaque and Vetrone, 2012; Wang et al., 2013b).

Luminescent thermal probes are derived from organic dyes, ruthenium complexes, spin crossover NPs, polymers, layered double hydroxides (LDHs), semiconductor quantum dots (QDs), and Ln^{3+}-based materials. Apart from these single-component systems, there are more complex examples in which the temperature dependence of the emission intensity of the probe (and/or the lifetime of a given emitting state) is induced by a second component. In most of the cases, this temperature-responsive material is a polymer,

TABLE 1 Summary of the Advantages, Disadvantages, and General Applications of High-Resolution Electrical, Near- and Far-Field Thermal Techniques (An Indicative Reference Is Included for Each Technique)

Method	Principle	Typical Resolution			Advantages	Disadvantages
		δx (μm)	δT (K)	δT (μs)		
HIGH-resolution thermal measurement techniques in micrometer–nanometer range						
Infrared thermography (Maldague and Marinetti, 1996)	Plank blackbody emission	10	10^{-1}	10	• Well-implemented commercial technique • Provides temperature image profile of the surface	• Detector saturation at high temperatures • Difficulties on the precise estimation of the emissivity of the surface materials, that is function of wavelength and temperature (Ferreira et al., 2013) (not all "hot bodies" are perfect blackbodies, in the physical meaning of the term) (Allison and Gillies, 1997) • Spatial resolution for the temperature detection, which is Rayleigh limited • Considerable temperature uncertainty, ∼1 K at room temperature (Rodrigues et al., 2016) • Strong dependence on the relative orientation between the camera and the measured surface (Benayas et al., 2015) • Maximum acquisition rate around 5 kHz, corresponding to a temporal resolution of 0.2 ms • Covering layers for emissivity correction can distort the thermal field and may be incompatible with the inspected sample (Millán et al., 2014)

Continued

TABLE 1 Summary of the Advantages, Disadvantages, and General Applications of High-Resolution Electrical, Near- and Far-Field Thermal Techniques (An Indicative Reference Is Included for Each Technique)—Cont'd

Method	Principle	Typical Resolution			Advantages	Disadvantages
		δx (μm)	δT (K)	δT (μs)		
Thermoreflectance (Cahill, 2004)	Temperature dependence of the reflection	10^{-1}	10^{-2}	10^{-1}	• High thermal and temporal resolution • Quantitative and qualitative measurement	• Requires the calibration of the reflectivity index • Spatial resolution limited by the diffraction limit (Löw et al., 2008) • Thermoreflectance coefficient is not available for every material and depends on excitation wavelength and thickness of the optical layer
Raman (Kim et al., 2006)	Inelastic scattering of monochromatic light	1	10^{-1}	10^{6}	• No sample preparation needed • Works in solids and liquids • Small volumes (<1 μm diameter) can be probed	• Highly time-consuming technique implying image point analysis as slow as 0.5 point s^{-1} • Low signal levels • Cross talk with fluorescent molecules
Microthermocouple (Watanabe et al., 2005)	Seebeck effect	10^{2}	10^{-1}	10	• Precise temperature calibration • Spatial resolution (at one dimension) of 25 nm	• The thermometer is separated from the active region of the device limiting, at very short timescales, the access to it • Additional fabrication effort required • Voltage reflections and capacitive coupling limit the timescale for transient thermometry of the device

Technique	Mechanism				Advantages	Disadvantages
Fluorescence thermography (Brites et al., 2012)	Temperature dependence of quantum efficiency/ lifetime/intensity	10^{-1}	10^{-2}	10	• Diverse experimental techniques to measure temperature • High temperature sensitivity • Ratiometric algorithms are independent of illumination source	• Photobleaching limits the long-term intensity and lifetime determination • High-expensive excitation sources and detectors to measure temperature using lifetime-based algorithms
Near-field scanning optical microscopy (Goodson and Asheghi, 1997)	Temperature dependence of the near-field radiation	10^{-2}	10^{-1}	10	• Spatial resolution below the Rayleigh limit (100 nm)	• Depends on the surface characteristics • Only access to surface temperature • Slow temperature acquisition • Vacuum and/or cryogenic temperatures required
Liquid crystal thermography (Lees, 1982; Windhorn and Cain, 1979; Yoder, 1979)	Crystal phase transitions (change color)	10	10^{-1}	10^2	• Diverse materials available commercially for different temperature ranges • Fully integrated with electronic devices	• Yields a semiquantitative temperature map, unless a detailed calibration is performed • A layer of the probe must be placed over the sample • Not compatible with liquid systems
Scanning thermal microscopy (Kim et al., 2012)	AFM with thermocouple or Pt thermistor tip	10^{-1}	10^{-1}	10^2	• Uses AFM tips to simultaneously measure temperature and determine the surface roughness • Submicrometric spatial resolution	• Slow acquisition times • Limited to solid samples • Requires fundamental knowledge of tip-sample heat transfer
Transmission electron microscopy (Gao et al., 2003)	Thermal expansion	10^{-2}	10^{-1}	10^1	• High spatial resolution • Compatible with different CNTs	• Vacuum required • Difficult to transpose for practical applications • Temperature determination by image analysis

TABLE 1 Summary of the Advantages, Disadvantages, and General Applications of High-Resolution Electrical, Near- and Far-Field Thermal Techniques (An Indicative Reference Is Included for Each Technique)—Cont'd

Method	Principle	Typical Resolution			Advantages	Disadvantages
		δx (μm)	δT (K)	δT (μs)		
Optical interferometry (Corke et al., 1983)	Thermal expansion or refractive index change	10^0	10^{-5}	10^{-3}	• Can be integrated in remote detection systems • All optical temperature determination	• Cross talk with other stimulus as strain/stress and bending • Low spatial resolution in the transverse direction
Nitrogen-vacancy (Kucsko et al., 2013)	Quantum mechanical spin	10^{-1}	10^{-3}	10^4	• Fully remote control of the system: manipulation of spin using microwave pulses and detection by laser radiation. • High spatial resolution	• High integration times required for low temperature uncertainty values • Critically depends of isotopically pure ^{12}C diamond • Sophisticated data analysis
Plasmon energy expansion thermometry (Mecklenburg et al., 2015)	Shift of electron energy loss peaks	10^{-2}	10^1	10^3	• High spatial resolution	• High temperature uncertainty • Needs a transmission electron microscope in high vacuum conditions to measure temperature
Thermal scanning electron microscopy (Wu and Hull, 2012)	Thermal diffuse scattering in electron backscatter diffraction	10^{-1}	10^1	10^4	• High spatial resolution	• High temperature uncertainty • Temperature determination requires a standard sample to calibrate the effect of beam current, beam voltage, stage-detector geometry, sample materials, etc.

Electron energy loss spectroscopy intensity (Vendelbo et al., 2013)	Intensity of electron energy loss peaks	10^{-2}	10^1	10^6	• High spatial resolution	• High temperature uncertainty • High acquisition times • Needs a transmission electron microscope in high vacuum conditions to measure temperature • Applicable only in solids
Motional-averaging NMR (Jarenwattananon et al., 2013)	NMR spectra linewidth	10^2	10^1	10^7	• Tunable temperature sensitivity • Robust relative to pressure, gas composition, reactor type, catalyst type, reaction rate, and steady-state conversion	• High temperature uncertainty • High acquisition times • Poor spatial resolution

The typical δx, δt, and δT resolutions of each method are also included.

eg, poly(*N*-isopropylacrylamide) (PNIPAM) (Gota et al., 2009; Graham et al., 2010), or an organic–inorganic hybrid host (Carlos et al., 2007).

Since organic dyes were patented in 1941 as "temperature indicator" (Jennings, 1941), many advances have been made. Molecular thermometers based on light-absorbing aromatic compounds (de Silva et al., 1997), rhodamine 101 (Clark et al., 1998), rhodamine B (RhB) (Ross et al., 2001), rhodamine 101 Rh B (Glawdel et al., 2009), fluorescein isothiocyanates (Guan et al., 2007), and cyanine dyes (Mikkelsen and Wallach, 1977) have become very popular in luminescence temperature determination, essentially in a biological context (Okabe et al., 2012). For a comprehensive review of the subject see, for instance, the works of Hoogenboom and collaborators (de la Rosa et al., 2016; Pietsch et al., 2011). Although the most available and used thermal probes are based on organic dyes, QDs and Ln^{3+}-based materials have been gaining relevance due to their higher photostability and relatively high emission quantum yields.

QDs have been proposed for submicron thermometry, since they present temperature-dependent luminescence (intensity changes or emission peak shifts) (Haro-Gonzalez et al., 2013; Li et al., 2007). Nanomedicine stands out as the most appealing area, since bioconjugation of QDs make them target selective. However, QDs are often composed of highly cytotoxic elements (eg, Cd), which make difficult their future use in clinical trials (Cho et al., 2007; Gnach et al., 2015). For a comprehensive review of the application of QDs in micro and nanothermometry, see, for instance, the works of Jaque and collaborators (Maestro et al., 2010a, 2013).

Ln^{3+}-based materials are versatile, stable, and narrow band emitters with, in general, high emission quantum yields (>50%) (Bünzli, 2010, 2015; Bünzli and Eliseeva, 2013; Comby and Bünzli, 2007). In fact, different emitting centers can cover the entire electromagnetic spectrum, ranging from UV (eg, Gd^{3+}) to IR (eg, Er^{3+}, Yb^{3+}, Nd^{3+}); thus, it is virtually possible to design on-demand luminescent probes for a large variety of applications (Binnemans, 2009; Bünzli, 2010; Carlos et al., 2009; Chen et al., 2013; Feng and Zhang, 2013). A large number of Ln^{3+}-based molecular thermometers covering temperatures from the cryogenic ($T < 100$ K) to the physiological (298–323 K) ranges have been reported, essentially in the last couple of years, involving chelate complexes (Brites et al., 2010; Peng et al., 2010a; Uchiyama et al., 2006), metal-organic frameworks (MOFs) (Cadiau et al., 2013; Cui et al., 2015b; Wang et al., 2015c), upconverting NPs (UCNPs) (Lojpur et al., 2014; Savchuk et al., 2014; Vetrone et al., 2010b), and downshifting nanomaterials (Balabhadra et al., 2015; Benayas et al., 2015; Rocha et al., 2014b). For a comprehensive review, see the works on high-temperature thermographic phosphors (Heyes, 2009; Rabhiou et al., 2011), on temperature-sensitive paints (the Ln^{3+} probe is incorporated into a polymer binder and the resulting paint sprayed onto a surface to map temperature distribution)

(Wolfbeis, 2008; Yu et al., 2010), on β-diketonate complexes (Brites et al., 2011, 2012), on organic–inorganic hybrids (Brites et al., 2012; Millán et al., 2016), and on NPs (Bettinelli et al., 2015; Fischer et al., 2011; Quintanilla et al., 2016; Wang and Zhang, 2015).

Luminescent thermometers based on the transient emission intensity response of Ln^{3+}-activated phosphors (eg, $Y_2O_2S:Eu^{3+}$ and $CaS:Eu^{3+}$) were firstly proposed by Kusama et al. in 1976 (Kusama et al., 1976) and by Samulski & Shrivastava four years later (Samulski and Shrivastava, 1980; Samulski et al., 1982). In 2002, the seminal paper of Wang et al. discussed the concept of using luminescent NPs for thermometry (Wang et al., 2002). The temperature-dependent emission characteristics of distinct semiconductor NPs were used as a proof of concept and ratiometric luminescent thermometers were proposed for the first time based on $ZnS:Mn^{2+}$, Eu^{3+} NPs, in which the ratio of the emission intensities of the two dopants—so-called fluorescence intensity ratio, FIR—provides a robust temperature measurement approach. A few years later, this same FIR concept was generalized to NPs doped only with Ln^{3+} ions, $BaTiO_3:Er^{3+}$ UCNPs (Alencar et al., 2004). In Er^{3+}-based systems, the FIR method involves measurements of the fluorescence intensities from two closely spaced electronic energy levels ($^2H_{11/2}$ and $^4S_{3/2}$) that are thermally coupled (eg, in a thermodynamically quasi equilibrium state) (Collins et al., 1998; Shinn et al., 1983), see Section 4.1.1.

We proposed a more recent breakthrough on luminescent nanothermometry in 2010 with the development of siloxane-based hybrid magnetic nanoclusters doped with Eu^{3+} and Tb^{3+} chelates (Brites et al., 2010). The key point in this approach is the temperature dependence of the energy transfer and back transfer rates between the host, the ligands, and the Ln^{3+} ions (Ln = Tb and Eu). The temperature dependence of the $^5D_4$ (Tb^{3+}) and $^5D_0$ (Eu^{3+}) emissions is essentially determined by the temperature dependence of the balance between i) host-to-Ln^{3+} and ligand-to-Ln^{3+} energy transfer rates, including pathways through excited singlet and triplet states; ii) Ln^{3+}-to-host and Ln^{3+}-to-ligand energy back transfer rates, and iii) non-radiative deactivations from upper excited 4f levels to the emitting $^5D_4$ and $^5D_0$ states. Since the Tb^{3+} and Eu^{3+} ions are well dispersed within the hybrid host (typically in concentrations lower than 5%), ion-ion energy transfer is unimportant. The $^5D_4 \rightarrow {}^7F_5/^5D_0 \rightarrow {}^7F_2$ relative intensity ratio guarantees the absolute measurement of temperature, with spatial resolution adjustable by the size of the nanoclusters to which the luminescent probes are anchored. We remark that similar energy resonance schemes may be obtained using other hybrid or polymer hosts or β-diketonate chelates with different ligands (Brites et al., 2013b, 2016). This mechanism involving the global balance between host-to-ions and ligand-to ions energy transfer and back transfer rates is different than that usually observed in Tb^{3+}/Eu^{3+}-doped materials in which the temperature dependence of the $^5D_4 \rightarrow {}^7F_5/^5D_0 \rightarrow {}^7F_2$ intensity ratio is determined by

the Tb^{3+}-to-Eu^{3+} energy transfer (Miyata et al., 2013) that occurs essentially through the dipole-quadrupole and quadrupole-quadrupole mechanisms (Rodrigues et al., 2014). The use of Tb^{3+}-to-Eu^{3+} energy transfer as a tool to temperature sensing was firstly proposed by Sato et al. in 1989 (Sato et al., 1989) and revisited by Liu et al. in 2005 (Liu et al., 2005).

In the last couple of years, the research on nanothermometry progressed toward the design of single nanoplatforms joining heaters and thermometers. Magnetic-, plasmonic-, and phonon-induced thermal heating of NPs are powerful noninvasive techniques with exciting potential for bio- and nanotechnology applications, such as drug release (Mura et al., 2013), remote control of single-cell functions (Stanley et al., 2012), plasmonic devices (Schuller et al., 2010), and hyperthermia therapy of cancer (Reddy et al., 2012) and other diseases (Stanley et al., 2012). To be effective, however, local heating requires measuring the nanoheater's local temperature. Since the first report by Tikhomirov et al. showing the phonon-induced heating of Yb^{3+}/Er^{3+}-based NPs through nonradiative emissions and the determination of its temperature rise using the $^2H_{11/2} \rightarrow {}^4I_{15/2}/{}^4S_{3/2} \rightarrow {}^4I_{15/2}$ intensity ratio (Tikhomirov et al., 2009), several intriguing reports on magnetic- (Dong and Zink, 2014; Piñol et al., 2015), plasmonic- (Debasu et al., 2013; Huang et al., 2015b), and phonon-induced (Carrasco et al., 2015; Wawrzynczyk et al., 2012) thermal heating of Ln^{3+}-based nanoplatforms have been published.

Apart from a few pioneering works published at the very end of the past century, the subject of investigating and developing temperature sensors working at the submicron scale has exploded in the last 10 years, particularly biased since 2010 by luminescent nanothermometry and its applications. Accordingly, the progress on high-resolution micro and nanothermometers, including luminescent and nonluminescent examples (Brites et al., 2012; Jaque and Vetrone, 2012; Wang et al., 2013b), intracellular measurements (Jaque et al., 2014a) and image-guided thermal treatments (Zhou et al., 2016), ceramic phosphors that can withstand extreme temperatures (Rabhiou et al., 2011), multiple optical chemical sensors (Stich et al., 2010), MOFs (Cui et al., 2015b), and temperature-stimuli polymers (de la Rosa et al., 2016; Pietsch et al., 2011), has been recently reviewed. Moreover, a comprehensive book (half way between a monograph and a reference book) has recently been published on this very multidisciplinary subject covering the fundamentals, luminescence-, and nonluminescence-based thermometry, applications, and future trends (Carlos and Palacio, 2016). Therefore, instead of just describing the progress achieved in the last couple of years, the present review focuses primarily on how to rationalize the thermal response of Ln^{3+}-based thermometers and how to precisely define the parameters governing their performance. After a brief overview of the two main approaches to determine temperature through luminescent thermometers (Section 2), we discuss in Sections 3 and 4 how the performance of ratiometric single- and dual-center luminescent thermometers should be

quantified accordingly to the relevant parameters: relative sensitivity, temperature uncertainty, spatial and temporal resolution, repeatability (or test–retest reliability), and reproducibility. The emission mechanisms supporting single- and dual-center emissions are reviewed, together with the advantages and limitations of each approach quantified essentially by the relative sensitivity and the temperature uncertainty. Illustrative examples of the rich variety of systems designed and developed to sense temperature are provided and explored in Section 5. Finally, we would attempt to summarize the chapter and provide a brief prospective outlook in Section 6.

2   LUMINESCENT THERMOMETERS

Historically, three main approaches to determine the temperature were followed in luminescent thermometry: (i) the spectral shift of a given transition, (ii) emission intensity measurements, using the integrated intensity of a single transition or of a pair of transitions, and (iii) lifetime measurements, using the decay profiles of emitting excited states (Fig. 1).

The most obvious approach to infer the absolute temperature from luminescence spectroscopy is to measure the intensities from two energy levels (or two Stark components of an excited state) in thermal equilibrium (see Section 4.1.1). The temperature scale is based exclusively upon the validity of the Boltzmann distribution and this nonempirical procedure was documented initially for the $^2H_{11/2} \rightarrow {}^4I_{15/2}$ and $^4S_{3/2} \rightarrow {}^4I_{15/2}$ Er^{3+} transitions (Shinn et al., 1983; Weber, 1967) and for two Stark components of the $^5D_{1,2}$ Eu^{3+} levels (Kusama et al., 1976). The noticeable feature of the $^2H_{11/2}/{}^4S_{3/2}$ Er^{3+} pair of excited levels is that they are energetically close, the energy gap being $\sim$800 cm^{-1} (Carnall et al., 1977), permitting the $^2H_{11/2}$ level to be populated from $^4S_{3/2}$ by thermal agitation ($k_B T \sim 200$ cm^{-1} at room temperature)
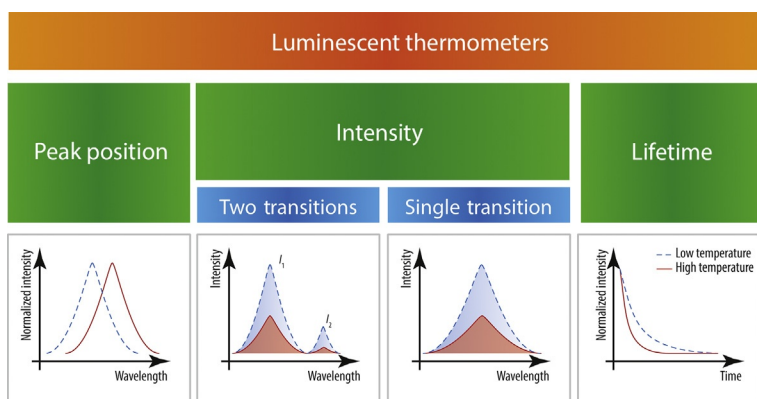
FIG. 1   Luminescent thermometers classification.
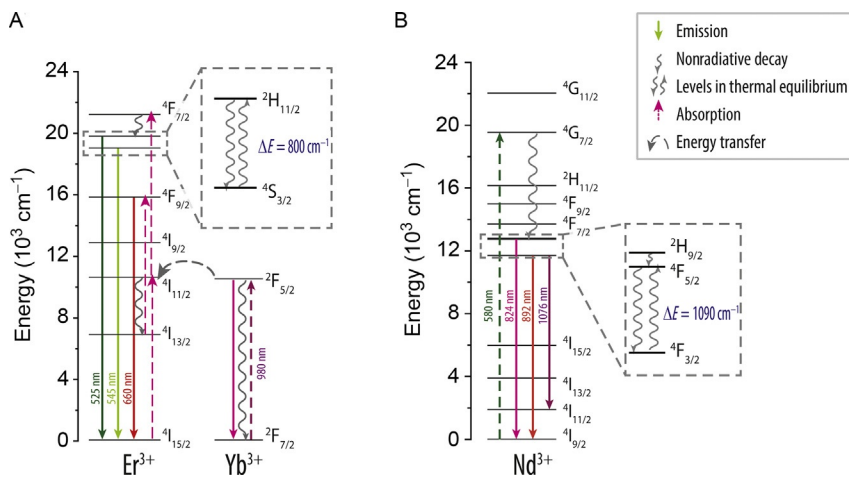
FIG. 2 Energy levels of (A) Yb^{3+}/Er^{3+} and (B) Nd^{3+} ions used for thermometry.

(Fig. 2). Optical-fiber temperature sensors were demonstrated in 1998 using the Er^{3+} emission lifetime at 1540 nm in Er-implanted Si samples (Kewell et al., 1998) and in 2007 through Er^{3+} fluorescence lines excited by means of a semiconductor laser-induced upconversion in Yb^{3+}/Er^{3+}-doped fluoride glasses (Berthou and Jörgensen, 1990). For a detailed description of fluorescence-based optical fiber thermometers, the review paper of Wade et al. (2003) is also worth mentioning.

Luminescent thermometers based on the emission intensity of a single transition depend critically on the illumination fluctuations and the local changes of the phosphor concentration. Thus, although it can be used, end-user applications are not compatible with recursive calibration procedures. In the literature, many examples, especially devoted to proof-of-concept luminescent thermometers, can be found describing single emission from Ln^{3+} ions (Peng et al., 2010a; Sun et al., 2010), QDs (Li et al., 2007; Liu et al., 2006; Maestro et al., 2011; Wang et al., 2008), and organic molecules (Chauhan et al., 2014; Donner et al., 2012; Gota et al., 2008; Okabe et al., 2012; Uchiyama et al., 2003; Yarimaga et al., 2011). All the recognized limitations of this emission approach can, however, be mitigated by the use of a second emission with the purpose to serve as an internal standard to calibrate the response of the luminescent probe. This is a truly long-standing concept discussed in the 1970s (Kusama et al., 1976; Mikkelsen and Wallach, 1977) and firstly implemented in 1980s using ZnCdS (Samulski and Shrivastava, 1980) and CdS:Eu^{3+} phosphors (Samulski et al., 1982) that have experienced a noteworthy advance in the last decade (Brites et al., 2012; Jaque and Vetrone, 2012; Wang et al., 2013b).

Lifetime-based sensing methods do not suffer from the above-mentioned disadvantages of the single-transition intensity technique. However, comparing with the ratiometric intensity response to temperature changes, they require longer acquisition times, postprocessing techniques, and the complexity and demands on the component instrumentation increase with the decreasing decay times (Berthou and Jörgensen, 1990; Brites et al., 2012; Peng et al., 2010b). Moreover, lifetime-based sensing methods are less appropriate for large-area gradient temperature measurements and very inappropriate to study dynamic measurements in which temperature variations occur at time intervals shorter than or equal to the lifetime of the probe.

According to the wide range of applications and as industry requires dedicated sensors for specific processes, it is highly improbable that a particular sensor can be simultaneously suitable for high ($T > 500$ K), physiological, or cryogenic monitoring ranges. Then, both the ratiometric intensity response and the lifetime-based sensing methods show considerable potential and have been extensively studied for a wide range of materials. Although the comparison between the performances of each method is of particular interest, it has not been done systematically. An interesting example is the pioneer work of Collins et al. for Cr^{3+}-, Er^{3+}-, and Pr^{3+}-based crystals (Fig. 3) (Collins et al., 1998). In general, the ratiometric intensity response provides higher relative sensitivity values ($5 \times$ larger in the Pr^{3+}-based crystal of Fig. 3). This is more evident for cryogenic temperatures as lifetime values are generally temperature independent in this range and, thus, the relative sensitivity approaches zero.

More recently, Paviolo et al. came to the same conclusion using a fluorescent molecular thermometer based on RhB to resolve temperature distributions within the volume of a single cell (Paviolo et al., 2013). The measure of temperature in the cytoplasm of an organic tissue via RhB emission intensity is more accurate and reliable than that performed using the RhB lifetime. Therefore, in general, the wisest luminescent thermometry choice should produce a ratiometric intensity response to temperature changes.

3 THERMOMETER PERFORMANCE

In this section, we will discuss how the emission intensity should be converted into temperature and how the performance of ratiometric luminescent thermometers should be quantified. The comparison of the performance of distinct luminescence thermometers is made using the following parameters:

- relative thermal sensitivity,
- temperature uncertainty,
- spatial and temporal resolution, and
- repeatability (or test–retest reliability) and reproducibility.
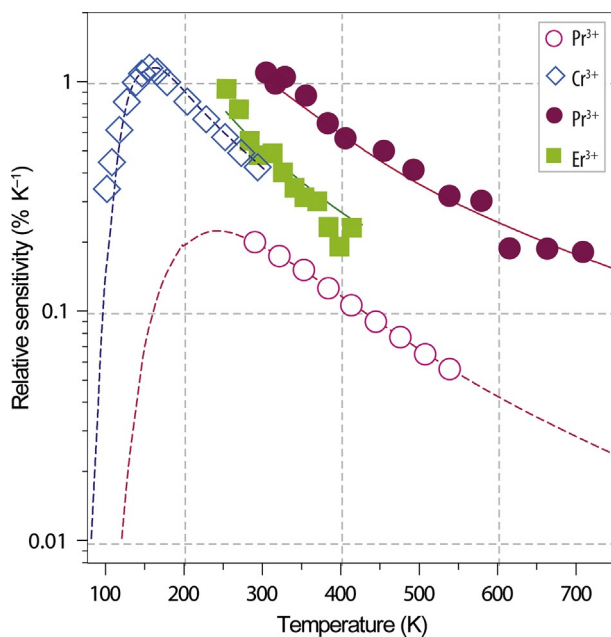
FIG. 3 Comparison of the relative sensitivities obtained through the FIR (*solid symbols*) and lifetime (*open symbols*) methods. The *solid* and *dashes curves* represent fits to the Boltzmann thermal equilibrium model and Collins' lifetime sensitivity equation (see the reference), respectively. *Adapted with permission from Collins, S., Baxter, G., Wade, S., Sun, T., Grattan, K., Zhang, Z., Palmer, A. 1998. Comparison of fluorescence-based temperature sensor schemes: theoretical analysis and experimental validation. J. Appl. Phys. 84, 4649–4654. © 1998 AIP Publishing.*

The conversion of integrated intensity in temperature is made through the thermometric parameter $\varDelta$ defined as:

$$\varDelta = \frac{I_1}{I_2} \tag{1}$$

where I_1 and I_2 are the integrated intensities of two transitions. Although some other empirical definitions can be found in literature, as, for instance (McLaurin et al., 2013)

$$\varDelta = \frac{I_1}{I_1 + I_2} \tag{2}$$

or (Brites et al., 2010)

$$\varDelta = I_1^2 - I_2^2, \quad I_1 > I_2 \tag{3}$$

the integrated intensity ratio of Eq. (1) is, by far, the commonly used thermometric parameter. Note that this equation lacks physical meaning in the limit

$I_2 \rightarrow 0$, since the thermometer readout reaches the system-operating limit, ie, a bound value defined in accordance with a reliability criterion (Robertson and Lee, 2002). In this case, a reasonable operating approach must consider as reliable intensity values only those that are 5% higher than the noise level (or baseline), thus ensuring the adequate consistency of the thermometer readout within the system-operating limit. This operational criterion is quite general, independently of the adopted form for Δ. Although in the limit $I_2 \rightarrow 0$ Eqs. (2) and (3) keep their physical meaning, variations in Δ lower than its intrinsic error (corresponding to negligible changes on I_1 and I_2) means that the system-operating limit is reached.

3.1   Relative Thermal Sensitivity

The relative thermal sensitivity S_r indicates the relative change of Δ per degree of temperature change and is defined by:

$$S_r = \frac{1}{\Delta} \left| \frac{\partial \Delta}{\partial T} \right| \qquad (4)$$

This parameter (usually expressed in units of % change per Kelvin of temperature change, $\% \, K^{-1}$) was defined in 2003 in the context of optical fiber point temperature sensing (Wade et al., 2003) and since our initial purpose in 2012 (Brites et al., 2012), has been commonly used as a figure of merit to compare different thermometers, independently of their nature (Benayas et al., 2015; Carrasco et al., 2015; Cerón et al., 2015; Cui et al., 2015b; McLaurin et al., 2013; Wang et al., 2015c; Zhou et al., 2014d). The maximum value of S_r is denoted as S_m. We note that $S_r > 0$ (negative sensitivities make no sense) and a negative signal in $\partial \Delta / \partial T$ means that Δ decreases as temperature increases. Compared to the absolute sensitivity (dos Santos et al., 1998),

$$S_a = \frac{\partial \Delta}{\partial T} \qquad (5)$$

S_r presents the critical advantage to be independent of the nature of the thermometer (ie, mechanical, electrical, optical) allowing direct and quantitative comparison between different samples, a powerful tool when different techniques are considered. Although frequently seen in the literature, S_a cannot be used to compare the performance of distinct luminescent thermometers as it depends on the sample characteristics (eg, absorption and lifetimes) and on the experimental setup.

3.2   Temperature Uncertainty

The temperature uncertainty (or temperature resolution) δT is the smallest temperature change that can be detected in a given measurement. Assuming that the temperature uncertainty of a thermometer results only from

changes in $\varDelta$, δT is given by the Taylor's series expansion of the temperature variation with $\varDelta$:

$$\delta T = \frac{\partial T}{\partial \varDelta}\delta\varDelta + \frac{1}{2!}\frac{\partial^2 T}{\partial \varDelta^2}(\delta\varDelta)^2 + \cdots + \frac{1}{n!}\frac{\partial^n T}{\partial \varDelta^n}(\delta\varDelta)^n \quad (6)$$

where $\delta\varDelta$ is the uncertainty in the determination of $\varDelta$. Considering that the expansion in T is dominated by the first term (Baker et al., 2005), Eq. (6) can be written in terms of S_r:

$$\delta T = \frac{1}{S_r}\frac{\delta\varDelta}{\varDelta} \quad (7)$$

pointing out that δT is dependent on the thermometer performance (quantified by the relative sensitivity) and experimental setup (that limits $\delta\varDelta/\varDelta$, as discussed in Section 3.2.1). For typical portable detection systems, $\delta\varDelta/\varDelta$ can reach 0.1%, at best, meaning that typical sensitivities of 1–10% K^{-1} (Brites et al., 2012) correspond to temperature uncertainties of 0.01–0.1 K, respectively. With more sensitive detectors, eg, photomultiplier tubes (PMTs) and charge-coupled devices (CCDs), $\delta\varDelta/\varDelta = 0.03\%$, and $\delta T < 0.003$ K. This is an impressive temperature resolution compared with that can be achieved with other techniques, such as wired thermistors (0.01 K) and noncontact infrared cameras (1.0 K).

3.2.1 Measuring the Intensity Uncertainty

The uncertainty on intensity measurements (δI) is mainly determined by the nature of the detector. Commercial detectors include, in ascending order of its sensitivity on intensity discrimination, photodiode arrays (PDAs), CCDs, and PMTs. The comparison of several detectors is not straightforward as different approaches use distinct parameters to quantify the device performance. Here we adopt the photosensitivity (S_Φ), measured in A W^{-1} (ampere of detection signal per Watt of incident photon). The conversion between the manufacturers' reported quantum efficiency (QE) and S_Φ is given by (Zalewski and Duda, 1983):

$$S_\Phi = QE\frac{\lambda}{hc} \quad (8)$$

where λ is the wavelength in nanometers, h is the Planck constant and c is the speed of light in vacuum.

The most common PDAs are typically fabricated using Si photodiodes covering the spectral range from the UV to the near infrared (NIR). The manufacturers point out high-speed response, high sensitivity and low noise, as the main advantages, and they are well implemented in portable spectrometers, due to their relatively low cost when compared with other detection devices. Typically, the maximum photosensitivity in the visible spectral region is

0.5 A W^{-1} (Saleh et al., 1991). The noncooled detectors present typical signal-to-noise ratio (SNR) of 1/500, whereas in cooled ones this value decreases to 1/1000, corresponding to a maximum relative δI of the order of 0.1% (Saleh et al., 1991). The main advantage of PDA detectors is the simultaneous access to all the covered spectral range, which is critical to avoid any delay between the acquisition of the two transitions used to measure temperature. On the other hand, their high acquisition rate ($\sim$5 Hz) precludes their use in submillisecond regime, which typically is not critical for dynamic nanothermometry applications.

CCDs are usually metal–oxide semiconductor structures (SiO$_2$ on Si and a layer of polycrystalline Si). The manufacturers report SNR values between 0.1% and 0.5% making these detectors appropriate for spectrometric measurements. The photosensitivity in the visible spectral range is about 2.5–4.0 A W^{-1} (Groom et al., 1999), meaning a fourfold increase in SNR, when compared with PDAs. The use of complementary metal–oxide semiconductors and the cooling of the detector can improve the dark–noise value resulting in low SNR values, 0.05% at best. The most obvious advantage of CCDs in comparison with other detecting solutions is that they are usually organized in bidimensional arrays giving access to spectral images. Spectrally resolved measurements can be implemented using bandpass filters for a set of channels (typically three CCDs for blue, green, and red spectral regions) or hyperspectral cameras. The last approach has been gaining a renovated interest since it allows the acquisition of spectral information on submicrometric sized domains. The most limiting factor for the spreading of the CCD technology is the cost: the price of a laboratory-grade CCD detector is one order of magnitude higher than that of the PDA equivalent in terms of photosensitivity.

Finally, PMTs are the most sensitive and the fastest response time detectors being constituted by a photocathode (photoemissive cathode), focusing electrodes, an electron multiplier and an anode (electron collector) in a vacuum tube. When photons impinge on the photocathode it emits photoelectrons that are focused by electrode voltages toward the electron multiplier, and finally collected by the anode as an output signal. The PMTs present typical overall photosensitivity in the visible range around 10^4 A W^{-1} (Dorenbos et al., 1993), one of the reasons justifying their wide use in most of the laboratory-grade spectrophotometers. Although most suppliers refer higher detection capabilities for these detectors, their incorporation in the actual spectrometers produce intensity fluctuations in steady-state conditions that degrades SNR to values of the order of 0.03%. Although commercially available devices allow covering the electromagnetic spectrum from the deep UV to the far IR, the experimental setups commonly use a set of gratings and moving optics that results in acquisition times of the order of a minute for a single spectrum, Table 2.

TABLE 2 State-of-the-Art Values for $\delta\varDelta/\varDelta$ for Different Detectors

Detector Type	Minimum $\delta\varDelta/\varDelta$ (%)	Observations
PDA	0.1	Low-cost detector incorporated in most portable spectrometers. Acquisition time on the millisecond range
CCD	0.05	Detector for large-area mapping. Acquisition time on the millisecond range
PMT	0.03	State-of-the-art radiation detector. Used in high-sensitive spectrometers. Acquisition time on the microsecond to the nanosecond range, per wavelength step

3.2.2 Experimental Determination of the Temperature Uncertainty

The δT values are experimentally determined from the distribution of temperature readouts of a luminescence thermometer when it is at a certain reference temperature. The temperature that corresponds to each spectrum is obtained using a calibration curve and the standard deviation of the resulting temperature histogram is the experimental δT of the luminescent thermometer. We illustrate this procedure for a chloroform suspension of $NaYF_4$:Yb^{3+}/Er^{3+} (18/2%) NPs at 3 g L^{-1} (Fig. 4). The details on the temperature measurement using the Er^{3+} emission upon 980 nm IR excitation are given in Section 4.1.1. We first calibrated the luminescent thermometer using a standard K-type thermocouple probe immersed in the suspension container. Then, setting the temperature of the sample to 308 K, we measured the emission spectra with 250 ms integration time during 60 s (total of 240 measurements). We computed $\varDelta$ according to Eq. (1), and the corresponding histogram presents a standard deviation of 0.0078. Computing the temperature corresponding to each emission spectrum using the calibration curve, a new histogram of temperature readouts is built (related with that based on $\varDelta$ by the calibration curve). Notice that higher relative sensitivity values narrow the histogram of T in comparison with that of $\varDelta$ (Fig. 4).

This experimental procedure also allows estimating potential effects of the excitation light on the thermometer readout. For UV-excited Ln^{3+} complexes, for example, the absence of drifts on the temperature readout indicates the absence of measurable heating by the ligand-induced Stokes shift (Fig. 5A). In contrast, the local temperature of Nd^{3+}- and Yb^{3+}/Er^{3+}-doped NPs noticeably increases under NIR excitation (Fig. 5B), a reason why they are being used as a single heater–thermometer platform (Rocha et al., 2014a; Wawrzynczyk et al., 2012; Ximendes et al., 2016).
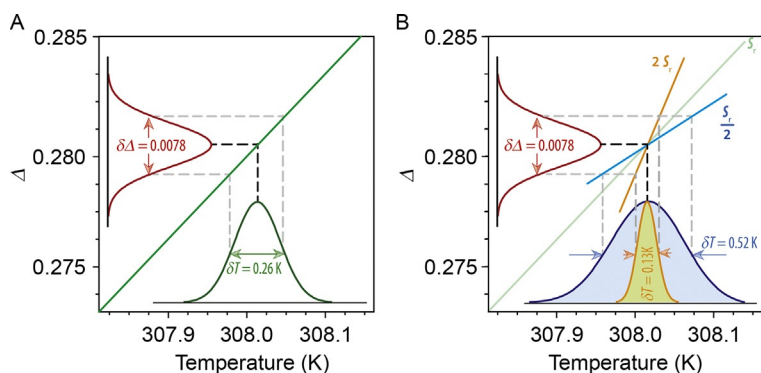
FIG. 4 Estimating δT by the readout fluctuations of a luminescent thermometer, example of an aqueous suspension (0.30 g L^{-1}) of NaYF$_4$:Yb^{3+}/Er^{3+} NPs, synthesized as described in Xie et al. (2013) and kindly providing by Prof. Dr. X. Liu from the National University of Singapore. (A) To get δT estimation we build the histogram of the $\varDelta$ and T measurements. The *black and gray interrupted lines* mark the position of the maximum and the standard deviation of the distributions, respectively. The conversion between the thermometric parameter and temperature is made using the calibration curve represented by the *solid green (dark gray in the print version) line*. In (B) we show that, if the sensitivity is decreased by half or increased twice, the resulting δT displays the opposite trend (increases twice or decreases by half, respectively).
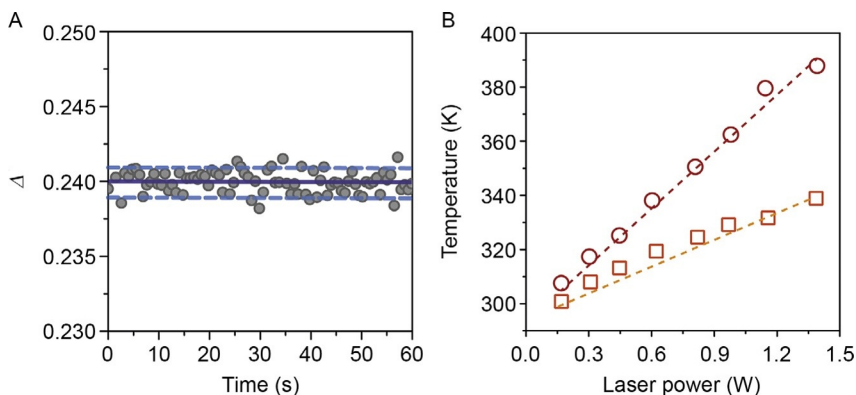
FIG. 5 (A) UV-excited [(Tb$_{0.914}$Eu$_{0.086}$)$_2$(PDA)$_3$(H$_2$O)]·2H$_2$O MOF (Wang et al., 2015c) under continuous exposition (365 nm, 30 μW cm^{-2}) presenting no drifts on the thermometric parameter, which indicates that the ligand-induced Stokes shift does not induce measurable local heating. The *solid line* corresponds to the mean $\varDelta$ at 298 K and the *interrupted lines* mark the region within $\pm$ the standard deviation of the measurement (2.6 K). (B) 808 nm laser-induced heating produced in LaF$_3$:Yb^{3+}/Er^{3+} (*orange (gray in the print version) squares*) and LaF$_3$:Yb^{3+}/Er^{3+}/Nd^{3+} (*red (dark gray in the print version) squares*) NPs as a function of the laser power. The *dots* are the experimental data and the *dashed lines* are guide for the eyes. The temperature was measured imaging the powder sample with an IR camera. Notice the higher augmentation of the temperature registered for the Nd^{3+} containing NPs. *Adapted with permission from Ximendes, E.C., Rocha, U., Jacinto, C., Kumar, K.U., Bravo, D., Lopez, F.J., Rodriguez, E.M., Garcia-Sole, J., Jaque, D. 2016. Self-monitored photothermal nanoparticles based on core–shell engineering. Nanoscale 8, 3057–3066. © 2016 The Royal Society of Chemistry.*

We should note, however, that recording a set of temperature readouts with statistical significance might not be always feasible. For instance, to record with high-resolution spectral region requested to define Δ, PMT detectors take typically one minute, which makes the evaluation of temporal fluctuations in temperature unpractical. Then, to overcome this limitation, δT can be computed using Eq. (7), with the relative uncertainty on Δ estimated through the integrated area of the transitions ($\delta I/I$). The typical $\delta\Delta/\Delta$ values reported in Table 2 should not be used as they correspond to the lower uncertainty limit (maximum SNR operating conditions). In generally, the detector operates above that maximum and, thus, the $\delta\Delta/\Delta$ values are always higher (eg, 0.5–2.5%) that those reported in the table. When the calibration curve is provided $\delta\Delta/\Delta$ is assessed as the root mean square value of the deviations, otherwise we have:

$$\frac{\delta\Delta}{\Delta}=\sqrt{\left(\frac{\delta I_1}{I_1}\right)^2+\left(\frac{\delta I_2}{I_2}\right)^2} \tag{9}$$

where $\delta I_i/I_i$ ($i=1, 2$) is estimated using the SNR values. Typically, dividing the readout fluctuations of the baseline by the maximum intensity value allows one to estimate the order of magnitude of $\delta I_i/I_i$. Assuming that the relative uncertainties on I_1 and I_2 are similar, we have:

$$\frac{\delta\Delta}{\Delta}=\sqrt{2}\frac{\delta I}{I} \tag{10}$$

Thus, to evaluate the error in temperature determination we use the thermal dependence of S_r (Eq. 7) and the SNR of the spectra, resulting in:

$$\delta T=\frac{\sqrt{2}}{S_r}\frac{\delta I}{I} \tag{11}$$

The error in the determination of the temperature uncertainty ($\sigma_{\delta T}$) can be accessed by calculating the error propagation for S_r and $\delta I/I$:

$$\frac{\sigma_{\delta T}}{\delta T}=\sqrt{\left(\frac{\sigma_{S_r}}{S_r}\right)^2+\left(\frac{\sigma_{\delta I/I}}{\delta I/I}\right)^2}\approx\frac{\sigma_{S_r}}{S_r} \tag{12}$$

considering that $\sigma_{\delta I/I}$ is negligible relatively to σ_{S_r}. The error in S_r is then given by:

$$\sigma_{S_r}=\sqrt{\left(\frac{\partial S_r}{\partial S_a}\sigma_{S_a}\right)^2+\left(\frac{\partial S_r}{\partial\Delta}\sigma_\Delta\right)^2}=S_r\sqrt{\left(\frac{\sigma_{S_a}}{S_a}\right)^2+\left(\frac{\sigma_\Delta}{\Delta}\right)^2} \tag{13}$$

where

$$\frac{\sigma_{S_a}}{S_a}=\sqrt{\left(\frac{\sigma_\Delta}{\Delta}\right)^2+\left(\frac{\sigma_{T_c}}{T_c}\right)^2} \tag{14}$$

Assuming that the error in the calibration temperature determination (σ_{T_c}) is negligible and the error in Δ is similar to its uncertainty, we get:

$$\frac{\sigma_{S_a}}{S_a} = \frac{\sigma_\Delta}{\Delta} \approx \frac{\delta\Delta}{\Delta} \tag{15}$$

and, thus, Eq. (13) becomes:

$$\frac{\sigma_{S_r}}{S_r} = \sqrt{2}\frac{\delta\Delta}{\Delta} \tag{16}$$

Finally, substituting Eq. (16) into Eq. (12), leads to:

$$\frac{\sigma_{\delta T}}{\delta T} = \sqrt{2}\frac{\delta\Delta}{\Delta} = 2\frac{\delta I}{I} \tag{17}$$

That means that the relative error on the temperature uncertainty is essentially determined by $\delta I/I$.

3.2.3 Temperature Uncertainty and Thermometer Size

A recent quantification of δT for distinct classes of nanothermometers (fluorescent polymers and proteins, CdSe QDs, and nanodiamonds) was recently done considering size and system-dependent properties and the spin-boson model (Alicki and Leitner, 2015):

$$\delta T = \left(\frac{4T}{3\sqrt{3}T_D}e^{3T_D/8T}\right)\frac{1}{\sqrt{N_a}}T \tag{18}$$

where N_a is the number of atoms in the sample and T_D its Debye temperature. For T_D in the range 100–2000 K, the term in parenthesis changes between 0.9 and 1.3 and

$$\delta T \approx \frac{1}{\sqrt{N_a}}T \tag{19}$$

For these authors, δT is termed "accuracy" in the sense that it represents how close a measured value is to the actual (true) value. Accuracy is defined in terms of systematic errors and should not be confused with precision that represents how close the measured values are to each other (random errors). Both for fluorescent organic- (with green fluorescent protein, GFP) and solid-state-based thermometers (with nanodiamonds or CdSe QDs) the model predicts an accuracy in accord with the experimental measurements, about 0.5 K for GFP (Takei et al., 2014), 44×10^{-3} K for nanodiamonds (Kucsko et al., 2013), and 0.6 K for CdSe QDs (Yang et al., 2011). Moreover, the system dimension determines the lowest temperature change that is possible to measure and in practice δT is controlled by the radius, r, of the thermometer, and varies as $r^{-3/2}$ (Alicki and Leitner, 2015). For instance, considering the criteria of temperature uncertainty referred earlier for portable ($\delta T < 0.5$ K)
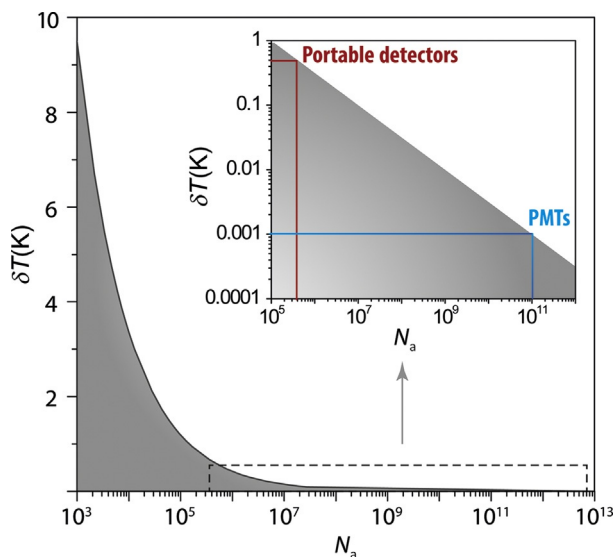
FIG. 6 Temperature uncertainty estimated from Eq. (19) for $T = 300$ K. The *gray shadowed area* represents the temperature uncertainty below the minimum values resulting from the spin-boson model (Alicki and Leitner, 2015). The *inset* shows a magnification of the region of $\delta T < 0.5$ K where the values assigned to portable detectors and PMTs are highlighted and the corresponding numbers of particles given.

and more sensitive detectors ($\delta T < 0.001$ K) at 300 K, we find $N_a > 3 \times 10^5$ and $N_a > 1 \times 10^{11}$, respectively, for the minimum number of atoms constituting the thermal probe (Fig. 6).

The model was also tested for $(Gd_{0.991}Nd_{0.009})_2O_3$ nanorods (Balabhadra et al., 2015). A temperature uncertainty of $\delta T = 0.14 \pm 0.05$ K (at 288 K) was calculated using the relative sensitivity and the $\delta\Delta/\Delta$ value, Eq. (7), while the value estimated with Eq. (18), $T_D = 362$ K and $N_a = (1.5 \pm 0.5) \times 10^5$, is $5 \times$ larger (Balabhadra et al., 2015). We emphasize that the number of atoms in a single nanorod is sufficient to assure, in the due time, equilibrium for any state function to be measured. Moreover, the calculus using Eq. (7) takes into account not a single NP but an ensemble of nanorods in thermal contact. In fact, considering 20–30 nanorods in contact, as shown in Fig. 2A of the reference, the agreement between theoretical (0.14–0.18 K) and experimental (0.16 K) uncertainties is very good and the theoretical temperature uncertainty (Eq. 7) should be the upper limit of the experimental temperature error.

3.3 Spatial and Temporal Resolution

When the temperature is measured in different spatial positions, the spatial resolution of the measurement (δx) is defined as the minimum distance

between points presenting a temperature difference higher than δT (or, equivalently, higher than the thermometer's sensitivity, Eq. 4) (Kim et al., 2012):

$$\delta x = \frac{\delta T}{|\vec{\nabla} T|_{max}} \qquad (20)$$

where $|\vec{\nabla} T|_{max}$ is the maximum temperature gradient of the mapping. For a one-dimensional temperature profile the temperature gradient is $|\vec{\nabla} T|_{max} = |dT/dx|_{max}$.

The temporal resolution of the measurement (δt) is the minimum time interval between measurements presenting a temperature difference higher than δT:

$$\delta t = \frac{\delta T}{|dT/dt|_{max}} \qquad (21)$$

where $|dT/dt|_{max}$ is the maximum temperature change per unit of time.

Both temporal and spatial resolutions are important to evaluate the applicability of a thermometer for dynamic temperature measurements. The technological areas with the highest spatiotemporal temperature discrimination demands are micro and optoelectronics, microelectromechanical (MEM) machines, memory chips, and Si-based biological sensors (Tao et al., 2012).

The spatial resolution of luminescent thermometers (Eq. 20) can be improved either by decreasing the temperature uncertainty or by increasing the measured temperature gradient. The first approach requires the use of lower noise detectors (eg, cooled detectors or PMTs, see Section 3.2.1). The increasing of the temperature gradient can be achieved either by increasing the value of the temperature step or by mapping with low scanning steps.

3.3.1 Comparison of Spatial and Temporal Resolutions from Different Techniques

The spatial and temporal resolutions (δx and δt) of luminescent thermometers were calculated in a handful of reports mapping the surface of thermographic films using optical fibers or scanning thermal microscopy (SThM) incorporating a fluorescent probe in the scanning tip. These values are compared with those obtained using other (nonluminescent) noncontact techniques, such as thermoreflectance and Raman spectroscopy (Fig. 7).

The use of SThMs adapted for fluorescence reading, by incorporating a fluorescent probe in the scanning tip, was initially reported by Aigouy et al. (Aigouy et al., 2005, 2009, 2011; Saïdi et al., 2009, 2011) to work in the subwavelength spatial resolution regime. Regarding high-resolution thermal imaging of integrated circuits, Saïdi et al. (2011) used a Yb^{3+}/Er^{3+}-doped PbF_2 nanocrystal as temperature sensor. The technique presents temperature uncertainty ~1.0 K, spatial resolution of 0.027 µm, despite the relatively long acquisition times (100 ms per pixel), that invalidates the transient mapping of
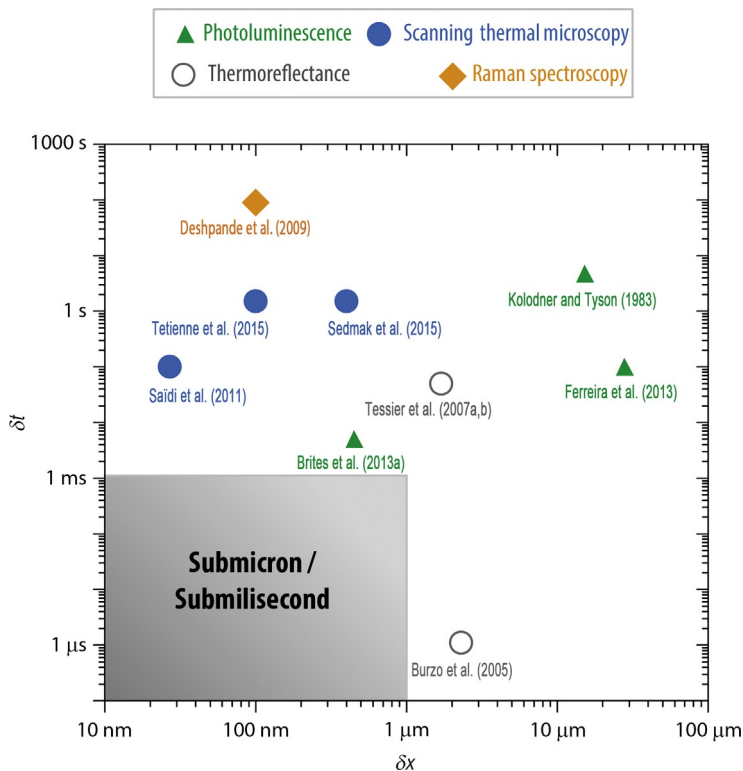
FIG. 7 Spatiotemporal resolution of noncontact thermometers. *Adapted with permission from Brites, C.D.S., Lima, P.P., Silva, N.J.O., Millán, A., Amaral, V.S., Palacio, F., Carlos, L.D. 2013a. Organic–inorganic Eu^{3+}/Tb^{3+} codoped hybrid films for temperature mapping in integrated circuits. Front. Chem. 1, 9.*

the device (Saïdi et al., 2011). In Section 5, we will discuss some examples of Yb^{3+}/Er^{3+}-doped UCNPs.

Very recently, the use of negatively charged nitrogen vacancy for SThM was reported by Tetienne et al. (2016). The spin of the nitrogen vacancy can be used as a sensitive thermometer by relying on the temperature dependence of the crystal field splitting parameter. The authors mapped the temperature of a plasmonic heated gold NP with a temperature uncertainty $\delta T = 30$ K and a spatial resolution of 0.1 μm. The temporal resolution of the measurement is defined by the pixel integration time (1.5 s) preventing the monitoring of the photodynamic heating process (Tetienne et al., 2016). Sedmak et al. incorporated in the scanning probe a Yb^{3+}/Er^{3+} transparent glass ceramic and a GFP (Sedmak et al., 2015). The transient heat-conduction experiments were performed in the 273–423 K range. A spatial resolution of 400 nm was achieved across an approximately 200×200 μm^2 field of view at an imaging frequency of 7 Hz, corresponding to a temporal resolution of $\delta t = 0.14$ s (Sedmak et al., 2015).

The seminal work of Kolodner and Tyson (1983) demonstrated the potential of noncontact Ln^{3+}-based thermometry to map integrated circuits. The authors reported the temperature mapping of a metal–oxide semiconductor field effect transistor (MOSFET) through the emission of a polymer film containing [Eu(tta)$_3$·2H$_2$O]. Based on shot noise of the collected light, a temperature uncertainty as low as 0.01 K was expected. However, experimental conditions (such as electric fluctuations of detection system) degrade this limit to the 0.1–1.0 K range. The spatial resolution is limited by the CCD smoothing to 15 μm and the temporal resolution by the exposure time of the camera, 5 s (Kolodner and Tyson, 1983).

Brites et al. reported the fabrication of diureasil films incorporating [Eu(btfa)$_3$(MeOH)(bpeta)] and [Tb(btfa)$_3$(MeOH)(bpeta)] complexes for temperature mapping in wired-board circuits. The films allowed temperature mapping with $\delta x = 34$ μm (Brites et al., 2010). A subsequent modification in the films production to include maghemite NPs increased the temperature gradient profile 10-fold, with concomitant improvement of the spatial resolution by an order of magnitude, $\delta x = 3.4$ μm (Brites et al., 2013c). In the Tb^{3+}/Eu^{3+}-doped diureasil films without maghemite NPs improving of the spatial resolution up to 0.42 μm was also achieved by decreasing the scanning step from 800 to 50 μm. For these films, the temporal resolution was computed as $\delta t = 4.8$ ms (Brites et al., 2013a). Afterward, analogous Tb^{3+}/Eu^{3+}-doped diureasil films were used to recover a Mach–Zehnder interferometer (Ferreira et al., 2013). This optoelectronic device operates with a temperature difference between the arms of ~ 1 K that results in a spatial resolution of $\delta x = 28$ μm. The temporal resolution of the measurement is of the order of the integration time of the detector (100 ms). In Section 5, we will address the thermometric features of diureasil films incorporating [Ln(btfa)$_3$(MeOH)(bpeta)] (Ln = Eu, Tb) complexes in more details.

Thermoreflectance thermal imaging is an optical technique for measuring, with external illumination, the relative change in surface reflectivity as a function of temperature (Burzo et al., 2005; Farzaneh et al., 2009; Kim et al., 2014). Burzo et al. used the thermoreflectance of a MOSFET device to map the temperature in a window of 15×50 μm^2, with uncertainty of 2.6 K and a spatiotemporal resolution of 2.3 μm–1.1 ms (Burzo et al., 2005). Using the transparency of a Si substrate in the NIR spectral region, Tessier et al. recorded a backside temperature map of a MOSFET with $\delta x = 1.7$ μm and $\delta t = 50$ ms, defined by the camera triggering (Tessier et al., 2007a).

Raman spectroscopy is an optical technique that uses the vibrational, rotational, and other low-frequency modes for temperature measurement (Beechem et al., 2007). In 2009, for instance, Deshpande et al. used the temperature-dependent spatially resolved Raman peak shift of a single suspended carbon nanotube (CNT) under electrical heating (Deshpande et al., 2009). The reduced temporal resolution of the measurement (set by the integration time, 60–120 s) and the temperature uncertainty ($\delta T \sim 10$ K) are balanced by the remarkable 0.1 μm spatial resolution. More recently,

Wang et al. used the same technique to evaluate the convective heat transfer coefficient of a suspended CNT with temperature uncertainty $\delta T \sim 4$ K and spatial resolution $\delta x = 0.05$ μm (Wang et al., 2013a).

The major outcome of the spatiotemporal resolution comparison performed in Fig. 7 is that there is not a single technique able to combine submicron and submillisecond resolutions. If a particular application requires high spatial resolution (<1 μm) and, simultaneously, a temporal resolution around 1 s, SThM is clearly the best suited technique. On the other hand, if the application demands a high temporal resolution ($<10^{-3}$ s) but can deal with spatial resolutions >1 μm, thermal reflectance is the more appropriate option. The combination of high spatial and temporal resolutions in the same technique remains a challenge, but we must stress that, up to now, the examples that have the best performance are those based on luminescent Ln^{3+}-doped organic–inorganic hybrid thermometers.

3.4 Repeatability and Reproducibility

Repeatability (or test–retest reliability) and reproducibility are the two components of precision in a measurement system, being major concerns among sensor engineering. Since the great majority of industrial and scientific applications require continuous monitoring, it is critical to achieve the same response under the same external stimulus. The terms "agreement," "reliability," "reproducibility," "accuracy," and "repeatability" are used with varying degrees of consistency in the scientific literature. The terminology adopted in this section follows the pivotal work of Bland and Altman in the context of clinical trials (Bland and Altman, 1986).

Repeatability refers to the variation in repeat measurements made under identical conditions. A given quantity is considered repeatable if different measurements made using the same instrument or method, over a certain period, give the same result. Variability in measurements made on the same subject in a repeatability study can then be ascribed only to errors due to the measurement process itself (Bartlett and Frost, 2008).

Reproducibility, on the other hand, refers to the variation in measurements of the same measurand carried out under modified conditions (Taylor and Kuyatt, 1994). The changing conditions may be due to different measurement methods or instruments being used, measurements being made by different observers, or measurements being made over a period of time within which the "error-free" level of the measurand could undergo nonnegligible change (Bartlett and Frost, 2008).

The repeatability of a thermometric probe indicates the accord between its ability to evaluate the temperature in comparison with a reference temperature probe (a thermocouple, for instance). If a probe method has poor thermal repeatability (ie, if there is a considerable variation in repeated measurements on the same temperature value) the agreement between the two probes is unavoidably degraded. According to the British Standards Institution, an
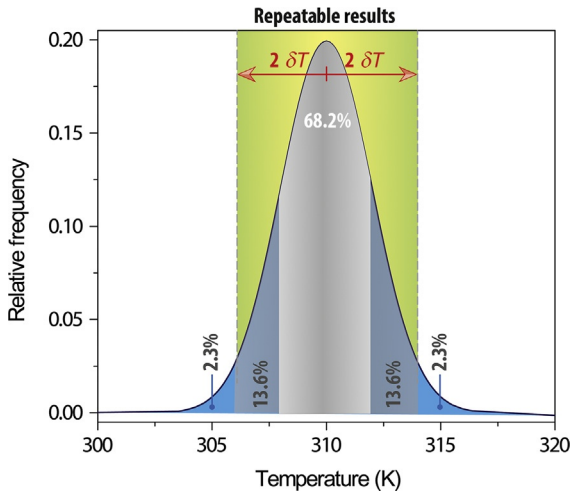
FIG. 8 The repeatability of a temperature measurement corresponds to compute the deviation relatively to the average measured temperature. If the distance to the mean temperature value is lower than $2\times$ the standard deviation of the data, this value is considered as a repetition of the mean value.

acceptable repeatability coefficient can be obtained when the deviation relative to the average measured temperature is lower than $2\times$ the standard deviation of the data (assumed here as δT)[2] (Fig. 8). This criterion ensures that, for stochastic processes, 95% of the measurements are less than two standard deviations away from the mean value of temperature.

In a typical procedure, the repeatability of a thermal probe is estimated by cycling the temperature in a given interval, ensuring that each measurement is performed with the probe in thermal equilibrium with the temperature controller (Fig. 9). The repeatability of a thermometer's readout upon temperature cycling is quantified using the expression:

$$R = 1 - \frac{\max\left(|\Delta_c - \Delta_i|\right)}{\Delta_c} \quad (22)$$

where Δ_c is the mean thermometric parameter (extracted from the calibration curve) and Δ_i is the value of each measurement of the thermometric parameter. Usually, 10 consecutive measurements are enough to have a minimal statistical significance of the computed results. For example, repeatability (expressed as a percentage) larger than 99.1% upon temperature cycling in a given range in 10 consecutive temperature cycles means that the maximum experimental deviation during the thermal cycling experiment is lower than 0.9% (Fig. 9). Notice that the maximum absolute deviation value and the

---

2. Accordingly to the International Standard ISO 5725-1: Accuracy (trueness and precision) of measurement methods and results—Part 1: General principles and definitions.
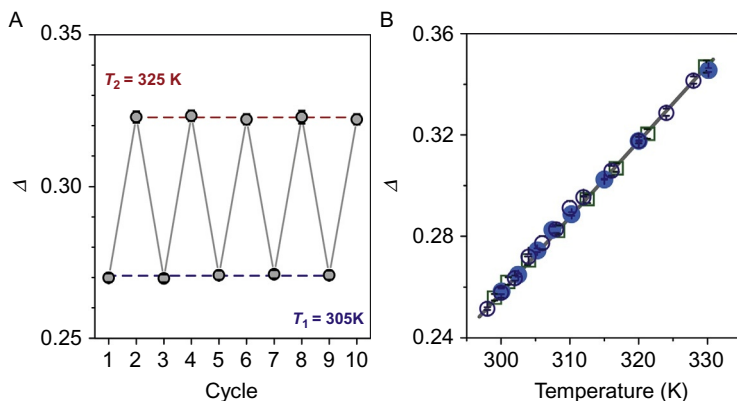
FIG. 9 Evaluating the reproducibility and repeatability of a luminescent thermometer readout, example of an aqueous suspension $(0.30 \, \mathrm{g \, L}^{-1})$ of NaYF$_4$:Yb^{3+}/Er^{3+} NPs, synthesized as described in Xie et al. (2013) and kindly providing by Prof. Dr. X. Liu from the National University of Singapore. (A) Thermometric parameter recorded in 10 heating–cooling temperature cycles showing reproducibility higher than 99.1% (Eq. 22). (B) Values obtained using different detectors (*open* and *filled circles*) and using the same detector in different days (*open squares*). The *error bars* represent $\delta\Delta$ and the *solid line* the calibration curve (built using any of the calibration runs, within the uncertainty of the fitting parameters).

temperature uncertainty must be compatible; otherwise the calibration procedure and/or the temperature uncertainty have been wrongly estimated.

Another key feature of the thermometer readout is the ability to reproduce the same results, even when different detectors are employed or the measurements are made in different days. Although the reproducibility of a thermometer cannot be numerically quantified, statistical analysis may be used to evaluate if distinct calibration procedures are significantly different. If the same calibration curve can be obtained in different measurements, within the resulting experimental uncertainty of the fitting parameters, we must conclude than the thermometer produces reproducible readouts under the tested conditions.

4 THERMAL RESPONSE RATIONALIZING

In general, the thermometric systems can be classified as primary or secondary. Primary thermometers are characterized by a well-established state equation that directly relate a particular measured value to the absolute temperature without the need of calibration, while secondary thermometers must be referred to a well-known temperature for their calibration (Brites et al., 2012). This might be a limitation when the thermometers are used in a different medium than that in which they were calibrated. The usual calibration procedure requires an independent measurement of the temperature (using, for instance, a thermocouple or an IR camera) to allow its conversion to luminescence intensity ratio, implying that a new calibration procedure is

required whenever the thermometer operates in a different medium. However, if this is not always possible (eg, at the submicrometric scale) a single calibration is assumed to be valid independently of the medium. Primary thermometers, on the contrary, overcome this limitation since the calibration factor can be computed whenever the thermometer operates in different media, as it depends on easily obtainable spectroscopic quantities. This is an obvious advantage making them ideal for temperature sensing at the nanoscale, although very few examples are reported so far. An interesting example is the single-center-based thermometers where the temperature is calculated by the ratio of the emission intensities of two distinct transitions from the same emitting center that can be rationalized assuming the simplest model of Boltzmann thermal equilibrium between two emitting states (Section 4.1). Another remarkable case comprises thermally excited state absorption in the Eu^{3+} ion in which Δ is defined by the variation of the intensity of the $^5D_0 \rightarrow {}^7F_4$ transition following direct excitation of the emitting $^5D_0$ level from specific $^7F_1$ or $^7F_2$ Stark components, thermally populated with respect to the $^7F_0$ nondegenerate ground state (Souza et al., 2016).

For secondary thermometers, two major trends for the temperature evolution of the thermometric parameter can be identified (Fig. 10):

- Emission arising from a single center, modeled by an exponential curve.
- Emission arising from two different centers, modeled by a sigmoidal (S-shaped) curve.

In fact, exponential curves are observed when I_1 and I_2 (Eq. 1) correspond to transitions of the same emitting center, whereas the S-shaped curve appears when the host matrix or the ligands play an important role in the energy transfer mechanisms. Whereas for the first group calibration is independent of the host material, in the second case the matrix can tune the thermometer's sensitivity (Brites et al., 2016; León-Luis et al., 2012). In Sections 4.1 and 4.2, single- and dual-center emissions will be addressed in detail.

Ratiometric luminescent thermometers

Single center

$$\frac{N_2}{N_1} = B \exp\left(-\Delta E / k_B T\right)$$

Dual center

$$\frac{N_2}{N_1} = \frac{A}{1 + \alpha \exp\left(-\Delta E / k_B T\right)}$$
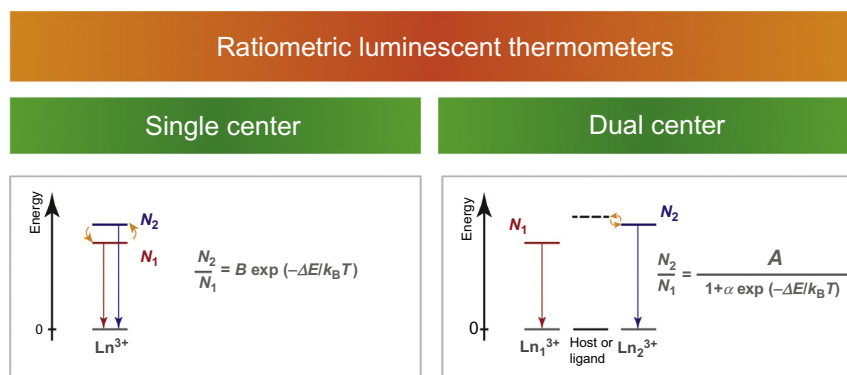
FIG. 10 Classification of ratiometric luminescent thermometers in single- and dual-center emissions.

4.1 Single-Center Emission

The ratio of the emission intensities of two distinct transitions from the same emitting center provides a robust temperature measurement approach, as mentioned earlier. The most common examples of Ln^{3+}-based ratiometric thermometers comprise Yb^{3+} ions as sensitizers and Er^{3+} (Alencar et al., 2004; Savchuk et al., 2014; Sedlmeier et al., 2012; Singh et al., 2009a, 2014; Vetrone et al., 2010a), Tm^{3+} (Dong et al., 2011; Lojpur et al., 2013; Pereira et al., 2015; Quintanilla et al., 2015; Sedlmeier et al., 2012), or Ho^{3+} (Lojpur et al., 2013; Savchuk et al., 2015; Sedlmeier et al., 2012; Xu et al., 2013) as upconverter activators. In fact, Maestro et al. demonstrated that $NaYF_4$:Yb/Er UCNPs are the most efficient multiphoton excited fluorescent NPs developed to date, displaying larger relative multiphoton excited upconversion efficiency (laser excitation intensities between 2×10^3 and 1×10^6 W cm^{-2}) compared with those of commercial QDs (approximately $2 \times$ larger) and Au nanorods (almost $10 \times$) presently used for multiphoton fluorescence bioimaging (Maestro et al., 2010b).

Less common examples involving Eu^{3+} (Meert et al., 2014; Yuasa et al., 2014), Nd^{3+}, using two Stark components of the $^4F_{3/2}$ multiplet (Benayas et al., 2015; Carrasco et al., 2015; Rocha et al., 2013, 2014a; Tian et al., 2014; Wawrzynczyk et al., 2012) or the $^4F_{5/2}$, $^4F_{3/2} \rightarrow ^4I_{9/2}$ transitions (Balabhadra et al., 2015; Tian et al., 2014), Pr^{3+} (Zhou et al., 2014b), Sm^{3+} (Dramićanin et al., 2014), Dy^{3+} (Boruc et al., 2012; Edge et al., 2000), and Gd^{3+} (Zheng et al., 2013) were also reported. Illustrative examples of these luminescent thermometers are addressed in detail in Section 5.

4.1.1 Boltzmann Law

The use of single-center luminescence line intensities as the thermometric parameter was described by Kusama et al. (1976) in a seminal work; for a review of the technique, see Collins et al. (1998) and Wade et al. (2003). The ratio of two energy-close emission intensities can be rationalized assuming the simplest model of Boltzmann thermal equilibrium between two emitting states, denoted by $|1>$ and $|2>$, where W_{10} is the absorption rate from the ground state $|0>$ to state $|1>$ and the I_{0i} ($i=1, 2$) intensity (Fig. 11) is:

$$I_{0i} \propto \hbar \omega_{0i} A_{0i} N_i \qquad (23)$$

where A_{01} and A_{02} and ω_{01} and ω_{02} are, respectively, the total spontaneous emission rates and the angular frequencies of the $1 \rightarrow 0$ and $2 \rightarrow 0$ transitions, and N_1 and N_2 are the populations of states $|1>$ and $|2>$.

If these two levels are in thermal equilibrium (they are designated by "thermally coupled levels," with separations of the order of the thermal energy), N_1 and N_2 are related by:

$$N_2 = N_1 \left(\frac{g_2}{g_1} \right) \exp \left(\frac{-\Delta E}{k_B T} \right) \qquad (24)$$
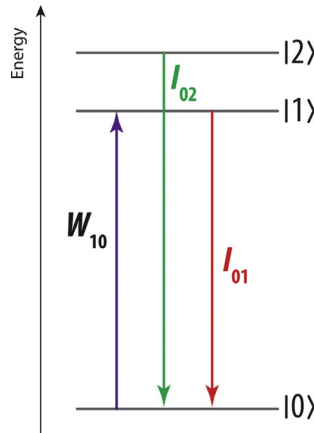
FIG. 11 Schematic energy-level diagram of the three-level model of a typical luminescent ion.

where g_1 and g_2 are the degeneracies of the 1 and 2 levels, ΔE is the energy difference between the barycenters of the $2 \rightarrow 0$ and $1 \rightarrow 0$ emission bands. The $2 \rightarrow 0$ ($I_{02} \equiv I_2$) and $1 \rightarrow 0$ ($I_{01} \equiv I_1$) intensity ratio (Δ) is given by:

$$\Delta = \frac{I_{02}}{I_{01}} = \frac{\hbar\omega_{02}A_{02}N_2}{\hbar\omega_{01}A_{01}N_1} = \frac{\omega_{02}A_{02}g_2}{\omega_{01}A_{01}g_1}\exp\left(-\frac{\Delta E}{k_BT}\right) = B\exp\left(-\frac{\Delta E}{k_BT}\right) \quad (25)$$

with

$$B = \frac{\omega_{02}A_{02}g_2}{\omega_{01}A_{01}g_1}.$$

The two levels cannot be too far apart, otherwise thermalization is no longer observed. For ΔE ranging from 200 to 2000 cm^{-1} the difference in the population of the emitting levels is such that they are considered "thermally coupled." These empirical limits guarantee that the levels are spectrally separated and not too far away so that the exponential temperature decay rate (determined by ΔE) is small (Khalid and Kontis, 2009). The response of the detection system in the frequency range of the two transitions was taken into account in the I_1 and I_2 intensities. The absolute temperature is then estimated from:

$$T = \frac{\Delta E}{k_B}\frac{1}{\ln(B/\Delta)} \quad (26)$$

in which ΔE is calculated using the formal definition of the barycenter of a J–J' transition or, when there are experimental difficulties in assigning precisely the Stark–Stark transitions, by fitting the envelope of the I_1 and I_2 transitions (Balabhadra et al., 2015). The constant B can be determined from the plot of Δ vs pump power extrapolating the curve (that is generally linear for laser power densities of 100–300 W cm^{-2}) to the limit of zero pump power ($\Delta \equiv \Delta_0$) corresponding to room temperature (Carlson et al., 2011; Debasu et al., 2013). Fig. 12A and B illustrates how the constants ΔE and B are
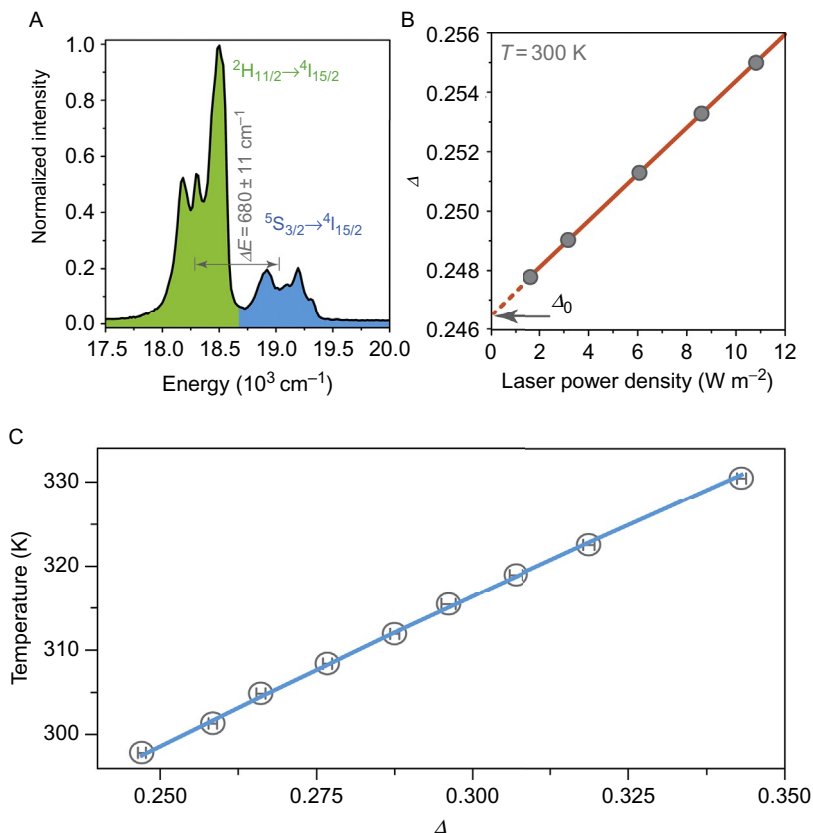
FIG. 12 (A) Determination of ΔE in an aqueous suspension of NaYF$_4$:Yb^{3+}/Er^{3+} NPs. The barycenter of each transition was determined using the procedure described in Section 4.1.1. (B) Determination of constant B in the same NPs via the plot of Δ vs laser power density. The *solid line* is the best fit to the experimental points ($r^2 > 0.998$). The value of Δ at no-laser excitation ($T = 300$ K), $\Delta_0 = 0.2465 \pm 0.0001$, was determined from the intercept of the fitting curve. The constant $B = 6.42 \pm 0.02$, computed from Eq. (26) with $T = 300$ K and $\Delta = \Delta_0$, is in agreement with previous reports, ie, $4.48 \leq B \leq 12.18$ (Debasu et al., 2013; Singh et al., 2010; Tikhomirov et al., 2009; Wang et al., 2007). (C) Computed temperature using Eq. (26), with $\Delta E = 680$ cm^{-1} and $B = 6.42$ (*solid line*), and comparison with the corresponding thermocouple readout (*open points*). The thermocouple error (not represented) is 0.1 K, whereas the *horizontal error bars* correspond to the error in the determination of Δ.

determined for an aqueous suspension (0.30 g L^{-1}) of NaYF$_4$:Yb^{3+}/Er^{3+} NPs, kindly providing by Prof. Dr. X. Liu from the National University of Singapore following a synthesis process described in Xie et al. (2013). When these parameters are determined independently of Eq. (25), the temperature can be estimated directly by Eq. (26), without needing any calibration, and the thermometer can be classified as a primary thermometer. Fig. 12C compares for the aqueous suspension of the NaYF$_4$:Yb^{3+}/Er^{3+} NPs the temperature

measured with a thermocouple immersed into the suspension and the temperature calculated using Eq. (26). We observe a perfect match between the two temperatures indicating that the local heating induced by the laser on the NPs is unimportant at this concentration and laser power density (1.6 W cm^{-2}).

4.1.2 Boltzmann Law for Overlapped Transitions

In the literature, we found several examples in which the temperature dependence of the intensity ratio of two-overlapped transitions was modeled through a slightly different form of Eq. (25):

$$\Delta = B \exp\left(-\frac{\Delta E}{k_B T}\right) + C \tag{27}$$

where C is a constant. These examples comprise either two Stark components of the same Ho^{3+} level (Savchuk et al., 2015) or two distinct transitions of Tm^{3+} (Xing et al., 2015; Xu et al., 2012; Zhou et al., 2014a), Fig. 13.

In general, the arguments used to apply Eq. (27) are based on the work developed by Wade et al. for optical fiber-based thermometers (Wade et al., 2003) in which:

$$\Delta = \left(\frac{n_2}{n_1}\right) B \exp\left(\frac{-\Delta E}{k_B T}\right) + \left(\frac{m_1}{n_1}\right) \tag{28}$$

where n_i (lower level $i=1$ and upper level $i=2$) defines the fraction of the total intensity of the transition originating from level i effectively measured by the detector for the i level and m_i defines the fraction of the total intensity from level i which is measured by the detector for the other thermalizing level (Wade et al., 2003). We should stress, however, that Wade's work addressed the problem of how to include intensities measured by two detectors with overlapped spectral ranges in Eq. (25), a limitation that does not occurs in the works mentioned earlier when the emission spectrum is measured by a single detector.

Although the use of Eq. (27) is being increasingly disseminated, we must draw attention on the fact that it underestimates S_r, as we will show next. Taking the example of NaYF$_4$:Yb^{3+}/Tm^{3+}@Pr^{3+} core–shell NPs (Zhou et al., 2014d), we can access to the integrated intensities of each transition without the overlap contribution fitting the emission spectrum to a set of Gaussian (or Lorentzian) functions, a routine procedure that overcomes the experimental difficulties in assigning precisely all the Stark components. For the spectrum recorded at 510 K (the one in which the overlap is more evident, Fig. 13A), we used four Gaussian peaks to reproduce the envelope of the $^1G_4 \rightarrow {}^3F_4$ and $^3F_{2,3} \rightarrow {}^3H_6$ Tm^{3+} transitions (Fig. 13B). The good agreement obtained between the ΔE value resulting from the barycenter of the deconvoluted transitions (2425 ± 15 cm^{-1}) and that reported by Bai et al. in LaF$_3$:Yb^{3+}/Tm^{3+} (1894–2635 cm^{-1}) (Bai et al., 2012) supports the procedure.
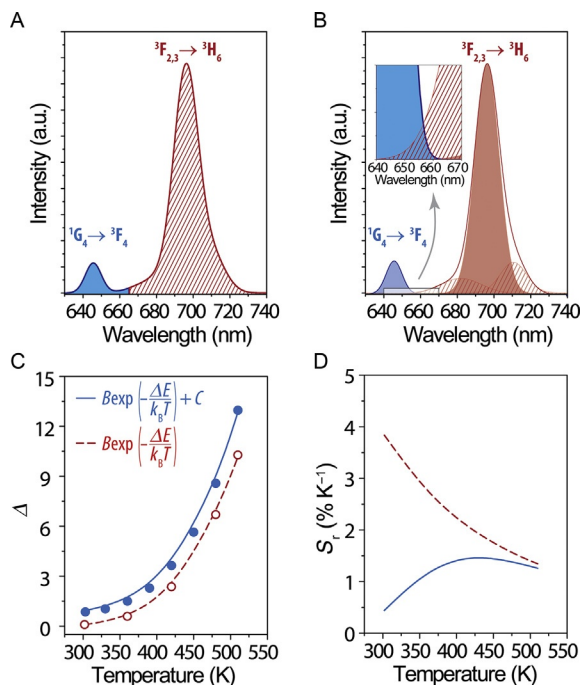
FIG. 13 (A) Overlap between the $^1G_4 \to {}^3F_4$ and $^3F_{2,3} \to {}^3H_6$ Tm^{3+} transitions in NaYF$_4$:Yb^3 $^+$/Tm^{3+}@Pr^{3+} core–shell NPs (980 nm excitation, 510 K) (Zhou et al., 2014a). The thermometric parameter is defined by integrating the emission spectrum between 625 and 665 nm (I_1) and between 655 and 740 nm (I_2). (B) Fit of the emission spectrum displayed in (A) using four Gaussians (three for $^3F_{2,3} \to {}^3H_6$ and one for $^1G_4 \to {}^3F_4$) to compute a new thermometric parameter using the fitted peak areas. (C) The calibration curves reported by Zhou et al. (2014a) (*solid circles*) and that computed using the ratio of the areas of the corresponding Gaussian peaks (*open circles*) are identical, apart from a vertical shift (different B values). The *solid* and *interrupted lines* correspond, respectively, to the best fit to data using Eq. (27) (as reported) and Eq. (25) ($r^2 > 0.998$). (D) The relative sensitivity computed using the different calibration curves converge for $T > 450$ K. For lower temperatures, however, the reported procedure (Zhou et al., 2014a) significantly underestimates the relative sensitivity.

The next step is to calculate the integrated area of each transition by the area of the sum of the Gaussians, for each spectrum recorded at different temperatures. As outcome, we are able to compute Δ, according to Eq. (1), and build a new calibration curve, which is vertically shifted from that reported by the authors (Fig. 13C). Fitting the calculated Δ to Eq. (25) gives $B = 9806$ and $\Delta E = 2431$ cm^{-1} ($r^2 > 0.998$). In comparing the sensitivity values resulting from the fitting to Eqs. (25) and (27), we realize that the latter underestimates the sensitivity, especially for lower temperatures (Fig. 13D). For this reason, we advocate the use of Eq. (25) instead of Eq. (27) that produces higher sensitivity values making clear the comparison between the different emitting centers, independently of the transitions overlap. This is exactly what was
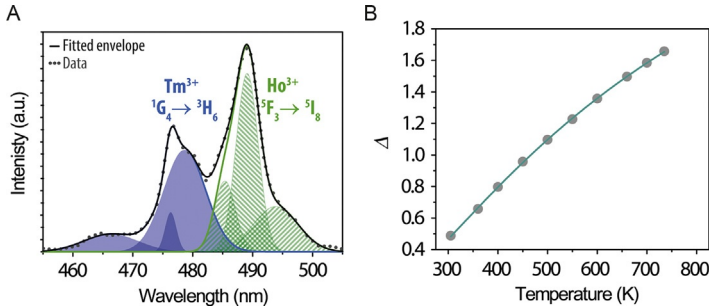
FIG. 14 (A) Upconverting emission spectrum of Y_2O_3:Yb^{3+}/Ho^{3+}/Tm^{3+} nanocrystals (303 K, 980 nm excitation). The $^5F_3 \rightarrow ^5I_8$ (Ho^{3+}) and $^1G_4 \rightarrow ^3H_6$ (Tm^{3+}) transitions were fitted to Gaussian functions showing a total overlap of 4.62%. (B) Calibration curve (*open points*). The *solid line* is the best fit to the data ($r^2 > 0.992$) using Eq. (39). *Panel (A) data extracted from Pandey, A., Rai, V.K. 2013. Optical thermometry using FIR of two close lying levels of different ions in Y_2O_3:Ho^{3+}–Tm^{3+}–Yb^{3+} phosphor. Appl. Phys. B 113, 221–225.*

observed by Pandey and Rai in Y_2O_3:Yb^{3+}/Tm^{3+}/Ho^{3+} (Pandey and Rai, 2013). The emission spectrum of this phosphor presents an overlap between the $^5F_3 \rightarrow ^5I_8$ (Ho^{3+}, I_1) and the $^1G_4 \rightarrow ^3H_6$ (Tm^{3+}, I_2) transitions and due to the close energetic position of the emitting levels (~470 cm^{-1}) that overlap affects the intensity ratio Δ (Fig. 14). The authors used the intensity maximum of I_1 and I_2, instead of the integrated areas (from peak fitting) to define Δ according to Eq. (1), and were able to fit $\Delta(T)$ to Eq. (25), and not to Eq. (27), since the peak maximum of each transition is proportional to the corresponding integrated (deconvoluted) area. This example will be further detailed in Section 4.2.1.

4.1.3 Relative Sensitivity and Temperature Uncertainty: The Example of Upconverting Nanoparticles

The main advantage of assigning a physical model to a thermometer readout is the possibility of predicting the thermal performance prior to synthesis and testing efforts. To quantify the relative sensitivity of the fluorescence intensity ratio of a single emitting center, we can use Eqs. (4) and (25) to write the relative sensitivity as (Collins et al., 1998; Wade et al., 2003):

$$S_r = \frac{\Delta E}{k_B T^2} \tag{29}$$

The corresponding uncertainty in temperature is calculated using Eq. (7):

$$\delta T = \frac{k_B T^2}{\Delta E} \frac{\delta \Delta}{\Delta} \tag{30}$$

Both S_r and δT can be tuned by a judicious choice of the emitting center, which determines ΔE. Although Eq. (29) points out that S_r increases using

energy levels pairs with larger energy differences, care needs to be taken to ensure that the levels are not too far apart, so that thermalization is no longer observed, as stressed earlier. Additionally, as the energy difference extends, the population (and hence the fluorescence intensity) of the upper thermalized level decreases with concomitant practical problems in measuring signals with low SNR values. As mentioned earlier when the limits of Eq. (1) were discussed, a reasonable operating approach must consider as reliable intensity values only those that are 5% higher than the noise level. Moreover, both Eqs. (29) and (30) are independent of the host matrix that supports the phosphor, meaning that the same ΔE gap induces similar S_r and δT values. This is emphasized in a recent publication on $NaYF_4$:Yb^{3+}/Er^{3+} UC nanowires, nanorods, and nanoplates (Li et al., 2013).

Until some time ago, the determination of δT was not very common. However, as the field is growing out of its infancy and develops toward applications, this parameter becomes a key factor to compare different thermometers. In what follows, we will compute δT using Eq. (7) for selected examples of UCNPs. The NPs are, most often, composed of a host crystal (usually fluorides, oxides, phosphates, or sulfides of metal ions) doped with up to three Ln^{3+} ions (Bettinelli et al., 2015; Chen et al., 2015b; Wang et al., 2010; Zhou et al., 2015a). UCNPs are known to display luminescence that varies strongly in the physiological temperature range, thus suggesting their use in biomedical applications, such as single-particle tracking, bioimaging and therapeutics, and thermal sensing (Bettinelli et al., 2015; Fischer et al., 2011; Gu et al., 2013; Il Park et al., 2015; Kumar et al., 2009; Wang and Liu, 2014; Wu et al., 2015; Zhou et al., 2015a). Among Ln^{3+} ions, Yb^{3+} and Nd^{3+} are by far the most used sensitizers, due to their large absorption cross sections at 980 and 808 nm, respectively, while Er^{3+}, Tm^{3+}, and Ho^{3+} are the most efficient activators (Bettinelli et al., 2015). The Yb^{3+}/Er^{3+} pair uses the Yb^{3+} large absorption cross section at 980 nm and subsequent energy transfer to Er^{3+} enabling upconversion emission in the green ($^2H_{11/2} \rightarrow {}^4I_{15/2}$ and $^5S_{3/2} \rightarrow {}^4I_{15/2}$ transitions, ca 510–565 nm) and red ($^4F_{9/2} \rightarrow {}^4I_{15/2}$ transition, ca 620–670 nm) spectral regions. The ratio of the integrated intensities of the $^2H_{11/2} \rightarrow {}^4I_{15/2}$ and $^5S_{3/2} \rightarrow {}^4I_{15/2}$ transitions is used to sense temperature since the pivotal work of Shinn et al. (1983). Near room temperature, this ratio of integrated intensities permits to get a relative sensitivity of the order of $1\% \, K^{-1}$ and a minimum temperature uncertainty of 0.5 K, assuming a practical limit of $\delta\Delta/\Delta = 0.5\%$ for commercial detectors. In Fig. 15, we compare the thermal uncertainty computed from the published data for a set of illustrative examples of single-center Yb^{3+}/Er^{3+}- and Yb^{3+}/$Tm^3{}^+$/Gd^{3+}-based thermometers. We suggest comparing the thermal uncertainty of the single-center thermometers by plotting δT as a function of a normalized temperature, T_{nor}, defined as:

$$T_{nor} = \frac{k_B T^2}{\Delta E} \tag{31}$$
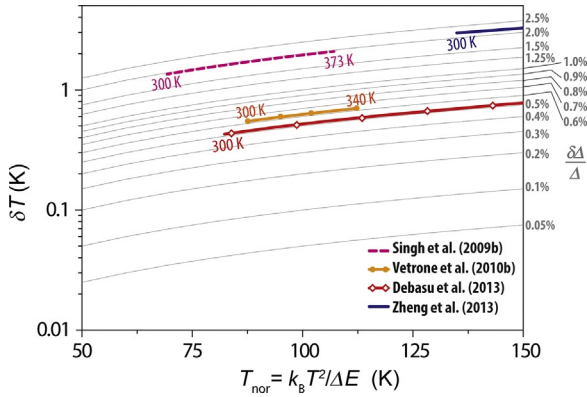
FIG. 15 Temperature uncertainty of single-center emission thermometers. Singh et al. (2009b), Vetrone et al. (2010b), and Debasu et al. (2013) used the $^2H_{11/2} \rightarrow {}^4I_{15/2}/^5S_{3/2} \rightarrow {}^4I_{15/2}$ transitions ratio in Er^{3+}/Yb^{3+}-doped materials. In the example reported by Sing et al. the host is Gd_2O_3, $\delta\Delta/\Delta = 2.0\%$, and $S_r < 0.8\% K^{-1}$ (Singh et al., 2009b). Vetrone et al. reported a cellular thermometer based on the $NaYF_4$ host with $S_r < 1.14\% K^{-1}$ and $\delta\Delta/\Delta = 0.6\%$ (Vetrone et al., 2010b), whereas Debasu et al. used the Gd_2O_3 host with $S_r < 1\% K^{-1}$ and $\delta\Delta/\Delta = 0.5\%$ (Debasu et al., 2013). Zheng et al. showed upconversion thermometry through the Gd^{3+} $^6P_{5/2} \rightarrow {}^8S_{7/2}$, $^6P_{7/2} \rightarrow {}^8S_{7/2}$ UV transitions in $NaLuF_4:Yb^{3+}/Tm^{3+}/Gd^{3+}$ UCNPs with $S_r < 0.74\% K^{-1}$ and $\delta\Delta/\Delta = 2.2\%$ (Zheng et al., 2013).

resulting in a set of lines with increasing slope for increasing values of $\delta\Delta/\Delta$. The results show that the temperature uncertainty of these UCNPs can be as low as $\delta T = 0.4$ K. Increasing the detection limit (up to 0.03%) and the integration time (>0.5 s), we can anticipate that single-center-based thermometers can have temperature uncertainties down to 0.1 K in the 300–340 K range.

4.2 Dual-Center Emission

Ratiometric Ln^{3+}-based thermometers in which the thermometric parameter involves the intensity ratio of two transitions belonging to two distinct emitting centers can be classified accordingly into five distinct classes:

(A) The Ln^{3+} ion is the probe and an organic dye is the reference. Examples include PMMA-btd/SiO_2 hybrid NPs embedding Eu-dt and OASN emitters (Peng et al., 2010b), RhB (or S-0378)/fluorescein (or NIR-797) decorated $NaYF_4:Yb^{3+}/Er^{3+}$ UCNPs (Gorris et al., 2011), ([Eu_2(qptca)(NO_3)$_2$(DMF)$_4$]· (CH_3CH_2OH)$_3$) MOF incorporating perylene into the porous (Cui et al., 2015a), and Eu-dsb and Tb-dsb MOFs (D'Vries et al., 2013).

(B) The Ln^{3+} ion is the reference and a QD is the probe, eg, $NaGdF_4:Nd^{3+}$ NPs and PbS/CdS/ZnS QDs embedded into poly(lactic-*co*-glycolic acid) (Cerón et al., 2015).

(C) Two Ln^{3+} ions indistinguishably employed as the probe and the reference and not interacting (no ion–ion energy transfer). An example is the $Y_2O_3:Tb^{3+}/Tm^{3+}$ phosphor (Ishiwada et al., 2011).

(D) Two Ln^{3+} ions indistinguishably employed as the probe or the reference, in which ion–ion energy transfer regulates the changes in the intensity ratio. Examples include Tb^{3+}/Eu^{3+} (Liu et al., 2005; Sato et al., 1989) and Yb^{3+}/Nd^{3+} (Marciniak et al., 2015).

(E) Two Ln^{3+} ions embedded into a polymer or an organic–inorganic hybrid host in which changes in Δ are controlled by thermally activated ion-to-host energy transfer, eg, Tb^{3+}/Eu^{3+} complexes incorporating into hybrid hosts (Brites et al., 2010, 2013b,c; Wang et al., 2014, 2015c).

Illustrative examples of these luminescent thermometers are addressed in detail in Section 5.

4.2.1 Intensity vs Temperature: Sigmoidal Dependence

Among the five classes listed earlier, examples involving direct ion→ion energy transfer and energy transfer through excited levels of the ligands or host matrix, listed as (D) and (E), respectively, show the same functional form for $\Delta(T)$: a S-shaped curve, which clearly deviates from an exponential intensity ratio profile, especially for $T < 200$ K, Fig. 16. Examples involving no-interacting Ln^{3+} ions, class (C), show a Boltzmann dependence for $\Delta(T)$, whereas those belonging to classes (A) and (B) do not present a unique trend and, thus, will not be discussed here.

Similarly to what was done using the Boltzmann law in single-center-based luminescent thermometers (Section 4.1), it is also possible to rationalize the $\Delta(T)$ dependence for dual-center-based ones. The analysis presented next follows the discussion of Cooke et al. (1998, 2004) that extends the classical Mott–Seitz model (Mott, 1938; Seitz, 1939) for competition between radiative
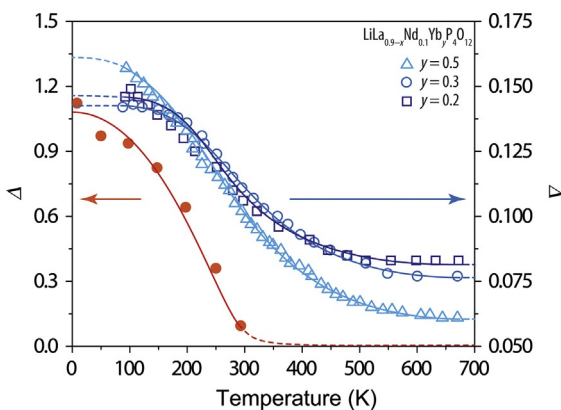
FIG. 16 Illustrative examples of S-shaped curves. The *full circles* correspond to Tb^{3+}-to-Eu^{3+} energy transfer (Liu et al., 2005) in sol–gel-derived glasses, whereas the *other symbols* correspond to Yb^{3+}-to-Nd^{3+} energy transfer in $LiLa_{0.9-x}\,Nd_{0.1}Yb_yP_4O_{12}$ (Marciniak et al., 2015). The *solid lines* are guides to the eyes.

and nonradiative transitions within a luminescence center. The model describes the total transition probability of an emitting level by the sum of radiative and nonradiative transition probabilities (A_R and A_{NR}, respectively). This can be evaluated by the inverse of the lifetime τ of the emitting level:

$$\frac{1}{\tau} = \frac{1}{\tau_R} + \frac{1}{\tau_{NR}} \tag{32}$$

where τ_R is the radiative lifetime (assumed to be temperature independent and equal to τ_0, the lifetime intensity at $T=0$ K) and τ_{NR} is the nonradiative lifetime that is described by the Arrhenius dependence: $\tau_{NR} = \tau_{NR}(0)\exp(-\Delta E/k_B T)$ where $\tau_{NR}(0)$ stands for the nonradiative decay time at $T=0$ K and ΔE for the activation energy of the thermal quenching process. Solving Eq. (32), we can write:

$$\tau = \frac{\tau_0}{1 + \alpha\exp(-\Delta E/k_B T)} \tag{33}$$

where $\alpha = A_{NR}/A_R$. When more than one quenching process is present, the above expression should be generalized including the deactivation though all the channels:

$$\tau = \frac{\tau_0}{1 + \sum_i \alpha_i \exp(-\Delta E_i/k_B T)} \tag{34}$$

The integrated luminescence intensity, I, may be related with τ as (Duarte et al., 1999; Stalder et al., 1992):

$$\frac{I}{\Gamma_0} = \frac{\tau}{\tau_0} \tag{35}$$

where Γ_0 is the beam intensity at $T=0$ K. Combining Eqs. (34) and (35) it follows:

$$I = \frac{\Gamma_0}{1 + \sum_i \alpha_i \exp(-\Delta E_i/k_B T)} \tag{36}$$

According to Eq. (1) (the definition of Δ), the temperature dependence of Δ is given by:

$$\Delta = \frac{\Gamma_{01}}{1 + \sum_i \alpha_{1i}\exp(-\Delta E_{1i}/k_B T)} \frac{1 + \sum_i \alpha_{2i}\exp(-\Delta E_{2i}/k_B T)}{\Gamma_{02}}$$
$$= \Delta_0 \frac{1 + \sum_i \alpha_{2i}\exp(-\Delta E_{2i}/k_B T)}{1 + \sum_i \alpha_{1i}\exp(-\Delta E_{1i}/k_B T)} \tag{37}$$

where $\Delta_0 = \Gamma_{01}/\Gamma_{02}$, α_{1i}, and α_{2i} stand for the ratios between the nonradiative and radiative probabilities of the i deactivation channel of transitions with

intensity I_1 and I_2, and ΔE_{1i}, and ΔE_{2i} are the activation energies for the thermal quenching process of transitions with intensity I_1 and I_2, respectively. There are two particular cases of Eq. (37) that we want to discuss here:

- One of the transitions (eg, I_2) exhibits a temperature dependence much smaller than the other.
- The exponential terms dominate the intensity of each transition, ie, $1 \ll \alpha_j \exp\left(-\Delta E_j/k_B T\right)$, $j = 1, 2$.

In the first case, Eq. (37) becomes:

$$\Delta \approx \frac{\Delta_0}{1 + \sum_i \alpha_{1i} \exp\left(-\Delta E_{1i}/k_B T\right)} \tag{38}$$

The temperature dependence of this equation changes from an almost linear relation (useful for a large temperature range, covering more than 100°) to a distinct S-shaped curve (of particular interest for a narrow temperature range, covering one or two tens of degrees), depending on ΔE_{1i} and α_{1i}. Although there are many luminescent thermometers presenting this functional form, eg, $Zn_x Mn_{1-x} Se/ZnCdSe$ nanocrystals (Vlaskin et al., 2010), polymer dots (Gota et al., 2009; Ye et al., 2011), Tb^{3+}/Eu^{3+} MOFs (Rao et al., 2013; Wei et al., 2015), and Tb^{3+}/Eu^{3+} organic–inorganic hybrids (Brites et al., 2010, 2013b,c, 2016), the calibration curve was fitted to this model only in two examples (Ananias et al., 2015; Wang et al., 2015c). Ananias et al. reported a cryogenic luminescent thermometer based on the Na $[(Gd_{0.8}Eu_{0.1}Tb_{0.1})SiO_4]$ silicate exhibiting uncommon photoluminescence properties due to structural disorder and a phase transition (Ananias et al., 2015). The calibration curve was fitted using Eq. (38) for two deactivation channels: Tb^{3+}-to-Tb^{3+} energy migration through multiple Tb^{3+} local sites, activation energy ΔE_1, and Tb^{3+}-to-Eu^{3+} energy transfer, with an activation energy ΔE_2. On the other hand, Wang et al. reported the $[(Tb_{0.914}Eu_{0.086})_2(pda)_3(H_2O)] \cdot 2H_2O$ nano-MOF, the first lanthanide-organic framework prepared by the spray-drying method, operating in the 10–325 K range (Wang et al., 2015c). The calibration curve was fitted using Eq. (38) with a single deactivation channel and the value obtained for the activation energy, $\Delta E = 52.4 \pm 2.0$ cm^{-1}, is in accord with the emission spectra suggesting that this nonradiative channel involves deactivation through the ligand levels, whose broad emission overlaps the $^5D_4$ state.

When the exponential terms dominate the intensity of each transition, Eq. (37) can be written as (assuming a single deactivation channel):

$$\Delta = \Delta_0 \frac{1 + \alpha_2 \exp\left(-\Delta E_2/k_B T\right)}{1 + \alpha_1 \exp\left(-\Delta E_1/k_B T\right)} \approx \Delta_0 \frac{\alpha_2}{\alpha_1} \exp\left(-\frac{\Delta E_2 - \Delta E_1}{k_B T}\right) \tag{39}$$

The most remarkable feature of this approximation is that Eqs. (39) and (25) have the same functional form and, thus, although we are dealing with

a dual-center emission the problem is reduced to the single-center case. An illustrative example is the Y_2O_3:Yb^{3+}/Ho^{3+}/Tm^{3+} UCNPs (Pandey and Rai, 2013) in which the thermometric parameter involves the intensity ratio of $^5F_3 \rightarrow {}^5I_8$ (Ho^{3+}, I_1) and $^1G_4 \rightarrow {}^3H_6$ (Tm^{3+}, I_2) transitions (Fig. 14). Due to the close energetic position of the emitting levels, ($\sim$470 cm^{-1}) the authors observed an overlap between the Ho^{3+} and Tm^{3+} transitions, see the discussion in Section 4.1.2. The resulting energetic separation between the levels was found to be $\Delta E_2 - \Delta E_1 = 443.82 \pm 7.72$ cm^{-1}, in good agreement with the actual energy gap between the (Ho^{3+}) and $^1G_4$ (Tm^{3+}) levels (473 cm^{-1}). This means that the difference between the activation energies for the two thermal quenching processes is mainly the energy gap between the two emitting levels, or, in other words, this suggests that both emitting levels are thermally depopulated through the same energy level.

Another interesting example of a dual-center emission thermometer that follows the same functional form of Boltzmann law (Eq. 25) is the Eu^{3+}/Tb^{3+}-doped APTES/TEOS organic–inorganic hybrid NPs (Brites et al., 2013b). The peculiar energetic position of the first excited triplet state of the acac ligand induces a continuous decrease of the integrated intensities of the $^5D_4 \rightarrow {}^7F_5$ (I_1) and $^5D_0 \rightarrow {}^7F_2$ (I_2) transitions in the 10–330 K range (Fig. 17). Two different regimes are clearly discernible: for $T < 175$ K the I_1 integrated area decreases stronger, when compared with that of I_2, whereas for $T > 200$ K both I_1 and I_2 decay almost linearly. The switch between the two regimes occurs in the 175–200 K range. When we plot, in the second regime, the natural logarithm of Δ with respect to the inverse of the temperature, we find a linear relationship compatible with Eq. (39). In this case, the activation energies ΔE_1 and ΔE_2 involve the triplet host (or ligand) level
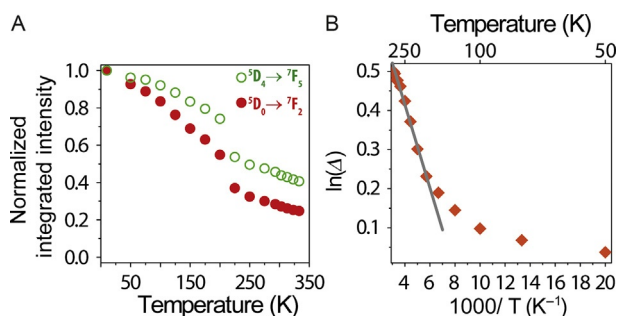
FIG. 17 (A) Normalized integrated $^5D_4 \rightarrow {}^7F_5$ and $^5D_0 \rightarrow {}^7F_2$ intensities in APTES/TEOS hybrid NPs doped with [Ln(acac)$_3 \cdot$3H$_2$O] (Ln = Eu, Tb) complexes (315 nm excitation). The intensities were normalized to the corresponding values at 10 K. (B) The linear dependence of ln(Δ) *(symbols)* with $1/T$ above 175 K follows the equation ln(Δ) = $-105.2/T + 0.8$ ($r^2 > 0.997$, *straight line*). *Adapted with permission from Brites, C.D.S., Lima, P.P., Silva, N.J.O., Millán, A., Amaral, V.S., Palacio, F., Carlos, L.D. 2013b. Ratiometric highly sensitive luminescent nanothermometers working in the room temperature range. Applications to heat propagation in nanofluids. Nanoscale 5, 7572–7580. © 2013 The Royal Society of Chemistry.*

and the $^5D_4$ ($20,336.6 \pm 10.1$ cm^{-1}) and $^5D_0$ ($17,205.8 \pm 9.0$ cm^{-1}) emitting states, respectively. Eq. (39) yields $E_1 - E_2 = 3277 \pm 14$ cm^{-1}, an energy difference in accord with an energetic scheme in which the $^5D_4$ depopulation occurs through the triplet of the acac ligand ($25,300 \pm 1250$ cm^{-1}) and the $^5D_0$ one via the triplet of the APTES/TEOS hybrid host ($20,768 \pm 2750$ cm^{-1}).

4.2.2 Relative Sensitivity and Temperature Uncertainty. Illustrative Examples

Whereas for the second particular case of Eq. (37), S_r and δT are given by Eqs. (29) and (30), respectively, for the first case S_r is given by (assuming a single deactivation channel):

$$S_r = \frac{\Delta E_1 \alpha_1 \exp(-\Delta E_1/k_B T)}{k_B T^2 [1 + \alpha_1 \exp(-\Delta E_1/k_B T)]} = \frac{\Delta E_1}{k_B T^2 [(1/\alpha_1) \exp(\Delta E_1/k_B T) + 1]} \quad (40)$$

Typically, $S_r(T)$ presents a bell-shaped profile that peaks at the inflection point of the S-shaped calibration curve and with a width determined by the activation energy ΔE_1 and the kinetic constant α_1. The correspondent uncertainty in temperature is given by:

$$\delta T = \frac{k_B T^2}{\Delta E_1} \left[\frac{1}{\alpha_1} \exp\left(\frac{\Delta E_1}{k_B T}\right) + 1 \right] \frac{\delta \Delta}{\Delta} \quad (41)$$

which depends critically on ΔE_1 and α_1 and its general form is a U-shaped curve, with minimum at the temperature of the maximum sensitivity S_m.

In order to compare the features of the single- and dual-center luminescent thermometers, we plot the calibration (Eqs. 25 and 38), sensitivity (Eqs. 29 and 40), and temperature uncertainty (Eqs. 30 and 41) curves in Fig. 18. The parameters used are $B = 4.0$, $\alpha = 3000$, $\Delta_0 = 0.5$, $\delta \Delta/\Delta = 0.5\%$, and $\Delta E = 600$, 800, 1000 cm^{-1}. Increasing or decreasing α by one order of magnitude only stretches or shrinks the profile of the S-shaped curve. Whereas dual-center thermometers seem to be more effective in the cryogenic range, in which values of $S_m = 3\%$ K^{-1} and $\delta T = 0.2$ K can be reached with portable spectrometers, single-center thermometers, however, are operative at higher temperatures ($T > 300$ K) with $S_m \sim 0.5$–1% K^{-1} and $\delta T \sim 0.5$ K. Furthermore, for the same ΔE value there is a notorious similarity of the S_r curves for higher temperatures ($T > 250$ K), corroborating the approximation that leads to Eq. (39) (the dominance of the exponential term) with the same functional form of Eq. (25).

Organic–inorganic hybrids comprising [Ln(btfa)$_3$(MeOH)(bpeta)] (Ln = Eu, Tb) complexes embedded into APTES/TEOS- and N-(triethoxysilylpropyl)-O-polyethylene oxide urethane/TEOS-based NPs and into diureasil films are examples following the temperature dependences of Eqs. (38), (40), and (41) (Fig. 19). The first excited triplet state of these three distinct hybrid hosts works as a "population storage reservoir," as it occurs in typical E-type
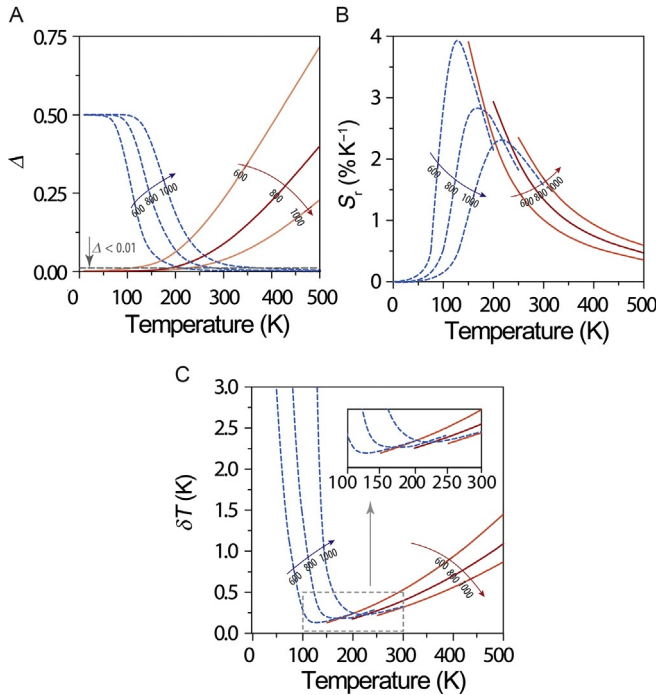
FIG. 18 (A) Calibration, (B) S_r, and (C) δT curves computed for single-center (*full lines*) and dual-center (*interrupted lines*) luminescent thermometers. The cutoff at $\Delta = 0.01$ represents the operational criterion in which reliable intensity values are only those 5% higher than the noise level. Below this limit, that corresponds to $\Delta/\Delta_0 < 2\%$ and $\Delta/B < 4\%$, in dual- and single-center thermometers, respectively, the S_r and δT values are not displayed because the thermometers are out of their operating range.

delayed fluorescence (Vlaskin et al., 2010), its energy being almost resonant with that of the $^5D_4$ level (Tb^{3+}); this allows thermally driven depopulation with the concomitant decrease of the Tb^{3+} intensity as temperature increases. On the contrary, the $^5D_0$ population is essentially constant since its relatively low energy hinders the thermally driven Eu-to-ligand back transfer. The fit of the corresponding calibration curves to Eq. (38) allows the estimation of S_r and δT for each material, according to Eqs. (40) and (41), respectively. Fig. 19 clearly points out that the feasibility of the fine-tuning of the temperature of maximum sensitivity and minimum thermal uncertainty by judicious engineering of ligands and hosts.

5 EXAMPLES

There are several factors determining the suitability of a thermometer for a given application. Some of them are obviously related to the sensing performance: working range, sensitivity, uncertainty, time resolution, and spatial
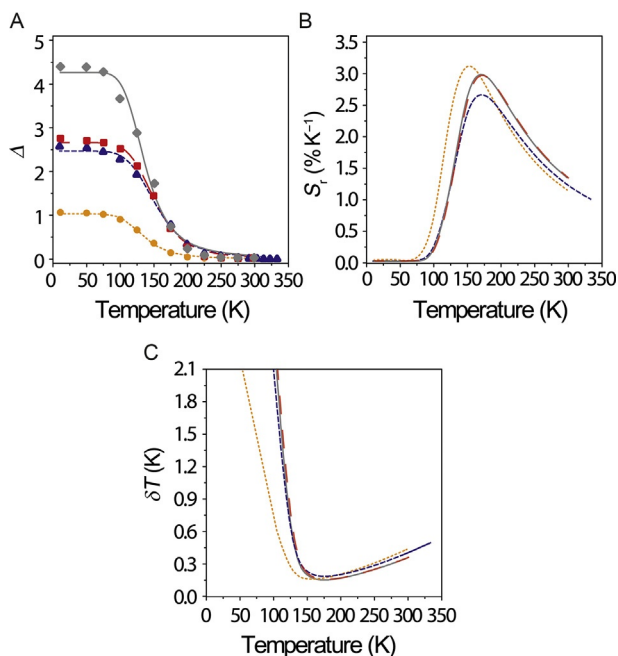
FIG. 19 Comparing the performance of Eu^{3+}/Tb^{3+} thermometers processed NP3-1.10 (*circles*), NP4-1.3 (*triangles*), and NP3-1.3 (*squares*) NPs (Brites et al., 2010, 2013b) and as a diureasil thin film (*solid diamonds*) (Brites et al., 2010). (A) Thermometric parameter, the *lines* are the best fit to the data using Eq. (38) with a single deactivation channel ($r^2 > 0.991$). (B) Relative sensitivity computed using Eq. (40). (C) Temperature uncertainty computed using Eq. (41) with $\delta\Delta/\Delta = 0.5\%$.

resolution of the system. However, others have to do with the material itself: physical state, mechanical properties, facility to be implemented, processability, versatility, and simplicity of the production method. This section considers both aspects in the diverse types of Ln^{3+}-based thermometric materials.

The shielding of 4*f* orbitals confers the excellent luminescence properties of Ln^{3+} ions but it is also the cause of a weak direct light absorption (Bünzli, 2006, 2015; Bünzli and Piguet, 2005; Malta and Carlos, 2003). To overcome this problem in optical thermometry, as well as for luminescence uses in general, the Ln^{3+} ions are coordinated by (i) organic chromophore ligands (eg, in β-diketonate complexes) or (ii) embedded into a host crystal (eg, MOFs and UCNPs) (Fig. 20). The mechanism of excitation, however, is different. The metal ions complexed by the light harvesting ligands are excited through absorption by the ligand and subsequent energy transfer (usually from an excited triplet state) to the ion (Malta, 1997, 2008; Malta and Silva, 1998), whereas inorganic crystals use directly the absorption band of the emitter Ln^{3+} ion (activator) or ion–ion energy transfer from another codopant ion (sensitizer) (Soukka and Härmä, 2011).
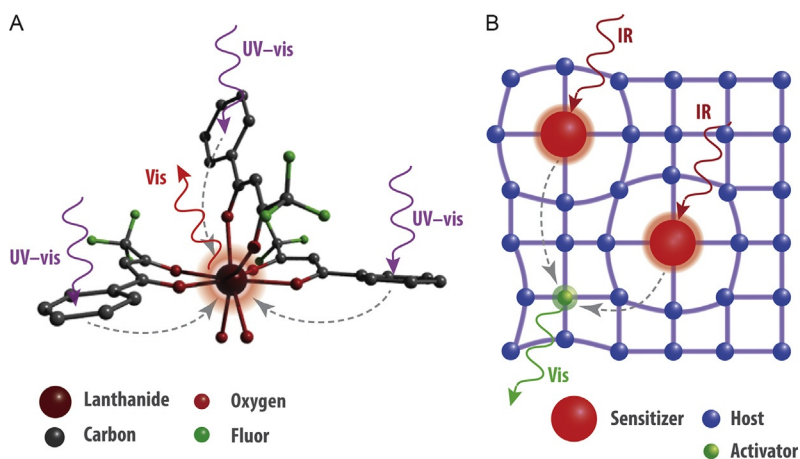
FIG. 20 Mechanisms of light harvesting in Ln^{3+}-based luminescent thermometers: (A) complexing with organic ligands and (B) doping in host crystals. The *solid arrows* represent light absorption or emission whereas the *interrupted arrows* sign the energy transfer within the materials. *Adapted with permission from Ding, M.Y., Chen, D.Q., Yin, S.L., Ji, Z.G., Zhong, J.S., Ni, Y.R., Lu, C.H., Xu, Z.Z. 2015. Simultaneous morphology manipulation and upconversion luminescence enhancement of β-NaYF$_4$:Yb^{3+}/Er^{3+} microcrystals by simply tuning the KF dosage. Sci. Rep.-UK 5, Article number: 12745. © 2015 Nature Publishing Group.*

Aromatic organic ligands serve as antennas for light harvesting and can multiply the photoluminescence intensity of Ln^{3+} ions by two orders of magnitude, at least (Shahi et al., 2015). Ligands and Ln^{3+} ions can be arranged in discrete molecules or in crystal lattices, such as MOFs. The ligands in discrete molecular compounds have β-diketonates (Binnemans, 2005), or polydentate azo compounds as binding groups (Fig. 21A), and residues with heterocyclic polycyclic aromatic rings (Fig. 21B), or N-base heterocycles (Fig. 21C) for light harvesting, and perfluoroalkyl residues to increase Lewis acidity (Binnemans, 2005). The residues also determine the energy of the singlet and triplet states of the ligand and, consequently, the luminescence properties of the Ln^{3+}-based materials. On the other hand, ligands in MOFs have dicarboxylic acids, as linking groups (Fig. 21A), and similar aromatic compounds for light harvesting (Fig. 21D).

A scheme of the different types of thermometric materials that are based on coordination compounds with organic ligands is shown in Fig. 22. It includes (i) micro and macrocrystals of lanthanide salts; (ii) discrete molecular complexes (molecular thermometers) embedded in amorphous matrices, such as polymers and organic–inorganic hybrids; and (iii) MOF micro and nanocrystals. In addition, we have to mention two other categories of luminescent thermometers: UCNPs and NIR-emitting NPs, which have also a crystalline nature.
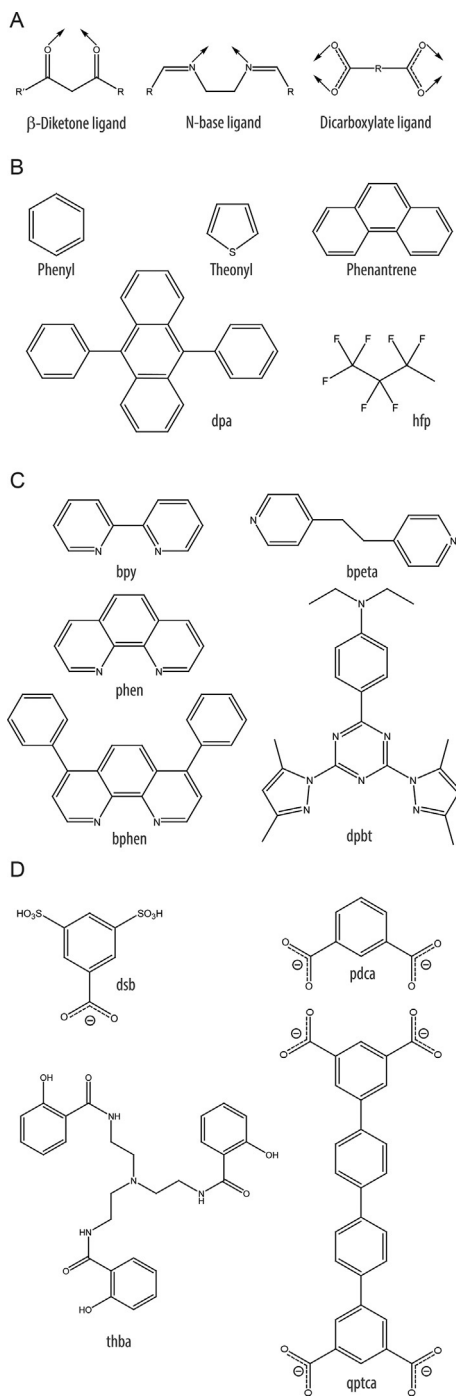
FIG. 21 Scheme of the most typical types of organic ligands in lanthanide coordination compounds for thermometry: (A) ligands used in molecular compounds and MOFs. (B) Structure of common aromatic cycles, polycycles, and heterocycles used as light harvesters in β-diketone ligands, and typical fluorocarbon ligand used as electron withdrawal group for enhancing ligand acidity. (C) Common N-based heterocycles in β-diketone ligands. (D) Common aromatic and polyaromatic ligands in MOFs.
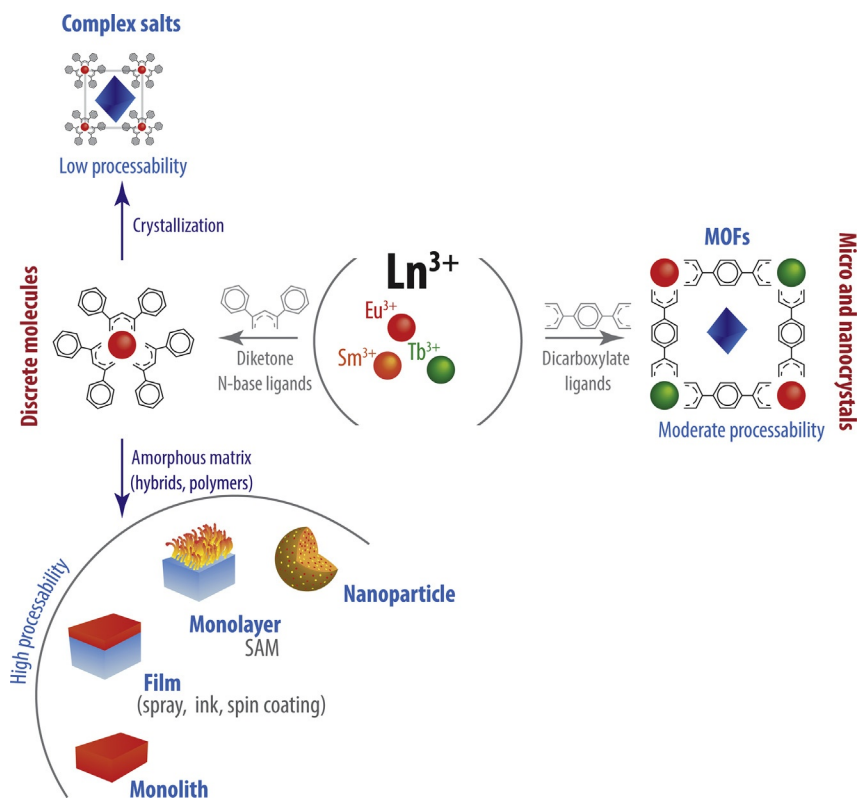
FIG. 22 Scheme of the different routes to design ratiometric luminescent thermometers based on Ln^{3+} complexes with organic ligands (eg, dicarboxylate and diketone N-based ligands).

Next, we show some illustrative examples of each type of material to gain a general view of their respective thermometric performance relatively to their composition and structure, and the methods for their production.

5.1 Crystals of Ionic Complexes

Thermometric systems based on crystals of ionic complexes are uncommon, but we can find a very early example reported by Sato et al. (1989). This thermometer was based on a physical mixture of Eu^{3+} and Tb^{3+} salts with β-diketone ligands, or on a chemical mixture of these ions in a double salt. The salts were powdered and spread on a glass substrate to form a thermometric layer. The authors considered that the thermally driven energy transition depopulating the radiative energy state occurred through the first excited triplet levels (T_1 and T'_1) of the ligands bound to different Ln^{3+} ions, $^5D_4 \rightarrow T_1 \rightarrow T'_1 \rightarrow {}^5D_0$. Therefore, it was stated that the two ions should be preferably in the same crystal lattice to favor the energy transfer between

the triplet energy states T_1 and T'_1 and the complexes were processed as double salts. The preparation method is very simple, it just requires the dissolution of ligands and Ln^{3+} salts in a solvent, usually an alcohol, and the evaporation of this solvent on a substrate to form a film. However, the processability and the practical application of salt powder films are quite reduced, limited to thermometry of some surfaces with salt adherence capacity, low mechanical requirements poor homogeneity, and low spatial resolution. The working range for a given composition is not wide but it can be tuned with the Tb/Eu ratio (from 4:1 to 49:1) and the type of ligand (btfa and hfa) in the region from 73 K to near 373 K. The sensitivity is not provided by the authors. Another interesting example is the cryogenic thermometer recently reported by Ren et al., the first example of a ratiometric Eu^{3+}/Tb^{3+} thermometer based on a lanthanide phosphonate (Ren et al., 2015). The compound presents a temperature-dependent emission under 393 nm excitation that enabling its use as a molecular thermometer with $S_m = 3.90\% \, K^{-1}$ and $\delta T = 0.15$ K, both at 38 K. There is another type of thermometer also based on the use of organic complexes, but operating with a very different mechanism of emission temperature dependence (Yuasa et al., 2014). In aqueous solution, the $[(Eu)_2(oda)_3(bp)]$ dinuclear complex displays two different structures in equilibrium. Consequently, the strongest $^5D_0 \rightarrow {}^7F_2$ transition is split into two levels at 613 and 616 nm. The thermometric parameter is the intensity ratio of these emissions that changes with the temperature in the physiological range.

5.2 Molecular Thermometers

In our classification, the luminescent thermometers based on the emission of discrete molecules of Ln^{3+} ions with organic ligands are referred to as molecular thermometers. This concept of molecular thermometry has been extended to several kinds of matrices (Fig. 22) (eg, polymers and organic–inorganic hybrids), and to a wide variety of forms, such as bulky materials, films, and NPs, being thus very versatile. They have even been incorporated in nonvolatile liquids such as anthracenes to make thermoresponsive liquids (Babu et al., 2013). Moreover, only a few molecules are necessary to give a thermometric response. These facts are determinant in the performance and processability of the thermometer. The molecular nature of the system introduces also another important advantage: the possibility to achieve a very high spatial resolution. Actually, it has been recently demonstrated that Ln^{3+} molecular thermometers can also be implemented as a self-assembled polymer monolayer on a Si surface (Rodrigues et al., 2016). This monolayer of Tb^{3+} and Eu^{3+} complexes behaves as a ratiometric thermometer with $S_m = 1.45\% \, K^{-1}$, a cycle–recycle reliability $R = 98.6\%$, and $\delta T = 0.3$ K. Moreover, this thermometer presents a unique behavior consisting in reversible bistability permitting that the Si-functionalized surface can operate as an optically active two-module

molecular demultiplexer. This opens the possibility of using this molecular thermometer in medical- and biotechnologies, such as blood diagnostics, "lab-on-a-molecule" systems, and molecular computational identification of small objects (de Silva, 2011).

5.2.1   In Polymer Matrices

Early examples of luminescent thermometers based on Ln^{3+} complexes embedded into polymer matrices comprise emission intensity variations of single-center emitters. However, one of the first examples studied the influence of ligands, polymers, and complex/polymer ratio using both decay lifetime and intensity variation (278–323 K) as the thermometric parameters (Khalil et al., 2004). The ligands were β-diketonates with different aromatic and fluorinated substituents, see Fig. 20. One of the ligands was tta that has an aromatic heterocycle linked to the diketonate group and a strong electron withdrawal group ($-CF_3$) that increases the ionicity of the ligand. Another ligand was F7 that has several electron withdrawal groups and therefore a stronger interaction with the metal (high Lewis acidity), but it does not have any aromatic ring. Other ligands employed in this comparative study were D2, with a high aromatic area, and 3p-hfb, with both an aromatic and electron withdrawal residues. Finally, they also used N-based bidentate ligands, as phen or bphen, to increase the coordination number of the β-diketonate complexes from 3 to 4. The different polymers were fluoroacrylic polymer, polycarbonate, and Teflon®. The loading of the complexes in the polymer was also varied between 1/10 and 1/600 ratios. The higher aromaticity of D2 in comparison with tta had the effect of shifting the excitation maximum from 350 to 400 nm. A high number of aromatic cycles in the ligands were also enhancing the maximum S_a values, which decreased from $4.42\% \, K^{-1}$, for $[Eu(D2)_3(phen)]$ complexes, to $0.9\% \, K^{-1}$, for $[Eu(F7)_3]$ ones; corresponding to S_m values, computed by us, of $1.77\% \, K^{-1}$ and $0.82\% \, K^{-1}$, respectively. Increasing the coordination number from tris to tetrakis was not beneficial due to the intensity photodegradation (from 7.2% to 16.2% intensity lost per hour of irradiation), despite the slightly increase of the maximum S_a values, from $2.27\% \, K^{-1}$ to $2.40\% \, K^{-1}$, corresponding to S_m values, computed by us, of $1.82\% \, K^{-1}$ and $1.49\% \, K^{-1}$, respectively. Whereas S_r increased with the concentration (up to 1/10), the relative sensitivity based on lifetime values was higher for the lowest concentration (1/600). The role of the polymer is obviously to provide the desired physical and chemical properties to the thermometer for a given application, but is also acting on the thermometric performance. In this case, the sensitivity in fluoroacrylic polymer was the highest followed close by polycarbonate and decreasing $4\times$ in Teflon. The thermometer was formulated as paint prepared by dispersion in dichloromethane or trifluorotoluene. The paint was sprayed or spin coated onto aluminum or glass substrates (Khalil et al., 2004).

Borisov and Wolfbeis (2006) and Stich et al. (2008) presented a dual sensor for temperature and O_2 in which the excitation maxima of tta and other β-diketonate ligands shifted into the visible region (410 nm) after addition of a N-based heterocyclic ligand, dpbt, with concomitant increase of the brightness. Ligand-to-Eu^{3+} energy transfer achieves visible light sensitization. When the thermometric parameter is the decay time, poly-(*tert*-butyl styrene) is used for complex encapsulation and poly(vinyl methyl ketone) is used as the binder, then, the working temperature range is extended to 273–343 K. The temperature-sensitive microparticles and the oxygen-sensitive microbeads are both dispersed in a polymer hydrogel solution and casted on a surface to give a dual temperature and oxygen sensor. The oxygen-sensitive microbeads were made of oxygen-sensitive complexes of palladium and porphyrin embedded in P(St-*co*-AN). Stich et al. (2008) suggest that the temperature can be monitored with very high spatial resolution by time-resolved fluorescence imaging because the luminescence lifetime of the temperature indicator is 10-fold longer than that of the oxygen indicator.

The crucial role of the matrix is also outlined by Sun et al. in comparing the thermometric performance of the $[Tb(thba)_3]$ complex when it is processed in several ways (Sun et al., 2010). The excitation wavelength of the complex is well in the UV (334 nm). The thermometric parameters are both intensity and lifetime and the working temperature range is 288–343 K. The $[Tb(thba)_3]$ complex was processed in three different ways:

- Dispersed in a polyurethane hydrogel and subsequently casted on a glass slide.
- Aqueous dispersion of precipitated NPs (10–20 nm in size) to make a colloid.
- NPs dispersed in acetonitrile mixed with a 10 wt% aqueous solution of PVA, knife coated onto a glass slide and evaporated to obtain transparent films.

The maximum relative sensitivity in polyurethane films is $S_m = 2.9\% \, K^{-1}$ (298–318 K) and that of NPs in water dispersions in this range is similar, $S_m = 2.8\% \, K^{-1}$. The big difference between the two materials is that the variation of the intensity with temperature is positive in the first case and negative in the second. Furthermore, the intensity/temperature ratio returned to negative values when the NPs were dispersed in PVA. The mechanism behind the temperature sensing was not entirely understood (Sun et al., 2010).

Polymers are also excellent matrices for dual-center emitters, despite the possibility of the energy transfer between the two Ln^{3+} ions quenches one of the emissions, as established by Sato et al. (1989). Dual-center emitters based on polymer matrices can also be made using nonlanthanide emitters as reference, as shown in Wang et al. (2015b). Moreover, this report is also demonstrating the capacity of polymer system for processing and multisensing. It presents a multisensor in the form of biocompatible sprayable thermogelating material (Fig. 23). In this case, the thermometric probe is $[Eu(dbm)_3(phen)]$ working in the range 298–328 K that is incorporated in
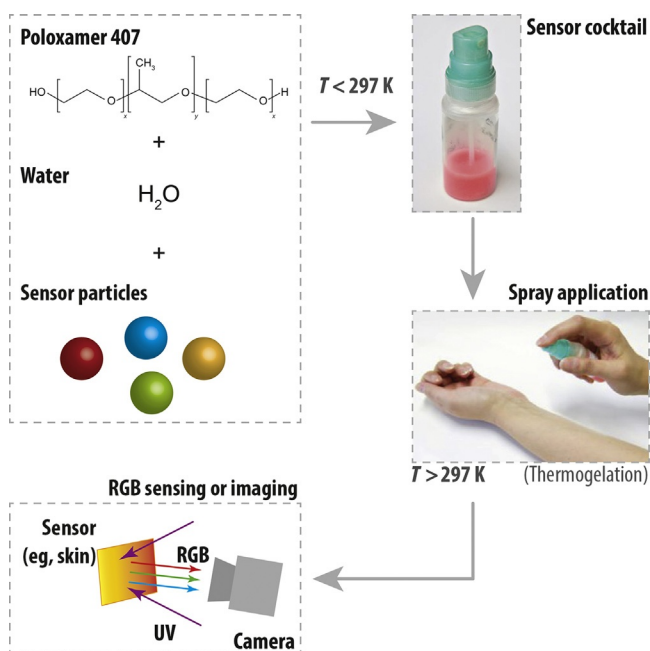
FIG. 23 Application of multisensor NPs by thermogelating spray on a wound. The NPs are dispersed in water with a thermogelating polymer, Poloxamer® 407. The dispersion is sprayed at a temperature below 297 K to remain fluid, and then is heated above this temperature to gelate. Sensing and imaging of the sensor can then be performed via ratiometric red–green–blue readout using a digital camera equipped with a blue or UV excitation light source. *Adapted with permission from Wang, X., Meier, R.J., Schmittlein, C., Schreml, S., Schäferling, M., Wolfbeis, O.S. 2015b. A water-sprayable, thermogelating and biocompatible polymer host for use in fluorescent chemical sensing and imaging of oxygen, pH values and temperature. Sens. Actuators B: Chem. 221, 37–44. © 2015 Elsevier B.V.*

poly(vinylidene chloride-*co*-acrylonitrile) polymer NPs. The reference chromophore is the dpa blue emitter that is incorporated as a dopant in PAN microparticles.

The use of polymers is quite suitable to make biocompatible nanothermometers that can be used in biomedical applications. A good example was reported by Takei et al. (2014) in which the thermosensitive and the reference fluorophores are, respectively, a [Eu(tta)$_3$] complex and Rh 101. Both emitters are embedded in PMMA NPs that were internalized in HeLa cells and observed by fluorescence microscope. An analysis of the fluorescence intensity yielded the temperature at each NP spot. This system was used to follow the effect of Ca^{2+} absorption in the cell. An increment of temperature was observed at certain spots that were associated to Ca^{2+} location in the cell, demonstrating that Ca^{2+} activity causes heat generation and the nanothermometer can be employed to follow that heating on a single cell.

An example that exploits the high versatility of lanthanide molecular thermometry can be found in Piñol et al. (2015). In this report, the thermometer

was implemented in a magnetic nanoheater consisting on a core–shell nanobead with a magnetic nucleus and a copolymer shell. The magnetic nucleus consists of iron oxide NPs that can be heated at a distance with an alternating magnetic field. The thermometric Ln^{3+} complexes are placed on the surface of the magnetic nucleus so they are sensing the temperature of the nanoheater core. The response of the molecular thermometer depends on the experimental setup and was measured as 0.25 s. Thus, the evolution of the nanoheater temperature could be followed in detail during relatively long heating and cooling periods, but also at the events of switching on and switching off the field (Fig. 24). In fact, the rapidity of the response is crucial at these events and the measurements revealed unexpected features on the process of heat diffusion from the nanoheater to the medium that cannot be explained with present theories (Piñol et al., 2015). The molecular nature of the thermometer and its optical character permitted also a high spatial resolution when the emission was captured on the camera of a fluorescence microscope. Given the biocompatibility of the materials used, its nanometric size, and the capacity of the object for conjugation with biovectors and other biological functionalities, it can be of great utility in biological applications. Actually, its capacity for temperature mapping of cells has been demonstrated (Piñol et al., 2015), and it can be a decisive tool for the development of local hyperthermia therapies of cancer. The concept of local hyperthermia is based on the generation of lethal temperature increments in small areas inside the cells instead of a global tissue temperature increase. To determine the feasibility of this concept it is necessary to use local temperature probes to measure the temperature gradients from the heater source and the exterior of the cell. Besides a reliable means to monitor temperature during magnetic hyperthermia treatments at a subcellular scale, these nanothermometers can potentially solving the paradox of "cold hyperthermia" (cellular death in the absence of a perceptible rise of the macroscopic temperature of the medium) (Périgo et al., 2015).

5.2.2 In Inorganic Matrices

The encapsulation of molecular thermometers in inorganic matrices is rare and mostly based on the use of clays. For instance, positively charged aminoclays have been used as a host for $Eu^{3+}:Tb^{3+}$ (1/7) complexes with btc (Wang et al., 2014). The material shows a linear temperature dependence of the I_{Tb}/I_{Eu} ratio in the 78–288 K range with $S_m = 0.74\% \, K^{-1}$ for Tb^{3+} and is dispersible in water, being therefore processed as a paint. Although proposed for pH sensing, the Eu-(tta) complex has also been encapsulated in other inorganic matrices, like laponite (Li et al., 2015).

5.2.3 In Organic–Inorganic Hybrid Matrices

Hybrid materials are also versatile matrices that can expand the processability and thermometric applications of powder-based thermometers presented in
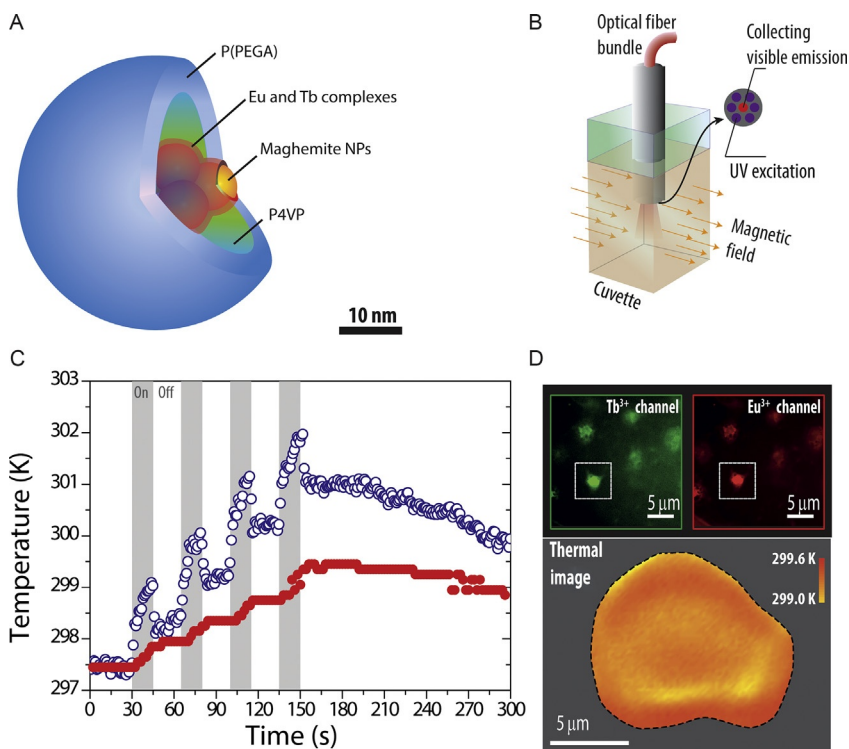
FIG. 24 Nanothermometer and nanoheater in a single NP. (A) The molecular ratiometric ther-
mometer is formed by Eu^{3+} and Tb^{3+} complexes placed around a magnetic nuclei that are heated
with an external ac magnetic field. (B) Hyperthermia experimental setup used to measure the tem-
perature dynamics. (C) The temperature of the heater can be followed in on–off heating cycles by
the luminescent thermometer (*open circles*) and with a control semiconductor-based thermal
probe immersed in the nanoparticle suspension (*full circles*). Whereas the control thermometer
measures the suspension's temperature, the luminescent thermometer is able to measure the tem-
perature of the heated NPs. (D) Temperature mapping of ex vivo HeLa cells using a multispectral
image of Eu^{3+} and Tb^{3+} emissions. The pixel-by-pixel Tb^{3+}/Eu^{3+} intensity ratio gives the temper-
ature of the medium with spatial resolution up to 200 nm. *Adapted with permission from Piñol, R.,
Brites, C.D.S., Bustamante, R., Martínez, A., Silva, N.J.O., Murillo, J.L., Cases, R., Carrey, J.,
Estepa, C., Sosa, C., Palacio, F., Carlos, L.D., Millán, A. 2015. Joining time-resolved thermome-
try and magnetic-induced heating in a single nanoparticle unveils intriguing thermal properties.
ACS Nano 9, 3134–3142. © 2015 American Chemical Society.*

Section 5.1. The physics of the thermometric process is radically different to
that of doped complexes, as mentioned in Section 1.

Thanks to the organic component, Ln^{3+} complexes are dispersible in
hybrid matrices (Lima et al., 2006, 2009). Besides, the inorganic component
provides mechanical properties that cannot be found in organic matrices,
so the judicious combination of both properties in materials result usually
on valuable add-on when compared with the separated counterparts

(Carlos et al., 2009). Among many interesting applications, organic–inorganic hybrids can be interesting as host matrices for Ln^{3+} molecular thermometry (Millán et al., 2016).

Thanks to their dual character, hybrids can gather the physical properties of inorganic materials and the processability of organic polymers (Escribano et al., 2008; Sanchez et al., 2005, 2011). Besides, they can also benefit from the synthetic facilities of sol–gel process that can be performed at room temperature and, like the polymerization of organic monomers, can be activated in a variety of forms. An example is the thermometric system proposed by us in 2010 (Brites et al., 2010). The matrix was a diureasil hybrid framework formed by a siliceous backbone in which PEG chains of different lengths are grafted on both sides by urea bridges (Carlos et al., 2000; de Zea Bermudez et al., 1998, 1999). The encapsulation of the complexes was performed by mixing them with the alkoxysilane diureasil hybrid precursors in solution. Then, the hydrolysis and condensation reactions of the alkoxy groups produce the intercrossing of the polymer chains forming a solid organic–inorganic hybrid framework with a uniform distribution of the Ln^{3+} thermometric complexes. The hybrids, processed as monoliths or thick and thin films, can be applied on the object on which the temperature must be determined by spraying, dip, or spin coating. Diureasil hybrid films were used as self-referenced and efficient luminescent probes to map temperature in microelectronic circuits and optoelectronic devices (Brites et al., 2010, 2013a,c; Ferreira et al., 2013).

The temperature mapping using Ln^{3+}-doped hybrid matrices was reported by Brites et al. using a diureasil film doped with [Eu(btfa)$_3$(MeOH)(bpeta)] and [Tb(btfa)$_3$(MeOH)(bpeta)] β-diketonate chelates (Brites et al., 2010). The absolute emission quantum yield is 0.16 ± 0.02 and $S_m = 1.9\% \, K^{-1}$, at 201 K, diminishing to 0.7–$0.4\% \, K^{-1}$ in the 300–350 K range. The high spatial resolution achievable with this system was demonstrated with a simple emission detector system consisting on scanning with an optical probe (Fig. 25), which improved that recorded with a state-of-the-art commercial IR thermal camera. With a small-scanning step the resolution can be improved up to 0.42 μm (see Section 3.3.1 for the discussion on spatial resolution of luminescent thermometers), below the Rayleigh limit of diffraction (1.89 μm) associated to the fibers diameter (200 μm). Afterward, the same research group measured the temperature gradient between the two Mach–Zehnder arms using diureasil films embedded the [Eu(btfa)$_3$(MeOH)(bpeta)] and [Tb(btfa)$_3$(MeOH)(bpeta)] complexes (Ferreira et al., 2013). When compared with the IR camera, the diureasil thermometer presents a better spatial resolution (28 μm instead of 128 μm) due to the significant temperature averaging of the camera that produces a smoothed readout of the temperature profile. This intrinsic limitation of the IR camera is critical to evaluate the temperature gradient in the region where the Mach–Zehnder was fabricated, which critically precludes the output modeling and prediction of the device optical performance (Ferreira et al., 2013).
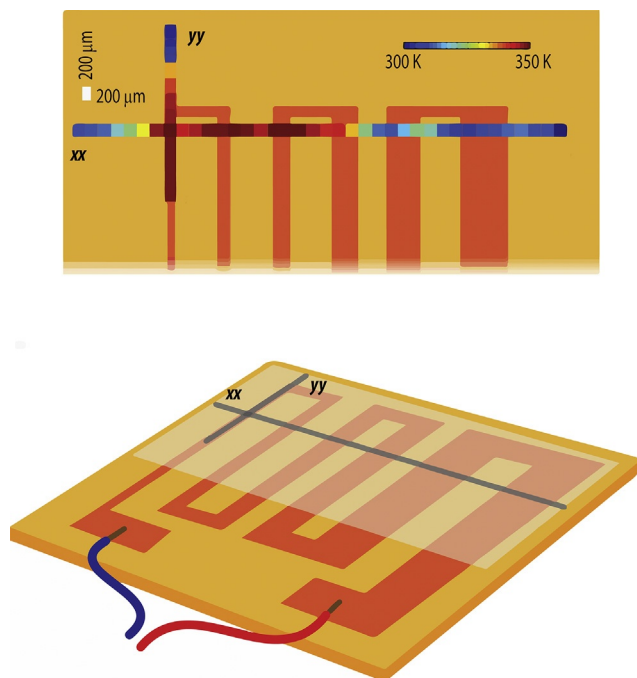
FIG. 25 Temperature pseudocolor map of an FR-4 wire-board covered by a molecular thermometer embedded into a diureasil organic–inorganic hybrid film. The emission of the film (excited at 365 nm) is used to map the temperature along the directions *xx* and *yy*.

5.3 Metal-Organic Frameworks

As pointed out earlier, Ln^{3+} ions and ligands can be arranged in MOFs that are also useful in luminescence thermometry. The working mechanism is similar to molecular thermometers but the ligands are carboxylic acids instead of ketonates, however they are crystals instead of molecules and they must be processed in a very different way. An extensive account on the processability of MOFs can be found in Falcaro et al. (2014). Their high advantage with respect to molecular thermometers is that ordered structure confers them a highly reproducible response. They are usually prepared by solvothermal (Cui et al., 2012) synthesis, although reverse micelles (Cadiau et al., 2013) and spray-drying methods (Wang et al., 2015c) have also been used.

Cui et al. (2012) and Cadiau et al. (2013) were the first to build self-referencing thermometers using MOFs and nano-MOFs, respectively. Cui et al. used dmbdc ligands and Eu^{3+} and Tb^{3+} ions mixed in a 7:1000 ratio. The thermometric crystals had micrometer size, a working temperature range of 10–300 K, and a constant $S_a = 0.38\% \, K^{-1}$ (corresponding to $S_m = 1.15\%$ K^{-1} at 200 K), can be computed from the published data. The working range of MOFs-based thermometers was increased (300–320 K) to reach

physiological values by Cadiau et al. using a similar ligand, bdc, and a 1/100 Eu/Tb ratio (Cadiau et al., 2013). In this case, $S_m = 0.37\%$ at 318 K, and the size of the thermometric crystals was reduced to the nanometric range, so they could be suspended in a liquid, opening the way for biological applications. Since then, most of the newly developed MOF nanothermometers have been proposed for this application. Later on Cui et al. reported the use of $Eu_{0.0069}Tb_{0.9931}$-dmbdc regarding the improvement relative sensitivity value in the physiological gamut, presenting a $S_m = 16\% \, K^{-1}$ at 300 K, by means of a simultaneous decrease of the $^5D_4 \rightarrow \, ^7F_5$ transition intensity and an increase of the $^5D_0 \rightarrow \, ^7F_2$ transitions intensity (Cui et al., 2014).

MOF thermometers can be obtained with a maximum absolute sensitivity $S_a \sim 30\% \, K^{-1}$ between 20 and 65 K ($S_m = 7.14\% \, K^{-1}$ at 65 K, calculated by us) using dsb ligands and combinations of $Eu_{0.02}Gd_{0.98}$ or $Eu_{0.05}Tb_{0.09}Gd_{0.86}$ ions (D'Vries et al., 2013). This thermometer, however, is only operative in the 10–300 K range, not covering physiological temperatures. In this system, temperature-dependent emission is the ligand triplet blue emission that decreases with the temperature, and the reference emission is that of the Eu^{3+} (or Tb^{3+}) ion. In this case, the structure is one-dimensional and the ions are arranged in the form of singular heptanuclear $[Ln_7(OH)_9]^{+12}$ metallic-cored secondary building unit surrounded by 4 dsb ligands.

Ratiometric mixed lanthanide-organic dye thermometers can also be constructed by absorption of organic dye emitters in the pores of the MOF structure. A proof-of-concept can be found in Cui et al. (2015a). The MOF consists of Eu^{3+} ions and qptc ligands, the absorbed dye is perylene that has an emission peak at 473 nm that decreases with the temperature. The thermometer's working range (388 nm excitation) is 293–353 K with an absolute sensitivity (based on the I_{615}/I_{473} ratio) constant and equal to $S_a = 1.28\% \, K^{-1}$ (corresponding to $S_m = 0.86\% \, K^{-1}$ at 301 K, calculated by us). The advantages introduced by this approach are to expand the available wavelength range for thermometry and to increase S_r near room temperature by dye-to-Ln^{3+} energy transfer.

A postfunctionalization method (Zhou et al., 2014d) has been used to produce MOF thermometers that show a good sensitivity ($S_a = 4.97\% \, K^{-1}$ and $r^2 = 0.996$ that corresponds to $S_m = 1.11\% \, K^{-1}$ at 283 K, calculated by us), even in the physiological range. The thermometers are prepared from In(OH)(bpydc) crystals with a three-dimensional framework structure consisting of chains of corner-sharing InO_6-octahedra interconnected by bpydc ligands. The Eu^{3+} and Tb^{3+} ions in a 0.005 ratio are introduced after synthesis by immersion in a solution of the lanthanides salts. The Ln^{3+} ions are fixed to the framework structure by coordination to the bipyridine (bpy) ligands. The excitation wavelength (315 nm) is well in the UV range, however, it can be increased to 487 nm with only a slight decrease in the absolute sensitivity to $3.69\% \, K^{-1}$ and $r^2 = 0.9993$ (corresponding to $S_m = 1.13\% \, K^{-1}$ at 283 K). It is also shown that S_a can be improved by decreasing the

Eu/Tb ratio, $S_a = 18.8\%\,K^{-1}$ for 0.1% Eu, corresponding to $S_m = 1.39\%\,K^{-1}$ at 283 K (calculated by us). However, the thermometer precision decreases as the correlation coefficient of the linear fit degrades to $r^2 = 0.9894$. The postfunctionalization method was also used to synthesize tunable white-light emitters nanocrystalline MOFs with $S_a = 47.98\%\,K^{-1}$ at 140 K (that corresponds to $S_m = 3.01\%\,K^{-1}$ at 180 K, calculated by us) (Zhou and Yan, 2015).

5.4 Upconverting Nanoparticles

Like in molecular thermometers, UCNPs-based thermometers are based on one or two emission bands showing a different variation with temperature. However, the excitation mechanism (Fig. 20) is quite different as the light is captured by a sensitizer ion in a host crystal (Sedlmeier et al., 2012). A detailed description of the mechanisms of the upconversion process can be found in several recent reviews (Bettinelli et al., 2015; Burbano et al., 2015; Chen et al., 2014; Liu, 2015; Liu et al., 2013; Wang and Liu, 2009; Zhou et al., 2015a,b). Moreover, the sensitizer, usually Yb^{3+}, that has a large absorption cross section, absorbs IR light (980 nm) transferring the energy to the activator in a double- or triple-photon processes. The activator releases this energy by multiple emission bands at shorter wavelengths (visible) that have different response to temperature variations. Common activators in UCNPs (eg, Er^{3+}, Tm^{3+}, Ho^{3+}, Tb^{3+}, and Eu^{3+}) are characterized by a ladder-like energy level structure and they are incorporated in the host lattice as dopants in a ratio lower than 2 mol% to minimize cross-relaxation energy losses. The $^2F_{7/2} \rightarrow {}^2F_{5/2}$ transition of Yb^{3+} is resonant with many f–f transitions of the activators, thus facilitating efficient energy transfer. Suitable host compounds are CaF_2, $NaYF_4$, $NaGdF_4$, NaY_2F_5O, LaF_3, Y_2O_3, Gd_2O_3, ZnO, Al_2O_3, $Y_2Ti_2O_7$, $Y_3A_5O_{12}$, $YNbO_4$, $CaMoO_4$, $BaTiO_3$, $SrWO_4$, $KLu(WO_4)_2$, and $LnPO_4$.

Like MOFs, UCNPs have a crystalline structure, and their thermometric response is very reproducible. On the other hand, they need high excitation power and they are normally operated with laser light sources. They also have lower sensitivities than hybrid NPs made with the same lanthanide ions (Dong et al., 2012).

Host compounds are sparingly soluble and form crystals of nanometric size by simple coprecipitation in water at moderate temperatures. However, this method yields high size dispersion, low crystallinity, and agglomeration. These drawbacks can be overcome by performing the synthesis at high temperature, Fig. 26. A frequent synthesis method is the hydrothermal reaction of lanthanide salts and fluorides that can be assisted by microwaves heating. They are also prepared by thermal decomposition of organic precursors in organic solvents at high temperature in the presence of surfactants. This method yields very low size dispersion, but it is obviously more expensive.
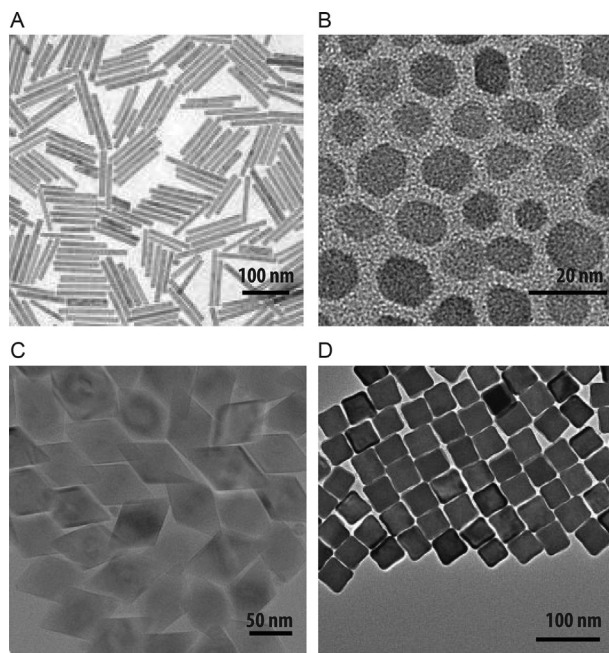
FIG. 26 UCNPs with high crystallinity and different shapes and sizes. (A) and (B) correspond to NaYF$_4$ and LaF$_3$, respectively, and were prepared by hydrothermal methods. (C) and (D) correspond to NaYF$_4$:Yb^{3+}/Er^{3+} and LiYF$_4$:Yb^{3+}/Er^{3+}, respectively, and were prepared by decomposition of organic precursors at high temperature in organic solvents. *Reproduced with permission from Wang, L., Li, Y. 2006. Na(Y$_{1.5}$Na$_{0.5}$)F$_6$ single-crystal nanorods as multicolor luminescent materials. Nano Lett. 6, 1645–1649. © 2006 American Chemical Society; Hu, H., Chen, Z., Cao, T., Zhang, Q., Yu, M., Li, F., Yi, T., Huang, C. 2008. Hydrothermal synthesis of hexagonal lanthanide-doped LaF3 nanoplates with bright upconversion luminescence. Nanotechnology 19, 375702. © 2008 IOP Science; Mahalingam, V., Vetrone, F., Naccache, R., Speghini, A., Capobianco, J.A. 2009. Colloidal Tm^{3+}/Yb^{3+}-doped LiYF4 nanocrystals: multiple luminescence spanning the UV to NIR regions via low-energy excitation. Adv. Mater. 21, 4025–4028. © 2009 Wiley-VCH Verlag GmbH; and Park, Y.I., Kim, J.H., Lee, K.T., Jeon, K.-S., Na, H.B., Yu, J.H., Kim, H.M., Lee, N., Choi, S.H., Baik, S.-I., Kim, H., Park, S.P., Park, B.-J., Kim, Y.W., Lee, S.H., Yoon, S.-Y., Song, I.C., Moon, W.K., Suh, Y.D., Hyeon, T. 2009. Nonblinking and nonbleaching upconverting nanoparticles as an optical imaging nanoprobe and T1 magnetic resonance imaging contrast agent. Adv. Mater. 21, 4467–4471. © 2009 Wiley-VCH Verlag GmbH.*

Other synthetic methods are solid and sol–gel reactions. In thermal decomposition methods in organic solvents, and often also in hydrothermal methods, surfactants are used to control the growth of the NPs. That permits a fine control of the size and shape of the crystallites (Fig. 26). However, the resulting NPs are hydrophobic, and they need to be surface modified to make them water dispersible.

Whereas the working temperature range of molecular thermometers is hardly reaching 373 K, that of upconversion thermometers covers a very wide

range of temperatures from a few degrees K to more than 1000 K, so they are especially suitable for high-temperature applications. Nevertheless, they are mainly proposed for in vivo applications (Hao et al., 2013; Zhang and Liu, 2013; Zhou et al., 2015a) because their IR excitation light has a large penetration depth into living tissue, >2 mm, in comparison with visible or UV light (del Rosal et al., 2015; Dong et al., 2011). It is also less damaging to cells, and it can be detected without interference from tissue autofluorescence (Tian et al., 2014).

The thermometric performance of UCNPs depends on the composition, the size, and the crystallinity of the host, and on the type and concentration of activators and sensitizers. UCNPs hosts should have low lattice phonon energies in order to minimize nonradiative loss (Bettinelli et al., 2015; Liu, 2015; Wang and Liu, 2009; Zhou et al., 2015b). That is the case of heavy metal halides. Among them, fluorides are the most chemically stable so that they are ideal for this purpose. $NaYF_4$ has often been the choice as an upconverting host, but it has recently been found that $NaLuF_4$ may comparatively increase the upconversion light intensity by 10-fold (Yang et al., 2012). For instance, $NaLuF_4$:Yb/Ho (10/0.5%) and $NaLuF_4$:Yb/Gd/Tm (20/20/0.7%) under 980 nm excitation and at 500 K have $S_r = 0.83$ and $0.267\% \, K^{-1}$, respectively, values higher than that of $0.263\% \, K^{-1}$ for $NaYF_4$:Pr (0.8%) at the same temperature (Zhou et al., 2014c). Moreover, the sensitivity of UCNPs with oxide ceramic matrices is comparable to that of fluorides. For instance, $S_r = 0.41$, 0.57, and $0.68\% \, K^{-1}$ at 500 K have been reported for $YNbO_4$:Yb/Er (2/0.3%), La_2O_2S:Nd (1%), and $Y_4Al_2O_9$:Dy (0.3%), respectively (Zhou et al., 2014c). A comparison of the thermal sensitivities of oxide ceramic hosts (eg, Gd_2O_3, $BaTiO_3$, Al_2O_3, $YNbO_4$, $LiNbO_3$, $CaWO_4$, $La_2(WO_4)_3$, $SrWO_4$, $CaMoO_4$, and $SrMoO_4$) with the Er^{3+}/Yb^{3+} activator/sensitizer pair can be found in Huang et al. (2015a). We note, however, that as the authors used S_a instead of S_r the comparison is useless; S_a critically depends on the constant B in Eq. (25) (that when experimentally determined depends on the setup used). Although they are mostly known for their use in IR thermometry, oxide ceramics can also be useful as luminescent thermometers under UV excitation. An example is that of scheelite-based $CaGd_{2(1-x)}Eu_{2x}(WO_4)_4$ solid solutions (Meert et al., 2014). The intensity ratio between the $^5D_1 \rightarrow {}^7F_1$ (535–545 nm) and the $^5D_0 \rightarrow {}^7F_1$ (585–600 nm) transitions has a temperature dependence in the range 300–500 K, with S_m ranging from $1.4\% \, K^{-1}$ (300 K) to $0.47\% \, K^{-1}$ (475 K). Actually, this compound has been used in the form of powders mixed with silicones to map the temperature of a resistive heater with the help of a photographic camera. A disadvantage of this system is the low relative intensity of the $^5D_1 \rightarrow {}^7F_2$ emission, as compared to the $^5D_0 \rightarrow {}^7F_2$ one, that makes acquisition times very long.

Upconverting materials have also been proposed for low temperature thermometry. For instance, for Y_2O_3:Yb^{3+}/Ho^{3+} submicron porous powders under 978 nm excitation Lojpur et al. reported maximum absolute sensitivities at

85 K of 9.7% K^{-1}, corresponding to $S_m = 1.61\% K^{-1}$, computed by us (Lojpur et al., 2013). Nevertheless, S_a decreases abruptly below and above this value. At 300 K, the value has decreased to 2% K^{-1}, corresponding to $S_r = 0.14\% K^{-1}$, as computed by us. According to the same authors, the maximum absolute sensitivity of Y_2O_3:Yb^{3+}/Tm^{3+} although lower is found at higher temperatures; near room temperature it is 7.8% K^{-1} (or $S_m = 0.55\% K^{-1}$, computed by us).

The feasibility of in vivo upconversion imaging has been demonstrated by subcutaneously injection of PA-coated Yb/Er/Mo-doped nanocrystal suspensions into the back of nude mice, and imaging with a 976 nm laser as the excitation light (power density ~ 0.2 W cm^{-2}) (Dong et al., 2012). However, the Er^{3+} emissions lie in the visible range, and to improve the penetration depth, both the excitation and the emission should be located within the first biological window (650–950 nm) (Cerón et al., 2015). An example is the two-photon NIR-to-NIR conversion observed in Yb^{3+}/Tm^{3+}-doped CaF_2 NPs (Dong et al., 2011). The penetration depth of Tm^{3+} fluorescence signal at 790 nm in phantom tissue was close to 2 mm, more than $4\times$ higher than that of Er^{3+} fluorescence visible signal at 655 nm in similar Yb^{3+}/Er^{3+}-doped CaF_2 NPs.

Most of UCNPs proposed for thermometry of biological applications are based on the Yb^{3+} sensitization at 980 nm. This excitation wavelength is overlapped with the maximum absorption band of water molecules (obviously abundant in biological tissues) and, therefore, the penetration depth in the tissues at this wavelength is reduced, with the associated increase of the local heating (McNichols et al., 2004). The optimal wavelength within the first biological window is around 800 nm (Kobayashi et al., 2010) that shows the lowest water absorption. Consequently, one has now the tendency to use excitation wavelengths around this value, see Shen et al. (2013) and Fig. 27.

A very intriguing example concerning UCNPs is the work of Zheng et al. that proposes a ratiometric temperature sensor based on core/shell NPs formed by a $NaGdF_4$:Yb^{3+}/Tm^{3+} core and an $NaGdF_4$:Eu^{3+}/Tb^{3+} shell (Zheng et al., 2014). The Yb^{3+}/Tm^{3+} pair harvests NIR photons at 980 nm exciting then the Gd^{3+} ions to the UV-lying levels via Yb^{3+}–Tm^{3+}–Gd^{3+} energy transfer process. Subsequently, energy is transferred from the Gd^{3+} ions in the core to the Gd^{3+} ions in the shell where, through another energy transfer process, it reaches the Tb^{3+} and Eu^{3+} ions resulting in green (545 nm) and red (615 nm) emissions, respectively. The thermal ratiometric parameter is the ratio between the intensities of these two emissions and $S_m = 0.50\% K^{-1}$ at 300 K is obtained. What is uncommon in this example is that the Tb^{3+} and Eu^{3+} excitation is reached through a two-step mechanism involving firstly a Yb^{3+}–Tm^{3+}–Gd^{3+} NIR-to-UV upconversion multiphoton process followed by energy migration between Gd^{3+} ions for a wide range of Ln^{3+} activators without long-lived intermediary energy states (Wang et al., 2011b). This design of core–shell nanostructures with different dopants in each layer,
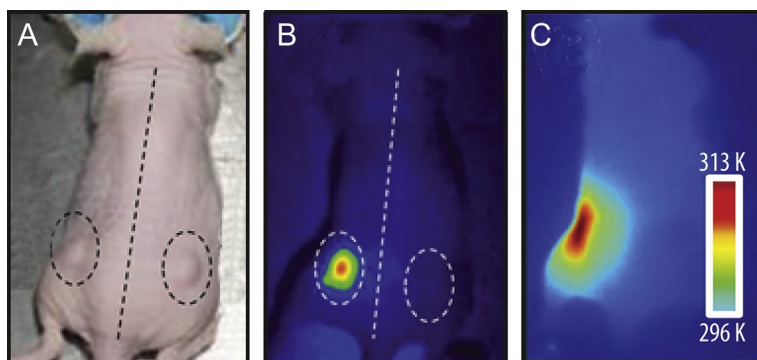
FIG. 27 (A) Optical image of a mouse with two tumors. $LaF_3:Nd^{3+}$ NPs were injected only in the left-side tumor whereas the right-side one was used as a control. (B) and (C) Infrared fluorescence and thermal images of the mouse under 808 nm (4 W cm^{-2}) laser irradiation, respectively. *Adapted with permission from Carrasco, E., del Rosal, B., Sanz-Rodríguez, F., de la Fuente, Á.J., Gonzalez, P.H., Rocha, U., Kumar, K.U., Jacinto, C., Solé, J.G., Jaque, D. 2015. Intratumoral thermal reading during photo-thermal therapy by multifunctional fluorescent nanoparticles. Adv. Funct. Mater. 25, 615–626. © 2015 Wiley-VCH Verlag GmbH.*

proposed by Wang and Liu in 2011, (Wang et al., 2011b) is an important breakthrough on the historical development of photon upconversion in Ln^{3+}-doped materials (Bettinelli et al., 2015). Based on this idea, a core–shell–shell NP design displaying tunable upconversion emissions spanning from UV to the visible spectral region by single wavelength excitation at 808 nm was suggested two years later (Wen et al., 2013). The design involved the growth of $NaYbF_4:Nd^{3+}$ (50 mol%) core NPs followed by successive deposition of two epitaxial shells of $Na(Yb,Gd)F_4:Er^{3+}$ (or $Na(Yb,Gd)F_4:Ho^{3+}/Tm^{3+}$) and $NaGdF_4$. The Nd^{3+} ions were used to harvest the NIR excitation, whereas the Yb^{3+} ions are designed to extract the excitation energy from Nd^{3+} and to subsequently transport the energy to the inner shell layer where upconverter ions (Er^{3+}, Ho^{3+}, or Tm^{3+}) were confined. The $NaGdF_4$ outermost shell layer passivates the active inner shell layer, protecting the upconverting process from surface quenchers (Han et al., 2014) and tuning the optical emission by encoding additional emitter ions (eg, Tb^{3+}, Eu^{3+}, Dy^{3+}) that are able to capture the upconverted energy through the Gd network of the sublattice (Wen et al., 2013).

The main advantage of a two-photon excitation process, relatively to one-photon absorption, is the substantial improvement that could be achieved in spatial resolution, due to the high order nature of the excitation process and the use of shorter emission wavelengths (Bettinelli et al., 2015; Pereira et al., 2015). Further spatial resolution improvement of temperature measurements would, therefore, be obtained if the thermosensitive luminescence would be excited under a three-, four-, or even five-photon excitation mechanism (Caillat et al., 2013). Three-photon excited Ln^{3+} emissions were

explored for thermal sensing in Yb^{3+}/Tm^{3+}- (dos Santos et al., 2001; Lojpur et al., 2013; Pereira et al., 2015) and Yb^{3+}/Ho^{3+}-doped (Xu et al., 2013) materials. An intriguing example of a five-photon excited Yb^{3+}/Er^{3+} β-NaLuF$_4$ nanothermometer involving the highest energy states for optical thermometry known so far (the $^4D_{7/2}$ and $^4G_{9/2}$ Er^{3+} levels) is recently reported (Zheng et al., 2015).

Naked crystals have limited light absorption due to the low doping concentration necessary to avoid quenching. However, the doping concentration can be increased without quenching problems when the excitation irradiation is increased. In this way, single crystal sensitivity has been achieved (Zhao et al., 2013). Light absorption and spectrum broadness can be greatly enhanced also by sensitization with NIR organic dye antennas (Zou et al., 2012). It has been observed that NaYF$_4$:Yb^{3+}/Er^{3+} NPs coated with the organic dye IR-806 increases their integrated spectral response in the 720–1000 nm range by more than 3000$\times$, with respect to uncoated NPs. The enhancement of upconversion efficiency occurs by absorption of NIR photons by the dye "antennae" and transfer of their excitation energy to the Yb^{3+} $^2F_{5/2}$ level by resonance energy transfer. Then the energy is typically transferred form Yb^{3+} to Er^{3+} leading to the Er^{3+} emission of upconverted light.

5.5 NIR-Emitting Nanoparticles

In particular, because Nd^{3+} has a ladder-like intra-4f energy level structure, the excitation and emission lie within the first biological window where the transparency of living tissues is high due to low optical absorption, offering much potential for deep-tissue luminescence imaging and temperature sensing (Carrasco et al., 2015; Cerón et al., 2015), as mentioned earlier. Only a limited number of reports on luminescent thermometry involving Nd^{3+}-doped nanocrystals are available, including LaF$_3$:Nd^{3+}, $S_m = 0.10\% K^{-1}$ at 283 K (Rocha et al., 2013, 2014a,b; Villa et al., 2014), NaYF$_4$:Nd^{3+}, $S_m = 0.12\%$ K^{-1} at 273 K (Tian et al., 2014; Wawrzynczyk et al., 2012), YAG:Nd^{3+}, $S_m = 0.15\% K^{-1}$ at 283 K (Benayas et al., 2015), and (Gd$_{0.991}$Nd$_{0.009}$)$_2$O$_3$ nanorods, $S_m = 1.75\% K^{-1}$ at 288 K (Balabhadra et al., 2015). Apart from their thermometric properties, UCNPs containing Nd^{3+} ions at high doping concentrations have also the capacity of heating by irradiation with a 808 nm laser beam (Carrasco et al., 2015). Actually, their use in controlled hyperthermia therapy has already been tested in animal tissues (Fig. 27). Mice with tumors formed by subcutaneous inoculation of cancer cells were injected with LaF$_3$:Nd^{3+} NPs directly in the tumor and then they were irradiated with the laser beam. The IR fluorescence of the NPs was captured with a camera and it was transformed to a thermal image that showed the NPs were heated up to temperatures around 323 K. The heating caused a selective size reduction of the tumors inoculated with the NPs, with respect to those inoculated with a phosphate-buffered saline solution.

6 CONCLUSION AND PERSPECTIVES

Luminescence thermometers have experienced a continuous and unprecedented growth over the past decade, after the handful of pioneering works published during the last quarter of the XXth century. The diversity of luminescent ratiometric thermometers reported so far (namely those operating at the nanoscale) points out the emergent interest of nanothermometry in microelectronics, microoptics, photonics, micro and nanofluidics, nanomedicine, and in many other conceivable applications, such as thermally induced drug release, phonon-, plasmonic-, and magnetic-induced hyperthermia and wherever exothermal chemical or enzymatic reactions occur at submicron scale. Examples are based on both individual thermal probes (eg, organic dyes, polymers, QDs, Ln^{3+}-based β-diketonates, and NPs) and more complex structures formed by probes encapsulated into polymer and organic–inorganic hybrid matrices. The total number of papers published since 2005 and dealing with luminescence thermometry or luminescent thermometers is around 400, a number that can substantially increase if publications describing potential or perspective systems are taken into account. Ln^{3+}-based thermometers, covering temperatures from cryogenic to physiological ranges and involving ionic and chelate complexes, clays, MOFs, and upconverting and downshifting NPs, account for approximately one-third of that number, as the majority of the papers involve organic dyes, polymers, and QDs. Moreover, the research on these different classes of Ln^{3+}-based thermometers has evolved in a distinctly different way, particularly concerning applications. While the research on MOFs, for instance, has been mainly focused on the synthesis and design of new structures and on the comparison of their thermometric performances, β-diketonates and NPs have already been used to map microelectronic and integrated optic components and to perform *in vivo* photothermal heating and intratumoral thermal sensing in mice, respectively. However, despite the actual promising progresses, the research on luminescence thermometry can be considered as in its early stages and more basic knowledge is still needed before prototypes become a commercial reality.

Up to now, the performance of the various reported luminescent thermometers has been essentially compared by means of the maximum relative sensitivity S_m (Eq. 4), introduced by us in 2012 as a figure of merit for luminescent and nonluminescent thermometric systems. In general, Ln^{3+}-based ratiometric thermometers have S_m values ranging from $0.1\% \, K^{-1}$ to $10\% \, K^{-1}$ (Fig. 28), similar to those reported for organic dyes-, polymers-, and QDs-based ones (Brites et al., 2012), covering a widespread temperature interval. For physiological temperatures, for instance, it is quite difficult to use the same polymer-based thermometer to cover the entire interval, as these systems are typically usable in a narrow range of ∼10 K (Brites et al., 2012).

The progress in the field requires undoubtedly the general use of quantitative parameters, such as temperature (δT), spatial (δx) and temporal (δt)
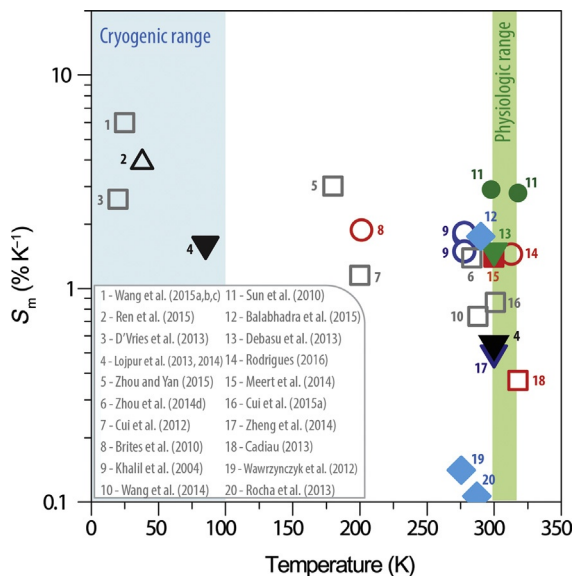
FIG. 28 Maximum thermal sensitivity values of illustrative examples of single- (*filled symbols*) and dual-center (*open symbols*) thermometers: ionic crystals (*up triangles*), molecular systems (*circles*), MOFs (*squares*), UCNPs (*down triangles*), and NIR NPs (*diamonds*).

resolutions, repeatability and reproducibility (R), errors in the thermometric parameter ($\delta\Delta$), temperature uncertainty ($\sigma_{\delta T}$), transition integrated areas ($\sigma_{\delta I/I}$), and relative sensitivity (σ_{S_r}) to optimize thermometer's performance and facilitate the comparison between distinct systems. For instance, in MOFs, upconverting and downshifting NPs it is necessary to establish the effect on these thermometric parameters of the size and the shape of the NPs, the relative concentration of the dopants and the host material. Therefore, instead of summarizing the latest advancements on Ln^{3+}-based thermometers, relatively well covered in a recent book (Carlos and Palacio, 2016) and in several reviews (Brites et al., 2012; Cui et al., 2015b; Jaque and Vetrone, 2012; Millán et al., 2016; Quintanilla et al., 2016; Wang and Zhang, 2015), the present manuscript focuses primarily on how to rationalize quantitatively the thermal response of luminescent thermometers, and how to precisely define the models and parameters governing their performance.

For secondary thermometers $\Delta(T)$ follows essentially two major trends: an exponential curve for single-center emission, eg, Yb^{3+}/Ln^{3+}- ($Ln = Er$, Tm, Ho) and Nd^{3+}-based thermometers, and a sigmoidal curve for dual-center emission, eg, Eu^{3+}/Tb^{3+}-based thermometers. The $\Delta(T)$, S_r, and δT curves computed for single- (Eqs. 25, 29, and 30) and dual-center (Eqs. 38, 40, and 41) thermometers (Fig. 18) permit to ascertain the following conclusions:

- Dual-center thermometers are more effective in the cryogenic range, reaching $S_m = 3\% \, K^{-1}$ and $\delta T = 0.2 \, K$, for $\Delta E = 600 \, cm^{-1}$ and $\delta \Delta / \Delta = 0.5\%$ (portable spectrometers).
- Although for $T < 70 \, K$, $S_m < 0.1\% \, K^{-1}$, and $\delta T > 1 \, K$, these values can be improved by one order of magnitude if PMT detectors are employed.
- To shift the operating range to temperatures around room temperature, the energy gap between the two thermally coupled levels must be larger than $1000 \, cm^{-1}$, which is much easier to accomplish if the Ln^{3+} ions are encapsulated into a polymer or an organic–inorganic hybrid host.
- Single-center thermometers are not effective in the cryogenic range, being more appropriate for high temperatures ($T > 200 \, K$), with thermometric parameters analogous to those obtained for dual-center examples (for similar ΔE values).
- The operating range can be shifted to higher temperatures increasing ΔE; however, as it is achieved at the cost of lowering the thermal coupling between the emitting states, caution must be taken to ensure that the two levels still remain thermalized in a thermodynamically quasi-equilibrium state.

The illustrative S_m values plotted in Fig. 28 are entirely in accord with these conclusions validating the general principles of the single- and dual-center models described in this review, and anticipating the possibility of employing these models to design new thermometers with optimized and predicted performance.

The main challenges that are currently facing scientists in the field are:

- To design nanothermometers for bioapplications and nanomedicine. New nanostructures whose emission and absorption bands lie within the so-called biological windows (650–950 and 1000–1350 nm), where tissue scattering and absorption are minimized (Cerón et al., 2015; Smith et al., 2009; Weissleder, 2001), optically active in biological medium, biocompatible, and easily uptaken by cells are mandatory to develop thermometry in nanomedicine.
- To record time-resolved intracellular temperature maps with spatial and temporal resolutions better than 1 μm and 1 s, respectively. Despite the considerable amount of research on intracellular thermometry carried out over the past 3–4 years, accurate and high-resolution temperature distributions within living cells have not yet been satisfactorily addressed.
- To improve the thermometers' spatiotemporal resolution below 1 μm–1 ms values. The temperature mapping in optoelectronic circuits is demanding for techniques combining high spatial and high temporal resolutions, compatible with the continuous high-rate data processing and miniaturization of the modern semiconductor devices. Luminescence will certainly play an important role in this process.

- To understand the energy transfer mechanisms that determine the thermal sensitivity of dual-center systems. Host-to-ion, ion-to-host, and ion-to-ion energy transfer mechanisms must be established and quantitatively described to clearly identify the functional form of $\Delta(T)$ and to compute the thermometric parameters. Malta's formalisms of ion-to-ion (Malta, 2008) and ligand-to-ion (Malta and Silva, 1998; Malta et al., 1997) energy transfer derived for luminescent complexes can be used to address this problem.

- To fully characterize heat transfer at the nanoscale (eg, in single heater–thermometer nanoplatforms and in nanofluids). For instance, continuous temperature monitoring with high-time resolution (1 s) under magnetic-, plasmonic-, or phonon-induced thermal heating opens intriguing possibilities in studies of the heat flow at the nanoscale, including thermal capacitance and conductivity across nanostructured media (Costescu et al., 2004), as for instance detailed studies in cellular thermal processes (Saunders and Verdin, 2009; Savitski et al., 2014). On the other hand, determining temperature gradients in a nanofluid (suspension of NPs) can pave the road to the quantitative characterization of the heat transport, a powerful tool to engineering the new generation of nanofluidic devices.

- To develop effective primary thermometers. The use of self-calibrated thermometers characterized by a well-established state equation, relating a specific measured value to the absolute temperature without the need of tedious calibrations for each particular conditions, are especially attractive when the thermometers are used in a different medium than that in which they are calibrated.

- To design multifunctional nanothermometers. A new generation of systems exploiting the synergetic integration of different functionalities in a single platform is required. Up to now, progresses have been essentially reported in assembling heaters and thermometers in the same NPs (Chen et al., 2015a; Debasu et al., 2013; Rohani et al., 2015; Song et al., 2015; Wang et al., 2015a). The integration of other functions in these heater–thermometer nanoplatforms, such as drug-delivery, MRI, PDT, and IR imaging is highly required and has an enormous potential in areas such as bio applications and nanomedicine.

- To integrate Ln^{3+}-based thermometers in commercial products. The notorious advantages of luminescence thermometry relatively to well-established techniques (eg, IR thermometry) will make possible the advent of prototypes in the near future.

In conclusion, Ln^{3+}-based luminescence thermometry is a versatile technique working in a wide range of the electromagnetic spectrum, from the UV to the IR and using peak shift, lifetime, risetime, or intensity ratios as thermometric parameters. The thermometers can operate from few to hundreds of Kelvin degrees, the operational interval of the majority of the thermal sensors

actually in the market, with suitable thermal sensitivity and temperature uncertainty, and a temperature acquisition readout, defined ultimately by the probe lifetime, that can be extended to the millisecond range. The gate to the field has only been ajar and there is still plenty of room at the bottom for developing this stimulating and exciting new field of research.

ACKNOWLEDGMENTS

LIST OF SYMBOLS

A_{0i}	total spontaneous emission rate from $|0>$ to $|i>$ state
A_{NR}	nonradiative transition probability
A_{R}	radiative transition probability
c	speed of light in vacuum
g_i	degeneracy of the ith energy level
h	Planck's constant
I	Luminescence intensity
k_B	Boltzmann's constant
N_a	number of atoms
N_i	population of the ith energy level
R	repeatability
S_a	absolute thermal sensitivity
S_m	maximum relative thermal sensitivity value
S_r	relative thermal sensitivity
T_D	Debye temperature
W_{0i}	angular frequency of the $i \rightarrow 0$ transition
α	kinetic constant
Δ	thermometric parameter
δ	uncertainty
δt	temporal resolution
δx	spatial resolution
σ	error
τ_i	lifetime of the ith energy level

ACRONYMS AND ABBREVIATIONS

3p-hfb	4,4,5,5,6,6,6-heptafluoro-1-phenanthren-3-yl-hexane-1,3-dione
APTES	3-aminopropyltriethoxysilane
bdc	1,4-benzenedicarboxylate
bp	2,2′-bipyridine-6,6′-dicarboxylic acid bis(N-hydroxy-succinimide) ester
bpeta	1,2-bis(4-pyridyl)ethane
bphen	4,7-diphenyl-1,10-phenantroline
bpy	2,2′-bipyridine
bpydc	2,2′-bipyridine-5,5′-dicarboxylic acid
btc	benzene-1,2,4,5-tetracarboxylate
btd	1,2-bis(trimethoxysilyl)decane
btfa	4,4,4-trifluoro-l-phenyl-1,3-butanedione
CCD	charge-coupled device
CNT	carbon nanotube
D2	1-phenanthren-3-yl-3-phenanthren-9-yl-propane-1,3-dione
dbm	dibenzoylmethane
dmbdc	2,5-dimethoxy-1,4-benzenedicarboxylate
DMF	dimethylformamide
dpa	9,10-diphenylanthracene
dpbt	2-(4-diethylamino-phenyl)-4,6-bis(3,5-dimethylpyrazol-1-yl)-1,3,5-triazine
dsb	3,5-disulfobenzoate
dt	tris(dinaphthoylmethane)-bis(trioctylphosphine) oxide
F7	1,1,1-trimethyl-5,5,6,6,7,7,7-heptafluoro-2,4-heptanedione
FIR	fluorescence intensity ratio
GFP	green fluorescent protein
HeLa	human cervical cancer cell line
hfa	hexafluoroacetylacetonate
hfp	heptafluoropropyl
IR	infrared
IR-806	2-[2-[2-chloro-3-[2-[1,3-dihydro-3,3-dimethyl-1-(4-sulfobutyl)-2H-indol-2-ylidene]-ethylidene]-1-cyclopentene-1-yl]-ethenyl]-3,3-dimethyl-1-(4-sulfobutyl)-3H-indolium hydroxide
LDH	layered double hydroxide
Ln³⁺	trivalent lanthanide
MEM	microelectromechanical
MeOH	methanol (CH_3OH)
MOF	metal-organic framework
MOSFET	metal–oxide semiconductor field effect transistor
MRI	magnetic resonance imaging
NIR	near infrared

NIR-797	1,1′-bis(4-sulfobutyl)-11-(4-isothiocyanatophenylthio)-3,3,3′,3′-tetramethyl-10,12-tri methyleneindotricarbocyanine monosodium salt
NP	nanoparticle
OASN	*N*-octyl-4-(3-aminopropyltrimethoxysilane)-1,8-naphthalimide
oda	diglycolic acid
P(St-*co*-AN)	poly(styrene-*co*-acrylonitrile)
pda	1,4-phenylenediacetate
PDA	photodiode array
pdca	2,6-pyridinedicarboxylate
PDT	photodynamic therapy
PEG	polyethyleneglycol
phen	1,10-phenanthroline
PMMA	poly(methyl methacrylate)
PMT	photomultiplier tube
PNIPAM	poly(*N*-isopropylacrylamide)
PVA	polyvinyl alcohol
QD	quantum dot
qptca	quaterphenyl-3,3′,5,5′ -tetracarboxylate
RhB	rhodamine B
S-0378	2-[2-[2-chloro-3-[2-[1,3-dihydro-3,3-dimethyl-1-(4-sulfobutyl)-2*H*-indol-2-ylidene]-ethylidene]-1-cyclopentene-1-yl]-ethenyl]-3,3-dimethyl-1-(4-sulfobutyl)-3H-indolium hydroxide, inner salt, sodium salt
SNR	signal-to-noise ratio
SThM	scanning thermal microscopy
TEOS	tetraethoxysilane
thba	tris[(2-hydroxy-benzoyl)-2-aminoethyl]amine
tta	thenoyltrifluoroacetonate
UCNP	upconverting nanoparticle
UV	ultraviolet
YAG	yttrium aluminum garnet

REFERENCES

Aigouy, L., Tessier, G., Mortier, M., Charlot, B., 2005. Scanning thermal imaging of microelectronic circuits with a fluorescent nanoprobe. Appl. Phys. Lett. 87, 184105.

Aigouy, L., Saïdi, E., Lalouat, L., Labeguerie-Egea, J., Mortier, M., Löw, P., Bergaud, C., 2009. AC thermal imaging of a microwire with a fluorescent nanocrystal: influence of the near field on the thermal contrast. J. Appl. Phys. 106, 074301.

Aigouy, L., Lalouat, L., Mortier, M., Löw, P., Bergaud, C., 2011. A scanning thermal probe microscope that operates in liquids. Rev. Sci. Instrum. 82, 036106.

Alencar, M.A.R.C., Maciel, G.S., de Araújo, C.B., Patra, A., 2004. Er^{3+}-doped $BaTiO_3$ nanocrystals for thermometry: influence of nanoenvironment on the sensitivity of a fluorescence based temperature sensor. Appl. Phys. Lett. 84, 4753–4755.

Alicki, R., Leitner, D.M., 2015. Size-dependent accuracy of nanoscale thermometers. J. Phys. Chem. B 119, 9000–9005.

Allison, S.W., Gillies, G.T., 1997. Remote thermometry with thermographic phosphors: instrumentation and applications. Rev. Sci. Instrum. 68, 2615–2650.

Ananias, D., Paz, F.A.A., Yufit, D.S., Carlos, L.D., Rocha, J., 2015. Photoluminescent thermometer based on a phase-transition lanthanide silicate with unusual structural disorder. J. Am. Chem. Soc. 137, 3051–3058.

Arai, S., Lee, S.C., Zhai, D., Suzuki, M., Chang, Y.T., 2014. A molecular fluorescent probe for targeted visualization of temperature at the endoplasmic reticulum. Sci. Rep. 4, 6701.

Arai, S., Suzuki, M., Park, S.J., Yoo, J.S., Wang, L., Kang, N.Y., Ha, H.H., Chang, Y.T., 2015. Mitochondria-targeted fluorescent thermometer monitors intracellular temperature gradient. Chem. Commun. 51, 8044–8047.

Asheghi, M., Yang, Y., 2005. Micro- and nano-scale diagnostic techniques for thermometry and thermal imaging of microelectronic and data storage devices. In: Breuer, K.S. (Ed.), Microscale Diagnostic Techniques. Springer, Berlin, pp. 155–196 (Chapter 4).

Babu, S.S., Hollamby, M.J., Aimi, J., Ozawa, H., Saeki, A., Seki, S., Kobayashi, K., Hagiwara, K., Yoshizawa, M., Mohwald, H., Nakanishi, T., 2013. Nonvolatile liquid anthracenes for facile full-colour luminescence tuning at single blue-light excitation. Nat. Commun. 4, 1969.

Bai, X., Li, D., Liu, Q., Dong, B., Xu, S., Song, H.W., 2012. Concentration-controlled emission in $LaF_3:Yb^{3+}/Tm^{3+}$ nanocrystals: switching from UV to NIR regions. J. Mater. Chem. 22, 24698–24704.

Baker, S.N., McCleskey, T.M., Baker, G.A., 2005. An ionic liquid-based optical thermometer. Ionic liquids IIIB: Fundamentals, Progress, Challenges and Opportunities, vol. 902. American Chemical Society, Washington, DC171–181 (Chapter 14).

Balabhadra, S., Debasu, M.L., Brites, C.D., Nunes, L.A., Malta, O.L., Rocha, J., Bettinelli, M., Carlos, L.D., 2015. Boosting the sensitivity of Nd^{3+}-based luminescent nanothermometers. Nanoscale 7, 17261–17267.

Barilero, T., Le Saux, T., Gosse, C., Jullien, L., 2009. Fluorescent thermometers for dual-emission-wavelength measurements: molecular engineering and application to thermal imaging in a microsystem. Anal. Chem. 81, 7988–8000.

Bartlett, J.W., Frost, C., 2008. Reliability, repeatability and reproducibility: analysis of measurement errors in continuous variables. Ultrasound Obstet. Gynecol. 31, 466–475.

Beechem, T., Graham, S., Kearney, S.P., Phinney, L.M., Serrano, J.R., 2007. Simultaneous mapping of temperature and stress in microdevices using micro-Raman spectroscopy. Rev. Sci. Instrum. 78, 061301.

Benayas, A., del Rosal, B., Perez-Delgado, A., Santacruz-Gomez, K., Jaque, D., Hirata, G.A., Vetrone, F., 2015. Nd:YAG near-infrared luminescent nanothermometers. Adv. Opt. Mater. 3, 687–694.

Berthou, H., Jörgensen, C.K., 1990. Optical-fiber temperature sensor based on upconversion-excited fluorescence. Opt. Lett. 15, 1100–1102.

Bettinelli, M., Carlos, L.D., Liu, X., 2015. Lanthanide-doped upconversion nanoparticles. Phys. Today 68, 38–44.

Binnemans, K., 2005. Rare earth beta-diketonates. In: Gschneidner Jr., K.A., Bünzli, J.-C.G., Pecharsky, V.K. (Eds.), Handbook on the Physics and Chemistry of Rare Earths, vol. 35. Elsevier Science, B. V., Amsterdam, pp. 107–272 (Chapter 225).

Binnemans, K., 2009. Lanthanide-based luminescent hybrid materials. Chem. Rev. 109, 4283–4374.

Bland, J.M., Altman, D.G., 1986. Statistical methods for assessing agreement between two methods of clinical measurement. Lancet 1, 307–310.

Borisov, S.M., Wolfbeis, O.S., 2006. Temperature-sensitive europium(III) probes and their use for simultaneous luminescent sensing of temperature and oxygen. Anal. Chem. 78, 5094–5101.

Boruc, Z., Kaczkan, M., Fetlinski, B., Turczynski, S., Malinowski, M., 2012. Blue emissions in Dy^{3+} doped $Y_4Al_2O_9$ crystals for temperature sensing. Opt. Lett. 37, 5214–5216.

Brites, C.D.S., Lima, P.P., Silva, N.J.O., Millán, A., Amaral, V.S., Palacio, F., Carlos, L.D., 2010. A luminescent molecular thermometer for long-term absolute temperature measurements at the nanoscale. Adv. Mater. 22, 4499–4504.

Brites, C.D.S., Lima, P.P., Silva, N.J.O., Millán, A., Amaral, V.S., Palacio, F., Carlos, L.D., 2011. Lanthanide-based luminescent molecular thermometers. New J. Chem. 35, 1177–1183.

Brites, C.D.S., Lima, P.P., Silva, N.J.O., Millán, A., Amaral, V.S., Palacio, F., Carlos, L.D., 2012. Thermometry at the nanoscale. Nanoscale 4, 4799–4829.

Brites, C.D.S., Lima, P.P., Silva, N.J.O., Millán, A., Amaral, V.S., Palacio, F., Carlos, L.D., 2013a. Organic–inorganic Eu^{3+}/Tb^{3+} codoped hybrid films for temperature mapping in integrated circuits. Front. Chem. 1, 9.

Brites, C.D.S., Lima, P.P., Silva, N.J.O., Millán, A., Amaral, V.S., Palacio, F., Carlos, L.D., 2013b. Ratiometric highly sensitive luminescent nanothermometers working in the room temperature range. Applications to heat propagation in nanofluids. Nanoscale 5, 7572–7580.

Brites, C.D.S., Lima, P.P., Silva, N.J.O., Millán, A., Amaral, V.S., Palacio, F., Carlos, L.D., 2013c. Thermometry at the nanoscale using lanthanide-containing organic–inorganic hybrid materials. J. Lumin. 133, 230–232.

Brites, C.D.S., Lima, P.P., Carlos, L.D., 2016. Tuning the sensitivity of Ln^{3+}-based luminescent molecular thermometers through ligand design. J. Lumin. 169 (B), 497–502.

Bünzli, J.-C.G., 2006. Benefiting from the unique properties of lanthanide ions. Acc. Chem. Res. 39, 53–61.

Bünzli, J.-C.G., 2010. Lanthanide luminescence for biomedical analyses and imaging. Chem. Rev. 110, 2729–2755.

Bünzli, J.-C.G., 2015. On the design of highly luminescent lanthanide complexes. Coord. Chem. Rev. 293, 19–47.

Bünzli, J.-C.G., Eliseeva, S.V., 2013. Intriguing aspects of lanthanide luminescence. Chem. Sci. 4, 1939–1949.

Bünzli, J.-C.G., Piguet, C., 2005. Taking advantage of luminescent lanthanide ions. Chem. Soc. Rev. 34, 1048–1077.

Burbano, D.C.R., Naccache, R., Capobianco, J.A., 2015. Near-IR triggered photon upconversion: imaging, detection, and therapy. In: Bünzli, J.-C.G., Pecharsky, V.K. (Eds.), Handbook of the Physics and Chemistry of Rare Earths, vol. 47. Elsevier, pp. 273–334 (Chapter 273).

Burzo, M.G., Komarov, P.L., Raad, P.E., 2005. Noncontact transient temperature mapping of active electronic devices using the thermoreflectance method. IEEE Trans. Compon. Pack. Technol. 28, 637–643.

Cadiau, A., Brites, C.D.S., Costa, P.M.F.J., Ferreira, R.A.S., Rocha, J., Carlos, L.D., 2013. Ratiometric nanothermometer based on an emissive Ln^{3+}-organic framework. ACS Nano 7, 7213–7218.

Cahill, D.G., 2004. Analysis of heat flow in layered structures for time–domain thermoreflectance. Rev. Sci. Instrum. 75, 5119–5122.

Cahill, D.G., Braun, P.V., Chen, G., Clarke, D.R., Fan, S.H., Goodson, K.E., Keblinski, P., King, W.P., Mahan, G.D., Majumdar, A., Maris, H.J., Phillpot, S.R., Pop, E., Shi, L., 2014. Nanoscale thermal transport. II. 2003–2012. Appl. Phys. Rev. 1, 011305.

Caillat, L., Hajj, B., Shynkar, V., Michely, L., Chauvat, D., Zyss, J., Pellé, F., 2013. Multiphoton upconversion in rare earth doped nanocrystals for sub-diffractive microscopy. Appl. Phys. Lett. 102, 143114.

Carlos, L.D., Palacio, F., 2016. Thermometry at the Nanoscale: Techniques and Selected Applications. Royal Society of Chemistry, Oxfordshire.

Carlos, L.D., Messaddeq, Y., Brito, H.F., Ferreira, R.A.S., De Zea Bermudez, V., Ribeiro, S.J.L., 2000. Full-color phosphors from europium(III)-based organosilicates. Adv. Mater. 12, 594–598.

Carlos, L.D., de Zea Bermudez, V., Amaral, V.S., Nunes, S.C., Silva, N.J.O., Ferreira, R.A.S., Rocha, J., Santilli, C.V., Ostrovskii, D., 2007. Nanoscopic photoluminescence memory as a fingerprint of complexity in self-assembled alkyl/siloxane hybrids. Adv. Mater. 19, 341–348.

Carlos, L.D., Ferreira, R.A.S., de Zea Bermudez, V., Ribeiro, S.J.L., 2009. Lanthanide-containing light-emitting organic–inorganic hybrids: a bet on the future. Adv. Mater. 21, 509–534.

Carlson, M.T., Khan, A., Richardson, H.H., 2011. Local temperature determination of optically excited nanoparticles and nanodots. Nano Lett. 11, 1061–1069.

Carnall, W.T., Crosswhite, H., Crosswhite, H.M., 1977. Energy level structure and transition probabilities in the spectra of the trivalent lanthanides in LaF3Argonne. Nat. Lab. Rep. IL, USA 78-XX-95.

Carrasco, E., del Rosal, B., Sanz-Rodríguez, F., de la Fuente, Á.J., Gonzalez, P.H., Rocha, U., Kumar, K.U., Jacinto, C., Solé, J.G., Jaque, D., 2015. Intratumoral thermal reading during photo-thermal therapy by multifunctional fluorescent nanoparticles. Adv. Funct. Mater. 25, 615–626.

Cerón, E.N., Ortgies, D.H., del Rosal, B., Ren, F., Benayas, A., Vetrone, F., Ma, D., Sanz-Rodríguez, F., Solé, J.G., Jaque, D., Rodríguez, E.M., 2015. Hybrid nanostructures for high-sensitivity luminescence nanothermometry in the second biological window. Adv. Mater. 27, 4781–4787.

Chapman, C.F., Liu, Y., Sonek, G.J., Tromberg, B.J., 1995. The use of exogenous fluorescent-probes for temperature-measurements in single living cells. Photochem. Photobiol. 62, 416–425.

Chauhan, V.M., Hopper, R.H., Ali, S.Z., King, E.M., Udrea, F., Oxley, C.H., Aylott, J.W., 2014. Thermo-optical characterization of fluorescent rhodamine B based temperature-sensitive nanosensors using a CMOS MEMS micro-hotplate. Sens. Actuators B: Chem. 192, 126–133.

Chen, G.Y., Yang, C.H., Prasad, P.N., 2013. Nanophotonics and nanochemistry: controlling the excitation dynamics for frequency up- and down-conversion in lanthanide-doped nanoparticles. Acc. Chem. Res. 46, 1474–1486.

Chen, G.Y., Qju, H.L., Prasad, P.N., Chen, X.Y., 2014. Upconversion nanoparticles: design, nanochemistry, and applications in theranostics. Chem. Rev. 114, 5161–5214.

Chen, C.W., Lee, P.H., Chan, Y.C., Hsiao, M., Chen, C.H., Wu, P.C., Wu, P.R., Tsai, D.P., Tu, D., Chen, X.Y., Liu, R.S., 2015a. Plasmon-induced hyperthermia: hybrid upconversion NaYF$_4$:Yb/Er and gold nanomaterials for oral cancer photothermal therapy. J. Mater. Chem. B 3, 8293–8302.

Chen, G.Y., Agren, H., Ohulchanskyy, T.Y., Prasad, P.N., 2015b. Light upconverting core–shell nanostructures: nanophotonic control for emerging applications. Chem. Soc. Rev. 44, 1680–1713.

Childs, P.R.N., Greenwood, J.R., Long, C.A., 2000. Review of temperature measurement. Rev. Sci. Instrum. 71, 2959–2978.

Cho, S.J., Maysinger, D., Jain, M., Roder, B., Hackbarth, S., Winnik, F.M., 2007. Long-term exposure to CdTe quantum dots causes functional impairments in live cells. Langmuir 23, 1974–1980.

Christofferson, J., Maize, K., Ezzahri, Y., Shabani, J., Wang, X., Shakouri, A., 2008. Microscale and nanoscale thermal characterization techniques. (Reprinted from Thermal Issues in Emerging Technologies: Theory and Application, January, 2007). J. Electron. Packag. 130, 041101–041106.

Clark, J.L., Miller, P.F., Rumbles, G., 1998. Red edge photophysics of ethanolic rhodamine 101 and the observation of laser cooling in the condensed phase. J. Phys. Chem. A 102, 4428–4437.

Collins, S., Baxter, G., Wade, S., Sun, T., Grattan, K., Zhang, Z., Palmer, A., 1998. Comparison of fluorescence-based temperature sensor schemes: theoretical analysis and experimental validation. J. Appl. Phys. 84, 4649–4654.

Comby, S., Bünzli, J.-C.G., 2007. Lanthanide near-infrared luminescence in molecular probes and devices. In: Gschneidner Jr., K.A., Bünzli, J.-C.G., Pecharsky, V.K. (Eds.), Handbook on the Physics and Chemistry of Rare Earths, vol. 37. Elsevier Science, B. V., New York, pp. 217–470 (Chapter 235).

Cooke, D.W., Muenchausen, R.E., Bennett, B.L., McClellan, K.J., Portis, A.M., 1998. Temperature-dependent luminescence of cerium-doped ytterbium oxyorthosilicate. J. Lumin. 79, 185–190.

Cooke, D.W., Bennett, B.L., Muenchausen, R.E., Lee, J.K., Nastasi, M.A., 2004. Intrinsic ultraviolet luminescence from Lu_2O_3, Lu_2SiO_5 and Lu_2SiO_5:Ce^{3+}. J. Lumin. 106, 125–132.

Corke, M., Kersey, A.D., Jackson, D.A., Jones, J.D.C., 1983. All-fiber Michelson thermometer. Electron. Lett. 19, 471–473.

Costescu, R.M., Cahill, D.G., Fabreguette, F.H., Sechrist, Z.A., George, S.M., 2004. Ultra-low thermal conductivity in W/Al_2O_3 nanolaminates. Science 303, 989–990.

Cui, Y.J., Xu, H., Yue, Y.F., Guo, Z.Y., Yu, J.C., Chen, Z.X., Gao, J.K., Yang, Y., Qian, G.D., Chen, B.L., 2012. A luminescent mixed-lanthanide metal-organic framework thermometer. J. Am. Chem. Soc. 134, 3979–3982.

Cui, Y.J., Zou, W.F., Song, R.J., Yu, J.C., Zhang, W.Q., Yang, Y., Qian, G.D., 2014. A ratiometric and colorimetric luminescent thermometer over a wide temperature range based on a lanthanide coordination polymer. Chem. Commun. 50, 719–721.

Cui, Y., Song, R., Yu, J., Liu, M., Wang, Z., Wu, C., Yang, Y., Wang, Z., Chen, B., Qian, G., 2015a. Dual-emitting MOF supersetdye composite for ratiometric temperature sensing. Adv. Mater. 27, 1420–1425.

Cui, Y., Zhu, F., Chen, B., Qian, G., 2015b. Metal-organic frameworks for luminescence thermometry. Chem. Commun. 51, 7420–7431.

Debasu, M.L., Ananias, D., Pastoriza-Santos, I., Liz-Marzán, L.M., Rocha, J., Carlos, L.D., 2013. All-in-one optical heater–thermometer nanoplatform operative from 300 to 2000 k based on Er^{3+} emission and blackbody radiation. Adv. Mater. 25, 4868–4874.

de la Rosa, R.V., Woisel, P., Hoogenboom, R., 2016. Supramolecular control over thermoresponsive polymers. Mater. Today 19, 44–55.

del Rosal, B., Sun, C., Yan, Y., Mackenzie, M.D., Lu, C., Bettiol, A.A., Kar, A.K., Jaque, D., 2014. Flow effects in the laser-induced thermal loading of optical traps and optofluidic devices. Opt. Express 22, 23938–23954.

del Rosal, B., Pérez-Delgado, A., Misiak, M., Bednarkiewicz, A., Vanetsev, A.S., Orlovskii, Y., Jovanović, D.J., Dramićanin, M.D., Rocha, U., Kumar, K.U., Jacinto, C., Navarro, E., Rodríguez, E.M., Pedroni, M., Speghini, A., Hirata, G.A., Martín, I.R., Jaque, D., 2015. Neodymium-doped nanoparticles for infrared fluorescence bioimaging: the role of the host. J. Appl. Phys. 118, 143104.

Deshpande, V.V., Hsieh, S., Bushmaker, A.W., Bockrath, M., Cronin, S.B., 2009. Spatially resolved temperature measurements of electrically heated carbon nanotubes. Phys. Rev. Lett. 102, 105501.

de Silva, A.P., 2011. Molecular logic gate arrays. Chem. Asian J. 6, 750–766.

de Silva, A.P., Gunaratne, H.Q.N., Gunnlaugsson, T., Huxley, A.J.M., McCoy, C.P., Rademacher, J.T., Rice, T.E., 1997. Signaling recognition events with fluorescent sensors and switches. Chem. Rev. 97, 1515–1566.

de Zea Bermudez, V., Carlos, L.D., Duarte, M.C., Silva, M.M., Silva, C.J.R., Smith, M.J., Assunção, M., Alcácer, L., 1998. A novel class of luminescent polymers obtained by the sol–gel approach. J. Alloys Compd. 277, 21–26.

de Zea Bermudez, V., Carlos, L.D., Alcácer, L., 1999. Sol–gel derived urea cross-linked organically modified silicates. 1. Room temperature mid-infrared spectra. Chem. Mater. 11, 569–580.

Dong, J., Zink, J.I., 2014. Taking the temperature of the interiors of magnetically heated nanoparticles. ACS Nano 8, 5199–5207.

Dong, N.N., Pedroni, M., Piccinelli, F., Conti, G., Sbarbati, A., Ramírez-Hernández, J.E., Maestro, L.M., Iglesias de la Cruz, M.C., Sanz-Rodríguez, F., Juarranz, A., Chen, F., Vetrone, F., Capobianco, J.A., Solé, J.G., Bettinelli, M., Jaque, D., Speghini, A., 2011. NIR-to-NIR two-photon excited $CaF_2:Tm^{3+}$, Yb^{3+} nanoparticles: multifunctional nanoprobes for highly penetrating fluorescence bio-imaging. ACS Nano 5, 8665–8671.

Dong, B., Cao, B.S., He, Y.Y., Liu, Z., Li, Z.P., Feng, Z.Q., 2012. Temperature sensing and in vivo imaging by molybdenum sensitized visible upconversion luminescence of rare-earth oxides. Adv. Mater. 24, 1987–1993.

Donner, J.S., Thompson, S.A., Kreuzer, M.P., Baffou, G., Quidant, R., 2012. Mapping intracellular temperature using green fluorescent protein. Nano Lett. 12, 2107–2111.

Dorenbos, P., Dehaas, J.T.M., Visser, R., Vaneijk, C.W.E., Hollander, R.W., 1993. Absolute light yield measurements on BaF_2 crystals and the quantum efficiency of several photomultiplier tubes. IEEE Trans. Nucl. Sci. 40, 424–430.

dos Santos, P.V., de Araujo, M.T., Gouveia-Neto, A.S., Medeiros Neto, J.A., Sombra, A.S.B., 1998. Optical temperature sensing using upconversion fluorescence emission in Er^{3+}/Yb^{3+}-codoped chalcogenide glass. Appl. Phys. Lett. 73, 578–580.

dos Santos, P.V., Vermelho, M.V.D., Gouveia, E.A., de Araujo, M.T., Gouveia-Neto, A.S., Cassanjes, F.C., Ribeiro, S.J.L., Messaddeq, Y., 2001. Efficient energy upconversion emission in Tm^{3+}/Yb^{3+}-codoped TeO_2-based optical glasses excited at 1.064 μm. J. Appl. Phys. 90, 6550–6552.

Dramićanin, M.D., Antić, Ž., Culubrk, S., Ahrenkiel, S.P., Nedeljkovic, J.M., 2014. Self-referenced luminescence thermometry with Sm^{3+} doped TiO_2 nanoparticles. Nanotechnology 25, 485501.

Duarte, M., Martins, E., Baldochi, S.L., Vieira, N.D., Vieira, M.M.M., 1999. De-excitation mechanisms of $BaLiF_3:Co^{2+}$ crystals. Opt. Commun. 159, 221–224.

D'Vries, R.F., Alvarez-Garcia, S., Snejko, N., Bausa, L.E., Gutierrez-Puebla, E., de Andres, A., Monge, M.A., 2013. Multimetal rare earth MOFs for lighting and thermometry: tailoring color and optimal temperature range through enhanced disulfobenzoic triplet phosphorescence. J. Mater. Chem. C 1, 6316–6324.

Edge, A.C., Laufer, G., Krauss, R.H., 2000. Surface temperature-field imaging with laser-induced thermographic phosphorescence. Appl. Optics 39, 546–553.

Escribano, P., Julián-López, B., Planelles-Aragó, J., Cordoncillo, E., Viana, B., Sanchez, C., 2008. Photonic and nanobiophotonic properties of luminescent lanthanide-doped hybrid organic–inorganic materials. J. Mater. Chem. 18, 23–40.

Falcaro, P., Ricco, R., Doherty, C.M., Liang, K., Hill, A.J., Styles, M.J., 2014. MOF positioning technology and device fabrication. Chem. Soc. Rev. 43, 5513–5560.

Farzaneh, M., Maize, K., Luerssen, D., Summers, J.A., Mayer, P.M., Raad, P.E., Pipe, K.P., Shakouri, A., Ram, R.J., Hudgings, J.A., 2009. CCD-based thermoreflectance microscopy: principles and applications. J. Phys. D Appl. Phys. 42, 143001.

Feng, J., Zhang, H.J., 2013. Hybrid materials based on lanthanide organic complexes: a review. Chem. Soc. Rev. 42, 387–410.

Feng, J., Tian, K.J., Hu, D.H., Wang, S.Q., Li, S.Y., Zeng, Y., Li, Y., Yang, G.Q., 2011. A triarylboron-based fluorescent thermometer: sensitive over a wide temperature range. Angew. Chem. Int. Ed. 50, 8072–8076.

Feng, J., Xiong, L., Wang, S., Li, S., Li, Y., Yang, G., 2013. Fluorescent temperature sensing using triarylboron compounds and microcapsules for detection of a wide temperature range on the micro- and macroscale. Adv. Funct. Mater. 23, 340–345.

Ferreira, R.A.S., Brites, C.D.S., Vicente, C.M.S., Lima, P.P., Bastos, A.R.N., Marques, P.G., Hiltunen, M., Carlos, L.D., André, P.S., 2013. Photonic-on-a-chip: a thermal actuated Mach–Zehnder interferometer and a molecular thermometer based on a single di-ureasil organic–inorganic hybrid. Laser Photon. Rev. 7, 1027–1035.

Fischer, L.H., Harms, G.S., Wolfbeis, O.S., 2011. Upconverting nanoparticles for nanoscale thermometry. Angew. Chem. Int. Ed. 50, 4546–4551.

Gao, Y.H., Bando, Y., Liu, Z.W., Golberg, D., Nakanishi, H., 2003. Temperature measurement using a gallium-filled carbon nanotube nanothermometer. Appl. Phys. Lett. 83, 2913–2915.

Glawdel, T., Almutairi, Z., Wang, S., Ren, C., 2009. Photobleaching absorbed rhodamine B to improve temperature measurements in PDMS microchannels. Lab Chip 9, 171–174.

Gnach, A., Lipinski, T., Bednarkiewicz, A., Rybka, J., Capobianco, J.A., 2015. Upconverting nanoparticles: assessing the toxicity. Chem. Soc. Rev. 44, 1561–1584.

Goodson, K.E., Asheghi, M., 1997. Near-field optical thermometry. Microsc. Thermophys. Eng. 1, 225–235.

Gorris, H.H., Ali, R., Saleh, S.M., Wolfbeis, O.S., 2011. Tuning the dual emission of photon-upconverting nanoparticles for ratiometric multiplexed encoding. Adv. Mater. 23, 1652–1655.

Gosse, C., Bergaud, C., Löw, P., 2009. Molecular probes for thermometry in microfluidic devices. In: Volz, S. (Ed.), Thermal Nanosystems and Nanomaterials, vol. 118. Springer-Verlag, Berlin, pp. 301–341 (Chapter 10).

Gota, C., Uchiyama, S., Yoshihara, T., Tobita, S., Ohwada, T., 2008. Temperature-dependent fluorescence lifetime of a fluorescent polymeric thermometer, poly(N-isopropylacrylamide), labeled by polarity and hydrogen bonding sensitive 4-sulfamoyl-7-aminobenzofurazan. J. Phys. Chem. B 112, 2829–2836.

Gota, C., Okabe, K., Funatsu, T., Harada, Y., Uchiyama, S., 2009. Hydrophilic fluorescent nanogel thermometer for intracellular thermometry. J. Am. Chem. Soc. 131, 2766–2767.

Graham, E.M., Iwai, K., Uchiyama, S., de Silva, A.P., Magennis, S.W., Jones, A.C., 2010. Quantitative mapping of aqueous microfluidic temperature with sub-degree resolution using fluorescence lifetime imaging microscopy. Lab Chip 10, 1267–1273.

Groom, D.E., Holland, S.E., Levi, M.E., Palaio, N.P., Perlmutter, S., Stover, R.J., Wei, M., 1999. Quantum efficiency of a back-illuminated CCD imager: an optical approach. Proc. SPIE 3649, 80–90.

Gu, Z.J., Yan, L., Tian, G., Li, S.J., Chai, Z.F., Zhao, Y.L., 2013. Recent advances in design and fabrication of upconversion nanoparticles and their safe theranostic applications. Adv. Mater. 25, 3758–3779.

Guan, X.L., Liu, X.Y., Su, Z.X., 2007. Preparation and photophysical behaviors of fluorescent chitosan bearing fluorescein: potential biomaterial as temperature/pH probes. J. Appl. Polym. Sci. 104, 3960–3966.

Han, S., Deng, R., Xie, X., Liu, X., 2014. Enhancing luminescence in lanthanide-doped upconversion nanoparticles. Angew. Chem. Int. Ed. 53, 11702–11715.

Hao, S., Chen, G., Yang, C., 2013. Sensing using rare-earth-doped upconversion nanoparticles. Theranostics 3, 331–345.

Haro-Gonzalez, P., Ramsay, W.T., Martinez Maestro, L., del Rosal, B., Santacruz-Gomez, K., Iglesias de la Cruz, M.C., Sanz-Rodríguez, F., Chooi, J.Y., Rodriguez Sevilla, P., Bettinelli, M., Choudhury, D., Kar, A.K., Solé, J.G., Jaque, D., Paterson, L., 2013. Quantum dot-based thermal spectroscopy and imaging of optically trapped microspheres and single cells. Small 9, 2162–2170.

Hartmann, M., 2006. Minimal length scales for the existence of local temperature. Contemp. Phys. 47, 89–102.

Hartmann, M., Mahler, G., Hess, O., 2004. Existence of temperature on the nanoscale. Phys. Rev. Lett. 93, 080402–080406.

Hayashi, T., Fukuda, N., Uchiyama, S., Inada, N., 2015. A cell-permeable fluorescent polymeric thermometer for intracellular temperature mapping in mammalian cell lines. PLoS One 10, E0117677.

Heyes, A.L., 2009. On the design of phosphors for high-temperature thermometry. J. Lumin. 129, 2004–2009.

Homma, M., Takei, Y., Murata, A., Inoue, T., Takeoka, S., 2015. A ratiometric fluorescent molecular probe for visualization of mitochondrial temperature in living cells. Chem. Commun. 51, 6194–6197.

Hu, X.L., Li, Y., Liu, T., Zhang, G.Y., Liu, S.Y., 2015. Intracellular cascade FRET for temperature imaging of living cells with polymeric ratiometric fluorescent thermometers. ACS Appl. Mater. Interfaces 7, 15551–15560.

Huang, H., Delikanli, S., Zeng, H., Ferkey, D.M., Pralle, A., 2010. Remote control of ion channels and neurons through magnetic-field heating of nanoparticles. Nat. Nanotechnol. 5, 602–606.

Huang, F., Gao, Y., Zhou, J.C., Xua, J., Wang, Y.S., 2015a. Yb^{3+}/Er^{3+} co-doped $CaMoO_4$: a promising green upconversion phosphor for optical temperature sensing. J. Alloys Compd. 639, 325–329.

Huang, Y., Rosei, F., Vetrone, F., 2015b. A single multifunctional nanoplatform based on upconversion luminescence and gold nanorods. Nanoscale 7, 5178–5185.

Il Park, Y., Lee, K.T., Suh, Y.D., Hyeon, T., 2015. Upconverting nanoparticles: a versatile platform for wide-field two-photon microscopy and multi-modal in vivo imaging. Chem. Soc. Rev. 44, 1302–1317.

Ishiwada, N., Fujioka, S., Ueda, T., Yokomori, T., 2011. Co-doped Y_2O_3:Tb^{3+}/Tm^{3+} multicolor emitting phosphors for thermometry. Opt. Lett. 36, 760–762.

Jaque, D., Vetrone, F., 2012. Luminescence nanothermometry. Nanoscale 4, 4301–4326.

Jaque, D., del Rosal, B., Rodriguez, E.M., Maestro, L.M., Haro-Gonzalez, P., Solé, J.G., 2014a. Fluorescent nanothermometers for intracellular thermal sensing. Nanomedicine 9, 1047–1062.

Jaque, D., Martinez Maestro, L., del Rosal, B., Haro-Gonzalez, P., Benayas, A., Plaza, J.L., Martin Rodriguez, E., Solé, J.G., 2014b. Nanoparticles for photothermal therapies. Nanoscale 6, 9494–9530.

Jarenwattananon, N.N., Gloggler, S., Otto, T., Melkonian, A., Morris, W., Burt, S.R., Yaghi, O.M., Bouchard, L.S., 2013. Thermal maps of gases in heterogeneous reactions. Nature 502, 537–540.

Jennings, G.W. 1941. Temperature indicator. US patent application US2261473 A. 4 Nov 1941.

Jung, W., Kim, Y.W., Yim, D., Yoo, J.Y., 2011. Microscale surface thermometry using SU8/rhodamine-B thin layer. Sens. Actuators A: Phys. 171, 228–232.

Ke, G.L., Wang, C.M., Ge, Y., Zheng, N.F., Zhu, Z., Yang, C.J., 2012. L-DNA molecular beacon: a safe, stable, and accurate intracellular nano-thermometer for temperature sensing in living cells. J. Am. Chem. Soc. 134, 18908–18911.

Kewell, A.K., Reed, G.T., Namavar, F., 1998. Integrated temperature sensor in Er-doped silicon. Sens. Actuators A: Phys. 65, 160–164.

Khalid, A.H., Kontis, K., 2009. 2D surface thermal imaging using rise-time analysis from laser-induced luminescence phosphor thermometry. Meas. Sci. Technol. 20, 025305.

Khalil, G.E., Lau, K., Phelan, G.D., Carlson, B., Gouterman, M., Callis, J.B., Dalton, L.R., 2004. Europium beta-diketonate temperature sensors: effects of ligands, matrix, and concentration. Rev. Sci. Instrum. 75, 192–206.

Kim, S.H., Noh, J., Jeon, M.K., Kim, K.W., Lee, L.P., Woo, S.I., 2006. Micro-Raman thermometry for measuring the temperature distribution inside the microchannel of a polymerase chain reaction chip. J. Micromech. Microeng. 16, 526–530.

Kim, K., Jeong, W.H., Lee, W.C., Reddy, P., 2012. Ultra-high vacuum scanning thermal microscopy for nanometer resolution quantitative thermometry. ACS Nano 6, 4248–4257.

Kim, D.U., Ryu, S.Y., Kim, J.K., Chang, K.S., 2014. Quantitative thermal characterization of microelectronic devices by using CCD-based thermoreflectance microscopy. In: SPIE MOEMS-MEMS. International Society for Optics and Photonics (89750Q-89750Q-7).

Kliesch, M., Gogolin, C., Kastoryano, M., Riera, A., Eisert, J., 2014. Locality of temperature. Phys. Rev. X 4, 031019.

Kobayashi, H., Ogawa, M., Alford, R., Choyke, P.L., Urano, Y., 2010. New strategies for fluorescent probe design in medical diagnostic imaging. Chem. Rev. 110, 2620–2640.

Kolodner, P., Tyson, J.A., 1983. Remote thermal imaging with 0.7-μm spatial resolution using temperature-dependent fluorescent thin films. Appl. Phys. Lett. 42, 117–119.

Kucsko, G., Maurer, P.C., Yao, N.Y., Kubo, M., Noh, H.J., Lo, P.K., Park, H., Lukin, M.D., 2013. Nanometre-scale thermometry in a living cell. Nature 500, 54–58.

Kumar, R., Nyk, M., Ohulchanskyy, T.Y., Flask, C.A., Prasad, P.N., 2009. Combined optical and MR bioimaging using rare earth ion doped NaYF$_4$ nanocrystals. Adv. Funct. Mater. 19, 853–859.

Kusama, H., Sovers, O.J., Yoshioka, T., 1976. Line shift method for phosphor temperature-measurements. Jpn. J. Appl. Phys. 15, 2349–2358.

Lees, D.E., 1982. Liquid-crystal thermometry. Anesth. Analg. 61, 803–804.

León-Luis, S.F., Rodríguez-Mendoza, U.R., Haro-Gonzalez, P., Martin, I.R., Lavin, V., 2012. Role of the host matrix on the thermal sensitivity of Er^{3+} luminescence in optical temperature sensors. Sens. Actuators B: Chem. 174, 176–186.

Li, S., Zhang, K., Yang, J.M., Lin, L.W., Yang, H., 2007. Single quantum dots as local temperature markers. Nano Lett. 7, 3102–3105.

Li, D.D., Shao, Q.Y., Dong, Y., Jiang, J.Q., 2013. Thermal sensitivity and stability of NaYF4:Yb^{3+}, Er^{3+} upconversion nanowires, nanorods and nanoplates. Mater. Lett. 110, 233–236.

Li, Z.Q., Li, P., Xu, Q.Q., Li, H.R., 2015. Europium(III)-beta-diketonate complex-containing nanohybrid luminescent pH detector. Chem. Commun. 51, 10644–10647.

Lima, P.P., Ferreira, R.A.S., Freire, R.O., Paz, F.A.A., Fu, L.S., Alves, S., Carlos, L.D., Malta, O.L., 2006. Spectroscopic study of a UV-photostable organic–inorganic hybrids incorporating an Eu^{3+} beta-diketonate complex. ChemPhysChem 7, 735–746.

Lima, P.P., Paz, F.A.A., Ferreira, R.A.S., de Zea Bermudez, V., Carlos, L.D., 2009. Ligand-assisted rational design and supramolecular tectonics toward highly luminescent Eu^{3+}-containing organic–inorganic hybrids. Chem. Mater. 21, 5099–5111.

Liu, G., 2015. Advances in the theoretical understanding of photon upconversion in rare-earth activated nanophosphors. Chem. Soc. Rev. 44, 1635–1652.

Liu, W.J., Yang, B.Z., 2007. Thermography techniques for integrated circuits and semiconductor devices. Sens. Rev. 27, 298–309.

Liu, Y., Qian, G.D., Wang, Z.Y., Wang, M.Q., 2005. Temperature-dependent luminescent properties of Eu-Tb complexes synthesized in situ in gel glass. Appl. Phys. Lett. 86, 071907.

Liu, T.C., Huang, Z.L., Wang, H.Q., Wang, J.H., Li, X.Q., Zhao, Y.D., Luo, Q.M., 2006. Temperature-dependent photoluminescence of water-soluble quantum dots for a bioprobe. Anal. Chim. Acta 559, 120–123.

Liu, H.X., Sun, W.Q., Xiang, A., Shi, T.W., Chen, Q., Xu, S.Y., 2012. Towards on-chip time-resolved thermal mapping with micro-/nanosensor arrays. Nanoscale Res. Lett. 7, 1–6.

Liu, Y.S., Tu, D.T., Zhu, H.M., Chen, X.Y., 2013. Lanthanide-doped luminescent nanoprobes: controlled synthesis, optical spectroscopy, and bioapplications. Chem. Soc. Rev. 42, 6924–6958.

Liu, J., Guo, X.D., Hu, R., Xu, J., Wang, S.Q., Li, S.Y., Li, Y., Yang, G.Q., 2015. Intracellular fluorescent temperature probe based on triarylboron substituted poly N-isopropylacrylamide and energy transfer. Anal. Chem. 87, 3694–3698.

Lojpur, V., Nikolić, M.G., Mancic, L., Milosevic, O., Dramićanin, M.D., 2013. Y_2O_3:Yb, Tm and Y_2O_3:Yb, Ho powders for low-temperature thermometry based on up-conversion fluorescence. Ceram. Int. 39, 1129–1134.

Lojpur, V., Nikolić, M.G., Dramićanin, M.D., 2014. Luminescence thermometry below room temperature via up-conversion emission of Y_2O_3:Yb^{3+}, Er^{3+} nanophosphors. J. Appl. Phys. 115, 203106.

Löw, P., Kim, B., Takama, N., Bergaud, C., 2008. High-spatial-resolution surface-temperature mapping using fluorescent thermometry. Small 4, 908–914.

Lowell, B.B., Spiegelman, B.M., 2000. Towards a molecular understanding of adaptive thermogenesis. Nature 404, 652–660.

Maestro, L.M., Rodríguez, E.M., Rodríguez, F.S., Iglesias de la Cruz, M.C., Juarranz, A., Naccache, R., Vetrone, F., Jaque, D., Capobianco, J.A., Solé, J.G., 2010a. CdSe quantum dots for two-photon fluorescence thermal imaging. Nano Lett. 10, 5109–5115.

Maestro, L.M., Rodriguez, E.M., Vetrone, F., Naccache, R., Ramirez, H.L., Jaque, D., Capobianco, J.A., Solé, J.G., 2010b. Nanoparticles for highly efficient multiphoton fluorescence bioimaging. Opt. Express 18, 23544–23553.

Maestro, L.M., Jacinto, C., Silva, U.R., Vetrone, F., Capobianco, J.A., Jaque, D., Solé, J.G., 2011. CdTe quantum dots as nanothermometers: towards highly sensitive thermal imaging. Small 7, 1774–1778.

Maestro, L.M., Haro-González, P., Iglesias de la Cruz, M.C., Sanz Rodríguez, F., Juarranz, A., Solé, J.G., Jaque, D., 2013. Fluorescent nanothermometers provide controlled plasmonic-mediated intracellular hyperthermia. Nanomedicine 8, 379–388.

Maldague, X., Marinetti, S., 1996. Pulse phase infrared thermography. J. Appl. Phys. 79, 2694–2698.

Malta, O.L., 1997. Ligand-rare-earth ion energy transfer in coordination compounds. A theoretical approach. J. Lumin. 71, 229–236.

Malta, O.L., 2008. Mechanisms of non-radiative energy transfer involving lanthanide ions revisited. J. Non Cryst. Solids 354, 4770–4776.

Malta, O.L., Carlos, L.D., 2003. Intensities of 4f–4f transitions in glass materials. Quim. Nova 26, 889–895.

Malta, O.L., Silva, F.R.G.E., 1998. A theoretical approach to intramolecular energy transfer and emission quantum yields in coordination compounds of rare earth ions. Spectrochim. Acta A 54, 1593–1599.

Malta, O.L., Brito, H.F., Menezes, J.F.S., Silva, F., Alves, S., Farias, F.S., deAndrade, A.V.M., 1997. Spectroscopic properties of a new light-converting device Eu(thenoyltrifluoroacetonate)(3) 2(dibenzyl sulfoxide). A theoretical analysis based on structural data obtained from a sparkle model. J. Lumin. 75, 255–268.

Mao, H.B., Yang, T.L., Cremer, P.S., 2002. A microfluidic device with a linear temperature gradient for parallel and combinatorial measurements. J. Am. Chem. Soc. 124, 4432–4435.

Marciniak, Ł., Bednarkiewicz, A., Stefanski, M., Tomala, R., Hreniak, D., Strek, W., 2015. Near infrared absorbing near infrared emitting highly-sensitive luminescent nanothermometer based on Nd^{3+} to Yb^{3+} energy transfer. Phys. Chem. Chem. Phys. 17, 24315.

McCabe, K.M., Hernandez, M., 2010. Molecular thermometry. Pediatr. Res. 67, 469–475.

McLaurin, E.J., Bradshaw, L.R., Gamelin, D.R., 2013. Dual-emitting nanoscale temperature sensors. Chem. Mater. 25, 1283–1292.

McNichols, R.J., Gowda, A., Kangasniemi, M., Bankson, J.A., Price, R.E., Hazle, J.D., 2004. MR thermometry-based feedback control of laser interstitial thermal therapy at 980 nm. Lasers Surg. Med. 34, 48–55.

Mecklenburg, M., Hubbard, W.A., White, E.R., Dhall, R., Cronin, S.B., Aloni, S., Regan, B.C., 2015. Nanoscale temperature mapping in operating microelectronic devices. Science 347, 629–632.

Meert, K.W., Morozov, V.A., Abakumov, A.M., Hadermann, J., Poelman, D., Smet, P.F., 2014. Energy transfer in Eu^{3+} doped scheelites: use as thermographic phosphor. Opt. Express 22, A961–A972.

Mikkelsen, R.B., Wallach, D.F.H., 1977. Temperature sensitivity of erythrocyte-membrane potential as determined by cyanine dye fluorescence. Cell Biol. Int. Rep. 1, 51–55.

Millán, J., Godignon, P., Perpiña, X., Perez-Tomas, A., Rebollo, J., 2014. A survey of wide bandgap power semiconductor devices. IEEE Trans. Power Electron. 29, 2155–2163.

Millán, A., Carlos, L.D., Brites, C.D.S., Silva, N.J.O., Piñol, R., Palacio, F., 2016. Organic–inorganic hybrids thermometry. In: Carlos, L.D., Palacio, F. (Eds.), Thermometry at the Nanoscale: Techniques and Selected Applications, vol. 38. The Royal Society of Chemistry, Oxfordshire, pp. 237–272 (Chapter 8).

Miyata, K., Konno, Y., Nakanishi, T., Kobayashi, A., Kato, M., Fushimi, K., Hasegawa, Y., 2013. Chameleon luminophore for sensing temperatures: control of metal-to-metal and energy back transfer in lanthanide coordination polymers. Angew. Chem. Int. Ed. 52, 6413–6416.

Mott, N.F., 1938. On the absorption of light by crystals. Proc. R. Soc. Lond. A Math. Phys. Sci. 167, 0384–0391.

Mura, S., Nicolas, J., Couvreur, P., 2013. Stimuli-responsive nanocarriers for drug delivery. Nat. Mater. 12, 991–1003.

Narberhaus, F., Waldminighaus, T., Chowdhury, S., 2006. RNA thermometers. FEMS Microbiol. Rev. 30, 3–16.

Okabe, K., Inada, N., Gota, C., Harada, Y., Funatsu, T., Uchiyama, S., 2012. Intracellular temperature mapping with a fluorescent polymeric thermometer and fluorescence lifetime imaging microscopy. Nat. Commun. 3, 705.

Pandey, A., Rai, V.K., 2013. Optical thermometry using FIR of two close lying levels of different ions in Y_2O_3:Ho^{3+}-Tm^{3+}-Yb^{3+} phosphor. Appl. Phys. B 113, 221–225.

Paviolo, C., Clayton, A.H., McArthur, S.L., Stoddart, P.R., 2013. Temperature measurement in the microscopic regime: a comparison between fluorescence lifetime- and intensity-based methods. J. Microsc. 250, 179–188.

Peng, H., Stich, M.I., Yu, J., Sun, L.N., Fischer, L.H., Wolfbeis, O.S., 2010a. Luminescent Europium(III) nanoparticles for sensing and imaging of temperature in the physiological range. Adv. Mater. 22, 716–719.

Peng, H.S., Huang, S.H., Wolfbeis, O.S., 2010b. Ratiometric fluorescent nanoparticles for sensing temperature. J. Nanopart. Res. 12, 2729–2733.

Pereira, A.F., Kumar, K.U., Silva, W.F., Santos, W.Q., Jaque, D., Jacinto, C., 2015. Yb^{3+}/Tm^{3+} co-doped $NaNbO_3$ nanocrystals as three-photon-excited luminescent nanothermometers. Sens. Actuators B: Chem. 213, 65–71.

Périgo, E.A., Hemery, G., Sandre, O., Ortega, D., Garaio, E., Plazaola, F., Teran, F.J., 2015. Fundamentals and advances in magnetic hyperthermia. Appl. Phys. Rev. 2, 041302.

Perpiñá, X., Jordà, X., Mestres, N., Vellvehi, M., Godignon, P., Millan, J., von Kiedrowski, H., 2004. Internal infrared laser deflection system: a tool for power device characterization. Meas. Sci. Technol. 15, 1011–1018.

Pietsch, C., Schubert, U.S., Hoogenboom, R., 2011. Aqueous polymeric sensors based on temperature-induced polymer phase transitions and solvatochromic dyes. Chem. Commun. 47, 8750–8765.

Piñol, R., Brites, C.D.S., Bustamante, R., Martínez, A., Silva, N.J.O., Murillo, J.L., Cases, R., Carrey, J., Estepa, C., Sosa, C., Palacio, F., Carlos, L.D., Millán, A., 2015. Joining time-resolved thermometry and magnetic-induced heating in a single nanoparticle unveils intriguing thermal properties. ACS Nano 9, 3134–3142.

Qiao, J., Chen, C.F., Qi, L., Liu, M.R., Dong, P., Jiang, Q., Yang, X.Z., Mu, X.Y., Mao, L.Q., 2014. Intracellular temperature sensing by a ratiometric fluorescent polymer thermometer. J. Mater. Chem. B 2, 7544–7550.

Quintanilla, M., Cantarelli, I.X., Pedroni, M., Speghini, A., Vetrone, F., 2015. Intense ultraviolet upconversion in water dispersible SrF2:Tm^{3+}, Yb^{3+} nanoparticles: the effect of the environment on light emissions. J. Mater. Chem. C 3, 3108–3113.

Quintanilla, M., Benayas, A., Naccache, R., Vetrone, F., 2016. Luminescent nanothermometry with lanthanide-doped nanoparticles. In: Carlos, L.D., Palacio, F. (Eds.), Thermometry at the Nanoscale: Techniques and Selected Applications, vol. 38. The Royal Society of Chemistry, Oxfordshire, pp. 124–166 (Chapter 5).

Rabhiou, A., Feist, J., Kempf, A., Skinner, S., Heyes, A., 2011. Phosphorescent thermal history sensors. Sens. Actuators A: Phys. 169, 18–26.

Rao, X., Song, T., Gao, J., Cui, Y., Yang, Y., Wu, C., Chen, B., Qian, G., 2013. A highly sensitive mixed lanthanide metal-organic framework self-calibrated luminescent thermometer. J. Am. Chem. Soc. 135, 15559–15564.

Reddy, L.H., Arias, J.L., Nicolas, J., Couvreur, P., 2012. Magnetic nanoparticles: design and characterization, toxicity and biocompatibility, pharmaceutical and biomedical applications. Chem. Rev. 112, 5818–5878.

Reif, F., 1965. Fundamentals of Statistical and Thermal Physics. McGraw-Hill, New York.

Ren, M., Brites, C.D., Bao, S.-S., Ferreira, R.A., Zheng, L.-M., Carlos, L.D., 2015. A cryogenic luminescent ratiometric thermometer based on a lanthanide phosphonate dimer. J. Mater. Chem. C 3, 8480–8484.

Robertson, D.G., Lee, J.H., 2002. On the use of constraints in least squares estimation and control. Automatica 38, 1113–1123.

Rocha, U., Jacinto da Silva, C., Ferreira Silva, W., Guedes, I., Benayas, A., Martínez Maestro, L., Acosta Elias, M., Bovero, E., van Veggel, F.C.J.M., Solé, J.G., Jaque, D., 2013. Subtissue thermal sensing based on neodymium-doped LaF3 nanoparticles. ACS Nano 7, 1188–1199.

Rocha, U., Kumar, K.U., Jacinto, C., Ramiro, J., Caamano, A.J., Solé, J.G., Jaque, D., 2014a. Nd^{3+} doped LaF_3 nanoparticles as self-monitored photo-thermal agents. Appl. Phys. Lett. 104, 053703.

Rocha, U., Kumar, K.U., Jacinto, C., Villa, I., Sanz-Rodríguez, F., Iglesias de la Cruz, M.C., Juarranz, A., Carrasco, E., van Veggel, F.C., Bovero, E., Solé, J.G., Jaque, D., 2014b. Neodymium-doped LaF_3 nanoparticles for fluorescence bioimaging in the second biological window. Small 10, 1141–1154.

Rodrigues, C.V., Luz, L.L., Dutra, J.D., Junior, S.A., Malta, O.L., Gatto, C.C., Streit, H.C., Freire, R.O., Wickleder, C., Rodrigues, M.O., 2014. Unusual photoluminescence properties of the 3D mixed-lanthanide-organic frameworks induced by dimeric structures: a theoretical and experimental approach. Phys. Chem. Chem. Phys. 16, 14858–14866.

Rodrigues, M., Piñol, R., Antorrena, G., Brites, C.D.S., Silva, N.J.O., Murillo, J.L., Cases, R., Díez, I., Palacio, F., Torras, N., Plaza, J.A., Pérez-García, L., Carlos, L.D., Millán, A., 2016. Implementing thermometry on silicon surfaces functionalized by lanthanide-doped self-assembled polymer monolayers. Adv. Funct. Mater. 26, 200–209. http://dx.doi.org/10.1002/adfm.201503889.

Rohani, S., Quintanilla, M., Tuccio, S., De Angelis, F., Cantelar, E., Govorov, A.O., Razzari, L., Vetrone, F., 2015. Enhanced luminescence, collective heating, and nanothermometry in an ensemble system composed of lanthanide-doped upconverting nanoparticles and gold nanorods. Adv. Opt. Mater. 3, 1606–1613.

Ross, D., Gaitan, M., Locascio, L.E., 2001. Temperature measurement in microfluidic systems using a temperature-dependent fluorescent dye. Anal. Chem. 73, 4117–4123.

Saïdi, E., Samson, B., Aigouy, L., Volz, S., Low, P., Bergaud, C., Mortier, M., 2009. Scanning thermal imaging by near-field fluorescence spectroscopy. Nanotechnology 20, 115703.

Saïdi, E., Babinet, N., Lalouat, L., Lesueur, J., Aigouy, L., Volz, S., Labeguerie-Egea, J., Mortier, M., 2011. Tuning temperature and size of hot spots and hot-spot arrays. Small 7, 259–264.

Saleh, B.E., Teich, M.C., Saleh, B.E., 1991. Fundamentals of Photonics. Wiley, New York.

Samulski, T., Shrivastava, P.N., 1980. Photo-luminescent thermometer probes—temperature-measurements in microwave fields. Science 208, 193–194.

Samulski, T.V., Chopping, P.T., Haas, B., 1982. Photo-luminescent thermometry based on europium-activated calcium sulfide. Phys. Med. Biol. 27, 107–114.

Samy, R., Glawdel, T., Ren, C.L., 2008. Method for microfluidic whole-chip temperature measurement using thin-film poly(dimethylsiloxane)/rhodamine B. Anal. Chem. 80, 369–375.

Sanchez, C., Julián-López, B., Belleville, P., Popall, M., 2005. Applications of hybrid organic–inorganic nanocomposites. J. Mater. Chem. 15, 3559–3592.

Sanchez, C., Belleville, P., Popall, M., Nicole, L., 2011. Applications of advanced hybrid organic–inorganic nanomaterials: from laboratory to market. Chem. Soc. Rev. 40, 696–753.

Sato, S., Yamaguchi, R., Nose, T., 1989. Temperature sensors by multicolor-fluorescent films of rare earth chelate compounds. IEICE J. C J72-C2, 906–911 (in Japanese).

Saunders, L.R., Verdin, E., 2009. Cell biology stress response and aging. Science 323, 1021–1022.

Savchuk, O.A., Haro-Gonzalez, P., Carvajal, J.J., Jaque, D., Massons, J., Aguilo, M., Diaz, F., 2014. Er:Yb:NaY$_2$F$_5$O up-converting nanoparticles for sub-tissue fluorescence lifetime thermal sensing. Nanoscale 6, 9727–9733.

Savchuk, O.A., Carvajal, J.J., Pujol, M.C., Barrera, E.W., Massons, J., Aguilo, M., Diaz, F., 2015. Ho, Yb:KLu(WO4)2 nanoparticles: a versatile material for multiple thermal sensing purposes by luminescent thermometry. J. Phys. Chem. C 119, 18546–18558.

Savitski, M.M., Reinhard, F.B.M., Franken, H., Werner, T., Savitski, M.F., Eberhard, D., Molina, D.M., Jafari, R., Dovega, R.B., Klaeger, S., Kuster, B., Nordlund, P., Bantscheff, M., Drewes, G., 2014. Tracking cancer drugs in living cells by thermal profiling of the proteome. Science 343, 1255784.

Schuller, J.A., Barnard, E.S., Cai, W.S., Jun, Y.C., White, J.S., Brongersma, M.L., 2010. Plasmonics for extreme light concentration and manipulation. Nat. Mater. 9, 193–204.

Sedlmeier, A., Achatz, D.E., Fischer, L.H., Gorris, H.H., Wolfbeis, O.S., 2012. Photon upconverting nanoparticles for luminescent sensing of temperature. Nanoscale 4, 7090–7096.

Sedmak, I., Urbančič, I., Štrancar, J., Mortier, M., Golobič, I., 2015. Transient submicron temperature imaging based on the fluorescence emission in an Er/Yb co-doped glass–ceramic. Sens. Actuators A: Phys. 230, 102–110.

Seitz, F., 1939. An interpretation of crystal luminescence. Trans. Faraday Soc. 35, 0074–0084.

Shahi, P.K., Singh, A.K., Rai, S.B., Ullrich, B., 2015. Lanthanide complexes for temperature sensing, UV light detection, and laser applications. Sens. Actuators A: Phys. 222, 255–261.

Shen, J., Chen, G.Y., Vu, A.M., Fan, W., Bilsel, O.S., Chang, C.C., Han, G., 2013. Engineering the upconversion nanoparticle excitation wavelength: cascade sensitization of tri-doped upconversion colloidal nanoparticles at 800 nm. Adv. Opt. Mater. 1, 644–650.

Shi, L., Dames, C., Lukes, J.R., Reddy, P., Duda, J., Cahill, D.G., Lee, J., Marconnet, A., Goodson, K.E., Bahk, J.-H., Shakouri, A., Prasher, R.S., Felts, J., King, W.P., Han, B., Bischof, J.C., 2015. Evaluating broader impacts of nanoscale thermal transport research. Nanosci. Microsc. Thermophys. Eng. 19, 127–165.

Shinn, M.D., Sibley, W.A., Drexhage, M.G., Brown, R.N., 1983. Optical-transitions of Er^{3+} ions in fluorozirconate glass. Phys. Rev. B 27, 6635–6648.

Singh, S.K., Kumar, K., Rai, S.B., 2009a. Er^{3+}/Yb^{3+} codoped Gd$_2$O$_3$ nano-phosphor for optical thermometry. Sens. Actuators A: Phys. 149, 16–20.

Singh, S.K., Kumar, K., Rai, S.B., 2009b. Multifunctional Er^{3+}-Yb^{3+} codoped Gd$_2$O$_3$ nanocrystalline phosphor synthesized through optimized combustion route. Appl. Phys. B: Lasers Opt. 94, 165–173.

Singh, S.K., Kumar, K., Rai, S., 2010. Diode laser pumped Gd$_2$O$_3$:Er^{3+}/Yb^{3+} phosphor as optical nano-heater. Appl. Phys. B: Lasers Opt. 100, 443–446.

Singh, B.P., Parchur, A.K., Ningthoujam, R.S., Ramakrishna, P.V., Singh, S., Singh, P., Rai, S.B., Maalej, R., 2014. Enhanced up-conversion and temperature-sensing behaviour of Er^{3+} and Yb^{3+} co-doped Y$_2$Ti$_2$O$_7$ by incorporation of Li$^+$ ions. Phys. Chem. Chem. Phys. 16, 22665–22676.

Smith, A.M., Mancini, M.C., Nie, S.M., 2009. Bioimaging: second window for in vivo imaging. Nat. Nanotechnol. 4, 710–711.

Somero, G.N., 1995. Proteins and temperature. Annu. Rev. Physiol. 57, 43–68.

Song, Y., Liu, G.X., Dong, X.T., Wang, J.X., Yu, W.S., Li, J.M., 2015. Au nanorods@NaGdF4/Yb^{3+}, Er^{3+} multifunctional hybrid nanocomposites with upconversion luminescence, magnetism, and photothermal property. J. Phys. Chem. C 119, 18527–18536.

Soukka, T., Härmä, H., 2011. Lanthanide nanoparticules as photoluminescent reporters. In: Hänninen, P., Härmä, H. (Eds.), Lanthanide Luminescence—Photophysical, Analytical and Biological Aspects, vol. 7. Springer-Verlag, Berlin, pp. 89–113 (Chapter 3).

Souza, A.S., Nunes, L.A.O., Silva, I.G.N., Oliveira, F.A.M., Luz, L.L., Brito, H.F., Felinto, M.C.F.C., Ferreira, R.A.S., Júnior, S.A., Carlos, L.D., Malta, O.L., 2016. Highly-sensitive Eu^{3+} ratiometric thermometers based on excited state absorption with predictable calibration. Nanoscale 8, 5327–5333.

Stalder, M., Bass, M., Chai, B.H.T., 1992. Thermal quenching of fluorescence in chromium-doped fluoride laser crystals. J. Opt. Soc. Am. B 9, 2271–2273.

Stanley, S.A., Gagner, J.E., Damanpour, S., Yoshida, M., Dordick, J.S., Friedman, J.M., 2012. Radio-wave heating of iron oxide nanoparticles can regulate plasma glucose in mice. Science 336, 604–608.

Stich, M.I.J., Nagl, S., Wolfbeis, O.S., Henne, U., Schaeferling, M., 2008. A dual luminescent sensor material for simultaneous imaging of pressure and temperature on surfaces. Adv. Funct. Mater. 18, 1399–1406.

Stich, M.I.J., Fischer, L.H., Wolfbeis, O.S., 2010. Multiple fluorescent chemical sensing and imaging. Chem. Soc. Rev. 39, 3102–3114.

Sun, L.N., Yu, J.B., Peng, H.S., Zhang, J.Z., Shi, L.Y., Wolfbeis, O.S., 2010. Temperature-sensitive luminescent nanoparticles and films based on a terbium (III) complex probe. J. Phys. Chem. C 114, 12642–12648.

Suzuki, M., Tseeb, V., Oyama, K., Ishiwata, S., 2007. Microscopic detection of thermogenesis in a single HeLa cell. Biophys. J. 92, L46–L48.

Takei, Y., Arai, S., Murata, A., Takabayashi, M., Oyama, K., Ishiwata, S., Takeoka, S., Suzuki, M., 2014. A nanoparticle-based ratiometric and self-calibrated fluorescent thermometer for single living cells. ACS Nano 8, 198–206.

Tao, F., Bernasek, S.L., Yuan, Z., Ying, W.C., Qu, Y., Han, K., Wong, K.T., Bent, S.F., Teplyakov, A.V., Yong, K.S., 2012. Functionalization of Semiconductor Surfaces. Wiley, Hoboken, NJ.

Taylor, B.N., Kuyatt, C.E., 1994. Guidelines for Evaluating and Expressing the Uncertainty of NIST Measurement Results. (NIST Technical Note 1297).

Tessier, G., Bardoux, M., Boue, C., Fournier, D., 2007a. Back side thermal imaging of integrated circuits at high spatial resolution. Appl. Phys. Lett. 90, 171112.

Tessier, G., Bardoux, M., Filloy, C., Boué, C., Fournier, D., 2007b. High resolution thermal imaging inside integrated circuits. Sens. Rev. 27, 291–297.

Tetienne, J.-P., Lombard, A., Simpson, D.A., Ritchie, C., Lu, J., Mulvaney, P., Hollenberg, L.C., 2016. A scanning nano-spin ensemble microscope for nanoscale magnetic and thermal imaging. Nano Lett. 16, 326–333 (arXiv preprint, arXiv:1509.00586).

Tian, X., Wei, X., Chen, Y., Duan, C., Yin, M., 2014. Temperature sensor based on ladder-level assisted thermal coupling and thermal-enhanced luminescence in $NaYF_4:Nd^{3+}$. Opt. Express 22, 30333–30345.

Tikhomirov, V., Driesen, K., Rodriguez, V., Gredin, P., Mortier, M., Moshchalkov, V., 2009. Optical nanoheater based on the Yb^{3+}-Er^{3+} co-doped nanoparticles. Opt. Express 17, 11794–11798.

Tsuji, T., Yoshida, S., Yoshida, A., Uchiyama, S., 2013. Cationic fluorescent polymeric thermometers with the ability to enter yeast and mammalian cells for practical intracellular temperature measurements. Anal. Chem. 85, 9815–9823.

Uchiyama, S., Matsumura, Y., de Silva, A.P., Iwai, K., 2003. Fluorescent molecular thermometers based on polymers showing temperature-induced phase transitions and labeled with polarity-responsive benzofurazans. Anal. Chem. 75, 5926–5935.

Uchiyama, S., de Silva, A.P., Iwai, K., 2006. Luminescent molecular thermometers. J. Chem. Educ. 83, 720–727.

Uchiyama, S., Tsuji, T., Ikado, K., Yoshida, A., Kawamoto, K., Hayashi, T., Inada, N., 2015. A cationic fluorescent polymeric thermometer for the ratiometric sensing of intracellular temperature. Analyst 140, 4498–4506.

Vendelbo, S.B., Kooyman, P.J., Creemer, J.F., Morana, B., Mele, L., Dona, P., Nelissen, B.J., Helveg, S., 2013. Method for local temperature measurement in a nanoreactor for in situ high-resolution electron microscopy. Ultramicroscopy 133, 72–79.

Vetrone, F., Naccache, R., de la Fuente, Á.J., Sanz-Rodriguez, F., Blazquez-Castro, A., Rodriguez, E.M., Jaque, D., Solé, J.G., Capobianco, J.A., 2010a. Intracellular imaging of HeLa cells by non-functionalized $NaYF_4$:Er^{3+}, Yb^{3+} upconverting nanoparticles. Nanoscale 2, 495–498.

Vetrone, F., Naccache, R., Zamarron, A., de la Fuente, Á.J., Sanz-Rodriguez, F., Maestro, L.M., Rodriguez, E.M., Jaque, D., Solé, J.G., Capobianco, J.A., 2010b. Temperature sensing using fluorescent nanothermometers. ACS Nano 4, 3254–3258.

Villa, I., Vedda, A., Cantarelli, I.X., Pedroni, M., Piccinelli, F., Bettinelli, M., Speghini, A., Quintanilla, M., Vetrone, F., Rocha, U., Jacinto, C., Carrasco, E., Rodríguez, F.S., Juarranz, Á., del Rosal, B., Ortgies, D.H., Gonzalez, P.H., Solé, J.G., Jaque, D., 2014. 1.3 μm emitting SrF_2:Nd^{3+} nanoparticles for high contrast in vivo imaging in the second biological window. Nano Res. 8, 649–665.

Vlaskin, V.A., Janssen, N., van Rijssel, J., Beaulac, R., Gamelin, D.R., 2010. Tunable dual emission in doped semiconductor nanocrystals. Nano Lett. 10, 3670–3674.

Wade, S.A., Collins, S.F., Baxter, G.W., 2003. Fluorescence intensity ratio technique for optical fiber point temperature sensing. J. Appl. Phys. 94, 4743.

Wang, F., Liu, X.G., 2009. Recent advances in the chemistry of lanthanide-doped upconversion nanocrystals. Chem. Soc. Rev. 38, 976–989.

Wang, F., Liu, X.G., 2014. Multicolor tuning of lanthanide-doped nanoparticles by single wavelength excitation. Acc. Chem. Res. 47, 1378–1385.

Wang, C., Zhang, F., 2015. Upconversion nanoparticles for thermal sensing. In: Zhang, F. (Ed.), Photon Upconversion Nanomaterials, vol. 46. Springer, Berlin, pp. 343–374 (Chapter 10).

Wang, S.P., Westcott, S., Chen, W., 2002. Nanoparticle luminescence thermometry. J. Phys. Chem. B 106, 11203–11209.

Wang, X., Kong, X.G., Yu, Y., Sun, Y.J., Zhang, H., 2007. Effect of annealing on upconversion luminescence of ZnO:Er^{3+} nanocrystals and high thermal sensitivity. J. Phys. Chem. C 111, 15119–15124.

Wang, J.H., Wang, H.Q., Li, Y.Q., Zhang, H.L., Li, X.Q., Hua, X.F., Cao, Y.C., Huang, Z.L., Zhao, Y.D., 2008. Modification of CdTe quantum dots as temperature-insensitive bioprobes. Talanta 74, 724–729.

Wang, F., Han, Y., Lim, C.S., Lu, Y.H., Wang, J., Xu, J., Chen, H.Y., Zhang, C., Hong, M.H., Liu, X.G., 2010. Simultaneous phase and size control of upconversion nanocrystals through lanthanide doping. Nature 463, 1061–1065.

Wang, C.L., Xu, R.Z., Tian, W.J., Jiang, X.L., Cui, Z.Y., Wang, M., Sun, H.M., Fang, K., Gu, N., 2011a. Determining intracellular temperature at single-cell level by a novel thermocouple method. Cell Res. 21, 1517–1519.

Wang, F., Deng, R.R., Wang, J., Wang, Q.X., Han, Y., Zhu, H.M., Chen, X.Y., Liu, X.G., 2011b. Tuning upconversion through energy migration in core–shell nanoparticles. Nat. Mater. 10, 968–973.

Wang, H.D., Liu, J.H., Guo, Z.Y., Zhang, X., Zhang, R.F., Wei, F., Li, T.Y., 2013a. Thermal transport across the interface between a suspended single-walled carbon nanotube and air. Nanosci. Microsc. Thermophys. Eng. 17, 349–365.

Wang, X.D., Wolfbeis, O.S., Meier, R.J., 2013b. Luminescent probes and sensors for temperature. Chem. Soc. Rev. 42, 7834–7869.

Wang, T., Li, P., Li, H., 2014. Color-tunable luminescence of organoclay-based hybrid materials showing potential applications in white LED and thermosensors. ACS Appl. Mater. Interfaces 6, 12915–12921.

Wang, J.H., Huang, H., Zhang, D.Q., Chen, M., Zhang, Y.F., Yu, X.F., Zhou, L., Wang, Q.Q., 2015a. Synthesis of gold/rare-earth-vanadate core/shell nanorods for integrating plasmon resonance and fluorescence. Nano Res. 8, 2548–2561.

Wang, X., Meier, R.J., Schmittlein, C., Schreml, S., Schäferling, M., Wolfbeis, O.S., 2015b. A water-sprayable, thermogelating and biocompatible polymer host for use in fluorescent chemical sensing and imaging of oxygen, pH values and temperature. Sens. Actuators B: Chem. 221, 37–44.

Wang, Z.P., Ananias, D., Carne-Sanchez, A., Brites, C.D.S., Imaz, I., Maspoch, D., Rocha, J., Carlos, L.D., 2015c. Lanthanide-organic framework nanothermometers prepared by spray-drying. Adv. Funct. Mater. 25, 2824–2830.

Watanabe, M.S., Kakuta, N., Mabuchi, K., Yamada, Y., 2005. Micro-thermocouple probe for measurement of cellular thermal responses. In: Proc. 27th Ann. Intl. Conf. IEEE EMBS 1–7, pp. 4858–4861.

Wawrzynczyk, D., Bednarkiewicz, A., Nyk, M., Strek, W., Samoc, M., 2012. Neodymium(III) doped fluoride nanoparticles as non-contact optical temperature sensors. Nanoscale 4, 6959–6961.

Weber, M.J., 1967. Probabilities for radiative and nonradiative decay of Er^{3+} in LaF_3. Phys. Rev. 157, 262–272.

Wei, Y., Sa, R., Li, Q., Wu, K., 2015. Highly stable and sensitive LnMOF ratiometric thermometers constructed with mixed ligands. Dalton Trans. 44, 3067–3074.

Weissleder, R., 2001. A clearer vision for in vivo imaging. Nat. Biotechnol. 19, 316–317.

Wen, H., Zhu, H., Chen, X., Hung, T.F., Wang, B., Zhu, G., Yu, S.F., Wang, F., 2013. Upconverting near-infrared light through energy management in core–shell–shell nanoparticles. Angew. Chem. Int. Ed. 52, 13419–13423.

Wickberg, A., Mueller, J.B., Mange, Y.J., Fischer, J., Nann, T., Wegener, M., 2015. Three-dimensional micro-printing of temperature sensors based on up-conversion luminescence. Appl. Phys. Lett. 106, 133103.

Windhorn, T.H., Cain, C.A., 1979. Optically-active binary-liquid crystal thermometry. IEEE Trans. Biomed. Eng. 26, 148–152.

Wolfbeis, O.S., 2008. Sensor paints. Adv. Mater. 20, 3759–3763.

Wu, X.W., Hull, R., 2012. A novel nano-scale non-contact temperature measurement technique for crystalline materials. Nanotechnology 23, 465707.

Wu, X., Chen, G.Y., Shen, J., Li, Z.J., Zhang, Y.W., Han, G., 2015. Upconversion nanoparticles: a versatile solution to multiscale biological imaging. Bioconjug. Chem. 26, 166–175.

Xie, X.J., Gao, N.Y., Deng, R.R., Sun, Q., Xu, Q.H., Liu, X.G., 2013. Mechanistic investigation of photon upconversion in Nd^{3+}-sensitized core–shell nanoparticles. J. Am. Chem. Soc. 135, 12608–12611.

Ximendes, E.C., Rocha, U., Jacinto, C., Kumar, K.U., Bravo, D., Lopez, F.J., Rodriguez, E.M., Garcia-Sole, J., Jaque, D., 2016. Self-monitored photothermal nanoparticles based on core–shell engineering. Nanoscale 8, 3057–3066.

Xing, L.L., Yang, W.Q., Ma, D.C., Wang, R., 2015. Effect of crystallinity on the optical thermometry sensitivity of Tm^{3+}/Yb^{3+} codoped $LiNbO_3$ crystal. Sens. Actuators B: Chem. 221, 458–462.

Xu, W., Gao, X.Y., Zheng, L.J., Zhang, Z.G., Cao, W.W., 2012. An optical temperature sensor based on the upconversion luminescence from Tm^{3+}/Yb^{3+} codoped oxyfluoride glass ceramic. Sens. Actuators B: Chem. 173, 250–253.

Xu, W., Zhao, H., Li, Y., Zheng, L., Zhang, Z., Cao, W., 2013. Optical temperature sensing through the upconversion luminescence from Ho^{3+}/Yb^{3+} codoped $CaWO_4$. Sens. Actuators B: Chem. 188, 1096–1100.

Yang, J.M., Yang, H., Lin, L.W., 2011. Quantum dot nano thermometers reveal heterogeneous local thermogenesis in living cells. ACS Nano 5, 5067–5071.

Yang, T.S., Sun, Y., Liu, Q., Feng, W., Yang, P.Y., Li, F.Y., 2012. Cubic sub-20 nm $NaLuF_4$-based upconversion nanophosphors for high-contrast bioimaging in different animal species. Biomaterials 33, 3733–3742.

Yarimaga, O., Lee, S., Ham, D.Y., Choi, J.M., Kwon, S.G., Im, M., Kim, S., Kim, J.M., Choi, Y.K., 2011. Thermofluorescent conjugated polymer sensors for nano- and microscale temperature monitoring. Macromol. Chem. Phys. 212, 1211–1220.

Ye, F.M., Wu, C.F., Jin, Y.H., Chan, Y.H., Zhang, X.J., Chiu, D.T., 2011. Ratiometric temperature sensing with semiconducting polymer dots. J. Am. Chem. Soc. 133, 8146–8149.

Yoder, R.D., 1979. Liquid-crystal thermometry. Anesth. Analg. 58, 351.

Yu, J.B., Sun, L.N., Peng, H.S., Stich, M.I.J., 2010. Luminescent terbium and europium probes for lifetime based sensing of temperature between 0 and 70°C. J. Mater. Chem. 20, 6975–6981.

Yuasa, J., Mukai, R., Hasegawa, Y., Kawai, T., 2014. Ratiometric luminescence thermometry based on crystal-field alternation at the extremely narrow $^5D_0 \rightarrow {}^7F_2$ transition band of europium (III). Chem. Commun. 50, 7937–7940.

Yue, Y., Wang, X., 2012. Nanoscale thermal probing. Nano Rev. 3, 11586.

Zalewski, E.F., Duda, C.R., 1983. Silicon photodiode device with 100% external quantum efficiency. Appl. Optics 22, 2867–2873.

Zhang, Y., Liu, X., 2013. Nanocrystals: shining a light on upconversion. Nat. Nanotechnol. 8, 702–703.

Zhao, J., Jin, D., Schartner, E.P., Lu, Y., Liu, Y., Zvyagin, A.V., Zhang, L., Dawes, J.M., Xi, P., Piper, J.A., Goldys, E.M., Monro, T.M., 2013. Single-nanocrystal sensitivity achieved by enhanced upconversion luminescence. Nat. Nanotechnol. 8, 729–734.

Zheng, K., Liu, Z., Lv, C., Qin, W., 2013. Temperature sensor based on the UV upconversion luminescence of Gd^{3+} in Yb^{3+}–Tm^{3+}–Gd^{3+} codoped $NaLuF_4$ microcrystals. J. Mater. Chem. C 1, 5502–5507.

Zheng, S.H., Chen, W.B., Tan, D.Z., Zhou, J.J., Guo, Q.B., Jiang, W., Xu, C., Liu, X.F., Qiu, J.R., 2014. Lanthanide-doped $NaGdF_4$ core–shell nanoparticles for non-contact self-referencing temperature sensors. Nanoscale 6, 5675–5679.

Zheng, K.Z., Song, W.Y., He, G.H., Yuan, Z., Qin, W.P., 2015. Five-photon UV upconversion emissions of Er^{3+} for temperature sensing. Opt. Express 23, 7653–7658.

Zhou, Y., Yan, B., 2015. Lanthanides post-functionalized nanocrystalline metal-organic frameworks for tunable white-light emission and orthogonal multi-readout thermometry. Nanoscale 7, 4063–4069.

Zhou, S.S., Jiang, G.C., Li, X.Y., Jiang, S., Wei, X.T., Chen, Y.H., Yin, M., Duan, C.K., 2014a. Strategy for thermometry via Tm^{3+}-doped $NaYF_4$ core–shell nanoparticles. Opt. Lett. 39, 6687–6690.

Zhou, S.S., Jiang, G.C., Wei, X.T., Duan, C.K., Chen, Y.H., Yin, M., 2014b. Pr^{3+}-doped β-$NaYF_4$ for temperature sensing with fluorescence intensity ratio technique. J. Nanosci. Nanotechnol. 14, 3739–3742.

Zhou, S.S., Jiang, S., Wei, X.T., Chen, Y.H., Duan, C.K., Yin, M., 2014c. Optical thermometry based on upconversion luminescence in Yb^{3+}/Ho^{3+} co-doped $NaLuF_4$. J. Alloys Compd. 588, 654–657.

Zhou, Y., Yan, B., Lei, F., 2014d. Postsynthetic lanthanide functionalization of nanosized metal-organic frameworks for highly sensitive ratiometric luminescent thermometry. Chem. Commun. 50, 15235–15238.

Zhou, B., Shi, B., Jin, D., Liu, X., 2015a. Controlling upconversion nanocrystals for emerging applications. Nat. Nanotechnol. 10, 924–936.

Zhou, J., Liu, Q., Feng, W., Sun, Y., Li, F., 2015b. Upconversion luminescent materials: advances and applications. Chem. Rev. 115, 395–465.

Zhou, H., Sharma, M., Berezin, O., Zuckerman, D., Berezin, M.Y., 2016. Nanothermometry: from microscopy to thermal treatments. ChemPhysChem 17, 27–36.

Zohar, O., Ikeda, M., Shinagawa, H., Inoue, H., Nakamura, H., Elbaum, D., Alkon, D.L., Yoshioka, T., 1998. Thermal imaging of receptor-activated heat production in single cells. Biophys. J. 74, 82–89.

Zou, W.Q., Visser, C., Maduro, J.A., Pshenichnikov, M.S., Hummelen, J.C., 2012. Broadband dye-sensitized upconversion of near-infrared light. Nat. Photonics 6, 560–564.

Index

Note: Page numbers followed by "*f*" indicate figures, and "*t*" indicate tables.